

# Geofluids in Deep Sedimentary Basins and their Significance for Petroleum Accumulation

Lead Guest Editor: Xiaorong Luo

Guest Editors: Zhijun Jin, Keyu Liu, and Shuichang Zhang





---

# **Geofluids in Deep Sedimentary Basins and their Significance for Petroleum Accumulation**

Geofluids

---

# **Geofluids in Deep Sedimentary Basins and their Significance for Petroleum Accumulation**

Lead Guest Editor: Xiaorong Luo

Guest Editors: Zhijun Jin, Keyu Liu, and Shuichang Zhang



---

Copyright © 2017 Hindawi. All rights reserved.

This is a special issue published in "Geofluids." All articles are open access articles distributed under the Creative Commons Attribution License, which permits unrestricted use, distribution, and reproduction in any medium, provided the original work is properly cited.

---

## Editorial Board

Mauro Cacace, Germany  
Timothy S. Collett, USA  
Cinzia Federico, Italy  
Tobias P. Fischer, USA  
Paolo Fulignati, Italy  
Salvatore Inguaggiato, Italy  
Francesco Italiano, Italy

Karsten Kroeger, New Zealand  
Cornelius Langenbruch, USA  
Stefano Lo Russo, Italy  
John A. Mavrogenes, Australia  
Ferenc Molnar, Finland  
Julie K. Pearce, Australia  
Daniele Pedretti, Finland

Marco Petitta, Italy  
Christophe Renac, France  
Andri Stefansson, Iceland  
Richard E. Swarbrick, UK  
Mark Tingay, Australia  
Micol Todesco, Italy

# Contents

## **Geofluids in Deep Sedimentary Basins and Their Significance for Petroleum Accumulation**

Xiaorong Luo, Zhijun Jin, Keyu Liu, and Shuichang Zhang

Volume 2017, Article ID 3571359, 4 pages

## **Diagenetic Heterogeneity of Deep Sandstones and Its Relationship to Oil Emplacement: A Case Study from the Middle Jurassic Toutunhe Formation in the Fukang Sag, Central Junggar Basin (NW China)**

Binfeng Cao, Xiaorong Luo, Likuan Zhang, Fenggui Sui, Huixi Lin, and Yuhong Lei

Volume 2017, Article ID 4292079, 23 pages

## **The Distribution and Origin of Carbonate Cements in Deep-Buried Sandstones in the Central Junggar Basin, Northwest China**

Wang Furong, He Sheng, Hou Yuguang, Dong Tian, and He Zhiliang

Volume 2017, Article ID 1020648, 13 pages

## **Seismic Characterization of Hypogenic Karst Systems Associated with Deep Hydrothermal Fluids in the Middle-Lower Ordovician Yingshan Formation of the Shunnan Area, Tarim Basin, NW China**

Hongtao Zhu, Xiu Zhu, and Honghan Chen

Volume 2017, Article ID 8094125, 13 pages

## **Experiment of Carbonate Dissolution: Implication for High Quality Carbonate Reservoir Formation in Deep and Ultradeep Basins**

Zhiliang He, Qian Ding, Yujin Wo, Juntao Zhang, Ming Fan, and Xiaojuan Yue

Volume 2017, Article ID 8439259, 8 pages

## **New Insight into the Kinetics of Deep Liquid Hydrocarbon Cracking and Its Significance**

Wenzhi Zhao, Shuichang Zhang, Bin Zhang, Kun He, and Xiaomei Wang

Volume 2017, Article ID 6340986, 11 pages

## **The Early Cambrian Mianyang-Changning Intracratonic Sag and Its Control on Petroleum Accumulation in the Sichuan Basin, China**

Shugen Liu, Bin Deng, Luba Jansa, Yong Zhong, Wei Sun, Jinmin Song, Guozhi Wang, Juan Wu, Zhiwu Li, and Yanhong Tian

Volume 2017, Article ID 6740892, 16 pages

## **Distribution and Thermal Maturity of Devonian Carbonate Reservoir Solid Bitumen in Desheng Area of Guizhong Depression, South China**

Yuguang Hou, Yaqi Liang, Sheng He, Yukun Liu, Zhiwei Fan, and Yingrui Song

Volume 2017, Article ID 4580416, 15 pages

## **Multiphase Calcite Cementation and Fluids Evolution of a Deeply Buried Carbonate Reservoir in the Upper Ordovician Lianglitag Formation, Tahe Oilfield, Tarim Basin, NW China**

Jiaqing Liu, Zhong Li, Lijuan Cheng, and Jiawei Li

Volume 2017, Article ID 4813235, 19 pages

## **Origin and Distribution of Carbonate Cement in Tight Sandstones: The Upper Triassic Yanchang Formation Chang 8 Oil Layer in West Ordos Basin, China**

Jin Lai, Guiwen Wang, Jing Chen, Shuchen Wang, Zhenglong Zhou, and Xuqiang Fan

Volume 2017, Article ID 8681753, 13 pages

**A Geochemical Model of Fluids and Mineral Interactions for Deep Hydrocarbon Reservoirs**

Jun Li, Raheel Ahmed, Qian Zhang, Yongfan Guo, and Xiaochun Li

Volume 2017, Article ID 3482603, 11 pages

**Pore Fluid Evolution Influenced by Volcanic Activities and Related Diagenetic Processes in a Rift Basin: Evidence from the Paleogene Medium-Deep Reservoirs of Huanghekou Sag, Bohai Bay Basin, China**

Zhongheng Sun, Hongtao Zhu, Changgui Xu, Xianghua Yang, Xiaofeng Du, Qingbin Wang, and Jinyang Qiao

Volume 2017, Article ID 9732575, 16 pages

**Deep-Buried Triassic Oil-Source Correlation in the Central Junggar Basin, NW China**

Ming Wu, Jun Jin, Wanyun Ma, Baoli Xiang, Ni Zhou, Jiangling Ren, and Jian Cao

Volume 2017, Article ID 7581859, 17 pages

**Genetic Types and Source of the Upper Paleozoic Tight Gas in the Hangjinqi Area, Northern Ordos Basin, China**

Xiaoqi Wu, Chunhua Ni, Quanyou Liu, Guangxiang Liu, Jianhui Zhu, and Yingbin Chen

Volume 2017, Article ID 4596273, 14 pages

**Hydrothermal Dissolution of Deeply Buried Cambrian Dolomite Rocks and Porosity Generation: Integrated with Geological Studies and Reactive Transport Modeling in the Tarim Basin, China**

Wenwen Wei, Daizhao Chen, Hairuo Qing, and Yixiong Qian

Volume 2017, Article ID 9562507, 19 pages

**A New Method to Identify Reservoirs in Tight Sandstones Based on the New Model of Transverse Relaxation Time and Relative Permeability**

Yuhang Guo, Baozhi Pan, and Lihua Zhang

Volume 2017, Article ID 6787038, 8 pages

## Editorial

# Geofluids in Deep Sedimentary Basins and Their Significance for Petroleum Accumulation

Xiaorong Luo,<sup>1</sup> Zhijun Jin,<sup>2</sup> Keyu Liu,<sup>3</sup> and Shuichang Zhang<sup>4</sup>

<sup>1</sup>Key Laboratory of Petroleum Resources Research, Institute of Geology and Geophysics, Chinese Academy of Sciences, Beijing 100029, China

<sup>2</sup>Petroleum Exploration and Production Research Institute, SINOPEC, Beijing 100083, China

<sup>3</sup>School of Geosciences, China University of Petroleum (East China), Shandong 266580, China

<sup>4</sup>PetroChina Research Institute of Petroleum Exploration & Development, Beijing 100083, China

Correspondence should be addressed to Xiaorong Luo; [luoxr@mail.iggcas.ac.cn](mailto:luoxr@mail.iggcas.ac.cn)

Received 11 September 2017; Accepted 19 September 2017; Published 5 December 2017

Copyright © 2017 Xiaorong Luo et al. This is an open access article distributed under the Creative Commons Attribution License, which permits unrestricted use, distribution, and reproduction in any medium, provided the original work is properly cited.

## 1. Motivation and Background

Geofluids, including water, liquid, and gaseous hydrocarbons and various nonhydrocarbon gases, not only are the products of geological processes but also actively participate in the geological processes. Understanding geofluids and their interaction with rocks under different geological conditions is fundamental to cognizing the geological processes.

Geofluids may continually flow and circulate underground in rock formations with suitable dynamics and pathways during geological evolution. Therefore the Geofluid Circulation System of Earth (GCSE) not only includes fluids from air, earth surface, and sedimentary basins but also includes fluids derived from deep crust and mantle. However, our understanding of GCSE is quite limited with scarce information because it is difficult to obtain geofluids from the deep crust.

It has been well documented that there exists rich petroleum and mineral resources in deep (>4500 m) sedimentary formations. Despite the huge cost involved in deep sedimentary basin exploration, thousands of deep wells have been drilled over the past few decades worldwide. By 2014, approximately 1600 deep oil and gas fields had been found in deep sedimentary formations. These discoveries not only have proven that there are huge quantities of petroleum resources in basinal deep formations (BDFs) but also provided rich geological information that enables us to understand much about the properties and phase behaviors

of deep geofluids and their chemical reactions with surrounding rock formations, as well as fluid flow and circulations in deep basins. The pioneering researches on geofluids in deep basins reveal a complete new realm, and much of our previous understanding about the geofluids and their evolution based on shallow sedimentary formations might be changed in the near future. They also allow us to better define the key research directions in the basinal geofluid discipline.

## 2. Contents of the Special Issue

The purpose of this special issue is to collate high-quality research articles in deep sedimentary basins. We hope to cover the most recent development on new discoveries, new data, new methodologies, and new understandings on geofluids in deep sedimentary basins and to discuss challenges and opportunities for future resource exploration in deep sedimentary basins.

*2.1. Petroleum Generation, Migration, and Accumulation in Deep Sedimentary Basins.* With petroleum exploration entering into deep strata, the traditional hydrocarbon generation models seem to confront numerous challenges in explaining the deep hydrocarbon discoveries [1, 2]. Hydrocarbon generation simulation and kinetics research suggested that gases from kerogen cracking could be extended to a relatively higher maturity stage [3, 4]. It is indicated that although the abundance of long, fatty chains in high-to-over-mature

kerogen decreases drastically, there is still certain amount of short branched aliphatic structures present, and the lower limit for gas from kerogen cracking can be extended to a maturity stage with Ro reaching 3.5% [5]. This suggests that high-to-over-mature kerogens in deep and ultradeep strata are still capable of providing material basis for gas generation.

W. Zhao et al. quantitatively reconstructed the yields of light hydrocarbons at different thermal evolution stages and established a set of hydrocarbon expulsion evolution curves for marine organic matters with different TOC values through computing pressurization during hydrocarbon generation and using light hydrocarbon online detection techniques. Based on the oil cracking simulation experiments and kinetics research of different liquid hydrocarbons, they also established a model for probing cracking evolution of different compositions of crude oil and heavy hydrocarbon gas ( $C_{2-5}$ ), as well as in-source and out-source pyrolysis gas generated from liquid hydrocarbons. Their work not only defines the cracking threshold for liquid hydrocarbons with different compositions and occurrences but also quantitatively estimates the contribution of pyrolysis gases to the deep natural gas resources.

Y. Hou et al. discussed the bitumen distribution and maturity in the Devonian carbonate reservoirs in South China. Due to the absence of vitrinite, organic matter maturity can only be obtained by indirect means. Their study found that the oil and gas in the Devonian reservoirs experienced a high temperature of 210°C to 260°C at the end of Permian, which was a critical period for paleo-oil reservoir cracking and also a critical period for marine natural gas generation. In combination with the regional tectonic evolution, the maturity of organic matters, which was determined by several techniques, is considered as a key parameter in reconstructing the formation and destruction processes of oil and gas accumulations.

There are multiple sets of hydrocarbon source rocks in the Junggar Basin, Western China, but the main source rocks vary greatly within the basin. Currently there is no consensus on the origin of the Triassic hydrocarbon accumulations in the Central Junggar Basin. M. Wu and coauthors suggested that there were two more sets of source rocks for the Triassic hydrocarbons, in addition to the traditionally perceived Permian source rocks. The Triassic source rocks contributed significantly to hydrocarbon accumulations. The lacustrine Triassic source rock is widely distributed in the Junggar Basin and can generate a significant amount of oil and gas under deep burial, constituting a potential set of effective source rocks. This new understanding further expands the oil and gas resource potential in the deep strata in the Junggar Basin. Based on whole oil carbon isotopes and various biomarker parameters and combined with the linear regression method, M. Wu et al. determined the contribution ratio of various sources rocks.

X. Wu and coauthors used geochemical data of the Upper Paleozoic tight gas in the Hangjinqi area of the Northern Ordos Basin in Western China to study the geochemical characteristics of tight gas. They found that the tight gas is mainly of coal-type and has been affected by mixing of oil-type gas in the wells from the Shilijiahan and Gongkahan zones adjacent

to the Wulanjilinmiao and Borjianghaizi faults. Gas-source correlation indicates that the coal-type gas in the Shiguhan zone is typical of a distal-source accumulation, whereas the natural gas in the Shilijiahan and Gongkahan zones is mainly characterized by a near-source accumulation.

*2.2. Petrology and Petrophysics of Deeply Buried Rocks and Reservoirs.* Generally, strata experiencing deep burial in a basin tend to encounter more types of diagenesis and more complex diagenetic processes. Thus, the reservoir porosity and the permeability generally become worse with increasing depths [6, 7]. The permeability of deeply buried reservoirs is rather low, which are often considered to be tight reservoirs. However, recent oil and gas exploration has revealed that, in the deep strata (below 4500 m) or the ultradeep strata (below 6000 m), some decent pore space of sedimentary rocks can still be maintained (F. Wang et al. and B. Cao et al.). In some carbonate plays, high porosity-permeability belts can still be present even below 7000 m to 8000 m (W. Wei et al.).

B. Cao et al. illustrate the diagenesis processes in the Jurassic formations in the Central Junggar Basin (NW China); ductile lithic-rich, very fine-grained sandstones deposited in all facies associations display compaction of easily deformed, clay-rich grains, resulting in a rapid loss of porosity during the earlier burial phase. They found that ductile lithic-rich, tightly compacted sandstones and calcite completely cemented sandstones can create permeability barriers embedded in permeable reservoir sandstones, resulting in heterogeneous flow. Especially when reservoirs come in contact with petroleum during the burial process, petroleum is prone to migrate and accumulate in rocks with better physical properties between barriers. The flux of oil and gas in reservoirs would alter the diagenetic environment, which may impede or terminate the diagenesis. The presence of late diagenetic calcite and sulphate cements is a good mineralogical indicator of oil charge and migration. Therefore, in different parts of the same reservoir, differential diagenetic discrepancy would be enhanced, which causes larger anisotropy in BDFs reservoir.

In tight clastic reservoirs, J. Lai et al. found two diagenetic stages of carbonate cements. The early diagenetic stage corresponds to a shallow burial with carbonate cements being pore-filling and grain-replacing calcite and dolomite. A late diagenetic stage occurred at a mesogenetic deep-burial depth with carbonate cements appearing as ferroan calcite and ferroan dolomite replacing framework grains and precipitating in intergranular pores.

B. Cao et al. regarded this to have been caused by different sedimentary facies, characterized by different reservoir particle sizes, granular components, and depositional structures. Various authigenic minerals with predominately patchy texture, including calcite, clays, analcime, anhydrite, barite, quartz overgrowth, and albite, are present in the fine-grained lithofacies deposited principally in fluvial channel, distributary channel, and distributary-mouth bar facies. Chlorite coats only occur in the distributary channel and distributary-mouth bar facies, whereas analcime and illite/smectite clays are most common in the fluvial channel facies. Hematite rims only occur in the fluvial channel facies.

W. Wei et al. investigated the diagenetic processes and porosity development tied to fault-controlled hydrothermal fluids in the deep Cambrian dolomite reservoirs in the ultradeep borehole TSI (~8408 m deep) in the Tarim Basin. Their studies focused on the critical diagenetic processes and their roles in pore generation and plugging. They present some prevalence evidence of dissolved, less-cemented open vugs in the deeper part of a well in the northern Tarim Basin and demonstrated that these pores and vugs were formed in association with fault-channeled hydrothermal fluids from greater depths.

### 2.3. Fluid Flow and Circulation in Deep Sedimentary Basins.

In sedimentary basins associated with deep hot fluids, the heat transmitted can also cause thermal alteration of the oil, thus forming “hydrothermal” oil which may not be consistent with the typical “thermogenic” oil [8, 9]. The Fischer-Tropsch reaction, considered to be a common inorganic chemical reaction in geothermal systems and ultrabasic rocks [10, 11], can produce the precursors of the critical organic molecules required for hydrocarbon generation. Fischer-Tropsch synthesis has been known to occur widely in deep hot fluid intrusion areas [12]. Under high temperature and pressure in the lower crust-upper mantle, considerable amounts of hydrocarbons of inorganic origin may be present. These hydrocarbons may be brought into basins via deep fluids to form reservoirs [13]. In addition, deep fluids are rich in CO<sub>2</sub> and Helium, which are likely to be preserved in the deep parts of basins so as to form important natural gas resources [14–16].

J. Li et al. construct a mutual solubility model to simulate the chemical reaction processes in CO<sub>2</sub>-CH<sub>4</sub>-brine systems under a wide range of temperatures (0–250°C), pressure (1–1500 bar), and salinity (NaCl molality from 0 to more than 6 mole/kgW). The result demonstrates that, in a deep basinal setting, calcite can be more stable than dolomite; and with the presence of CH<sub>4</sub> and H<sub>2</sub>S in the gas phase, hydrocarbons tend to become “sour.”

J. Liu et al. document the origin of diagenetic fluids of a deeply buried carbonate reservoir in the Tarim Basin in NW China by using a combination of petrology, in situ Secondary Ion Mass Spectrometry (SIMS) analysis, fluid inclusion analysis, and radiogenic isotope analysis of pore-filling calcite cements. The multiple cement stages produced poor matrix porosity, whereas caves and fractures formed during epigenetic karstification constitute the dominant reservoir spaces. A corresponding diagenesis-related reservoir evolution model was established which favors exploration and prediction in deeply buried reservoir in the Tahe area.

The pore fluid evolution of the Paleogene medium-deep reservoirs in the Huanghekou Sag of the Bohai Bay Basin in China was investigated by Z. Sun et al. The authors demonstrated that volcanic activities may exert a significant influence on the pore fluid properties depending on the volcanic activity intensity. The evolution of pore fluids can be divided into three stages corresponding to volcanic activities. The vertical distribution of pore fluids with varied properties in different intervals controls the diagenetic processes and reservoir quality.

Organic fluids have an obvious effect on diagenesis. J. Lai et al. observed that the content of carbonate cement has good correlation with its distance to the source rock. They believed that the dissolution of Ca-feldspars by organic acid-rich fluids together with clay mineral transformations such as illitization of smectite would provide Ca<sup>2+</sup> and Mg<sup>2+</sup> ions for carbonate cementation. Organic acids and CO<sub>3</sub><sup>2-</sup>-rich fluids would charge into reservoirs together with hydrocarbons. When CO<sub>2</sub> and acids were buffered by the framework grain dissolution, carbonate cements would precipitate, causing a decrease in CO<sub>2</sub> concentration.

### 2.4. Methodologies for Understanding Geofluids in Basinal Deep Formations.

Data for geofluids in BDFs are quite scarce overall due to limited drilling, challenging environments, and high sampling cost [17]. Recent observation, measurements, and laboratory physical simulations indicate that there do not appear any fundamental differences in the ways of fluid-rock interactions between the deeply buried formations and their shallow counterparts [6, 18]. Therefore, some of the conventional simulation algorithms developed for shallow reservoirs can be used to simulate fluid-rock interaction in BDFs with elevated pressures and temperatures.

As demonstrated by papers in this special issue, the main methodologies commonly used for studying geofluids in sedimentary basins are similar to those used for shallow reservoirs including (1) analyzing natural analogues, (2) physical simulation in the laboratory, and (3) numerical simulations.

The reservoir rocks in deep basin tend to become tighter [7]. The accurate measurements of permeability of ultralow permeability rock are imperious for reservoir quality evaluation. Y. Guo et al. proposed a new transformation model between the NMR transverse relaxation time and the relative permeability of the wetting phase, where a piecewise method was used to calculate relationship between the transverse relaxation time and relative permeability. The authors also demonstrated a way to determine the piecewise points by the mutation position of the fractal dimensions, with pore radius ranges of 0.03 μm and 1 μm in their case. The method provided a theoretical basis for interpreting relative permeability curve with depth through the NMR logging data.

The works of S. Liu et al. and H. Zhu et al. presented two case studies of BDFs in the Sichuan Basin and the Tarim Basin, respectively. Both works are on the Paleozoic carbonate petroleum systems that are currently under active exploration. S. Liu et al. illustrate an effective basin analysis technique for investigation of BDFs and corresponding petroleum systems, while H. Zhu et al. demonstrate how new seismic interpretation techniques and procedures can help identify reservoir sweet spots or zones in BDFs.

The experimental work by Z. He et al. provided some new insights into carbonate dissolution in BDFs. Through laboratory experiments and field observation, they concluded that high poroperm carbonate reservoirs in BDFs would require an open or semiopen fluid system in the subsurface with the types of formation water primarily determining the dissolution capability, whereas close fluid systems can only preserve preexisting reservoir spaces.

J. Li et al. present a mutual solubility model for CO<sub>2</sub>-CH<sub>4</sub>-brine systems under high pressure and temperature (up to 250°C and 150 MPa), which is applicable to BDFs. By combining with the PHREEQC functionalities, they computed the CO<sub>2</sub>-CH<sub>4</sub>-brine-carbonate-sulfate equilibrium and concluded that, for CO<sub>2</sub>-CH<sub>4</sub>-brine-carbonate systems in BDFs, magnesium is more likely to be dissolved in aqueous phase, while calcite could be more stable than dolomite.

W. Wei et al. investigated the diagenetic processes and porosity development based on the petrographic investigation and petrophysical data integrated with fluid reactive transport modeling using TOUGHREACT. Their modeling results indicate that pores and vugs may be effectively formed in the deeply buried dolomites associated with faults, where hydrothermal fluids flow upward from deeper formations.

## Acknowledgments

We are grateful to all the authors for their great contributions to this special issue and for their dedication and perseverance during the revision process. We are indebted to the 60 or so reviewers who helped evaluate and improve those papers.

Xiaorong Luo  
Zhijun Jin  
Keyu Liu  
Shuichang Zhang

## References

- [1] F. Behar, S. Roy, and D. Jarvie, "Artificial maturation of a Type I kerogen in closed system: Mass balance and kinetic modelling," *Organic Geochemistry*, vol. 41, no. 11, pp. 1235–1247, 2010.
- [2] K. He, S. Zhang, J. Mi, and G. Hu, "The speciation of aqueous sulfate and its implication on the initiation mechanisms of TSR at different temperatures," *Applied Geochemistry*, vol. 43, pp. 121–131, 2014.
- [3] A. S. Pepper and P. J. Corvi, "Simple kinetic models of petroleum formation. Part I: oil and gas generation from kerogen," *Marine and Petroleum Geology*, vol. 12, no. 3, pp. 291–319, 1995.
- [4] N. Mahlstedt and B. Horsfield, "Metagenetic methane generation in gas shales I. Screening protocols using immature samples," *Marine and Petroleum Geology*, vol. 31, no. 1, pp. 27–42, 2012.
- [5] J. Mi, S. Zhang, J. Chen et al., "Upper thermal maturity limit for gas generation from humic coal," *International Journal of Coal Geology*, vol. 152, pp. 123–131, 2015.
- [6] S. Bloch, R. H. Lander, and L. Bonnell, "Anomalously high porosity and permeability in deeply buried sandstone reservoirs: Origin and predictability," *AAPG Bulletin*, vol. 86, no. 2, pp. 301–328, 2002.
- [7] S. N. Ehrenberg and P. H. Nadeau, "Sandstone vs. carbonate petroleum reservoirs: A global perspective on porosity-depth and porosity-permeability relationships," *AAPG Bulletin*, vol. 89, no. 4, pp. 435–445, 2005.
- [8] R. C. Burruss and C. D. Laughrey, "Carbon and hydrogen isotopic reversals in deep basin gas: Evidence for limits to the stability of hydrocarbons," *Organic Geochemistry*, vol. 41, no. 12, pp. 1285–1296, 2010.
- [9] B. R. T. Simoneit, "Petroleum generation, an easy and widespread process in hydrothermal systems: an overview," *Applied Geochemistry*, vol. 5, no. 1-2, pp. 3–15, 1990.
- [10] T. M. McCollom and J. S. Seewald, "A reassessment of the potential for reduction of dissolved CO<sub>2</sub> to hydrocarbons during serpentinization of olivine," *Geochimica et Cosmochimica Acta*, vol. 65, no. 21, pp. 3769–3778, 2001.
- [11] Q. Fu, B. Sherwood Lollar, J. Horita, G. Lacrampe-Couloume, and W. E. Seyfried Jr., "Abiotic formation of hydrocarbons under hydrothermal conditions: Constraints from chemical and isotope data," *Geochimica et Cosmochimica Acta*, vol. 71, no. 8, pp. 1982–1998, 2007.
- [12] E. M. Galimov, "Isotope organic geochemistry," *Organic Geochemistry*, vol. 37, no. 10, pp. 1200–1262, 2006.
- [13] X. Wang, Z. Ouyang, S. Zhuo, M. Zhang, G. Zheng, and Y. Wang, "Serpentinization, abiogenic organic compounds, and deep life," *Science China Earth Sciences*, vol. 57, no. 5, pp. 878–887, 2014.
- [14] J. X. Dai, J. Li, W. W. Ding et al., "Geochemical characters of the giant gas accumulations with over one hundred billion cubic meters reserves in China," *Petroleum Exploration and Development*, vol. 32, no. 4, pp. 16–23, 2005.
- [15] J. Wang, W. H. Liu, J. Z. Qin, J. Zhang, and B. J. Shen, "Reservoir forming mechanism and origin characteristics in Huangqiao-carbon dioxide gas field, North Jiangsu Basin," *Natural Gas Geoscience*, vol. 19, no. 6, pp. 826–834, 2008.
- [16] Q. Y. Liu, J. X. Dai, Z. Y. Jin et al., "Abnormal hydrogen isotopes of natural gases from the Qingshen gas field, the Songliao Basin," *Geochimica*, vol. 43, no. 5, pp. 460–468, 2014.
- [17] Z. Li, "Research frontiers of fluid-rock interaction and oil-gas formation in deep-buried basins. bulletin of mineralogy," *Petrology and Geochemistry*, vol. 35, pp. 807–816, 2017.
- [18] C. Fan, Z. Wang, A. Wang et al., "Identification and calculation of transfer overpressure in the northern Qaidam Basin, northwest China," *AAPG Bulletin*, vol. 100, no. 1, pp. 23–39, 2016.

## Research Article

# Diagenetic Heterogeneity of Deep Sandstones and Its Relationship to Oil Emplacement: A Case Study from the Middle Jurassic Toutunhe Formation in the Fukang Sag, Central Junggar Basin (NW China)

Binfeng Cao,<sup>1,2</sup> Xiaorong Luo,<sup>1,2</sup> Likuan Zhang,<sup>1</sup> Fenggui Sui,<sup>3</sup> Huixi Lin,<sup>3</sup> and Yuhong Lei<sup>1</sup>

<sup>1</sup>Key Laboratory of Petroleum Resources Research, Institute of Geology and Geophysics, Chinese Academy of Sciences, Beijing 100029, China

<sup>2</sup>University of Chinese Academy of Sciences, Beijing 100049, China

<sup>3</sup>Institute of Western Frontier Area, Shengli Oilfield Company, SINOPEC, Dongying 257000, China

Correspondence should be addressed to Binfeng Cao; cao.binfeng@126.com

Received 4 March 2017; Accepted 27 June 2017; Published 25 September 2017

Academic Editor: Stefano Lo Russo

Copyright © 2017 Binfeng Cao et al. This is an open access article distributed under the Creative Commons Attribution License, which permits unrestricted use, distribution, and reproduction in any medium, provided the original work is properly cited.

The Middle Jurassic Toutunhe Formation at depths of approximately 4000–6000 m has increasingly come into focus as a current deep reservoir target in the central Junggar Basin (NW China). Based on petrography, SEM, stable isotopes, and fluid inclusion analyses, the goals of this study were to investigate the effect of depositional lithofacies on sandstone diagenetic heterogeneity and to examine the relationship between diagenetic evolution and oil charge within a heterogeneous reservoir. Grain size controls the overall abundance of cement and porosity and reservoir properties through its effect on ductile lithic sand grains and hence on mechanical compaction. Early diagenetic calcite cement is an exception to this trend. Ductile lithic-rich, very fine-grained sandstones featured compaction of easily deformed, clay-rich grains, resulting in a very rapid loss of porosity during burial. In contrast, dissolution and cementation occurred as well as ductile compaction in the fine-grained sandstones. Two episodes of oil charge occurred in the relatively coarser-grained sandstone lithofacies. Diagenesis progressed alternately with oil emplacement, and some diagenetic alterations and oil charge occurred simultaneously. Ductile lithic-rich, highly compacted sandstones and tightly calcite-cemented sandstones can create permeability barriers embedded in permeable reservoir sandstones, probably resulting in heterogeneous flow.

## 1. Introduction

Reservoir heterogeneity refers to spatial variability of a system property (e.g., porosity, permeability, and pore structure) at a specified scale [1–4]. The intrinsic complexity of a reservoir is the result of various geological processes, including depositional environment, diagenesis, and tectonic imprint. The heterogeneity is a critical factor affecting fluid flow and distribution within a reservoir [5, 6]. Diagenetic studies that are pertinent to reservoir characterization have been confined almost entirely to the identification and quantification of mineral components and porosity types by combined use of scanning electron microscope (SEM) and thin section and

surely do not characterize diagenetic heterogeneity, especially at scales larger than microscopic scale. The primary texture and detrital compositions of sandstones, sand body geometry, and architecture, ultimately controlled by depositional environment, are of decisive importance in determining the rate and pathways of fluid flow affecting the extent and distribution of early diagenetic alterations in sandstones [7–12]. Early diagenesis in turn exerts a substantial control on the deep-burial diagenetic evolution of the sandstones [9, 10, 13]. It seems plausible that a significant component of sandstone diagenetic heterogeneity arises from initial variations in texture and grain compositions in principle [8, 14]. Thus, linking diagenetic alterations to depositional environments

and lithofacies has been an important concept for evaluating a degree of large-scale heterogeneity characterizing diagenetic features [9, 10]. This is essential to achieve a complete and adequate spatial representation of a heterogeneous reservoir.

Hydrodynamic fluctuations and varying depositional facies associations directly determine textural and compositional parameters of sandstone sediments, producing differential compaction and diagenetic processes, as well as reservoir quality evolutions [15–17]. Some sandstone lithofacies have experienced a very rapid loss of porosity through compaction or cementation and have achieved a high capillary entry pressure during early diagenesis and have acted as low-permeability barriers to late fluid (hydrocarbons included) flow in a reservoir [17–19]. However, studies of differential sandstone diagenesis and porosity evolutions at a reservoir scale level are still far from being fully explored in the literature.

In recent years, the Jurassic lithologic and stratigraphic traps have become a major focus of deep reservoir exploration in the central Junggar Basin (NW China). Some oil fields such as Mobei, Mosuowan, and Moxizhuang oil fields have been discovered in the Jurassic sandstones (Figure 1(a)), reflecting promising prospects for deep exploration. No significant discoveries have been obtained in the Fukang Sag. By the end of 2014, the Shengli Oilfield Company, SINOPEC, has completed seven wells in this area (Figure 1(b)) and has obtained substantial findings in the Lower-Middle Jurassic sandstones. The recoverable oil original reserves were estimated to be approximately  $2109.35 \times 10^4$  t (155 million bbl). The focus of this study is the Middle Jurassic Toutunhe Formation (Figures 2 and 3). This formation is buried at depths of approximately 4000–6000 m. The sandstones have strongly heterogeneous petrophysics with porosities of 2.1–16.4% and permeabilities of 0.02–28.9 mD. The inhomogeneity of oil shows has been noted from core description, well logs to well tests. The aim of the study is to investigate the effect of depositional environments and lithofacies on sandstone diagenetic heterogeneity and to decipher the diagenetic evolution pathways of a heterogeneous reservoir and its impact on hydrocarbon migration.

## 2. Geological Setting

The Fukang Sag is located in the Junggar Basin, which covers an area of approximately  $136,000 \text{ km}^2$  ( $52,509 \text{ mi}^2$ ) north of Xinjiang Uygur Autonomous Region, northwest China (Figure 1(a)). The Junggar Basin is triangle-shaped and is confined by the Qinggelidi and Kelameili Mountains to the northeast, by the Yilinheibiergen and Bogda Mountains to the south, and by the Zhayier and Halalate Mountains to the northwest. The basin lies at a three-block junction between Kazakhstan, Siberia, and Tarim and is a part of the Kazakhstan block [20]. The Junggar Basin is floored by Precambrian crystalline basement and part of Hercynian folded basement [21] and is an Upper Paleozoic, Mesozoic, and Cenozoic superimposed basin. The basin has experienced the Hercynian, Indosinian, Yanshanian, and Himalaya orogenies. Three main phases of deformation have been recognized in the basin: the Middle-Late Permian rift stage, Triassic to Paleogene depression

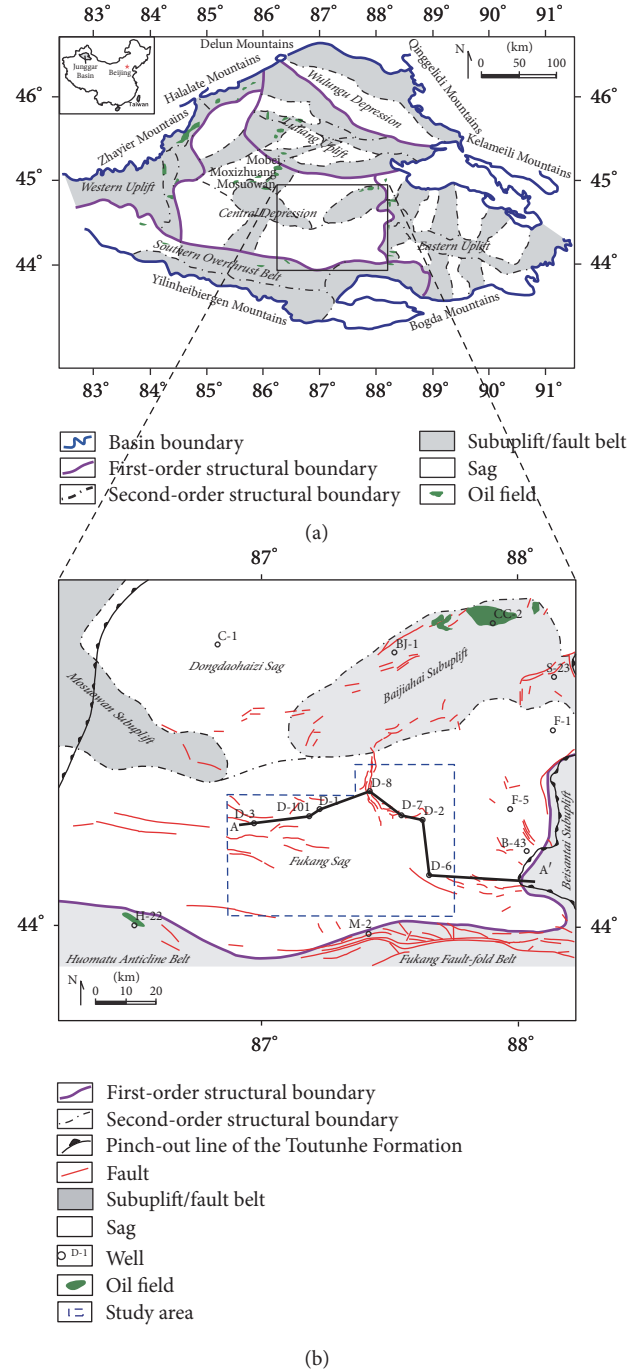


FIGURE 1: (a) Regional geological map showing structural features of the Junggar Basin and location of the study area [24]. (b) Location of the studied wells.

stage, and Neogene to Quaternary foreland stage [22, 23] (Figure 3). The Junggar Basin contains six structural units: the Wulungu Depression, Luliang Uplift, Western Uplift, Central Depression, Southern Overthrust Belt, and Eastern Uplift [24]. Each structural unit has a distinct structural style and tectonic history. The Fukang Sag lies in the Central Depression (Figure 1(b)). The main structure within the sag is a northeast-southwest trending monocline (Figure 2), which

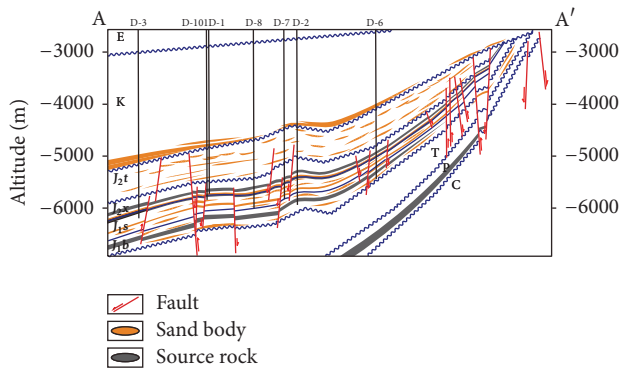


FIGURE 2: Schematic structural section crossing the studied wells.

formed as a result of the uplift of the Bogda Mountains at the southern margin of the basin since the Paleogene [24]. The Jurassic strata are relatively flat lying or dip gently to the southwest with a dip angle of 2–3° (Figure 2). Most of the observed faults are northeast-directed and east-west-directed normal faults confined to the Jurassic strata (Figures 1(b) and 2). Throw of the fault is generally tens to hundreds of meters and strike length is less than 2 km. These normal faults and deep reversed faults, in some localities, show a flower structure (Figure 2).

The central basin contains Carboniferous to Quaternary sediment fills up to 10 km thick (Figure 3). Rather than attempting an encyclopedic coverage of all the sediments, here, we only summarize general depositional evolution of the Jurassic succession. During the Early Jurassic and early Middle Jurassic period, the central basin was an intracontinental shallow lacustrine basin under the low-amplitude oscillating tectonic regime. Depositional facies identified in the central basin include alluvial fan and fluvial, deltaic, and lacustrine facies [25, 26]. The deposits are typical of a coal-bearing succession and consist of conglomerates, sandstones, and mudstones (Figure 3). Due to the Early Yanshanian orogeny, the lacustrine area began to shrink rapidly during the late Middle-Late Jurassic period. Fluvial, deltaic, and shallow lacustrine facies are included. The deposits are sandstones and mudstones (Figure 3). The contact between the Toutunhe Formation and the underlying Xishanyao Formation is unconformable. The Toutunhe Formation has local erosions, and the Upper Jurassic succession is entirely absent (Figure 3).

Previous exploration and geochemical studies indicate that the Fukang Sag contains four sets of potential source rocks (i.e., Carboniferous, Permian, Triassic, and Jurassic) (Figure 3). Among these source rocks, most discovered hydrocarbons in the Jurassic strata are generally believed to be originated from both the Permian and Jurassic source facies [27–29]. As these source rocks are deeply buried and not easily penetrated by the drill, previous published organic geochemistry studies have been almost entirely restricted to the northern and eastern slope of the sag [29, 30]. The Lower Permian Pingdiqian Formation contains deep lacustrine black mudstones, oil shales, and dolomitic mudstones with a total thickness of 50–650 m [30]. The mudrocks have total

organic carbon (TOC) contents ranging from 0.5 to 10.2%. The organic matter is of type I-II kerogen with vitrinite reflectance ( $R_o$ ) values of 1.2–2.0% [29]. It can be inferred that the source rocks are mature to over mature towards the sag center [30]. The source rocks in the Lower Jurassic and lower Middle Jurassic succession are composed of lacustrine-swamp deep gray mudstones and carbargilites interbedded with thin coal-beds. The mudstones have a total thickness of up to 500 m [30]. The TOC contents range from 0.3 to 3.7%. The organic matter is of type II-III kerogen with  $R_o$  values of 0.6–1.0% [29]. The Badaowan Formation's source rocks are of better quality than the Sangonghe and Xishanyao Formation. It is speculated that these source rocks are mature to highly mature towards the sag center [30].

In the Fukang Sag, the Toutunhe Formation's deposits were derived from Kelameili Mountains in the northeast and Bogda Mountains in the south [31–33]. During deposition of the Toutunhe Formation, the study area witnessed a variety of depositional environments ranging from shallow lacustrine through to delta to meandering fluvial system with a total thickness of 700–900 m [33]. The formation can be subdivided into three lithological units (Figure 4). The lower unit ( $J_{113}$ ) consists of grayish-green mudstones and siltstones interbedded with very fine- to fine-grained sandstones. The middle ( $J_{112}$ ) unit includes grayish-green very fine- to fine-grained sandstones, siltstones, and mudstones. The upper unit ( $J_{111}$ ) comprises mainly greyish-brown gravel-bearing medium-grained sandstones, fine-grained sandstones, very fine-grained sandstones, and interlaminated siltstones and mudstones. The Lower Cretaceous mudstones are widely distributed with a total thickness of 140–180 m and can act as the main regional seals for the Jurassic hydrocarbon plays.

### 3. Samples and Methods

Cores were logged and sampled from the D-1, D-2, D-3, D-6, D-7, and D-8 wells (Figure 4). The specific lithofacies and depositional facies associations of the sandstones were defined based on core description (proportion of sand to shale, bed thickness, grain size, degree of bioturbation and deformation, sedimentary structure, presence of bioclasts and mudstone intraclasts, carbonate cement distribution, etc.). This was combined with wireline logging interpretation to delineate the overall depositional environments for the Toutunhe Formation. All cores were examined under ultraviolet (UV) light for reservoir properties (oil saturation, oil immersion, oil patch, fluorescence, and no show).

Twenty-eight conventional core samples were selected to represent the various depositional facies and lithofacies and the different reservoir properties (Figure 4). Mineralogical, stable carbon and oxygen isotope, and fluid inclusion analyses were performed at the Institute of Geology and Geophysics, Chinese Academy of Sciences, Beijing, China.

All samples were impregnated with blue epoxy resin under vacuum to indicate porosity prior to preparing polished thin sections. Sandstone petrographic compositions were quantified by 300-pointed modal analysis. In addition, the thin sections were studied to identify growth occurrence and habits of interstitial diagenetic minerals and to define

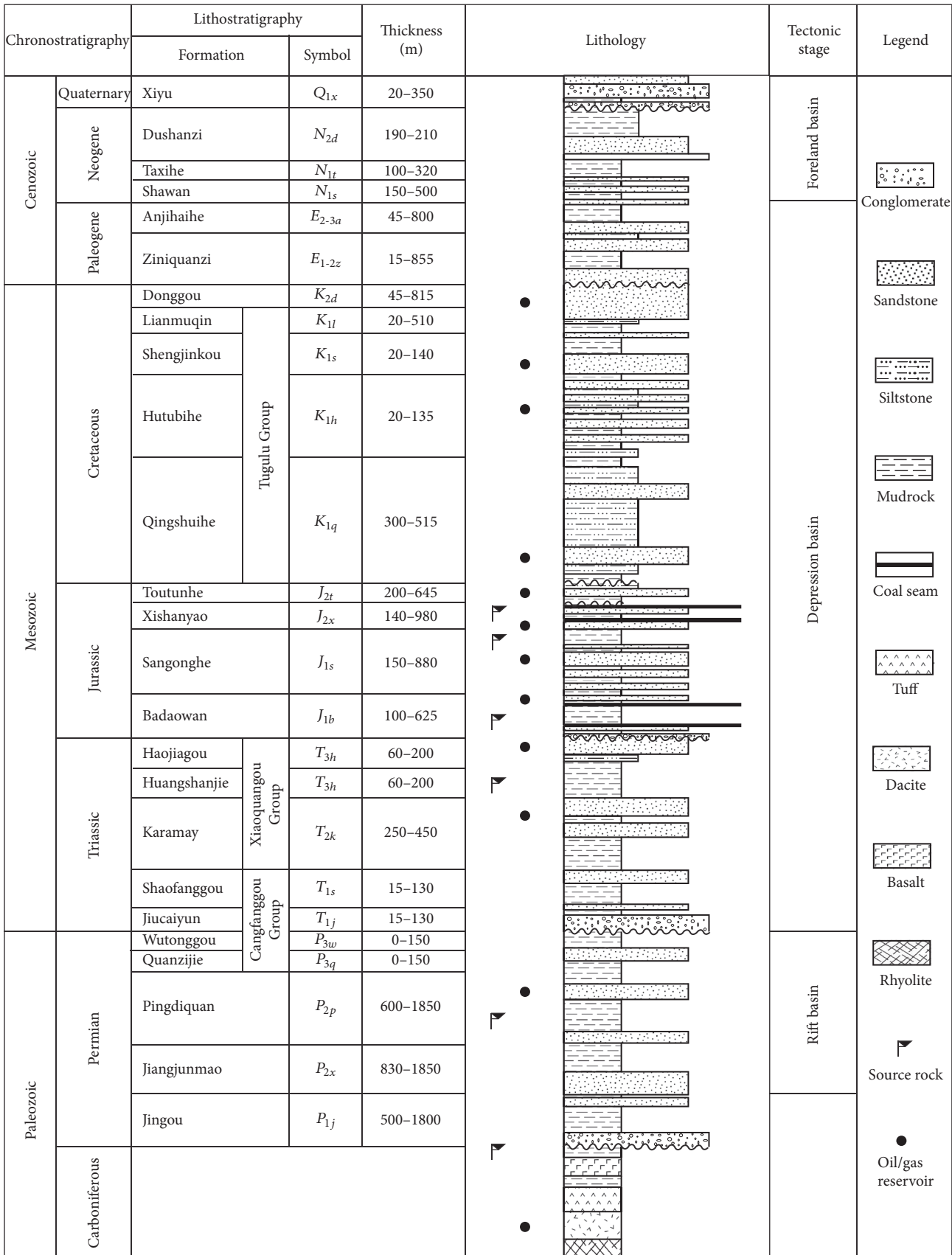


FIGURE 3: Generalized stratigraphic column of the central Junggar Basin. Tectonic stages refer to Wu [22] and Zhao [23].

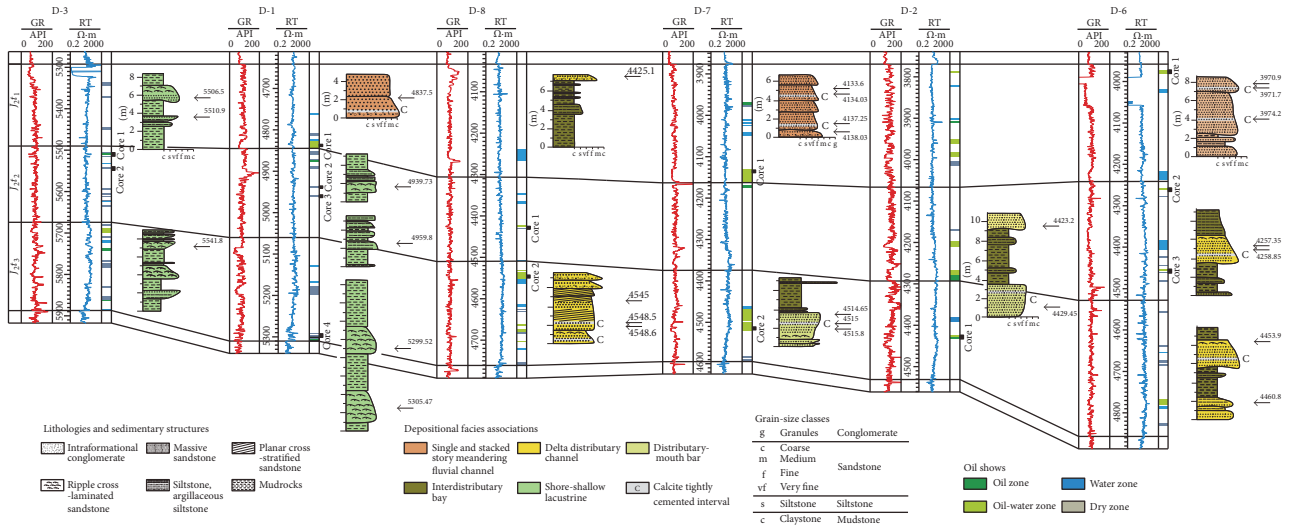


FIGURE 4: Wireline logs of the Toutunhe Formation in the studied wells showing sample depths. Only the point-counted samples are included. Depositional facies associations and lithofacies are interpreted based on core description. Calcite tightly cemented intervals are shown. GR/API: natural gamma-ray log; RT/ $\Omega$ -m: formation true resistivity.

textural relationships between different cements. Cathodoluminescence (CL) observations were made using a Relion III cold-cathode device at beam voltages of up to 15 keV and 500  $\mu$ A. To further determine their textural relationships, selected samples were examined using a high-resolution field-emission Nova NanoSEM 450 scanning electron microscope equipped with an integrated analysis system of the Oxford Aztec Energy Dispersive X-ray Spectrometry (EDS) and electron backscatter diffraction (EBSD). Carbon-coated thin sections were mounted on gold grids. All backscatter electron (BSE) images were acquired at 20 keV at a working distance of 5–8 mm. EDS was used for qualitative identification of minerals.

Fourteen samples containing a single generation of calcite cement (either early or late) were selected for carbon and oxygen isotope analysis. The samples were ground to >200 mesh and then soaked overnight in 3% sodium hypochlorite to remove organic matter. Subsequently, the powder samples were reacted with 100% phosphoric acid at 25°C for 4 hours, and CO<sub>2</sub> was extracted and analyzed. The entire process was finished using a Finnigan Delta S mass spectrometer. Oxygen isotopic compositions were calculated using a phosphoric acid-CO<sub>2</sub> fractionation factor of 1.0125 at 25°C. All results were represented in standard notation relative to PDB standard. The reproducibility of duplicate analyses generally was better than  $\pm 0.2\%$ .

Nine samples were collected to prepare 100  $\mu$ m thick doubly polished sections for petrographic observation and microthermometric measurement of fluid inclusions. Petrography of pore bitumen (free oils and solid bitumens) and fluid inclusion and fluid inclusion assemblages were firstly examined using a Nikon 80I microscope under both transmitted and UV light. The wavelength of the emission fluorescence is greater than 420 nm. Homogenization temperature measurement of fluid inclusions was carried out using a calibrated Linkam THMSG600 heating-freezing

stage. A step-heating and temperature cycling technique [35] was adopted to record the homogenization temperatures. The precision is  $\pm 0.1^\circ\text{C}$ . Fluids inclusions displaying textural or microthermometric evidence for stretching, necking down, leakage, or decrepitation were excluded from the study.

### 4. Results

**4.1. Core Description.** Sedimentological description of all cores from six wells with a total length of 53.5 m has been done (Figure 4). Five depositional facies associations of the sandstones have been distinguished: (1) single and stacked story meandering fluvial channel, (2) delta distributary channel, (3) distributary-mouth bar, (4) interdistributary bay, and (5) shore-shallow lacustrine facies association. These facies associations have been identified based on core sections and well log data and are briefly described as follows. Single and stacked story channels are up to 5 m thick, fining-up units ranging mainly from blocky gravel-bearing medium- to very fine-grained sandstones, with minor siltstone and mudstone laminae. The meandering channel facies association dominates the whole upper Toutunhe Formation in the study area. Delta distributary channels are fine-grained sandstones, grading upwards into siltstones. The individual channel units are up to 3 m and sometimes are erosional-based. Sedimentary structures, in some localities, are blocky lamination at the base, changing gradually upwards into planar cross bedding towards the top of the unit, where current ripple is common. Distributary-mouth bars comprise up to 3 m thick, coarsening-up units from siltstones to fine-grained sandstones. The very fine-grained sandstones often display current ripple. Interdistributary bay sediments are almost mudstones interlaminated with thin and lenticular very fine-grained sandstones and siltstones (10 to 20 cm thick). The sandstones often exhibit plane parallel lamination in which bioclasts are common. Delta distributary channel,

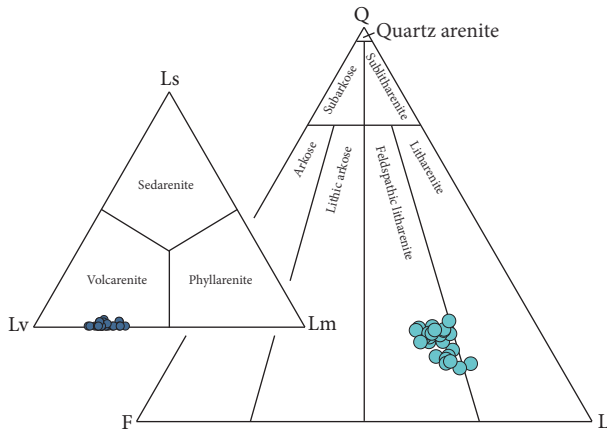


FIGURE 5: Sandstone QFL triangular classification of the Toutunhe Formation (after Folk [34]).

distributary-mouth bar, and interdistributary bay facies associations are mostly limited to the middle and lower units of the Toutunhe Formation in the D-2, D-6, D-7, and D-8 wells. Shore-shallow lacustrine fills are bioturbated mudstones and interbedded very fine-grained sandstones and siltstones displaying current ripple and plane parallel lamination. Mud intraclast-bearing fine-grained sandstones are seen locally. Patchy pyrite and bioclasts are commonly found. Shore-shallow lacustrine facies association dominates the middle and lower Toutunhe Formation in the D-1 and D-3 wells. In the first three facies associations, calcite commonly forms discrete and tightly cemented concretions (up to 30 cm) embedded in weakly cemented or uncemented sandstones (Figure 6(e)), in particular, in the relatively coarse-grained part of graded sand beds (Figure 4).

**4.2. Sandstone Petrology.** The Toutunhe Formation's sandstones are very fine- to fine-grained sandstones with the median grain size values of 0.08–0.25  $\mu\text{m}$ . Sorting ranges from moderate to well-sorted. The roundness of detrital sand grains varies from subangular to subrounded.

The sandstones are mostly feldspathic litharenite and litharenite (Figure 5; [34]). The average framework composition is 20.4% quartz, 23.3% feldspar, and 56.4% rock fragments ( $Q_{20.4}F_{23.3}L_{56.3}$ ). The detrital components of the sandstones are dominated by volcanic rock fragments, averaging approximately 36% of the whole rock volume (WRV). The igneous textures recognized in thin sections include lathwork, microlithic, cryptocrystalline, felsitic, and vitric types. Most volcanic rock fragments are composed of euhedral lathwork and microlithic feldspar phenocrysts in the cryptocrystalline groundmass which displays characteristic alteration to clays (Figures 6(a)–6(d)). Metamorphic rock fragments have an average content of about 12%<sub>WRV</sub> and comprise metamorphosed siltstone, mica schist, slate, and phyllite. Sedimentary rock fragment contents are generally less than 2%<sub>WRV</sub>. They are mostly shale and chert. Some of the lithic fragments are variably altered or deformed and have vague or irregular outlines (Figures 6(a)–6(d)) and termed as “ductile” lithic sand grains. The percentage of the ductile

grains is 3–40%<sub>WRV</sub>. Detrital quartz as a fraction of the whole rock averages 17%<sub>WRV</sub> and is mostly monocrystalline with minor amounts of polycrystalline grains. The polycrystalline quartz features sharp extinction and resorption embayments, which is interpreted as metamorphic origin. Total detrital feldspar averages 20%<sub>WRV</sub>. Plagioclase is the most abundant feldspar type observed, with an average ratio of plagioclase to total feldspar of about 0.7. In addition, detrital clay matrix is locally abundant, up to 8%<sub>WRV</sub>.

**4.3. Diagenetic Heterogeneity.** Three major sandstone petrofacies have been defined on the basis of texture and detrital compositions, diagenetic features, and pore space properties (i.e., pore abundance and type). Diagenetic features of the three defined sandstone petrofacies are described below.

**4.3.1. Ductile Lithic-Rich Sandstone.** Ductile lithic-rich sandstones are mainly ripple cross-laminated very fine-grained sandstones (median grain size: 0.08–0.13  $\mu\text{m}$ ) that occur in all facies associations (Figure 4). Ductile lithic grains constitute 22–40% of the whole rock in these samples; the contents of detrital matrix are 5–8%<sub>WRV</sub> (Table 1). Diagenesis of the sandstones is characterized by compaction of easily deformed, clay-rich grains. Ductile grains are severely deformed by mechanical compaction and are squeezed between rigid detrital grains, blocking pore throats (Figures 6(a)–6(c)). In addition to clay minerals almost indiscernible in thin sections, pyrite is an important authigenic phase in the ductile lithic-rich sandstones, ranging from 1%<sub>WRV</sub> to 3%<sub>WRV</sub>. Pyrite occurs mainly as clusters of cubes in interstitial pores and is an early diagenetic product (Figures 8(f) and 9(h)). The sandstones have no visible thin porosity (Figures 6(a)–6(c)).

**4.3.2. Tightly Calcite-Cemented Sandstone.** Tightly calcite-cemented sandstones occur in the relatively coarse-grained lithofacies of a graded sand bed (Figure 4), having the median grain size values of 0.17–0.19  $\mu\text{m}$  (Table 1). Tightly calcite-cemented sandstones contain calcite in excess of 20%<sub>WRV</sub>. The calcite cements, which are composed mostly of anhedral calcite crystals (Figure 9(a)), represent a poikilotopic texture and local replacement of framework grains (Figures 6(f) and 6(g)). The calcite precipitated before significant compaction, thereby limiting further diagenetic modifications and resulting in a high intergranular volume. The contents of ductile lithic grains are 3–5%<sub>WRV</sub> in these samples. The early diagenetic calcite cements exhibit orange-red luminescence emission (Figure 6(g)). The EDS analysis indicates that the calcite has homogeneous almost 100%  $\text{CaCO}_3$  (Figure 8(g)). The calcite has  $\delta^{13}\text{C}$  values of –4.3 to –1.4‰ and  $\delta^{18}\text{O}$  values of –13.4 to –11.2‰ (Table 2). The sandstones have also no visible porosity in thin sections (Figure 6(f)).

**4.3.3. Permeable Reservoir Sandstone.** Permeable reservoir sandstones are blocky to planar cross-stratified, fine-grained sandstones deposited predominately in the fluvial channel, distributary channel, and distributary-mouth bar facies associations. Ductile grains are less abundant in these samples than in ductile lithic-rich sandstones, ranging from 13%<sub>WRV</sub>

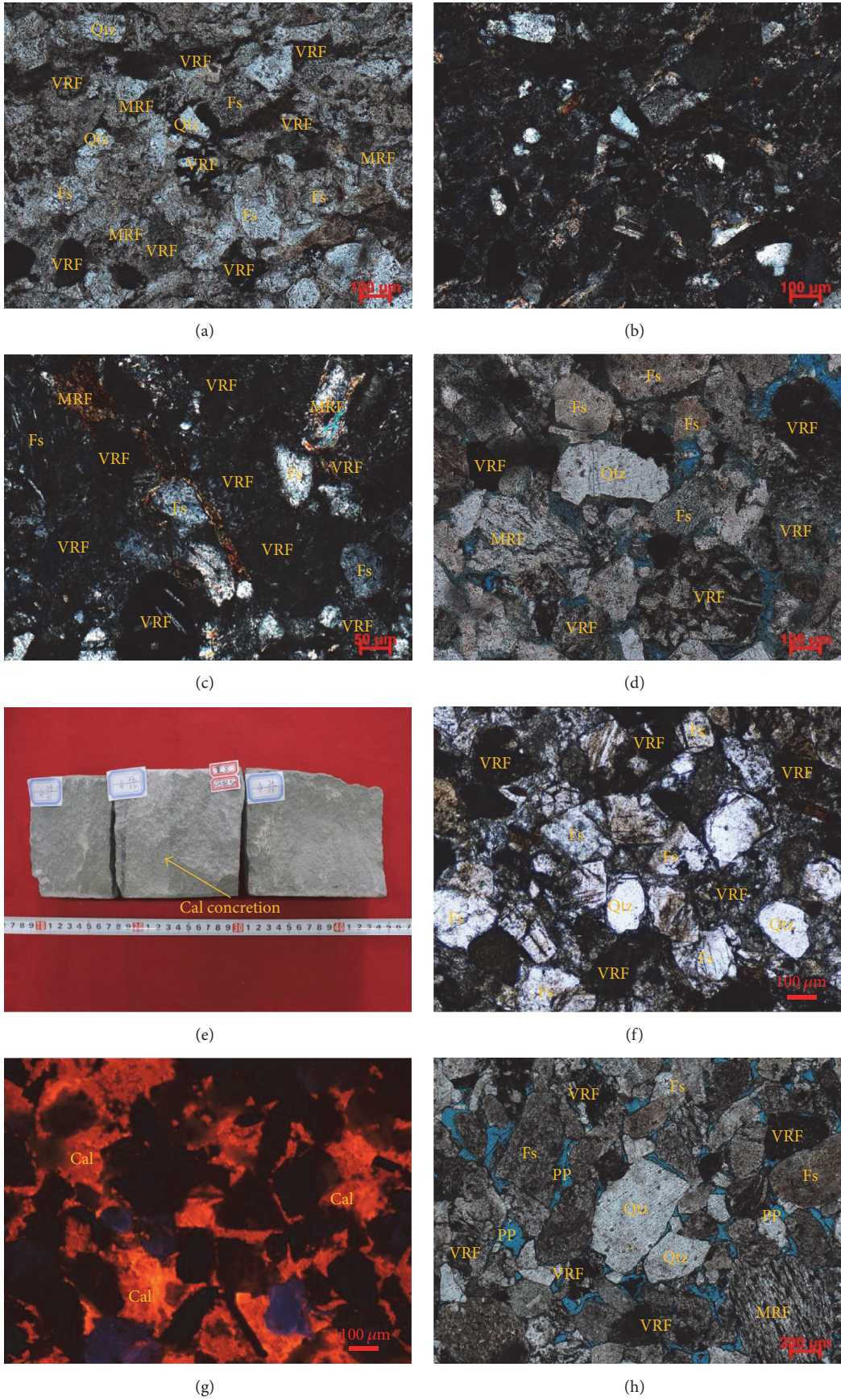


FIGURE 6: Continued.

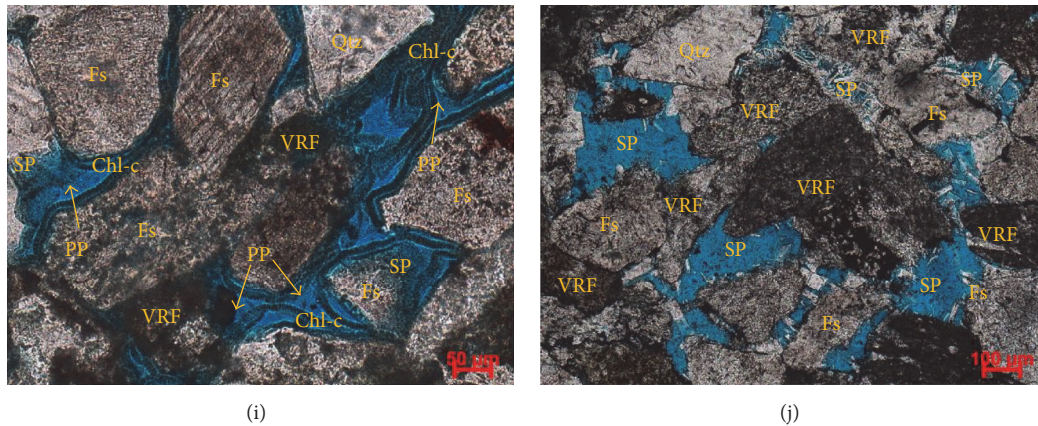


FIGURE 6: Thin section images and core photographs of sandstones (pore space is highlighted in blue). ((a) and (b)) Sample 4959.8 m, well D-1, plane-polarized light (PPL), and cross-polarized light (XPL), respectively: the predominance of volcanic rock fragments with various igneous textures. Note that some volcanic rock fragments exhibit a typical characteristic alteration of matrix to clays. (c) Sample 4939.73 m, well D-1, and XPL: volcanic and metamorphic rock fragments deformed between detrital quartz and feldspar grains and smeared on the surfaces of these rigid detrital grains. (d) Sample 4425.1 m, well D-8, and PPL: altered and deformed volcanic and metamorphic rock fragments. (e) Sample 4548.5 m, well D-8: calcite commonly forming white concretions in cores. ((f) and (g)) Sample 4548.5 m, well D-8, PPL, and CL, respectively: calcite representing a poikilotopic texture and local replacement of framework grains. The calcite exhibits orange-red luminescence emission. (h) Sample 4138.03 m, well D-7, and PPL: primary intergranular porosity. (i) Sample 4514.65 m, well D-7, and PPL: primary intergranular porosity and chlorite coats. Partial dissolution along the detrital grain margins is frequently observed. (j) Sample 4837.5 m, well D-1, and PPL: secondary porosity derived from dissolution of detrital grains. Framework grains: quartz (Qtz), feldspar (Fs), volcanic rock fragment (VRF), metamorphic rock fragment (MRF); cement: calcite (Cal), chlorite coat (Chl-c); primary porosity (PP) and secondary porosity (SP).

to 20%<sub>WRV</sub>; the contents of detrital matrix are less than 3%<sub>WRV</sub> (Table 1). Authigenic minerals include calcite, clay, analcime, anhydrite, barite, quartz overgrowth, albite, and hematite. These cements display a patchy or sporadic texture. Primary intergranular porosity (Figures 6(h) and 6(i)) as counted in thin sections averages 3.9%<sub>WRV</sub>, while secondary porosity averages 1.6%<sub>WRV</sub> and is affiliated with feldspars and lithic fragments and even minor cements (Figures 6(i), 6(j), and 7(d)).

The calcite contents are low, generally less than 7%<sub>WRV</sub>, and display a rather patchy and local cementation (Figures 7(a), 7(b), and 9(b)). The calcite cements formed after significant compaction and postdated chlorite coats, quartz overgrowths, and feldspar overgrowths or authigenic albite (Figures 8(a) and 8(c)). The calcite displays yellow to orange luminescence (Figure 7(b)). The EDS analysis reveals that the calcite contains Mn in some samples (Figure 8(h)). They have  $\delta^{13}\text{C}$  values of  $-8.4$  to  $-5.9\text{‰}$  and  $\delta^{18}\text{O}$  values of  $-19.0$  to  $-16.4\text{‰}$  (Table 2).

Chlorite has contents of less than 4%<sub>WRV</sub>. Chlorite cement seems to be facies-related and has been only observed in the distributary channel and distributary-mouth bar facies associations. The chlorite occurs as thick, continuous grain coats and not as pore-filling cement (Figures 6(i), 7(c)–7(e), 8(a), 8(b), and 9(c)). Chlorite coats represent the growth outward from detrital grain surfaces and are absent at points of grain-to-grain contact. Chlorite coats underlie quartz overgrowths, analcime, authigenic albite, barite, and calcite (Figures 7(c)–7(e), 8(a), 8(b) and 9(c)). In addition, minor

amounts of illite/smectite are present (Figures 9(d) and 9(e)), particularly in the fluvial channel facies.

There is large variation in the volume of analcime, ranging from 0 to 5%<sub>WRV</sub>. Analcime cements are the most abundant in the fluvial channel facies. The analcime is almost completely extinct and isotropic under crossed-polarized light and shows mainly pore-filling cementation (Figures 7(d), 7(e), 8(e), and 9(e)). Analcime cements are underlain by chlorite coats and replaced by calcite (Figures 7(d)–7(g)) and are intimately intergrown with authigenic albite and illite/smectite clays (Figures 9(d) and 9(e)).

Anhydrite contents are very variable with a maximum of 7%<sub>WRV</sub>. Barite is rare, however, in some samples; up to 2%<sub>WRV</sub> barite is present. Sulfate cements fill pores in patches and locally replace detrital grains (Figures 7(h), 8(b)–8(d) and 9(f)). Both anhydrite and barite grow over and engulf chlorite coats, quartz overgrowths, feldspar overgrowths, or authigenic albite (Figures 7(i), 7(j), 8(b), 8(c), and 9(f)) and are commonly juxtaposed with some of calcite cements (Figures 7(k), 8(c), and 8(d)).

Authigenic quartz has low contents, generally less than 3%<sub>WRV</sub>. Quartz cements occur as overgrowths on detrital quartz grains (Figures 7(c), 7(i), 8(a), and 9(g)), underlain by chlorite coats (Figure 7(c)) and enclosed by calcite and sulfate cements (Figures 7(i) and 8(a)). The contents of albite cements are less than 2%<sub>WRV</sub>. Albite pore fills and overgrowths occur. Pore-filling albite crystals are euhedral tabular and prismatic-shaped and are underlain by chlorite coats and hematite rims and engulfed by calcite and sulfate cements

TABLE 1: Point count data summary and sample petrophysical properties. Petrofacies A: ductile lithic-rich sandstone; petrofacies B: calcite tightly cemented sandstone; petrofacies C: permeable reservoir sandstone.

Well	Sample depth (m)	Reservoir properties (class)	Interpretated petrofacies	Core measurement			Thin section porosity (%)			Textural characteristic			Detrital grains (%)			
				Total porosity (%)	Permeability (mD)	Secondary	Total	Primary	Secondary	Median grain size (mm)	Roundness (class)	Sorting (class)	Quartz	K-Feldspar	Plagioclase	Volcanic rock fragment
D-1	4837.5	Fluorescence	C	8.6	2.09		3.3	2.0	1.3		SA-SR	M	18.6	5.0	13.5	33.4
D-1	4939.73	No show	A	3.5	0.04						SA-SR	M	14.0	6.9	14.7	40.5
D-1	4959.8	No show	A	4.5	0.12						SA-SR	M	11.7	4.5	15.0	42.3
D-1	5299.52	No show	A	5.1	0.07		0.5		0.5		SA-SR	M	12.8	6.0	15.7	40.0
D-1	5305.47	No show	A	6.3	0.09						SA-SR	G	13.0	7.3	13.0	40.5
D-2	4423.2	Fluorescence	C	11.8	0.82		4.0	2.3	1.7		SA-SR	M-G	20.5	4.4	14.0	35.9
D-2	4429.45	Fluorescence	C	14.4	1.70		5.4	4.4	1.0		SA-SR	M-G	21.9	3.0	13.1	33.0
D-3	5506.5	Fluorescence	C	9.2	1.32		1.8	1.3	0.5		SA-SR	G	17.0	7.2	16.3	34.0
D-3	5510.9	Fluorescence	C	11.4	2.31		2.0	1.5	0.5		SA-SR	G	19.4	7.0	14.0	35.3
D-3	5542.8	No show	A	6.3	0.18		0.5		0.5		SA-SR	M	15.2	8.0	16.3	38.0
D-6	3970.9	Oil stain	C	14.9	1.83		8.7	6.3	2.4		SA-SR	G	17.0	5.8	15.0	33.6
D-6	3971.7	No show	B	4.5	0.03						SA-SR	G	18.4	6.0	15.7	30.5
D-6	3974.2	No show	B	4.3	0.06						SA-SR	G	17.0	7.3	10.2	32.0
D-6	4257.35	Fluorescence	C	13.6	5.16		6.0	4.0	2.0		SA-SR	G	18.5	7.0	13.5	35.0
D-6	4258.85	Fluorescence	C	11.7	2.79		7.5	4.5	3.0		SA-SR	G	18.5	6.0	14.0	33.8
D-6	4453.9	No show	A	5.3	0.15						SA-SR	G	14.7	5.8	15.0	39.4
D-6	4460.8	No show	A	4.5	0.09						SA-SR	M	12.6	3.0	13.8	42.4
D-7	4133.6	Fluorescence	C	10.3	0.57		3.3	2.3	1.0		SA-SR	M-G	19.2	7.0	15.0	36.5
D-7	4134.03	Fluorescence	C	12.2	1.66		5.2	3.7	1.5		SA-SR	M-G	18.0	6.4	16.7	34.7
D-7	4137.25	Fluorescence	C	15.9	11.50		6.2	5.0	1.2		SA-SR	M	21.5	7.0	13.7	35.0
D-7	4138.03	Fluorescence	C	14.7	3.82		5.3	4.8	0.5		SA-SR	M-G	20.9	3.0	15.9	34.8
D-7	4514.65	Fluorescence	C	12.5	0.95		7.1	5.1	2.0		SA-SR	G	18.8	6.0	14.3	36.0
D-7	4515	No show	B	3.5	0.04						SA-SR	G	17.9	5.5	10.0	31.7
D-7	4515.8	Fluorescence	C	12.9	1.83		8.0	6.0	2.0		SA-SR	G	15.0	7.0	11.0	38.0
D-8	4425.1	Fluorescence	C	13.7	5.42		7.5	5.0	2.5		SA-SR	M-G	21.0	8.7	14.7	29.7
D-8	4545	Fluorescence	C	12.9	1.33		5.0	3.5	1.5		SA-SR	G	19.0	7.4	15.0	32.5
D-8	4548.5	No show	B	3.3	0.05						SA-SR	M-G	16.5	7.0	8.0	32.4
D-8	4548.6	Fluorescence	C	13.0	1.86		6.0	4.0	2.0		SA-SR	G	17.4	6.0	13.6	34.0

TABLE 1: Continued.

Well	Sample depth (m)	Metamorphic rock fragment	Detrital grains (%)				Ductile grain	Detrital matrix	Albite	Quartz overgrowth	Authigenic minerals (%)						
			Sedimentary rock fragment	Micas	Chert	Ductile grain					Chlorite	Calcite	Analcime	Anhydrite	Barite	Pyrite	
D-1	4837.5	10.1			1.0	13.8	1.5	2.0	1.0		1.0	3.5	4.0	2.0			
D-1	4939.73	13.3		2.0		32.0	6.3									2.3	
D-1	4959.8	13.0	1.0	1.5		35.0	8.0									3.0	
D-1	5299.52	12.3	1.0	2.0		28.3	7.5				tr.					1.7	
D-1	5305.47	12.5		2.2		25.7	8.0									3.0	
D-2	4423.2	13.0	0.5			19.1	2.2				4.0		tr.				
D-2	4429.45	15.3				18.8	3.5	0.5			3.0		0.5				
D-3	5506.5	10.5		0.7	0.5	16.7	2.3		2.0			tr.	0.5				
D-3	5510.9	11.7				15.2	1.5		1.8				7.0				
D-3	5542.8	15.7		0.8		21.9	5.0						5.0	0.3			
D-6	3970.9	8.3			0.3	13.5	1.0		1.5		2.2	5.0	tr.	1.6		1.0	
D-6	3971.7	9.4				5.0	0.5				20.0						
D-6	3974.2	11.5				3.0	1.0				22.0						
D-6	4257.35	9.0				14.9	1.8				6.0	2.7	tr.	0.5			
D-6	4258.85	11.9				13.1			1.0		6.8	0.5					
D-6	4453.9	13.1	1.5	2.0		25.1	5.7				tr.					2.8	
D-6	4460.8	14.2	1.0	2.3		40.0	7.7									3.0	
D-7	4133.6	12.0				20.0	3.4		1.0		0.5	2.0					
D-7	4134.03	14.0		0.5		19.0	2.0		0.5		0.5	1.5					
D-7	4137.25	12.0	0.5		0.5	15.6	1.5				0.7	1.0	tr.				
D-7	4138.03	15.6	1.0			16.2	1.0				0.5	2.0					
D-7	4514.65	10.3		0.5		18.1	2.0	1.0			0.3	1.0					
D-7	4515	11.9				4.0					23.0						
D-7	4515.8	12.5			1.0	18.9	3.0				3.5	0.5					
D-8	4425.1	15.0				12.7		0.5				0.5					
D-8	4545	14.5	1.0			19.8	2.0		2.4		1.2	2.0					
D-8	4548.5	10.8		0.5		5.0					24.8						
D-8	4548.6	15.5				15.0	3.2	0.5				0.5	tr.				

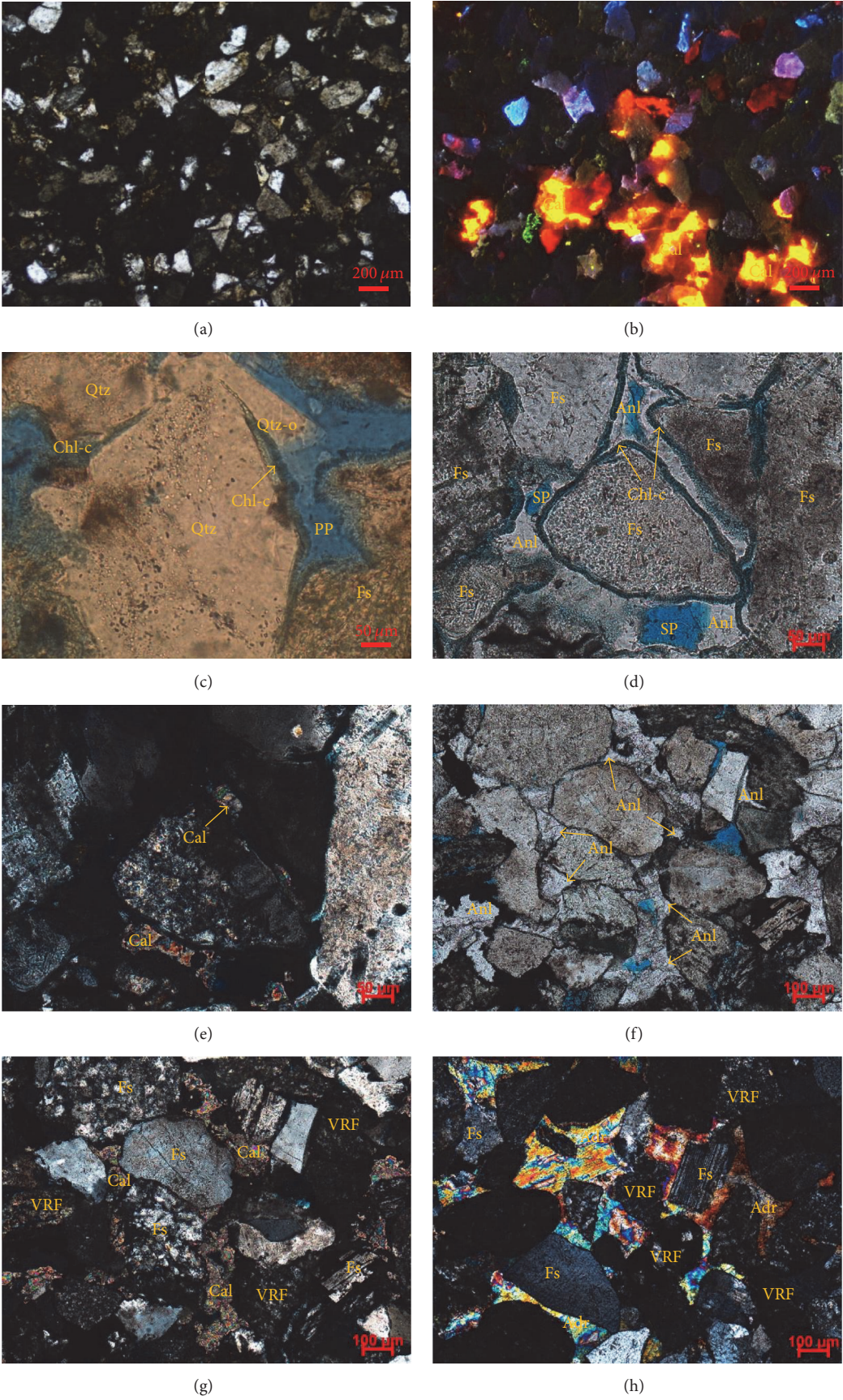


FIGURE 7: Continued.

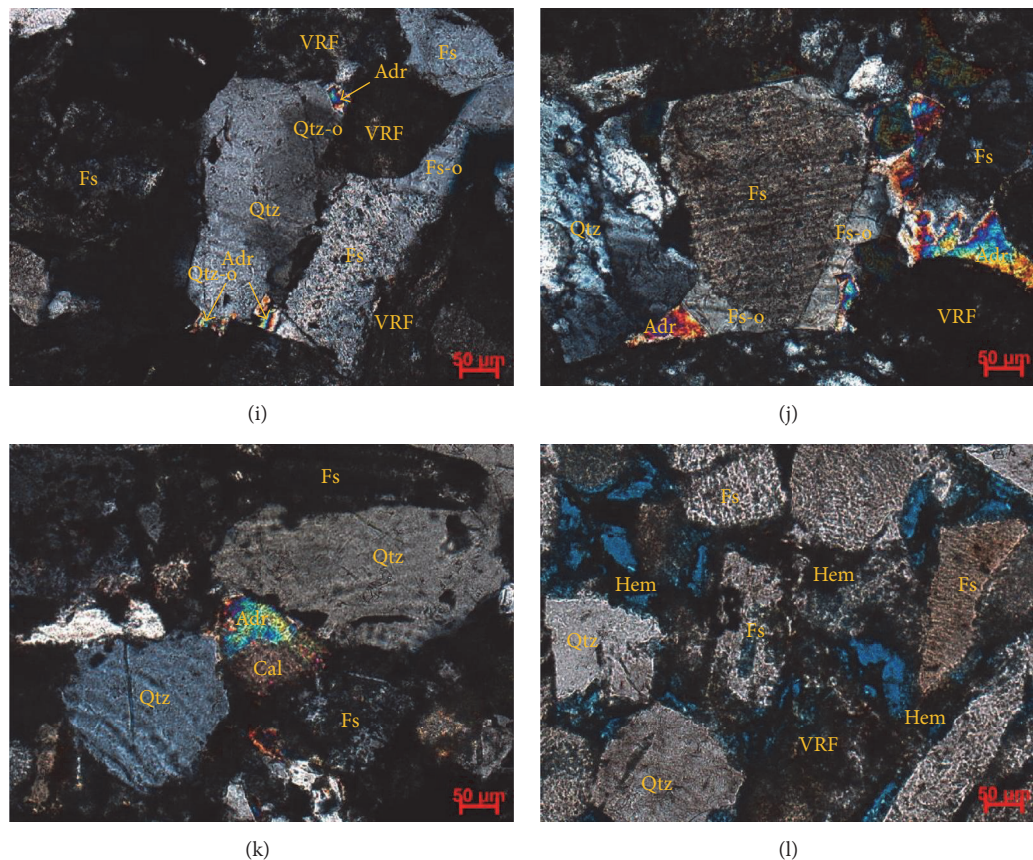


FIGURE 7: Thin section images of sandstones (pore space is highlighted in blue). ((a) and (b)) Sample 4133.6 m, well D-7, PPL, and CL, respectively: calcite displaying a rather patchy and local cementation and having yellow to orange luminescence. (c) Sample 4429.45 m, well D-2, and PPL: quartz overgrowth precipitated on a detrital quartz grain where there is a break in the continuity of the chlorite coat. ((d) and (e)) Sample 4514.65 m, well D-7, PPL, and XPL: partially dissolved analcime postdating chlorite coats and replaced by calcite. ((f) and (g)) Sample 4258.85 m, well D-6, PPL, and XPL: partially dissolved analcime replaced by calcite. (h) Sample 4837.5 m, well D-1, and XPL: anhydrite cements filling pores in patches and locally replacing detrital grains. (i) Sample 5506.5 m, well D-3, and XPL: quartz overgrowths engulfed by anhydrite. (j) Sample 4837.5 m, well D-1, and XPL: feldspar overgrowths overlain by anhydrite. (k) Sample 5506.5 m, well D-3, and XPL: anhydrite cements commonly juxtaposed with some of calcite cements. (l) Sample 4133.6 m, well D-7, and PPL: hematite occurring as very thin rims around detrital grains. Framework grains: quartz (Qtz), feldspar (Fs), volcanic rock fragment (VRF); cement: calcite (Cal), chlorite coat (Chl-c), analcime (Anl), anhydrite (Adr), quartz overgrowth (Qtz-o), feldspar overgrowth (Fs-o), and hematite (Hem); primary porosity (PP) and secondary porosity (SP).

(Figures 8(b), 8(c), 9(c), 9(d), and 9(f)). The albite crystals, in some samples, have been observed to be closely associated with analcime and illite/smectite clays (Figure 9(d)).

Hematite occurs in trace amounts as very thin rims around detrital grains (Figures 7(l) and 8(c)). The grain-rimming hematite is generally absent at points of grain-to-grain contact, indicating that it is not syndepositional precipitation. Precipitation of the iron oxides likely occurred from general phreatic oxidation during the late Jurassic uplift [36].

**4.4. Pore Bitumens and Fluid Inclusions.** Oil shows are localized in cores, indicating the heterogeneous nature of oil migration in a reservoir. Ductile lithic-rich sandstones and tightly calcite-cemented sandstones do not contain oil shows in cores, pore bitumens, or oil-filled fluid inclusions in thin sections. This suggests that oil charge never occurred in these sandstones. By contrast, permeable reservoir sandstones

generally have oil shows in cores. Pore bitumens and oil-filled inclusions are present, indicating that oil charged the sandstones. Therefore, permeable reservoir sandstones have been targeted for study of pore bitumens and fluid inclusions.

**4.4.1. Petrography.** Abundant pore-free oils and solid bitumens have been found. In contrast to nonfluorescent solid bitumens, pore-free oils have yellow and blue-white fluorescence under UV light. The yellow fluorescence dominates. These pore bitumens mostly fill pores and rare feldspar cleavage planes (Figures 10(a)–10(h)). Oil-stained chlorite coats display a yellow fluorescence (Figures 10(a) and 10(b)), indicating that oil charge postdated the precipitation of chlorite coats.

With respect to oil-filled inclusions, two fluorescence colors, yellow and blue-white, have been observed. Similar to pore bitumens, the dominant fluorescence color is

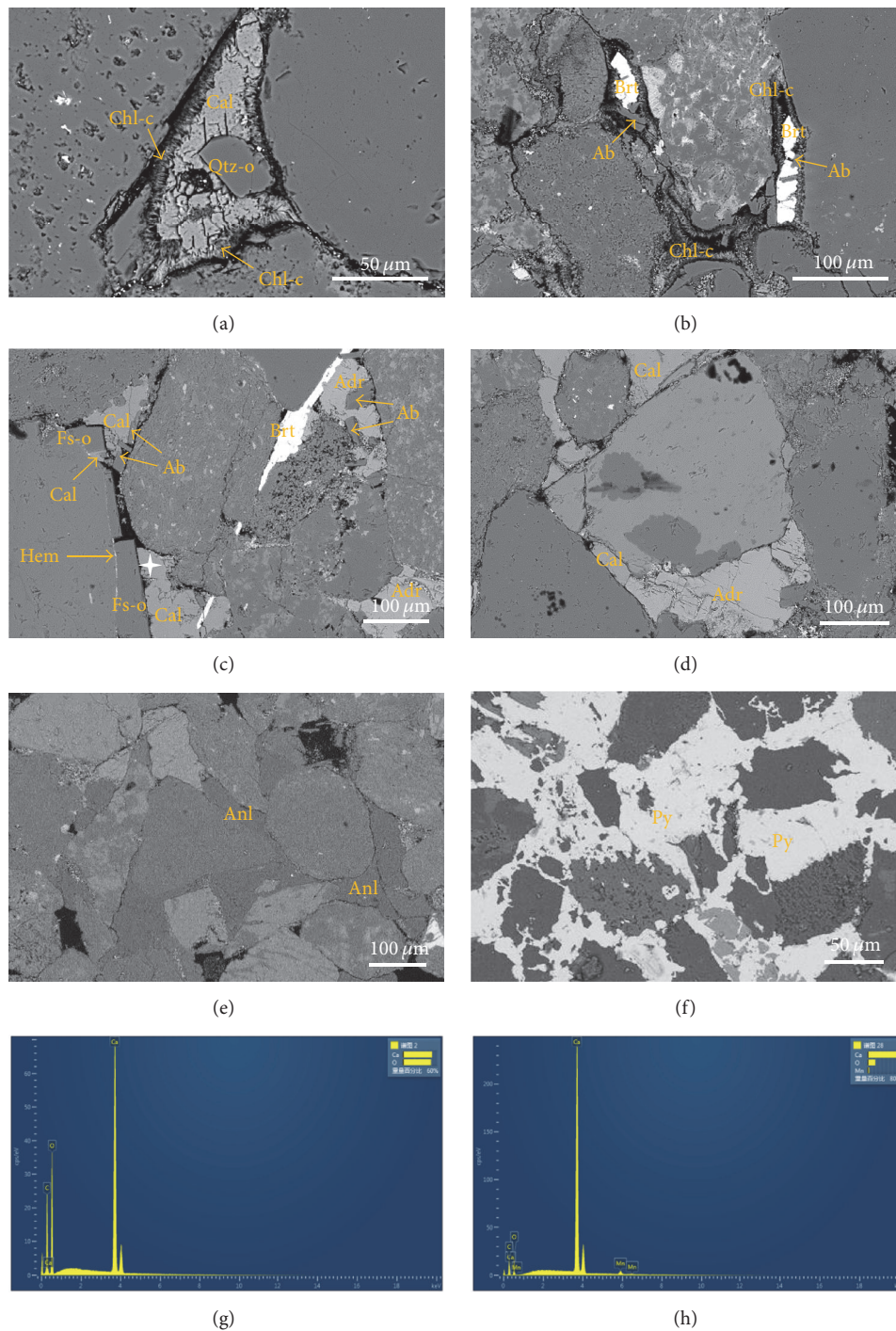


FIGURE 8: SEM BSE images of sandstones. (a) Sample 4514.65 m, well D-7: calcite postdating grain-coating chlorite and quartz overgrowths. (b) Sample 4514.65 m, well D-7: chlorite coats and authigenic albite engulfed by barite. (c) Sample 4837.5 m, well D-1: authigenic albite or feldspar overgrowths postdating hematite rims in contact with detrital grains and engulfed by calcite and anhydrite that are possibly synchronous with barite. (d) Sample 4837.5 m, well D-1: calcite possibly simultaneous with anhydrite. (e) Sample 3970.9 m, well D-6: analcime filling intergranular pores. (f) Sample 5299.52 m, well D-1: pyrite filling intergranular pores and replacing detrital grains locally. (g) Calcite having homogeneous almost 100%  $\text{CaCO}_3$ ; the location refers to Figure 9(a). (h) Calcite containing Mn; the location refers to Figure 8(c). Cement: calcite (Cal), chlorite coat (Chl-c), analcime (Anl), anhydrite (Adr), barite (Brt), quartz overgrowth (Qtz-o), feldspar overgrowth (Fs-o), albite (Ab), pyrite (Py), and hematite (Hem).

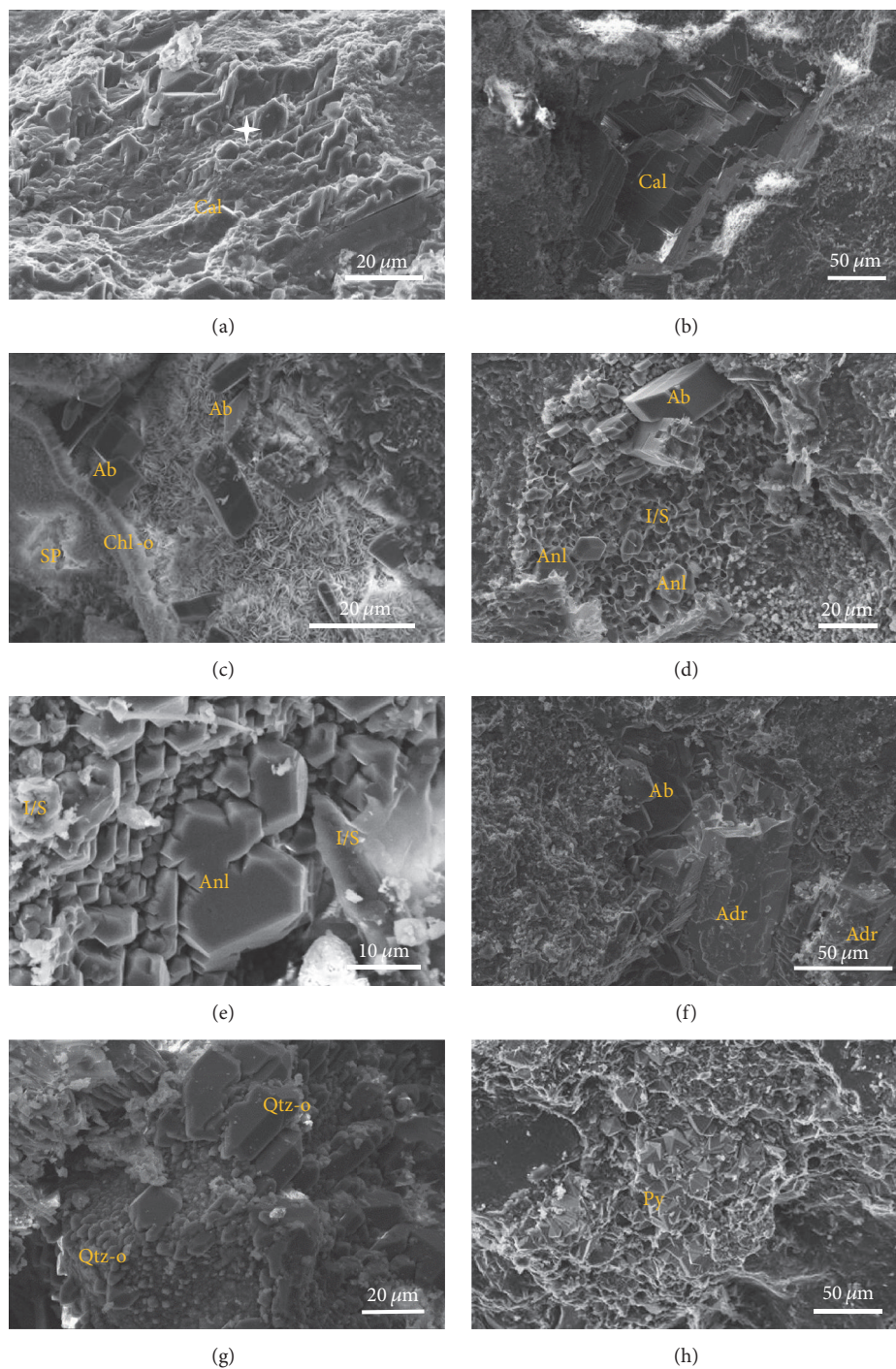


FIGURE 9: SEM images of sandstones. (a) Sample 4515 m, well D-7: calcite composed mostly of anhedral calcite crystals. (b) Sample 4514.65 m, well D-7: calcite filling pore in patches. (c) Sample 4548.6 m, well D-8: secondary porosity created by complete dissolution of a detrital grain and authigenic albite growing over chlorite coats. Note that relict chlorite coats remain. (d) Sample 4837.5 m, well D-1: analcime and authigenic albite growing over illite/smectite clays. (e) Sample 3970.9 m, well D-6: analcime associated with illite/smectite clays. (f) Sample 5510.9 m, well D-3: anhydrite growing over authigenic albite. (g) Sample 3970.9 m, well D-6: quartz overgrowth. (h) Sample 5299.52 m, well D-1: pyrite filling intergranular pores. Cement: calcite (Cal), chlorite coat (Chl-c), analcime (Anl), anhydrite (Adr), quartz overgrowth (Qtz-o), albite (Ab), and pyrite (Py).

TABLE 2: Stable carbon and oxygen isotopic compositions of calcite cements in the Toutunhe Formation.

Well	Depth (m)	Calcite type	$\delta^{13}\text{C}$ (VPDB)	$\delta^{18}\text{O}$ (VPDB)
D-1	4837.5	Late	-6.0	-18.0
D-2	4423.2	Late	-8.4	-16.4
D-3	5506.5	Late	-6.7	-18.0
D-6	3970.9	Late	-7.8	-18.9
D-6	3971.7	Early	-3.1	-13.0
D-6	3974.2	Early	-4.3	-13.4
D-6	4258.85	Late	-8.4	-17.8
D-7	4133.6	Late	-6.8	-17.9
D-7	4138.03	Late	-7.4	-19.0
D-7	4514.65	Late	-5.9	-18.3
D-7	4515	Early	-4.1	-12.9
D-8	4545	Late	-6.5	-17.4
D-8	4548.5	Early	-1.4	-11.2
D-8	4548.6	Late	-8.3	-16.8

yellow. Oil inclusions are subspherical and elongated in shape, and some irregularly shaped varieties also occur. Oil inclusions are mostly two-phase inclusions containing less than 30 vol.% vapor at 20°C. Three-phase inclusions that contain a hydrocarbon liquid phase (or nonfluorescent solid bitumen), an aqueous liquid phase, and a vapor phase are present occasionally. Most oil inclusions occur within healed microfractures confined to individual quartz grains (Figures 10(i)–10(l)). These oil inclusions generally range in diameter from 3 to 5  $\mu\text{m}$ . In such a case, it is readily easy to find the coexisting aqueous inclusions. A small proportion of oil inclusions also lie in cements (Figures 10(m) and 10(n)), indicating that they were trapped at the time of the precipitation or recrystallization. No oil inclusions have been observed in syntaxial quartz overgrowths, suggesting that quartz precipitated prior to oil arrival. Oil inclusions and associated aqueous inclusions in calcite cements are smaller than within healed microfractures, often less than 3  $\mu\text{m}$  in diameter.

**4.4.2. Fluid Inclusion Microthermometry.** Oil inclusions and aqueous inclusions in calcite cements are too small to reliably measure their homogenization temperatures, and some of the inclusions appear to have stretched or decrepitated. The aqueous inclusions that are coeval with oil inclusions hosted within quartz microfractures were selected for homogenization temperature measurement. A total of seventy-two homogenization temperature measurements were obtained from twenty-four fluid inclusion assemblages (Table 3). The homogenization temperature values display a bimodal distribution pattern: one population ranges from 80 to 100°C, and the other falls between 110 and 120°C (Figure 11). Noteworthy is the fact that the homogenization temperature values of the aqueous inclusions that are coeval with blue-white fluorescing oil inclusions are marginally lower than those associated with yellow fluorescing ones.

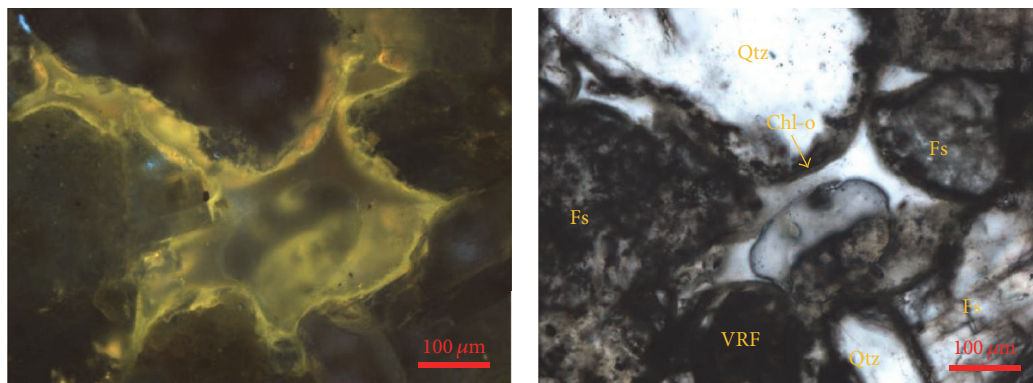
## 5. Discussion

**5.1. Differential Diagenetic Sequences of Sandstones.** Fluid inclusion data indicate that two episodes of oil charge took place in permeable reservoir sandstones in the Toutunhe Formation. Different episodes of oil emplacement, here, can be used to distinguish between preoil minerals that formed prior to oil charge, oil-stage minerals whose formation either resulted directly from the charge process or overlapped at least partly in time, and postoil minerals that precipitated after oil arrival in the reservoir. In terms of hydrocarbon migration and accumulation, such a partition is of great significance for understanding the temporal and spatial characteristics of rock-fluid interactions and assessing reservoir quality during the critical period of hydrocarbon charge [17, 18].

Based on textural relationships between authigenic minerals themselves and pore bitumens or oil inclusions, a general paragenetic sequence is presented in Figure 12. The dominant diagenetic features before the first oil charge in permeable reservoir sandstones were mechanical compaction, dissolution of detrital grains, and the formation of hematite rims, chlorite coats, illite/smectite clay, analcime, authigenic albite, and quartz overgrowths. The earliest formed minerals were chlorite coats and hematite rims, which were followed by analcime, authigenic albite, and quartz overgrowths. Most of these diagenetic alterations were controlled by the interaction of subaerial meteoric water with unstable volcanic rock fragments and detrital feldspars. Synchronous with the first oil arrival, quartz cementation was retarded. Anhydrite, barite, and calcite precipitated. When late oil charge occurred, calcite cementation continued. These reactions were controlled by high temperatures and increasingly complicated pore water chemistry arising from the interactions between hydrocarbon fluids and rocks as burial progressed.

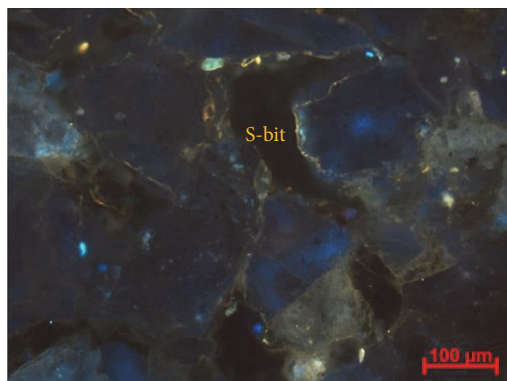
In contrast to permeable reservoir sandstones, the compaction of easily deformed, clay-rich grains and associated authigenic clays dominated ductile lithic-rich sandstones before the first oil emplacement. Trace amounts of pyrite precipitated at this period. The ductile compaction continued but reduced with increasing burial. Almost no fluids entered the sandstones later. For tightly calcite-cemented sandstones, calcite cements significantly filled and occluded intergranular pores prior to the first oil arrival. Similar to ductile lithic-rich sandstones, no other diagenetic reactions occurred within the sandstones later.

**5.2. Texture-Dependent Mechanical Compaction.** The mechanical compaction of lithic sandstones is controlled by the amount and type of lithic fragments [11, 37, 38]. Volcanic rock fragments are the dominant framework component of sandstones in the Toutunhe Formation and are commonly altered. Breakdown of volcanic rock fragments initiated probably during transportation or weathering [38, 39] and continued during burial. When altered by weathering or diagenesis, volcanic rock fragments are extremely ductile [37]. Therefore, the altered volcanic rock fragments are the most important contributor to the mechanical compaction of the sandstones. Upon burial, these ductile grains were deformed between

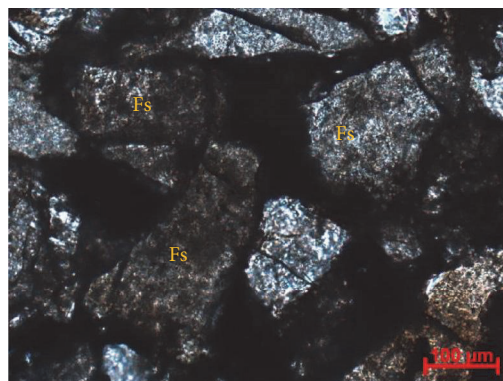


(a)

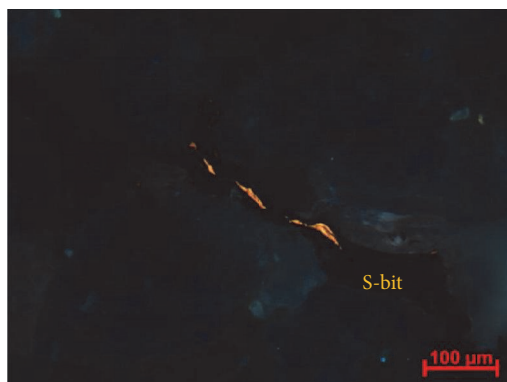
(b)



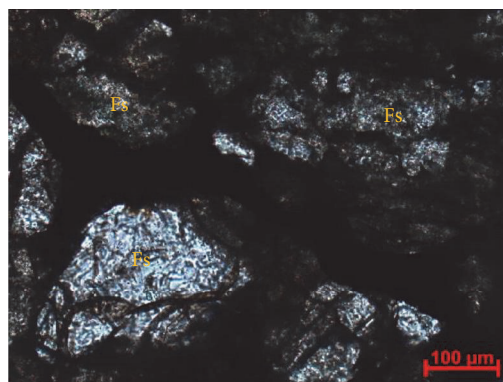
(c)



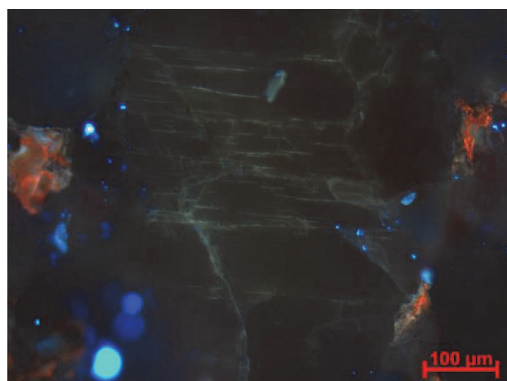
(d)



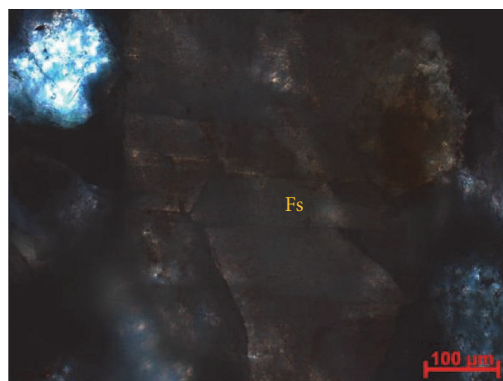
(e)



(f)



(g)



(h)

FIGURE 10: Continued.

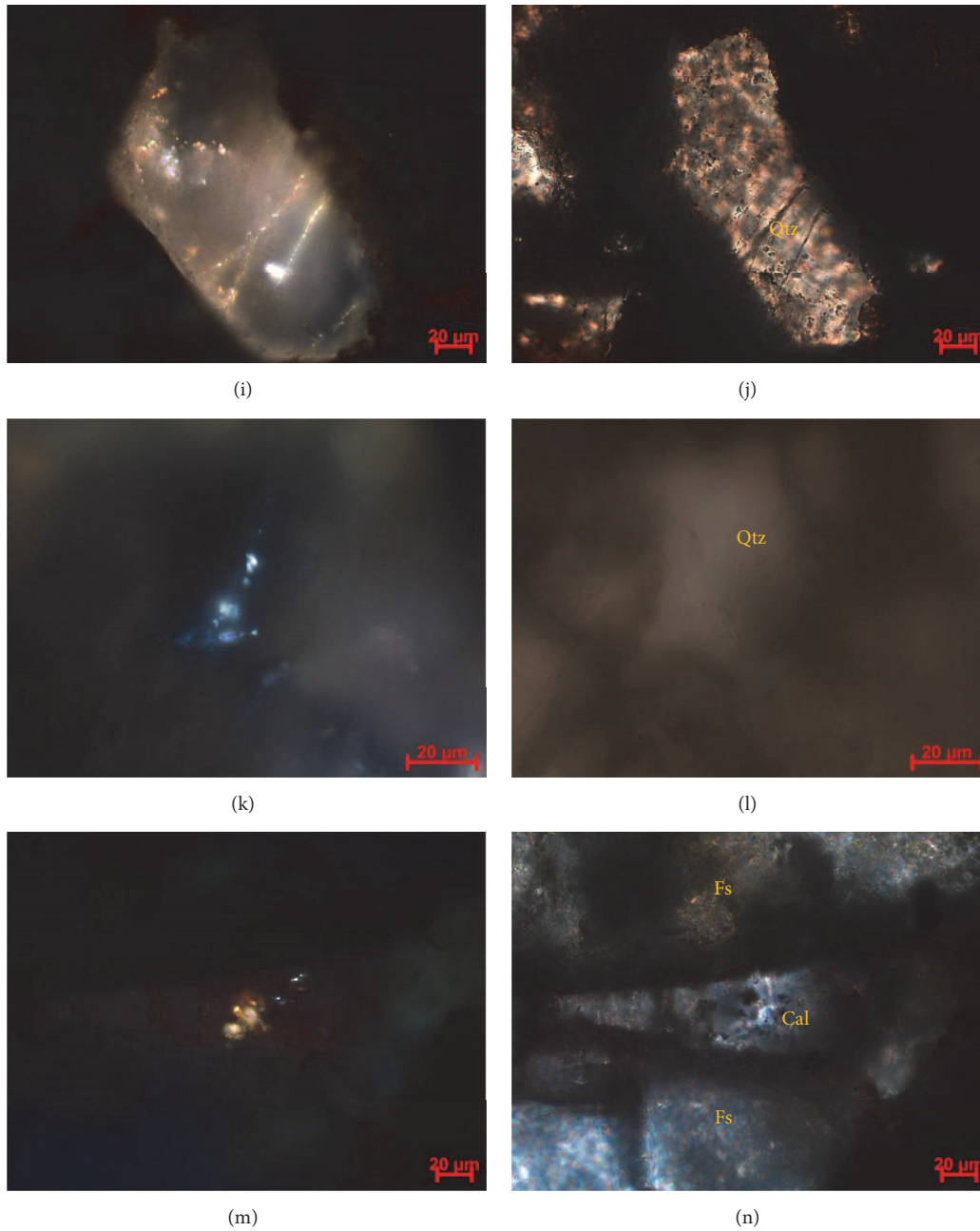


FIGURE 10: Thin section images of pore bitumens and oil-filled inclusions under transmitted light (a, c, e, g, i, k, m) and UV light (b, d, f, h, j, l, n). ((a) and (b)) Sample 4514.65 m, well D-7: yellow fluorescing oils absorbed over chlorite coats. ((c) and (d)) Sample 4548.6 m, well D-8: pore solid bitumens with yellow fluorescing oils absorbed on walls. ((e) and (f)) Sample 4548.6 m, well D-8: intergranular pore filled with nonfluorescent solid bitumens with yellow fluorescing oils absorbed inside. ((g) and (h)) Sample 4138.03 m, well D-7: blue-white fluorescing oils occurring within cleavage planes of detrital feldspars. ((i) and (j)) Sample 4837.5 m, well D-1: yellow fluorescing oil inclusions occurring along healed microfractures terminating at detrital quartz margin. ((k) and (l)) Sample 3970.9 m, well D-6: blue-white fluorescing oil inclusions healed microfractures in detrital quart. ((m) and (n)) Sample 4258.85 m, well D-6: yellow fluorescing oil inclusions in calcite cements. Framework grains: quartz (Qtz), feldspar (Fs), and volcanic rock fragment (VRF); cement: calcite (Cal) and chlorite coat (Chl-c); solid bitumen (S-bit).

rigid detrital grains. They became smeared over the surfaces of the rigid grains and were squeezed into pore throats leading to significant porosity loss (Figures 6(a)–6(d)). A moderate inverse correlation between porosity and permeability and ductile grain content is presented after excluding

the tightly calcite-cemented sandstone samples from the plots in Figure 13, indicating that the ductile compaction is a major cause of porosity loss in the sandstones. Ductile lithic-rich sandstones containing ductile grains in excess of 20%<sub>WRV</sub> have an average porosity of 5%, ranging from 3.5 to 6.3%,

TABLE 3: Summary of microthermometry of fluid inclusions.

Well	Sample depth (m)	Reservoir properties (class)	Number of fluid inclusions assemblages	Range of homogenization temperature (°C)
D-1	4837.5	Fluorescence	3	90.7–107.3 (7)
D-2	4429.45	Fluorescence	2	87.5–98.7 (2)
D-3	5510.9	Fluorescence	1	84.3–95.1 (3)
D-6	3970.9	Fluorescence	2	86.6–101.5 (9)
D-6	4258.85	Fluorescence	1	117.2–121.6 (5)
D-7	4133.6	Fluorescence	4	82.3–124.7 (15)
D-7	4137.25	Fluorescence	1	83.2–93.2 (2)
D-7	4514.65	Fluorescence	4	81.6–112.4 (15)
D-8	4545	Fluorescence	6	83.2–113.3 (14)

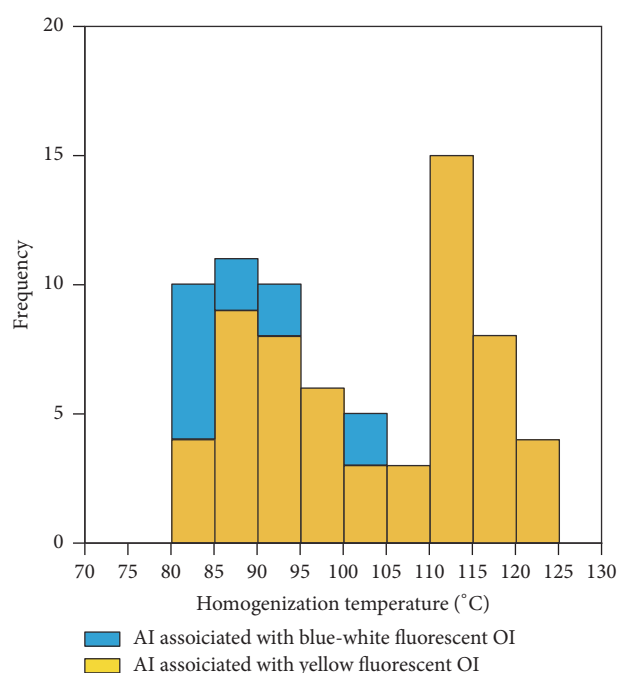


FIGURE 11: Histograms of homogenization temperatures for aqueous inclusions that are coeval with oil inclusions. Aqueous inclusion (AI) and oil inclusion (OI).

and an average permeability of 0.10 mD, ranging from 0.04 to 0.18 mD. In comparison, permeable reservoir sandstones with less than 20%<sub>WRV</sub> ductile grain content have an average porosity of 13%, ranging from 8.6 to 15.9%, and an average permeability of 2.76 mD, ranging from 0.57 to 11.50 mD. A threshold value of 20% abundance seems to apply to these ductile grains.

Notably, it is clear from Figure 14 that the ductile grain abundance has a rough negative correlation with grain size. Most of the finer-grained sandstones (ripple cross-laminated) tend to have greater amounts of ductile grains and hence lower porosity and poorer reservoir properties. This suggests that depositional facies and lithofacies were important for predicting ductile components [11, 15, 38].

### 5.3. Origins of Authigenic Minerals and Their Effects on Reservoir Quality

**5.3.1. Chlorite.** Chlorite precursor phases and source and transportation of Fe<sup>2+</sup> ions, almost entirely controlled by paleoclimate, paleosoil, and river system development, significantly affect the formation of chlorite coats [40]. Volcanic rock fragments are the most likely source of Fe<sup>2+</sup> and Mg<sup>2+</sup> ions for chlorite coats in the Toutunhe Formation. Five out of seventeen permeable reservoir sandstone samples contain chlorite coats (Table 1), so, while not frequent, they indicate that chlorite coats nonuniformly precipitate in sandstone.

Chlorite coats on quartz grains can prevent pervasive cementation of quartz overgrowths by limiting nucleation sites and inhibit the occlusion of primary intergranular porosity in sandstones [41, 42]. Figure 7(c) illustrates that minor breaks in the continuity of chlorite coats on quartz grains allow precipitation of quartz overgrowth. This is a compelling argument for the preservation of primary porosity by chlorite coats. The sandstones that contain chlorite coats are expected to have relatively high porosity values with a given composition, texture, and burial/temperature. The role of chlorite coats in the preservation of primary porosity, however, is not that important in the Toutunhe Formation. Clay grain coats have no effect on the precipitation of cements other than quartz [42]. Because of the mineralogically immature nature of the sandstones, quartz precipitation is almost volumetrically negligible in the Toutunhe Formation. Therefore, chlorite coats have little impact on primary porosity preservation.

**5.3.2. Analcime.** The mechanisms reported in the literature which may cause the formation of authigenic analcime in sandstones include direct precipitation from pore water or lake water, reaction of saline and alkaline pore water with detrital silicates, formation from a gel, and alteration of precursor zeolites [43]. In the Toutunhe Formation, no evidence for a precursor zeolite other than analcime has been found. The precipitation of analcime from sodium aluminosilicate gels is generally considered to have been associated with hydrothermal alterations [44]. No hydrothermal gels or other types of gels have been observed. Analcime cements



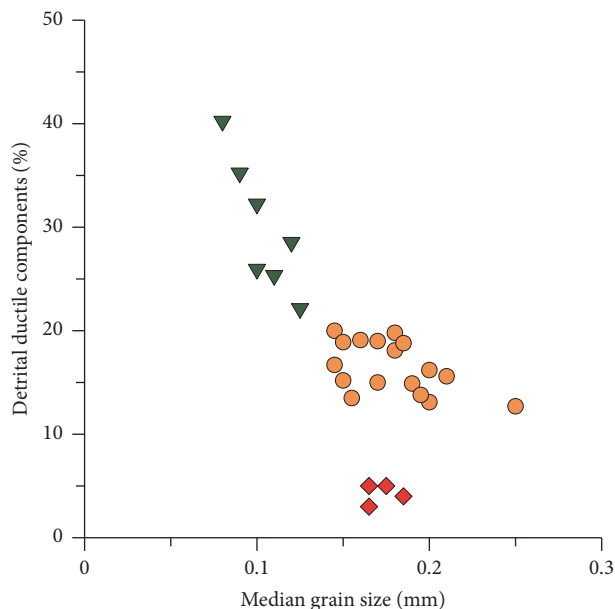


FIGURE 14: Cross-plot of median grain size versus ductile grain content showing that medium grain size is critical to ductile grain content. Green triangles denote ductile lithic-rich sandstone, red rhombi denote calcite tightly cemented sandstone, and orange circles denote permeable reservoir sandstone.

negative  $\delta^{13}\text{C}$  values are probably related to a significant carbon contribution from soil-derived bicarbonate or oxidation of organic matter during early diagenesis. The cementation of early calcite, especially in completely cemented sandstones, causes substantial porosity loss. As discussed previously, the calcite forms discrete and tightly cemented concretions in the relatively coarse-grained part of a graded sand bed. This is consistent with an outcrop study from Jiao et al. [49] which indicated that the early calcite concretions occur commonly in the relatively coarse-grained sandstones at the central part of a fining-upward delta distributary channel sequence. They indicated that these concretions, in some localities, are up to 4 m in size and are heterogeneously distributed.

With respect to late calcite cements, the negative  $\delta^{13}\text{C}$  signature suggests that they were related to the supply of  $\text{CO}_2$  derived from decarboxylation of organic matter and  $\text{Ca}^{2+}$  ions in the formation water. The lower  $\delta^{18}\text{O}$  values are related to increasing temperatures and fluid-rock interactions during burial diagenesis. The presence of oil inclusions (Figures 10(m) and 10(n)) suggests that, during the formation of the late calcite, the ratio of hydrocarbons to aqueous fluids was high. In addition, the late calcite cements show slight enrichment in  $\text{Mn}^{2+}$  ions (Figure 6(d)). Cao et al. [50] proposed that  $\text{Mn}^{2+}$  is most likely derived from volcanic materials in the Junggar Basin and that the enrichment of  $\text{Mn}^{2+}$  ions in the pore water is closely associated with the dissolution of volcanic materials by “hot” hydrocarbon fluids in the deep Permian source rocks rather than volcanic fragments themselves in shallow sandstones. Therefore, we conclude that some of the late calcite precipitated from a  $\text{Mn}^{2+}$ -rich

hydrocarbon fluid that was introduced from depths into the Toutunhe Formation. It is fair to say that an episode of oil charge, ultimately sourced from the Permian source facies in the deep parts of the Fukang Sag, occurred in the Toutunhe Formation. This is entirely consistent with the analyses of biomarker compositions and geochemical origin of crude oils in the Toutunhe Formation by Hao et al. [51] who indicated that the oils were derived from the Permian and Jurassic source facies in the Toutunhe Formation.

**5.3.4. Anhydrite and Barite.** A source of  $\text{SO}_4^{2-}$  and  $\text{Ba}^{2+}$  ions is required for sulphate cements. These are considered to be outside the Toutunhe Formation. The Permian source rocks contain thin seams of gypsum [52]. These gypsum deposits can spatially provide  $\text{SO}_4^{2-}$  ions for the sulphate cements. A possible source for  $\text{Ba}^{2+}$  ions is the underlying Middle-Lower Jurassic coals [53, 54]. Both anhydrite and barite precipitated during late diagenesis, possibly temporally responding to the northeast-southwest trending tilting of the Fukang Sag due to the uplift of the Bogda Mountains since the Paleogene [24]. We tentatively suggest that a great proportion of deep-seated hydrocarbons that were derived from the Permian source facies possibly migrated up along faults from depths and leaked into the Toutunhe Formation. Synchronous with the up-fault migration of deep hydrocarbons,  $\text{SO}_4^{2-}$  and  $\text{Ba}^{2+}$  invaded the Toutunhe Formation and were precipitated as barite and anhydrite. Although no oil inclusions have been found in the sulphate cements because of limited thin sections for fluid inclusion study, petrographic evidence indicates that barite and anhydrite cements are possibly simultaneous with late calcite, which contain oil inclusions. Thus the precipitation of the sulphate cements may be lined to oil charge. This further confirms that there was once an episode of charge in the Toutunhe Formation, ultimately sourced from the Permian source facies. The preferential occurrence of the sulphate cements in relatively coarse-grained sandstones may be due to the easier movement of fluids through these sandstones. These sulphate cements generally reduce porosity and permeability but do not completely prevent late flow as they occur in localized patchy areas similar to late calcite.

**5.4. Timing of Secondary Dissolution.** Determining the timing of secondary dissolution is difficult. Detrital feldspars and volcanic rock fragments are very unstable during near-surface meteoric water flushing [55]. However, the early diagenetic analcime cements, in some samples, have been observed to be partly dissolved (Figures 7(d)–7(g)). Additionally, relic chlorite coats represent delicate textures (Figure 9(c)), suggesting late dissolution. This is because such fabric, if formed relatively early, should have been destroyed or reoccupied by later minerals [56]. Therefore, secondary dissolution most likely continued throughout burial.

A geochemically nearly closed system for burial diagenesis has been accepted [42, 57]. In such a system below the reach of freshwater, the pore water flow is limited and the bulk chemical composition of the sediments does not change significantly. The idea that significant net increases in porosity

may occur during burial diagenesis due to leaching of framework grains by organic acids has mostly been problematic [42, 57]. Furthermore, organic acid quantities are insufficient to significantly influence bulk rock-water equilibria, albeit being present extensively in oilfield formation water [58, 59]. Organic acids may also be neutralized during expelling from source rocks and migration in sandstones [57]. Therefore, we concluded that most of secondary porosity formed by meteoric water influx through the sandstones at shallow burials.

*5.5. Effect of Diagenetic Heterogeneity on Fluid Flow.* The two sandstone petrofacies, highly compacted, ductile lithic-rich, very fine-grained sandstones, and tightly calcite-cemented sandstones may create permeability barriers or baffles embedded in porous reservoir sandstones. For reasons discussed previously, these permeability barriers are of early diagenetic origin. Depositional environment and lithofacies and the pore water chemistry under near-surface conditions are all key parts in their formation and distribution. These barrier interbeds vary widely in the abundance and occurrence. If they are continuous over large areas in a reservoir, they have a significant effect on fluid flow [6, 19, 60].

Due to reservoir compartmentalization by the intersecting barrier interbeds, oil migration and accumulation in a reservoir are inevitably hindered. An invasion-percolation-based model of oil migration by Luo et al. [18, 19] indicated that oils migrate laterally through a larger fraction of a heterogeneous reservoir than a homogeneous one. Luo et al. [18, 19] thought that not all permeable reservoir compartments separated by the intersecting barrier interbeds act as the pathways for migration or trap for accumulation and a considerable portion of them are filled with formation water. Although the oil-water contact in individual permeable compartments is essentially horizontal, the blocking effect of the intersecting barrier interbeds causes the differences in the oil-water contact between compartments, resulting in an uneven oil-water contact at a reservoir scale. In the Toutunhe Formation, well testing shows that oil and water zones are commonly interbedded; there exists a complex oil-water relationship. Reservoir heterogeneity most likely gives a good explanation for the complex oil-water distribution in the Toutunhe Formation.

In addition, the intra-sand-body barrier interbeds may significantly increase the tortuosity of fluid flow and alter the sweep efficiency, affecting recovery during waterflooding [6, 60].

The study concentrated on reservoir heterogeneity at the core scale. The combination of outcrop study and subsurface data will be used to predict the regional distribution of both the ductile lithic-rich sandstones and tightly calcite-cemented sandstones and thus to characterize reservoir heterogeneity at the macroscale and higher hierarchies. This necessitates single-well heterogeneity characterization and interwell correlation of the area of interest, especially when cores are strictly limited for deep drilling. Therefore, well log responses to these barrier interbeds can be quantified at first. Our future work is to construct regional barrier interbed networks and modeling oil migration.

## 6. Conclusions

We emphasize that the evaluation of sandstone diagenetic heterogeneity requires systematic examinations of depositional environment and lithofacies that basically determine the primary texture and compositions of sandstones.

Five depositional facies associations of the sandstones have been distinguished based on core sections and well log data: single and stacked story meandering fluvial channel, delta distributary channel, distributary-mouth bar, interdistributary bay, and shore-shallow lacustrine facies association.

The Toutunhe Formation's sandstones consist mostly of feldspathic litharenite and litharenite. Grain size and the abundance of ductile-lithic sand grains are the most important primary detrital controls on diagenesis, porosity, and reservoir properties. These controls operate largely through their effect on mechanical compaction.

Three major sandstone petrofacies have been defined in the Toutunhe Formation. Ductile lithic-rich, very fine-grained sandstones, which occur in all facies associations, are dominated by compaction of easily deformed, clay-rich grains, resulting in a very rapid loss of porosity during burial. Tightly calcite-cemented sandstones occur commonly in the relatively coarse-grained lithofacies of a graded sand bed. By contrast, fine-grained permeable reservoir sandstones, deposited predominately in the fluvial channel, distributary channel, and distributary-mouth bar facies associations, contain relatively less abundant ductile-lithic grains. Various authigenic minerals are present in the relatively coarser-grained sandstone lithofacies with predominately a patchy texture. Chlorite coats only occur in the distributary channel and distributary-mouth bar facies. Analcime and illite/smectite clays are commonly found in the fluvial channel facies. Diagenesis progressed alternately with oil charge, and some diagenetic alterations and oil charge occurred simultaneously. Late diagenetic calcite and sulphate cements may have an indication for oil migration.

Highly compacted, ductile lithic-rich sandstones and tightly calcite-cemented sandstones can create permeability barriers embedded in a porous reservoir, resulting in heterogeneous flow.

## Disclosure

The authors accept full responsibility for the ideas and conclusions expressed in the manuscript.

## Conflicts of Interest

The authors declare that they have no conflicts of interest.

## Acknowledgments

This work was supported by the Strategic Priority Research Program of the Chinese Academy of Sciences (no. XDA14010202) and by the National Natural Science Foundation of China (no. 41372151). The authors are indebted to Mr. Tao Xu at the Shengli Oilfield Company, SINOPEC, for helpful suggestions.

## References

- [1] F. J. Petrijohn, P. E. Potter, and R. Siever, *Sand and Sandstone*, Springer-Verlag, New York, NY, USA, 1972.
- [2] K. J. Weber, "How heterogeneity affects oil recovery," in *Reservoir Characterization*, L. W. Lake and H. B. Carroll Jr., Eds., pp. 487–544, Academic Press, Orlando, Florida, USA, 1986.
- [3] C. E. Koltermann and S. M. Gorelick, "Heterogeneity in sedimentary deposits: A review of structure-imitating, process-imitating, and descriptive approaches," *Water Resources Research*, vol. 32, no. 9, pp. 2617–2658, 1996.
- [4] P. J. R. Fitch, M. A. Lovell, S. J. Davies, T. Pritchard, and P. K. Harvey, "An integrated and quantitative approach to petrophysical heterogeneity," *Marine and Petroleum Geology*, vol. 63, no. 5, pp. 82–96, 2015.
- [5] C. P. North and K. S. Taylor, "Ephemeral-fluvial deposits: Integrated outcrop and simulation studies reveal complexity," *AAPG Bulletin*, vol. 80, no. 6, pp. 811–830, 1996.
- [6] S. P. Dutton, C. D. White, B. J. Willis, and D. Novakovic, "Calcite cement distribution and its effect on fluid flow in a deltaic sandstone, Frontier Formation, Wyoming," *AAPG Bulletin*, vol. 86, no. 12, pp. 2007–2021, 2002.
- [7] S. Bloch and J. H. McGowen, "Influence of depositional environment on reservoir quality prediction," in *Reservoir Quality Assessment and Prediction in Clastic Rocks*, M. D. Wilson, Ed., vol. 30 of *SEPM Short Course*, pp. 41–57, 1994.
- [8] L. F. De Ros, S. Morad, and P. S. G. Paim, "The role of detrital composition and climate on the diagenetic evolution of continental molasses: evidence from the Cambro-Ordovician guaritas sequence, southern Brazil," *Sedimentary Geology*, vol. 92, no. 3–4, pp. 197–228, 1994.
- [9] S. Morad, J. M. Ketzer, and L. R. De Ros, "Spatial and temporal distribution of diagenetic alterations in siliciclastic rocks: Implications for mass transfer in sedimentary basins," *Sedimentology*, vol. 47, no. S1, pp. 95–120, 2000.
- [10] S. Morad, K. Al-Ramadan, J. M. Ketzer, and L. F. De Ros, "The impact of diagenesis on the heterogeneity of sandstone reservoirs A review of the role of depositional facies and sequence stratigraphy," *AAPG Bulletin*, vol. 94, no. 8, pp. 1267–1309, 2010.
- [11] K. L. Milliken, "Diagenetic heterogeneity in sandstone at the outcrop scale, Breathitt formation (Pennsylvanian), eastern Kentucky," *AAPG Bulletin*, vol. 85, no. 5, pp. 795–815, 2001.
- [12] S. Henares, L. Caracciolo, C. Viseras, J. Juan Fernández, and L. M. Yeste, "Diagenetic constraints on heterogeneous reservoir quality assessment: a triassic outcrop analog of meandering fluvial reservoirs," *AAPG Bulletin*, vol. 100, no. 09, pp. 1377–1398, 2016.
- [13] J. M. Ajdukiewicz and R. H. Lander, "Sandstone reservoir quality prediction: the state of the art," *AAPG Bulletin*, vol. 94, no. 8, pp. 1083–1091, 2010.
- [14] K. Bjørlykke, "Relationships between depositional environments, burial history and rock properties. Some principal aspects of diagenetic process in sedimentary basins," *Sedimentary Geology*, vol. 301, no. 3, pp. 1–14, 2014.
- [15] Y. Jiao, J. Yan, S. Li, R. Yang, F. Lang, and S. Yang, "Architectural units and heterogeneity of channel reservoirs in the Karamay Formation, outcrop area of Karamay oil field, Junggar basin, northwest China," *AAPG Bulletin*, vol. 89, no. 4, pp. 529–545, 2005.
- [16] E. Hammer, M. B. E. Mørk, and A. Næss, "Facies controls on the distribution of diagenesis and compaction in fluvial-deltaic deposits," *Marine and Petroleum Geology*, vol. 27, no. 8, pp. 1737–1751, 2010.
- [17] B. Cao, X. Luo, L. Zhang, F. Sui, H. Lin, and Y. Lei, "Diagenetic evolution of deep sandstones and multiple-stage oil entrapment: A case study from the Lower Jurassic Sangonghe Formation in the Fukang Sag, central Junggar Basin (NW China)," *Journal of Petroleum Science and Engineering*, vol. 152, no. 3, pp. 136–155, 2017.
- [18] X. R. Luo, L. K. Zhang, Y. H. Lei, C. Z. Hu, H. Shi, and B. F. Cao, "Structural heterogeneity of reservoirs and its implication on hydrocarbon accumulation in deep zones," *China Petroleum Exploration*, vol. 21, no. 1, pp. 28–36, 2016.
- [19] X. Luo, C. Hu, Z. Xiao et al., "Effects of carrier bed heterogeneity on hydrocarbon migration," *Marine and Petroleum Geology*, vol. 68, no. 12, pp. 120–131, 2015.
- [20] S. J. Ren, C. F. Jiang, Z. K. Zhang, and D. Y. Qin, *The Geotectonic Evolution of China*, Science Press, Beijing, China, 1980.
- [21] B. Zhao, "Nature of basement of Junggar Basin," *Xinjiang Petroleum Geology*, vol. 13, no. 2, pp. 95–99, 1992.
- [22] Q. F. Wu, "Growth stage, classification of structural units and cause of partial tectonic of Junggar Basin," *Xinjiang Petroleum Geology*, vol. 71, no. 1, pp. 29–37, 1986.
- [23] B. Zhao, "Formation and Evolution of Junggar Basin," *Xinjiang Petroleum Geology*, vol. 13, no. 3, pp. 191–196, 1992.
- [24] P. L. Li, J. H. Feng, Y. C. Lu et al., *Structure, sedimentation, and petroleum accumulation in the Junggar Basin*, Geological Publishing House, Beijing, China, 2010.
- [25] Z. H. Tang, Y. Huang, and H. L. Zhang, "Sedimentary facies and sequences of Jurassic in eastern Junggar Basin," *Xinjiang Petroleum Geology*, vol. 18, no. 4, pp. 330–337, 1997.
- [26] M. L. Zhang, X. M. Zhu, and Q. Zhang, "Jurassic sedimentary system of east Junggar Basin and its hydrocarbon significance," *Oil Gas Geology*, vol. 21, no. 3, pp. 272–278, 2000.
- [27] C. G. Wang, T. G. Wang, J. P. Chen, X. P. Shi, S. Z. Xiang, and T. Jin, "Recognition of crude oil types in the Jurassic Reservoirs of Cainan oilfield, east Junggar Basin," *Petroleum Geology Experiment*, vol. 25, no. 3, pp. 183–189, 2003.
- [28] J. P. Chen, C. P. Deng, D. G. Liang et al., "The Cainan Oilfield: a typical mixed crude oil of three-endmember," *Acta Sedimentol. Sin.*, vol. 22, pp. S91–S97, 2004.
- [29] H. Kuang, *Accumulation Regularity of Lithology reservoirs in Jurassic Baijiahai area, Junggar Basin [ Ph.D. Dissertation]*, Yangtzi University, Wuhan, China, 2009.
- [30] J. Chen, D. Liang, X. Wang et al., "Mixed oils derived from multiple source rocks in the Cainan oilfield, Junggar Basin, Northwest China. Part I: genetic potential of source rocks, features of biomarkers and oil sources of typical crude oils," *Organic Geochemistry*, vol. 34, no. 7, pp. 889–909, 2003.
- [31] Q. Zhang, M. L. Zhang, X. M. Zhu, D. K. Zhong, and G. W. Wang, "Analysis of Jurassic sources in east Fukang slope of Junggar Basin," *Xinjiang Petroleum Geology*, vol. 20, no. 6, pp. 501–546, 1999.
- [32] J. Jin, H. G. Wen, B. L. Xiang, L. Q. Qi, J. W. Yu, and L. L. Li, "Provenance analysis of Middle Jurassic Toutunhe Formation in eastern Fukang slope, Junggar Basin," *Lithologic Reservoirs*, vol. 26, no. 2, pp. 54–58, 2014.
- [33] M. Zhang, J. L. Xiu, L. Chen, and T. Xu, "The provenance system and characteristic of sedimentary evolution of Jurassic Toutunhe Formation in the second and fourth Blocks of central Junggar Basin," *Journal of Oil and Gas Technology*, vol. 36, no. 6, pp. 45–50, 2014.

- [34] R. L. Folk, *Petrology of Sedimentary Rocks*, Hemphills, Austin, Texas, USA, 1974.
- [35] R. H. Goldstein and T. J. Reynolds, "Systematics in fluid inclusions in diagenetic minerals," *SEPM Short Course*, vol. 31, 1994.
- [36] Y.-Q. Jiao, L.-Q. Wu, Y.-C. Lu, and J.-Y. Ren, "Evolution of the Chepaizi-Mosuowan paleo-uplift, Junggar Basin, China: Evidence from diagenesis of late Jurassic red beds," *Journal of China University of Geosciences*, vol. 33, no. 2, pp. 219–226, 2008.
- [37] E. D. Pittman and R. E. Larese, "Compaction of lithic sands: experimental results and applications," *American Association of Petroleum Geologists Bulletin*, vol. 75, no. 8, pp. 1279–1299, 1995.
- [38] R. H. Worden, M. Mayall, and I. J. Evans, "The effect of Ductile-Lithic sand grains and quartz cement on porosity and permeability in Oligocene and lower Miocene clastics, South China Sea: prediction of reservoir quality," *AAPG Bulletin*, vol. 84, no. 3, pp. 345–359, 2000.
- [39] H. Kashiwagi, Y. Ogawa, and N. Shikazono, "Relationship between weathering, mountain uplift, and climate during the Cenozoic as deduced from the global carbon-strontium cycle model," *Palaeogeography, Palaeoclimatology, Palaeoecology*, vol. 270, no. 1–2, pp. 139–149, 2008.
- [40] P. J. Dowey, D. M. Hodgson, and R. H. Worden, "Pre-requisites, processes, and prediction of chlorite grain coatings in petroleum reservoirs: a review of subsurface examples," *Marine and Petroleum Geology*, vol. 32, no. 1, pp. 63–75, 2012.
- [41] S. Bloch, R. H. Lander, and L. Bonnell, "Anomalously high porosity and permeability in deeply buried sandstone reservoirs: origin and predictability," *AAPG Bulletin*, vol. 86, no. 2, pp. 301–328, 2002.
- [42] T. R. Taylor, M. R. Giles, L. A. Hathorn et al., "Sandstone diagenesis and reservoir quality prediction: models, myths, and reality," *AAPG Bulletin*, vol. 94, no. 8, pp. 1093–1132, 2010.
- [43] R. W. Renaut, "Zeolitic diagenesis of late Quaternary fluvio-lacustrine sediments and associated calcrete formation in the Lake Bogoria Basin, Kenya Rift Valley," *Sedimentology*, vol. 40, no. 2, pp. 271–301, 1993.
- [44] R. C. Surdam and H. P. Eugster, "Mineral reactions in the sedimentary deposits of the Lake Magadi region, Kenya," *Bulletin of the Geological Society of America*, vol. 87, no. 12, pp. 1739–1752, 1976.
- [45] Q. Gall and R. Hyde, "Analcime in lake and lake-margin sediments of the Carboniferous Rocky Brook Formation, Western Newfoundland, Canada," *Sedimentology*, vol. 36, no. 5, pp. 875–887, 1989.
- [46] R. L. Hay, "Silicate reactions in three lithofacies of a semi-arid basin, Olduvai Gorge Tanzania," *Mineralogical society of America*, vol. 3, pp. 237–255, 1970.
- [47] Y. S. Sun and Z. Q. Cao, "Characteristics and distribution of Zeolite group minerals in Karamay Oilfields," *Xinjiang Petroleum Geology*, vol. 12, no. 3, pp. 253–261, 1991.
- [48] S. F. Zhu, X. M. Zhu, X. L. Wang, and Z. Y. Liu, "Zeolite diagenesis and its control on petroleum reservoir quality of Permian in northwestern margin of Junggar Basin, China," *Science China Earth Sciences*, vol. 55, no. 3, pp. 386–396, 2012.
- [49] Y. Q. Jiao, S. T. Li, S. G. Yang, and J. L. Chen, "An outcrop study on internal architecture and heterogeneity of lacustrine delta-front sand bodies," *Journal of China University of Geosciences, Earth Science*, vol. 18, no. 4, pp. 441–451, 1993.
- [50] J. Cao, W. Hu, S. Yao et al., "Content of reservoir calcite cement: A novel inorganic geotracer of secondary petroleum migration in the structurally complex Junggar Basin (NW China)," *Science China Earth Science*, vol. 37, no. 10, pp. 1358–1369, 2007.
- [51] F. Hao, Z. Zhang, H. Zou, Y. Zhang, and Y. Yang, "Origin and mechanism of the formation of the low-oil-saturation Moxizhuang field, Junggar Basin, China: implication for petroleum exploration in basins having complex histories," *AAPG Bulletin*, vol. 95, no. 6, pp. 983–1008, 2011.
- [52] L. Kuang, Y. Tang, D. Lei et al., "Formation conditions and exploration potential of tight oil in the Permian saline lacustrine dolomitic rock, Junggar Basin, NW China," *Petroleum Exploration and Development*, vol. 39, no. 6, pp. 700–711, 2012.
- [53] J. Gluyas, L. Jolley, and T. Primmer, "Element mobility during diagenesis: Sulphate cementation of Rotliegend sandstones, Southern North Sea," *Marine and Petroleum Geology*, vol. 14, no. 7–8, pp. 1001–1011, 1997.
- [54] B. McNeil, H. F. Shaw, and A. H. Rankin, "The timing of cementation in the Rotliegend sandstones of the southern North Sea: a petrological and fluid inclusion study of cements," *Journal of Petroleum Geology*, vol. 21, no. 3, pp. 311–328, 1998.
- [55] R. C. Surdam and J. R. Boles, "Diagenesis of volcanogenic sandstones," in *Aspects of Diagenesis*, P. A. Scholle and P. R. Schluger, Eds., vol. 26 of *Special Publication*, pp. 227–247, Society for Sedimentary Geology, Tulsa, USA, 1979.
- [56] Z. Tang, J. Parnell, and F. J. Longstaffe, "Diagenesis and reservoir potential of Permian-Triassic Fluvial/Lacustrine sandstones in the southern Junggar basin, northwestern China," *AAPG Bulletin*, vol. 81, no. 11, pp. 1843–1865, 1997.
- [57] K. Bjørlykke and J. Jahren, "Open or closed geochemical systems during diagenesis in sedimentary basins: constraints on mass transfer during diagenesis and the prediction of porosity in sandstone and carbonate reservoirs," *AAPG Bulletin*, vol. 96, no. 12, pp. 2193–2214, 2012.
- [58] T. Barth and K. Bjørlykke, "Organic acids from source rock maturation: generation potentials, transport mechanisms and relevance for mineral diagenesis," *Applied Geochemistry*, vol. 8, no. 4, pp. 325–337, 1993.
- [59] P. D. Lundegard and Y. K. Kharaka, "Distribution and occurrence of organic acids in subsurface waters," in *Organic Acids in Geological Processes*, E. D. Pittman and M. D. Lewan, Eds., pp. 38–69, Springer-Verlag, New York, NY, USA, 1994.
- [60] M. D. Jackson and A. H. Muggeridge, "Effect of discontinuous shales on reservoir performance during horizontal waterflooding," *SPE Journal*, vol. 5, no. 4, pp. 446–455, 2000.

## Research Article

# The Distribution and Origin of Carbonate Cements in Deep-Buried Sandstones in the Central Junggar Basin, Northwest China

Wang Furong,<sup>1</sup> He Sheng,<sup>1</sup> Hou Yuguang,<sup>1</sup> Dong Tian,<sup>2</sup> and He Zhiliang<sup>3</sup>

<sup>1</sup>Key Laboratory of Tectonics and Petroleum Resources, China University of Geosciences, Ministry of Education, Wuhan 430074, China

<sup>2</sup>Department of Earth & Atmospheric Sciences, University of Alberta, Edmonton, AB, Canada T6G 2E3

<sup>3</sup>SINOPEC Petroleum Exploration and Production Research Institute, Beijing 100083, China

Correspondence should be addressed to Hou Yuguang; [sporthyg@126.com](mailto:sporthyg@126.com)

Received 4 March 2017; Revised 19 May 2017; Accepted 4 June 2017; Published 14 September 2017

Academic Editor: Xiaorong Luo

Copyright © 2017 Wang Furong et al. This is an open access article distributed under the Creative Commons Attribution License, which permits unrestricted use, distribution, and reproduction in any medium, provided the original work is properly cited.

Extremely high porosities and permeabilities are commonly discovered in the sandstones of the Xishanyao Formation in the central Junggar Basin with the burial depth greater than 5500 m, from which hydrocarbons are currently being produced. High content of carbonate cements (up to 20%) is also observed in a similar depth range. Our study aimed to improve our understanding on the origin of carbonate cements in the Xishanyao Formation, in order to provide insights into the existence of high porosity sandstones at greater depths. Integrated analyses including petrographic analysis, isotopic analysis, fluid-inclusion, and core analysis were applied to investigate the distribution and origin of carbonate cements and the influence of high fluid pressure on reservoir quality. Textural evidences demonstrate that there are two generations of carbonate cements, precipitated at the temperature of 90°C and 120°C, respectively. The carbonate cements with low  $\delta^{13}\text{C}_{\text{PDB}}$  ranging from  $-19.07$  to  $-8.95\%$  dominantly occurred near the overpressure surface and especially accumulated at approximately 100 m below the surface. Our interpretation is that high content of carbonate cements is significantly influenced by early carbonate cements dissolution and migration under overpressure. Dissolution of plagioclase resulted in the development of internal pores and porosities of as much as 10% at 6500 m depth presumably.

## 1. Introduction

Carbonate cements in sandstones have variable mineralogy, texture, and chemical compositions and therefore exhibit significant effects on reservoir properties because it is commonly concentrated rather than being uniformly distributed. It is challenging to quantify the influence of concretionary carbonate cements on fluid flow in reservoirs because it is difficult to determine the distribution of diagenetic heterogeneity based on subsurface data. If the carbonate cements formed during early diagenetic stage, it could provide a framework that resists burial compaction and retains primary porosity until decarbonatization at greater burial depth [1–3]. Microlitic carbonate cements formed at early diagenetic stage can undertake partial overburden load that can slow compaction and can be dissolved into secondary pores under favorable geologic conditions. Extensive studies have been performed on carbonate cementation-dissolution reactions

from the viewpoints of fluid-rock, organic-inorganic, and sandstone-mudstone interactions in the past 40 years by traditional geochemical methods, such as stable isotope and major and trace elements analysis [4–17] (Tan Jianxiong et al., 1999; dos Anjos et al., 2000; Hendry et al., 2000; Taylor et al., 2000; Fayek et al., 2001; Geoffrey Thyne, 2001; Ni Shijun et al., 2002; Wang Zhizhang et al., 2003; Xie Xinong et al., 2006; Wilkinson et al., 2006; Machent et al., 2007; Cao Jian et al., 2007).

It is observed that the favorable sandstone reservoirs are developed at the depth of 4500–6000 m in the central Junggar Basin. The average porosity is approximately 10% and the average permeability is  $1 \times 10^{-3} \mu\text{m}^2$ . Although many studies have been carried out in this area, including petrographic analysis, formation-water geochemistry, fluid inclusions analysis, and overpressure characterization [13, 18–23], there is still a lot of debate on the origins and types of

porosity in this area. Some studies assumed that the primary residual pores are the dominant pore type and other studies assumed that secondary pores resulting from the dissolution of carbonate cements make more contributions to forming favorable reservoirs [24–26]. The negative correlation between porosity and the carbonate cements content indicates that the formation of secondary pores and carbonate cement dissolution probably have genetic relationships. It is unexpected that in sandstones high secondary porosity and high content of carbonate cements superimpose at the same depth. In this study, we attempt to investigate the origin of carbonate cements in deep-buried sandstones in the central Junggar Basin by applying a multidisciplinary approach, including petrographic, microthermometric, fluid-inclusion, and geochemical analysis. The main objectives of the study are as follows: (1) to quantify the chemical composition, size, and spatial distribution of carbonate cements and (2) to provide further insights into the effect of carbonates cements on petrophysical properties of deep-buried reservoirs.

## 2. Geological Setting

The Junggar Basin is one of the most prolific oil basin in China (Jiang and Fowler, 1986), covering an area of 136,000 km<sup>2</sup>. It is an intramontane basin bounded by multiple orogenic belts, including the Qinggelidi Mountains, the Kelameili Mountains, the Yilinheibergen Mountains, the Bodega Mountains, and the Zhayier Mountains (Figure 1). The Junggar Basin is Late Palaeozoic-Cenozoic in age which is developed on the Junggar terrane, consisting of both Precambrian crystalline basement formed at 800 Ma ago and slightly metamorphic Palaeozoic basement [28–33]. Our study area in this paper belongs to SINOPEC, located in the central depression of the hinterland of the basin which mainly consists of the west segment of the Changji Sag in the south (Figure 1).

The central depression area is one of the important areas for petroleum exploration. The characteristics of source rocks and reservoirs in the central Junggar Basin have been extensively studied. There were two sets of source rocks, including the Permian shales dominated by lacustrine-facies and the Jurassic mudstones dominated by swamp coal-bearing. The deeply buried Jurassic sandstones dominated by fluvial-delta facies were main reservoirs with low porosity and permeability generally. However, relatively high porosity and permeability in sandstones display at some depth. At the same time, extensive development of overpressure is displayed over much of the central Junggar Basin. Much more hydrocarbon generated from Permian and Jurassic source rocks accumulated in the overpressured system (Wu Hengzhi et al., 2006; Li Pingping et al., 2006; Yang Zhi et al., 2007) (Figure 2).

Figure 3 shows the modelling burial history of Y1 well (Yongjin area) in Block 3 (see Figure 1 for its location). The erosion event generated an unconformity between Later Jurassic and Early Cretaceous. Therefore, the heat flow is the only variable that needs to be adjusted to match the present-day vitrinite reflectance data. Our modelling results indicated that the paleotemperature decreased gradually from the Permian to the present. This result is consistent with previous studies [34–37]. Drilling data demonstrated that the vitrinite

reflectance ( $R_o$ ) ranges within 0.65~0.82% in the Middle Jurassic Xishanyao Formation. To match the measured and the predicated vitrinite reflectance data, BasinMod simulation software aims to rebuild the geothermal history. At present, the temperature of Jurassic strata was approximately between 120°C and 150°C, giving a gradient of 2.2°C/100 m. With the results of homogenization temperature, the main oil pools in the third central block formed from the end of the early Cretaceous to the early stage of Paleogene (from 75 Ma to 60 Ma) [38]. At the same time, the crude oil was detected in high levels of 25-norhopane from Y1 well, which explained that an early stage of hydrocarbon charging occurred in the late Jurassic [38].

## 3. Samples and Methods

125 core samples were obtained from six wells (Y1, Y2, Y3, Y6, Y7, and Y8) at a depth range of 5500–6200 m from Jurassic Xishanyao Formation (Figure 1). The strategy of sample collection is based on the characteristics of lithology. Generally, an interval of one meter is between the two samples, if the cores have homogeneous qualities. The ternary plot indicates that the Xishanyao Formation sandstones are dominantly litharenite and feldspathic litharenite as they have an average framework composition of Q<sub>28</sub>F<sub>13</sub>L<sub>59</sub> (Figure 4).

Carbonate cements were investigated by using epoxy-impregnated thin sections, cathodoluminescence, and SEM/EDX images. Conventional core samples and epoxy-impregnated thin sections analysis was conducted on the MIAS 2000 microscopes by the Experimental Research Center of Wuxi Research Institute of Petroleum Geology of SINOPEC and Research Center of Shengli Oilfield Institute of Geology of SINOPEC. Analysis was performed at the room temperature of 25°C and the relative humidity of 60%.

Cathodoluminescence analysis was conducted on the CL8200 MK5 cathodoluminescence microscopy by the Experimental Research Center of Wuxi Research Institute of Petroleum Geology of SINOPEC. Analysis was performed at the room temperature of 27°C and the relative humidity of 40%.

SEM/EDX analysis was performed on the sem-xl30 and EDX-INCA scanner by the Experimental Research Center of Wuxi Research Institute of Petroleum Geology of SINOPEC. Analysis was performed at the room temperature of 22°C and the relative humidity of 60%.

Carbon and oxygen isotope analysis was carried out on the MAT253 Gas isotope mass spectrometer made in Germany Firmigan company. Analysis was performed at the sample tray temperature of 72°C, chromatography temperature of 40°C, and helium gas pressure of 100 KPa.

Electron microprobe analysis was conducted on the JXA-8100 electron probe microanalyser at the State Key Laboratory of Geological Processes and Mineral Resource. Analysis was performed at the room temperature of 23°C and the relative humidity of 65%.

## 4. Results

*4.1. Thin Section Analysis.* Thin section images demonstrate that the dominant cements are carbonates, which consists

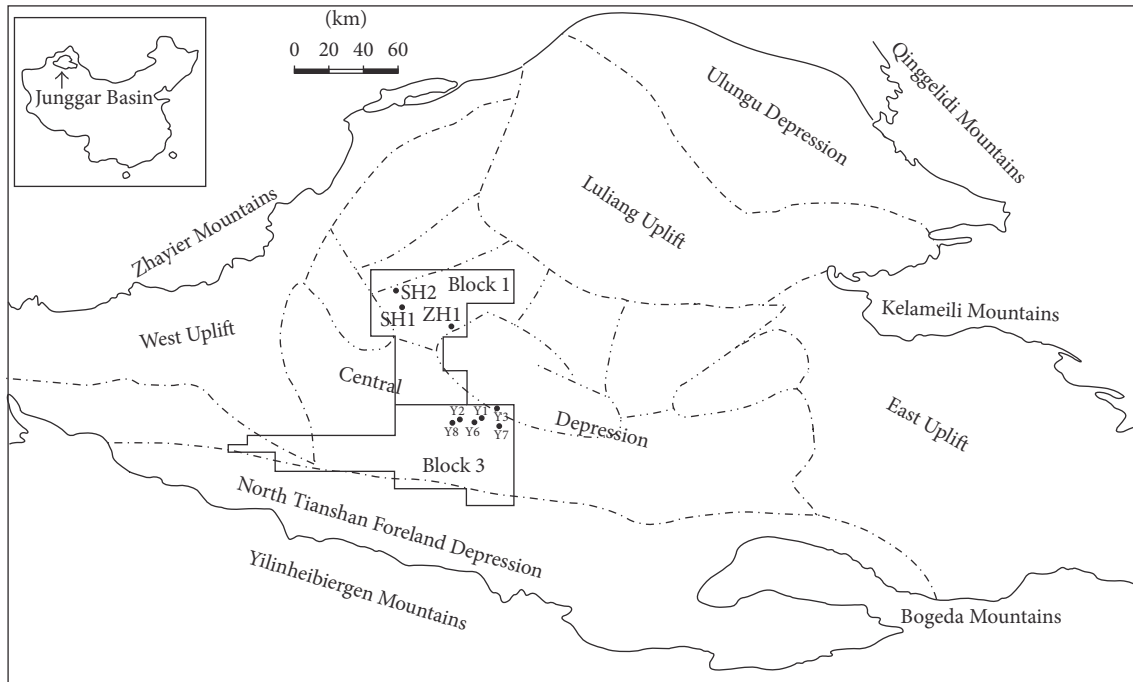


FIGURE 1: Map showing the tectonic units and studied well locations in the central Junggar Basin.

of a high volume of ferroan calcite and ankerite. At the same time, a small amount of dolomite developed in some wells. Thin section images show that both ferroan and nonferroan calcites commonly occurred as extensive, single-crystal poikilotopes that filled with the intergranular pores (Figure 5(a)). In contrast, ankerite cements are regular to rhombic, replacing calcites with an undulating extinction characteristic (Figures 5(b) and 5(c)). Dolomite cements were also observed in the form of replacing calcites (Figure 5(d)). Some calcite crystal filled in intergranular pores and postdated quartz overgrowth (Figures 5(e) and 5(f)). Some thin section images show that carbonate cements replaced detrital quartz, feldspar, or rock fragments. The abundance of carbonate can be up to 20% and generally in the range of 1–10% within the six studied wells (Figure 6). At the same time, particle contact modes were different because of maldistributed distribution. Some particles were in point contact where carbonate cements develop, while others were in straight of concavoconvex contact. Moreover, carbonates with different mineral compositions distributed in different wells, such as ankerite cements, generally distributed in wells Y2, Y6, and Y8 with an average concentration of 4.5% and calcite cements generally distributed in wells Y1, Y3, and Y7 with an average content of 4.1%.

**4.2. Cathodoluminescence.** Under the cathodoluminescent (CL) images, the relative content of manganese (Mn) and iron (Fe) in carbonate cements can be used to provide insights into the redox conditions when the pore fluid formed. Mn in calcites is an activator in CL, while Fe acts as a quencher. Carbonate cements with  $Mn > Fe$  show bright luminescence, whereas calcite cements with  $Fe > Mn$  exhibit dull-luminesce. In Block 3, the carbonate cements partially

show bright luminescence (Figure 5(g)) and others show shade of bright luminescence (Figure 5(h)). Cathodoluminescence of these calcite cements can be interpreted by their origin in sandstones.

**4.3. EDX Analysis.** The trace element data of 14 core samples, determined by EDX analysis, are presented in Table 1. Carbonate cements are generally rich in Fe with low content of Mn and Mg, and the concentration of Ca increases with increasing burial depth.

**4.4. Stable Isotopes.**  $\delta^{13}C$  and  $\delta^{18}O$  of the carbonate cements, together with burial and thermal histories, can be used to reveal the origin of the cements. Stable isotopes data in Yongjin area are presented in Table 2. Carbon isotope values range from  $-19.07$  to  $-5.87\text{‰}$  (PDB) with average value of  $-8.95\text{‰}$  (PDB). The oxygen isotope values range from  $-21.08$  to  $-13.96\text{‰}$  (PDB) with average value of  $-17.5\text{‰}$  (PDB). The  $\delta^{13}C$  and  $\delta^{18}O$  values increase with increasing burial depth and there is a positive correlation between the  $\delta^{13}C$  and  $\delta^{18}O$  values.

## 5. Discussion

**5.1. Origins of Carbonate Cements and Source of Fluid.** Petrographic observations revealed at least two generations of carbonate cements. The first-generation carbonate occurred as blocky crystalline calcite, which filled within the intergranular pores reduced considerably by mechanical and chemical compaction. This kind of cements occurred in the form of coating quartz grains, preventing authigenic quartz from overgrowing (Alaa et al., 2007). And they dominated in the deeply buried sandstones and filled with iron (Fe) content,

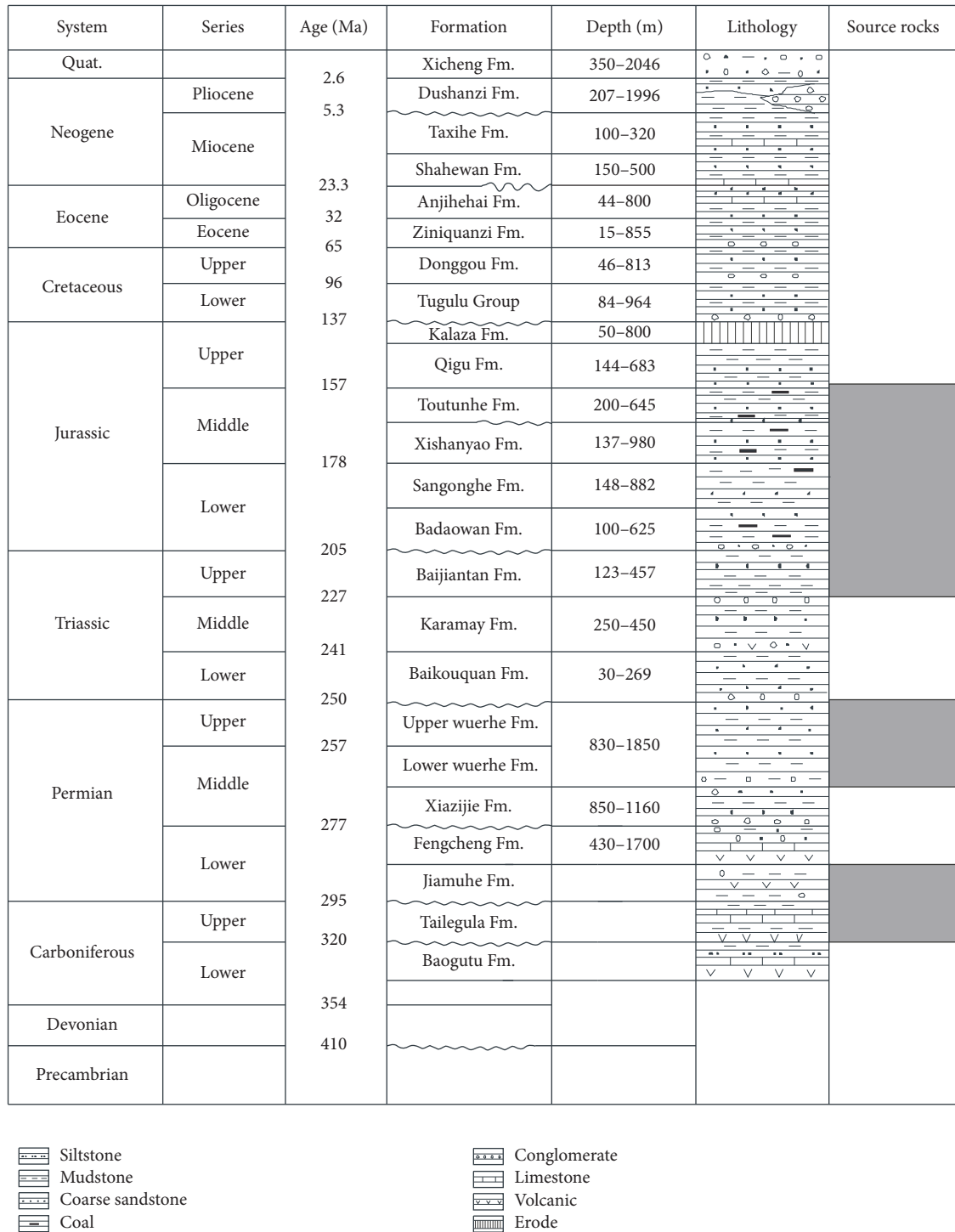


FIGURE 2: Stratigraphic column and correlation of stratum in the center of Junggar Basin (2002).

which belonged to late diagenesis cements. The second-generation carbonate cement was ankerite, which replaced calcite (Figure 5(c)).

$\delta^{13}\text{C}$  and  $\delta^{18}\text{O}$  in the carbonate cements can be used to unravel the origins of the cements. The main mechanisms of generation of  $\delta^{13}\text{C}$ -depleted  $\text{CO}_2$  in large amounts during burial are discussed by Irwin et al. [39], including diagenetic

carbonate in area I, carbonate relating to biogas in area II, and carbonate relating to organic acid in area III (Jansa et al., 1990; Wang Darui, 2000; Wilkinson et al., 2006) (Figure 7). 29 samples from Xishanyao Formation (J2x) and 11 samples from Toutunhe formation (J2t) were collected between 5500 m and 6200 m for the carbon and oxygen stable isotopic analysis. The results were shown in Figure 7 as

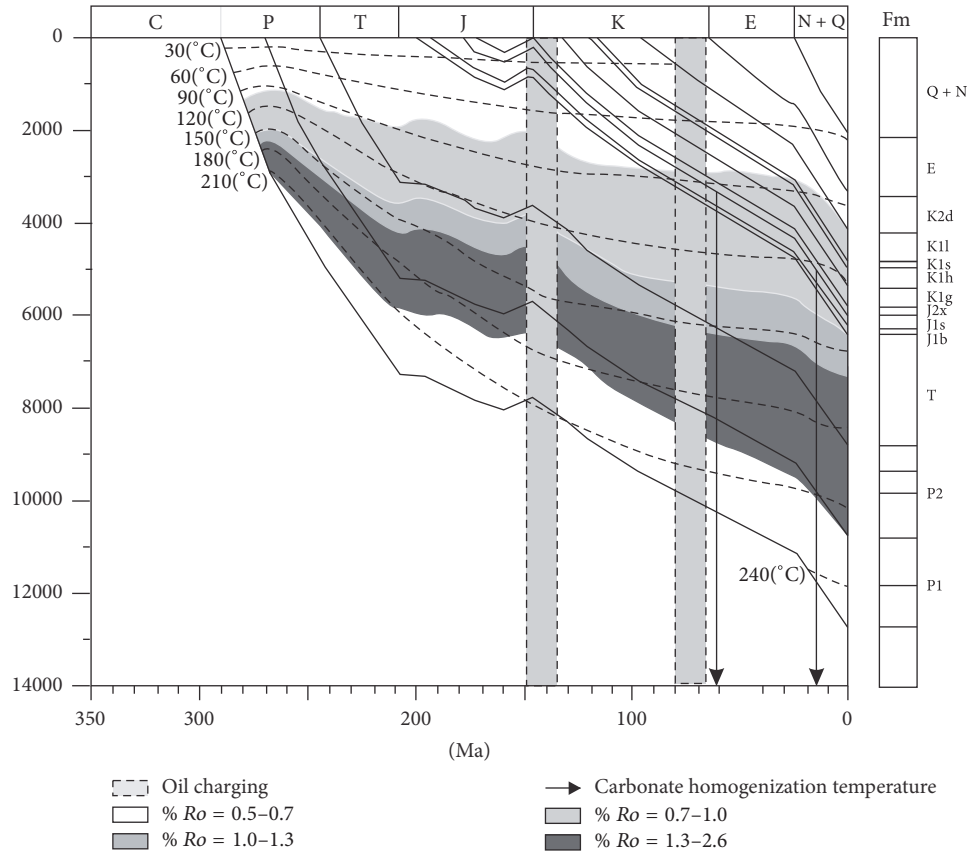


FIGURE 3: Generalized burial and thermal histories of Y1 well from Block 3 in the central Junggar Basin. Location of the example well is marked in Figure 1.

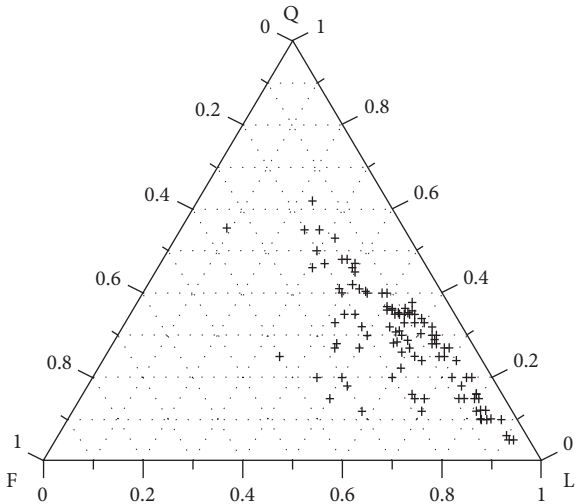


FIGURE 4: Ternary plot showing sandstone compositions according to Folk's (1980) classification scheme.

a plot of  $\delta^{18}\text{O}$  (PDB) versus  $\delta^{13}\text{C}$  (PDB) that more negative  $\delta^{13}\text{C}$  values are generally accompanied by more negative  $\delta^{18}\text{O}$  values indicating that the carbonate cements were significantly influenced by organic matter alteration during burial (Figure 7) in area III. Rare input of  $\delta^{12}\text{C}$  with increasing

burial and temperature from thermal alteration of organic matter is indicated by the strong correlation between  $\delta^{13}\text{C}$  and  $\delta^{18}\text{O}$  [39–41].

With limited fluid-inclusion data of carbonate cements and quartz overgrowth, the precipitation was formed at about 100°C and 80–130°C, respectively (Table 3). From Figures 5(e) and 5(f), the phenomena that carbonate crystal postdates quartz overgrowth revealed that at least part of carbonate cement deposited at 120°C (inclusion homogenization temperature of overgrowth concentrating in 120°C). From Figure 3, the carbonate formation mainly resulted from the later hydrocarbon charging.

**5.2. Effect on Reservoir Properties.** Reservoir physical properties data indicate that porosity near the overpressure surface is relatively high, mainly concentrating in the depth range +50 m~–250 m of the overpressure top surface, and the carbonate cements are concentrated in these high porosity zone (Figure 8). Thin section images and microscope analysis were used to investigate the origin that why do the high porosity and carbonate cements superimpose in depth, when the formation water flowed and broke through the overpressure surface, causing the precipitation and concentration of calcite near the overpressure surface because of the unstable temperature and pressure [42, 43] (Yang Zhi, 2011).

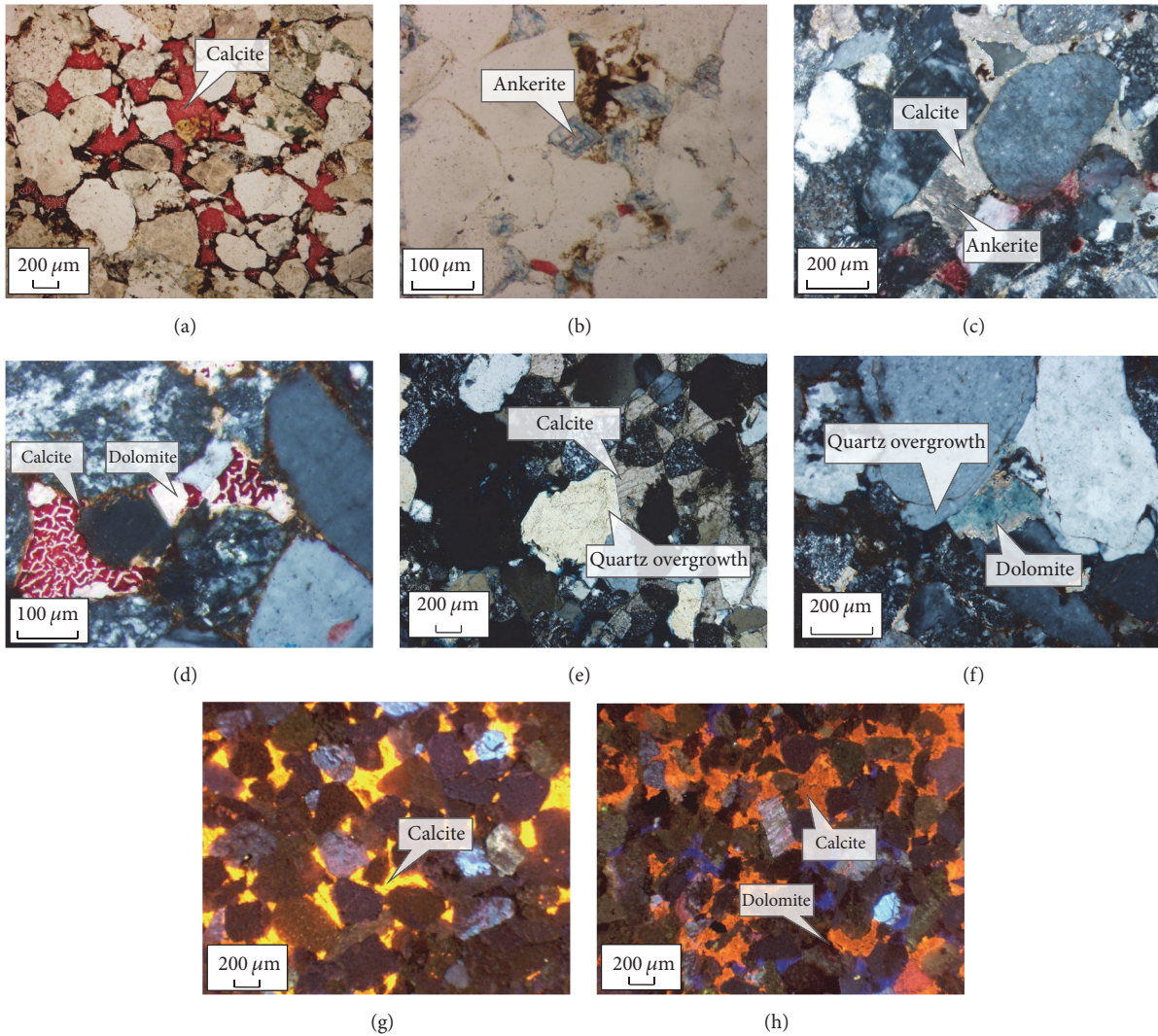


FIGURE 5: Photomicrographs showing petrographic features of the Xishanyao Formation sandstones. Most common types of mineralogy variations in sandstone cement, including (a) secondary pores were mainly filled by crystal calcite, major pores were filled by asphalt at the edges, and the photomicrograph is a stained red-epoxy-impregnated thin sections of conventional core samples by plane-polarized light with magnification of 40 (Y6 well at 6,048.59 m); (b) single-crystal rhombus ankerite, the photomicrograph is a stained blue-epoxy-impregnated thin sections of conventional core samples by plane-polarized light with magnification of 200 (Y6 well at 6028.52 m); (c) a few ankerites replace calcites in a red-epoxy-impregnated thin sections of conventional core samples with cross-polarized light with magnification of 100 (Y2 well at 5966.02 m); and (d) a few dolomites replace calcites in a stained red-epoxy-impregnated thin sections of conventional core samples with cross-polarized light with magnification of 200 (Y2 well at 5967.02 m); (e) crystal calcite filled in pores, and crystal postdate quartz overgrowth in a stained blue-epoxy-impregnated thin sections of conventional core samples by cross-polarized light with magnification of 40 (Y1 well at 5876 m); (f) dolomites develop in a stained blue-epoxy-impregnated thin sections of conventional core samples by plane-polarized light with magnification of 100 (Y2 well at 6000.25 m); (g) calcite cements show bright yellow luminescence in cathodoluminescence photomicrograph with magnification of 40 (Y7 well at 6095 m); (h) calcite cements show saffron luminescence and dolomites cements are disphotic in cathodoluminescence photomicrograph with magnification of 40 (Y8 well at 6099.46 m).

Observation from thin section images indicate that secondary intergranular pores are the dominant pore type (Figure 9). In contrast to the characteristics of minerals by plane-polarized and cross-polarized light, the remnant of calcite can be found after dissolution developing in the surrounding pores. Data from electron microprobe analysis indicate that the secondary intergranular pores resulted from dissolving intergranular carbonate cements and feldspar (Figure 10, Table 4), mainly generated by calcite dissolution. Megapores

were mostly formed by the dissolution of albite and less by K-feldspar and kaolinite in situ deposit which shows that pore configuration has good connection. These evidences demonstrate that the large-scale dissolution of intergranular carbonate cements can generate more intergranular pores and make the pore more connected.

Although sandstones experienced extensive mechanical compaction and chemical compaction, the point or straight grain contact and the pervasive development of intergranular

TABLE 1: Composition from EDX analysis of carbonate cements in sandstone of Block 3.

Well	Depth/m	Content/%							
		Na <sub>2</sub> O	MgO	Al <sub>2</sub> O <sub>3</sub>	SiO <sub>2</sub>	CaO	MnO	Fe <sub>2</sub> O <sub>3</sub>	K <sub>2</sub> O
Y1	6117.38			2.22	5.54	82.59	4.31	5.35	
Y2	5970.53		17.48		5.55	47.38	4.43	25.16	
	6001.23		19.00		6.79	63.28	6.41	4.52	
Y3	5614.22	1.37	13.92	3.33	8.70	43.33	3.47	24.45	
	5868.00		1.59	3.04	4.78	79.22	5.95	5.04	0.37
Y6	6028.60		21.22			52.30	3.63	22.85	
	6084.00			1.36	5.26	91.04		2.34	
Y7	6095.00			1.27	2.45	92.39	1.76	2.13	
	6101.55		3.84	4.56	15.13	45.61	7.50	22.51	0.84
Y8	6088.55		21.43	2.44	1.99	51.05		23.08	
	6096.20			0.95	9.21	85.44		4.02	0.38

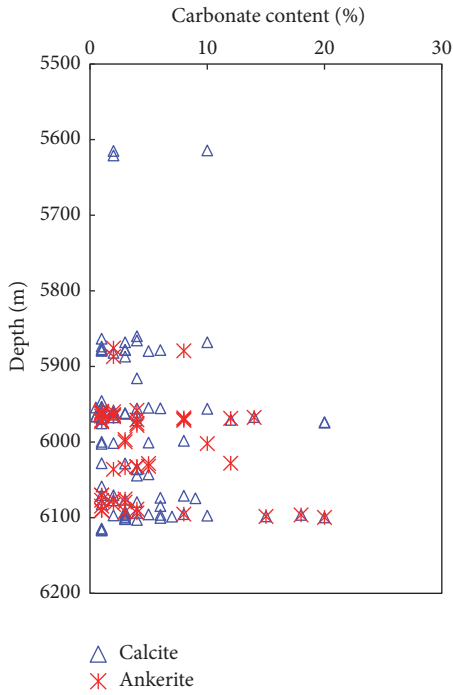


FIGURE 6: Regional abundance of carbonate cements versus depth in the Jurassic Formation. Text data from 125 core samples show that carbonate is abundant from below 5800 m and increases with depth down to about 6100 m burial depth. The contents of calcite have little changes with the depth. However, ankerite has a sharp interface of 5850 m burial depth and the content increases with the depth.

pores suggest that the formation of carbonate cements predated intensive physical compaction. Firstly, early carbonate cements occupied the intergranular pore space which increased rock mechanical strength and resisting ability to compaction. Therefore, the sandstone reservoir can develop high primary porosity even in deeply buried conditions. Secondly, early carbonate cements provided materials for dissolution which can form a large amount of secondary intergranular porosity and feldspar dissolution further improved

TABLE 2: Carbon and oxygen isotope values in Xishanyao formation sandstones of Block 3.

Well	Depth/m	$\delta^{13}\text{C}_{\text{PDB}}/\text{‰}$	$\delta^{18}\text{O}_{\text{PDB}}/\text{‰}$	Isotopic temperature/ $^{\circ}\text{C}$
Y1	5880.00	-8.21	-19.05	128.92
	6095.00	-7.55	-18.53	124.17
	6095.50	-7.37	-16.44	106.21
Y7	6096.80	-8.18	-19.95	137.06
	6098.60	-7.52	-17.87	118.36
	6099.59	-7.60	-17.53	115.42
	6101.80	-7.49	-16.15	103.82
Y8	6103.60	-7.65	-18.17	120.99
	6088.50	-11.63	-16.68	108.21
	6088.80	-12.38	-16.88	109.89
	6092.00	-10.82	-17.65	116.46
	6093.30	-11.08	-16.04	102.92
	6093.50	-10.72	-17.86	118.28
	6094.30	-10.80	-16.78	109.05
Y3	6099.50	-7.34	-17.40	114.31
	5614.90	-7.05	-17.36	113.97
	5620.80	-7.10	-18.17	120.99
	5621.10	-7.61	-18.43	123.28
	5865.60	-5.87	-21.08	147.73
	5866.35	-19.07	-14.68	92.04
	5867.90	-5.92	-21.28	149.65
Y6	5977.00	-8.31	-13.96	86.5
	6034.90	-6.52	-17.72	117.06
	6044.80	-6.95	-19.03	128.64
	6076.50	-7.08	-16.29	104.97
	6084.60	-7.04	-19.20	130.18
Y2	6098.50	-9.70	-18.35	122.57
	5961.50	-6.36	-15.06	95.03
	6004.30	-9.97	-17.87	118.36

Isotopic temperature ( $^{\circ}\text{C}$ ) =  $16.45 - 4.31(\delta\text{c} - \delta\text{w}) + 0.14(\delta\text{c} - \delta\text{w})^2$ , according to Epstein et al. [27].

TABLE 3: Fluid-inclusion data from quartz overgrowth and carbonate cements.

Well	Depth, m	Numbers of inclusion	Carbonate homogenization temperature, °C	Quartz overgrowth homogenization temperature, °C
Y1	5828.2	1	100	
	5876.38	4		115, 120, 125, 127
	6114.7	1	98	
	6116.87	2	92, 98	
Y2	5953.66	6	96	85, 88, 116, 120, 132
	5970.53	3		102, 117, 127
	6002.15	2	98, 102	
Y6	6027.44	2	96, 102	
	6028.6	2		80, 134

TABLE 4: Electron microprobe analysis of residual mineral contents in secondary pores of wells in studied area.

Well	Position	Content/%										
		SiO <sub>2</sub>	TiO <sub>2</sub>	Al <sub>2</sub> O <sub>3</sub>	FeO	MnO	MgO	CaO	Na <sub>2</sub> O	K <sub>2</sub> O	Cr <sub>2</sub> O <sub>3</sub>	Total
SH1	a	63.55	0.00	17.89	0.00	0.00	0.00	0.00	1.00	16.10	0.00	98.54
	b	0.16	0.00	0.03	0.03	0.00	0.40	53.50	0.00	0.00	0.00	54.12
ZH1	c	68.13	0.00	19.57	0.05	0.00	0.00	0.00	12.03	0.02	0.00	99.80
	d	64.13	0.03	18.02	0.05	0.00	0.00	0.00	0.31	16.65	0.00	99.19
SH2	e	51.02	0.00	18.75	0.05	0.00	0.00	0.31	8.17	0.00	0.00	78.30
	f	0.00	0.00	0.00	0.59	0.62	0.44	60.92	0.00	0.00	0.00	62.57
	g	0.08	0.00	0.00	58.11	0.00	0.00	0.00	0.00	0.00	0.00	58.19
Y1	h	0.81	0.00	0.13	1.49	1.34	0.17	52.45	0.00	0.00	0.02	56.41
	i	64.73	0.00	18.32	0.00	0.00	0.00	0.00	0.30	16.69	0.00	100.04
	j	70.41	0.00	20.46	0.10	0.00	0.00	0.16	10.48	0.00	0.00	101.61

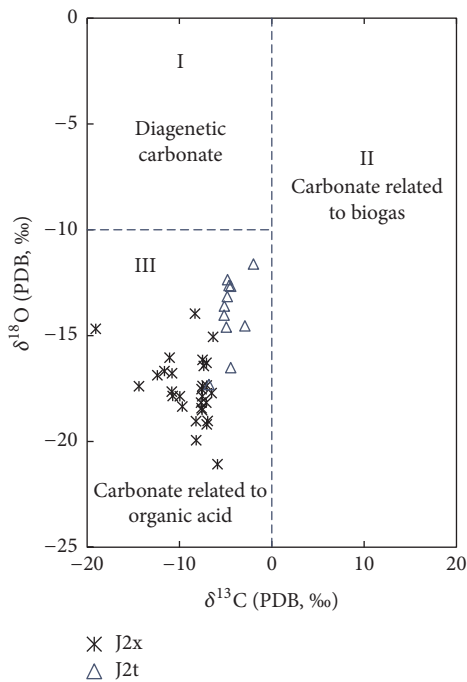


FIGURE 7: Stable isotopic data of carbon and oxygen for carbonate cements of Block 3.

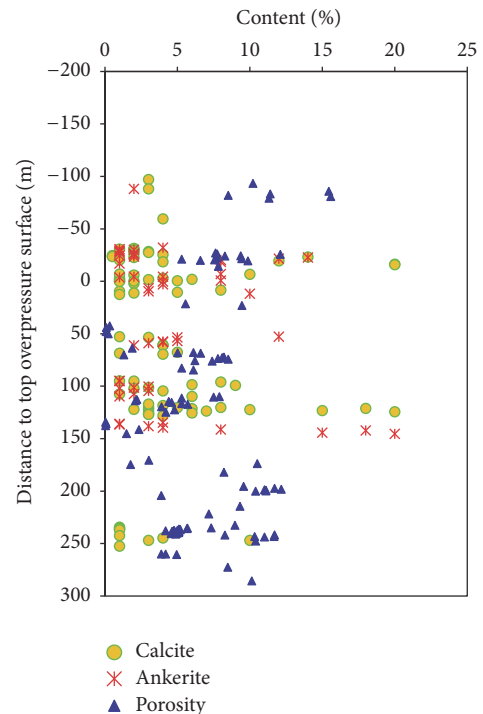


FIGURE 8: Relations between carbonate content, porosity, and distance to top overpressure surface of Block 3.

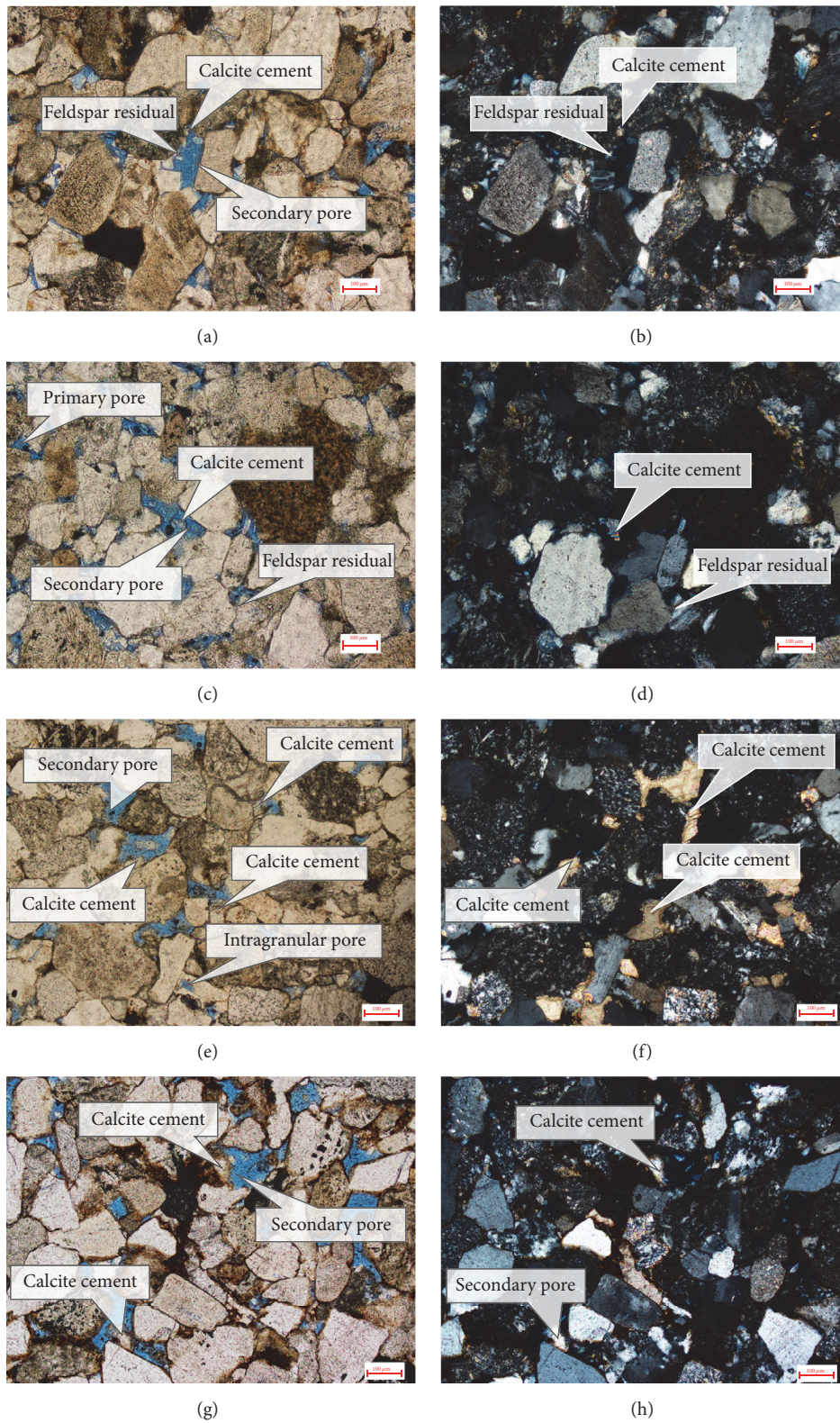


FIGURE 9: Photomicrographs of petrographic features of the Xishanyao Formation sandstones. Full view of pores and intergranular secondary pores develops from a blue-epoxy-impregnated thin sections of conventional core samples. The remnant of calcite and feldspar can be found after dissolution. (a), (b) Y2 well at 5961.5 m with magnification of 40; (c), (d) Y6 well at 5978 m with magnification of 40; (e), (f) Y1 well at 5876.3 m with magnification of 40; (g), (h) Y7 well at 6102.95 m with magnification of 40.

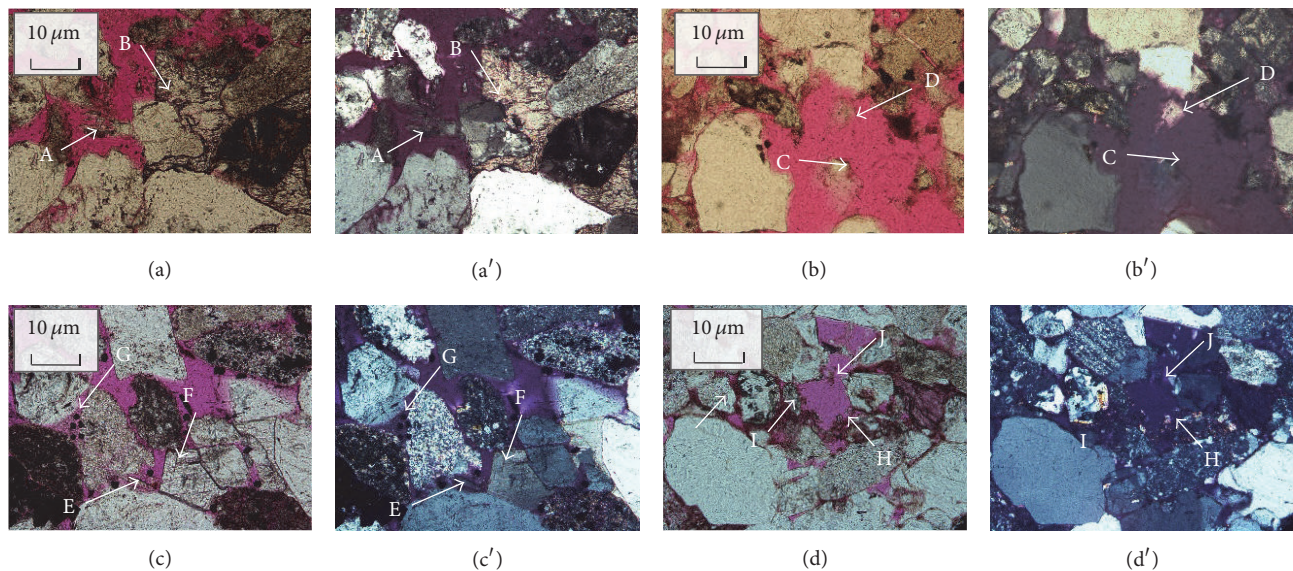


FIGURE 10: Photomicrographs of pore types by electron microprobe analysis of sandstones in central Junggar Basin. (a) and (a') Intergranular secondary pore develops, and measuring point A shows that the remnant is K-feldspar and the measuring point B is calcite. The photomicrograph is a red-epoxy-impregnated thin sections of conventional core samples with magnification of 10 (Sha 1 well at 3656.6 m with Jurassic) and photo (a) by plane-polarized light and photo (a') by cross polarization; (b) and (b') intergranular secondary pore develops, and measuring point C shows that the remnant is albite and measuring point D is K-feldspar. The photomicrograph is a red-epoxy-impregnated thin sections of conventional core samples with magnification of 10 (Zhuang 1 well at 4375.23 m with Jurassic), and photo (b) by plane-polarized light and photo (b') by cross polarization; (c) and (c') intergranular secondary pore develops, measuring point E shows that the remnant is albite. Measuring point F is calcite and measuring point G is siderite, and the photomicrograph is a red-epoxy-impregnated thin sections of conventional core samples with magnification of 10 (Sha 2 well at 3439 m with Jurassic) and photo (c) by plane-polarized light and photo (c') by cross-polarized light; (d) and (d') intergranular secondary pore develops, and measuring point H shows that the remnant is calcite, measuring point I is K-feldspar, and measuring point J is albite. The photomicrograph is a red-epoxy-impregnated thin sections of conventional core samples with magnification of 10 (Y1 well at 5877 m with Jurassic) and photo (d) by plane-polarized light and photo (d') by cross-polarized light.

the porosity. In these two ways, the high porosity and high content of carbonate cements developed in the same burial depth [44].

Carbonate cements commonly occurred as irregularly distributed concretions even at the same depth, so it is challenging to predict porosity and permeability in the subsurface from spaced wells. Thin sections can provide a continuous image of heterogeneity produced by concretionary calcite cements. Our thin section images indicate a negative correlation between the carbonate cements and porosity development. Perhaps this phenomenon elaborates that intergranular pores, developing in deeply buried sandstones, result from early carbonate cements dissolving and migration. Therefore, early carbonate cements develop widely and secondary porosity is higher at later diagenetic phase.

The late generation of poikilotopic calcite is interpreted as a result of plagioclase and early calcite dissolution, which releases cations into pore water and may also be responsible for the precipitation of clay minerals and the silica cements [45]. From Figure 3,  $R_o$  were in 0.7–1.0%. Thin section observations show that calcite formation is strongly associated with alteration of plagioclase. Among the common rock-forming minerals, plagioclase (especially calcium-rich plagioclase) is dissolved more rapidly than the other silicate phases [46], indicating that porosity generation may primarily result

from plagioclase dissolution in deeply burial location. With the increasing of depth, temperature, and thermal maturity, calcite dissolution will be gradually weakened [5]. According to thin sections, primary porosity developed before the depth 3500 m, secondary porosity mainly developed between 3500–6200 m, and cracks begin to develop from 6200 m [47, 48]. Therefore, during the deep-burial water-rock interaction processes, a lower secondary porosity zone resulting from plagioclase dissolution at depth greater than 6500 m would develop (Figure 11).

## 6. Conclusions

In Block 3 of the central Junggar Basin, carbonate cements are the predominant cements. Conventional core samples, epoxy-impregnated thin section analysis, and cathodoluminescence analysis indicate that the growth of carbonate cements has two stages and mostly formed at the late diagenetic stage, generating ferroan calcite and ankerite cements.

Data from the six wells demonstrate that carbonate cements of most of the samples are less than 20% and generally in the range of 1–10%. The concentration of carbonate cements increases with increasing burial depth. Carbonate cements mainly concentrate in the depth range +50 m–200 m to the top overpressure surface.

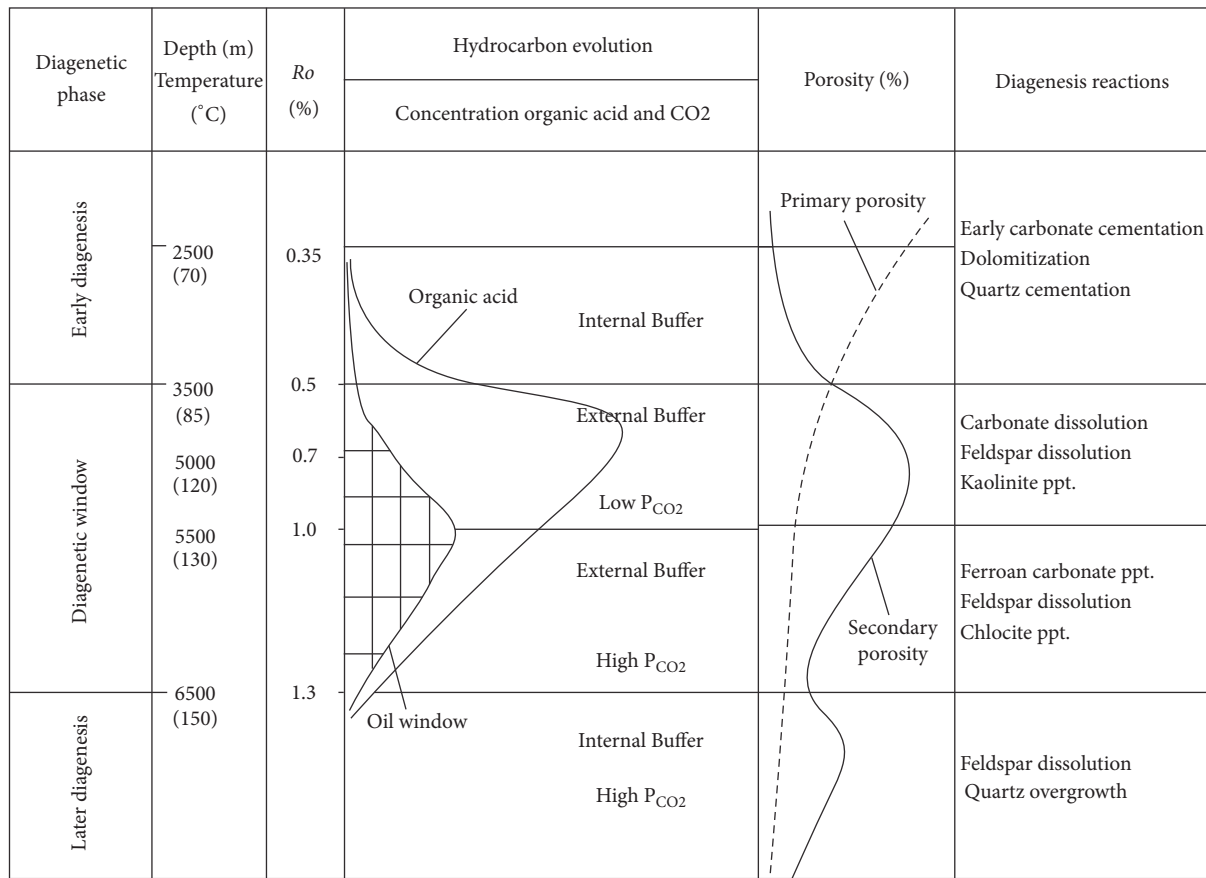


FIGURE 11: Diagenetic reactions, porosity, and hydrocarbon evolution of the different diagenetic phase in Block 3.

Stable isotopic data shows that  $\delta^{13}C_{PDB}$  ranges from -19.07 to -5.87‰ and  $\delta^{18}O_{PDB}$  ranges from -21.08 to -13.96‰. This suggests that the carbonate cements in these sandstones were significantly influenced by organic matter during burial history.

Electron microprobe analysis documents that the secondary intergranular pores primarily resulted from dissolving intergranular carbonate cements and feldspar. The chemical compaction and large-scale cementation restricted the dissolving capability of organic acid on late carbonate cements.

Textural data suggest that the late poikilotopic calcite, near the top overpressure surface, is rich in Fe and high porosity is developed in the same depth interval. This can be interpreted as a result of the dissolution of plagioclase. Therefore, another secondary porosity zone is supposed to develop, resulting from plagioclase dissolution at depth greater than 6500 m. However, because of the chemical compaction and quartz overgrowth, the porosity scale will be smaller than the porosity developed at the depth of 5500 m.

**Conflicts of Interest**

The authors declare that there are no conflicts of interest regarding the publication of this paper.

**References**

- [1] R. Hesse and L. A. Abid, "Carbonate cementation-the key to reservoir properties of four sandstone levels (cretaceous) in the hibernia oil field, jeanne d'arc basin, newfoundland, Canada," in *Carbonate Cementation in Sandstones: Distribution Patterns and Geochemical Evolution, International Association of Sedimentologists Special Publication*, vol. 26, pp. 363-393, Wiley Online Library, Oxford, UK, 1998.
- [2] S. Liu, S. Huang, Z. Shen, Z. Lü, and R. Song, "Diagenetic fluid evolution and water-rock interaction model of carbonate cements in sandstone: An example from the reservoir sandstone of the Fourth Member of the Xujiahe Formation of the Xiaoquan-Fenggu area, Sichuan Province, China," *Science China Earth Sciences*, vol. 57, no. 5, pp. 1077-1092, 2014.
- [3] D. Xiong, K. Azmy, and N. J. F. Blamey, "Diagenesis and origin of calcite cement in the Flemish Pass Basin sandstone reservoir (Upper Jurassic): Implications for porosity development," *Marine and Petroleum Geology*, vol. 70, pp. 93-118, 2016.
- [4] C. D. Curtis, "Possible links between sandstone diagenesis and depth-related geochemical reactions occurring in enclosing mudstones," *Journal of the Geological Society*, vol. 135, no. 1, pp. 107-117, 1978.
- [5] R. C. Surdam, L. J. Crossey, E. S. Hagen, and H. P. Heasler, "Organic-inorganic interactions and sandstone diagenesis," *AAPG Bulletin*, vol. 73, no. 1, pp. 1-23, 1989.
- [6] S. D. Weedman, S. L. Brantley, R. Shiraki, and S. R. Poulson, "Diagenesis, Compaction, and Fluid Chemistry Modeling of a

- Sandstone Near a Pressure Seal: Lower Tuscaloosa Formation, Gulf Coast," *AAPG Bulletin*, vol. 80, no. 7, pp. 1045–1064, 1996.
- [7] K. Bjorlykke, "Geofluids: Origin, migration and evolution of fluids in sedimentary basins," in *Fluid-flow processes and diagenesis in sedimentary basins*, L. Parnell, Ed., vol. 78 of *Geological Society Special Publication*, pp. 127–140, 1994.
- [8] F. L. Lynch, "Mineral/water interaction, fluid flow, and Frio sandstone diagenesis: evidence from the rocks," *AAPG Bulletin*, vol. 80, no. 4, pp. 486–504, 1996.
- [9] Z. Zhihuan, H. Wenxuan, Z. Jianhui, Y. Bingsong, and L. Xiancai, "Study of fluid-rock interaction in Eocene Formation in Dongying Depression, Bohai Gulf Basin," *Acta Sedimentologica Sinica*, vol. 18, no. 4, pp. 560–566, 2000.
- [10] S. P. Dutton, C. D. White, B. J. Willis, and D. Novakovic, "Calcite cement distribution and its effect on fluid flow in a deltaic sandstone, Frontier Formation, Wyoming," *AAPG Bulletin*, vol. 86, no. 12, pp. 2007–2021, 2002.
- [11] K. Al-Ramadan, S. Morad, J. N. Proust, and I. Al-Aasm, "Distribution of diagenetic alterations in siliciclastic shoreface deposits within a sequence stratigraphic framework: evidence from the Upper Jurassic, Boulonnais, NW France," *Journal of Sedimentary Research*, vol. 75, no. 5, pp. 943–959, 2005.
- [12] R. Jonk, A. Hurst, D. Duranti, J. Parnell, A. Mazzini, and A. E. Fallick, "Origin and timing of sand injection, petroleum migration, and diagenesis in Tertiary reservoirs, south Viking Graben, North Sea," *AAPG Bulletin*, vol. 89, no. 3, pp. 329–357, 2005.
- [13] F. Hao, H. Zou, Y. Fang, and J. Hu, "Kinetics of organic matter maturation and hydrocarbon generation in overpressure environment," *Shiyou Xuebao/Acta Petrolei Sinica*, vol. 27, no. 5, pp. 9–18, 2006.
- [14] M. I. Odigi and L. C. Amajor, "Geochemistry of carbonate cements in Cretaceous sandstones, southeast Benue Trough, Nigeria: Implications for geochemical evolution of formation waters," *Journal of African Earth Sciences*, vol. 57, no. 3, pp. 213–226, 2010.
- [15] B. T. T. Nguyen, S. J. Jones, N. R. Goult, et al., "The role of fluid pressure and diagenetic cements for porosity preservation in Triassic fluvial reservoirs of the Central Graben, North Sea," *AAPG Bulletin*, vol. 97, no. 8, pp. 1273–1302, 2013.
- [16] F. García-García, R. Marfil, G. A. De Gea et al., "Reworked marine sandstone concretions: A record of high-frequency shallow burial to exhumation cycles," *Facies*, vol. 59, no. 4, pp. 843–861, 2013.
- [17] S. L. Nyman, R. M. Gani, J. P. Bhattacharya, and K. Lee, "Origin and distribution of calcite concretions in Cretaceous Wall Creek Member, Wyoming: Reservoir-quality implication for shallow-marine deltaic strata," *Cretaceous Research*, vol. 48, pp. 139–152, 2014.
- [18] Z. Ming, Z. Weihai, and Q. Jiangxiu, "The character and origin of overpressure and its explorational significance in Junggar Basin," *Petroleum Exploration and Development*, vol. 27, no. 2, pp. 31–35, 2000.
- [19] W.-H. Zhang, M. Zha, and J.-X. Qu, "Overpressure and mechanisms of hydrocarbon accumulation in tertiary of southern Junggar Basin," *Journal of the University of Petroleum*, vol. 28, no. 1, pp. 10–12, 2004.
- [20] W. Kongyou, Z. Ming, W. Xulong, Q. Jiangxiu, and X. Chen, "Further researches on the tectonic evolution and dynamic setting of the Junggar Basin," *Acta Geoscientifica Sinica*, vol. 26, no. 3, pp. 217–222, 2005.
- [21] S. He, Z.-L. He, Z. Yang, H.-Z. Wu, F.-R. Wang, and W.-Z. Shi, "Characteristics, well-log responses and mechanisms of overpressures within the Jurassic formation in the central part of Junggar basin," *Diqiu Kexue - Zhongguo Dizhi Daxue Xuebao/Earth Science - Journal of China University of Geosciences*, vol. 34, no. 3, pp. 457–470, 2009.
- [22] K. Xi, Y. Cao, Y. Wang et al., "Diagenesis and porosity-permeability evolution of low permeability reservoirs: A case study of Jurassic Sangonghe Formation in Block 1, central Junggar Basin, NW China," *Petroleum Exploration and Development*, vol. 42, no. 4, pp. 475–485, 2015.
- [23] Z. Yang, S. He, Q. Li, S. Lin, and S. Pan, "Geochemistry characteristics and significance of two petroleum systems near top overpressured surface in central Junggar Basin, NW China," *Marine and Petroleum Geology*, vol. 75, pp. 341–355, 2016.
- [24] J. Kuang, Y. Genshun, and Z. Guohua, "The Origin of Favorable Sandstone Reservoirs of Sangonghe Formation, Lower Jurassic in Central Junggar Basin," *Petroleum Exploration and Development*, vol. 28, no. 6, pp. 34–37, 2001.
- [25] S. Jianfeng, Z. Xingping, S. Chunsong, Z. Huiliang, and G. Mozhen, "Basic Types of High-quality Clastic Reservoirs Deep-buried in Superimposed Basins in China," *China Petroleum Exploration*, vol. 11, no. 1, pp. 11–16, 2006.
- [26] X. Guosheng, L. Jianlin, Z. Ping, L. Feng, and L. Yisha, "Diagenesis and pore formation mechanism of jurassic and cretaceous reservoirs in block 3 in the middle of Junggar Basin," *Journal of Oil and Gas Technology*, vol. 29, no. 3, pp. 1–7, 2007.
- [27] S. Epstein, R. Buchsbaum, H. A. Lowenstam, and H. C. Urey, "Revised carbonate-water isotopic temperature scale," *Bulletin of the Geological Society of America*, vol. 64, no. 11, pp. 1315–1326, 1953.
- [28] H. Li, M. Jiang, Y. Wang, L. Zhang, and G. Yu, "Image of crust and upper mantle structure along the array from fuyun to kuerle by P-to-S converted waves," *Acta Geologica Sinica*, vol. 80, no. 1, pp. 135–141, 2006.
- [29] K. Yuzhu, "Targets of Paleozoic in Junggar Basin," *Petroleum Prospect and Exploration*, vol. 31, no. 5, pp. 449–453, 2010.
- [30] K. Zhihong, "Evolution of paleozoic sedimentation of the junggar basin," *Journal of Geomechanics*, vol. 17, no. 2, pp. 158–174, 2011.
- [31] S. Jiye, Q. Mingkuan, C. Yuqi, and H. Zhongbo, "Basement characteristics of junggar basin and its effect on sandstone-type uranium metallogenesis," *Geological Review*, vol. 61, no. 1, pp. 128–138, 2015.
- [32] X. Wu, D. He, D. Yang, X. Qi, and Y. Tang, "Structural character and hydrocarbon accumulation in the Luliang uplift, Junggar Basin," *Scientia Geologica Sinica*, vol. 47, no. 1, pp. 73–91, 2012.
- [33] Z. He, S. Gao, and M. Zheng, "Regional tectonic framework and evolution of superimposed basins in northwestern China," *Earth Science Frontiers*, vol. 22, no. 3, pp. 227–240, 2015.
- [34] P. Changchun, Z. Zhongyi, F. Shanfa, X. Qilai, W. Xulong, and W. Yutao, "Thermal history of Junggar Basin," *Geochimica*, vol. 26, no. 6, pp. 1–7, 1997.
- [35] W. Xulong, Y. Haibo, and Q. Yongxin, "Basin modeling technique and JunMod basin modeling software," *Computer Application of Petroleum*, vol. 2, pp. 18–24, 2001.
- [36] Q. Nansheng, Z. Ming, and W. Xulong, "Simulation of geothermal evolution history in junggar basin," *Xinjiang Petroleum Geology*, vol. 21, no. 1, pp. 38–41, 2000.
- [37] N. Qiu, H. Yang, and X. Wang, "Tectono-thermal evolution in the Junggar Basin," *Chinese Journal of Geology*, vol. 37, no. 4, pp. 423–429, 2002.

- [38] W. Yin, B.-W. Bie, and G.-L. Liu, "The characteristics of fluid inclusions and its application to identifying oil accumulating stages in central depression, Junggar Basin," *Bulletin of Mineralogy, Petrology and Geochemistry*, vol. 28, no. 1, pp. 53–60, 2009.
- [39] H. Irwin, C. Curtis, and M. Coleman, "Isotopic evidence for source of diagenetic carbonates formed during burial of organic-rich sediments," *Nature*, vol. 269, no. 5625, pp. 209–213, 1977.
- [40] R. C. Surdam, S. W. Boese, and L. J. Crossey, "The chemistry of secondary porosity," in *Clastic Diagenesis*, D. A. McDonald and R. C. Surdam, Eds., pp. 127–149, AAPG Memoir, 1984.
- [41] S. Morad, "Carbonate cementation in sandstones; distribution patterns and geochemical evolution," in *Carbonate Cementation in Sandstones*, S. Morad, Ed., vol. 26 of *Special Publication*, pp. 1–26, International Association of Sedimentologists, Oxford, UK, 1998.
- [42] L.-Q. Zhang, "Distribution and origin of ferrocalcite cements in Paleogene overpressure sandstones on the south margin of Junggar Basin, Xinjiang, China," *Journal of Chengdu University of Technology. Science and Technonogy*, vol. 38, no. 6, pp. 625–632, 2011.
- [43] Y.-Z. Wang, Y.-C. Cao, S.-M. Zhang, F.-L. Li, and F.-C. Meng, "Genetic mechanisms of secondary pore development zones of Es 4x in the north zone of the Minfeng Sag in the Dongying Depression, East China," *Petroleum Science*, vol. 13, no. 1, pp. 1–17, 2016.
- [44] H. Sijing, H. Peipei, W. Qingdong, L. Haonian, W. Meng, and Z. Mingliang, "The significance of cementation in porosity preservation in deep-buried sandstones," *Lithologic Reservoirs*, vol. 19, no. 3, pp. 7–13, 2007.
- [45] R. M. Siebert, G. K. Moncure, and R. W. Lahann, "A theory of framework grain dissolution in sandstones," in *Clastic Diagenesis*, D. A. McDonald and R. C. Surdam, Eds., vol. 37, AAPG Memoir, Tulsa, OK, 1984.
- [46] R. H. McNutt, S. K. Frape, P. Fritz, M. G. Jones, and I. M. MacDonald, "The  $^{87}\text{Sr}$   $^{86}\text{Sr}$  values of Canadian Shield brines and fracture minerals with applications to groundwater mixing, fracture history, and geochronology," *Geochimica et Cosmochimica Acta*, vol. 54, no. 1, pp. 205–215, 1990.
- [47] Z. Yang, S. He, F. Wang, Z. He, H. Wu, and X. Meng, "Characteristics and genetic mechanism of carbonate cement in sandstone reservoirs of Yongjin area in central Junggar Basin," *Acta Petrologica et Mineralogica*, vol. 28, no. 2, pp. 169–178, 2009.
- [48] W. Furong and H. Sheng, "The reservoir characteristic of deeply-buried sandstone in the Center of Junggar Basin," *Petroleum Geology and Experiment*, vol. 32, no. 6, pp. 547–552, 2010.

## Research Article

# Seismic Characterization of Hypogenic Karst Systems Associated with Deep Hydrothermal Fluids in the Middle-Lower Ordovician Yingshan Formation of the Shunnan Area, Tarim Basin, NW China

Hongtao Zhu, Xiu Zhu, and Honghan Chen

Key Laboratory of Tectonics and Petroleum Resources, China University of Geosciences, Ministry of Education, Wuhan 430074, China

Correspondence should be addressed to Hongtao Zhu; htzhu@cug.edu.cn

Received 3 March 2017; Revised 11 May 2017; Accepted 27 July 2017; Published 13 September 2017

Academic Editor: Zhijun Jin

Copyright © 2017 Hongtao Zhu et al. This is an open access article distributed under the Creative Commons Attribution License, which permits unrestricted use, distribution, and reproduction in any medium, provided the original work is properly cited.

Two fundamental forms of hypogenic karst systems (lateral stratiform hypogenic and cross-formational fault-vein hypogenic karst system) are distinguished mainly by differential effects of preexisting faults. In seismic cross sections, hypogenic karst systems are expressed as complex *string-beads*-like seismic reflections associated with faults. In this study, a new seismic characterization workflow was developed including seismic amplitude thresholding, fault interpretation, pickup, and merge display to enhance the description of the spatial distribution and coupling of hypogenic karst system and faults. The results suggest that the lateral stratiform hypogenic karst systems are predominantly developed at the top of the secondary faults, presenting an overall of “layered distribution and finger-like interaction” features. The cross-formational fault-vein hypogenic karst systems are developed around faults and characterized by dendritic distribution. Furthermore, we infer that the development pattern of hypogenic karst systems has been produced by the interplay of the faults, preexisting epigenic karst systems, and lateral carrier-beds, which together combine the complex hydrothermal migration pathways of fluids with the characteristics of vertical and horizontal combined pathways. In addition, some possible controlling factors (e.g., sequence stratigraphic boundaries, paleogeomorphology, and sedimentary facies) that can influence the development of these hypogenic karst systems have been discussed in detail.

## 1. Introduction

It has been well documented that there exists tremendous exploratory potential of the deep subsurface, which has recently drawn attention of petroleum geologists worldwide (e.g., [1–3]). One of the forming mechanisms of deeply buried carbonate reservoirs (>4500 m) is related to dissolution effects by fluids in the deep subsurface (e.g., [4, 5]). The fluids here are not meteoric in origin but typically refer to hydrothermal fluids, which enter the relatively shallow subsurface from deep along the faults. Hypogenic karst systems influenced by deep hydrothermal fluids contribute to the formation of the quality deep carbonate reservoirs and have been found in the Yingshan Formation (>6000 m) of the Shunnan area, Tarim Basin, NW China. In addition, hydrothermal minerals (calcite, quartz, and tabular anhydrites) provide evidence that hypogenic karst systems

affected by hydrothermal fluids are also found in the Yingshan Formation. Clearly understanding the characteristics of hypogenic karst systems developed in Yingshan Formation is therefore of significance to optimizing petroleum exploration and increasing reserves.

Hypogenic karst is a genic type of karst, regardless of the lithologies in which it develops [6, 7]. Speleogenesis is often considered as the primary mechanism of the formation of karst because almost all essential attributes of karst owe their origin to speleogenesis [7]. Two fundamental types of speleogenesis, hypogene and epigene, are differentiated mainly by the distinct hydrodynamic characteristics of the respective groundwater flow systems: (1) stratiform confined aquifer systems or across-formational fracture-vein flow systems, of varying depths and degrees of confinement, and (2) hydrodynamically open, near-surface unconfined systems

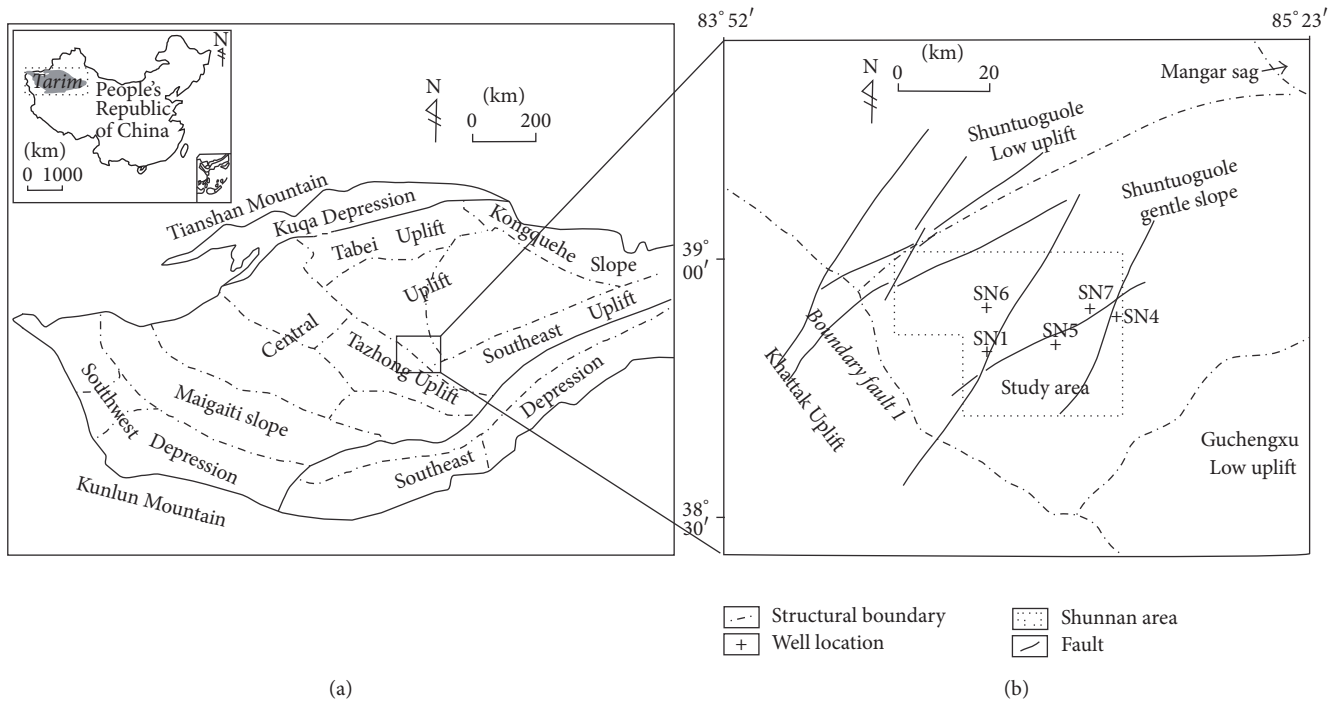


FIGURE 1: Location of the Shunnan area in the Central Tarim Basin, NW China. (a) Location of the Tarim Basin in China and the Tazhong uplift in Tarim Basin. (b) Main tectonic units of the Shunnan area.

[7]. Accordingly, the principal difference between hypogenic and epigenic karst systems lies in the modes (confined versus unconfined) and principal vectors (ascending versus descending) of fluid circulation and in the source of recharge to a given unit (recharge from depth versus recharge from the overlying or immediately adjacent surface) [6, 7].

There have been many case studies on carbonate karst over the past six decades, but they deal mainly with epigenic karst systems (e.g., [8–14]). The progress on the characterization of the hypogenic karst systems (e.g., [15–19]) predominantly focuses on the planar- or section-view delineations of lateral stratiform hypogenic karst system zones and relevant fault system zones individually. The “lateral stratiform hypogenic karst system zone” is used to denote the zone where fluids are directed transversely flow across layers and formation and in which fluids related to upwelling flows from the deep subsurface and upwards migrate along the faults. The relevant “fault system zone” in this paper not only denotes the migration pathways (faults) of ascending fluids that contribute to the formation of hypogenic karst system but also refers to the “cross-formational fault-vein hypogenic karst system,” which is characterized by developing parallel around faults.

The Shunnan area is a three-level structural unit within the Tarim Basin, located at the downthrown side of the boundary fault I of the Tazhong Low uplift (Figure 1). It is bounded to the west by the Khattak Uplift, north by the Shuntuoguole Low uplift, south by the Guchengxu Low uplift, and east by the Mangar sag (Figure 1). In recent years, hydrothermal minerals (calcite and quartz in veins and tabular anhydrites) at depths (>6000 m) and distinctive seismic

reflections that are expressed by a series of individual string-beds lateral spreading have been found in the Shunnan area. These provide the potential conditions to characterize the distribution of the hypogenic karst systems.

The aim of this paper is to understand the spatial distribution and controlling factors of hypogenic karst development and develop a model of the karst systems in the Middle-Lower Ordovician Yingshan Formation of Shunnan area, Tarim Basin, NW China. In this paper, the hypogenic karst systems and faults were first distinguished on the basis of an integrated approach of seismic data with available conventional cores, wells, and a scanning electron microscope analysis, and then a new seismic characterization workflow was developed, including seismic amplitude thresholding, fault interpretation, pickup, and merge display, to enhance the description of the spatial distribution and coupled hypogenic karst systems and faults. The proposed workflow will provide new insight into 3D seismic characterization of the hypogenic karst systems and can be used extensively in hypogenic-related karst basins around the world.

## 2. Geological Setting

The Tarim Basin in western China (Figure 1) is a composite basin with a number of uplifts and depressions that developed as a result of a long and complicated tectonic history (e.g., [20–26]). It is located between the Tianshan Mountain and Kunlun mountains, occupying an area of  $56 \times 10^4 \text{ km}^2$ . The basin's east-west length is 1400 km while the maximum width reached 520 km with the altitude ranges between 800 m and 1300 m. Collectively, the development of the basin's

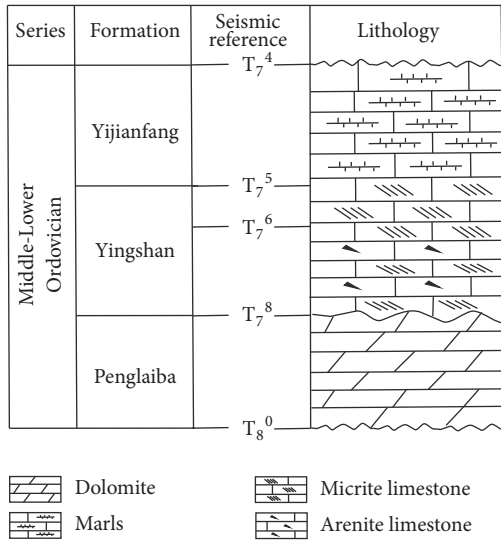


FIGURE 2: Generalized stratigraphic column of the Middle-Lower Ordovician of the Tarim Basin, showing lithology and seismic reference. The study interval is the Yingshan Formation.

current configuration and the geometry of tectonic elements are controlled mainly by multiple tectonic activities. The Tarim Basin is mainly divided into three uplifts and four depressions. From the north to the south, there are the Kuqa Depression, Tabei Uplift, Northern Depression, Central Uplift, Southwest Depression, Southeast Uplift, and Southeast Depression (e.g., [27–29]; Figure 1(a)).

The Tazhong Low uplift is located in the middle part of the Central Uplift in the Tarim Basin, covering an area of  $2.9 \times 10^4 \text{ km}^2$ , and the terrain dips to northwest, generally like a bird foot or a broom (e.g., [29]; Figure 1(a)). The Middle Ordovician in the Tazhong area is subdivided into Yingjianfang and Yingshan Formations. The Lower Ordovician is subdivided into Yingshan and Penglaiba Formations. After the deposition of Lower Ordovician Penglaiba Formation, Tazhong area, subjected to compression, started to uplift.

The study area (Figure 1(b)) is a three-level structural unit, located at downthrown side of the boundary fault I of Tazhong Low uplift within Tarim Basin. It adjoins Khattak Uplift bounded by the boundary fault I on the western side; to the north, it is adjacent to the Shuntuoguole Low uplift. The gentle slope connects Guchengxu Low uplift to the south and Mangar sag to the east, respectively. The lower part of the Yingshan Formation was subjected to long-term exposure, forming intensive epigenetic karst systems. To the contrary, the upper part of the Yingshan Formation did not experience exposure after deposition, and a large amount of hypogenic karst systems was found in the upper part of the Yingshan Formation. Seismic references  $T_8^0$  and  $T_7^4$  are the base and top of the Middle-Lower Ordovician,  $T_7^8$  and  $T_7^5$  are the base and top of the Middle-Lower Ordovician Yingshan Formation, and  $T_7^6$  is the interface between the upper and lower Yingshan Formation. Those seismic references are shown in Figure 2.

The hypogenic karst systems are defined as the formation of caves by water that recharges the soluble formation from below, driven by hydrostatic pressure or other sources of energy and independent of the recharge from the overlying or immediately adjacent surface (e.g., [15]). It has been proved that carbonates may produce a series of geological and geochemical changes in the hydrothermal process and these changes may be reflected by mineralogy and geochemistry [30]. The hydrothermal fluids often contain some acid gases such as  $\text{CO}_2$  and  $\text{H}_2\text{S}$  [31], dissolve the original carbonates by the water-rock reaction, and form the hydrothermally associated minerals such as the fluorite, chlorite, sphalerite, and barite and even the hydrothermal mineral association [32]. Hydrothermal processes commonly form the associated minerals such as calcite, quartz, and tabular anhydrite in well SN4 (Figure 3). Present temperature is the highest temperature in the geological buried process of the Yingshan Formation [33], and geothermal gradient of the Shunnan area is  $2.0\sim 2.3^\circ\text{C}/100 \text{ m}$  [34, 35]. Therefore, the highest temperature in well SN4 of the Yingshan Formation is about  $153\sim 173^\circ\text{C}$ . The homogenization temperature of the original inclusion represents the temperature of the hydrothermal fluid [30]. The main homogenization temperatures of primary fluid inclusions in calcite and quartz are higher than the highest temperature of about  $25^\circ\text{C}$  in well SN4 [33], so the calcite and quartz must have been formed in high-temperature condition which may be mainly caused by hydrothermal fluids from the deep subsurface.

### 3. Seismic Facies Variations between Epigenetic and Hypogenic Karst Systems

Classic seismic facies are groups of the characteristics of seismic reflections which differ from those of adjacent areas (e.g., [36]). Paleokarst seismic facies are extremely complex. Previously published studies provide valuable insights into seismic evidence of paleokarst facies (e.g., [23, 24, 37, 38]). Key seismic parameters include reflection amplitude, continuity of seismic events, apparent frequency, external form, and internal reflection configuration. The variations are utilized to infer the underlying geology (e.g., [23, 24, 39]). In this paper, two typical seismic facies referred to as the individual string-beads-like and complex string-beads-like are identified to describe the seismic reflections of epigenetic and hypogenic karst systems, respectively, in the Middle-Lower Ordovician Yingshan Formation. Detailed differences between both string-beads-like individuals and complexes are expounded in the following.

**3.1. Seismic Facies of Epigenetic Karst Systems.** As noted in Klimchouk [7], epigenetic karstification occurs in the near-surface conditions and is directly linked with recharge from the immediately overlying or adjacent surface. The individual string-beads-like seismic reflection has been interpreted as the evidences of “epigenetic karst system” in the Tarim Basin in the published papers, which is always linked with the terms “unconformities, weathering crusts, exposure, etc.” (Guo et al. 2012; Chen et al. 2014) [40, 41]. These terms are further related to the epigenetic karst system development. Guo et al.

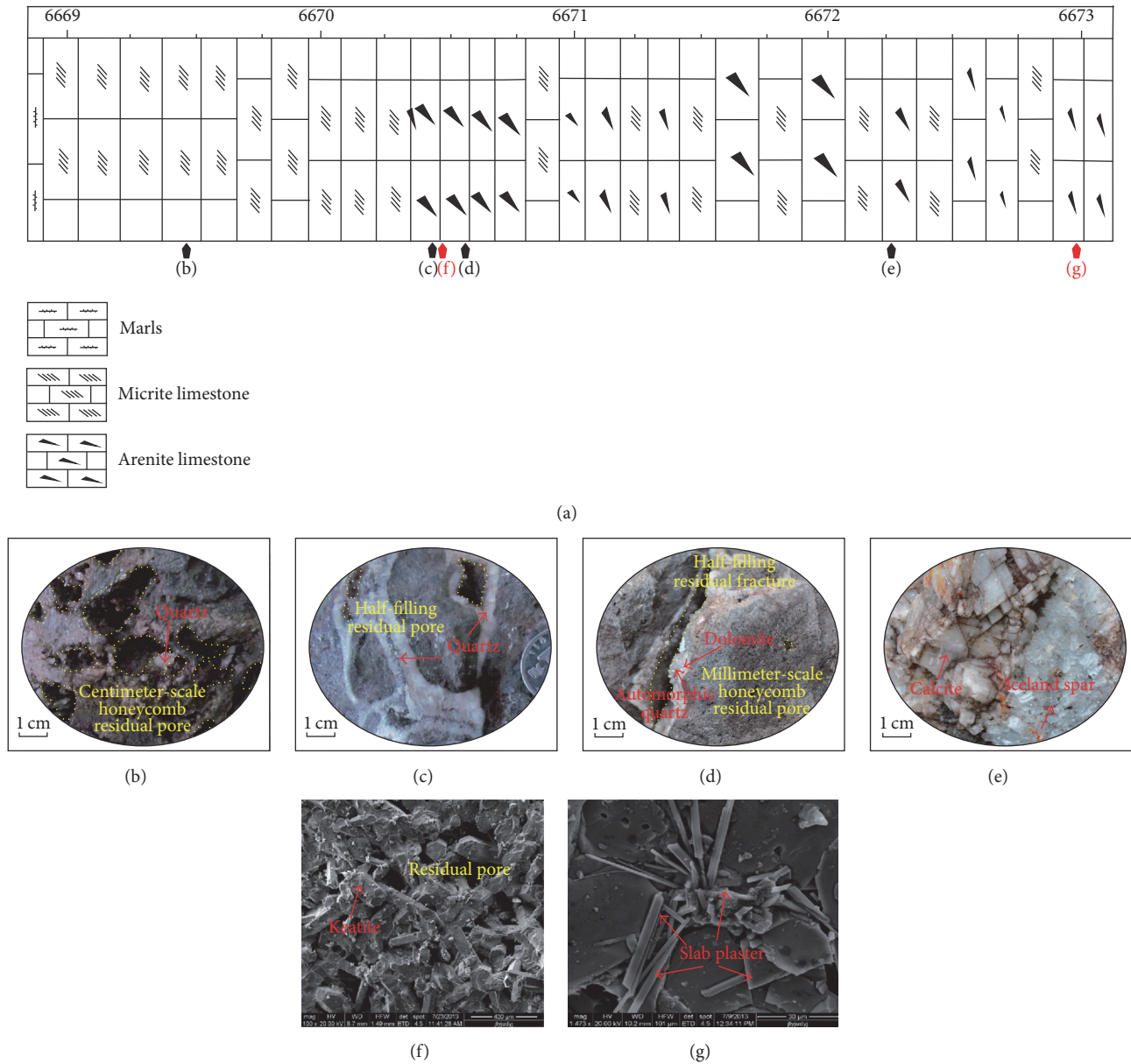


FIGURE 3: Petrologic characteristics of the Yingshan Formation determined from well SN4. (a) Lithology of well SN4 from 6668.3 to 6673.5 m. (b) Centimeter-scale honeycomb residual pores, 6669.47 m. (c) Half-filling residual pores along the fractures, 6670.44 m. (d) Half-filling residual pores along the fracture and millimeter-scale honeycomb residual pores, 6670.57 m. (e) Iceland spar (calcite), 6672.25 m. (f) Quartz in vein, 6670.48 m. (g) Tabular anhydrite, 6672.98 m.

(2012) pointed out the individual *string-beads*-like seismic reflection in Yingshan Formation is attributed to weathering karst (epigenic karst). Chen et al. (2014) demonstrated the individual *string-beads*-like seismic reflection (strong or weak amplitude) is attributed to “epigenic karst system” on the basis of analysis of conventional cores, wells, and loggings in Yingshan Formation, Tarim Basin. In this paper, the author thought the development of karst system in Yingshan Formation is linked with the exposure environment and related to meteoric fluids. Gao et al. [40] demonstrated that the individual *string-beads*-like seismic reflection in the

Tazhong area is linked with the exposure environment. In this paper, the moldic and dissolution pores in well Shun2 (at depth of 6879.5 m) are formed in the meteoric fresh water environment as a result of the repeated exposure of the carbonate platform. In addition, fibrous calcite cementation in well Shun6 (at the depth of 6646.9 m) is also the indicator of the meteoric fresh water environment.

In the study area, many high-amplitude, low-continuous, individual *string-beads*-like seismic reflections were recognized in the lower part of the Yingshan Formation in the seismic cross sections (Figures 4(a) and 4(b)). These seismic

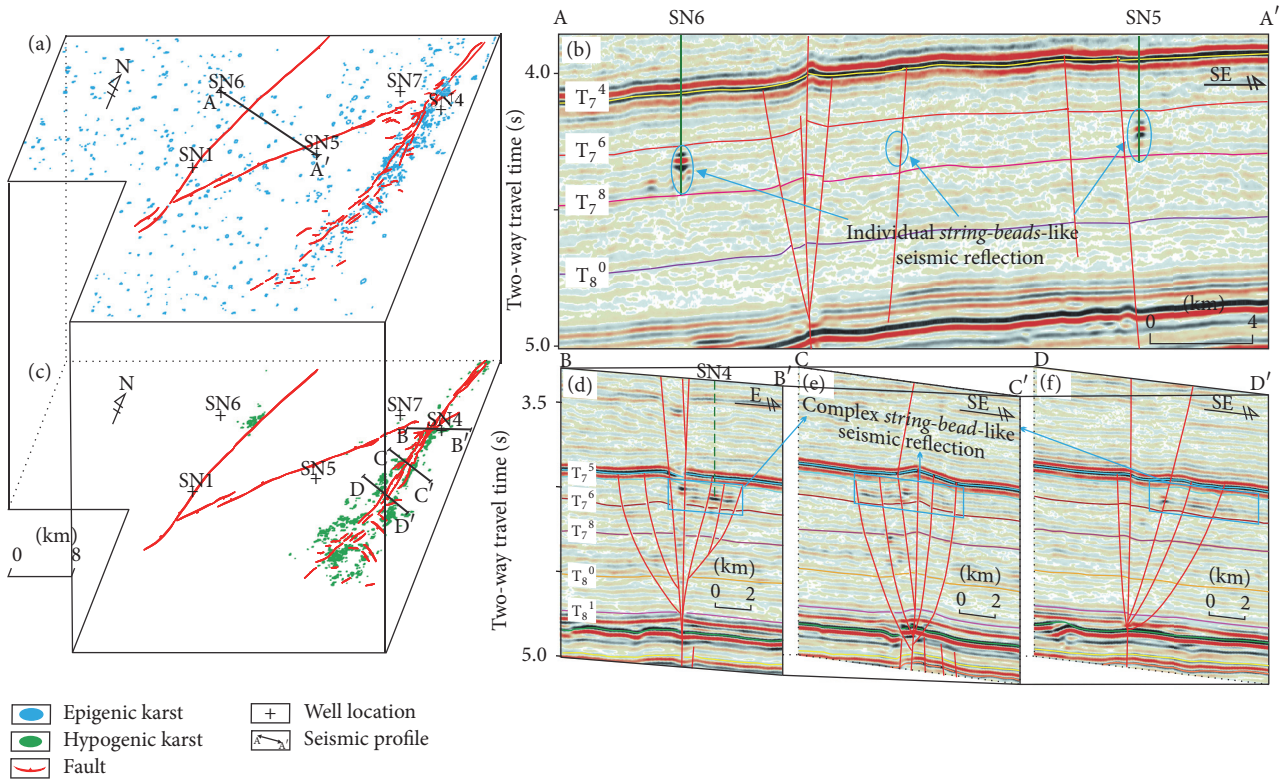


FIGURE 4: Seismic facies of epigenic karst systems and hypogenic karst systems of the Yingshan Formation in the study area. (a) Seismic attribute RMS (root mean square) map of the lower part of the Yingshan Formation. (b) Epigenic karst systems marked by the blue oval line across wells SN6 and SN5 seismic section, showing the typical individual *string-beads*-like seismic reflections. (c) Seismic attribute RMS (root mean square) map of the upper part of the Yingshan Formation. (d) Complex *string-beads*-like seismic reflections of hypogenic karst systems across well SN4 seismic section, developed associated with the faults. (e) and (f) Other seismic section showing complex *string-beads*-like seismic reflections of hypogenic karst systems, developed associated with the faults. The blue color indicates epigenic karst systems, distributed widely in the entire study area with the isolated punctate distributions; the green color indicates hypogenic karst systems, showing belt-shaped distributions along the SN4 fault zone.

reflections are characterized by multiple strong amplitudes with vertical build-ups and worm-like short-axis appearances, forming near-vertical columns, referred to as *string-beads*. [41]. They predominantly reflect the distribution of the epigenic karst systems. Apart from the individual *string-beads*-like seismic reflections, the strata are characterized by continuous parallel or subparallel seismic reflections (Figure 4(a); see [42]).

The seismic amplitude attribute (root mean square-RMS) map indicates that the isolated punctate anomalies caused by the individual *string-beads*-like seismic reflections of epigenic karst systems are widely distributed across the entire study area. This reveals that the epigenic karst systems are well developed in the lower part of the Yingshan Formation of the study area (Figure 4(a)).

**3.2. Seismic Facies of Hypogenic Karst Systems.** A set of hypogenic karst systems (lateral stratiform hypogenic and cross-formational fault-vein hypogenic karst systems) was recognized in the Upper Yingshan Formation of well SN4 area and the cross-well seismic sections. Differing with parallel or subparallel seismic reflections of the strata and individual *string-beads*-like seismic reflections of the epigenic

karst systems, seismic reflections of hypogenic karst systems are usually composed of a series of individual string-beads, defined as a *string-beads* complex (Figures 4(c), 4(d), 4(e), and 4(f)). Furthermore, compared with the isolated distribution of epigenic karst system in planar view, the *string-beads* complex of hypogenic karst systems is belt-shaped distributed along the faults in the planar view and the section view: (1) lateral stratiform hypogenic karst systems are well developed at the top of the secondary faults, and cross-formational fault-vein hypogenic karst systems are developed around the faults through the seismic cross sections (Figures 4(d), 4(e), and 4(f)); (2) lateral stratiform hypogenic and cross-formational fault-vein hypogenic karst systems are well developed along the SN4 fault zone in the seismic attribute RMS map, showing the characteristics of a belt-shaped distribution and string-beads complexes with distinctive strong amplitude anomalies (Figure 4(c)).

#### 4. 3D Seismic Characterization of Hypogenic Karst Systems

Investigations of hypogenic karst systems predominantly focus on the section- or planar-view delineation of a lateral

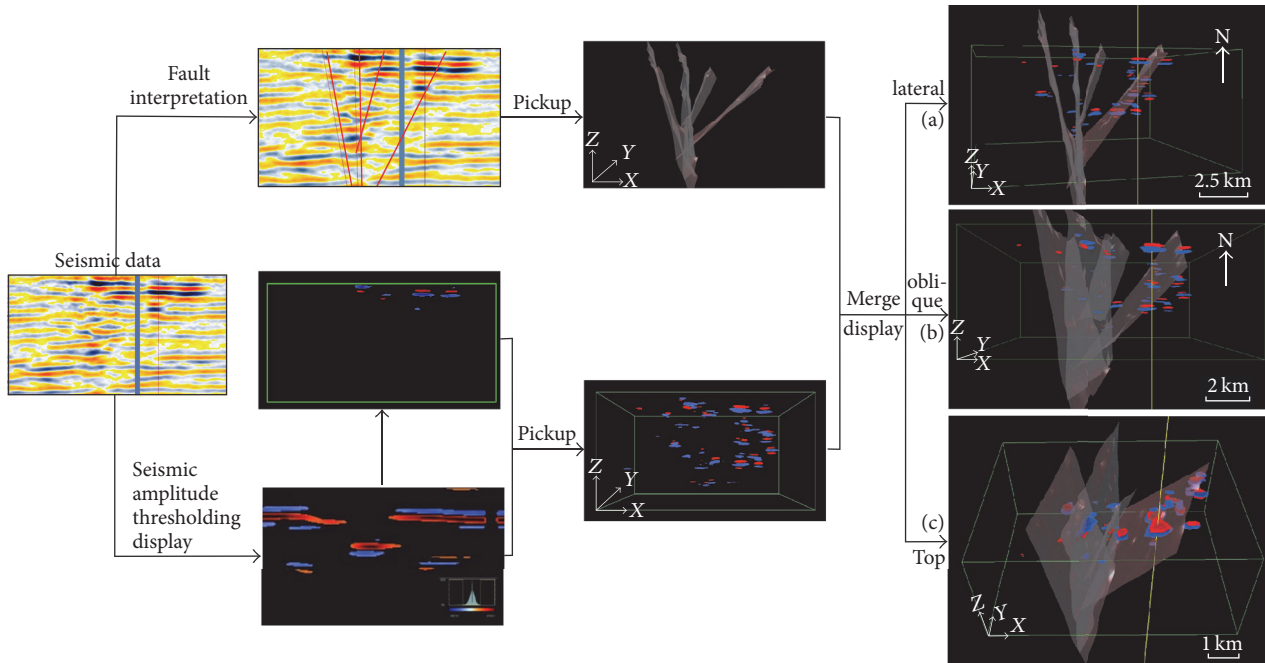


FIGURE 5: A new 3D seismic characterization workflow for hypogenic karst systems, including seismic amplitude thresholding, fault interpretation, pickup, and merge displays; 3D view of hypogenic karst systems in the study area ((a), (b), and (c)). (a) Coupling relationships between faults (multilevel faults) and hypogenic karst systems. (b) and (c) showing the lateral, oblique, and top distributions of hypogenic karst systems, respectively. Red and blue color represent hypogenic karst systems.

stratiform hypogenic karst system and the relevant fault system zone individually (e.g., [38, 43–47]).

Recently acquired 3D seismic data, covering the entire study area, make it possible to investigate the seismic facies and distributions of hypogenic karst systems [23, 24]. A new seismic characterization workflow has been developed in this study, including seismic amplitude thresholding, fault interpretation, pickup, and merge display to conduct a joint investigation of the spatial distribution and coupling of the lateral stratiform hypogenic karst system and relevant fault system zones (Figure 5). The relevant fault system zones are used in this paper to denote the migration pathways (relevant faults) of hydrothermal fluids and the cross-formational fault-vein hypogenic karst systems around faults.

The workflow includes the following steps (Figure 5):

- (1) Carry out the logging and seismic facies analysis based on 3D seismic data and drilling data, taking into account detailed comparisons of well-to-seismic ties, and then conclude with the characteristics of lateral stratiform hypogenic karst systems and their relevant fault system zone by analyzing seismic facies across different seismic lines.
- (2) Characterize the hypogenic karst systems (lateral stratiform hypogenic and cross-formational fault-vein hypogenic karst systems) on the basis of the attributes of strong seismic amplitude and high continuity:

- (a) Firstly, picking the overall attributes of the root mean square to determine the seismic amplitude classification standards and then defining the seismic amplitude distribution ranges of the hypogenic karst system, especially, the minimal seismic amplitude value is required.
- (b) Secondly, display the part of the amplitude that is higher than the minimum amplitude value through seismic amplitude thresholding and strong amplitude pickup.
- (c) Finally, characterize the spatial distribution of hypogenic karst system according to the above results.

- (3) Display the spatial distribution of relevant faults through fault interpretation, pickup, and thresholding display.
- (4) Merge displays lateral stratiform hypogenic karst systems and fault system zones.

## 5. Characterization Results of Hypogenic Karst Systems

Applying the proposed new seismic characterization workflow, a series of the spatial configuration diagrams show hypogenic karst systems and relevant faults, further analyzing their coupling relationship from different perspectives (Figures 5(a), 5(b), and 5(c)).

Hypogenic karst systems constituted lateral stratiform hypogenic karst system and cross-formational fault-vein hypogenic karst system [7, 48]. Deep fluids upwards flowed along the faults and at the same time transversely migrated along the soluble formation and lateral stratiform hypogenic karst system is thus formed. Lateral stratiform hypogenic karst systems are predominantly characterized by an overall view of “horizontal layered distribution with certain lateral continuity” (Figure 5(a)). With the accumulation of fluids, lateral stratiform hypogenic karst systems are integrated and cut-through, making the layered characteristic apparent (Figures 5(a), 5(b), and 5(c)). It is shown in Figure 5(c) that lateral stratiform hypogenic karst systems formed in different locations at the top of the same faults generally exhibit the obvious amplitude abnormalities. Seismic amplitudes decrease gradually away from faults or top downwards of faults, revealing the karstified range and intensity decreasing gradually downwards in the lateral stratiform hypogenic system zones. Cross-formational fault-vein hypogenic karst system is usually formed around the faults; that is, the fault systems zone is cross-formational fault-vein hypogenic karst development zone.

The importance of faults in hypogenic karst system is reflected in two aspects. On the one hand, faults are vertical migration pathways of hydrothermal fluids, which are important for upwelling cross-communication between shallow and deep subsurface and further for lateral stratiform hypogenic karst system development. Because fluids in fault systems encounter the lateral carrier-beds (the unconformities, weathering crusts, and preexisting epigenic karst systems), fluids occur in lateral selective dissolution due to the high permeability of lateral carrier-beds, and the lateral stratiform hypogenic karst systems are developed (Figure 5(a)). On the other hand, fault zones are also cross-formational fault-vein hypogenic karst development zones where ascending flows cross soluble and insoluble rocks. Accordingly, cross-formational fault-vein hypogenic karst systems are developed around faults by the dissolution effects of fluids on massive rocks [6, 7]. In addition, the faults comprised the primary faults and secondary faults with different characteristics. Primary faults are much rougher and their cross sections often exhibit the circular or elliptic physical characteristics. Conversely, the secondary faults are developed in three directions, vertical, horizontal, and bending and divergence in multiple directions, and their shape sizes have distinct differences, small to large (Figure 5(b)).

## 6. Development Pattern of Hypogenic Karst Systems

Based on the detailed characterization of hypogenic karst systems in the study area, the development pattern of hypogenic karst systems is proposed, where deep hydrothermal fluids migrated vertically through primary and secondary faults and flowed laterally through lateral carrier-beds (including unconformities, weathering crusts, the preexisting epigenic karst system, porous, or vuggy layers). The pattern shows that the hypogenic karst system has overall “vertical and

horizontal combination, dendritic distribution, layered distribution, and finger-like interaction” features (Figure 6).

The vertical faults formed by primary and secondary faults have a positive effect on the development of hypogenic karst systems. The deep hydrothermal fluids flowed upwards along the multilevel faults, presenting “dendritic distribution” features. Subsequently, fluids migrated along the lateral carrier-beds horizontally, presenting “layered distribution” characteristics. The strata were subjected to selective dissolution in the course of the lateral migration, presenting typical “finger-like interaction” characteristics. Faults and lateral carrier-beds together formed a “vertical and horizontal combination” of hydrothermal migration pathways. Hypogenic karst systems have an overall “dendritic distribution, layered distribution, and finger-like interaction” features (Figure 6).

“Dendritic distribution” means that the hypogenic karst system is characterized by a multiple-level “dendritic” morphology. Primary faults are the “trunks” of vertical channels and secondary faults are “branches” accompanied by the diffusion of the hydrothermal fluids. In addition, the dissolved pores, karst cave, and dolomite reservoirs are further branches developed at the top of the secondary faults (Figure 6).

Hydrothermal fluids migrated upwards along the secondary faults, forming an intensive dissolution area. Then, hydrothermal fluids migrate horizontally along the lateral carriers, forming the “layered distribution” of dissolved pores systems. In addition, the dissolved pore systems formed by different secondary faults were fused and penetrated, making the “layered distribution” apparent. At the same time, when the hydrothermal fluids converged on the top of the secondary faults, selective dissolution gave priority to soluble sparry calcarenite compared with micrite. Altered soluble sparry calcarenite and unaltered micrite presented the characteristics of interbedding and alternative occurrence. More specifically, the strata consisted of altered sparry calcarenite accompanied by unaltered micrite interbed.

In summary, hypogenic karst systems can be interpreted as a tree-like cave system with an erect trunk in the bottom, bending in multiple directions upwards and changing into horizontal at the top, showing overall “vertical and horizontal combination, dendritic distribution, layered distribution, and finger-like interaction” features (Figure 6).

## 7. Controlling Factors for Hypogenic Karst Systems

The main controlling factors of the Ordovician karst systems are uplift, unconformity, fault systems, rock physical properties, and sedimentary facies [13, 26]. In order to illustrate the spatial distributions, this paper will present the controlling factors of the hypogenic karst system through the analysis of fault systems, sequence stratigraphic boundaries, preexisting epigenic karst systems, paleogeomorphology, and sedimentary facies.

*7.1. Relationships between Fault Systems and Hypogenic Karst Systems.* Based on the distinct seismic reflections between

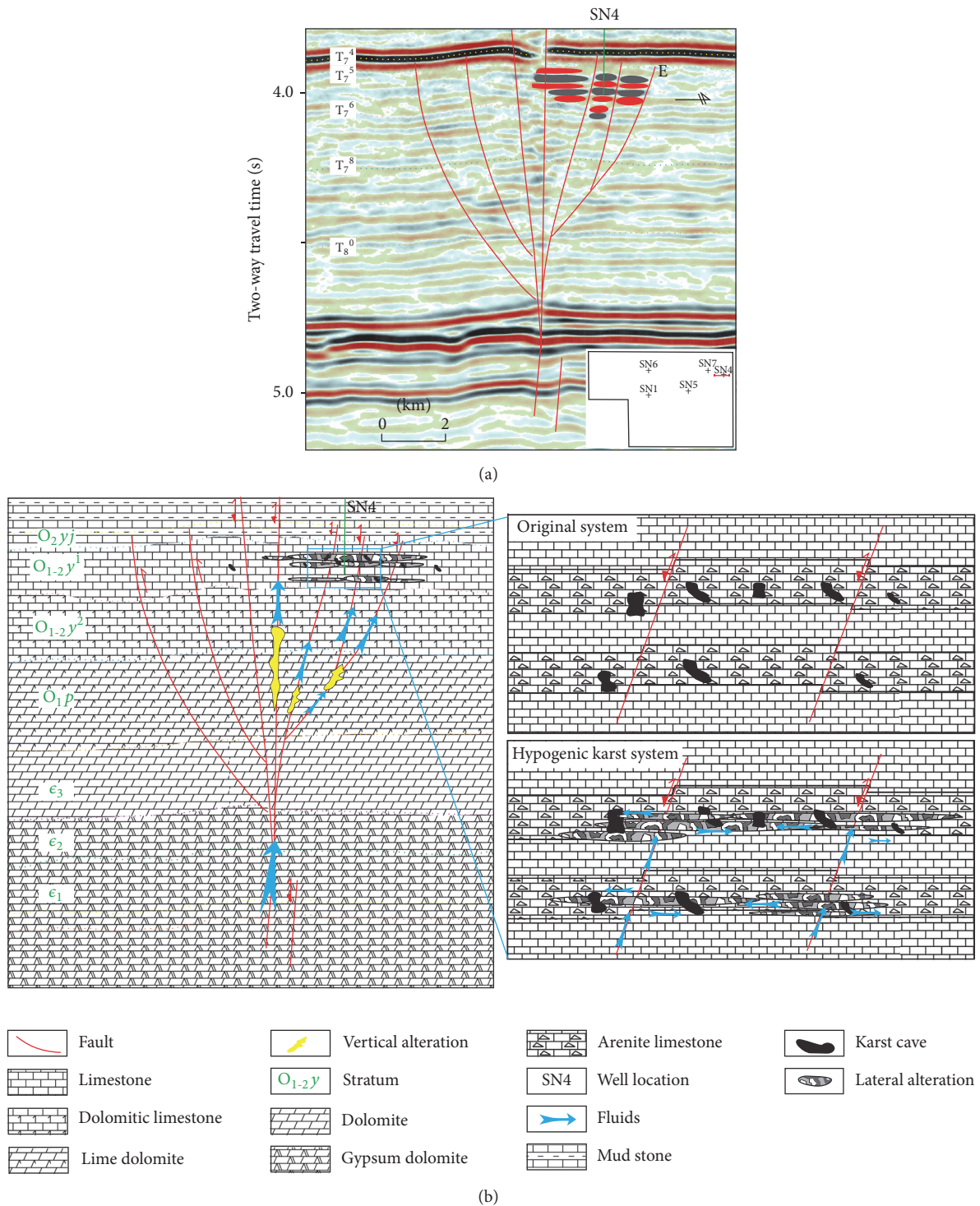


FIGURE 6: Development pattern of hypogenic karst systems of the study area. (a) Seismic dip section DD' showing complex *string-beads*-like seismic reflections of hypogenic karst systems in the Yingshan Formation. (b) Hydrothermal fluids pathways derived from the deep subsurface, showing vertical pathways (primary-secondary faults) and lateral carrier-beds (preexisting epigenic karst systems, unconformities, soluble layers, etc.). Accumulations of hydrothermal fluids make it possible for the scattered lateral carrier-beds to communicate with one another and formed hypogenic karst systems with such features as dendritic distribution, layered distribution, and finger-like interaction.

the karst systems (low continuity and strong seismic amplitude) and surrounding rocks (high continuity and weak seismic amplitude), the planar distributions of epigenic and hypogenic karst systems in the Yingshan Formation were shown in Figures 4(a) and 4(c) by using the seismic amplitude attribute (RMS, root mean square).

The seismic attribute RMS map shows that isolated punctate anomalies are widely distributed across the entire study area, as recognition indicators of epigenic karst systems in the lower part of the Yingshan Formation. Conversely, a large amount of hypogenic karst systems are developed along the SN4 fault zone in the upper part of the Yingshan Formation, located at the top of the secondary faults (Figures 4(d), 4(e), and 4(f)). Therefore, preexisting epigenic karst systems and faults influenced the distributions of hypogenic karst systems, which were also utilized to interpret the reason why hypogenic karst systems focused distributing along the faults in the upper part of the Yingshan Formation. It is explained further below.

**7.1.1. Faults.** There are four periods of tectonic activities in the Shunnan area of the Tarim Basin: the Early and Middle Caledonian phases, the Late Caledonian to the Early Hercynian phases, and the Late Hercynian phases. The tectonic stress intensity developed moderately during the Early Caledonian phases and then subsequently increased during the Middle-Late Caledonian to the Early Hercynian phases, after which the strength gradually weakened during the Late Hercynian stage.

The structural fractures of compressional torsional strike-slip faults are wider and easily developed in comparison to transtensional strike-slip faults, which depend on the properties of strike-slip faults and petrophysical characteristics of carbonate rocks [49]. Two major strike-slip fault systems trending NE and NNE are present in the Shunnan area under control of the compressional torsional strike-slip fault tectonic activity of Episode I of the mid-Caledonian. Because the intensity of the NNE strike-slip fault activity is comparatively weak, the fracture scale is smaller and it does not have hereditability in the late period. Conversely, the NE strike-slip fault cuts through multiple layers and reaches the Sinian system. Hydrothermal fluids below the basement migrate upwards along the strike-slip fault and react with the Ordovician carbonate strata [30, 33].

The SN4 fault system is a typical instance of the northeast-southwest-trending strike-slip faults systems, and the structure style of which was strongly influenced by the transtensional tectonic stress from the Late Caledonian to early Hercynian. The positive flower structure occurred as tectonic inversion, finally forming a series of tensile normal faults. The tensile normal faults are good vertical migration pathways, which provide favorable conditions for the hydrothermal fluids to migrate upward. In addition, the vertical conduction through faults is superior to the lateral conduction through the effective carbonate reservoir, so fluids will choose effective and opened faults while migrating upward; thus, hypogenic karst systems are developed around and at the end of opened faults (Figures 4(d), 4(e), and 4(f)), showing a belt-shaped distribution along the SN4 fault belt (Figure 4(c)).

**7.1.2. Epigenic Karst Systems.** Epigenic karst systems are developed in the lower part of the Yingshan Formation, because the Shunnan area was subjected to intensive dissolution as a result of long-term exposure as sea level descends though with no strong tectonic uplift activities this time. On the contrary, epigenic karst systems are comparatively less developed in the upper part of the Yingshan Formation without exposure condition, because the area was under control of the tectonic activity of Episode I in mid-Caledonian and located at downthrown side of fault, resulting in no exposure at surface after the deposition of Yingshan and Yijianfang Formations.

However, recent interpretations considered the importance of preexisting epigenic karst systems, as effective permeability formations [33]. They provide conducive conditions for the lateral dissolution and are beneficial for the formation of lateral stratiform hypogenic karst systems. Hydrothermal fluids from the deep migrate to the top of secondary faults and then along preferential permeability formation to migrate laterally, making it possible for *string-beads*-like individuals of the scattered epigenic karst systems to communicate with each other and become *string-beads*-likes complexes of a massive hypogenic karst systems.

**7.2. Relationships between Sequence Boundaries and Preexisting Epigenic Karst Systems.** Based on the principles of sequence stratigraphy and taking into account the empirically derived base level, volumetric partitioning, and facies variations, we proposed sequence stratigraphic framework for the Yingshan Formation. It includes two third-order sequences, namely, SQ2 and SQ3 from bottom to top (Figure 7). Sequences SQ2 and SQ3 correspond to the lower and upper parts of the Yingshan Formation, respectively.

Karst systems of the Yingshan Formation were meticulously identified, calibrated, and correlated by well log data combined with previous studies [40, 50]. The results speculated that two different types of the karst system are present in the sequences SQ2 and SQ3, respectively.

Sequence SQ2 is predominantly characterized by individual *string-beads*-like seismic reflection (Figure 7). The distributions of epigenic karst systems and sequence boundaries are related, showing the developments of epigenic karst systems correspondingly migrated to top from bottom of the sequence boundary from highlands to lowlands (Figure 7). The reason is that highlands experienced long-term intensive erosion and surface denudation than that of lowlands as the sea level falls geomorphically, causing wide ranges of epigenic karst systems developed close to the bottom of the sequence boundary.

Sequence SQ3 is predominantly characterized by complex *string-beads*-like seismic reflections (Figures 4(c), 4(d), 4(e), and 4(f)). The carbonate platforms began to enter the burial stage after experiencing multiple tectonic subsidence. Faults caused by the tectonic activities provide the potential pathways for the hydrothermal fluids to migrate upwards. Thus, deep hydrothermal fluids entered the overlying carbonate strata near the fault and dissolved soluble layers, producing the formation of hypogenic karst systems.

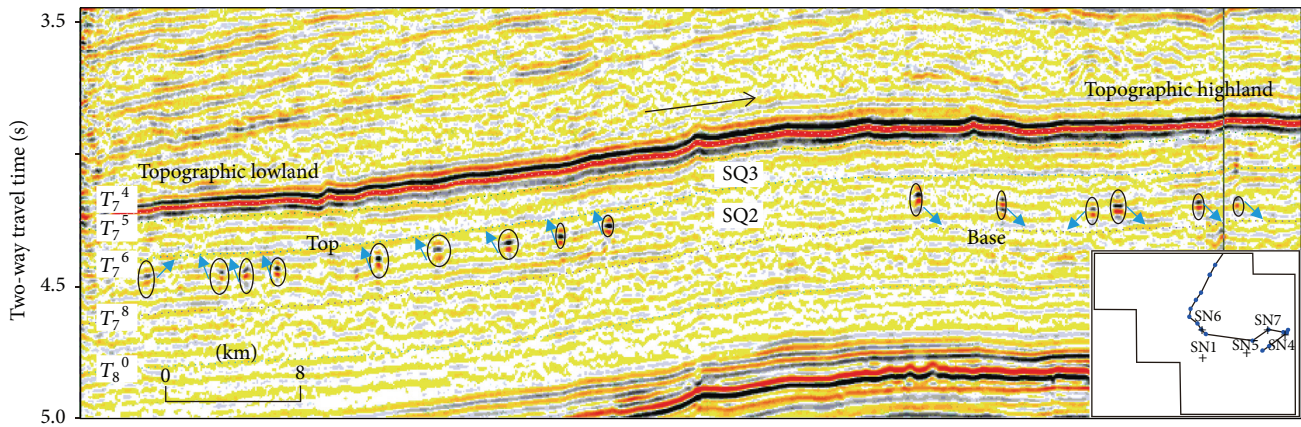


FIGURE 7: Seismic dip section showing individual *string-beads*-like seismic reflections of epigenic karst systems in the lower part of the Yingshan Formation, which developed near the base and top of sequence boundary in the topographic highland and lowland, respectively.

**7.3. Relationships between Geomorphology and Hypogenic Karst System.** Paleogeomorphology is a comprehensive response of what a study area has experienced, including structural deformation, depositional infilling, differential compaction, weathering, and erosion (e.g., [37]). Previous studies and exploration efforts have confirmed that paleogeomorphology is one of the key controlling factors for the development of epigenic karst (e.g., [51]), also applicable in Shunnan area.

The Shunnan area is dominated by platform facies deposits during Middle-Lower Ordovician, which were denuded to different degrees in different zones under control of multiphased Caledonian-Hercynian tectonic uplift. To better understand the relationship between seismic geomorphology and the distribution of hypogenic karst systems in this area, the paper is based primarily on interpretations of an integrated data set, including 3D seismic data and well data. The paleogeomorphology in the upper part of the Yingshan Formation was reconstructed, including topographic features of low uplifts, gentle slopes, and sags of the intraplatform (Figure 8). The paleogeomorphology framework is marked by widely distributed sags northwest and comparatively developed low uplifts southeast, whereas gentle slopes are overall less developed (Figure 8).

In addition, the paleogeomorphological map shows that hypogenic karst systems in the upper part of the Yingshan Formation are widely distributed along the faults, which are located in the low uplifts of the intraplatform. The reason why hypogenic karst systems are easily distributed in the highlands is that geomorphically highlands of the intraplatform are easier places to develop a lot of dissolved pores with good connectivity, which are characterized by the well development of vadose zones. Furthermore, the dissolved pores with good connectivity not only provide much reservoir space for the original dense carbonate but also superimpose faults to provide upward pathways for the fluids migration. These factors contribute to the epigenic karst systems development and preexisting epigenic karst systems in the lower part of the Yingshan Formation were a precursor for subsequent hypogene karstification.

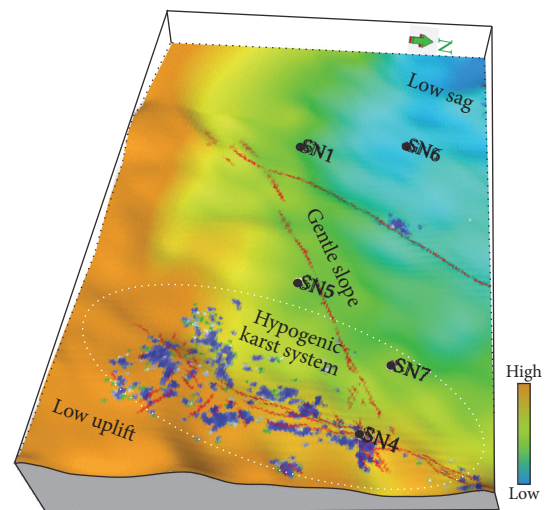


FIGURE 8: Relationships of paleogeomorphology and hypogenic karst systems of the upper part of the Yingshan Formation, showing belt-shaped distributions at the highlands of the margin of intraplatform along the SN4 fault zone.

**7.4. Relationships between Sedimentary Facies and Hypogenic Karst Systems.** The Middle-Lower Ordovician Penglaiba and Yingshan Formations are mainly a set of marine carbonate platform facies deposits, and they are also a typical restricted-open sedimentary sequence platform of transgression type. A dolomitic to limestone lithological trend exists from the Penglaiba to Yingshan Formation, primarily showing the variations from pure dolomite, gray dolomite, and dolomitic limestone in the Penglaiba Formation to the granular and micrite limestone in the Yingshan Formation (e.g., [52–54]).

During the deposition of the Penglaiba Formation, the restricted platform facies are primarily composed of microcrystalline argillaceous dolomite and dolomudstone. It corresponds to a deposit formed in a restricted (partially closed) environment, probably, associated with poor water circulation caused by the sea-floor topography barrier. In contrast,

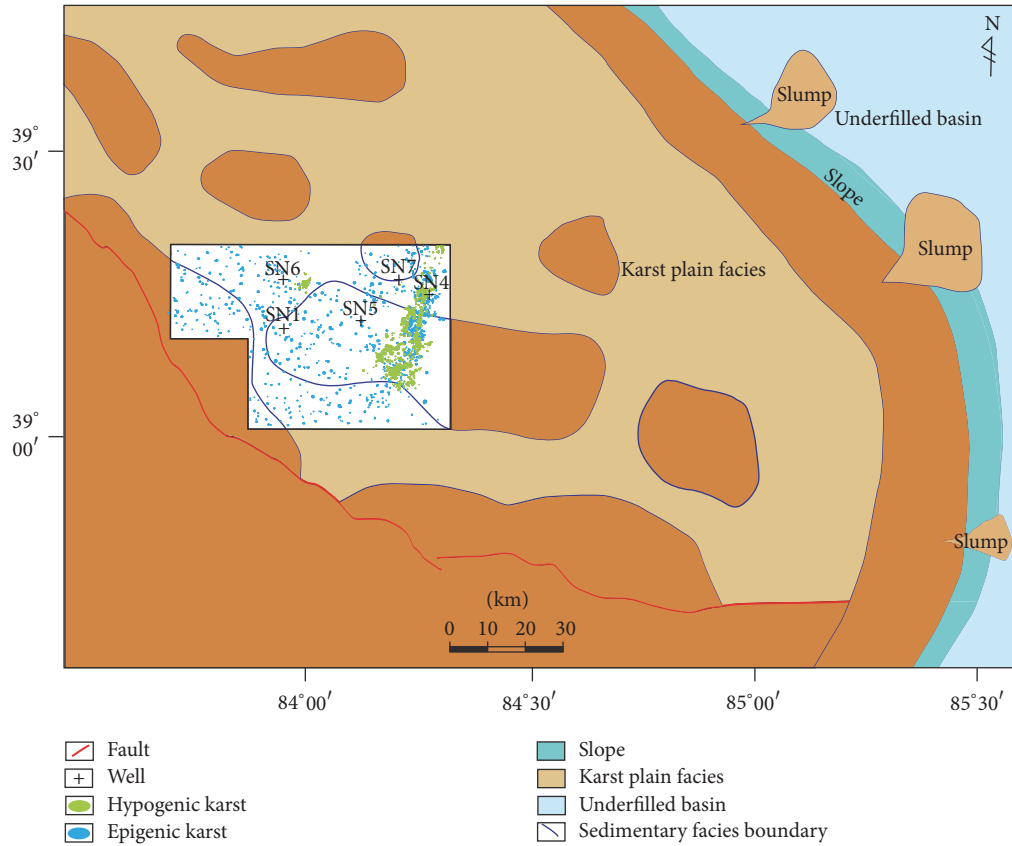


FIGURE 9: Relationships of the sedimentary facies and hypogenic karst systems of the upper and lower part of the Yingshan Formation, showing well coupling between the distribution of intraplateform shoals and the development of hypogenic karst systems.

with the ascent of sea level, a small amount of limestone occurs as thin layer and intercalated in the dolomite during the deposition of the Yingshan Formation, indicating smooth water circulation.

More previous studies revealed that a large number of intraplateform shoals deposited in the Yingshan Formation [55–57]. Sparry calcarenite is the main lithology of the intraplateform shola facies in the Tazhong area [58]. The lithology gradually varies from the sparry calcarenite to micrite away from the intraplateform shola facies. Compared with the micrite, original porosities of sparry calcarenite are easily developed and more easily dissolved by the meteoric or high-temperature fluids, and thus karst systems (epigenic karst and hypogenic karst) are easily developed in the area of the intraplateform sholas. In the study area, Figure 9 also shows the close relationships between the intraplateform shoals and the karst systems (epigenic and hypogenic karst systems). Intraplateform shoals are generally developed in geomorphically highlands of the local super-shallow water.

### 8. Conclusions

This study documented the presence of hypogenic karst systems (lateral stratiform hypogenic and cross-formational fault-vein hypogenic karst system) characterized by complex *string-beads*-like seismic reflections in a data set from the

Tarim Basin. The features are clustered near known faults in the data set, and this, coupled with a new workflow using seismic amplitude thresholding, fault interpretation, pickup, and merge display to characterize the coupling relationship between them, leads us to propose the development pattern of hypogenic karst systems. Fluids expelled from the deep subsurface move upwards along the vertical pathways (multilevel faults), creating an aggressive fluid that is transported to horizontally lateral carrier-beds, further forming selective dissolution. The accumulations of fluids at the top of the secondary faults make it possible for the formation of a massive hypogenic karst system of *string-beads* complexes with such features as dendritic distribution, layered distribution, and interfingering bead strings.

Potential controlling factors that influenced the development of hypogenic karst systems have been illustrated by a variety of end-member attributes that are distinct in terms of faults, sequence boundaries, preexisting epigenic karst systems, paleogeomorphology, and sedimentary facies. The hypogenic karst systems are not evenly distributed across the study area but are most common in the highlands along the faults, where epigenic karst systems are usually developed because the residual space of an epigenic karst system is conducive to the convergence of hydrothermal fluids. Trapped hydrothermal fluids from the deep scattered epigenic karst systems communicate with one another and form

massive hypogenic karst systems. In addition, karst systems develop in association with both the sequence boundaries and sedimentary facies. The development of epigenic karst systems migrates to the top from the bottom of the sequence boundary from the highlands to lowlands. It also has a close relationship with the presence of intraplatform shoals.

## Conflicts of Interest

The authors declare that they have no conflicts of interest.

## Acknowledgments

This research is sponsored by the National 973 research program on “Tectonic evolution and the differences of hydrocarbon accumulation process of the Upper Paleozoic in the Tarim Basin” (no. 2012CB214804).

## References

- [1] S. Bloch, R. H. Lander, and L. Bonnell, “Anomalously high porosity and permeability in deeply buried sandstone reservoirs: origin and predictability,” *AAPG Bulletin*, vol. 86, no. 2, pp. 301–328, 2002.
- [2] J. M. Ajdukiewicz, P. H. Nicholson, and W. L. Esch, “Prediction of deep reservoir quality using early diagenetic process models in the jurassic norphlet formation, gulf of Mexico,” *AAPG Bulletin*, vol. 94, no. 8, pp. 1189–1227, 2010.
- [3] X. Pu, L. Zhou, W. Wang et al., “Medium-deep clastic reservoirs in the slope area of Qikou sag, Huanghua depression, Bohai Bay Basin,” *Petroleum Exploration and Development*, vol. 40, no. 1, pp. 38–51, 2013.
- [4] S. J. Mazzullo and P. M. Harris, “Mesogenetic dissolution: its role in porosity development in carbonate reservoirs,” *AAPG Bulletin*, vol. 76, no. 5, pp. 607–620, 1992.
- [5] A. N. Palmer, “Geochemical models for the origin of macroscopic solution porosity in carbonate rocks,” in *Unconformities and Porosity in Carbonate Strata*, A. D. Budd, A. H. Saller, and P. M. Harris, Eds., vol. 63 of *AAPG Memoir*, pp. 77–101, 1995.
- [6] A. Klimchouk, “Speleogenesis, hypogenic,” in *Encyclopedia of Caves*, D. C. Culver and W. B. White, Eds., pp. 748–765, Elsevier, Academic Press, Chennai, India, 2nd edition, 2012.
- [7] A. Klimchouk, “The karst paradigm: changes, trends and perspectives,” *Acta Carsologica*, vol. 44, no. 3, pp. 289–313, 2015.
- [8] D. C. Ford and P. W. Williams, *Karst Geomorphology and Hydrology*, Unwin Hyman, London, UK, 1989.
- [9] D. Ford and P. Williams, *Karst Hydrogeology and Geomorphology*, Wiley, Chichester, UK, 2007.
- [10] A. N. Palmer, “Origin and morphology of limestone caves,” *Geological Society of America Bulletin*, vol. 103, no. 1, pp. 1–21, 1991.
- [11] A. N. Palmer, “Distinction between epigenic and hypogenic maze caves,” *Geomorphology*, vol. 134, no. 1–2, pp. 9–22, 2011.
- [12] H. Hu, Z. Y. Wang, and Y. F. Zhang, “The characteristics of the interbedding weathering crust karst in the Yingshan Formation, North slope of the Tazhong Uplift,” *Xinjiang Petroleum Geology*, vol. 34, no. 1, pp. 277–281, 2013.
- [13] F. Renwei, O. Cheng, P. Yanjun et al., “Evolution modes of interbedded weathering crust karst: a case study of the 1<sup>st</sup> and 2<sup>nd</sup> members of Ordovician Yingshan Formation in EPCC block, Tazhong, Tarim Basin,” *Petroleum Exploration and Development*, vol. 41, no. 1, pp. 49–59, 2014.
- [14] Z. M. Wang, L. J. Zhang, and C. H. Sun, “Classification period and exploration for carbonate karst in the Ordovician, Tarim Basin,” *Journal of Palaeogeography*, vol. 17, pp. 635–644, 2015.
- [15] A. B. Klimchouk, *Hypogene Speleogenesis: Hydrogeological and Morphogenetic Perspective*, vol. 36 of *Special Paper No. 1*, National Cave and Karst Research Institute, Carlsbad, New Mexico, 2007.
- [16] K. W. Stafford, L. Land, and A. Klimchouk, “Hypogenic speleogenesis within seven rivers evaporites: coffee cave, eddy county, New Mexico,” *Journal of Cave and Karst Studies*, vol. 70, no. 1, pp. 47–61, 2008.
- [17] K. Stafford, L. Land, and G. Veni, *Advances in Hypogene Karst Studies*, National Cave and Karst Research Institute, Carlsbad, Calif, USA, 2009.
- [18] A. B. Klimchouk and D. C. Ford, *Hypogene Speleogenesis and Karst Hydrogeology of Artesian Basins*, Ukrainian Institute of Speleology and Karstology, Simferopol, Crimean, 2009.
- [19] T. Chavez and P. Reehling, “Proceedings of Deep Karst: Origins, Resources, and Management of Hypogene Karst. National Cave and Karst Research Institute, Carlsbad,” 2016.
- [20] Z. Q. Gao, T. L. Fan, Z. F. Jiao, and Y. Li, “The structural types and depositional characteristics of carbonate platform in the cambrian-ordovician of tarim basin,” *Acta Sedimentologica Sinica*, vol. 24, no. 1, pp. 19–27, 2006.
- [21] T. L. Fan, B. S. Yu, and Z. Q. Gao, “Characteristics of carbonate sequence stratigraphy and its control on oil-gas in Tarim Basin,” *Geoscience*, vol. 21, pp. 57–65, 2007.
- [22] A. J. Shen, W. Q. Pan, X. P. Zheng, L. J. Zhang, Z. F. Qiao, and N. Y. Mo, “Types and characteristics of Lower Paleozoic karst reservoirs in Tarim Basin,” *Marine Origin Petroleum Geology*, vol. 15, pp. 20–29, 2010.
- [23] H. Zeng, R. Loucks, X. Janson et al., “Three-dimensional seismic geomorphology and analysis of the Ordovician paleokarst drainage system in the central Tabei Uplift, northern Tarim Basin, western China,” *AAPG Bulletin*, vol. 95, no. 12, pp. 2061–2083, 2011.
- [24] H. Zeng, G. Wang, X. Janson et al., “Characterizing seismic bright spots in deeply buried, Ordovician Paleokarst strata, Central Tabei uplift, Tarim Basin, Western China,” *Geophysics*, vol. 76, no. 4, pp. B127–B137, 2011.
- [25] L. Yun and Z. Cao, “Hydrocarbon enrichment pattern and exploration potential of the Ordovician in Shunnan area, Tarim Basin,” *Oil and Gas Geology*, vol. 35, no. 6, pp. 788–797, 2014.
- [26] G. Zhiqian, L. Zhongbao, G. Shanlin, D. Qunan, W. shiqiang, and L. Shilin, “Characteristics and genetic models of Lower Ordovician carbonate reservoirs in southwest Tarim Basin, NW China,” *Journal of Petroleum Science and Engineering*, vol. 144, pp. 99–112, 2016.
- [27] C. Z. Jia, *Structural Characteristics and Oil & Gas in the Tarim Basin*, Petroleum Industry Press, Beijing, China, 1997.
- [28] D. F. He, X. Y. Zhou, C. J. Zhang, W. J. Yang, and X. Shi, “Characteristics of geologic framework of multicycle superimposed basin in Tarim basin,” *China Petroleum Exploration*, vol. 11, no. 1, pp. 31–41, 2006 (Portuguese).
- [29] X. Lan, X. Lü, Y. Zhu, and H. Yu, “The geometry and origin of strike-slip faults cutting the Tazhong low rise megaanticline (central uplift, Tarim Basin, China) and their control on hydrocarbon distribution in carbonate reservoirs,” *Journal of Natural Gas Science and Engineering*, vol. 22, pp. 633–645, 2015.

- [30] M. Wu, Y. Wang, M. Zheng, W. Zhang, and C. Liu, "The hydrothermal karstification and its effect on Ordovician carbonate reservoir in Tazhong uplift of Tarim Basin, Northwest China," *Science in China, Series D: Earth Sciences*, vol. 50, no. 2, pp. 103–113, 2007.
- [31] J. W. Hedenquist and R. W. Henley, "The importance of CO<sub>2</sub> on freezing point measurements of fluid: evidence from active geothermal systems and implications for epithermal ore deposition," *Economic Geology*, vol. 80, no. 5, pp. 1379–1406, 1985.
- [32] M. Jébrak, "Hydrothermal breccias in vein-type ore deposits: a review of mechanisms, morphology and size distribution," *Ore Geology Reviews*, vol. 12, no. 3, pp. 111–134, 1997.
- [33] P. J. Li, H. H. Chen, D. Q. Tang et al., "Coupling relationship between ne strike-slip faults and hypogenic karstification in middle-lower ordovician of Shunnan Area, Tarim Basin, Northwest China," *Earth Science*, vol. 42, no. 1, pp. 93–104, 2017.
- [34] H. L. Li, N. S. Qiu, Z. J. Jin, and Z. L. He, "Geothermal history of Tarim basin," *Oil and Gas Geology*, vol. 26, no. 5, pp. 613–617, 2005.
- [35] D. Y. Zhu, Q. Q. Meng, W. X. Hu, and Z. J. Jin, "Differences between fluid activities in the Central and North Tarim Basin," *Geochimica*, vol. 42, no. 1, pp. 82–94, 2013.
- [36] R. M. Mitchum, P. R. Vail, and J. B. Sangree, "Seismic stratigraphy and global changes of sea level, Part 6: stratigraphic interpretation of seismic reflection patterns in depositional sequences," *AAPG Memoir*, vol. 62, pp. 117–134, 1977.
- [37] H. Zhu, X. Yang, X. Zhou, and K. Liu, "Three-dimensional facies architecture analysis using sequence stratigraphy and seismic sedimentology: example from the paleogene dongying formation in the bz3-1 block of the bozhong sag, Bohai Bay Basin, China," *Marine and Petroleum Geology*, vol. 51, pp. 20–33, 2014.
- [38] C. M. Burberry, C. A. Jackson, and S. R. Chandler, "Seismic reflection imaging of karst in the Persian Gulf: Implications for the characterization of carbonate reservoirs," *AAPG Bulletin*, vol. 100, no. 10, pp. 1561–1584, 2016.
- [39] P. R. Vail, R. M. Mitchum, and R. G. Todd, "Seismic stratigraphy and global changes of sea level," *AAPG Memoir*, vol. 26, pp. 49–212, 1977.
- [40] Y. F. Gao, H. Fu, T. Wang, H. F. Yang, and L. X. Zhao, "The features of ordovician sequence boundaries and its controls on carbonate karst in tarim basin," *Xinjiang Petroleum Geology*, vol. 33, no. 10, pp. 362–367, 2015.
- [41] X. Zhu, H. T. Zhu, H. H. Chen, L. Qi, P. J. Li, and L. Yun, "Characterization of hypogenic karst systems in the Middle-Lower Ordovician of Shunnan area, Tarim Basin," *Oil and Gas Geology*, vol. 37, no. 5, pp. 653–662, 2016.
- [42] A. McDonnell, R. G. Loucks, and T. Dooley, "Quantifying the origin and geometry of circular sag structures in northern Fort Worth Basin, Texas: paleocave collapse, pull-apart fault systems, or hydrothermal alteration?" *AAPG Bulletin*, vol. 91, no. 9, pp. 1295–1318, 2007.
- [43] G. R. Davies and L. B. Smith Jr., "Structurally controlled hydrothermal dolomite reservoir facies: an overview," *AAPG Bulletin*, vol. 90, no. 11, pp. 1641–1690, 2006.
- [44] P. Eichhubl, N. C. Davatzes, and S. P. Becker, "Structural and diagenetic control of fluid migration and cementation along the Moab fault, Utah," *AAPG Bulletin*, vol. 93, no. 5, pp. 653–681, 2009.
- [45] E. Frankowicz and K. R. McClay, "Extensional fault segmentation and linkages, Bonaparte Basin, outer North West Shelf, Australia," *AAPG Bulletin*, vol. 94, no. 7, pp. 977–1010, 2010.
- [46] H. J. Yang, K. K. Li, W. Q. Pan, Z. Y. Xiao, and C. F. Cai, "Burial hydrothermal dissolution fluid activity and its transforming effect on the reservoirs in Ordovician in Central Tarim," *Acta Petrologica Sinica*, vol. 28, no. 3, pp. 783–792, 2012.
- [47] G. Wu, H. Yang, S. He, S. Cao, X. Liu, and B. Jing, "Effects of structural segmentation and faulting on carbonate reservoir properties: a case study from the Central Uplift of the Tarim Basin, China," *Marine and Petroleum Geology*, vol. 71, pp. 183–197, 2016.
- [48] A. Klimchouk, A. S. Auler, F. H. R. Bezerra, C. L. Cazarin, F. Balsamo, and Y. Dublyansky, "Hypogenic origin, geologic controls and functional organization of a giant cave system in Precambrian carbonates, Brazil," *Geomorphology*, vol. 253, pp. 385–405, 2016.
- [49] Q. Miao, M. Pan, H. L. Gao, and B. Zhang, "The 3-D visualization characterization of the complex buried-hill fracture structure," *Xinjiang Petroleum Geology*, vol. 29, no. 21, pp. 364–366, 2008 (Chinese).
- [50] W. Q. Pan, Z. M. Wang, C. H. Sun et al., "Classifications of sequence boundaries in the Lower Paleozoic carbonates in Tarim Basin and their significances," *Oil and Gas Geology*, vol. 32, no. 1, pp. 531–541, 2011.
- [51] Z. H. Kang, "The karst paleogeomorphology of carbonate reservoir in Tahe Oilfield," *Xinjiang Petroleum Geology*, vol. 27, pp. 522–525, 2006.
- [52] L. D. Wang, *Formation mechanics and distribution forecast of Carbonates Paleokarst reservoir in T<sub>7</sub><sup>4</sup> Interface from Central Tarim Basin [Ph.D. thesis]*, PhD Dissertation in China University of Geosciences, Beijing, China, 2007.
- [53] S. W. Xie, *A Study on Sequence Stratigraphy and Geological Characteristics for Yingshan Formation in the Central Uplift Aera of Tarim Basin, China [Ph.D. thesis]*, PhD Dissertation in Chengdu University of Technology, 2011.
- [54] Z. F. Zhai, *A Study on the Sequence stratigraphy and Sedimentary Characteristic of Ordovician in Tazhong area of Tarim basin [Ph.D. thesis]*, PhD Dissertation in Chengdu University of Technology, 2012.
- [55] W. Liu, X. Y. Zhang, and J. Y. Gu, "Corrosion inhibition and adsorption properties of methocarbamol on mild steel in acidic medium," *Portugaliae Electrochimica Acta*, vol. 27, no. 1, pp. 435–442, 2009.
- [56] C. L. Wang, G. H. Wu, W. J. Cui et al., "Characteristics and distribution of intra-platform beach of the lower-middle ordovician yingshan formation carbonate," *Acta Sedimentologica Sinica*, vol. 29, pp. 1048–1058, 2011.
- [57] Z. K. Jin, L. Shi, B. S. Gao, and K. H. Yu, "Carbonate facies and facies models," *Acta Sedimentologica Sinica*, vol. 31, no. 1, pp. 965–980, 2013.
- [58] J. H. Zhang, B. S. Yu, Z. L. Qi, Z. K. Bai, Z. Ruan, and L. R. Li, "Seismic facies and the distribution of the intraplatform sholas in the Ordovician Yingshan Formation in the Ka-1 three-dimensional seismic area, Central Tarim Basin, Xinjiang," *Sedimentary Geology and Tethyan Geology*, vol. 36, no. 3, pp. 104–112, 2016.

## Research Article

# Experiment of Carbonate Dissolution: Implication for High Quality Carbonate Reservoir Formation in Deep and Ultradeep Basins

Zhiliang He,<sup>1,2</sup> Qian Ding,<sup>1,2</sup> Yujin Wo,<sup>1,2</sup> Juntao Zhang,<sup>1,2</sup> Ming Fan,<sup>1,3</sup> and Xiaojuan Yue<sup>4</sup>

<sup>1</sup>State Key Laboratory of Shale Oil and Gas Enrichment Mechanisms and Effective Development, Beijing 100083, China

<sup>2</sup>Laboratory of Structural and Sedimentological Reservoir Geology, Petroleum Exploration and Production Research Institute, SINOPEC, Beijing 100083, China

<sup>3</sup>Wuxi Research Branch of Petroleum and Production Research Institute, SINOPEC, Wuxi 214151, China

<sup>4</sup>China University of Petroleum-Beijing, Beijing 102249, China

Correspondence should be addressed to Qian Ding; [dingqian.syky@sinopec.com](mailto:dingqian.syky@sinopec.com)

Received 26 February 2017; Revised 22 June 2017; Accepted 12 July 2017; Published 11 September 2017

Academic Editor: Keyu Liu

Copyright © 2017 Zhiliang He et al. This is an open access article distributed under the Creative Commons Attribution License, which permits unrestricted use, distribution, and reproduction in any medium, provided the original work is properly cited.

As the most frontiers in petroleum geology, the study of dissolution-based rock formation in deep carbonate reservoirs provides insight into pore development mechanism of petroleum reservoir space, while predicting reservoir distribution in deep-ultradeep layers. In this study, we conducted dissolution-precipitation experiments simulating surface to deep burial environments (open and semiopen systems). The effects of temperature, pressure, and dissolved ions on carbonate dissolution-precipitation were investigated under high temperature and pressure (~200°C; ~70 Mpa) with a series of petrographic and geochemical analytical methods. The results showed that the window-shape dissolution curve appeared in 75~150°C in the open system and 120~175°C in the semiopen system. Furthermore, the dissolution weight loss of carbonate rocks in the open system was higher than that of semiopen system, making it more favorable for gaining porosity. The type of fluid and rock largely determines the reservoir quality. In the open system, the dissolution weight loss of calcite was higher than that of dolomite with 0.3% CO<sub>2</sub> as the reaction fluid. In the semiopen system, the weight loss from dolomitic limestone prevailed with 0.3% CO<sub>2</sub> as the reaction fluid. Our study could provide theoretical basis for the prediction of high quality carbonate reservoirs in deep and ultradeep layers.

## 1. Introduction

Oil and gas formed in carbonate formations take up to 60% of the total oil and gas resources worldwide [1–3]. The deep carbonate reservoirs in China mainly distribute in Ordos, Tarim Basin of Ordovician, Sichuan Basin of Triassic, Permian, Carboniferous, Cambrian, and Sinian, and the depth of those reservoirs ranges from 3000 m to 8000 m [4, 5]. The exploration practice on Well TS1 from Tarim Basin and well MS1 from Sichuan Basin found good dissolved pores in the ultradeep carbonate rocks with buried depths of 6,000 to 8400 m [6]. High quality dolomite reservoir was observed at 8408 m in well TS1 with porosity around 9.1%. Dolostone with an average porosity of 12% was found in Sichuan Basin at 6000 m [7]. The hydrocarbon exploration in Tahe Oil field,

Jingbian Gas Field, Puguang Gas Field, Yuanba Gas Field, Anyue Gas Field, and other marine gas and oil fields indicated that marine carbonate, especially to deep layers, showed promising prospects.

After the deposition of carbonate sediments, it went through the penecontemporaneous stage, the early, the middle, and the late diagenetic stage, and the epigenetic stage. The valuable reservoir porosity of carbonate rocks is largely related to the fluid transformation process in the diagenetic process. Pore was destructed and developed in early meteoric zone diagenesis. In late stage of dissolution, porosity developed due to hydrocarbon maturation and destruction [8]. Based on the fluid source, the fluid in the carbonate fluid-rock interaction can be divided into surface fluid, formation fluid, and deep source fluid. Based on the fluid source and

interaction model, the geological fluid environment of carbonate reservoir formation can be divided into three categories: open environment, semiopen environment, and closed environment.

With the simulation experiment and numerical simulation, it is possible to clarify the relationship between the dissolution process of limestone and dolostone and temperature, pressure, and fluid. Plummer et al. [9], Busenberg and Plummer [10], and Sjöberg [11] investigated that the effects of  $a_{\text{H}^+}$ ,  $p\text{CO}_2$ , and temperature on the dissolution rate of calcite and dolomite through simulation experiments. Fan et al. [12, 13] investigated the dissolution characteristics of different types of carbonate rocks in acetic acid/ $\text{CO}_2$ / $\text{H}_2\text{S}$  solutions and found the positive relationship between dissolution strength and temperature. A high dissolution strength was thus maintained in a certain temperature range, and a “dissolution window” was formed. She et al. [14, 15] found that the dissolution rate of dolomite is close to micrite limestone. These studies have deepened the understanding of the formation and development of carbonate reservoirs. However, previous studies focused on the dissolution rate of carbonates in weak acidic fluid from room temperature to medium temperature ( $\sim 150^\circ\text{C}$ ) and its dissolution control factors; few attentions were paid on the dissolution patterns of carbonate rock/carbonate mineral-fluid reactions under different system and high temperature/pressure [16–20]. In this study, the dissolution process with carbonate samples/minerals under different fluid environment and different fluid/rock ratio was carried out using a self-made simulation experimental instrument, and the favorable fluid environment for developing high quality carbonate reservoir was discussed.

## 2. Experiments

The carbonate and fluid interaction can be regarded as a solid-gas-liquid three-phase coexisting reaction system. In the system, carbonate rock served as the solid phase for dissolution or precipitation; the liquid and gas filled in the porosity served as the fluid. The main factors influencing the interaction between solid and liquid are temperature, pressure, pH, fluid/solid ratio, mineral surface structure, reaction surface area, and so on [21]. The burial depth determines the temperature and pressure of the system. The reaction between carbonate mineral and fluid is as follows:



M represents alkali metal element (Ca, Mg, etc.). During reaction,  $\text{CaCO}_3$  or  $\text{CaMg}(\text{CO}_3)_2$  dissolved and  $\text{Ca}^{2+}$  and  $\text{Mg}^{2+}$  entered into the fluid. The reaction progress can be monitored quantitatively by the change of metal cation concentration or the mineral weight loss before and after the reaction.

*2.1. Experiment Setting.* This experiment is carried out on carbonate reservoir dissolution rate instrument which is designed and manufactured by our lab (Figure 1) [12, 22, 23]. An electrical heater was used to heat the reactor. The temperature of the reactor was monitored and controlled



FIGURE 1: Carbonate reservoir dissolution simulation instrument (Type XYD-II).

by a temperature sensor (Pt100). The designed temperature and pressure of the instrument are  $250^\circ\text{C}$  and 70 Mpa. The pressure and flow rate of the reaction system are controlled by a constant pressure constant current pump. Surface structure was observed by scanning electron microscope (SEM; Zeiss EVO MA 10, Germany); the concentrations of  $\text{Ca}^{2+}$  and  $\text{Mg}^{2+}$  before and after the reaction were measured by ICP-OES (Agilent, 715 OES, USA) with detection limit of  $0.3 \mu\text{g/L}$  and  $0.1 \mu\text{g/L}$ , respectively. The type and constituents of the minerals were measured by X-ray diffractometer (XRD; Bruker D8, Germany).

*2.2. Experiment Steps.* During the experiment, the temperature and pressure of the reactor were gradually raised to the setting values. The fluid was pressurized in the reservoir tank and then flowed into the high-temperature and high-pressure reactor through the pipeline (Hastelloy). Six parallel quartz reaction tubes could be placed in the reactor. The fluid first flowed through the tube and then react with the carbonate sample. Following (1), the weight loss of the carbonate minerals during the reaction could quantitatively describe the magnitude of dissolution process.

Following a geothermal gradient of  $2.5^\circ\text{C}/100 \text{ m}$ , the temperature and pressure from earth surface to the formation depth (7000 m) ranged from  $25\sim 200^\circ\text{C}$  and  $1\sim 70 \text{ Mpa}$ , respectively. The temperature of the reactor was heated gradually around  $5^\circ\text{C}/\text{min}$ . The fluid flow rates were set at 1 ml/min and 0 ml/min for the open and the semiopen geological fluid system, respectively (Table 1). The reaction time for each temperature/pressure set was 3 to 4 hours till the calcium and magnesium ions concentrations in the fluid no longer changed and then extended for two more hours to ensure that the equilibrium of the fluid-rock interaction was reached. When the reaction was completed, the calcium and magnesium ions in the fluid were measured and the dissolution rate was determined by weighing the mass loss of the samples.

At the end of the experiment, the dissolution characteristics of the two kinds of fluid systems and various carbonate samples with temperature and pressure were investigated by measuring the change of dissolution weight loss and the change of ion concentrations.

TABLE 1: Experimental conditions.

	Reaction fluid	Temperature (°C)	Water/rock ratio	Flow rate (ml/min)
Open system	0.3% CO <sub>2</sub> solution	35°C to 200°C	1:30	1
Semiopen system	0.3% CO <sub>2</sub> solution	35°C to 200°C	1:1	0

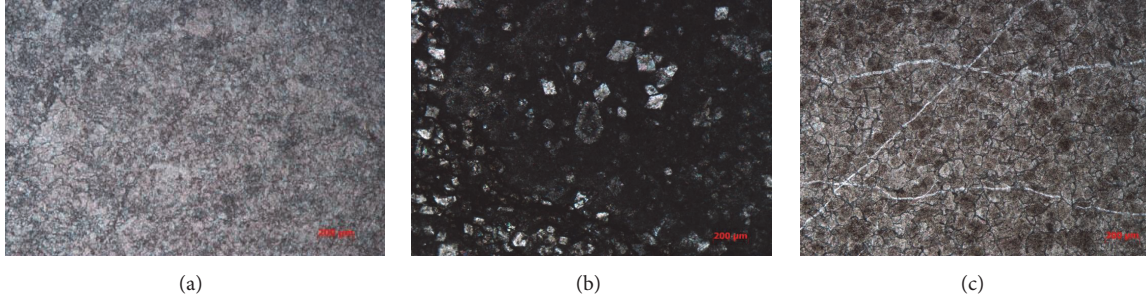


FIGURE 2: Carbonate rock sample types: (a) micritic limestone; (b) dolomitic limestone; (c) fine crystalline dolostone.

**2.3. Experimental Subject.** In this study, samples were standard calcite mineral, standard dolomite mineral, and micritic limestone samples from Ordovician Pingliang Formation, dolomitic limestone samples, and fine crystalline dolostone samples from Ordovician Majiagou Formation. The microscopic characteristics of the samples are shown in Figure 2. The collecting positions and formations of the samples are listed in Table 2. The mineral composition and content of the carbonate samples are listed in Table 3.

The samples were crushed into particles of 2.8 mm to 4.2 mm in diameter to fit the sample tube. The samples were ultrasonically cleaned with deionized water and dried in the oven at 105°C for 24 hours. CO<sub>2</sub> aqueous solution was selected as the acidic fluid medium, to simulate the in situ acidic fluid environment [24]. The mass fraction of CO<sub>2</sub> in the aqueous solution is 0.3% with pH of 4.2.

### 3. Results and Discussion

**3.1. Carbonate Weight Loss in the Open System.** In the open system simulation, the dissolution of calcite generally exceeded that of dolomite, so as limestone and dolostone (Figure 3). The dissolution weight loss of each carbonate sample showed a dissolution window, during which the weight loss first ascends and then declines along with rising temperature [12, 22, 23, 25]. The temperature that showed the dissolution window ranged from 35°C to 150°C. The dissolution weight loss of the standard calcite sample increased between 35°C and 100°C, reached the peak value at 100°C, and then declined slowly. For the standard dolomite sample, the range when dissolution weight loss increased was between 35°C and 125°C, and the maximum dissolution weight loss was reached at 125°C. The response time of dolomite on temperature variation was slower than that of calcite, and the maximum dissolution weight loss of calcite was twice of the dolomite. These results indicated that the calcite was dissolute more than that of dolomite in the open environment and

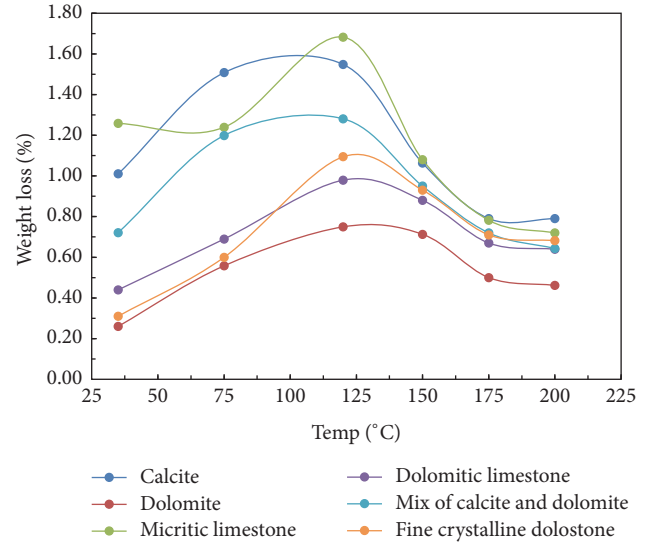


FIGURE 3: The relationship between carbonate dissolution weight loss and temperature in the open system.

was consistent with the former study carried out in the open system [23]. Through thermodynamic simulations, Huang et al. [26] found that carbonate minerals in the depth of less than 700 meters of the formation tend to dissolve, and Zhu et al. [27] found that the dissolution performance of carbonate rocks increased first and then decreased with the increase of temperature. The results in this study are in accordance with the above simulations.

**3.2. Carbonate Weight Loss in the Semiopen System.** In the semiopen system simulation, the dissolution weight loss of dolomitic limestone was the largest among all the samples. The dissolution weight loss of calcite was higher than that of dolomite for the whole temperature range. Limestone and dolomite shared similar dissolution weight losses between

TABLE 2: Collecting location of the samples.

Sample number	Sample name	Lithology	Formation
C1	Calcite standard mineral	Calcite	—
D1	Dolomite standard mineral	Dolomite	—
A1	XLG-O <sub>2</sub> P-16	Micritic limestone	Ordovician Pingliang Formation
A2	TWD-O <sub>2</sub> P-7	Dolomite limestone	Ordovician Tiewadian Formation
A3	Mixed standard mineral	Half calcite, half dolomite	—
A4	XF3 well	Fine crystalline dolostone	Ordovician Majiagou Formation

TABLE 3: Components and contents of the minerals.

Sample number	Calcite	Dolomite	Quartz	Pyrite	Clay mineral
C1	100%	—	—	—	—
D1	—	100%	—	—	—
A1	95.8%	—	2.3%	1.9%	—
A2	68.2%	26.6%	2.3%	—	2.9%
A3	50%	50%	—	—	—
A4	—	90.1%	4.2%	2.5%	3.2%

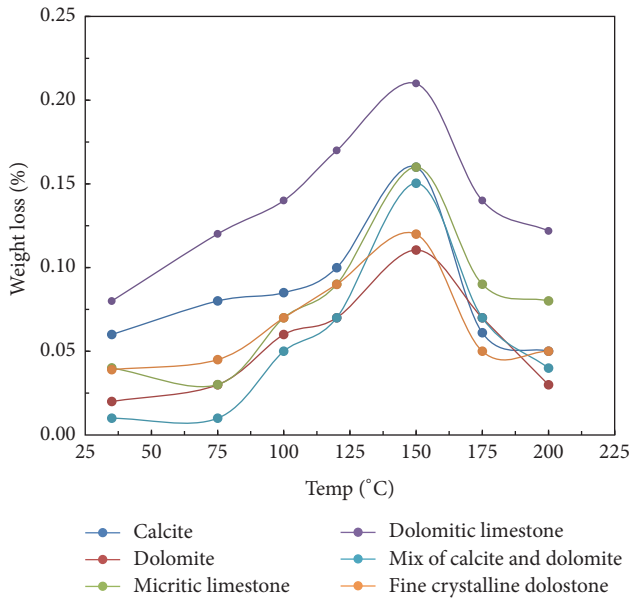


FIGURE 4: The relationship between carbonate dissolution weight loss and temperature in the semiopen system.

35°C~125°C, and the dissolution rate of the former exceeded the latter when temperature was higher than 125°C. The dissolution weight loss of all the samples came to the peak around 150°C. The highest dissolution weight loss of calcite is about 1.5 times that of dolomite. The temperature range for the dissolution window was from 120°C to 175°C. The dissolution window in the semiopen system appeared at higher temperature/pressure than that in the open system (Figure 4).

In the semiopen system, dolomitic limestone (with a dolomite content < 30%) had a higher weight loss than other carbonate samples. Taylor et al. [28] also found that the dissolution weight loss of the limestone from Kluff formation with a dolomite content of 30–40% was the largest in 1 M HCl solution and at room temperature. Davis et al. [29] suggested that Mg<sup>2+</sup> generated from dolomite dissolution destroyed the internal crystal structure of calcite and enhanced the dissolution of calcite. It is also observed in the field that the dolomitized limestone reservoirs are generally well developed for the dissolution of the pores.

The simulation experiment of the semiopen system is close to the actual deep-ultradeep carbonate stratum. The opening of the fault systems associated with episodic tectonics or the specific fluid developed from adjacent formations such as CO<sub>2</sub>, organic acids which form hydrocarbon generation, or H<sub>2</sub>S from TSR could make it favorable for the fluid entering the fault or fractures to react with carbonate rock. The water/rock ratio is relatively small due to the small amount of the liquid. In that case, the fluid became supersaturation in a short time during the reaction, following the equilibrium of the dissolution/precipitation process. Such short period of reactions affected little on creating porosity but could maintain the preexisting pores formed in the open system and prevent the porosity loss through cementation.

In this study, the average weight loss of the standard calcite sample in the open system was 14 times larger than that of the semiopen system. For the standard dolomite samples, the average weight loss in the open system was 11 times of that in the semiopen system. As a result, the dissolution weight loss of carbonate rocks in the open system was higher under the same temperature and pressure conditions (corresponding to the burial depth), which is also favorable for porosity creation (Figure 5).

In the dissolution process of carbonate minerals, H<sup>+</sup> in the solution diffused into the diffusion boundary layer between the mineral and the solution and reacted with the surface of the mineral. Ca<sup>2+</sup> and Mg<sup>2+</sup>, as the reaction product, diffused from the mineral surface into the solution. The thickness of the boundary layer determines the diffusion time and the reaction rate. The dissolution rate could be limited. When the flow rate of the fluid was low, a relatively thicker diffusion boundary layer was made, and the slow mass transfer velocity became the limiting factor of a higher dissolution rate and vice versa [30–32]. In the open system, the stronger hydrodynamic condition and a thinner DBL than

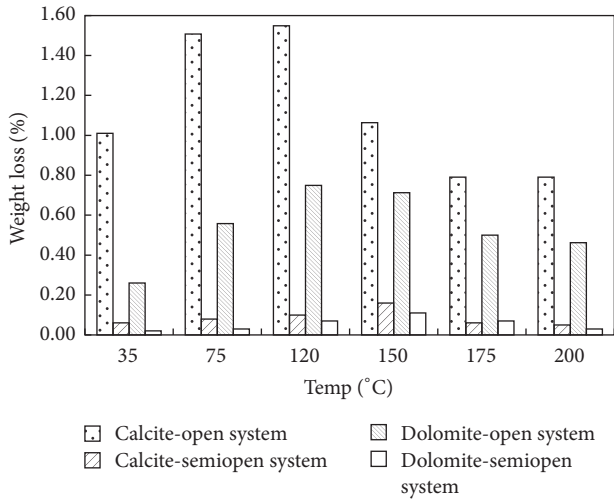


FIGURE 5: The comparison of dissolution weight loss of carbonate rock samples in the open systems and semiopen systems.

that in the semiopen system could lead to a higher diffusion rate.

When the pH of fluid was below 4, the mineral dissolution rate was proportional to  $H^+$  concentration [33, 34]. The open fluid system is continually replenished with fresh acidic fluid (pH ~ 4) during the reaction. Nevertheless, the total amount of fluid in the semiopen fluid system was relatively small and the average pH of the fluid increased to ~5.45 after  $H^+$  depletion. Thus, a lower pH of the fluid could guarantee the open system with a higher reaction rate. As a result, both the higher diffusion rate and the reaction rate indicated that the dissolution of carbonate rocks in the open system, with a larger total dissolution amount, was more significant than those in the semiopen system.

In addition, simulation experiments of water-rock interaction of carbonate rocks in the closed system showed that the whole carbonate rock tended to precipitation and cementation as temperature and pressure increased [35]. However, we also observed that a few single points tended to dissolve, which indicated a dynamic equilibrium of dissolution/precipitation process in the reaction. Since water/rock ratio is quite small in the closed system, precipitation merely had an influence on the whole porosity status.

**3.3. Surface Observation of the Carbonate Samples.** The carbonate samples were observed by scanning electron microscopy (SEM) before and after the reaction in the open system. The characteristics of carbonate dissolution are as follows: the calcite surface was flat before the reaction (Figure 6(a)), and then small dissolved pores were formed along the calcite cleavage surface or the weak point on the surface (Figure 6(b)). Some newly white mineral precipitated on the surface, which was later identified as  $CaCO_3$  by Energy Dispersive Spectrometer (Figure 6(c)). Dolomite dissolved mainly on the crystal edge from rhombus to ellipsoid (Figure 6(d)). Small pores formed on the dolomite crystal edge were then connected to form larger pores (Figures 6(e)

and 6(f)). Herman and White [36] observed the selective dissolution of dolomite along the grain edge. The initial interface of the fluid and the rock determines the interface morphology after dissolution. Generally, the dissolution was extended and connected along the contact surface of the mineral cleavage, the fracture, and the weak points.

**3.4. Characteristics of Different Fluid Environments**

**3.4.1. Open Geological Fluid System.** When we applied the experimental results to the corresponding actual geological fluid system of which deep-ultradeep carbonate reservoir was formed, (1) open environment with a higher water/rock ratio would lead to a fluid with unsaturated  $CaCO_3$ . In that case, the water-rock reaction kept moving towards the dissolution direction. New pores were formed, and the original pores or fractures were expanded. The new formed pores offered a larger surface area for the dissolution reaction. Carbonate strata continue to dissolve into scaled reservoir, along with the development of large pore and fracture system.

In the geological history, open geological environment mainly existed in the penecontemporaneous stage of long-term exposure sedimentary diagenesis such as reef, beach, and tidal flat with frequent exposures or the epigenesis stage of tectonic uplift such as near-surface karst environment and deep cycle fresh water dissolution environment. The long term and large scale of such dissolution could form considerable storage space. Despite the filling effect from mechanical, chemical, or biochemical processes, open environment is the main forming environment for high quality carbonate reservoirs. In addition, the scale and quality of the reservoir were further determined by the composition and structure of the carbonate rock, the interaction intensity and time of fluid, and the filling patterns and magnitude. For example, the quality of late karst reservoir may be degraded due to the effects of over dissolution and filling.

**3.4.2. Semiopen Geological Fluid Environment.** The water/rock ratio in the semiopen geological fluid system was relatively small. The fluid was prone to rapidly reach saturation or supersaturation state during the reaction. There was a dynamic equilibrium of dissolution/precipitation process between the fluid and the rock. Mineral dissolves and precipitates along the fluid flow pathway simultaneously. Some preexisting porosity may be expanded while some porosity may get cementation by calcite and dolomite.

In geological history, such environment is characterized by periodic fault, active fold, and special fluid event during basin evolution, which change the original fluid environment and break the chemical balance inside the formation to form a new fluid environment. As a result, episodic fluid-rock interaction happened. The exchange of material and energy in the formation would cause a series of processes including dissolution, metasomatism, dolomitization, recrystallization, and cementation and lead to the increase/decrease of porosity. Along with burial process, hydrocarbon generation, BSR, and TSR occurred in the strata, and some acid/alkali fluid may also enter the carbonate formation along with magmatic activity to form a new fluid environment and alter the storage

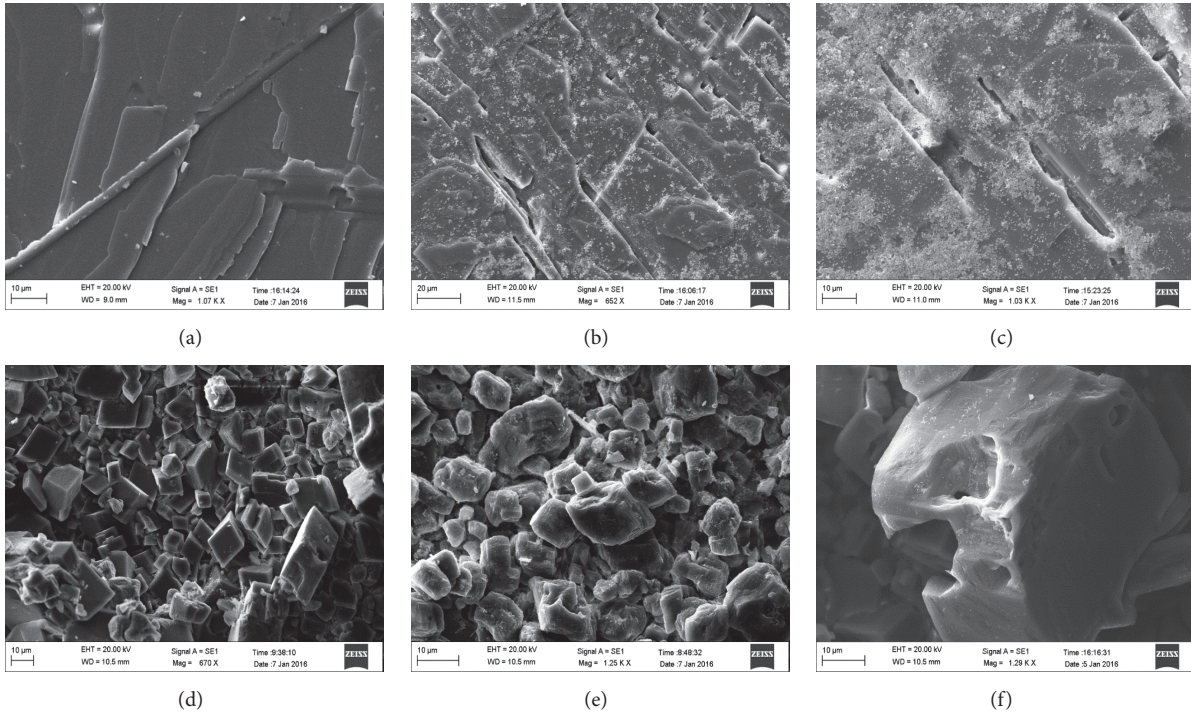


FIGURE 6: Surface morphology of the carbonate samples before and after the dissolution experiment: (a) calcite sample before dissolution; (b) dissolution fractures on the calcite surface; (c) expanded dissolution fracture after dissolution; (d) dolomite before the dissolution; (e) dolomite dissolved on the edge; (f) etch pits on the dolomite surface.

space. Chemical aggressive fluid during fluid-rock interaction, charged with  $\text{CO}_2$ ,  $\text{H}_2\text{S}$ , organic acids, mainly came from organic matter maturation, hydrocarbon degradation, TSR, and BSR [24, 37, 38]. Those fluids could significantly dissolve the rock and enhance porosity [39, 40]. Moreover, some semiopen environment such as strong tectonic-hydrothermal movement could also form high quality carbonate reservoirs. For example, scaled hydrothermal dolostone reservoir is one of the key oil and gas exploration areas.

**3.4.3. Closed Geological Fluid Environment.** The remaining pore water in the closed geological fluid system was saturated, and the fluid-rock interaction reached an equilibrium state. There was no scaled dissolution or precipitation, and the preexisting porosity was maintained. Although fluid flow was limited, changes in burial depth may break the reaction equilibrium by temperature or pressure change. Minor precipitation, dissolution, or recrystallization would appear along with the change of burial depth, but porosity was barely altered in this environment. The main function of a closed environment is the maintenance of reservoir space. The closed fluid environment requires a stable tectonic background and good cap conditions, which are the foundation and prerequisite of oil and gas accumulation, transformation, adjustment, and preservation.

In summary, open and semiopen fluid environment are the key to the formation of reservoir space, and closed fluid environment is essential to the maintenance of reservoir space.

## 4. Conclusions

In this study, we reached the following understandings through the comprehensive analysis of the experiments results:

- (1) Open is the key. Almost all the high quality reservoirs had experienced one or more open or semiopen geologic fluid environments in the geological evolution history. Long-term precipitation leaching during penecontemporaneous stage and epigenesis stage and acid dissolution in the middle and late stages of deep burial diagenesis could significantly improve the physical properties of the reservoirs.
- (2) The type of the fluid and rock determines the dissolution rate and reservoir quality. The flow pattern, intensity, and reaction time of the fluid determine the dissolution strength and the dissolution rate. The structure, composition, and contact surface of rock affect the quality of the reservoir. The various channel types of the fluid flow could form reservoir space such as dissolution pores, fractures, and holes.
- (3) Closed geological fluid environment is essential for the preservation of preexisting reservoir space. If the preexisting pores of the carbonate reservoirs were well formed in the early diagenesis stage, the deep-ultradeep closed environment could provide effective

preservation conditions. The burial or uplifting process of the formation will change the system temperature and pressure and lead to microcirculation of the fluid in the reservoir. Although the migration and minor adjustment of the materials may occur, the porosity barely changed along with the obvious variation of permeability and heterogeneity.

## Conflicts of Interest

The authors declare that they have no conflicts of interest.

## Acknowledgments

The assistance of Dr. Ming Xue is acknowledged. The help on the experiment and reference material from Dr. Donghua You, Dr. Shoutao Peng, and Dr. Lingjie Yu is acknowledged. This work is supported by Strategic Priority Research Program of the Chinese Academy of Sciences (Grant no. XDA14010201) and National Natural Science Foundation of China (Grants no. 41702134 and no. U1663209).

## References

- [1] Z. R. Beydoun, "Arabian plate oil and gas: why so rich and so prolific?" *Episodes*, vol. 21, no. 2, pp. 74–81, 1998.
- [2] T. P. Burchette, "Carbonate rocks and petroleum reservoirs: a geological perspective from the industry," *Geological Society Special Publication*, vol. 370, no. 1, pp. 17–37, 2012.
- [3] H. G. Machel, M. L. Borrero, E. Dembicki, H. Huebscher, L. Ping, and Y. Zhao, "The grosmont: the world's largest unconventional oil reservoir hosted in carbonate rocks," *Geological Society Special Publication*, vol. 370, no. 1, pp. 49–81, 2012.
- [4] Y. Ma, X. Cai, and P. Zhao, "The research status and advances in porosity evolution and diagenesis of deep carbonate reservoir," *Earth Science Frontiers*, vol. 18, no. 4, pp. 181–192, 2011.
- [5] Z. He, X. Jin, and Y. Wo, "Hydrocarbon accumulation characteristics and exploration domains of ultra-deep marine carbonate in China," *China Petroleum Exploration*, vol. 21, no. 1, pp. 3–14, 2016.
- [6] C. Jiao, Z. He, X. Xing, H. Qing, B. He, and C. Li, "Tectonic hydrothermal dolomite and its significance of reservoirs in Tarim basin," *Acta Petrologica Sinica*, vol. 27, no. 1, pp. 277–284, 2011.
- [7] G. Zhu, S. Zhang, Y. Liang, Y. Ma, J. Dai, and G. Zhou, "Dissolution and alteration of the deep carbonate reservoirs by TSR: an important type of deep-buried high-quality carbonate reservoirs in Sichuan basin," *Acta Petrologica Sinica*, vol. 22, no. 8, pp. 2182–2194, 2006.
- [8] P. W. Choquette and N. P. James, "Diagenesis# 12. Diagenesis in Limestones-3. The deep burial environment," *Geoscience Canada*, vol. 14, no. 1, pp. 3–35, 1987.
- [9] L. N. Plummer, T. M. L. Wigley, and D. L. Parkhurst, "The kinetics of calcite dissolution in CO<sub>2</sub>-water systems at 5 to 60°C and 0.0 to 1.0 atm CO<sub>2</sub>," *American Journal of Science*, vol. 278, no. 2, pp. 179–216, 1978.
- [10] E. Busenberg and L. N. Plummer, "The kinetics of dissolution of dolomite in CO<sub>2</sub>-H<sub>2</sub>O systems at 1.5 to 65°C and 0 to 1 atm PCO<sub>2</sub>," *American Journal of Science*, vol. 282, no. 1, pp. 45–78, 1982.
- [11] E. L. Sjöberg, "Kinetics and mechanism of calcite dissolution in aqueous solutions at low temperatures," in *Stockholm Contributions in Geology Stockholm*, vol. 92, Almquist Wiksell, 1978.
- [12] M. Fan, X. Jiang, and W. Liu, "Dissolution of carbonate rocks in CO<sub>2</sub> solution under the different temperature," *Acta Sedimentologica Sinica*, vol. 25, no. 6, pp. 825–830, 2007.
- [13] M. Fan, Z. He, and Z. Li, "Dissolution window of carbonate rocks and its geological significance," *Oil and Gas Geology*, vol. 32, no. 4, pp. 499–505, 2011.
- [14] M. She, Y. Zhu, A. Shen, X. Zheng, and X. He, "Simulation experiment for the dissolution of carbonate rocks of the Yingshan formation on the northern slope of Tazhong uplift," *Carsologica Sinica*, vol. 31, no. 3, pp. 234–239, 2012.
- [15] M. She, J. Shou, and A. Shen, "Experimental simulation of dissolution for carbonate rocks in organic acid under the conditions from epigenesis to deep burial environments," *Geochimica*, vol. 43, no. 3, pp. 276–286, 2014.
- [16] J. W. Morse and R. S. Arvidson, "The dissolution kinetics of major sedimentary carbonate minerals," *Earth-Science Reviews*, vol. 58, no. 1-2, pp. 51–84, 2002.
- [17] O. S. Pokrovsky, S. V. Golubev, and J. Schott, "Dissolution kinetics of calcite, dolomite and magnesite at 25°C and 0 to 50 atm pCO<sub>2</sub>," *Chemical Geology*, vol. 217, no. 3-4, pp. 239–255, 2005.
- [18] O. S. Pokrovsky, S. V. Golubev, J. Schott, and A. Castillo, "Calcite, dolomite and magnesite dissolution kinetics in aqueous solutions at acid to circumneutral pH, 25 to 150°C and 1 to 55 atm pCO<sub>2</sub>: new constraints on CO<sub>2</sub> sequestration in sedimentary basins," *Chemical Geology*, vol. 265, no. 1-2, pp. 20–32, 2009.
- [19] L. N. Plummer and T. M. L. Wigley, "The dissolution of calcite in CO<sub>2</sub>-saturated solutions at 25°C and 1 atmosphere total pressure," *Geochimica et Cosmochimica Acta*, vol. 40, no. 2, pp. 191–202, 1976.
- [20] L. N. Plummer and E. Busenberg, "The solubilities of calcite, aragonite and vaterite in CO<sub>2</sub>-H<sub>2</sub>O solutions between 0 and 90°C, and an evaluation of the aqueous model for the system CaCO<sub>3</sub>-CO<sub>2</sub>-H<sub>2</sub>O," *Geochimica et Cosmochimica Acta*, vol. 46, no. 6, pp. 1011–1040, 1982.
- [21] S. L. Brantley and C. F. Conrad, "Analysis of rates of geochemical reactions," in *Kinetics of Water-Rock Interaction*, S. L. Brantley, J. D. Kubicki, and A. F. White, Eds., Springer, New York, NY, USA, 2008.
- [22] X. Jiang, S. Wang, and M. Fan, "Study of simulation experiment for carbonate rocks dissolution in burial diagenetic environment," *Petroleum Geology and Experiment*, vol. 30, no. 6, pp. 643–647, 2008.
- [23] M. Fan, K. Hu, and X. Jiang, "Effect of acid fluid on carbonate reservoir reconstruction," *Geochimica*, vol. 38, no. 1, pp. 20–26, 2009.
- [24] S. J. Mazzullo and P. M. Harris, "An overview of dissolution porosity development in the deep-burial environment, with examples from carbonate reservoirs in the permian basin," in *Permian Basin Plays—Tomorrow's Technology Today*, M. P. Candelaria, Ed., West Texas Geological Society Publication, Midland, Texas, Tex, USA, 1991.
- [25] Z. He, X. Wei, and Y. Qian, "Forming mechanism and distribution prediction of quality marine carbonate reservoirs," *Oil and Gas Geology*, vol. 32, no. 4, pp. 489–498, 2011.
- [26] S. Huang, K. Huang, X. Zhang, L. Liu, and Q. Zhong, "Chemical thermodynamics foundation of retrograde solubility for carbonate: solution media related to CO<sub>2</sub>," *Journal of Chendu University of Technology*, vol. 36, no. 5, pp. 457–464, 2009.

- [27] D. Zhu, Z. Jin, and W. Hu, "Hydrothermal alteration dolomite reservoir in Tazhong area," *Acta Petrolei Sinica*, vol. 30, no. 5, pp. 698–704, 2009.
- [28] K. C. Taylor, H. A. Nasr-El-Din, and S. Mehta, "Anomalous acid reaction rates in carbonate reservoir rocks," *SPE Journal*, vol. 11, no. 4, pp. 488–496, 2006.
- [29] K. J. Davis, P. M. Dove, and J. J. De Yoreo, "The role of  $Mg^{2+}$  as an impurity in calcite growth," *Science*, vol. 290, no. 5494, pp. 1134–1137, 2000.
- [30] W. Dreybrodt, J. Lauckner, L. Zaihua, U. Svensson, and D. Buhmann, "The kinetics of the reaction  $CO_2 + H_2O \rightarrow H^+ + HCO_3^-$  as one of the rate limiting steps for the dissolution of calcite in the system  $H_2O-CO_2-CaCO_3$ ," *Geochimica et Cosmochimica Acta*, vol. 60, no. 18, pp. 3375–3381, 1996.
- [31] R. Orton and P. R. Unwin, "Dolomite dissolution kinetics at low pH: a channel-flow study," *Journal of the Chemical Society, Faraday Transactions*, vol. 89, no. 21, pp. 3947–3954, 1993.
- [32] Z. Liu and D. Wolfgang, "Kinetics and rate-limiting mechanisms of dolomite dissolution at various  $CO_2$  partial pressures," *Science in China, Series B: Chemistry*, vol. 44, no. 5, pp. 500–509, 2001.
- [33] E. L. Sjöberg and D. T. Rickard, "Calcite dissolution kinetics: surface speciation and the origin of the variable pH dependence," *Chemical Geology*, vol. 42, no. 1-4, pp. 119–136, 1984.
- [34] R. A. Berner and J. W. Morse, "Dissolution kinetics of calcium carbonate in sea water; IV, Theory of calcite dissolution," *American Journal of Science*, vol. 274, no. 2, pp. 108–134, 1974.
- [35] Y. Yang, B. Liu, and S. Qin, "Re-recognition of deep carbonate dissolution based on the observation of in-situ simulation experiment," *Acta Scientiarum Naturalium Universitatis Pekinensis*, vol. 50, no. 2, pp. 316–322, 2014.
- [36] J. S. Herman and W. B. White, "Dissolution kinetics of dolomite: effects of lithology and fluid flow velocity," *Geochimica et Cosmochimica Acta*, vol. 49, no. 10, pp. 2017–2026, 1985.
- [37] R. Sassen and C. H. Moore, "Framework of hydrocarbon generation and destruction in eastern smackover trend," *American Association of Petroleum Geologists Bulletin*, vol. 72, no. 6, pp. 649–663, 1988.
- [38] S. Zhang, G. Zhu, and K. He, "The effects of thermochemical sulfate reduction on occurrence of oil-cracking gas and reformation of deep carbonate reservoir and the interaction mechanisms," *Acta Petrologica Sinica*, vol. 27, no. 3, pp. 809–826, 2011.
- [39] V. Schmidt and D. A. McDonald, "The role of secondary porosity in the course of sandstone diagenesis," in *Aspects of Diagenesis*, P. R. Schluger, Ed., SEPM Society for Sedimentary Geology, Oklahoma, Okla, USA, 1979.
- [40] C. H. Moore, *Carbonate Diagenesis and Porosity*, Elsevier, New York, NY, USA, 1989.

## Research Article

# New Insight into the Kinetics of Deep Liquid Hydrocarbon Cracking and Its Significance

Wenzhi Zhao, Shuichang Zhang, Bin Zhang, Kun He, and Xiaomei Wang

Research Institute of Petroleum Exploration and Development, Beijing 100083, China

Correspondence should be addressed to Shuichang Zhang; sczhang@petrochina.com.cn

Received 31 March 2017; Accepted 20 July 2017; Published 6 September 2017

Academic Editor: Paolo Fulignati

Copyright © 2017 Wenzhi Zhao et al. This is an open access article distributed under the Creative Commons Attribution License, which permits unrestricted use, distribution, and reproduction in any medium, provided the original work is properly cited.

The deep marine natural gas accumulations in China are mainly derived from the cracking of liquid hydrocarbons with different occurrence states. Besides accumulated oil in reservoir, the dispersed liquid hydrocarbon in and outside source also is important source for cracking gas generation or relayed gas generation in deep formations. In this study, nonisothermal gold tube pyrolysis and numerical calculations as well as geochemical analysis were conducted to ascertain the expulsion efficiency of source rocks and the kinetics for oil cracking. By determination of light liquid hydrocarbons and numerical calculations, it is concluded that the residual bitumen or hydrocarbons within source rocks can occupy about 50 wt.% of total oil generated at oil generation peak. This implies that considerable amounts of natural gas can be derived from residual hydrocarbon cracking and contribute significantly to the accumulation of shale gas. Based on pyrolysis experiments and kinetic calculations, we established a model for the cracking of oil and its different components. In addition, a quantitative gas generation model was also established to address the contribution of the cracking of residual oil and expelled oil for natural gas accumulations in deep formations. These models may provide us with guidance for gas resource evaluation and future gas exploration in deep formations.

## 1. Introduction

The natural gas accumulations of deep marine strata in China are mainly derived from the cracking of liquid hydrocarbons [1–5]. Previous research believed that natural gas has been mainly derived from accumulated paleoreservoirs of liquid hydrocarbons via cracking [6, 7]. However, the dispersed liquid hydrocarbons could also act as an important source for natural gas accumulations. Residual petroleum refers to those retained in source rocks and along migration pathways. Since there is no systematic evaluation method for quantifying residual petroleum, there remains a great controversy on this issue [8–18]. The amount of residual petroleum in source rocks could be calculated using expulsion efficiency. Pepper and Corvi [9] proposed that liquid hydrocarbons could be expelled from source rocks via kerogen or inorganic pore system, and the greatest expulsion efficiency for marine and lacustrine source rocks could reach 80%, and the residual petroleum in the source rocks is of 5%~20%, using the ORGAS model.

Ritter [11] first proposed the application of swelling-theory in expulsion efficiency calculation and demonstrated

that different geochemical fractions have different expulsion efficiency and the expulsion efficiency of saturates could achieve as high as 80%. Kelemen et al. [14] discovered chemical fractionation during hydrocarbon expulsion based on the swelling-theory and thus established the Exxon CS-CYM model to predict hydrocarbon compositions on the basis of chemical structures and production [15, 19]. Stainforth [17] thought that hydrocarbon expulsion is achieved by diffusion via organic pore system and set a generation and expulsion model, ShellGenex, including both the transition state theory and the free volume theory. The model suggests that hydrocarbon expulsion is a continuous process with decreasing GOR of the expelled petroleum and increasing density of the expelled oil. The dispersed hydrocarbons that occurred in the migration pathways are even more difficult to quantitative evaluation due to the reservoir and structure condition or the secondary modification of later structural evolution. Zhao et al. [4] demonstrated the significance of dispersed liquid hydrocarbons on gas accumulations and divided them into three occurrence states based on paleostructure: accumulated, half-accumulated, and dispersed.

TABLE 1: Basic geochemical characteristics of source rock samples.

Well	Strata	Depth (m)	Basin	TOC (%)	Tmax (°C)	S <sub>1</sub> (mg/g)	S <sub>2</sub> (mg/g)	HI (mg/g·TOC)	R <sub>o</sub> (%)
Chao 73-87	K	834.6	Songliao Basin	4.89	435	1.39	42.06	860	0.5
Da 11	K	1710	Songliao Basin	3.71	434	0.91	30.74	829	0.5
Da 11	K	1712	Songliao Basin	4.14	442	0.74	36.70	886	0.6
Da 11	K	1722	Songliao Basin	3.31	447	0.51	27.19	821	0.8
X28	J	1996	Sichuan Basin	3.03	447	2.96	12.07	398	0.9
PL 10	J	1995	Sichuan Basin	2.54	449	3.65	10.21	402	1.0
PL10	J	1997	Sichuan Basin	2.81	449	2.45	10.40	370	1.0

TABLE 2: The physical characteristics and geochemical compositions of oil samples.

Well	Oil type	Location	Density (g/cm <sup>3</sup> )	Group composition (%)		
				Saturates	Aromatics	Resin + asphaltenes
ND 1	Light oil	Bohai Bay Basin	0.76	95.90	2.34	1.76
ZG 6			0.78	78.56	20.54	0.90
YH 7			0.79	82.06	15.47	2.47
DH11	Normal oil	Tarim Basin	0.87	80.00	15.00	5.00
YM201			0.86	30.91	48.45	20.64
LN 1	Heavy oil		0.97	29.00	31.00	40.00

Previous researches on liquid hydrocarbon cracking mainly focused on high temperature cracking mechanisms, and it is generally believed that the liquid hydrocarbons begin to crack and are terminated at about 200°C [20, 21]. Recently, many researches on kinetics of gas generation have been proposed as more and more oil cracking gas accumulations are being discovered [3, 6, 7, 15, 21–29]. Dieckmann et al. [30] obtained kinetic parameters of gas generation at different maturity stages using microscale sealed vessel (MSSV) thermal cracking of the Toarcian Shale and deduced that when the geothermal heating rate is about 5.3°C/ma, the initiation temperature of oil cracking happened at 150°C, with  $R_o$  of 1.2%, and the peak gas generation corresponds to 180°C. Tsuzuki et al. [31] proposed that the peak gas generation from oil cracking corresponds to 220°C, based on the kinetics parameters of cracking experiments of different fractions of oil, and believed that the gas accumulations of oil cracking could only be found beyond 5000 m. Vandenbroucke et al. [32] divided the  $C_{14+}$  fraction into compositions of NSOs,  $C_{14+}$ Aro-1,  $C_{14+}$ Aro-2,  $C_{14+}$ sat( $n$ ),  $C_{14+}$ sat(iso + cyclo), and so forth and calculated the kinetics parameters of each composition. Behar et al. [33, 34] calculated hydrocarbon generation potentials under laboratory and natural conditions based on the above kinetic parameters.

In this paper, we discuss the categories of oil occurrences, their cracking mechanism, and gas potential, which can provide a new insight into evaluation of the deep gas resource prospects.

## 2. Samples and Experiments

**2.1. Samples.** In order to quantify the residual petroleum during the generation process, source rock samples of different

maturities are needed. Since the marine strata in China have all experienced deep burial, the organic matters in the source rocks are at mature to overmature stages. Thus, the Cretaceous source rock samples from the Songliao Basin, with relatively low thermal maturity, and the Jurassic source rock samples from the Sichuan Basin, with peak oil generation maturity, were chosen for our pyrolysis experiments. The basic geochemical characteristics of these samples are listed in Table 1.

Eight oil samples for dynamic analysis of thermal cracking and gas generation were obtained from the Tarim Basin and the Bohai Bay Basin, including heavy, normal, and light oils, with densities ranging from 0.76 g/cm<sup>3</sup> to 0.97 g/cm<sup>3</sup>. The geochemical compositions of these oil samples are listed in Table 2.

### 2.2. Experimental Methods

**2.2.1. Gold Tube Simulation Experiment of Liquid Hydrocarbons.** Thermal cracking of the liquid hydrocarbons was achieved using the gold tube simulation apparatus, under the conditions of high temperature and high pressure. The procedures for adding samples into the gold tube were as follows. One side of gold tube (60 mm × 5 mm) was sealed by welding under constant argon flow condition; then certain amount of samples was added to the gold tube through the other open side. Afterwards, the added tube was fixed in a cold water bath, and the air was swept out by argon flow for 5 minutes. Then, the gold tube was sealed by welding to provide a complete closed environment. The completely sealed gold tube was put into a reaction still, and simulation experiment was performed under the programmed temperature conditions. The sealed gold tube was weighed both before and after the simulation experiment in order to exclude the possibility of potential leakage.

The gold tube simulation experiment was designed to include two procedures, with heating rate of 2°C/h and 20°C/h, heating duration time (4 h, 8 h, and 16 h), and thermal cracking under the thermostatic conditions (400°C), with different reaction medium conditions. The pressure of the reaction system was set at 50 MPa, and the deviation range is within 0.1 MPa. The temperature and pressure of the reactor were controlled by the computer terminal program, and the range of the temperature deviation is within 0.1°C.

The collection and quantification of gas from the gold tubes were performed by a custom-made device which was connected to a vacuum pump. Prior to piercing the tube, the gas collection unit was pumped at a residual pressure ( $P_1$ ,  $<10^{-3}$  bar). The pressure of the collection unit was recorded after the gold tube was ruptured ( $P_2$ ). The volumes of gas products were calculated according to the following equation:  $V = (P_2 - P_1) \times V_0 / P_0$  ( $V_0$  is the volume of gas collection unit and  $P_0$  is atmosphere pressure).

Identification and quantification of the individual hydrocarbon and nonhydrocarbon gas components were carried out using a two-channel Wasson-Agilent 7890 Series gas chromatograph (GC). The temperature of the heating program for the GC oven started from 20°C to 68°C (held isothermal for 7 min), then increased to 90°C (at a rate of 10°C/min and then held isothermal for 1.5 min), and finally reached 175°C (at a rate of 15°C/min and then held isothermal for 5 min). An external standard was used for the chromatographic calibration. The certified gas standards were prepared at a precision of better than  $\pm 1$  mol% for each component made by BAPB Inc.

**2.2.2. Other Analyses Methods.** The hydrocarbon pyrolysis analysis of the source rock was performed on a Rock-Eval 6 instrument. The  $S_1$  peak was an adsorbed hydrocarbon, which was released in a helium atmosphere at 300°C for 3 minutes, representing the residual petroleum in the source rock. The pyrolysis hydrocarbon was those hydrocarbons released when the temperature rose to 600°C at a heating rate of 50°C/min for 3 minutes.

The hydrocarbon content in the rock was obtained by chloroform extraction. A soxhlet extraction method was used, and the process involved wrapping about 150 g sample by filter paper extracted by chloroform, putting the samples in an extractor, adding dichloromethane and methanol (93 : 7, v/v) to the cycling bottles with a small piece of copper, heating at a constant bath temperature of 75°C, and afterwards extracting 72 hours at circulating water cooling extraction.

The quantification of oil group components was gained by TLC-FID. The liquid hydrocarbons were dissolved in chloroform and boiled in a sintered silica column. The dissolved hydrocarbons were separated into saturates, aromatics, resin, and asphaltenes based on the different polarity and were identified by the flame ion detector. The mass percentage of each of the group components was calculated with the method of peak area normalization. The solvents utilized included hexane, dichloromethane, chloroform, and isopropanol.

Gas chromatographic analysis of the saturate was obtained by the Agilent 7890 gas chromatograph. The

chromatographic column was HP-5MS (30 m  $\times$  0.25 mm  $\times$  0.25  $\mu$ m). Helium was the carrier gas. The programmed heating procedures were set as follows: the initial temperature was 100°C and held for 5 min. Then the temperature increased to 300°C with a heating rate of 4.0°C/min, detected by FID detector after heated for 15 min.

### 3. Results and Discussion

**3.1. Category of Petroleum Occurrence in Sedimentary Basins.** There are three categories of petroleum occurrences. One remained in source rocks, the second is dispersed along the migration pathways, and the third is trapped in the structural or lithology-stratigraphic reservoirs. The third type of hydrocarbons is conventional oil and gas exploration target. However, under the conditions of high temperature in deep strata, the former two types of petroleum could also act as significant sources for gas accumulations when the secondary cracking happened. Zhao et al. [4, 5, 12, 18] discussed the concept of “relaying gas generation” model (gas generated from kerogen primary cracking followed by gas from petroleum secondary cracking) of the residual petroleum within the sources and the dispersed petroleum in reservoirs, indicating that both can become the main sources of deep gas.

**3.1.1. Retained Petroleum in Source Rocks.** In the traditional study of hydrocarbon source rock evaluation, free hydrocarbons (“ $S_1$ ”) or chloroform bitumen “A” of the rock pyrolysis parameters is approximately used as retained petroleum [20, 35]. With the discovery of shale oil and gas, the evaluation accuracy of the hydrocarbon source rocks is further improved, and the quantitative evaluation of the residual petroleum is not satisfied with these two parameters. Volatile light components of free hydrocarbons (“ $S_1$ ”) cannot be detected during the experimental analysis, and at 300°C, some of the heavy components cannot be completely desorbed and detected; therefore “ $S_1$ ” can only represent a portion of the residual petroleum [35]. Usually chloroform bitumen “A” mainly represents the medium-heavy components in residual petroleum. However, during the sample processing and analysis process, the light component would volatilize significantly. Thus, the components heavier than  $C_{13}$  can be detected using the conventional analysis, and the components lighter than  $C_{13}$  almost completely disappeared, so chloroform bitumen “A” also only represents a part of the residual petroleum (Figure 1).

The generation of hydrocarbons generally experienced the process of kerogen—intermediate products—oil and gas. Behar et al. [33, 34] suggested that the intermediate products are mainly strong polar compounds which are rich in N, O, S, and other heteroatoms. These compounds are soluble in n-pentane dichloromethane and other organic solvents. Among them, the compound which is soluble in n-pentane is roughly equivalent to pyrolysis “ $S_1$ ”, and for those which are soluble in methylene chloride, their contents are roughly comparable to the same as those of chloroform bitumen “A” (Figure 2). It can be seen that pyrolysis “ $S_1$ ” and chloroform bitumen “A” mainly represent the intermediate product in

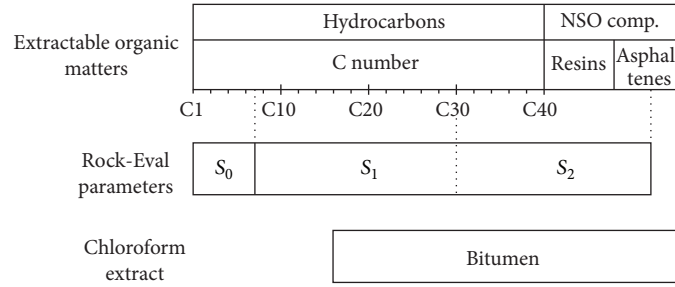


FIGURE 1: Relationship between pyrolysis parameters  $S_1$ , chloroform extracts, and residual petroleum (modified after [35]).

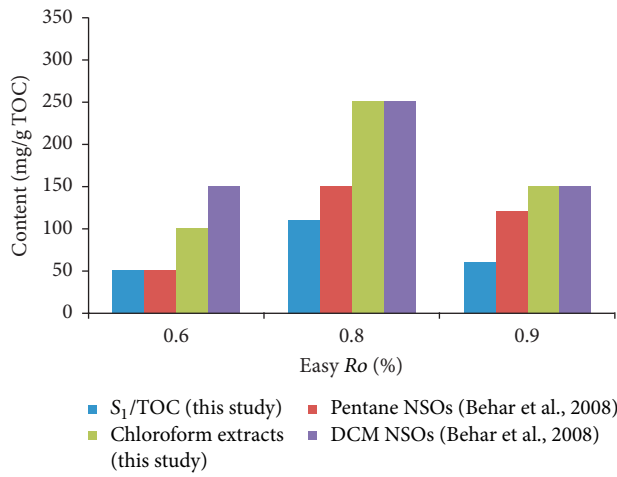


FIGURE 2: Relationships between Rock-Eval  $S_1$ , chloroform extracts, and soluble organic matters.

the conversion process from kerogen to oil, which is rich in NSO components. Some volatile hydrocarbon components may be largely dissipated and cannot be detected.

In order to achieve the accurate quantification of residual petroleum, it is necessary to restore the light components of chloroform bitumen “A”. Zhu et al. [36] pointed out that the recovery coefficient of light hydrocarbons in chloroform bitumen “A” was between 1.2 and 1.6 ( $R_o = 0.8\% \sim 1.6\%$ ) when studying residual petroleum in source rocks from the Dongying Depression. After the light hydrocarbon recovery, the quantity of residual petroleum in the source rocks during the oil generation peak stage was about 50% of the total hydrocarbons generated.

A new method to recover the light components in the residual petroleum was provided in this paper. First, put the fresh rock sample as shown in Table 1 and some steel balls into a sealed container, then freeze them in liquid nitrogen, then let the steel balls grind rock samples in the container, and finally analyze the hydrocarbon component by online GC. For the oil generation peak samples (Xi 28 and PL 10 of the Sichuan Basin in Table 1), the light components in the residual petroleum inside the source at the oil generation peak stage accounted for about one-third of the total hydrocarbons, and this part would not be detectable using conventional methods. After the light components lost due to the analysis

process are added back to the original components, it is found that the residual petroleum at the peak of oil production also accounts for about 50% of the total hydrocarbon production.

In addition, Zhang et al. [37] used the model of hydrocarbon generation and pressurization [38–40] to calculate the change of pressure within source rock. Results showed that oil and gas generation resulted in overpressure, and the maximum was more than 100 MPa during the peak stage of oil generation if no hydrocarbon expelled. In order to keep the pressure unchanged, there should be about 25%–50% of the hydrocarbon expelled.

As the maturity increases, the residual liquid hydrocarbons will be further cracked to form more light components and gaseous hydrocarbons, and the pressure in the source rocks will be further increased to promote more hydrocarbon expulsion outside the source rocks [14, 15, 17]. Thus, as the maturity increases, the content of residual petroleum in the source rocks will gradually decrease while the light component content will increase.

**3.1.2. Petroleum outside the Source Rocks.** The expelled hydrocarbons from source rocks might escape to the surface, or accumulate in traps, or disperse along the migration pathways. Due to the geological factors, such as the structural movement at the timing of reservoir formation, the reservoir conditions, and the later tectonic evolution, the proportions of the concentrated or dispersed liquid hydrocarbons are difficult to determine [52, 53]. Wang et al. [54] provided two methods to discuss the occurrence of the dispersed liquid hydrocarbons both in Sichuan Basin and in Tarim Basin. For example, the Sinian and Cambrian source rocks in the Sichuan Basin were at low mature stage ( $R_o$  value is about 0.7%) in the early Silurian, and the Gaoshiti-Moxi structure had not yet been developed; thus the region cannot form large-scale oil and gas accumulations. The source rocks reached peak petroleum generation stages ( $R_o$  value increased from 0.7% to 2.0%) at the Late Permian-Triassic and formed paleo-oil reservoirs in the local reign and dispersed liquid hydrocarbons in the slope area [4]. The occurrence of the liquid hydrocarbons was partly controlled by the topographic gradient during the time of expulsion. When the gradient of slope areas exceeded  $3^\circ$ , expelled hydrocarbons tended to accumulate at paleohighs, forming significant hydrocarbon accumulations, while the abundance of hydrocarbons was lower and quite dispersed at the lower

TABLE 3: Kinetics parameters for the cracking of individual organic compounds.

Compound	Activation energy (kcal/mol)	Preexponential factor ( $s^{-1}$ )	Reference
$n-C_{14}$	67.6	$7.20E + 18$	[41]
$n-C_{16}$	59.6	$3.10E + 14$	[42]
$n-C_{16}$	74	$3.00E + 19$	[43]
$n-C_{25}$	68.2	$6.10E + 15$	[44]
Tetralin	58	$3.50E + 12$	[45]
Dodecylbenzene	53.3	$1.30E + 13$	[46]
Pentadecylbenzene	55.5	$1.10E + 14$	[47]
Butylbenzene	52.9	$1.10E + 12$	[48]
Ethylbenzene	62.3	$4.70E + 13$	[49]
3-Methylphenanthrene	49	$4.50E + 10$	[50]
Dibenzothiophene	59	$1.90E + 11$	[51]

gradient slopes and failed to form significant hydrocarbon accumulations.

**3.2. Gas from Cracking of Liquid Hydrocarbons.** The results of simulation experiments indicated that the stability of hydrocarbons is controlled by many factors. Among the intrinsic properties, chemical compositions are the primary ones. In order to elucidate the thermal stability of the liquid hydrocarbons with different compositions, the cracking kinetics of specific compounds were investigated.

**3.2.1. Cracking Kinetic Parameters of Specific Compounds.** The cracking of the alkanes is dominated by the C-C bond. The covalent bond first undergoes a homogeneous reaction under the action of thermal stress or the free radical initiators (such as S and R) to generate free radicals and then triggers the free radical chain reaction [55, 56]. The rate at the free radical initiation reaction (mainly the dissociation reaction of the C-C bond) occurs as a rate step in the free radical chain reaction determining the rate of the alkane cracking reaction. The dissociation energy of C-C bond increases with alkane carbon number decreasing [57]. That is to say, it is more difficult for alkanes with lower carbon number to crack. Actually, there exists linear relationship between the reaction rate constant ( $k$ ) and the carbon number ( $i$ ):  $k_i [s^{-1}] = (2.3i - 15.6) \times 10^{-5}$  [58].

During the cracking process, cycloalkanes might experience side chain cleavage, aromatization, and cyclization of paraffin [59]. Cycloalkanes with side chains might subject to  $\beta$ -cleavage to transform methyl-cycloalkanes and straight chain alkanes when heated. Methyl-cycloalkanes would further undergo the ring splitting or aromatization to form more stably aromatic hydrocarbon. The labile aromatics, such as those with long side chain, would experience side chain cleavage [56]. However, for the relatively stable aromatics, mainly those with short side chain or the polycyclic aromatics, there are two possible pathways for further thermal evolution: transformation to cycloalkanes via hydrogenation or transformation to condensed aromatics via polymerization [60]. Since polycyclic aromatics are more thermally stable than monoaromatics or aromatics with free energy, it is more easily for aromatics to transform to condensed aromatics

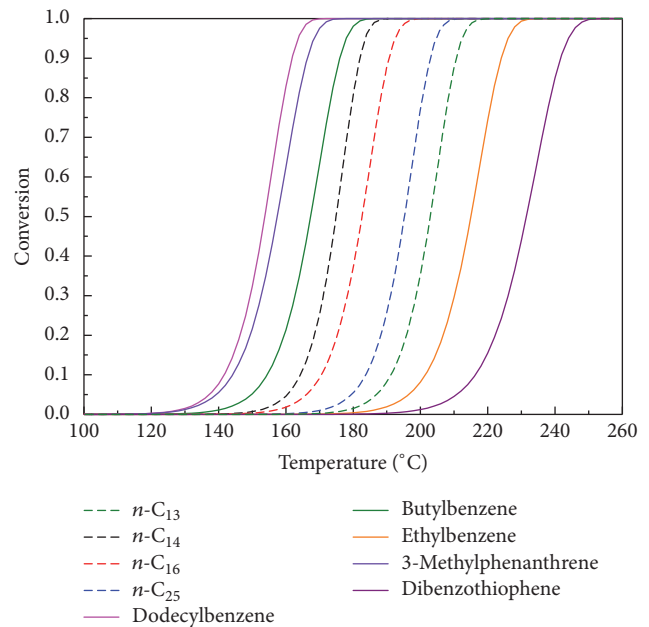


FIGURE 3: Cracking curves of individual compounds under geological heating rate ( $2^{\circ}C/ma$ ).

via polymerization. Polymerization of aromatics (dehydrogenation) is usually accompanied by the pyrolysis of normal alkanes (hydrogenation), which is referred to as disproportionation. These disproportionation reactions could provide hydrogen sources for the hydrocarbon generation, and as a result, the relative proportion of light hydrocarbons and asphaltenes would increase.

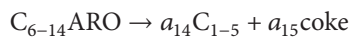
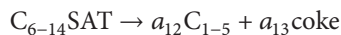
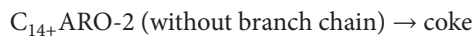
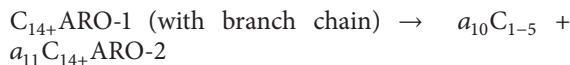
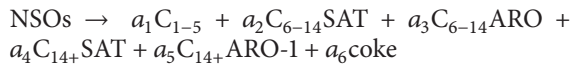
The activation energy and preexponential factor for various compounds during cracking process are different greatly (Table 3). The activation energy and preexponential factor of n-alkane cracking are markedly higher than aromatics. Based on the molecular collision theory, with the same ambient temperature, the effective collision number of n-alkanes is markedly more than aromatics, of course with much higher energy barrier.

The cracking kinetics parameters of individual compounds could be deduced to geological conditions (Figure 3).

It is obvious that the aromatics with no or short side chains have higher thermal stability than alkanes, whereas the aromatics with long side chains are of lower thermal stability. The reason is that the dissociation energy needed for  $\beta$ -cleavage of aromatics with long side chains is generally lower than C-C cleavage of alkanes. Thus, aromatics with long side chains are susceptible to side chain cleavage, transforming to more thermally stable methyl-aromatics and alkanes.

**3.2.2. Cracking Kinetics Parameters of Liquid Hydrocarbons with Different Compositions.** Differences in chemical composition and pyrolysis pathways will inevitably lead to different thermal stability during the liquid hydrocarbon cracking and it also determines the cracking temperature thresholds of hydrocarbons for the different compositions. The thermal stability of light components ( $C_{6-14}$  saturates and aromatics) is obviously higher than that of heavy hydrocarbons ( $C_{14+}$  saturates and aromatics) and heavy components (resin and asphaltenes). Tsuzuki et al. [31] divided the cracking of Sarukawa crude oil into seven components: gaseous hydrocarbons ( $C_{1-5}$ ), light saturates ( $C_{6-14}$  saturates), light aromatics ( $C_{6-14}$  aromatics), heavy saturates ( $C_{15+}$  saturates), heavy concentrated aromatics, heavy nonconcentrated aromatics, and coke fractions

The oil and gas reservoir components can be divided into the following parts according to the difference of chemical compositions and thermal stability: (1) the lowest cracking activation energy of resin and asphaltenes ( $C_{14+}$  NSO compounds) (50~55 kcal/mol); (2) intermediate activation energy of  $C_{14+}$  unstable aromatics (including alkyl side chain aromatic and naphthenic condensed aromatic components) and  $C_{14+}$  polycyclic condensed aromatics and methyl-aromatics; (3) high activation energy (60~70 kcal/mol) of  $C_{14+}$  saturates, light aromatics ( $C_{6-13}$ ), and light saturates ( $C_{6-13}$ ); (4) wet gas ( $C_{2-5}$ ) with high stability (cracking activation energy greater than 70 kcal/mol) and  $CH_4$  [31–33]. Different components have diverse thermal stabilities and cracking reaction paths and the secondary transformation process in the process of cracking. According to the cracking process of six different components, crude oil cracking could be divided into the following [31–33]:



The total amount of crude oil  $c_{(oil)} = \sum x_i c_i = x_1 c_1 + x_2 c_2 + \dots + x_n c_n$ . The total rate of cracking of crude oil  $k_{(oil)} = \sum x_i k_i = x_1 k_1 + x_2 k_2 + \dots + x_n k_n$ ; that is,  $k_i = A_i \exp(-E_{ai}/RT)$ . The kinetic parameters of crude oil cracking are matched with  $A \exp(-E_a/RT) = \sum x_i A_i \exp(-E_{ai}/RT)$ .

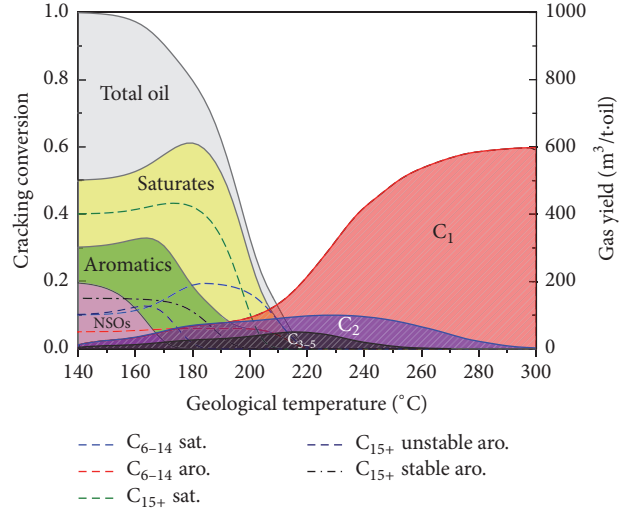


FIGURE 4: Gas generation model of crude oil and its components (heating rate  $2^\circ C/ma$ ).

Among them,  $x_i$ ,  $c_i$ ,  $k_i$ ,  $A_i$ , and  $E_{ai}$  represent the relative content, the absolute amount, the rate constant, the pre-exponential factor, and the activation energy of the cracking reaction of the component, respectively.  $X_i$  ( $i = 1-6$ ) represent  $C_{6-14}$  saturates,  $C_{14+}$  saturates,  $C_{6-14}$  aromatics,  $C_{14+}$  stabilized aromatics (polycyclic aromatics),  $C_{14+}$  unstable aromatics (including long chain), and nonhydrocarbon pitch (NSOs);  $\sum x_i = 1$ .

By geological extrapolation based on the conversion coefficient ( $a_i$ ) and kinetic parameters obtained by previous experimental works [31, 33], a cracking model for crude oil with specific compositions can be established as indicated in Figure 4.

Under the geological conditions (heating rate  $2^\circ C/Ma$ ), resin and asphaltenes began to crack at  $135^\circ C$  and cracked completely at about  $170^\circ C$ . Aromatics began to crack at about  $160^\circ C$  and cracked completely at  $220^\circ C$ . Aromatics started to crack at about  $160^\circ C$  and completely finished at  $220^\circ C$ . The starting cracking temperature of  $C_{15+}$  unstable aromatics was  $160^\circ C$ ,  $C_{15+}$  stable aromatics was over  $170^\circ C$ , and  $C_{6-14}$  aromatics started over  $200^\circ C$ . Saturates were the most stable components, with peak cracking temperature exceeding  $180^\circ C$ , and completely cracked at  $220^\circ C$ . The  $C_{15+}$  saturates started to crack at  $175^\circ C$  and the  $C_{6-14}$  saturates began to crack at  $185^\circ C$ . When the temperature exceeded  $220^\circ C$  wet gas components ( $C_{3-5}$ ) began to crack.

**3.2.3. Amount of Cracked Gas from Liquid Hydrocarbons with Various Compositions.** The gas generation potential of the liquid hydrocarbons is influenced by the H/C atomic ratio and thermal reaction pathways. The highest yield of gaseous hydrocarbon production of per unit waxy oil or light oil could reach 800 ml/g (with mass production of 600 mg/g), obviously higher than normal oil and heavy oils, with high quantities of resins and asphaltenes. The maximum hydrocarbon yield of normal oil and heavy oil is 680 ml/g and 599 ml/g, and the peak mass production is 500 mg/g and 450 mg/g, respectively (Figure 5).

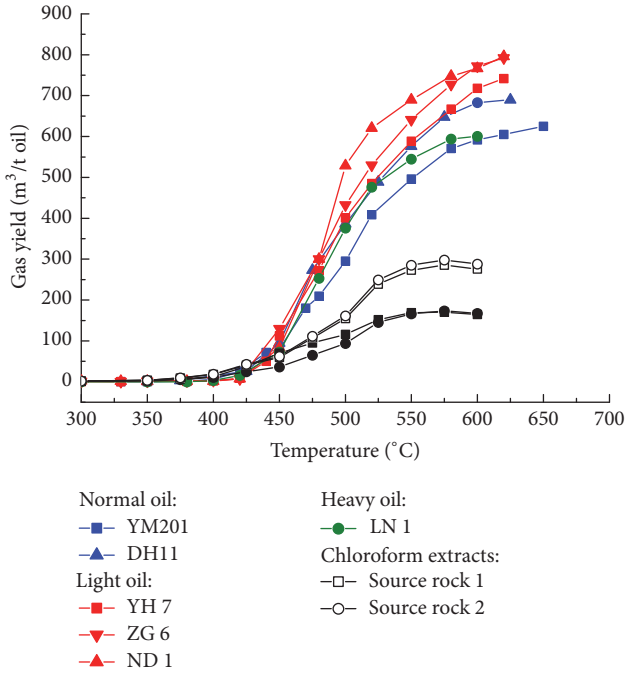


FIGURE 5: The volume production of gaseous hydrocarbons from liquid hydrocarbons with different compositions (heating rate: 20°C/min, 50 MPa).

The maximum gas production has a positive relationship with saturates and negative relationship with heavy components. It is indicated that saturates with high hydrogen percentage (especially paraffin) generally experience C-C bond cracking to form micromolecule hydrocarbon and gaseous hydrocarbons during pyrolysis process. For resins and asphaltenes, gaseous hydrocarbon mainly originated from the cracking of branched chain structure and and finally aromatic ring condensed to form heavy asphaltenes.

The correlation mathematical relationship of gas production of secondary cracking and group compositions could be expressed as follows:

Gas production:

$$M \text{ (mg/g oil)} = 95.2 \times \left[ \frac{\text{saturated fraction}}{\text{aromatic fraction}} \right] - 564.9 \times (\text{polar fraction percentage}) + a \text{ (constant)} \quad (1)$$

Kinetic characterizations of gaseous hydrocarbons are different for liquid residual in source rocks and that of outside sources, which is mainly caused by hydrocarbon expulsion, resulting in a higher proportion of heavy fractions in the residuals hydrocarbons retained in the source rocks. Shale and argillaceous source rocks usually contain clay minerals with catalytic capabilities. Based on the group composition of residual petroleum retained in source rocks and gas production calculation, maximum gas production of residual hydrocarbon in source rocks and crude oil outside source could be obtained, averagely 500 ml/g and 690 ml/g.

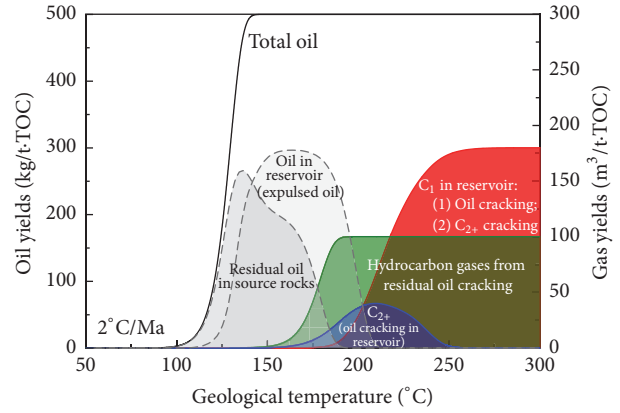


FIGURE 6: Gas generation model for the cracking of residual oil in Type-II source rocks and expelled crude oil in reservoir under geological conditions (heating rate: 2°C/Ma). The conversion of the generation and cracking of oil and gas were obtained by kinetic extrapolation based on their kinetic parameters, wherein the kinetic parameters ( $E_a$  and  $A_f$ ) applied in this model for oil generation were 51.4 kcal/mol and  $8.14E+13 \text{ s}^{-1}$  [9], for oil cracking in reservoir were 59.8 kcal/mol and  $2.13E+13 \text{ s}^{-1}$  [2], and for residual oil cracking in source were 56.1 kcal/mol and  $1.0E+13 \text{ s}^{-1}$  [61].

Previous studies revealed that the average activation energy of the residual oil cracking is 234.1 kJ/mol, which is significantly lower than the liquid hydrocarbon cracking outside sources [2, 3]. This is mainly due to the significantly high levels of residual heavy hydrocarbon components and the possible catalytic effect of clay minerals in the source rocks.

Based on the abroad research results from hydrocarbon generation, evolution, and the trend of overpressure in the sources, a gas general model from the cracking of residual oil (in source) and expelled oil (in reservoir or out of source) derived from Type-II kerogen can be established (Figure 6). If we supposed the maximum oil potential for the Type-II kerogen as 500 mg/g TOC, the amount of the gas generation from the cracking oil or liquid hydrocarbons with different occurrence states can be evaluated. At the stage of oil generation peak (about 135°C), the amounts of the liquid hydrocarbons from in and out the sources account for about 50%, respectively. Due to the fractionation during expulsion, the components of two states of oil may differ a lot. For example, the liquid hydrocarbons trapped inside the sources contain heteroatom compounds of N, O, and S, and the cracked gas production from the liquid hydrocarbons inside the sources is less than those from the liquid hydrocarbons outside the sources.

The liquid hydrocarbons inside the sources began to crack at 135°C, cracked rapidly at 170°C, and terminated at 200°C. However, the cracking of hydrocarbons outside the sources started at 175°C and exhausted at 220°C.

At the early stage of the liquid hydrocarbon cracking, the content of the wet gas is higher. With higher strata temperature, the content of the methane gradually increases, until the content of methane exceeds the wet gas, and then the wet gas starts to crack at 220°C.

### 3.3. Potential and Significance of Secondary Cracking Gas

**3.3.1. Potential of Cracked Gas from Residual Oil in Source Rocks.** Large amount of thermally cracked gas can become an important gas source kitchen for shale gas, which is formed in the mature/overmature stages by dispersed liquid hydrocarbons inside the sources [53, 62]. Before 2000, many experts thought that there is no exploration potential in the area where the source rocks are highly mature to overmature, because the hydrocarbon generation is thought to have been exhausted at those maturities [20]. In fact, there are still a considerable number of liquid hydrocarbons trapped in the source rocks after hydrocarbon source rocks enter the “oil window” stage. Based on the simulation experiment of hydrocarbon generation and expulsion and dynamics analysis of gas generation, Zhao et al. [12, 18] concluded that (1) large amount of liquid hydrocarbons discharged from the source rocks occurred in the stage of “oil window,” with  $R_o$  values range within 0.6%~1.2%, the expulsion efficiency of the source rocks is generally 40%~60%, and the oil shale has the highest hydrocarbon efficiency (80%); (2) kerogen degrades in the early stage of maturity/high maturity, and  $R_o$  value ranges within 1.2%~1.6%, and the gas cracking from the hydrocarbons entrapped in source rocks happen in the stage of high maturity/overmaturity with a  $R_o$  value over 1.6%. The  $R_o$  value of the main gas generation is 1.5%~3.2%. Although the gas generated from the liquid hydrocarbons is later than those degraded from the kerogen, the amount of the gas from the former is 2~4 times more than the gas from the latter. Therefore, the quantity of liquid hydrocarbons trapped in the source rocks can be considerable, and the amount of natural gas formed in the high to overmaturity stage is much larger than the amount of natural gas formed by the degradation of kerogen. Therefore it is a kind of late accumulation natural gas and becomes an effective gas source kitchen.

The black shale in the Silurian Longmaxi Formation in the Sichuan Basin is a high quality source rock with high organic matter abundance and TOC in the lower black shale section is between 3% and 6%, average 3.5%. The maturity of the organic matter is high. The equivalent vitrinite reflectance ( $R_o$ ) is between 2.0% and 4.0%, in the mature stage. In recent years, the black shale which is similar to the Longmaxi Formation has been found in several shale gas fields such as Fuling, Changning, and Weiyuan. The methane and ethane carbon isotopes of the shale gas are significantly reversed [62, 63]. The main reason for this reversal is the mixing of gas cracked from the liquid hydrocarbons in the high mature/overmature stages of the shale and the gas degraded from the kerogen in the early stage [63, 64], which is also supported by widely distributed solid asphaltene in shale [1]. The thermogenic shale gas is a kind of unconventional gas mainly distributing in the organic-rich shale with a thickness greater than 15 m and  $R_o$  value within 1.1%~3.0%. Higher or lower maturity values do not appear to be beneficial to the formation and preservation of cracked gas. So the discovery of the thermogenic shale gas is a strong evidence of the retention of hydrocarbons in situ.

**3.3.2. Contribution of Liquid Hydrocarbons outside Source Rocks to the Gas Accumulations.** The secondary cracking of liquid hydrocarbon was the main source of most marine deep gas fields. Lower Paleozoic marine source rocks of three major Chinese marine basins are all at mature/overmature stages ( $R_o$  value ranges from 2.5% to 3.5%). It is commonly reported that discovery of large gas fields from gas cracked liquid hydrocarbon accumulation (paleo-oil accumulations) under high temperature [52, 53]. Asphaltene is a secondary cracking product from the liquid hydrocarbons, and its abundance could be used as an evidence for oil secondary cracking. Generally, in the high parts of the slope with steep strata angle (the higher area of the paleogeography), liquid hydrocarbons could form large-scale oil accumulations. This kind of paleo-oil reservoirs usually has high content of asphaltene. These accumulated liquid hydrocarbons are mainly controlled by paleostructures. Paleouplift is a favorable area for the liquid hydrocarbons to accumulate. The concentrated liquid hydrocarbon is mainly controlled by paleo-strata temperature. The Paleozoic paleouplifts of the Sichuan Basin are well developed and the paleo-geothermal gradient temperature was high; therefore, the scales of the cracking gas resources from liquid hydrocarbons may be tremendous.

The dispersed liquid hydrocarbons outside the sources also contribute to the formation of the conventional gas accumulations. The tectonic patterns of the Sichuan and Tarim basins in China are mostly in the form of “big uplift and big depression.” The distribution of oil and gas is mainly controlled by these large paleouplifts and relatively stable large-scale paleoslopes. Based on the accumulation of the liquid hydrocarbons, the paleo-terrain slope of the reservoirs is an important controlling factor for the enrichment degree and the pattern of the liquid hydrocarbons. In the slope area with low strata angle, the differentiation action of the liquid hydrocarbons is small.

In previous studies [4, 54], “five-step-method” has been used to calculate the gas potential of the Sichuan Basin. The liquid hydrocarbons retained in source rocks, dispersed along migration pathways, and accumulated in paleostructures were cracked into gas of 886, 588, and 298 trillion cubic meters, respectively. Based on the factors such as tectonic movement, accumulation and preservation conditions in the main gas generation period and the later period, the amount of effective resources is 0.89, 1.76, and 1.49 trillion cubic meters, respectively. The contribution ratio of the three categories oil to gas resource is 21%, 43%, and 36%, respectively. Therefore the liquid hydrocarbons can be cracked and formed large gas accumulations in the late stage, contributing to the deep gas resources.

Because of the contribution of the aggregated paleo-oil reservoirs and dispersed liquid hydrocarbons, the largest single gas field in the Sinian and Cambrian old formations of the Gaoshiti-Moxi area has been formed in the Sichuan Basin, which has been explored for nearly 100 years [52, 53]. The proven natural gas reserves in the Longwangmiao Formation of the Moxi area reach  $440.38 \times 10^9 \text{ m}^3$ , and controlled reserves in the fourth section of the Sinian Dengying

Formation amount to  $204.29 \times 10^9 \text{ m}^3$ , illustrating great potentials for deep gas exploration.

The production evidence declare that the high source rock maturity would not retain or maintain gas contents in reservoir, although at some locations %Ro values greater than 3% to 3.5%Ro are found in both China and North America. It is uncertain whether this is due to loss of containment of the gas or chemical alteration. This is a risk factor for commercial shale gas exploration and needs further studies.

#### 4. Conclusions

There are three categories of petroleum occurrence, that is, residues in the source rocks, retained along migration pathways and trapped in paleoreservoirs. All of them are important sources for deep gas accumulations. At the peak stage of oil generation, the amount of hydrocarbons retained in the source rock is about 50%.

The pyrolysis kinetic parameters of different types of liquid hydrocarbons differ greatly, depending mainly on their compositions. Saturates are the most stable components, requiring high pyrolysis activation energy and high pyrolysis temperature, while the pyrolysis of bitumen only needs low temperature and the activation energy is low. At mature to overmature stages, the required cracking temperature of residual petroleum in source rocks is lower than that of the migrated-out hydrocarbons. The cracked gas generations yield from the residual petroleum in source rocks generally lower that of the migrated-out hydrocarbons.

The cracking of deeply buried liquid hydrocarbons becomes an important source to different types of gas accumulations. The cracking of residual petroleum in source rocks not only becomes the sole source for shale gas but also contributes to the conventional deep natural gas accumulations when expelled. The dispersed liquid hydrocarbons along migration pathways or elsewhere can also be cracked to form natural gas under high temperature and accumulated under suitable geological conditions. The paleo-oil accumulations become the main source for conventional gas accumulations after cracking. The trapped paleo-oil reservoir and the dispersed liquid hydrocarbons along migration pathways can jointly form giant deep natural gas accumulations.

#### Conflicts of Interest

The authors declare that there are no conflicts of interest regarding the publication of this paper.

#### References

- [1] J. Dai, C. Zou, S. Liao et al., "Geochemistry of the extremely high thermal maturity Longmaxi shale gas, southern Sichuan Basin," *Organic Geochemistry*, vol. 74, pp. 3–12, 2014.
- [2] K. He, S. C. Zhang, X. M. Wang, and J. K. Mi, "Research on the kinetics and controlling factor for oil cracking," *Natural Gas Geoscience*, vol. 22, pp. 211–218, 2011.
- [3] S. C. Zhang, G. Y. Hu, J. K. Mi et al., "Time-limit and yield of natural gas generation from different origins and their effect on forecast of deep oil and gas resources," *Acta Petrolei Sinica*, vol. 34, no. S1, pp. 41–50, 2013.
- [4] W. Zhao, S. Hu, W. Liu, T. Wang, and H. Jiang, "The multi-staged "golden zones" of hydrocarbon exploration in superimposed petroliferous basins of onshore China and its significance," *Petroleum Exploration and Development*, vol. 42, no. 1, pp. 1–12, 2015.
- [5] W. Zhao, Z. Wang, D. Wang, J. Li, Y. Li, and G. Hu, "Contribution and significance of dispersed liquid hydrocarbons to reservoir formation," *Petroleum Exploration and Development*, vol. 42, no. 4, pp. 439–453, 2015.
- [6] A. S. Pepper and T. A. Dodd, "Simple kinetic models of petroleum formation. Part II: oil-gas cracking," *Marine and Petroleum Geology*, vol. 12, no. 3, pp. 321–340, 1995.
- [7] H. J. Schenk, R. Di Primio, and B. Horsfield, "The conversion of oil into gas in petroleum reservoirs. Part I: Comparative kinetic investigation of gas generation from crude oils of lacustrine, marine and fluviodeltaic origin by programmed-temperature closed-system pyrolysis," *Organic Geochemistry*, vol. 26, no. 7–8, pp. 467–481, 1997.
- [8] G. P. Cooles, A. S. Mackenzie, and T. M. Quigley, "Calculation of petroleum masses generated and expelled from source rocks," *Organic Geochemistry*, vol. 10, no. 1–3, pp. 235–245, 1986.
- [9] A. S. Pepper and P. J. Corvi, "Simple kinetic models of petroleum formation. Part I: oil and gas generation from kerogen," *Marine and Petroleum Geology*, vol. 12, no. 3, pp. 291–319, 1995.
- [10] D. Leythaeuser, M. Radke, and R. G. Schaefer, "Efficiency of petroleum expulsion from shale source rocks," *Nature*, vol. 311, no. 5988, pp. 745–748, 1984.
- [11] U. Ritter, "Solubility of petroleum compounds in kerogen: Implications for petroleum expulsion," *Organic Geochemistry*, vol. 34, no. 3, pp. 319–326, 2003.
- [12] Z. W. Zhao, Y. Z. Wang, and C. S. Zhang, "Successive generation of natural gas from organic materials and its significance in future exploration," *Petroleum Exploration and Development*, vol. 32, no. 2, pp. 1–7, 2005.
- [13] D. Ertas, S. R. Kelemen, and T. C. Halsey, "Petroleum expulsion part 1. Theory of kerogen swelling in multicomponent solvents," *Energy and Fuels*, vol. 20, no. 1, pp. 295–300, 2006.
- [14] S. R. Kelemen, C. C. Walters, D. Ertas, H. Freund, and D. J. Curry, "Petroleum expulsion part 3. A model of chemically driven fractionation during expulsion of petroleum from kerogen," *Energy and Fuels*, vol. 20, no. 1, pp. 309–319, 2006.
- [15] H. Freund, C. C. Walters, S. R. Kelemen et al., "Predicting oil and gas compositional yields via chemical structure-chemical yield modeling (CS-CYM): Part 1 - Concepts and implementation," *Organic Geochemistry*, vol. 38, no. 2, pp. 288–305, 2007.
- [16] D. M. Jarvie, R. J. Hill, T. E. Ruble, and R. M. Pollastro, "Unconventional shale-gas systems: the Mississippian Barnett Shale of north-central Texas as one model for thermogenic shale-gas assessment," *AAPG Bulletin*, vol. 91, no. 4, pp. 475–499, 2007.
- [17] J. G. Stainforth, "Practical kinetic modeling of petroleum generation and expulsion," *Marine and Petroleum Geology*, vol. 26, no. 4, pp. 552–572, 2009.
- [18] W. Zhao, Z. Wang, H. Wang, Y. Li, G. Hu, and C. Zhao, "Further discussion on the connotation and significance of the natural gas relaying generation model from organic matter," *Petroleum Exploration and Development*, vol. 38, no. 2, pp. 129–135, 2011.
- [19] C. C. Walters, H. Freund, S. R. Kelemen, P. Peczak, and D. J. Curry, "Predicting oil and gas compositional yields via

- chemical structure-chemical yield modeling (CS-CYM): Part 2 - Application under laboratory and geologic conditions," *Organic Geochemistry*, vol. 38, no. 2, pp. 306–322, 2007.
- [20] K. A. Kvenvolden, "Petroleum geochemistry and geology," *Organic Geochemistry*, vol. 24, no. 1, pp. 109–110, 1996.
- [21] D. W. Waples, "The kinetics of in-reservoir oil destruction and gas formation: Constraints from experimental and empirical data, and from thermodynamics," *Organic Geochemistry*, vol. 31, no. 6, pp. 553–575, 2000.
- [22] A. K. Burnham and R. L. Braun, "Development of a detailed model of petroleum formation, destruction, and expulsion from lacustrine and marine source rocks," *Organic Geochemistry*, vol. 16, no. 1–3, pp. 27–39, 1990.
- [23] B. Horsfield, H. J. Schenk, N. Mills, and D. H. Welte, "An investigation of the in-reservoir conversion of oil to gas: compositional and kinetic findings from closed-system programmed-temperature pyrolysis," *Organic Geochemistry*, vol. 19, no. 1–3, pp. 191–204, 1992.
- [24] R. I. McNeil, "Thermal stability of hydrocarbons: Laboratory criteria and field examples," *Energy & Fuels*, vol. 10, no. 2, pp. 60–67, 1996.
- [25] F. Dominé, D. Dessort, and O. Brévar, "Towards a new method of geochemical kinetic modelling: Implications for the stability of crude oils," *Organic Geochemistry*, vol. 28, no. 9–10, pp. 597–612, 1998.
- [26] V. Dieckmann, H. J. Schenk, B. Horsfield, and D. H. Welte, "Kinetics of petroleum generation and cracking by programmed-temperature closed-system pyrolysis of Toarcian Shales," *Fuel*, vol. 77, no. 1–2, pp. 23–31, 1998.
- [27] R. J. Hill, Y. Tang, and I. R. Kaplan, "Insights into oil cracking based on laboratory experiments," *Organic Geochemistry*, vol. 34, no. 12, pp. 1651–1672, 2003.
- [28] W. Zhao, Z. Wang, S. Zhang, H. Wang, and Y. Wang, "Oil cracking: An important way for highly efficient generation of gas from marine source rock kitchen," *Chinese Science Bulletin*, vol. 50, no. 22, pp. 2628–2635, 2005.
- [29] H. Tian, X. Xiao, L. Yang et al., "Pyrolysis of oil at high temperatures: Gas potentials, chemical and carbon isotopic signatures," *Chinese Science Bulletin*, vol. 54, no. 7, pp. 1217–1224, 2009.
- [30] V. Dieckmann, P. G. Caccialanza, and R. Galimberti, "Evaluating the timing of oil expulsion: About the inverse behaviour of light hydrocarbons and oil asphaltene kinetics," *Organic Geochemistry*, vol. 33, no. 12, pp. 1501–1513, 2002.
- [31] N. Tsuzuki, N. Takeda, M. Suzuki, and K. Yokoi, "The kinetic modeling of oil cracking by hydrothermal pyrolysis experiments," *International Journal of Coal Geology*, vol. 39, no. 1–3, pp. 227–250, 1999.
- [32] M. Vandenbroucke, F. Behar, and J. L. Rudkiewicz, "Kinetic modelling of petroleum formation and cracking: Implications from the high pressure/high temperature Elgin Field (UK, North Sea)," *Organic Geochemistry*, vol. 30, no. 9, pp. 1105–1125, 1999.
- [33] F. Behar, F. Lorant, and L. Mazeas, "Elaboration of a new compositional kinetic schema for oil cracking," *Organic Geochemistry*, vol. 39, no. 6, pp. 764–782, 2008.
- [34] F. Behar, S. Roy, and D. Jarvie, "Artificial maturation of a Type I kerogen in closed system: Mass balance and kinetic modelling," *Organic Geochemistry*, vol. 41, no. 11, pp. 1235–1247, 2010.
- [35] M. Bordenave, *Applied Petroleum Geochemistry*, Technip, Paris, 1993.
- [36] F. R. Zhu, Y. L. Zhang, and Y. Li, "Quantitative evaluation residual liquid hydrocarbons in shale," *Acta Petrolei Sinica*, vol. 36, no. 1, pp. 13–18, 2015.
- [37] B. Zhang, J. Hu, and J. Yang, "Controlling effect of source rocks on the occurrence of tight oil – taking the Da'anzhai reservoir of Sichuan Basin as an example," *Bulletin of Mineralogy, Petrology and Geochemistry*, vol. 34, no. 1, pp. 45–54, 2015.
- [38] X. Guo, S. He, K. Liu, G. Song, X. Wang, and Z. Shi, "Oil generation as the dominant overpressure mechanism in the Cenozoic Dongying depression, Bohai Bay Basin, China," *AAPG Bulletin*, vol. 94, no. 12, pp. 1859–1881, 2010.
- [39] X. Guo, S. He, K. Liu, and L. Zheng, "Quantitative estimation of overpressure caused by oil generation in petroliferous basins," *Organic Geochemistry*, vol. 42, no. 11, pp. 1343–1350, 2011.
- [40] X. W. Guo, K. Y. Liu, S. He, Z. Yang, and T. T. Dong, "Quantitative estimation of overpressure caused by gas generation and application to the Baiyun Depression in the Pearl River Mouth Basin, South China Sea," *Geofluids*, vol. 16, no. 1, pp. 129–148, 2016.
- [41] C. Song, W.-C. Lai, and H. H. Schobert, "Condensed-phase pyrolysis of n-tetradecane at elevated pressures for long duration. Product distribution and reaction mechanisms," *Industrial & Engineering Chemistry Research*, vol. 33, no. 3, pp. 534–547, 1994.
- [42] T. J. Ford, "Liquid-phase thermal decomposition of hexadecane: Reaction mechanisms," *Industrial and Engineering Chemistry Fundamentals*, vol. 25, no. 2, pp. 240–243, 1986.
- [43] K. J. Jacksón, A. K. Burnham, R. L. Braun, and K. G. Knauss, "Temperature and pressure dependence of n-hexadecane cracking," *Organic Geochemistry*, vol. 23, no. 10, pp. 941–953, 1995.
- [44] F. Behar and M. Vandenbroucke, "Experimental determination of the rate constants of the n-C25 thermal cracking at 120, 400, and 800 bar: Implications for high-pressure/high-temperature prospects," *Energy and Fuels*, vol. 10, no. 4, pp. 932–940, 1996.
- [45] J. Yu and S. Eser, "Thermal decomposition of jet fuel model compounds under near-critical and supercritical conditions. 2. Decalin and tetralin," *Industrial and Engineering Chemistry Research*, vol. 37, no. 12, pp. 4601–4608, 1998.
- [46] F. Behar, F. Lorant, H. Budzinski, and E. Desavis, "Thermal stability of alkylaromatics in natural systems: Kinetics of thermal decomposition of dodecylbenzene," *Energy and Fuels*, vol. 16, no. 4, pp. 831–841, 2002.
- [47] P. E. Savage and M. T. Klein, "Asphaltene reaction pathways. 2. Pyrolysis of n-pentadecylbenzene," *Industrial and Engineering Chemistry Research*, vol. 26, no. 3, pp. 488–494, 1987.
- [48] H. Freund and W. N. Olmstead, "Detailed chemical kinetic modeling of butylbenzene pyrolysis," *International Journal of Chemical Kinetics*, vol. 21, no. 7, pp. 561–574, 1989.
- [49] S. B. Domke, R. F. Pogue, F. J. R. Van Neer, and C. M. Smith, "Investigation of the kinetics of ethylbenzene pyrolysis using a temperature-scanning reactor," *Industrial and Engineering Chemistry Research*, vol. 40, no. 25, pp. 5878–5884, 2001.
- [50] F. Behar, H. Budzinski, M. Vandenbroucke, and Y. Tang, "Methane generation from oil cracking: Kinetics of 9-methylphenanthrene cracking and comparison with other pure compounds and oil fractions," *Energy and Fuels*, vol. 13, no. 2, pp. 471–481, 1999.
- [51] C. Dartiguelongue, F. Behar, H. Budzinski, G. Scacchi, and P. M. Marquaire, "Thermal stability of dibenzothiophene in closed system pyrolysis: Experimental study and kinetic modelling," *Organic Geochemistry*, vol. 37, no. 1, pp. 98–116, 2006.

- [52] J. Du, C. Zou, C. Xu et al., "Theoretical and technical innovations in strategic discovery of a giant gas field in Cambrian Longwangmiao Formation of central Sichuan paleo-uplift, Sichuan Basin," *Shiyou Kantan Yu Kaifa/Petroleum Exploration and Development*, vol. 41, no. 3, pp. 268–277, 2014.
- [53] C. Zou, J. Du, C. Xu et al., "Formation, distribution, resource potential and discovery of the sinian-cambrian giant gas field, sichuan basin, SW China," *Petroleum Exploration and Development*, vol. 41, no. 3, pp. 278–293, 2014.
- [54] Y. Z. Wang, Z. W. Zhao, and L. D. Wang, "Quantitative assessment of pyrolysis gas generated by dispersed liquid hydrocarbon," *Acta Geologica Sinica*, vol. 90, no. 1, pp. 68–79, 2016.
- [55] Y. V. Kissin, "Catagenesis and composition of petroleum: Origin of n-alkanes and isoalkanes in petroleum crudes," *Geochimica et Cosmochimica Acta*, vol. 51, no. 9, pp. 2445–2457, 1987.
- [56] M. L. Poutsma, "Fundamental reactions of free radicals relevant to pyrolysis reactions," *Journal of Analytical and Applied Pyrolysis*, vol. 54, no. 1, pp. 5–35, 2000.
- [57] Y. Tang, J. K. Perry, P. D. Jenden, and M. Schoell, "Mathematical modeling of stable carbon isotope ratios in natural gases," *Geochimica et Cosmochimica Acta*, vol. 64, no. 15, pp. 2673–2687, 2000.
- [58] H. H. Voge and G. M. Good, "Thermal cracking of higher paraffins," *Journal of the American Chemical Society*, vol. 71, no. 2, pp. 593–597, 1949.
- [59] P. Castaño, J. M. Arandes, M. Olazar, J. Bilbao, B. Pawelec, and U. Sedrán, "Effect of hydrogen on the cracking mechanisms of cycloalkanes over zeolites," *Catalysis Today*, vol. 150, no. 3-4, pp. 363–367, 2010.
- [60] L. Fusetti, F. Behar, R. Bounaceur, P.-M. Marquaire, K. Grice, and S. Derenne, "New insights into secondary gas generation from the thermal cracking of oil: Methylated monoaromatics. A kinetic approach using 1,2,4-trimethylbenzene. Part I: A mechanistic kinetic model," *Organic Geochemistry*, vol. 41, no. 2, pp. 146–167, 2010.
- [61] K. He, S. Zhang, X. Wang, J. Mi, R. Mao, and G. Hu, "Effect of gas generation from in-situ cracking of residual bitumen in source on hydrocarbon generation from organic matter," *Shiyou Xuebao/Acta Petrolei Sinica*, vol. 34, no. 1, pp. 57–64, 2013.
- [62] R. Yang, S. He, Q. Hu, D. Hu, and J. Yi, "Geochemical characteristics and origin of natural gas from Wufeng-Longmaxi shales of the Fuling gas field, Sichuan Basin (China)," *International Journal of Coal Geology*, vol. 171, pp. 1–11, 2017.
- [63] S. Zhang, K. He, G. Hu et al., "Unique chemical and isotopic characteristics and origins of natural gases in the Paleozoic marine formations in the Sichuan Basin, SW China: Isotope fractionation of deep and high mature carbonate reservoir gases," *Marine and Petroleum Geology*, 2016.
- [64] X. Xia, J. Chen, R. Braun, and Y. Tang, "Isotopic reversals with respect to maturity trends due to mixing of primary and secondary products in source rocks," *Chemical Geology*, vol. 339, pp. 205–212, 2013.

## Research Article

# The Early Cambrian Mianyang-Changning Intracratonic Sag and Its Control on Petroleum Accumulation in the Sichuan Basin, China

Shugen Liu,<sup>1</sup> Bin Deng,<sup>1</sup> Luba Jansa,<sup>2</sup> Yong Zhong,<sup>3</sup> Wei Sun,<sup>1</sup> Jinmin Song,<sup>1</sup> Guozhi Wang,<sup>1</sup> Juan Wu,<sup>1</sup> Zhiwu Li,<sup>1</sup> and Yanhong Tian<sup>1</sup>

<sup>1</sup>State Key Laboratory of Oil and Gas Reservoir Geology and Exploitation, Chengdu University of Technology, Chengdu 610059, China

<sup>2</sup>Geological Survey of Canada-Atlantic, Dartmouth, NS, Canada

<sup>3</sup>Sichuan Geophysical Company of CNPC Chuanqing Drilling Engineering Company Limited, Chengdu 610213, China

Correspondence should be addressed to Shugen Liu; [lsg@cduet.edu.cn](mailto:lsg@cduet.edu.cn) and Bin Deng; [dengbin3000@163.com](mailto:dengbin3000@163.com)

Received 2 March 2017; Accepted 1 June 2017; Published 16 August 2017

Academic Editor: Xiaorong Luo

Copyright © 2017 Shugen Liu et al. This is an open access article distributed under the Creative Commons Attribution License, which permits unrestricted use, distribution, and reproduction in any medium, provided the original work is properly cited.

The older and deeper hydrocarbon accumulations receive increasing attention across the world, providing more technical and commercial challenges to hydrocarbon exploration. We present a study of an asymmetrical, N-S striking intracratonic sag which developed across the Sichuan basin, south China, from Late Ediacaran to Early Cambrian times. The Mianyang-Changning intracratonic sag is ~50 km wide, with its steepest part in the basin center. In particular the eastern margin shows its greatest steepness. Five episodes in the evolutions of the sag can be recognized. It begins in the Late Ediacaran with an uplift and erosion correlated to Tongwan movement. Initial extension occurred during the Early Cambrian Maidiping period, when more strata of the Maidiping Formation were deposited across the sag. Subsequently, maximum extension occurred during the Early Cambrian Qiongzhusi period that resulted in 450–1700 m thick Maidiping-Canglangpu Formations being deposited in the sag. Then, the sag disappeared at the Longwangmiao period, as it was infilled by the sediments. The intracratonic sag has significant influence on the development of high-quality reservoirs in the Dengying and Longwangmiao Formations and source-rock of the Niutitang Formation. It thus indicates that a high probability for oil/gas accumulation exists along the intracratonic sag, across the central Sichuan basin.

## 1. Introduction

Continental rift basins are widespread extensional structures on the Earth's surface and are known from the Archean up to the present. They account for ~30% of global hydrocarbon discoveries [1]. In particular, the Neoproterozoic assembly and break-up of two supercontinents, that is, Rodinia and Greater Gondwana, were marked by the development of a long series of rift valleys, half-graben, pull-apart basins, and intramontane molasse basins, along the Peri-Gondwanan Margin, from Australia through Pakistan, Oman and North Africa, and South China block (Figure 1(a)) [2, 3]. A series of studies was undertaken to unravel the generation and accumulation of hydrocarbons in this unique geological time [4–7]. The area which was particularly intensively studied is

the South Oman Salt Basin [8, 9]. In most of these areas, the Neoproterozoic-Early Cambrian organic-rich strata are widespread, forming the Neoproterozoic-Early Cambrian (“Infra-Cambrian” [10]) hydrocarbon plays. The occurrence of prolific source-rocks was controlled by strong postglacial sea-level rise, following the major Neoproterozoic glaciations [2]. Furthermore, deposits of evaporites and black shale are widespread in rift-related basins, providing effective seal and source-rock across from Oman, Pakistan, and India to South China [3, 11]. This generated an interest in exploring for the Infra-Cambrian plays along the Peri-Gondwanan Margin. Despite the existence of proven Infra-Cambrian hydrocarbon plays in many parts of the world, the petroleum prospective is associated with much higher exploration risks than in conventional Phanerozoic petroleum systems, as the strata

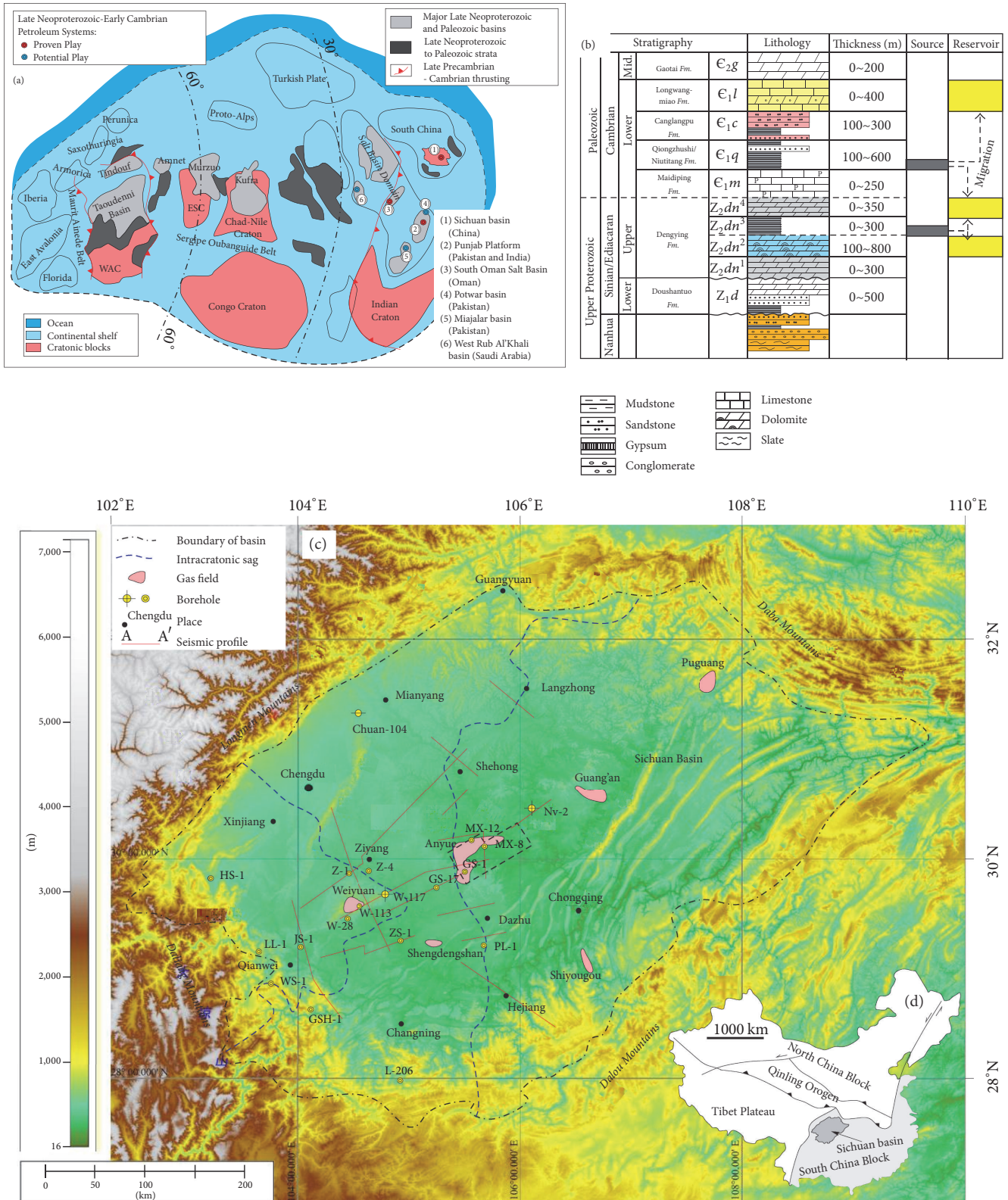


FIGURE 1: (a) Generalized Late Neoproterozoic-Early Cambrian palaeogeography of the “Peri-Gondwanan Margin” and its petroleum system (modified from Craig et al. [2]). (b) Late Neoproterozoic-Middle Cambrian Stratigraphic column for the South China block. (c) The Digital Elevation Map (DEM) showing the topography and intracratonic sag in the Sichuan basin, the red lines indicating 2D seismic profiles to unravel the sag structure, and the black dotted line showing 3D seismic data of the Gaoshiti-Moxi area. (d) Insert: map of the basic tectonic framework of China.

are usually much more deeply buried and relatively poorly known.

The Sichuan basin located in the South China continental block has generated interest for brine/natural gas exploration since the ~1100 AD [12] and is one of the largest sedimentary basins rich in petroleum resources in China (Figure 1). It is noteworthy to mention that workers in the old salt industry have used bamboo casing and piping to drill for gas near Zigong, in the southern Sichuan basin. This idea inspired the first significant gas pools discovery in the Shiyougou and Shengdengshan structures in the 1930s, followed later by a series of oil/gas discoveries in the Sichuan basin (Figure 1), for example, Well Nv-2 in 1958 and the Ediacaran Weiyuan gas fields in 1964 (with a proven in-place gas volume of  $408.6 \times 10^8 \text{ m}^3$  (1.5 tcf), etc.) [13–15]. In particular, recent major discoveries are genetically related to Neoproterozoic–Paleozoic extensional tectonics across the basin, for example, Puguang gas field with a proven in-place gas volume of  $3500 \times 10^8 \text{ m}^3$  (12.4 tcf) [16] and the Anyue gas field with a volume of  $4403.8 \times 10^8 \text{ m}^3$  (15.6 tcf) [17]. The later Ediacaran–Cambrian carbonate gas field is also the biggest gas field presently in China. Based on seismic data, structural features, hydrocarbon condition, and so on, we reconstruct the Early Cambrian extensional structure, that is, the Mianyang–Changning intracratonic sag located in the basin center, and discuss its influence on petroleum accumulation. It may stimulate further exploration in these hydrocarbon rich provinces.

## 2. Geological Setting

The Sichuan basin is located at the western margin of the South China block, which is comprised of the Yangtze platform in the northwest and the Cathaysian Block in the southeast (Figure 1). To the north, it is separated from the North China block by the Late Paleozoic to Middle Mesozoic Qinling Orogen [19], and to the west from the Mesozoic–Cenozoic Eastern Tibetan Plateau by the Longmen–Daliang thrust fold belt [20, 21]. Within the South China block, the Sichuan basin is separated from a 1300-km wide Mesozoic intracontinental orogenic belt by the Qiyueshan–Daloushan structure [22, 23]. Thus, the Sichuan basin is a superimposed basin influenced by its peripheral orogens and dominated by four stages of basin evolution: (a) a rift at the cratonic margin in the Neoproterozoic, (b) a marine carbonate platform from the Early Cambrian to Middle Triassic, (c) a foreland basin from Late Triassic to Late Cretaceous, and (d) subsequent exhumation and structural modification. The sedimentary cover is comprised mainly of Paleozoic and Middle Mesozoic strata of shallow-marine deposits, and post-Late Triassic terrestrial strata, of a total thickness ~8 km to 12 km.

The South China block is generally considered being a part of the Precambrian Rodinia supercontinent [24–26]. Along its western and northern margins, the Proterozoic basement of the craton, that is, the Kongling complex or Banxi group, is characterized by the presence of migmatitic granites and gneiss, a metamorphosed greywacke-slate succession, unconformably overlain by the Sinian/Ediacaran sedimentary rocks. The Sinian/Ediacaran Doushantuo and Dengying formations deposited during a major marine

transgression are predominantly comprised of shallow water dolomitic carbonates. Due to the Tongwan tectonic movement, Sinian (Ediacaran) dolomites were exposed to fresh-water karstification, resulting in widespread development of caverns and dissolution porosity in the upper of Dengying Formation and at unconformities (Figure 1(b)) [27, 28]. That becomes a favorable niche for petroleum accumulation in the Proterozoic Dengying Formation, as demonstrated by the Weiyuan gas field with proven gas reserves of  $408.61 \times 10^8 \text{ m}^3$  (1.5 tcf) [29]. Furthermore, the major extensional movements in the Sichuan basin were the Xinkai taphrogenesis or “extensional movement,” which is coeval with assembly and breakup of the Rodinia supercontinent [30–33]. It resulted in the formation of deep extensional faults representing favorable conduits for thermal fluids migration from the deep basin. The evidence is widespread dissolution, precipitation of silica, occurrence of zebra structures, and saddle dolomite in the Late Proterozoic strata, improving the reservoir quality of the Dengying Formation, which widely host the lead-zinc deposits of MVT type and barite-fluorite and hydrothermal chert along the western margin of the South China block [34–36]. The Early Cambrian strata paraconformably overlie the Sinian (Ediacaran) rocks. In particular, the Qiongzhusi Formation (or Niutitang Formation) is one of the most important source-rocks (dominated by Type I-kerogen) in the basin, which generated hydrocarbons found in the Upper Sinian and Early Cambrian formations reservoirs [37–39]. Recently, another giant gas field has been discovered in coarsely crystalline dolomite facies, in the Cambrian Longwangmiao Formation, with proven gas reserves of  $4403.8 \times 10^8 \text{ m}^3$  (16.2 tcf).

During Mesozoic to Cenozoic times, the area was affected by several phases of tectonic movements, including the Caledonian movement and Indosinian and Yanshannian movements [40, 41]. This resulted in most of the upper Silurian, Devonian, and Carboniferous strata being absent across the South China block, in the development of several regional unconformities and an E-W trending Leshan–Longnvshi paleouplift in the Sichuan basin center. These structures significantly influenced the formation of the carbonate reservoirs and hydrocarbon accumulations across the Sichuan basin and its periphery [7, 29, 38]. Furthermore, those multi-phase tectonic movements gave rise to a complicated tectonic evolution and sedimentary history of the basin [42, 43].

## 3. The Early Cambrian Mianyang–Changning Intracratonic Sag

*3.1. Precambrian Extensional Faults across the Sichuan Basin.* Stratigraphic horizons were mapped in the Gaoshiti–Moxi area, located in the center of the Sichuan basin, using the three-dimensional seismic data and well control (Figure 1(c)). We observed that extensional faults are extremely common in most of the Precambrian strata (Figure 2) (see Supplementary Material, available online at <https://doi.org/10.1155/2017/6740892>). There are at least two extensional faults present with an opposite dip, indicating a rift. The continuity of reflectors indicates presence of syn-rift deposits. Furthermore, an offset of extensional faults is well imaged in the

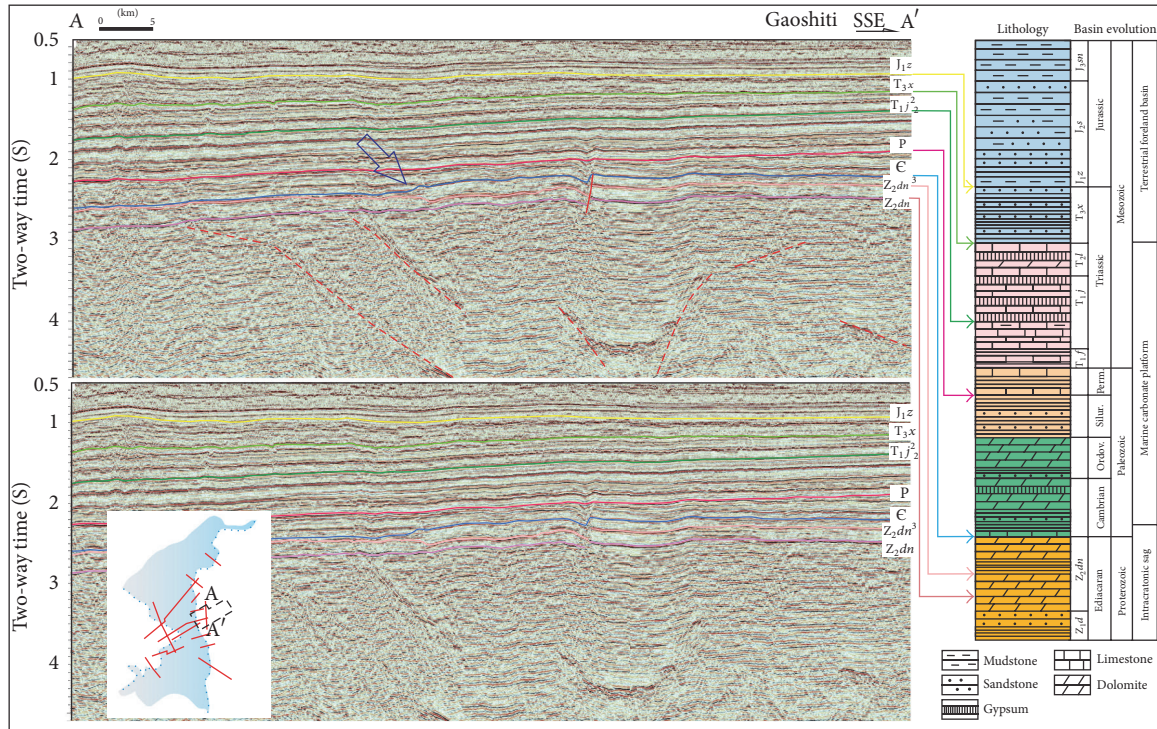


FIGURE 2: 3D seismic profile indicating Precambrian extensional structure in the center of the Sichuan basin (please find the original data in Supplementary Material). The red dotted line and blue arrow show the pre-Sinian extensional faults and eastern boundary of extensional structure; the inset box shows the location ( $J_1z$ : base of Lower Jurassic Zhiliujing Formation,  $T_{3x}$ : base of Upper Triassic Xujiache Formation,  $T_{1j}^2$ : base of the second member of Lower Triassic Jialingjiang Formation, P: base of Permian, E: base of Cambrian,  $Z_{2dn}^3$ : base of the third member of Sinian Dengying Formation).

seismic data. This structural model was used as the basis for our 2D and 3D interpretation across the Sichuan basin. The density of seismic profiles is 5–30 km across most of the basin. The data shows that there are many extensional faults and related structures in the Precambrian strata, across the Sichuan basin. Most of these structures have NE-strike; some of extensional structures further show the influence of the deformation of the overlain strata. In particular, some of the strata overlying the extensional structures (i.e., Upper Sinian Dengying and Lower Cambrian sequences) are characterized by distinctly increased thickness (Figure 2).

### 3.2. Boundary of the Mianyang-Changning Intracratonic Sag.

As borehole data for pre-Sinian strata are lacking, therefore there is much of uncertainty about the rifts. However, based on regional geology studies [30–33], we argue that such extensional tectonics extended across the Ediacaran (Sinian) to Early Cambrian periods. Occurrence of extensional tectonics is supported by the borehole data of the Sinian strata and related seismic data, which indicate presence of Early Cambrian extensional structures across the Sichuan basin. The borehole data indicates that there is distinct increased thickness of the Early Cambrian Qiongzhusi Fm in the GS-17 and Z-4 wells, located at the hanging walls of the extensional faults mentioned above, in comparison with W-28 and GS-1 wells located at the footwalls. In particular, there is an additional strata, the Maidiping Fm, in the center of the

extensional structure, compared to other places (Table 1, Figure 3). Thus, we argue that there is an extensional structure across the center of Sichuan basin, named the Mianyang-Changning intracratonic sag. We use the term “intracratonic sag” according to P. A. Allen and J. R. Allen [44], as it is difficult to identify how large the offset of extensional faults was during the Early Cambrian periods.

Most of the seismic profiles across the Mianyang-Changning intracratonic sag show significant changes in the thickness of Early Cambrian strata; those strata westwards and eastwards onlap onto the Sinian strata, with decreasing thickness from the center of the sag to its sides. It should be noted that the underlain Late Sinian strata show decreasing thickness towards the boundary of the sag. The continuity of reflection horizons suggests asymmetric geometry of the Mianyang-Changning intracratonic sag, with a steep boundary at the eastern margin, where the discontinuous reflections indicate that it probably accommodated some extensional faults to result in a dustpan-like geometry.

From north to south, the seismic data shows an increasing steepness along the eastern margin of the sag, for example, from the Langzhong to the Shehong sections (Figure 4 D-D' section), where the orientation of eastern margin changes from NE-striking to NS-striking in the Shehong area. At the center of the Sichuan basin the increased thickness of Early Cambrian strata is consistent with overlain extensional faults in pre-Cambrian strata in the Gaoshiti-Moxi area

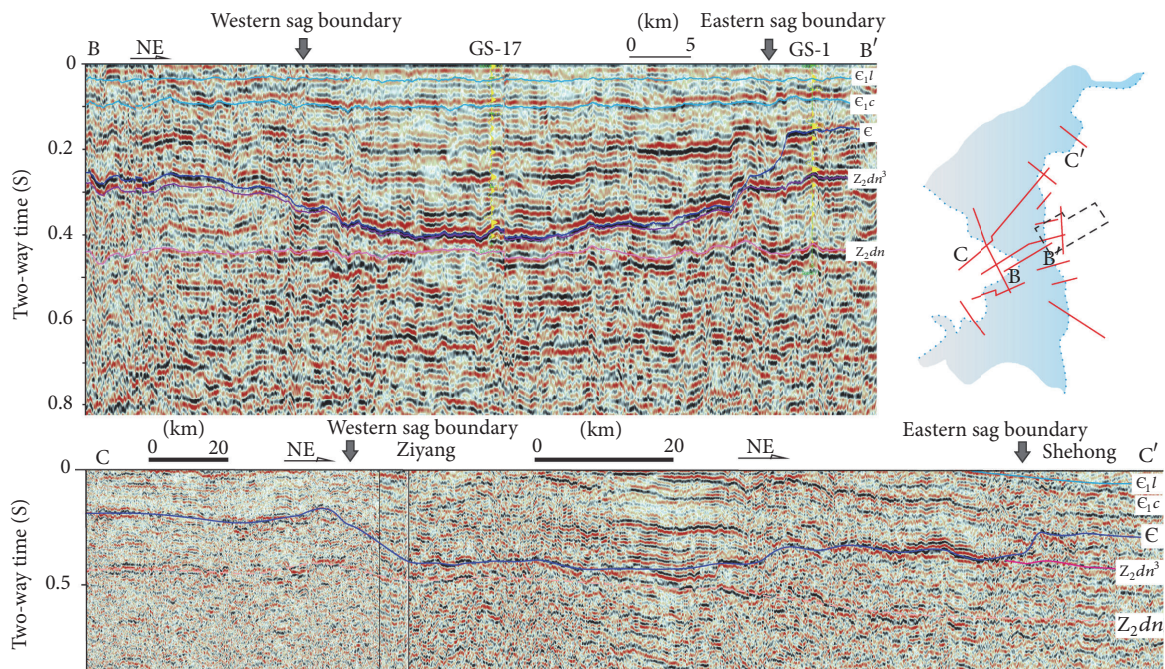


FIGURE 3: The key seismic profiles indicating presence of Early Cambrian extensional intracratonic sag across the Sichuan basin. (B-B': NE-striking Weiyuan-Gaoshiti cross-section across the intracratonic sag. The yellow lines show log-data for well picks of the horizon; based on GS-1 and GS-17 wells. Grey arrows show western and eastern sag boundaries.  $E_{1l}$  and  $E_{1c}$  are bases of Lower Cambrian Longwangmiao and Canglangpu *Fm.* C-C': NE-striking Ziyang-Shehong section. All the seismic profiles are rotated back with the Middle Cambrian Gaotai *Fm.* The inset map shows locations of cross-sections).

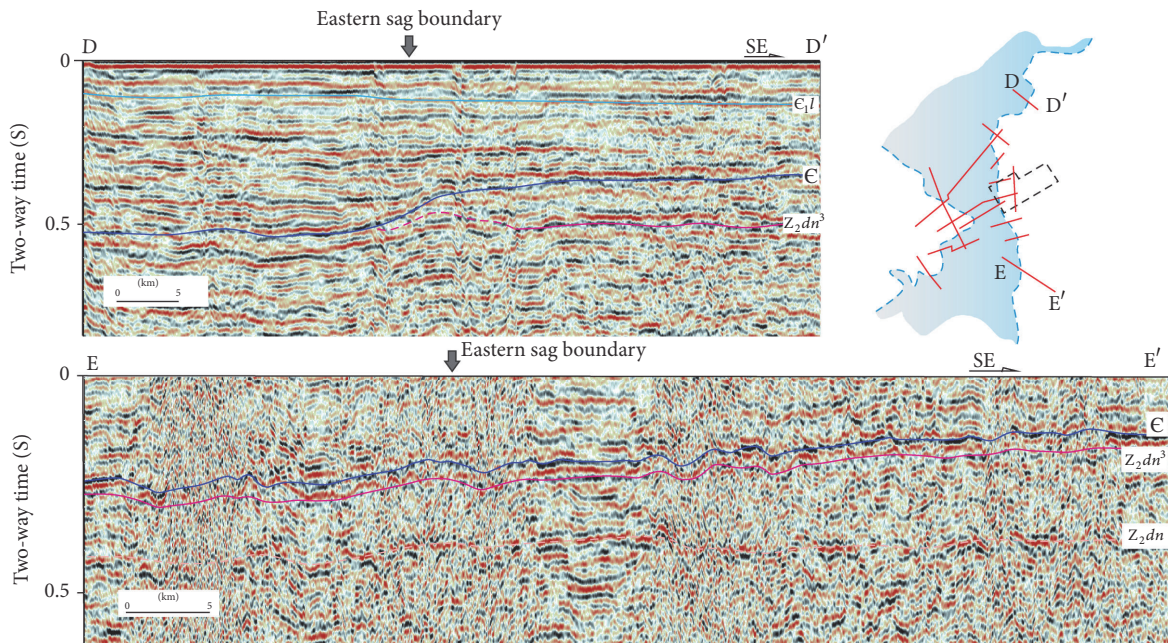


FIGURE 4: 2D seismic profile across eastern margin of the Mianyang-Changning intracratonic sag. D-D': SE-striking Langzhong section in northern segment of the sag; E-E': SE-striking Hejiang section in southern segment. It should be noted that there is a distinct decrease in the steepness of the eastern boundary from the north to the south.

TABLE 1: The thickness of Sinian (Ediacaran)-Early Cambrian strata in wells across the intracratonic sag.

Formation	Western margin		Center of the Miayang-Changning intracratonic sag				Eastern margin			
	LL-1# (m)	W-28# (m)	WS-1# (m)	Z-4# (m)	GSH-1# (m)	ZS-1# (m)	GS-17# (m)	L-206# (m)	GS-1# (m)	PL-1# (m)
Longwangmiao Fm.	51	81	164	76	211	138	92	555.5	87	124
Canglangpu Fm.	88	135	182	267	196	129	214	239.5	91.1	191
Qiongzhusi Fm.	223	356	578	386	459	430	398	210.3	157	247
Maidiping Fm.	24.5	/	53	198	/	45	285	0.6	/	/
Fourth member of Dengying Fm.	223.5	32	118	/	81	39	/	29.1	262.5	59
Third member of Dengying Fm.	6	5.5	11	76	4	6	11	No data	67.15	57

(For locations, see Figure 1.)

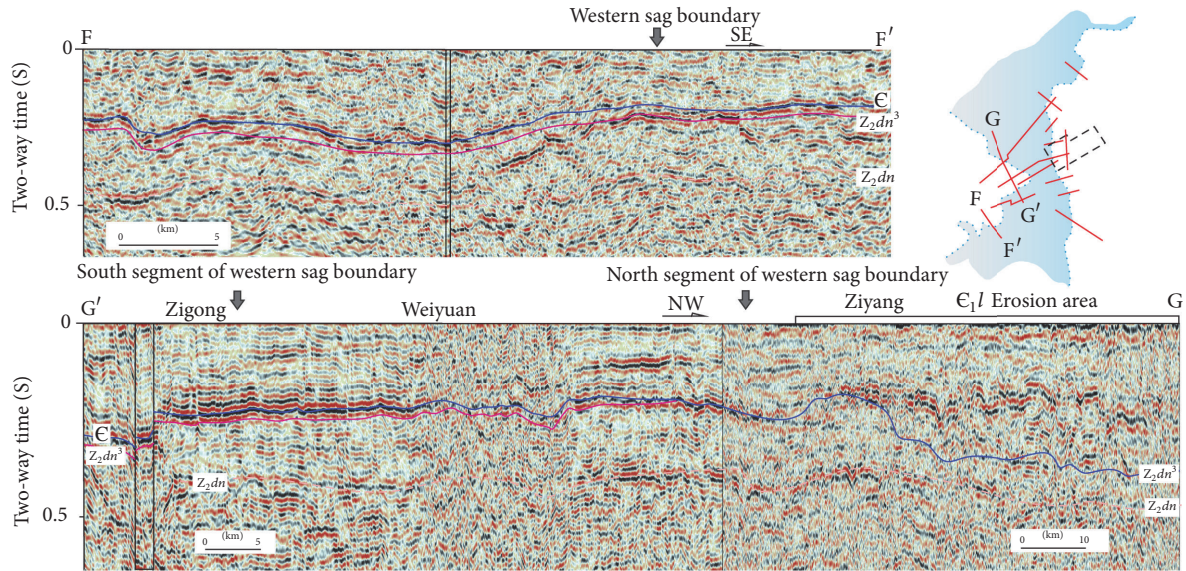


FIGURE 5: 2D seismic profile across western margin of the Mianyang-Changning intracratonic sag. F-F': SE-striking Qianwei section in southern segment of the sag; G-G': NW-striking Zigong-Ziyang section, showing a distinct decrease in steepness of the western sag boundary from the north to the south.

(Figure 2). The discontinuous reflections at the base of the Early Cambrian strata suggest a steeper margin of the Mianyang-Changning intracratonic sag than at its northern segment (Figure 3). Further to the south, the steepness of eastern margin substantially decreases, as can be observed at, for example, the Dazhu and Hejiang areas (Figure 4 E-E' section).

The western margin of the sag as indicated by seismic profiles is characterized by less steep beds and more complicated strata orientation than that of the eastern margin. The western margin can be subdivided into two segments, one is NW-striking and the other NE-striking, separated by the Weiyuan-Zigong area. In the south, both the south segment of western margin and south segment of the eastern margin are characterized by low steepness (Figure 5 F-F' section and Figure 4 E-E' section). Although the western margin of the Mianyang-Changning intracratonic sag shows generally less steepness than the eastern margin (Figure 3), the northern segment of western margin of the sag is much steeper than its southern segment (Figure 5 G-G' section). It should be noted that the underlying Dengying Formation is thinner along the western margin than at the eastern margin of the sag. That is a result of the uplift and erosion which occurred during the end of the Ediacaran epoch [30–32].

### 3.3. Geometry of the Mianyang-Changning Intracratonic Sag.

We have used seismic lineups at the base of the Early Cambrian Maidiping and Canglangpu formations to unravel spatial thicknesses of the deposits during Early Cambrian times. It demonstrates syn-extension sedimentation during that time and shows geometry of the Mianyang-Changning intracratonic sag across the Sichuan basin (Figure 6). The isopach map (Figure 6(a)) shows thickest Maidiping-Canglangpu Formations to be located in the center of the

Sichuan basin, where the thickness is about 450–1700 m higher than 0–600 m at any other place. It suggests that a geometry of the Early Cambrian Mianyang-Changning intracratonic sag is with its eastern margin along the Bazhong-Shehong-Dazhu-Hejiang zone, and its western margin along the Xinjing-Weiyuan-Qianwei zone. To the east of the sag, the thickness of the Maidiping-Canglangpu Formations is about 300–600 m, with a thickness center at the Guan'an-Hechuan area. To the west, the thickness is about 0–500 m, with a westward decrease in thickness due to the erosion.

The Mianyang-Changning intracratonic sag can be separated into three segments, roughly separated by the Weiyuan-Gaoshiti area. The northern segment located at the north of the Shehong-Xinjing area has thicker Maidiping-Canglangpu Formations than the other two segments. Also its width increases northwards. In particular, some extensional faults developed in the center of the sag during the Early Cambrian times. The middle segment with a N-S striking strata is characterized by the greatest steepness of both margins of the sag. The narrowest place in the middle segment has about 50 km width. Furthermore, more strata of Maidiping Formation was deposited in the center, which resulted in the thickness of Maidiping-Canglangpu Formations being significantly larger than that outside the sag. The southern segment located at south of the Dazhu-Qianwei area is characterized by the least steepness of the margins and thinnest Maidiping-Canglangpu Formations than in other segments. Due to erosion, the western margin of the southern segment is not very distinct, resulting in a roughly southwestward increase in its width.

### 3.4. Evolution of the Mianyang-Changning Intracratonic Sag.

Based on E-W-striking seismic sections of the Mianyang-Changning sag, the balanced cross-sections were constructed considering the template line as flat (e.g., the top of

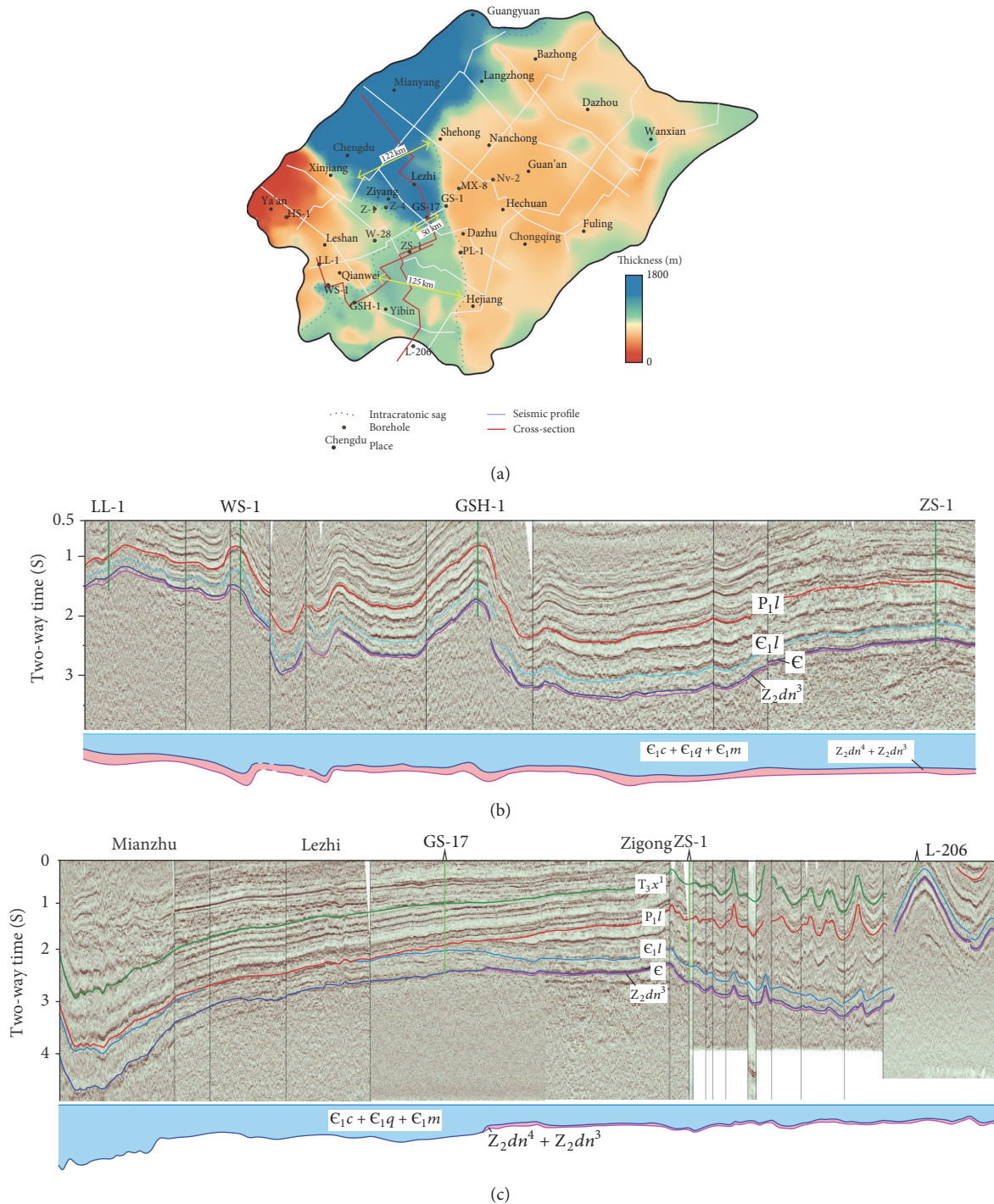


FIGURE 6: Cross-sections showing Early Paleozoic strata geometries in the intracratonic sag. ((a) spatial distribution of the sag indicated by the isopach map of the Maidiping-Canglangpu Formations; the sag is characterized by asymmetrical, N-S striking geometry. The sag can be subdivided into three segments; in particular, the eastern margin is much steeper than the western margin. (b) E-W striking cross-section of the sag in Leshan-Yibin-Zigong area. (c) N-S striking cross-section of the sag in Mianzhu-Changning area.)

Longwangmiao Formation, Canglangpu Formation, and Qiongzhusi Formation), to unravel the multistage history of the Mianyang-Changning intracratonic sag. Thus, the evolution of the intracratonic sag can be divided into five episodes: presag period (i.e., uplifting and erosion) at the end of Late

Sinian Dengying period, an early stage at the Early Cambrian Maidiping period, a main stage of extension during the Early Cambrian Qiongzhusi period, and a decay and dispersal stages of extension at the Early Cambrian Canglangpu and Longwangmiao periods, respectively (Figure 7).

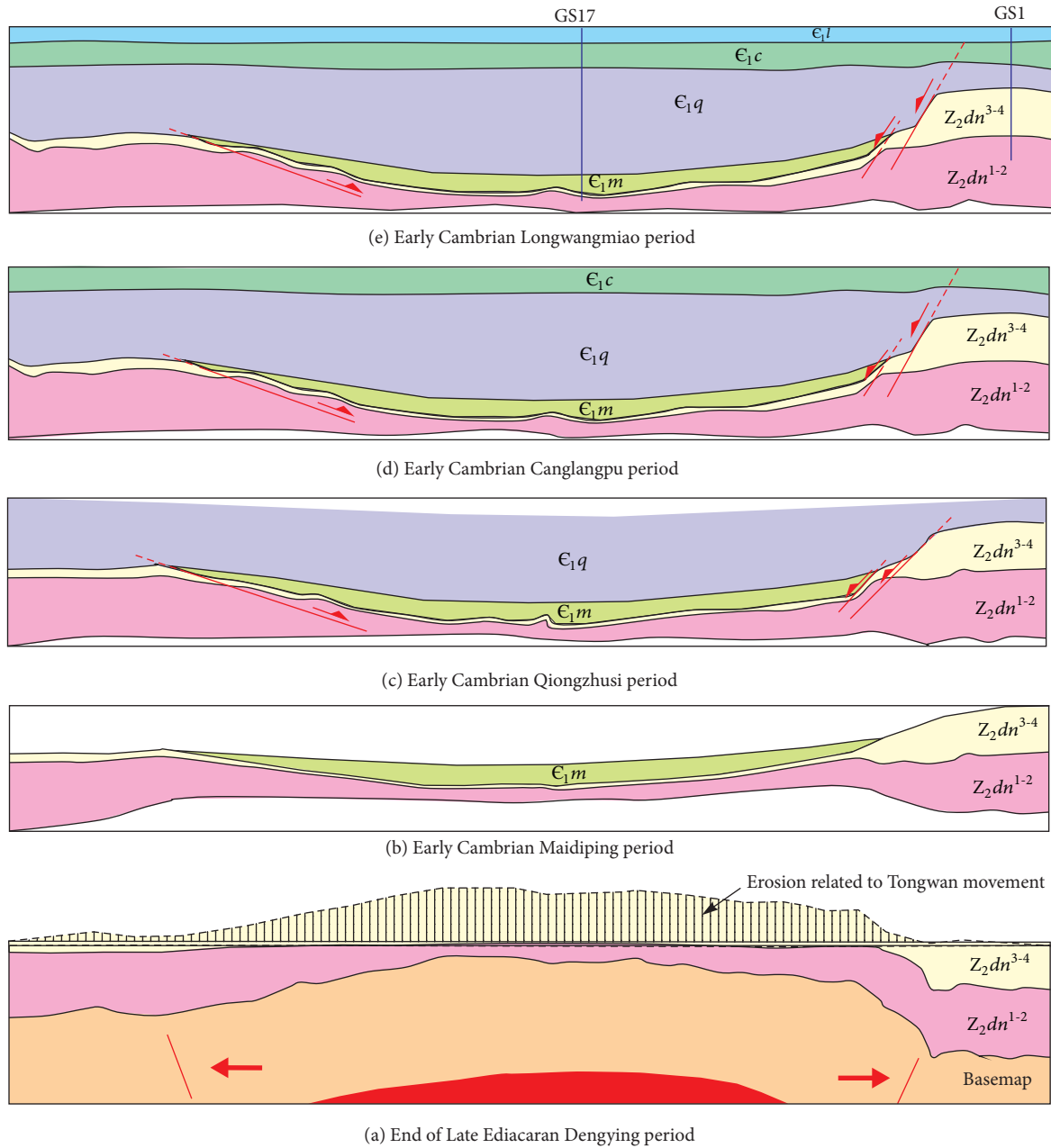


FIGURE 7: Evolution of the Early Cambrian Mianyang-Changning intracratonic sag (it should be noted that there is more strata of Maidiping Formation and much thicker Niutitang Formation in the center of the Mianyang-Changning sag, indicating that the initial extension as well as maximum of extension occurred during the Early Cambrian Maidiping to Niutitang periods).

Widespread uplift and erosion across the Sichuan basin occurred at the end of Late Sinian Dengying period, named the “Tongwan movement” [30–32]. It is associated with different magnitudes of erosion across the sag, for example, the Z-4 and GS-17 wells located in the center of the sag lack the third and fourth members of the Dengying Formation (Table 1). This indicates that uplift and erosion across the sag were stronger than at other outside places during this time.

Early in the Early Cambrian Maidiping period, the Maidiping Formation was deposited where in presag time there was maximum erosion. This unit is characterized by

deposits of black phosphorus silicic shale and phosphorus dolomite, interbedded with cellophane beds. Their occurrence is related to submarine volcanism and hydrothermal processes in a deep oceanic environment [45, 46], which indicates rapid subsidence and extensional tectonics. The Qiongzhusi Formation is characterized by the occurrence of black shale and mudstone at its base, and by grey-to-black muddy siltstone in the upper part of the formation, of which the geochemistry suggests it is dominated with I-type source-rocks with high TOC content [17, 18]. The latter indicate some shallowing, or progressive basin filling during the final stage

of extension. The thickness of black shale in the center of the sag is up to 180 m, for example, in the GS-17 well, which is greatly important for petroleum occurrences in the center of the Sichuan basin. The extension and sedimentation across the intracratonic sag decreased distinctly during the decay and dispersal stages at the Canglangpu and Longwangmiao periods. The Longwangmiao Formation is comprised of carbonate rocks of roughly consistent thickness across the center of Sichuan basin, indicating that the Mianyang-Changning intracratonic sag already disappeared.

#### 4. Control of the Intracratonic Sag on Oil/Gas Occurrences

The development of the Mianyang-Changning intracratonic sag significantly influenced the Late Proterozoic to Early Cambrian oil/gas occurrences in the Sichuan basin, that is, chiefly through its influence on the distribution of high-quality reservoirs in the Late Proterozoic Dengying and Early Cambrian Longwangmiao formations and of source-rocks in the Niutitang Formation.

*4.1. High-Quality Reservoir of Late Proterozoic Dengying Formation.* The reservoir characteristics of the Late Proterozoic Dengying Formation in the boreholes across the intracratonic sag indicate distinct differences in karst development, burial and hydrothermal dissolution, porosity and permeability, and so on (Table 2). There were variable magnitudes of erosion across the Mianyang-Changning intracratonic sag (Table 1, Figure 7); therefore there are variable occurrences of karst caves impacting the reservoir. The Z-1 and GS-1 wells located around the edges of the intracratonic sag have much higher density of karst caves than the JS-1 and W-113 wells, located further away from the western sag boundary. Furthermore, there are different volumes of bitumen in the reservoir of the Dengying Formation, indicating different magnitudes of burial dissolution. Westward of the intracratonic sag, no bitumen is present in the 2nd and 4th member of the Dengying Formation at the JS-1 well. Eastward, near the sag boundary, the W-113 well shows widespread bitumen in the 2nd and 4th members of the Dengying Formation, extending for 96.42 m in a 110.42 m long core in the 2nd member and for 14.82 m in a 23.6 m long core of the 4th member, respectively. The bitumen impregnated 1%~6% in porosity, in both the 2nd and 4th members of the Dengying Formation, as well as in the Z-1 well, located at the western margin of the sag. In particular, a core 31.05 m long in the GS-1 well, located at the eastern margin of the sag, is totally impregnated by bitumen in the 4th member of the Dengying Formation, indicating much more burial dissolution along the eastern margin.

It should be noted that the porosity and permeability across the sag show significant differences. The strata in JS-1 well show poor porosity and permeability. The reservoir is comprised of dissolution pores and fractures, with most of them totally or partially filled with dolomite. To the east along the intracratonic sag, the Z-1 and GS-1 wells Dengying Formation strata have much better porosity and permeability than the JS-1 and W-113 wells, in which the reservoir is represented by dissolution pores and caverns. In particular, the

thickness of reservoir in the GS-1 well is up to 184.05 m, with a gas production of  $10^6 \text{ m}^3$  per day. It indicates that a better porosity and permeability in the reservoir is located along the border of the intracratonic sag. That is consistent with a distinct increase in the karst weathering, dissolution pores occurrence, presence of bitumen in the reservoir, and intensity of burial and hydrothermal dissolution towards the sag.

*4.2. High-Quality Source-Rock of Early Cambrian Niutitang Formation.* During development of the Early Cambrian Mianyang-Changning intracratonic sag, the 50–450 m thick Qiongzhusi/Niutitang Formation comprised of black shale was deposited (Figure 8). It should be noted that the geometry and thickness of Qiongzhusi Formation show much difference than those of the Early Cambrian Maidiping-Canglangpu Formations (shown in Figure 6), which could be attributed to the interpolation of different thickness between them (i.e., the 50–450 m thick Qiongzhusi Formation and the 450–1700 m thick Maidiping-Canglangpu Formations). However, the thickness isopach of the Qiongzhusi Formation roughly parallels the orientation of the sag, indicating that the maximum thickness of the Qiongzhusi Formation is controlled by the morphology of the sag. Strata located around the intracratonic sag provided most of the hydrocarbons to charge its Late Proterozoic to Lower Cambrian petroleum systems [7, 18, 38, 39].

*4.3. High-Quality Reservoir of Early Cambrian Longwangmiao Formation.* Based on thin-section analyses from three wells across the intracratonic sag, different diagenesis regimes were noted in the Early Cambrian Longwanmiao Formation. A 20–60 m thick high-quality reservoir in the Anyue supergiant gas field shows dolomitization, cementation, compaction, and pressure solution. Dolomitization, selective freshwater dissolution, and liquid hydrocarbon filling had significant roles in the reservoir development, in particular the last two processes. The Longwangmiao Formation reservoir in the MX-12 well located at the eastern margin of the sag shows strong selective freshwater karstification and hydrocarbon charging, indicated by multiple episodes of bitumen filling. Also it has indications of moderate epigenic karstification and hydrothermal activity (Table 3). However, the reservoir in the boreholes located in the center of the sag shows strong epigenic karstification and hydrothermal dolomite, for example, the GS-17 well. To the west of the sag, magnitude of hydrocarbon charging, epigenic karstification, and hydrothermal dolomite decrease in the Longwangmiao Formation. For example, the JS-1 well demonstrates only weak epigenic karstification and no hydrocarbon charging. Thus, it suggests that the high-quality reservoir in the Longwangmiao Formation is associated with the intracratonic sag development. Most importantly, the best reservoirs of Longwangmiao Formation are located at the eastern margin of the sag.

There are two reasons which may explain the occurrence of a high-quality reservoir at the eastern margin of the sag in the Early Cambrian Longwanmiao Formation. During extensional tectonics, the footwall of the intracratonic sag may have formed a paleohigh along its margins. Although the difference in elevation between the paleohigh of the

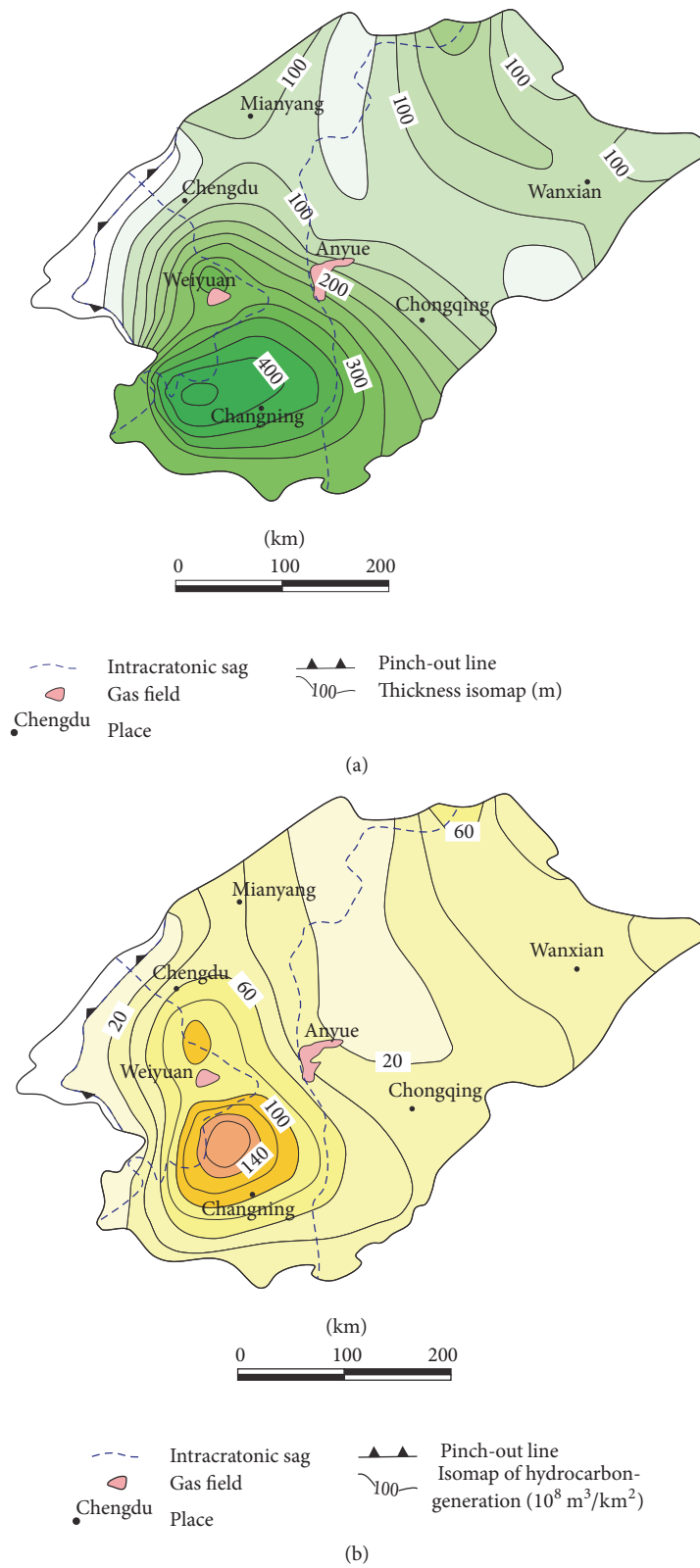


FIGURE 8: The thickness and hydrocarbon-generating intensity of the Lower Cambrian mudstone across the Sichuan basin ((a) Thickness isopach map of the Qiongzhusi/Niutitang Formation; (b) isomap of hydrocarbon-generating of the Qiongzhusi/Niutitang Formation, modified from Huang et al., 2002 [18]).

TABLE 2: Reservoir features of the Ediacaran Dengying Formations across the intracratonic sag.

Wells	JS-1#	W-113#	Z-1#	GS-1#
Locations		Western margin of the sag		Eastern margin
Reservoir	2nd member	3rd and 4th members	2nd and 3rd members	2nd and 4th members
Porosity	3.02%–4.05%	1%–5%	1%–2%	2.45%–4.85%
Permeability	0.0063–5.9317 mD	0.1–1.92 m	0.00225–88.2 mD	1.005–8.02 mD
Bitumen content	No	1%~6%	1%~5%	1%~5%
Pore type	Dissolved pore	Fracture and pore	Dissolved pore	Dissolved pore
Fracture density	15.3/m	24.75/m	4.22/m	1.4/m
Density of karst cave	0.75/m	1.3/m	25/m	11.4/m
Vugs-filling minerals	Dolomite	Dolomite-saddle dolomite-bitumen	Saddle dolomite-bitumen	Saddle dolomite-bitumen
Weathering karst	Weak	Medium	Strong	Very strong
Burial dissolution	Weak	Moderate strong	Strong	Very strong
Hydrothermal dissolution	Weak	Moderate strong	Strong	Very strong

(For locations, see Figure 1.)

TABLE 3: Differential diagenesis of Early Cambrian Longwangmiao Formation across the intracratonic sag.

Well	JS-1	GS-17	MX-12
Location	Western margin of sag	Center of sag	Eastern margin
Lithology	Crystalline dolomite	Dolomitic grainstone, crystalline dolomite	Dolomitic grainstone
Mudstone recrystallization	No	Weak	Weak
Dolomitization	Strong	Strong	Strong
Cementation	Weak	Moderate	Strong
Freshwater karstification	Weak	Moderate	Strong
Compaction, pressure solution	Moderate	Moderate	Moderate
Recrystallization	Strong	Strong	Strong
Epigenic karstification	Weak	Moderate to strong	Moderate
Hydrothermal dolomite	Moderate	Strong	Moderate
First charging of hydrocarbon and bitumen	No	Moderate	Strong
Second charging of hydrocarbons	No	Moderate	Strong

(For locations, see Figure 1.)

footwall and hanging wall may not be substantial, it had significant influence on reservoir development. Our studies of seismic data support existence of such a paleohigh during deposition of the Longwanmiao Formation. The Moxi-Gaoshiti area (in Figure 1 the MX-GS area) had maximum paleoelevation during that time period. Thus, we suggest that the paleohigh formed at the sag margin was conducive for a grainstone-bank facies deposition during Longwangmiao Formation time. The thickness of this facies is 20–70 m at the Moxi-Gaoshiti area. Subsequent surface exposure resulted in freshwater karstification and development of intergranular and intragranular dissolution porosity.

The lower part of the Lower Cambrian had significant capacity to generate oil/gas, which together with hydrocarbons from the Ediacaran Sinian strata migrated to Early Paleozoic traps [7, 37, 38]. The critical time periods for hydrocarbons generation, migration, and transformation were the Silurian, which was the initial period for liquid hydrocarbons generation, Late Permian to Late Triassic period for peak

hydrocarbon-generation, and the Middle Jurassic to Late Cretaceous interval for hydrocarbon-cracking into gas [7, 47]. Furthermore, the paleouplift of Leshan-Longnvshi formed during Late Carboniferous-Early Permian period and is roughly prior to the period of peak hydrocarbon-generation [48, 49]; we argue that the paleohigh along the margins of the intracratonic sag has the highest probability to be charged by hydrocarbons, as maturity of the source-rocks was increasing with increased burial.

Study of thin-sections indicates that there are two periods of hydrocarbon charging: the first one during shallow-moderate burial of the strata and the second one during moderate-to-deep burial. The first one followed a period of uplift and freshwater karstification of exposed carbonate strata, which occurred at the Sinian-Cambrian boundary, and is marked by the unconformity. Occurrence of trace amounts of bitumen suggests that limited hydrocarbon-generation may have occurred due to the presence of hot hydrothermal fluids, indicated by Pb-Zn mineralization near the boundary. The

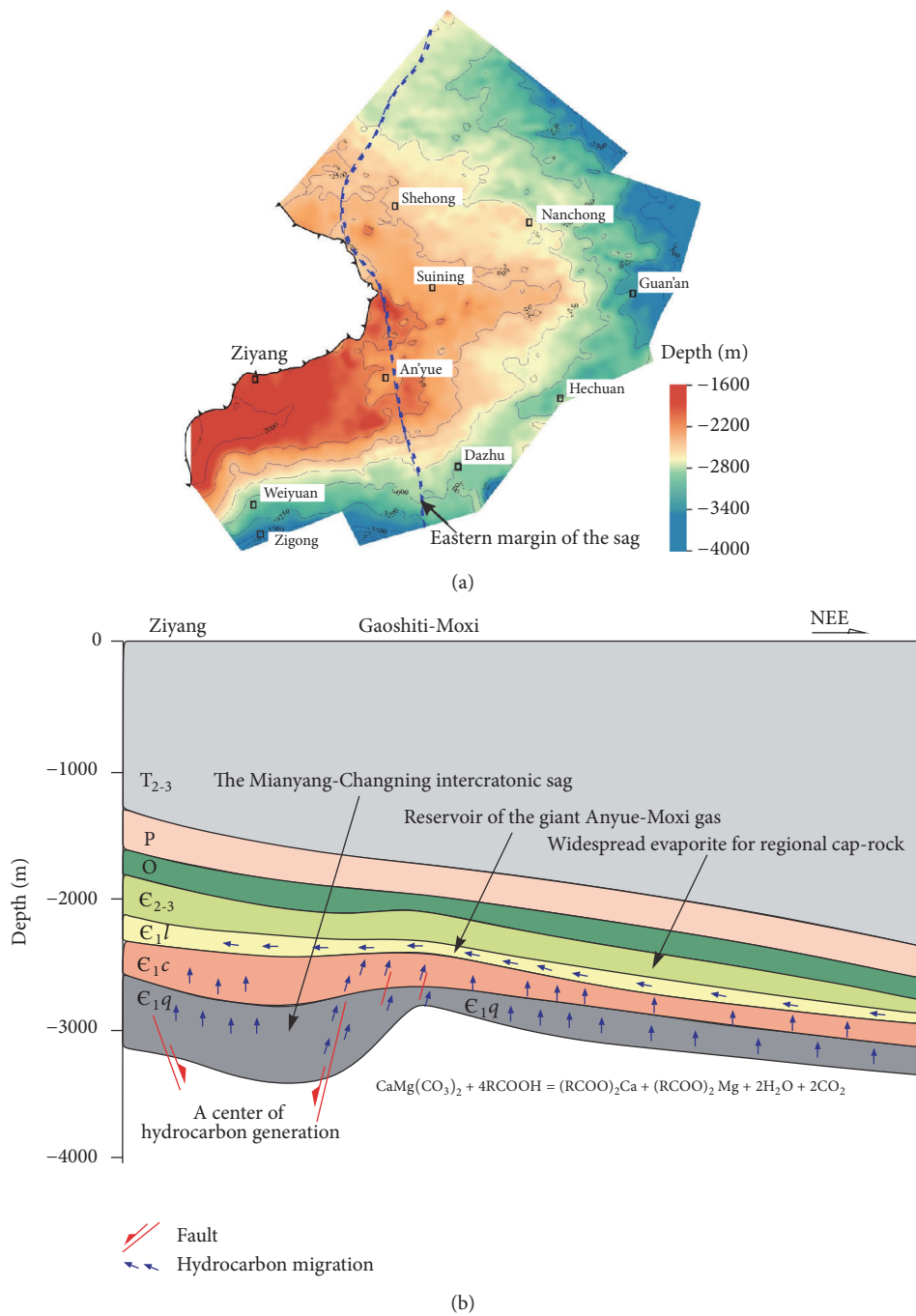


FIGURE 9: Conceptual model of high-quality reservoir rocks of Early Cambrian Longwangmiao *Fm* in the central Sichuan basin. ((a) Paleo-structure of Longwangmiao *Fm* at the end of Permian, (b) hydrocarbon charging model of Qiongzhusi *Fm*).

increased burial resulted in increased thermal maturity of the source-rocks and the main peak of hydrocarbon-generation during the Permian. The Gaoshiti-Moxi and Weiyuan-Ziyang areas located at the eastern and western margins of the sag represent the best area for hydrocarbon charging and migration (Figure 9). Both of those areas contain high-quality reservoirs in the Longwangmiao Formation. Also there is a steeper margin at the eastern margin of the sag

than its west, which would contribute to a better efficiency of hydrocarbon migration. Furthermore, the Gaoshiti-Moxi and Weiyuan-Ziyang areas were located at the paleohigh and upper slope during the deposition of Longwangmiao Formation. Both of them account for most of high-quality reservoirs in the Gaoshiti-Moxi area. Therefore, we suggest that the most prospective areas characterized by occurrence of high-quality reservoirs and hydrocarbons accumulation in

Longwangmiao Formation are at the eastern part of the overlapping areas of the Mianyang-Changning intracratonic sag and the paleouplift, represented by the Gaoshiti-Moxi area.

## 5. Conclusions

The Neoproterozoic break-up of the Rodinia supercontinent, that is, Xinkai taphrogenesis in the South China block, had significant influence on the Neoproterozoic-Early Cambrian hydrocarbon occurrences in the Sichuan basin. Our study shows an asymmetrical, S-N striking intracratonic sag, that is, the Mianyang-Changning intracratonic sag, which developed across the Sichuan basin from the Late Ediacaran to Early Cambrian time. The sag can be divided into three segments, with margins roughly along the Bazhong-Shehong-Dazhu-Hejiang area at the eastern margin and the Xinjing-Weiyuan-Qianwei area at the western margin. In particular, the eastern margin shows much greater steepness than the western margin. The narrowest part of the sag is ~50 km across, and its greatest steepness is in the basin center. Five episodes of evolutions of the sag can be established. It begins in the Late Ediacaran with an uplift and erosion correlated to Tongwan movement preceding extension. Initial extension occurred in the Early Cambrian Maidiping period, with strata of the Maidiping Formation deposited across the Mianyang-Changning sag. Subsequently, maximum of extension took place at the Early Cambrian Qiongzhusi period that resulted in deposition of the 450–1700 m thick Maidiping-Canglangpu Formations in the center of the sag. Finally, the sag was infilled by sediments at the end of the Early Cambrian (i.e., the Longwangmiao period) and as structural entity disappeared.

The Mianyang-Changning intracratonic sag had significant influence on the Late Proterozoic to Early Cambrian hydrocarbon occurrences in the Sichuan basin. It is chiefly through its influence on the presence of high-quality reservoirs rocks in the Late Proterozoic Dengying and Early Cambrian Longwangmiao formations and distribution of source-rocks of the Niutitang Formation. During the evolution of the Mianyang-Changning sag, the paleohighs and erosion account for the development of high-quality reservoirs in the Late Proterozoic Dengying and Early Cambrian Longwangmiao formations. Furthermore, it was the sag development which provided conditions favorable for the deposition of I-type source-rock of the Niutitang Formation. Considering all of these factors there is a high probability of oil/gas accumulation along the Mianyang-Cangning intracratonic sag, particularly along its eastern margin across the center of the Sichuan basin.

## Conflicts of Interest

The authors declare that they have no conflicts of interest.

## Acknowledgments

This work was supported by the National Basic Research Program of China (no. 2012CB214805) and the Natural Science Foundation (nos. 41230313, 41402119, and 41472017).

The authors are thankful to Frank Thomas for review of the English in the manuscript.

## References

- [1] S. I. Fraser, A. J. Fraser, M. R. Lentini, and R. L. Gawthorpe, "Return to rifts - The next wave: Fresh insights into the petroleum geology of global rift basins," *Petroleum Geoscience*, vol. 13, no. 2, pp. 99–104, 2007.
- [2] J. Craig, J. Thurow, B. Thusu, A. Whitham, and Y. Abutarruma, "Global Neoproterozoic petroleum systems: The emerging potential in North Africa," *Geological Society Special Publication*, vol. 326, pp. 1–25, 2009.
- [3] F. Lottaroli, J. Craig, and B. Thusu, "Neoproterozoic-Early Cambrian (Infracambrian) hydrocarbon prospectivity of North Africa: A synthesis," *Geological Society Special Publication*, vol. 326, pp. 137–156, 2009.
- [4] A. A. Meyerhoff, "Geology and petroleum fields in Proterozoic and lower Cambrian strata, Lena-Tunguska petroleum province, Eastern Siberia, USSR," in *Giant Oil and Gas Fields of the Decade 1968-1978*, M. T. Halbouty, Ed., vol. 30, pp. 225–252, AAPG Memoir, 1980.
- [5] K. A. R. Ghorri, J. Craig, B. Thusu, S. Lüning, and M. Geiger, "Global Infracambrian petroleum systems: A review," *Geological Society Special Publication*, vol. 326, pp. 109–136, 2009.
- [6] G. M. Bhat, J. Craig, M. Hafiz et al., "Geology and hydrocarbon potential of neoproterozoic-cambrian basins in asia: An introduction," *Geological Society Special Publication*, vol. 366, no. 1, pp. 1–17, 2012.
- [7] S. G. Liu, C. Qin, L. Jansa et al., "Transformation of oil pools into gas pools as results of multiple tectonic events in Upper Sinian (Upper Neoproterozoic), deep part of Sichuan Basin, China," *Energy Exploration and Exploitation*, vol. 29, no. 6, pp. 679–698, 2011.
- [8] J. M. Peters, J. B. Filbrandt, J. P. Grotzinger, M. J. Newall, M. Shuster, and H. A. Al-Siyabi, "Surface-piercing salt domes of interior North Oman, and their significance for the Ara carbonate 'stringer' hydrocarbon play," *GeoArabia*, vol. 8, no. 2, pp. 231–270, 2003.
- [9] J. Schoenherr, R. Littke, J. L. Urai, P. A. Kukla, and Z. Rawahi, "Polyphase thermal evolution in the Infra-Cambrian Ara Group (South Oman Salt Basin) as deduced by maturity of solid reservoir bitumen," *Organic Geochemistry*, vol. 38, no. 8, pp. 1293–1318, 2007.
- [10] A. Wyatt, *Challinors Dictionary of Geology*, University of Wales Press, Cardiff, Wales, 6th edition, 1986.
- [11] A. G. Smith, "A review of the ediacaran to early cambrian ('Infra-Cambrian') evaporites and associated sediments of the middle east," *Geological Society Special Publication*, vol. 366, no. 1, pp. 229–250, 2012.
- [12] C. Zhong and J. Huang, *Drilling and Gas Recovery Technology in Ancient, Zigong Salt Industry Museum, Sichuan, China*, 1997.
- [13] R. J. Korsch, M. Huazhao, S. Zhaocai, and J. D. Gorter, "The Sichuan basin, southwest China: a late proterozoic (Sinian) petroleum province," *Precambrian Research*, vol. 54, no. 1, pp. 45–63, 1991.
- [14] Y. C. Xu and P. Shen, "A study of natural gas origins in China," *AAPG Bulletin*, vol. 80, no. 10, pp. 1604–1614, 1996.
- [15] J. Zhang and Q. Zhang, "The review and prospects of oil and gas exploration in Sichuan basin," *Natural Gas Industry*, vol. 22, pp. 3–7, 2002.

- [16] Y. Ma, X. Guo, T. Guo, R. Huang, X. Cai, and G. Li, "The Puguang gas field: New giant discovery in the mature Sichuan Basin, southwest China," *AAPG Bulletin*, vol. 91, no. 5, pp. 627–643, 2007.
- [17] C. N. Zou, J. H. Du, C. C. Xu et al., "Formation, distribution, resource potential and discovery of the Sinian-Cambrian giant gas field, Sichuan Basin, SW China," *Petroleum Exploration and Development*, vol. 41, no. 3, pp. 278–293, 2014.
- [18] X. P. Huang, S. Q. Wang, and Q. H. Luo, *Oil and Gas Resource Evaluation in Sichuan Basin*, PetroChina Southwest Oil & Gas Field Company, Chengdu, China, 2002.
- [19] Y. Dong, G. Zhang, F. Neubauer, X. Liu, J. Genser, and C. Hauzenberger, "Tectonic evolution of the Qinling orogen, China: review and synthesis," *Journal of Asian Earth Sciences*, vol. 41, no. 3, pp. 213–237, 2011.
- [20] F. Roger, M. Jolivet, and J. Malavieille, "The tectonic evolution of the Songpan-Garzê (North Tibet) and adjacent areas from Proterozoic to Present: A synthesis," *Journal of Asian Earth Sciences*, vol. 39, no. 4, pp. 254–269, 2010.
- [21] S. Liu, B. Deng, Z. Li et al., "Geological evolution of the longmenshan intracontinental composite orogen and the eastern margin of the Tibetan Plateau," *Journal of Earth Science*, vol. 24, no. 6, pp. 874–890, 2013.
- [22] S. Li, M. Santosh, G. Zhao, G. Zhang, and C. Jin, "Intracontinental deformation in a frontier of super-convergence: A perspective on the tectonic milieu of the South China Block," *Journal of Asian Earth Sciences*, vol. 49, pp. 313–329, 2012.
- [23] Z.-X. Li and X.-H. Li, "Formation of the 1300-km-wide intracontinental orogen and postorogenic magmatic province in Mesozoic South China: A flat-slab subduction model," *Geology*, vol. 35, no. 2, pp. 179–182, 2007.
- [24] X.-H. Li, "U-Pb zircon ages of granites from the southern margin of the Yangtze Block: Timing of Neoproterozoic Jinning Orogeny in SE China and implications for Rodinia assembly," *Precambrian Research*, vol. 97, no. 1-2, pp. 43–57, 1999.
- [25] M.-F. Zhou, D.-P. Yan, P. M. Vasconcelos, J.-W. Li, and R.-Z. Hu, "Structural and geochronological constraints on the tectono-thermal evolution of the Danba domal terrane, eastern margin of the Tibetan plateau," *Journal of Asian Earth Sciences*, vol. 33, no. 5-6, pp. 414–427, 2008.
- [26] J.-H. Yu, S. Y. O'Reilly, L. Wang et al., "Where was South China in the Rodinia supercontinent?. Evidence from U-Pb geochronology and Hf isotopes of detrital zircons," *Precambrian Research*, vol. 164, no. 1-2, pp. 1–15, 2008.
- [27] F. H. Hou, S. X. Fang, X. Z. Wang et al., "Review of Sinian Dengying formation reservoir and permeability in Sichuan basin," *Acta Petrolei Sinica*, vol. 20, pp. 16–21, 1999.
- [28] W. Li, J. Liu, S. Deng, B. Zhang, and H. Zhou, "The nature and role of Late Sinian-Early Cambrian tectonic movement in Sichuan Basin and its adjacent areas," *Shiyou Xuebao/Acta Petrolei Sinica*, vol. 36, no. 5, pp. 546–563, 2015.
- [29] S. G. Liu, W. Sun, Y. H. Zhao et al., "Differential accumulation and distribution of natural gas and their main controlling factors in the Upper Sinian Dengying Fm, Sichuan Basin," *Natural Gas Industry*, vol. 35, no. 1, pp. 10–23, 2015.
- [30] J. Q. Huang, J. S. Ren, and C. F. Jiang, *Tectonic and Geotectonic Evolution of China: A Brief Introduction of the Tectonic Map of China (1: 4 000 000)*, Science Press, Beijing, China, 1980.
- [31] Z. L. Luo, "The influence on the formation oil and mineral resources from taphrogenesis movement since the late Paleozoic in southwest China," *Acta Geologica Sichuan*, vol. 2, pp. 1–22, 1981.
- [32] Z. L. Luo, "A discussion of taphrogenesis and hydrocarbon distribution in China," *Acta Geologica Sichuan*, vol. 3, pp. 93–101, 1984.
- [33] Z. X. Li, S. V. Bogdanova, A. S. Collins et al., "Assembly, configuration, and break-up history of Rodinia: a synthesis," *Precambrian Research*, vol. 160, no. 1-2, pp. 179–210, 2008.
- [34] Z. Chen M and Q. Chen Y, "The Paleogeography in early Meizhucun period of Early Cambrian at Yangtze platform and distribution of phosphorite," *Scientia Geologica Sinica*, vol. 3, pp. 246–256, 1987.
- [35] G. Z. Wang, S. G. Liu, C. H. Chen, D. Wang, and W. Sun, "The genetic relationship between MVT Pb-Zn deposits and paleo-oil/gas reservoirs at Heba, Southeastern Sichuan Basin," *Earth Science Frontiers*, vol. 20, no. 1, pp. 107–116, 2013.
- [36] S. G. Liu, W. M. Huang, L. F. Jansa et al., "Hydrothermal Dolomite in the Upper Sinian (Upper Proterozoic) Dengying Formation, East Sichuan Basin, China," *Acta Geologica Sinica—English Edition*, vol. 88, no. 5, pp. 1466–1487, 2014.
- [37] S. G. Liu, Y. S. Ma, W. Sun et al., "Studying on the differences of Sinian natural gas pools between Weyuan gas field and Ziyang gas-brone area, Sichuan basin," *Acta Geologica Sinica*, vol. 82, no. 3, pp. 328–337, 2008.
- [38] G. Wei, G. Chen, S. Du, L. Zhang, and W. Yang, "Petroleum systems of the oldest gas field in China: Neoproterozoic gas pools in the Weyuan gas field, Sichuan Basin," *Marine and Petroleum Geology*, vol. 25, no. 4-5, pp. 371–386, 2008.
- [39] G. Zhu, T. Wang, Z. Xie, B. Xie, and K. Liu, "Giant gas discovery in the Precambrian deeply buried reservoirs in the Sichuan Basin, China: Implications for gas exploration in old cratonic basins," *Precambrian Research*, vol. 262, pp. 45–66, 2015.
- [40] B. C. Burchfiel and L. H. Royden, "Tectonics of the Longmen Shan and adjacent regions, central China," *International Geology Review*, vol. 37, no. 8, pp. 661–735, 1995.
- [41] Z. Jin, Y. Yuan, Q. Liu, and Y. Wo, "Controls of Late Jurassic-Early Cretaceous tectonic event on source rocks and seals in marine sequences, South China," *Science China Earth Sciences*, vol. 56, no. 2, pp. 228–239, 2013.
- [42] J. Wang, "Relationship between tectonic evolution and hydrocarbon in the foreland of the Longmen mountains," *Journal of Southeast Asian Earth Sciences*, vol. 13, no. 3-5, pp. 327–336, 1996.
- [43] S. Liu, B. Deng, Z. Li, and W. Sun, "Architecture of basin-mountain systems and their influences on gas distribution: A case study from the Sichuan basin, South China," *Journal of Asian Earth Sciences*, vol. 47, pp. 204–215, 2012.
- [44] P. A. Allen and J. R. Allen, *Basin Analysis: Principles and Application to Petroleum Play Assessment*, Wiley-Blackwell, Chichester, UK, 2013.
- [45] W.-H. Zhang, L.-J. Jiang, H. Gao, and R.-D. Yang, "Study on sedimentary environment and origin of black siliceous rocks of the Lower Cambrian in Giuzhou Province," *Bulletin of Mineralogy Petrology and Geochemistry*, vol. 22, no. 2, pp. 174–178, 2003.
- [46] J. Wang, D. Chen, D. Wang, D. Yan, X. Zhou, and Q. Wang, "Petrology and geochemistry of chert on the marginal zone of Yangtze Platform, western Hunan, South China, during the Ediacaran-Cambrian transition," *Sedimentology*, vol. 59, no. 3, pp. 809–829, 2012.
- [47] J. Z. Huang, S. J. Cheng, L. S. Song Wang Jr., X. M. Gou, T. D. Wang, and H. M. Dai, "Hydrocarbon system of the Sichuan basin and formation of the medium-to-large gas fields," *Science in China (Series D)*, vol. 26, pp. 504–510, 1996.

- [48] Y. C. Kang, "The formation and development of Paleo-uplift in central Sichuan and its oil/gas prospect," *Experimental Petroleum Geology*, vol. 10, pp. 12–23, 1988.
- [49] Y. Zhong, Y.-L. Li, X.-B. Zhang et al., "Evolution characteristics of Central Sichuan palaeouplift and its relationship with early Cambrian Mianyang-Changning intracratonic sag," *Journal of Chengdu University of Technology (Science and Technology Edition)*, vol. 41, no. 6, pp. 703–712, 2014.

## Research Article

# Distribution and Thermal Maturity of Devonian Carbonate Reservoir Solid Bitumen in Desheng Area of Guizhong Depression, South China

Yuguang Hou,<sup>1</sup> Yaqi Liang,<sup>1,2</sup> Sheng He,<sup>1</sup> Yukun Liu,<sup>1</sup> Zhiwei Fan,<sup>3</sup> and Yingrui Song<sup>1</sup>

<sup>1</sup>China University of Geosciences Key Laboratory of Tectonics and Petroleum Resources, Ministry of Education, Wuhan 430074, China

<sup>2</sup>Geological Experimental Testing Center of Hubei Province, Wuhan 430034, China

<sup>3</sup>Petroleum Exploration Branch Company, Sinopec, Chengdu 610041, China

Correspondence should be addressed to Yuguang Hou; [sporthyg@126.com](mailto:sporthyg@126.com) and Sheng He; [shenghe@cug.edu.cn](mailto:shenghe@cug.edu.cn)

Received 3 March 2017; Revised 18 May 2017; Accepted 28 June 2017; Published 15 August 2017

Academic Editor: John A. Mavrogenes

Copyright © 2017 Yuguang Hou et al. This is an open access article distributed under the Creative Commons Attribution License, which permits unrestricted use, distribution, and reproduction in any medium, provided the original work is properly cited.

The distribution of solid bitumen in the Devonian carbonate reservoir from well Desheng 1, Guizhong Depression, was investigated by optical microscope and hydrocarbon inclusions analysis. Vb and chemical structure indexes measured by bitumen reflectance, laser Raman microprobe (LRM), and Fourier transform infrared spectroscopy (FTIR) were carried out to determine the thermal maturity of solid bitumen. Based on the solid bitumen thermal maturity, the burial and thermal maturity history of Devonian carbonate reservoir were reconstructed by basin modeling. The results indicate that the fractures and fracture-related dissolution pores are the main storage space for the solid bitumen. The equivalent vitrinite reflectance of solid bitumen ranges from 3.42% to 4.43% converted by Vb (%) and LRM. The infrared spectroscopy analysis suggests that there are no aliphatic chains detected in the solid bitumen which is rich in aromatics C=C chains (1431–1440  $\text{cm}^{-1}$ ). The results of Vb (%), LRM, and FTIR analysis demonstrate that the solid bitumen has experienced high temperature and evolved to the residual carbonaceous stage. The thermal evolution of Devonian reservoirs had experienced four stages. The Devonian reservoirs reached the highest reservoir temperature 210–260°C during the second rapid burial-warming stage, which is the main period for the solid bitumen formation.

## 1. Introduction

Reservoir bitumen, a type of solid and amorphous organic matter, is the product of maturation of organic matter and can be regarded as a critical symbol to prospect hydrocarbon reservoirs [1–5]. The origin of reservoir solid bitumen is generally attributed to thermal cracking and nonthermal cracking. The thermal events, such as the high overburden temperature and the activity of igneous rocks, can generate the thermal gradual change bitumen and the thermal spikes bitumen, respectively [6]. In the high temperature geothermal-system, the light component chains of bitumen are eventually alkanoylated to generate methane, and the heavy component is condensed to form a polycyclic coke

bitumen residue characterized by a high carbon compound. The pyrolytic bitumen represents the end product of oil thermal cracking. The accumulation of pyrolytic bitumen in reservoirs usually can be used to indicate industrial oil-gas reservoirs. The formation of nonthermal cracking reservoir bitumen is basically due to oxidation, biodegradation, water washing, and deasphalting. Biodegradation is thought to be the most common trigger to secondary alteration of hydrocarbon and accounts for most of heavy oil in the world [7–9].

The occurrence state and geochemical characteristics of solid bitumen record the processes of hydrocarbon generation, migration, and accumulation. There is abundant geological information which is useful for exploration and

exploitation activities in oil and gas bearing basin. The formation and evolution of bitumen are closely related to the evolution history of oil-gas reservoirs, which are of great significance to understand the history of oil and gas reservoirs formation, reconstruction, and destruction [10–12].

Determination of the thermal maturity of solid bitumen is very important to reconstruct the evolution history of reservoirs. Comparing with the bitumen reflectance detection, the laser Raman microprobe (LRM) and Fourier transform infrared spectroscopy (FTIR) can provide maturity information from the chemical structure of solid bitumen. Depending on the ordering degree of the molecular structure arrangement and the change of chemical composition during the thermal evolution, the Raman spectrum characteristic peaks of carbonaceous organic matter show a systematic change with the increase of maturity. Therefore, it can be used as an indicator of Raman spectroscopy that reflects the maturity of carbonaceous organic matter [13, 14]. The correlation between the parameters of laser Raman spectroscopy and the vitrinite reflectance of organic carbonaceous matter has been studied, and several corresponding regression relationships have been proposed [15–18]. Infrared spectroscopy is proven to be an effective method in determining the structure and composition of hydrocarbon organic matter [19, 20]. With increasing maturity, the change of functional groups on FTIR corresponds to the chemical structure conversion of organic matter. During the process of thermal evolution, the aliphatic bands are gradually reduced, to vanish eventually. However, the absorption band of aromatic hydrocarbon will correspondingly increase.

Guizhong Depression is one of the most important areas for oil and gas exploration in the marine carbonate rocks, southern China [21–24]. It is characterized by complex tectonic evolution, multiple sedimentary systems, and multi-stage hydrocarbon accumulations. Abundant oil-gas seepages in the Guizhong Depression including 31 oil-gas seepages and 57 bitumen displays (32 of Devonian, 35 of Carboniferous, 15 of Permian, and 6 of Triassic) have been found previously [25]. The abundant reservoir bitumen and oil sands not only indicate the history of large-scale hydrocarbon generation, migration, and accumulation in this area but also imply the complexity and risk for oil and gas exploration in this area. After having experience of oil and gas exploration in this area for more than 40 years, it is generally accepted that this area has the primitive geological conditions for the formation of medium to large size oil-gas field. Although the ancient reservoirs have undergone frequent destruction and alteration, they may still have residual reservoirs [22, 23, 26].

In 2014, Sinopec deployed the deepest prospecting well Desheng-1 (in what follows named as DS1) on the Desheng biohermal lithologic traps in the Yishan fault depression, north of Guizhong Depression. The drilling depth of well DS1 was 5170.00 m, and its target drilling stratigraphic unit was the Lower Devonian Yujiang Formation. There are no obvious oil and gas shows in the target layer, but some reservoir bitumen shows were found in the Devonian carbonate reservoir. The major objectives of this study were to (1) investigate the distribution characteristics of solid bitumen in the Devonian carbonate reservoir of well DS1 by physical

property observation; (2) document the thermal maturity of the reservoir solid bitumen by reflectivity detection and chemical structure indexes analysis; (3) reconstruct the burial and thermal maturity history of bituminous reservoir based on the erosion thickness restoration and basin modeling technique. Our results not only have theoretical significance but also provide scientific guidance to oil and gas assessment, strategic area selection, and exploration deployment in the study area.

## 2. Geological Setting

The Guizhong Depression is located at the junction zone between the southern margin of the Yangtze plate and the southern Caledonian fold belt (Figure 1(a)). The Guizhong Depression, covering approximately  $4.6 \times 10^4 \text{ km}^2$  is an important part of the Nanpanjiang-Youjiang Basin [21, 27, 28]. This depression can be further divided into 13 subtectonic units. The study area is located in the Yishan fault sag of the Guizhong Depression (Figure 1(b)).

The Guizhong Depression is a large Late Paleozoic marine sedimentary depression overlying the Caledonian movement, which is mainly composed of the Upper Paleozoic marine strata (Figure 2) [30]. During the Hercynian period ( $D - P_1$ ), the study area gradually entered the passive continental margin depression stage. The sedimentary thickness from Devonian to Early Permian is more than 14,000 m [23, 31]. The Lower Devonian was deposited in the tidal flat-shore environment. During Middle and Late Devonian stage, this depression was mainly filled with carbonate and mudstone deposits, formed in the platform and interplatform environment. The Middle and Late Devonian was the main period of reef development [26, 32]. After a brief erosion of the Dongwu movement, the study area entered the Indosinian period. Thick layer of clastic rocks was deposited from the Late Permian to Middle Triassic in the study area [24]. By the late stage of Middle Triassic, the marine sedimentary history of the study area came to an end due to the basin-mountain transition. During the Yanshan-Himalayan period, the Guizhong Depression suffered continuous extrusion uplift. There is less deposition of Triassic-Cretaceous deposit retained by synclines in this study area, and the thickness is about 1500 m [33].

The hydrocarbon accumulation condition of Guizhong Depression was superior in the geological history [22]. The residual bitumen stored in the famous Middle Devonian paleoreservoir of Dachang reef is estimated to be tens of millions of tons. Previous studies suggest that the original oil accumulation could be more than 100 million tons [22, 24]. Therefore, the Devonian is the main target strata for the oil and gas exploration in the study area (Figures 2 and 3). The mudstone of the Middle Devonian Tangding Formation and Luofu Formation deposited in the interplatform basin are the main source rocks, and the dolomite and biohermal limestone deposited in the platform are the main reservoir. Both the mudstone and limestone of Upper Devonian deposited in the interplatform basin and foreslope could be the potential cap rock.

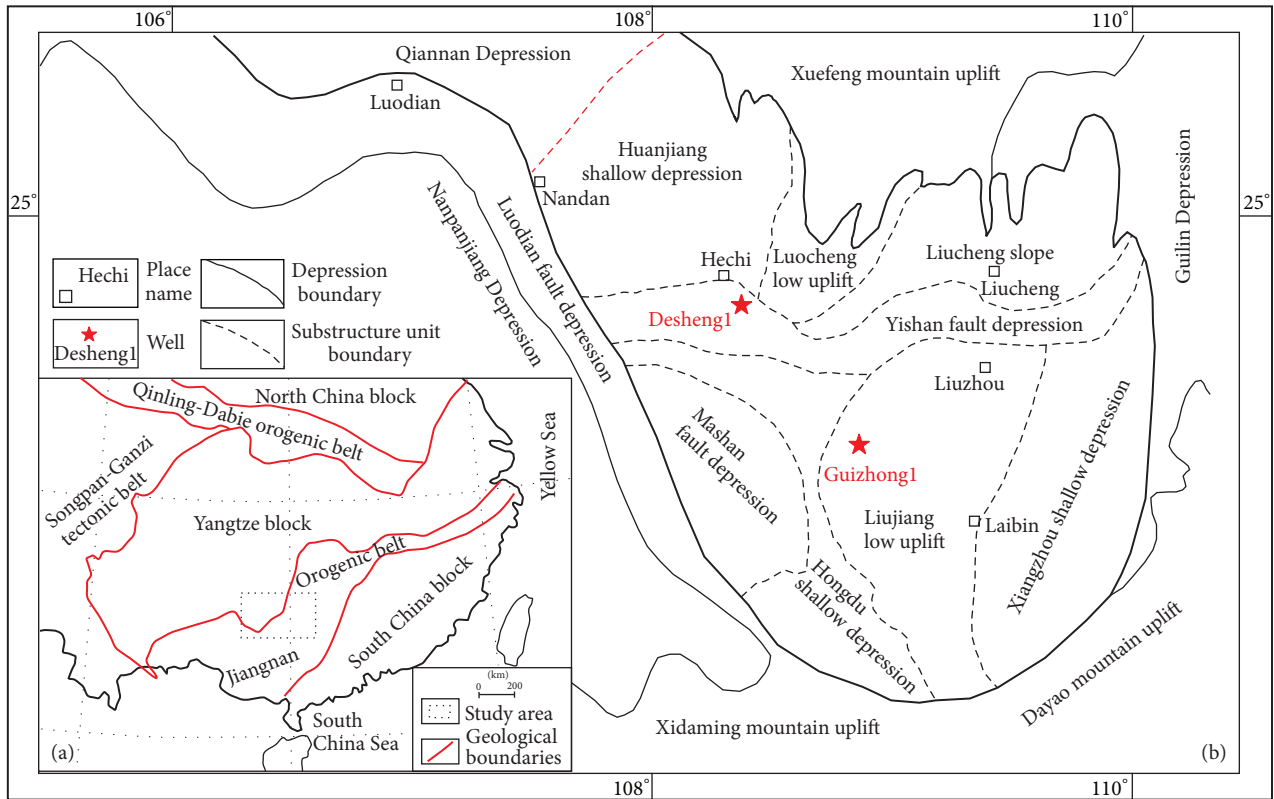


FIGURE 1: (a) The location of the Guizhong Depression. (b) The subtectonic units of Guizhong Depression and the location of sampling wells.

### 3. Samples and Methods

**3.1. Samples.** We collected carbonate samples from Upper Devonian Rongxian Formation and Middle Devonian Yingtang Formation and Donggangling Formation (Figure 2). These formations were deposited in the reef subfacies of the carbonate platform-platform edge. Yingtang Formation is comprised of algal marl and black-gray dolomite. The brachiopod fossils are distributed in the algae marlite, and the thin layer of tiny asphalt particles can be observed on the core cross-section. The 1st section of Donggangling Formation is composed of a set of black-gray algae marl. Rongxian formation developed the oolitic limestone and algal mudstone, and gray-black sheet of highly evolved bitumen can be seen on their core cross-section. Porosity types of the carbonate reservoir can be divided into intraparticle pore and interparticle pore within ooids, intergranular pore within dolomite, dissolution pore and cave, microfracture, and so forth.

In this study, reservoir solid bitumen observation and hydrocarbon inclusions detection were carried out on the carbonate reservoir samples. The laser Raman microprobe analysis was used to determine the composition of the bitumen and hydrocarbon inclusions. The bitumen reflectance detection, laser Raman microprobe, and Fourier transform infrared spectroscopy (FTIR) were used to determine the thermal maturity of solid bitumen. The burial and thermal maturity history of carbonate reservoir bearing solid bitumen of well DS1 were reconstructed by using Basin Model

Simulation Software. FTIR analysis was performed at the Materials and Chemical Analysis and Testing Center, China University of Geosciences (Wuhan). All the other tests were completed at the Key Laboratory of Structural and Oil and Gas Resources, Ministry of Education, China University of Geosciences (Wuhan).

**3.2. Identification on Solid Bitumen and Hydrocarbon Inclusions.** 15 carbonate samples were selected to make the casting thin section slides. The distribution characteristics of solid bitumen and pore structure in these carbonate rocks were studied by using the transmission microscope of Nikon Eclipse LV100 POL, 5x (+). The surface porosity (within bitumen or not) was also be estimated.

Six carbonate samples and 13 calcite vein samples were selected to make double-side polishing thin sections and were analyzed on the identification of hydrocarbon inclusions by using Nikon Eclipse LV100N POL, 100x (+).

**3.3. Laser Raman Microprobe Analysis.** The composition of solid bitumen and hydrocarbon inclusions were analyzed by the laser Raman spectroscopy. The Raman microprobe analyses were collected with a JY/Horiba LabRam HR800 Raman system at room temperature of 25°C, equipped with a frequency doubled Nd:YAG laser (532.06 nm) where output laser power is 14 mW, and laser hit the surface of the sample power is generally 2~12 mW with the line width <0.1 nm. It was equipped with a 50x long-work-distance Olympus

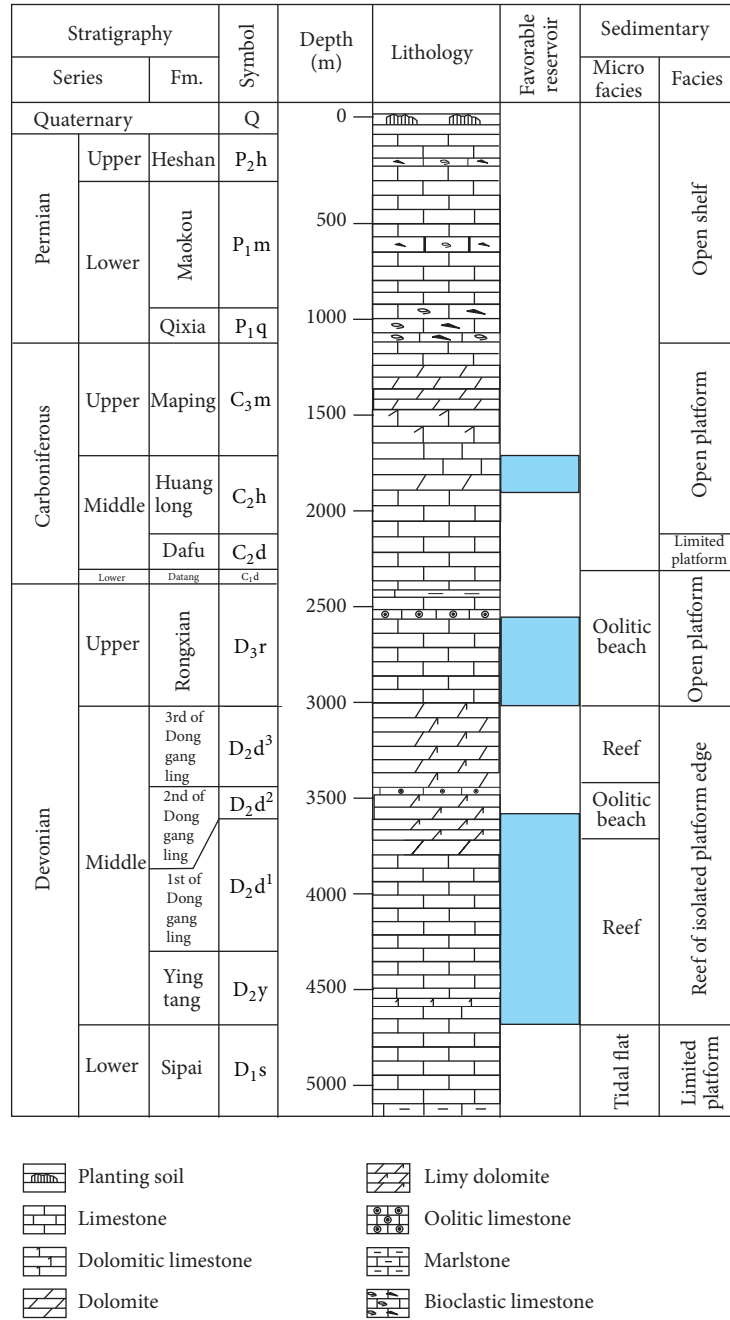


FIGURE 2: The stratigraphic framework of well DS1, Guizhong Depression (see well location in Figure 1).

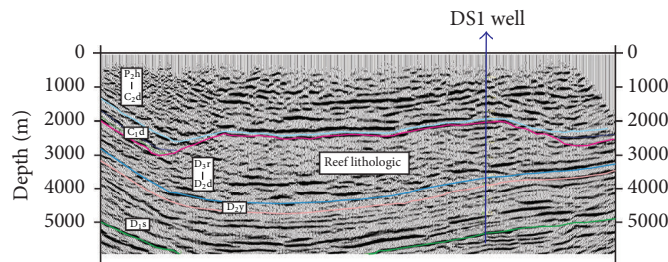


FIGURE 3: Seismic profile of reef lithologic at Desheng area (strata correspond to Figure 2).

objective with a numerical aperture of 0.5. The aperture of the confocal hole was set to 200  $\mu\text{m}$ . Raman peak position was regularly calibrated with the  $\sim 520.7\text{ cm}^{-1}$  band of a polished silicon wafer. The spatial resolution was 0.1  $\mu\text{m}$  in the transverse direction and 0.3  $\mu\text{m}$  in the longitudinal direction, and the data was collected every 40 seconds.

**3.4. Bitumen Reflectance Analysis.** Limited by the sample weight of the test required, only two solid bitumen samples from 1st section of Upper Devonian Donggangling Formation were selected for bitumen reflectance analysis. Jacob [34] proposed that bitumen reflectance could be used as a maturity parameter, due to the stochastic linear relationship between the reflectances of vitrinite and bitumen. Several conversion formulas between the bitumen reflectance and the vitrinite were summarized by Jacob [34], Feng and Chen [35], and Liu and Shi [36]:

$$R_o = 0.6180R_b + 0.4000 \quad [34],$$

$$R_o = 0.6790R_b + 0.3195$$

base on pyrolysis simulation experiment [35],

$$R_o = 0.6569R_b + 0.3364 \quad (1)$$

base on natural thermal evolution [35],

$$R_o = 0.6880R_b + 0.3460 \quad [36],$$

where  $R_o$  is the vitrinite reflectance and  $R_b$  the bitumen reflectance.

Thermal maturity of the two solid bitumen samples was determined by measuring bitumen reflectance and then converting into the vitrinite reflectance by using the above equations.

**3.5. Fourier Transform Infrared (FTIR) Spectroscopy Analysis.** The solid bitumen samples from Upper Devonian Rongxian Formation were analyzed by FTIR. Prior to the experiment, 2 g of the bitumen powder sample was placed in a low-temperature drying oven and dried less than 80°C. Samples were fully mixed with potassium bromide in a ratio of 1:150, and then we placed the mixture in tablet press tested by Thermo Infrared spectrometer. The test is based on GB/T6040-2002 with the detection-ambient temperature of 23°C and the relative humidity of 53%. The infrared spectrum of the bitumen organic matter is in the range of 4000~400  $\text{cm}^{-1}$ .

**3.6. Basin Modeling.** One-dimensional modeling technology can be used to simulate hydrocarbon generation and primary migration, defined as movement of hydrocarbon through and out of the source rocks [37]. BasinMod software was used to carry out the one-dimensional modeling of burial and thermal maturity history. According to the geological background of the study area and conceptual model [15], the instantaneous heat flow history model and the EASY% Ro mature history model are used to simulate the thermal evolution history of well DSI. The equivalent reflectivity of

bitumen and inclusions was used to calibrate modeling results in this study [38, 39].

## 4. Results

**4.1. Distribution Characteristics of Solid Bitumen.** Thin section analysis suggests that the solid bitumen is mainly concentrated in the Upper Devonian Rongxian Formation (2860 m–2870 m), Middle Devonian Donggangling Formation (4210 m–4220 m), and the Yingtang Formation (4640 m–4655 m). The surface porosity filled with solid bitumen ranges from 3% to 8% and is slightly higher in the Rongxian Formation.

Three main filling types of solid bitumen in the reservoir have been observed: fracture filling, dissolution pore filling, and recrystallization pore filling.

**Fracture Filling.** This filling type is mainly developed in the limestone reservoirs. According to the characteristics of fractures filled with solid bitumen, the fractures can be divided into two types: structural fractures and diagenetic dissolution fractures. Structural fractures are mainly found in oolitic limestone of the Upper Devonian Rongxian Formation (Figure 4(a)). The combination of main fracture with branch fractures has the shear characteristics and is distributed in the form of horsetail. The morphology of the ooids on the two sides of the fractures is quite different. The surrounding ooids were always cut through by the fractures, and the broken ooids were filled or disseminated by the bitumen (Figure 4(b)). Diagenetic dissolution fractures display bending and irregular shape and are commonly found in the limestone reservoirs of all layers (Figures 4(c)–4(f)). In the algae marl of the Middle Devonian Donggangling Formation, these fractures are developed around large blocks of calcite crystals (Figures 4(c) and 4(d)). In the black-gray limestone and algae marl of the Middle Devonian Yingtang Formation, it was shown that different fractures filling bitumen interpenetrated each other (Figures 4(e) and 4(f)). This type of fracture is generally filled with bitumen and a small amount of microcrystalline calcite or fine-grained calcite.

**Dissolution Pore Filling.** This filling type of solid bitumen is mainly distributed in the oolitic limestones of the Upper Devonian Rongxian Formation. The dissolution pores of ooids filled with solid bitumen are commonly distributed around the microfractures (Figure 4(a)). The ooids close to the fractures are inclined to be disseminated by bitumen, but the ooids far away from the fractures are well preserved. The solid bitumen within the dissolved ooids displays flocculent and pure black. The filling substance between ooids is mainly composed of microcrystalline calcite or fine-grained calcite. The calcite crystals that are large in size and well-crystallized can be seen occasionally but are not affected by bitumen. In the Donggangling Formation, a small amount of dissolution pore is distributed around the dissolution fractures, and the pores have been filled with carbonaceous bitumen (Figure 4(c)).

**Recrystallization Pore Filling.** They are mainly distributed in dolomitic limestones of the Middle Devonian Yingtang

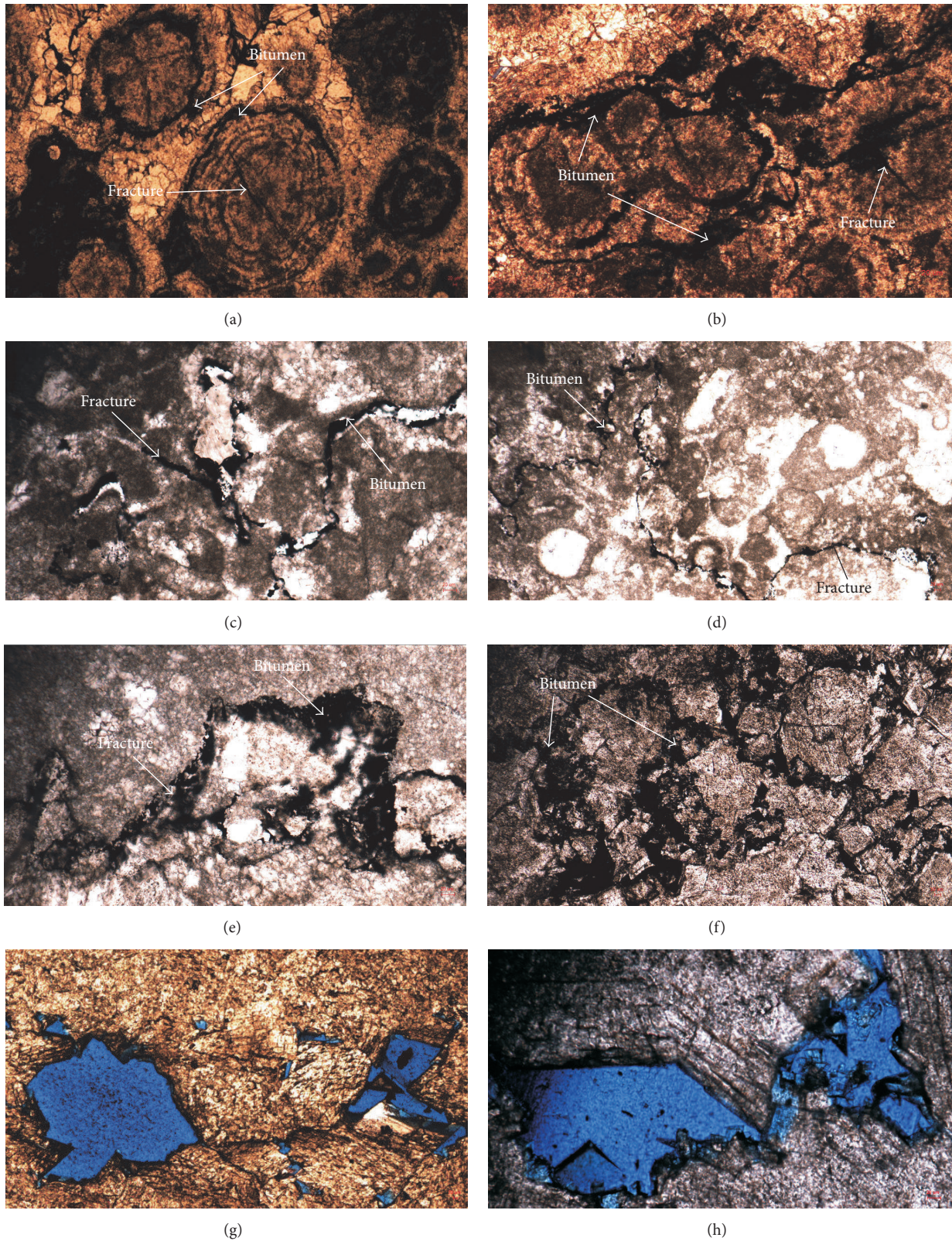


FIGURE 4: Distribution of bitumen in the carbonate reservoirs of well DS1 in Guizhong Depression. ((a) and (b)) DS-X06, 2864.44–2864.49 m, oolitic limestones, 5x (–). Bitumen filled in the fractures and dissolved pores in Rongxian Formation. (c) DS-X44, 4211.21 m, algal mudstone, 10x (–) and (d) DS-X44, 4211.21 m, algal mudstone, 20x (–). Dissolution fractures are filled with bitumen and sparry calcite in the 1st section of Donggangling Formation. (e) DS-X51, 4648.27 m, algal mudstone, 5x (–), and (f) DS-X53, 4648.76–4648.81 m, dolomite, 5x (–). Dissolution fractures are filled with bitumen in Yingtang Formation. (g) DS-X16, 3889.97–3890.05 m, dolomite, 5x (–), and (h) DS-X19, 3894.05–3894.09 m, dolomite, 5x (–), no bitumen filled in the pores and fractures in the upper 1st section of Donggangling Formation.

Formation. The dolomitic limestone shows well-developed and well-crystallized calcite crystals. The recrystallization pores are distributed as a network, concentrate between the calcite crystals, and completely filled with bitumen (Figure 4(f)). The edge of solid bitumen is commonly straight, and some of solid bitumen shows polygonal shape. In addition, the recrystallization pores are also well developed in the dolomite reservoir in the upper 1st section of Middle Devonian Donggangling Formation. However, almost no solid bitumen within these pores was observed based on the cores and casting thin sections analysis (Figures 4(g) and 4(h)). There are some straight structural fractures in the Yingtang Formation without bitumen filling and without or partially filled with secondary calcite.

**4.2. Characteristics of Fluid Inclusions.** Fluid inclusion analysis suggests that there are a large amount of gas-liquid two-phase salt-water inclusions observed in the carbonate reservoirs and calcite veins in the Middle Devonian Yingtang Formation and the Donggangling Formation (Figures 5(a) and 5(b)). Basically, these inclusions are small in size, which are generally 3–5  $\mu\text{m}$  in size (the smallest is less than 3  $\mu\text{m}$  and the largest is close to 9  $\mu\text{m}$ ). The ratio of gas to liquid in the salt-water inclusions is approximately 6–12%. They display oblong or irregular shape, occurring in small clusters along the direction of fracture or paralleling mineral joints. A small amount of bitumen inclusions and methane-containing fluid inclusions were also detected, but no fluorescent hydrocarbon inclusions were observed (Figures 5(c) and 5(d)). The solid bitumen inclusions are dark gray or black in the single polarized opaque and characterized by different size and rectangular or irregular in shape. The methane-containing fluid inclusions display isolated distribution in the dolomite and calcite veins, which were gray-black in the transmission of low transparency light, and have a wide range of shapes such as oval, rectangular, and irregular shape (Figure 5(d)).

**4.3. LRM of Solid Bitumen and Hydrocarbon Inclusions.** Laser Raman Microprobe is a molecular spectral microanalysis technique, and it becomes an effective method for the study of carbonaceous particles in sedimentary and metamorphic sedimentary rocks [16–18]. Based on the principle of “different substances correspond to the corresponding peak position,” organic carbonaceous matters have two characteristic peaks in the frequency range of 1000  $\text{cm}^{-1}$  to 2000  $\text{cm}^{-1}$  on the spectra. The position of the two characteristic peaks are located from 1580  $\text{cm}^{-1}$  to 1600  $\text{cm}^{-1}$  and 1350  $\text{cm}^{-1}$  to 1380  $\text{cm}^{-1}$ , respectively. The formation of the former peak is due to the vibration of the C=C bond on the aromatic configuration plane of the molecule, and the latter is due to the defect between the disordered structure and the aromatic structural unit. The characteristic peaks of hydrocarbon gas are mainly distributed 2890–2594  $\text{cm}^{-1}$ .

**Solid Bitumen.** The laser Raman Microprobe analysis indicates that the dark materials filled within the microfractures and around ooids of the Upper Devonian Rongxian Formation (Figure 6(a)), in the intergranular pores and

fractures of the Middle Devonian Donggangling Formation (Figure 6(b)) and the reticular recrystallized pores of the Middle Devonian Yingtang Formation (Figures 6(c) and 6(d)), manifesting obvious spectral peak characteristics of organic matter. By comparing with the typical laser Raman spectra of carbonaceous bitumen and pyrobitumen reported by Liu et al. [18] (Figures 6(e) and 6(f)), these dark materials can be determined as solid bitumen.

**Hydrocarbon Inclusions.** The laser Raman spectra of suspected bitumen inclusions in the gray dolomite of Donggangling Formation are shown in Figures 7(a) and 7(b). In the spectrums of bitumen inclusions, two typical organic characteristic peaks appeared in the frequency range of 1000  $\text{cm}^{-1}$ –2000  $\text{cm}^{-1}$ , indicating that the inclusions contained bitumen organic matter. As the inclusions are small and not clear, the test location is mostly gas-liquid-mineral mixed phase. Therefore, the spectrums often contain the characteristic peaks of the background minerals, mainly including calcite or some other carbonate minerals. Additionally, the peaks of water can also be displayed on the spectrograms, which have larger width and lower height.

The laser Raman spectra of suspected methane-containing fluid inclusions in the dolomite reservoirs of the Donggangling Formation and the calcite veins of the Yingtang Formation are shown in Figures 7(c) and 7(d). The response level of the inclusions' component may be limited by the size of the inclusions and their hydrocarbon content. The positions of the Methane Raman scattering peak ( $V_1$ ) in the spectrograms of the Donggangling Formation are mainly in the range of 2910–2945  $\text{cm}^{-1}$  (Figure 7(c)). The reason for such a wide peak may be affected by the ethane composition that existed in the inclusion. In the Yingtang Formation (Figure 7(d)), the  $V_1$  peak in the spectrograms has higher response where the position is around 2925.99  $\text{cm}^{-1}$ .

#### 4.4. Thermal Maturity of Solid Bitumen

(1) **Bitumen Reflectance.** Thermal maturity of solid bitumen can be determined by measuring their reflectance and converting into the vitrinite reflectance [6]. The bitumen reflectance values (%  $R_b$ ) of the two samples from the 1st section of Donggangling Formation are 5.35% and 5.44%, respectively (Table 1). The equivalent vitrinite reflectances are ranging from 3.70%  $R_o$  to 4.09%  $R_o$  based on the different conversion formulas.

(2) **Equivalent Vitrinite Reflectance by LRM.** Due to the regular change of the distance between vibration peaks G and D and the ratio of their heights with the increase of maturity, Liu et al. [18] proposed that equivalent reflectance ( ${}_{\text{Rmc}}R_o\%$ ) converted by the Raman spectroscopy analysis parameters could be used as a maturity parameter. The equivalent reflectivity of solid bitumen can be calculated through the equation “ ${}_{\text{Rmc}}R_o\% = 1.1659h \text{ (Dh/Gh)} + 2.7588$ ” (where  $h$  (Dh/Gh) is the ratio of peak height of peaks G and D), which is suitable for thermal evolution stage from overmature to granular graphitization.

TABLE 1: Results of equivalent vitrinite reflectance by bitumen reflectance.

Sample number	Formation	Lithology of reservoir	Bitumen reflectance (%)	Equivalent vitrinite reflectance (%)			
				Jacob, 1989	Feng and Chen, 1988 Pyrolysis	Natural Liu and Shi, 1994	
DSI-5-1	D <sub>2</sub> d <sup>1</sup>	Muddy Limestone	5.35	3.70	3.95	3.85	4.03
DSI-5-4	D <sub>2</sub> d <sup>1</sup>		5.44	3.76	4.01	3.91	4.09

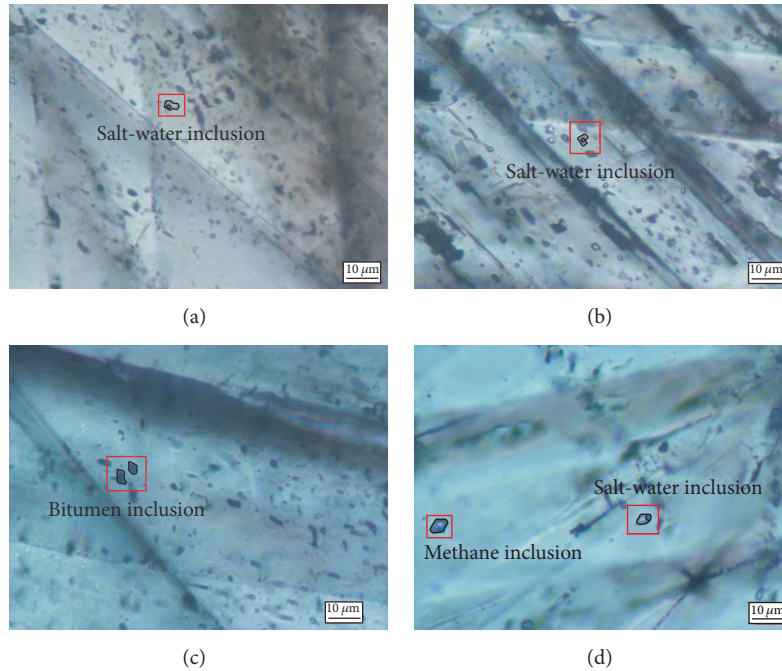


FIGURE 5: Photomicrographs of fluid inclusions trapped in calcite veins. ((a) and (b)) Gas-liquid two-phase salt-water inclusions in the calcite veins of carbonate reservoirs of the 1st section of Donggangling Formation, 3802.22 m, transmitted light. (c) Solid bitumen inclusions in the calcite veins of carbonate reservoirs of Yingtang Formation, 4653.16 m, transmitted light. (d) Gas-liquid two-phase salt-water inclusion and methane-containing fluid inclusion in the calcite veins of carbonate reservoirs of Yingtang Formation, 4653.16 m, transmitted light.

The equivalent vitrinite reflectance calculated from the laser Raman characteristic peaks of the bitumen in thin sections are shown in Table 2, and the values range between 3.42 and 4.43%. The equivalent vitrinite reflectance values of the bitumen inclusions range from 3.80% to 4.23% (Table 2). The conversion values are consistent with the vitrinite reflectance calculated from the measured bitumen reflectivity, and both results indicate that the Devonian carbonate reservoirs of well DSI have experienced high thermal evolution to the quasi-metamorphism stage.

**4.5. Infrared Spectroscopy of Solid Bitumen.** Limited by the amount of samples, only several solid bitumen samples from the Upper Devonian Rongxian Formation are eligible for this experiment. The results are shown in Figure 8.

According to the principles of infrared spectroscopy and organic chemistry, as well as the most likely distribution of the various bands summarized by the predecessors [3, 5, 40–42], the most likely functional groups represented by the absorption peaks in the solid bitumen infrared spectrum of this test can be summarized as follows: (1) the peaks of free

water, adsorbed water, crystal water, and structured water are shown, respectively, in the vicinity of  $3756\text{ cm}^{-1}$ ,  $3435\text{ cm}^{-1}$ ,  $3200\text{--}3250\text{ cm}^{-1}$ , and  $3640\text{ cm}^{-1}$ , which are related to stretching vibration of -OH groups in molecular water; (2) the bands locating in  $1600\text{--}1550\text{ cm}^{-1}$  and  $1450\text{ cm}^{-1}$  are mainly related to the C=C group skeleton vibration of aromatic hydrocarbons; (3) the bands locating in  $3100\text{--}3000\text{ cm}^{-1}$  show the stretching vibration of the chemical bond of the C-H on the aromatic ring; (4) the absorption peak at the  $1154.74\text{--}1021.46\text{ cm}^{-1}$  position may be related to the structure of the Si-O chemical bond of the clay mineral; (5) the weakly continuous bands at  $880\text{ cm}^{-1}$  to  $680\text{ cm}^{-1}$  are related to the out-of-plane bending vibration of the chemical bond of C-H of various aromatic hydrocarbons and depend on the number of adjacent protons; and (6) the bands locating in the vicinity of  $1420\text{ cm}^{-1}$ ,  $955\text{--}954\text{ cm}^{-1}$ , and below  $680\text{ cm}^{-1}$  are heteroatom absorption peaks.

The results show that the band peak of the oxygen-containing groups (C=O) displayed at  $1710\text{ cm}^{-1}$  have disappeared completely (Figure 8). Only a very little band peak

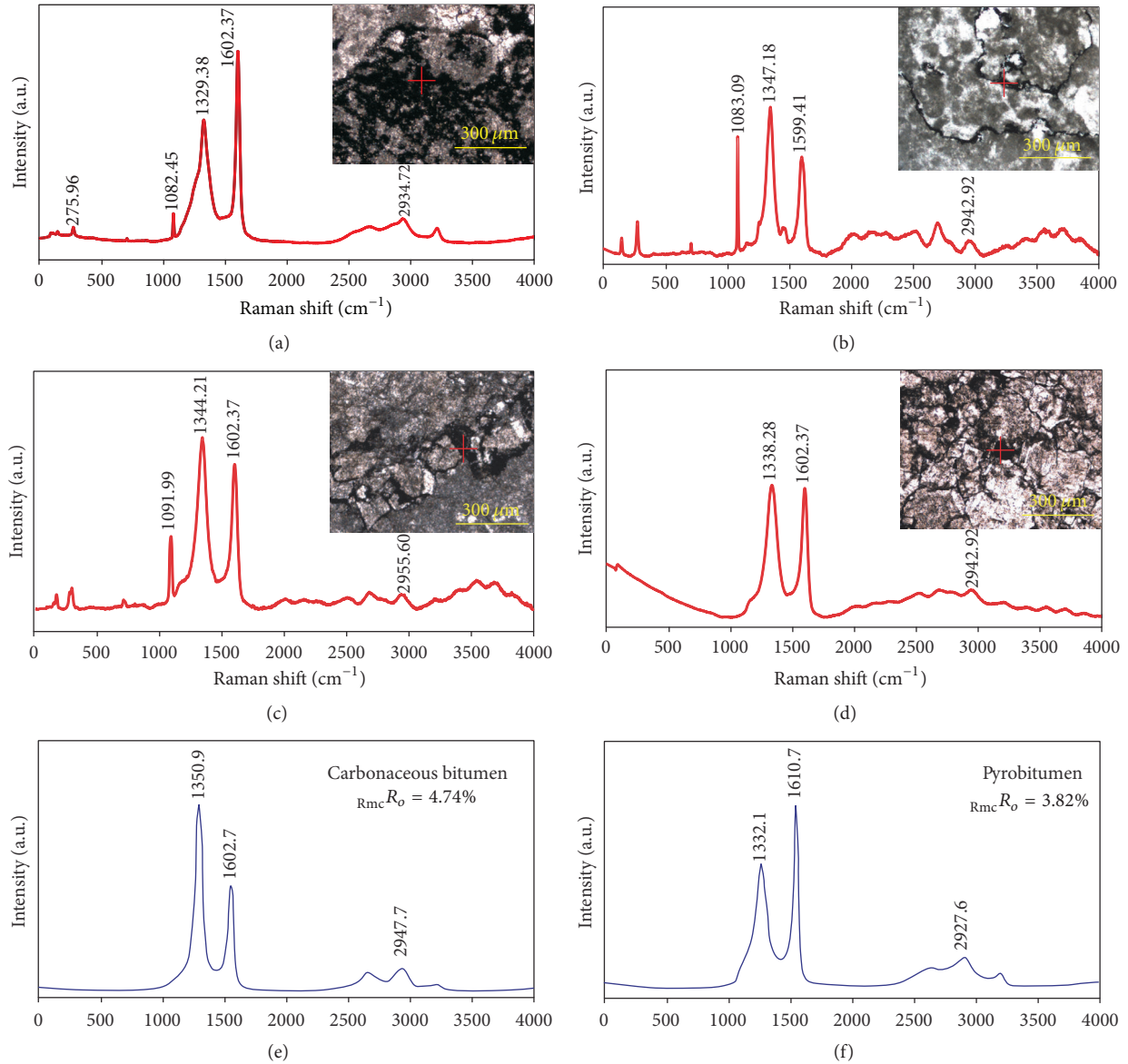


FIGURE 6: Laser Raman spectra of the solid bitumen in well DS1 and typical bitumen from previous publication. (a) DS-X06, 2864.44–2864.49 m, Rongxian Formation, oolitic limestones, 5x (–). (b) DS-X44, 4211.21 m, 1st section of Donggangling Formation, algal mudstone, 10x (–). (c) DS-X51, 4648.27 m, Yingtang Formation, algal mudstone, 5x (–). (d) DS-X53, 4648.76–4648.81 m, Yingtang Formation, dolomite, 5x (–). (e) Carbonaceous bitumen with  $R_{mc}R_o = 4.74\%$  and (f) pyrobitumen with  $R_{mc}R_o = 3.82\%$  taken from Liu et al. [18]. +: the exact location of the laser Raman analysis.

of aliphatic chain located in 2800–3000  $\text{cm}^{-1}$  exist on the FTIR spectrum (Figure 8). Except for the slight absorption peak near 875  $\text{cm}^{-1}$  and 710  $\text{cm}^{-1}$ , the bands of out-of-plane bending vibration of C-H chemical bond have also all disappeared. It indicates that the alkyl hydrocarbon chains in the bitumen samples almost have been depleted. On the other hand, the peaks associated with aromatics C=C or C-C bonds located in 1431–1440  $\text{cm}^{-1}$  are apparently higher than any other band peaks (Figure 8). Such characteristic FTIR spectrum generally represents the organic matter except low maturity samples, which indicates that the high thermal mature bitumen samples are enriched with aromatics and

have a relatively high condensation degree of aromatic rings [4, 5, 29].

4.6. *Thermal Evolution History of Devonian Carbonate Reservoirs.* Based on the geothermal gradient map and the geothermal flow chart of China [43–45], the present geothermal gradient of the Guizhong Depression is about 3.5°C/100 m and the heat flux is ranging from 45 to 55  $\text{mW}/\text{m}^2$ . According to the regional paleogeographic data, the paleogeothermal gradient in the Guizhong Depression prior to the late Indosinian uplift is estimated to be 2.82°C/100 m. There are two important uplift erosion movements in the

TABLE 2: Equivalent vitrinite reflectance of bitumen converted by LRM.

Sample number	Formation	Type of sample	Lithology of reservoir	Equivalent vitrinite reflectance (%)
DS-D01				3.55
DS-D02				3.79
DS-D05	D <sub>3</sub> r	Bitumen Samples	Oolitic limestone	3.74
DS-X06				3.42
DS-X10			Algal mudstone	3.64
DS-X44	D <sub>2</sub> d <sup>1</sup>	Bitumen Samples	Algal mudstone	4.43
DS-X51	D <sub>2</sub> y	Bitumen Samples	Algal mudstone	4.09
DS-X53			Dolomite	3.46
DS-X19-8-1				4.23
DS-X19-9				3.80
DS-X19-10	D <sub>2</sub> d <sup>1</sup>	Bitumen Inclusions	Dolomite	3.86
DS-X20-4				3.77
DS-X20-5				3.76

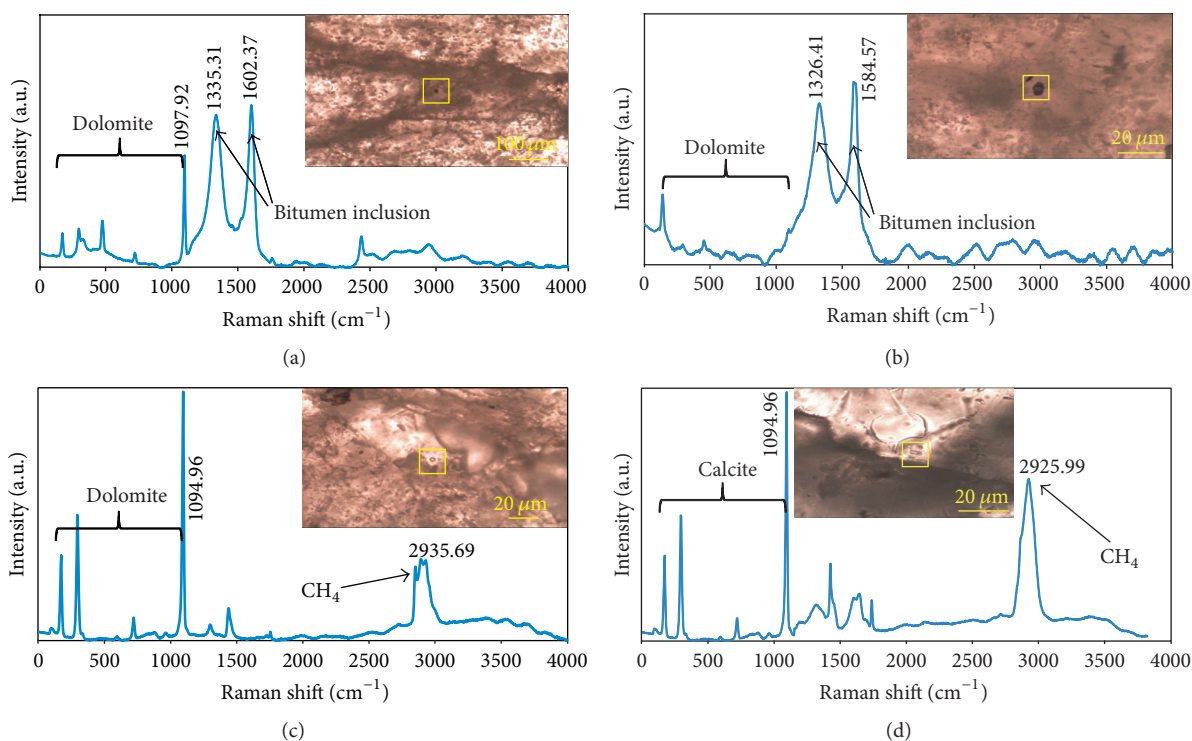


FIGURE 7: Laser Raman spectra for the bitumen and methane-containing fluid inclusion in the calcite vein and dolomite of well DS1. (a) DS-X19, 3894.07 m, Bitumen inclusion within the dolomite of 1st section of Donggangling Formation. ((b) and (c)) DS-X20, 3895.49 m, Bitumen and methane-containing fluid inclusion within the dolomite of 1st section of Donggangling Formation. (d) DS-X64, 4653.16 m, methane-containing fluid inclusion within the calcite vein of Yingtang Formation.

Guizhong Depression. By using the Easy% *Ro* model simplified by Wang et al. [46], the erosion thickness of the main tectonic uplift-denudation stage (late Indosinian-Yanshan-Himalayan period) in well DS1 can be restored as approximately 4012.9 m according to the measured equivalent *Ro* data in this study. The erosion thickness of the Guizhong Depression during Yanshan-Himalayan Period was calculated by the previous study to be around 4000 m based on the homogenization temperature of fluid inclusions and

vitrinite reflectivity [23, 33]. The erosion thickness of Dongwu movement, which occurred during the early Indosinian, could not be calculated accurately. Its thickness roughly ranges from 300 to 500 m according to previous publications [47, 48]. In this paper, we assigned erosion thickness of 400 m for the Dongwu movement.

The detailed maturity history of Devonian carbonate reservoirs in well DS1 is modeled (Figure 9(a)). A very good correlation between measured and modeled temperatures

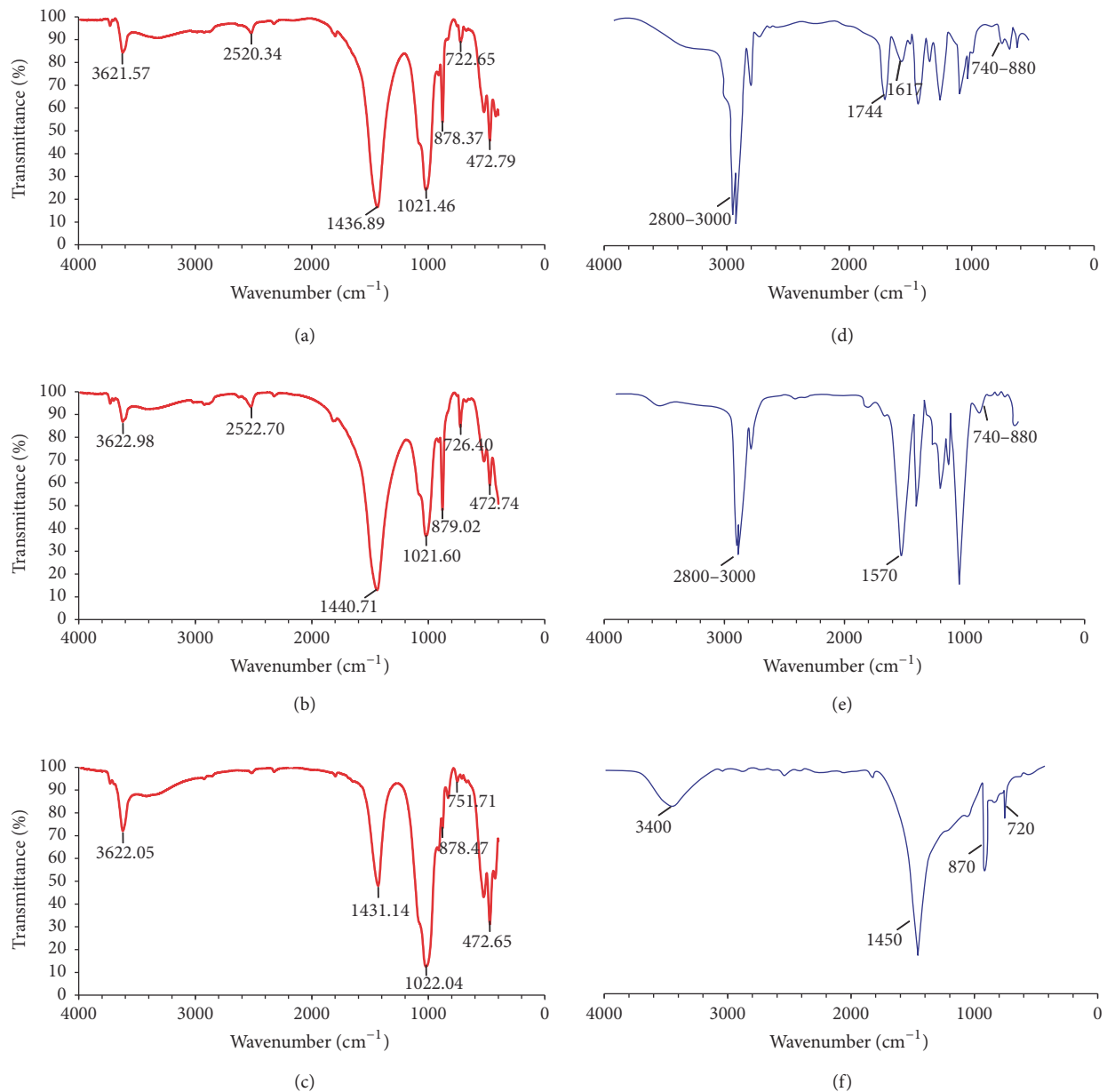


FIGURE 8: Infrared spectroscopy of solid bitumen in Rongxian Formation of well DS1 and other area. (a) DS-D02, 2866.70 m, (b) DS-D09, 2866.78 m, and (c) DS-D12, 2868.08 m of oolitic limestone in well DS1. (d) Silurian bitumen from well H1 (6081 m) of Tarim Basin,  $R_o$  (%) = 0.36% [29], characterized with richness in aliphatic chains (2800–3000 cm<sup>-1</sup>). (e) Carboniferous bitumen from well LN14 (5070 m) of Tarim Basin,  $R_o$  (%) = 0.64% [29], characterized with richness in aliphatic chains (2800–3000 cm<sup>-1</sup>). (f) Cambrian bitumen from Northwestern Hunan, depth = 335 m,  $R_o$  (%) = 4.88% [3], characterized with lack of aliphatic chains and richness in aromatics C=C chains (1450 cm<sup>-1</sup>).

and equivalent  $R_o$  values implies that thermal and maturity history model are a good fit for this study area (Figure 9(b)). As shown in Figure 9, the Devonian Formation began to enter early mature threshold ( $R_o = 0.5\%$ ) at a depth range of 1800–2000 m and at a temperature range of 105–115°C during the deposition of 2nd section of Donggangling Formation. Beginning at the early stage of Triassic deposition (around 240 Ma), the Devonian reservoirs passed the overmature stage threshold ( $R_o > 2.0\%$ ), successively. The maximum experienced temperature of Yingtang Formation and Rongxian Formation of well DS1 occurred during Middle Triassic

and reached the highest temperature of 265°C and 225°C, respectively.

## 5. Discussion

**5.1. Distribution Characteristics of Solid Bitumen.** The fractures and the dissolution pores associated with the fracture are the main existing forms of solid bitumen in the limestone reservoirs, whereas the recrystallized pores are the main storage space for the solid bitumen in the dolomitic limestone.

There are obvious differences in the size of the ooids on both sides of the diagenetic fractures of the Upper Devonian

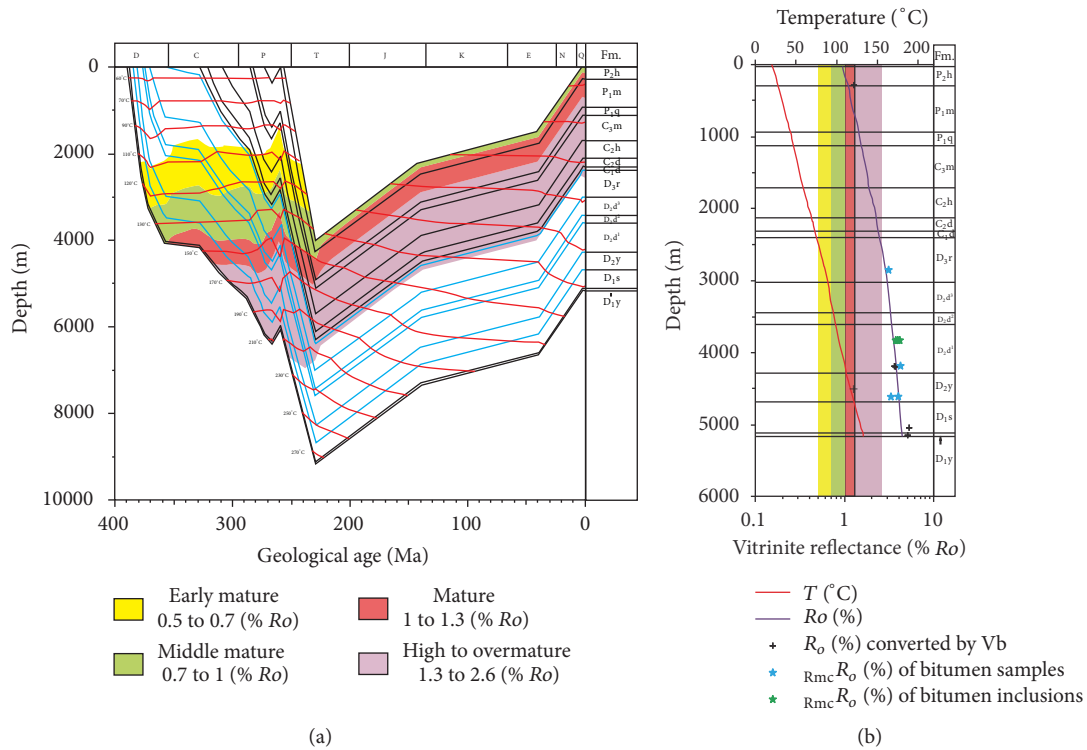


FIGURE 9: Thermal maturity history modeling of well DS1 (a) (see well location in Figure 1 and stratigraphic units in Figure 2) and temperature and maturity calibration (b) (right). +: the measured temperature ( $^{\circ}\text{C}$ ) and the bottom hole temperature. The red line is modelling temperature. The dark line is modelling  $R_o$ .

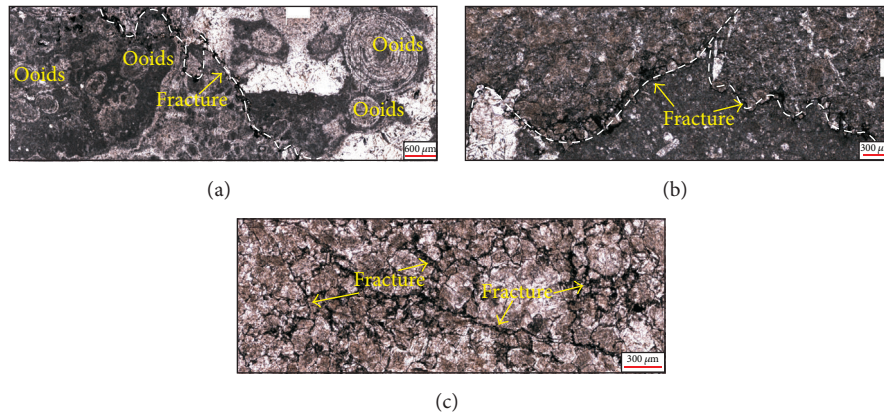


FIGURE 10: Distribution of bitumen in the carbonate reservoirs of well DS1 in Guizhong Depression. (a) DS-X08, 2866.24–2866.35 m, 5x (-), differences in ooids size on both sides of the diagenetic fracture in oolitic limestones of Rongxian Formation. (b) DS-X51, 4648.27 m, 5x (-), differences in size of calcite crystals on both sides of the dissolution fractures in algal mudstone of Yingtang Formation. (c) DS-X53, 4648.76–4648.81 m, 5x (-), grid-like dissolution fractures in dolomite of Yingtang Formation.

Rongxian Formation (Figure 10(a)), and there are also some differences in the size of calcite crystals on both sides of the diagenetic dissolved fractures (Figure 10(b)). It is speculated that these fractures are formed by mechanical compaction or tectonic stress during early diagenetic stage. These fractures were then dissolved to dissolution fractures by the liquid hydrocarbons and other acidic fluids generated at later stage. Finally, the liquid hydrocarbons were transferred into bitumen. Dissolution and recrystallization play an important

role in the formation of dissolved pores and the filling of the bitumen in the dolomitic limestone of the Middle Devonian Yingtang Formation. The network distribution of the solid bitumen in the Middle Devonian Yingtang Formation indicates that it may be associated with the early developed diagenetic fractures (Figure 10(c)). The diagenetic fractures not only provide main channels for the hydrocarbons and dissolved fluids flow but also expand the distribution range of dissolution pores due to the dissolution. These crossed

fractures are favorable to bitumen and secondary calcite filling. The fractures and pores filled with solid bitumen are supposed to be formed at the early stage of oil production and injection.

In the upper section of Donggangling Formation, there is no obvious bitumen filling in the pores of high quality dolomite reservoirs. However, bitumen inclusions and methane-containing fluid inclusions found in these reservoirs could be considered as the evidences for the oil and gas activities (Figures 6 and 7). There are two possible reasons for this phenomenon: one is that the reservoirs were formed before the main period of liquid hydrocarbon generation and migration but were not in the favorable place for the hydrocarbon accumulation in the reef traps. They are only the carrier beds, even not on the main migration path for the hydrocarbons. Thus, these reservoirs only captured a small amount of hydrocarbon inclusions. The other reason could be that the reservoirs were formed after the significant hydrocarbon generation and charging. Only a small amount of hydrocarbon inclusions was captured during the hydrocarbon migration process of fluid activity after the reservoir destruction. With the same reason, there were no obvious bitumen deposits in the flat tectonic fractures of the reservoir (Figures 4(g) and 4(h)). Few inclusions of bitumen and methane were found in some calcite veins (Figure 5), indicating that these fractures probably formed during the adjustment and reform stage of liquid hydrocarbon accumulation.

**5.2. Thermal Maturity of Solid Bitumen.** The bitumen observed on the core DS1 was described as hard, brittle, steel-gray, insoluble in chloroform, conchoidal fracture, and nonfluorescent. These features are similar to the carbon bitumen with high thermal evolution degree in paleoreservoirs of Nanpanjiang area [1, 24]. This suspected solid bitumen observed by microscope mainly filled in the microfractures, intergranular pores, dissolved holes, and intercrystal pores and display several regular morphologies (Figure 4). They show some clear characteristics of pyrobitumen and similar to the solid bitumen in the carbonate reservoir of well Guizhong 1, Sichuan Basin [1, 49]. This pyrobitumen is different from the precipitation bitumen and biodegraded bitumen which are grainy and irregular in shape.

The spectra of the laser Raman spectroscopy and infrared spectroscopy suggest that the solid bitumen has characteristics of highly evolved aromatic compounds. The vitrinite reflectances calculated by the laser Raman spectra are strongly consistent with the vitrinite reflectances converted from bitumen reflectance (Tables 1 and 2), indicating that the solid bitumen has reached a mature stage of metamorphism. In order to highlight the high thermal maturity characteristics of the solid bitumen in this study, the infrared spectra of the solid bitumen in Rongxian Formation are compared with the different maturity bitumen published by previous researchers (Figure 8). The infrared spectroscopy of the low maturity bitumen from Tarim Basin is characterized as aliphatic chains enrichment ( $2800\text{--}3000\text{ cm}^{-1}$ ) (Figures 8(d) and 8(e)), which is obviously different from the solid bitumen in this study [4, 29]. The solid bitumen of Rongxian

Formation is similar to the anthraxolite of Cambrian ( $R_o\%$  is 4.88%) reported by Cao et al. [3], which is characterized with lack of aliphatic chains but richness in aromatics C=C chains ( $1450\text{ cm}^{-1}$ ). The result of comparison demonstrates that the solid bitumen had undergone a very high thermal evolution degree and had evolved to the residual carbonaceous stage such as pyrobitumen and schungite [2, 5].

**5.3. Thermal Evolution History of Devonian Reservoirs.** According to the comprehensive analysis of basin simulation and the thermal maturity of solid bitumen, the thermal evolution history of Devonian reservoirs in well DS1 can be divided into four stages:

- (1) The early rapid burial-warming stage from Early and Middle Devonian to Middle and Late Permian: the Rongxian Formation entered the medium mature stage and the bottom temperature of the reservoir reached  $140^\circ\text{C}$ . The 1st sections of Donggangling Formation and the Yingtang Formation were in stage of mature to overmature, and the temperature of the reservoir reached up to  $190^\circ\text{C}$ . After this stage, the liquid crude oil that filled the Devonian carbonate reservoir has been cracked into wet gas and lower maturity bitumen.
- (2) During the Late Permian, the study area entered into a temporary uplift-cooling stage caused by Donggwu movement. The Devonian reservoir was uplifted several hundred meters, and the reservoir temperature decreased by about  $10\text{--}20^\circ\text{C}$ .
- (3) The rapid burial-warming stage from Late Permian to Early and Middle Triassic: at the end of the Permian, the 1st section of Donggangling Formation and the Yingtang Formation completely entered the overmature stage, and the temperature of the reservoirs was over  $200^\circ\text{C}$ . The lower part of Rongxian Formation also entered into overmature stage at Early Triassic ( $R_o = 2.0\%$ ). As a result of this rapid burial and warming up, the entire Devonian reservoirs in well DS1 have experienced the stage of overmature and metamorphism. And they have reached the highest reservoir temperature of  $210\text{--}260^\circ\text{C}$  before the tectonic uplift caused by late Indosinian orogeny occurred at the late period of Early Triassic. At this stage, the lower maturity bitumen was further thermally cracked into pyrobitumen because of high temperature.
- (4) Since Middle Triassic, the study area entered a slow uplift and cooling stage. The uplift and erosion that occurred during Yanshan-Himalayan period have significant influence on the thermal maturity evolution of the Devonian reservoirs. From 230Ma to present, there was no increase in the maturity probably because of the uplift and having no deeper burial. The temperature of Devonian reservoirs has been reduced by  $120^\circ\text{C}$  due to the uplift to the present-day depth.

## 6. Conclusions

The following conclusions can be drawn in this study:

- (1) Fractures and fracture-related dissolution pores are the main storage space for solid bitumen.
- (2) The equivalent vitrinite reflectance of the solid bitumen in well DSI ranges from 3.42% to 4.43%, and no aliphatic chains were detected by the FTIR.
- (3) The pyrobitumen in Devonian carbonate reservoir is supposed to be the result of thermal cracking in the high temperature after crude oil charged into the reservoir at the early stage.
- (4) The thermal maturity history demonstrates that the Devonian reservoirs have experienced four stages. The entire Devonian reservoirs reached the highest reservoir temperature 210–260°C during the second rapid burial-warming stage, which is the main period for solid bitumen formation.

## Conflicts of Interest

The authors declare that they have no conflicts of interest.

## Acknowledgments

The study was financially supported by the National Science Foundation of China (no. 41302111; no. 41672139), the Program of Introducing Talents of Discipline to Universities (no. B14031), the Foundation of China Geological Survey (no. 12120114046901), and the thirteenth research plan of the Ministry of Science and Technology of China (nos. 2016ZX05034002-003 and 2017ZX05049005-007). The authors are very grateful to the Petroleum Exploration Branch Company of Sinopec for their kind help and support to complete this study and the permission to publish the results.

## References

- [1] M. Zhao, S. Zhang, L. Zhao, and J. Da, "Geochemical features and genesis of the natural gas and bitumen in paleo-oil reservoirs of Nanpanjiang Basin, China," *Science in China, Series D: Earth Sciences*, vol. 50, no. 5, pp. 689–701, 2007.
- [2] W. G. Li, Y. H. Duan, L. K. Yan, and Z. Z. Sun, "Study on measuring method of asphalt using infrared spectrum characteristic of petroleum pitch," *Petroleum Asphalt*, vol. 26, pp. 9–14, 2012 (Chinese).
- [3] D. Y. Cao, X. S. Zhu, J. M. Deng, Z. N. Li, and Y. D. Wu, "Analysis on features of anthraxolite from Northwestern Hunan Wanrongjiang Mine and geological meaning," *Coal Science and Technology*, vol. 41, pp. 109–112, 2013.
- [4] T. S. Song, L. Liu, Q. A. Meng, N. Liu, and X. R. Ming, "Characteristics of reservoir bitumen and its influence on reservoir properties in Fuyu oil layer, Daqing Placanticline," *Global geology*, vol. 34, pp. 1079–1083, 2015 (Chinese).
- [5] R. H. Zhang, C. S. Si, L. Huang et al., "Genesis and evolution of reservoir bitumen in Xiaocaoba paleo-oil reservoir, Qianbei Depression," *Petroleum Geology & Experiment*, vol. 39, pp. 99–105, 2017 (Chinese).
- [6] Y. Xiong, W. Jiang, X. Wang et al., "Formation and evolution of solid bitumen during oil cracking," *Marine and Petroleum Geology*, vol. 78, pp. 70–75, 2016.
- [7] A. J. Lomando, "The influence of solid reservoir bitumen on reservoir quality," *AAPG Bull.*, vol. 76, pp. 1137–1152, 1992.
- [8] L. F. Liu, J. Z. Zhao, S. C. Zhang, J. H. Fang, and Z. Y. Xiao, "Genetic types and characteristics of the Silurian asphaltic sandstones in Tarim Basin," *Acta Petrolei Sinica*, vol. 21, no. 6, pp. 12–17, 2000 (Chinese).
- [9] J. C. Jin, J. Z. Qin, Z. R. Zhang, M. Fan, and Q. Zhang, "Genetic analysis of the high matured bitumen in Songpan-Aba area," *Petroleum Geology & Experiment*, vol. 26, no. 4, pp. 370–374, 2004.
- [10] Rogers, "Significance of reservoir bitumens to thermal maturation studies, Western Canada Basin," *AAPG*, vol. 58, no. 9, pp. 1806–1824, 1974.
- [11] L. D. Stasiuk, "The origin of pyrobitumens in Upper Devonian Leduc Formation gas reservoirs, Alberta, Canada: An optical and EDS study of oil to gas transformation," *Marine and Petroleum Geology*, vol. 14, no. 7-8, pp. 915–929, 1997.
- [12] R. J. Hwang, S. C. Teerman, and R. M. Carlson, "Geochemical comparison of reservoir solid bitumens with diverse origins," *Organic Geochemistry*, vol. 29, no. 1-3, pp. 505–517, 1998.
- [13] S. R. Kelemen and H. L. Fang, "Maturity trends in Raman spectra from kerogen and coal," *Energy and Fuels*, vol. 15, no. 3, pp. 653–658, 2001.
- [14] Y. Zeng and C. Wu, "Raman and infrared spectroscopic study of kerogen treated at elevated temperatures and pressures," *Fuel*, vol. 86, no. 7-8, pp. 1192–1200, 2007.
- [15] J. J. Sweeney and A. K. Burnham, "Evolution of a simple modal of vitrite reflectance on chemical kinetics," *AAPG Bull.*, vol. 74, pp. 1559–1570, 1990.
- [16] J. W. Schopf, A. B. Kudryavtsev, D. G. Agresti, A. D. Czaja, and T. J. Wdowiak, "Raman imagery: A new approach to assess the geochemical maturity and biogenicity of permineralized Precambrian fossils," *Astrobiology*, vol. 5, no. 3, pp. 333–371, 2005.
- [17] J. W. Schopf and A. B. Kudryavtsev, "Confocal laser scanning microscopy and Raman imagery of ancient microscopic fossils," *Precambrian Research*, vol. 173, no. 1-4, pp. 39–49, 2009.
- [18] D. Liu, X. Xiao, H. Tian et al., "Sample maturation calculated using Raman spectroscopic parameters for solid organics: Methodology and geological applications," *Chinese Science Bulletin*, vol. 58, no. 11, pp. 1285–1298, 2013.
- [19] L. Wei, Y. Wang, and M. Mastalerz, "Comparative optical properties of macerals and statistical evaluation of mis-identification of vitrinite and solid bitumen from early mature Middle Devonian – Lower Mississippian New Albany Shale: Implications for thermal maturity assessment," *International Journal of Coal Geology*, vol. 168, pp. 222–236, 2016.
- [20] A. Grobe, J. L. Urai, R. Littke, and N. K. Lünsdorf, "Hydrocarbon generation and migration under a large overthrust: The carbonate platform under the Semail Ophiolite, Jebel Akhdar, Oman," *International Journal of Coal Geology*, vol. 168, pp. 3–19, 2016.
- [21] H. D. Chen, M. C. Hou, W. J. Liu, and J. C. Tian, "Basin evolution and sequence stratigraphic framework of south of China during Hercynian cycle to Indo-Chinese epoch," *Journal of Chengdu University of Technology: Science & Technology Edition*, vol. 31, no. 6, pp. 629–635, 2004 (Chinese).

- [22] M. C. Hou, H. D. Chen, and J. C. Tian, "Study on reservoir characteristics of the Late Paleozoic reef in Youjiang basin, China," *Journal of Chendu University of Technology (Science & Technology Edition)*, vol. 32, no. 3, pp. 231–238, 2005 (Chinese).
- [23] Z. L. Chen, G. S. Yao, Q. X. Guo et al., "Hydrocarbon accumulation and thermal reconstruction of Neopaleozoic marine strata in Guizhong Depression," *Marine Origin Petroleum Geology*, vol. 15, no. 3, pp. 1–10, 2010 (Chinese).
- [24] X. Y. He, G. S. Yao, X. S. He et al., "Bitumen genesis and hydrocarbon accumulation pattern of Well Guizhong-1 in Guizhong Depression," *Acta Petrolei Sinica*, vol. 31, no. 3, pp. 420–431, 2010 (Chinese).
- [25] L. Huang, Z. Y. Xu, P. W. Wang, and S. Y. Xiong, "An analysis of resource potential of Upper Paleozoic shale gas in Guizhong depression," *Geology in China*, vol. 39, no. 2, pp. 497–506, 2012 (Chinese).
- [26] P. W. Wang, G. S. Yao, Z. L. Chen et al., "Characteristics and evolution of Devonian reef reservoirs in Guizhong (central Guangxi) depression," *Geology in China*, vol. 38, no. 1, pp. 170–179, 2011 (Chinese).
- [27] S. G. Liu and Z. L. Luo, "Study on the distribution characteristics of petroleum deposits from the plate tectonic evolution in South China," *Acta Petrolei Sinica*, vol. 22, no. 4, pp. 24–30, 2001 (Chinese).
- [28] M. J. Zhao, S. C. Zhang, and L. Zhao, "Geochemistry and genesis of bitumen in paleo-oil reservoir in the Nanpanjiang Basin, China," *Acta Geologica Sinica*, vol. 80, pp. 893–901, 2006.
- [29] D. M. Liu, K. L. Jin, H. L. Mao, W. M. Du, and Hu. J. Study of, "Study of macerals in hydrocarbon source rocks by fourier transform infrared microspectroscopy," *Acta Petrologica Sinica*, vol. 14, pp. 222–231, 1998 (Chinese).
- [30] Z. C. Mao, Y. S. Du, M. Zhang, J. X. Yan, and F. Zeng, "Organic geochemical characterization and depositional paleoenvironments of the Devonian strata in Guizhong region, Guangxi, China," *Science in China, Series D: Earth Sciences*, vol. 52, no. 1, pp. 88–95, 2010.
- [31] J. W. Kang, X. B. Lin, J. C. Tian, and X. Zhang, "Reservoir characteristics within the Devonian sequence stratigraphic framework in the southern Guizhou-central Guangxi region," *Sedimentary Geology and Tertiary Geology*, vol. 30, pp. 76–83, 2010.
- [32] L. X. Fu, P. Yu, S. L. Li, Q. J. Zhang, and Y. Gao, "Prediction of devonian reef distribution in guizhong deperssion," *Marine Origin Petroleum Geology*, vol. 14, pp. 35–41, 2009 (Chinese).
- [33] Z. H. Lou, C. J. Shang, G. S. Yao, Z. L. Chen, and A. M. Jin, "Hydrocarbon preservation conditions in marine strata of the Guizhong depression and its margin," *Acta Petrolei Sinica*, vol. 32, no. 3, pp. 432–441, 2011 (Chinese).
- [34] H. Jacob, "Classification, structure, genesis and practical importance of natural solid oil bitumen ("migrabitumen")," *International Journal of Coal Geology*, vol. 11, no. 1, pp. 65–79, 1989.
- [35] G. X. Feng and S. J. Chen, "Relationship between the reflectance of bitumen and vitrinite in rock," *Nature Gas Industry*, vol. 8, no. 3, pp. 20–25, 1988.
- [36] D. H. Liu and J. Y. Shi, "Discussion on unconventional evaluation method of high maturated carbonate source rock," *Petroleum Exploration and Development*, vol. 21, no. 3, pp. 113–115, 1994.
- [37] B. P. Tissot and D. H. Welte, *Petroleum Formation and Occurrence*, Springer, Berlin, Germany, 2nd edition, 1984.
- [38] P. A. Allen and J. R. Allen, *Basin Analysis: Principles and Application*, Blackwell Scientific Publications, Oxford, England, 1990.
- [39] J. M. Hunt, *Petroleum Geochemistry and Geology*, Springer, Berlin, Germany, 1996.
- [40] H. Ganz and W. Kalkreuth, "Application of infrared spectroscopy to the classification of kerogen types and the evaluation of source rock and oil shale potentials," *Fuel*, vol. 66, no. 5, pp. 708–711, 1987.
- [41] S. R. Dalal, S. K. Menon, and Y. K. Agrawal, "Infrared spectroscopic studies of EOM from Cambay Basin," *Journal of the Indian Chemical Society*, vol. 73, pp. 247–253, 1996.
- [42] A. A. Christy, B. Dahl, and O. M. Kvalheim, "Structural features of resins, asphaltenes and kerogen studied by diffuse reflectance infrared spectroscopy," *Fuel*, vol. 68, no. 4, pp. 430–435, 1989.
- [43] E. X. Jiang, "Terrestrial heat flow pattern and thermo-tectonic domains in continental area of China," *Journal of the Graduate School of the Chinese Academy of Sciences*, vol. 18, no. 1, pp. 51–58, 2001 (Chinese).
- [44] S. B. Hu, L. J. He, and J. Y. Wang, "Compilation of heat flow data in the China continental area (3rd edition)," *Chinese Journal of Geophysics*, vol. 44, no. 5, pp. 611–626, 2001 (Chinese).
- [45] Y. S. Yuan, Y. S. Ma, S. B. Hu, T. L. Guo, and X. Y. Fu, "Present-day geothermal characteristics in South China," *Chinese Journal Geophysics*, vol. 49, no. 4, pp. 1118–1126, 2006 (Chinese).
- [46] W. Wang, Z. Zhou, and P. Yu, "Relations between vitrinite reflectance, peak temperature and its neighboring thmperature variation rate: a comparison of methods," *Chinese Journal Geophysics*, vol. 48, no. 6, pp. 1375–1386, 2005 (Chinese).
- [47] B. He, Y. G. Xu, Y. M. Wang, and L. Xiao, "Nature of the Dongwu movement and its temporal and spatial evolution," *Earth Science — Journal of China University of Geosciences*, vol. 30, pp. 89–96, 2005 (Chinese).
- [48] C. Q. Zhu, M. Xu, J. N. Shan, Y. S. Yuan, Y. Q. Zhao, and S. B. Hu, "Quantifying the denudations of major tectonic events in Sichuan basin: Constrained by the paleothermal records," *Geology in China*, vol. 36, pp. 1268–1277, 2009 (Chinese).
- [49] S. Z. Hu, S. F. Li, X. W. Fu, Y. J. Li, and T. D. Wang, "Identification of highly to over mature gas interval using reservoir bitumen features: Sichuan basin of Southwest China," *Petroleum Science and Technology*, vol. 32, no. 12, pp. 1437–1442, 2014.

## Research Article

# Multiphase Calcite Cementation and Fluids Evolution of a Deeply Buried Carbonate Reservoir in the Upper Ordovician Lianglitag Formation, Tahe Oilfield, Tarim Basin, NW China

Jiaqing Liu,<sup>1</sup> Zhong Li,<sup>1</sup> Lijuan Cheng,<sup>1</sup> and Jiawei Li<sup>2</sup>

<sup>1</sup>*Institute of Geology and Geophysics, Chinese Academy of Sciences, Beijing 100029, China*

<sup>2</sup>*Research Institute of Tsinghua, Pearl River Delta, Guangzhou 510530, China*

Correspondence should be addressed to Zhong Li; [lizhong@mail.igcas.ac.cn](mailto:lizhong@mail.igcas.ac.cn)

Received 2 March 2017; Revised 9 May 2017; Accepted 28 May 2017; Published 1 August 2017

Academic Editor: Zhijun Jin

Copyright © 2017 Jiaqing Liu et al. This is an open access article distributed under the Creative Commons Attribution License, which permits unrestricted use, distribution, and reproduction in any medium, provided the original work is properly cited.

Oil and gas have been found in the Upper Ordovician Lianglitag Formation carbonates in the Tahe Oilfield, Tarim Basin, NW China. This study documents the origin of diagenetic fluids by using a combination of petrology, SIMS, fluid inclusion, and radiogenic isotope analysis. Six stages of calcite cements were revealed. C1-C2 formed in marine to early burial environments. C3 has relatively low  $\delta^{18}\text{O}_{\text{VPDB}}$  values ( $-8.45\text{‰}$  to  $-6.50\text{‰}$ ) and likely has a meteoric origin. Meteoric water probably fluxed into aquifers during the Early Paleozoic and Late Paleozoic uplift. C4 has  $\delta^{18}\text{O}_{\text{VPDB}}$  values typically 3‰ higher than those of C3, and probably formed during shallow burial. C5 displays relatively negative  $\delta^{18}\text{O}_{\text{VPDB}}$  values ( $-8.26\text{‰}$  to  $-5.12\text{‰}$ ), and the moderate-to-high fluid-inclusion temperatures imply that it precipitated in burial environments. C6 shows homogenization temperatures (up to 200°C) higher than the maximum burial and much lower salinities ( $<10.61\text{ wt\% NaCl}$ ), which may suggest that the fluid was deeply recycled meteoric water. The average  $^{87}\text{Sr}/^{86}\text{Sr}$  ratios of fracture- and vug-filling calcite cements are much higher, indicative of incorporation of radiogenic Sr. Caves and fractures constitute the dominant reservoir spaces. A corresponding diagenesis-related reservoir evolution model was established that favors exploration and prediction.

## 1. Introduction

Fluid origin and flow in sedimentary basins have an important influence on various diagenetic alteration processes, including cementation, dissolution, recrystallization, and dolomitization, which have significant impacts on reservoir development [1–10]. Thus, constraining the origin and evolution of fluid and fluid flow events is of considerable significance for hydrocarbon exploration and reservoir development. Fluid is not only a component of the fluid-rock interaction but also a carrier of matter and energy in the fluid-rock interaction. Fluid is an active control factor of the fluid-rock interaction system [7, 10, 11]. However, for deeply buried reservoirs, due to their complicated burial and tectonic history, the fluid chemical composition and flow are very complicated; therefore, understanding and predicting fluid flow are still challenging.

The Tahe Oilfield, located within the Tabei tectonic block in the northern part of the basin, is the largest Paleozoic

marine oilfield in China. For the Tahe Oilfield, the current main oil-gas production layer is the Middle Ordovician Yijianfang Formation and the Early Middle Ordovician Yingshan Formation, and considerable previous works have been done on these layers [12–17]. By contrast, carbonate rocks of the Upper Ordovician Lianglitag Formation are potential exploration strata, which have received little attention. The carbonates of the Upper Ordovician Lianglitag Formation are deeply buried, with depths  $> 4500\text{ m}$ . Previous studies mainly focused on the biostratigraphy, lithostratigraphy [18–20], and sedimentary environment [21–23]. Lu et al. [24] analyzed the main reservoir characteristics of the Lianglitag Formation: the matrix of the Lianglitag Formation is characterized by low porosity and permeability, with strong reservoir heterogeneity.

In situ Secondary Ion Mass Spectrometry (SIMS) has provided a powerful technique for studying basin fluid activities [25–30]. SIMS can solve the traditional test difficulties; for example, a small number of samples cannot meet the test

requirements or the analysis results are often the average value of multiphase fluid mixing. In this paper, for the first time, in situ SIMS analysis has been used to characterize different fluids and discriminate their nature in study areas.

This paper takes the carbonate reservoirs of the Upper Ordovician Lianglitag Formation as a typical example and focuses on the activities of diagenetic fluids as well as their effects on reservoir development under a complex multistage tectonic setting. This work can provide useful insights into fluid evolution during diagenesis for typical deeply buried reservoirs. Specifically, we address the following questions:

- (1) What are the petrological and geochemical characteristics of diagenetic calcites in the Late Ordovician Lianglitag Formation?
- (2) What is the nature of the fluids and their impact on the Lianglitag Formation?
- (3) What mechanisms were responsible for the formation of the carbonate reservoir of the Lianglitag Formation in the Tahe Oilfield in the Tarim Basin?
- (4) What is the model for diagenetic fluid flow and reservoir performance in deeply buried carbonate successions?

## 2. Geological Background

The Tarim Basin, located in southern Xinjiang province, northwestern China, is surrounded by the Tian Shan, Kunlun, and Altyn mountains to the north, southwest, and southeast, respectively (Figure 1(a)). It is a multicycle composite basin with continental crust, composed of pre-Sinian basaltic basins, which are formed by prototypical basins with different properties in different periods [32, 33]. The basin can be divided into seven tectonic units: Kuqa Depression, Tabei Uplift, North Depression (Manjiaer-Awati Depressions), Central Uplift, Southwest Depression, Southeast Uplift, and Southeast Depression [32] (Figure 1(a)). The Tahe Oilfield, covering an area of 2400 km<sup>2</sup>, is located in the Akekule uplift in the eastern part of the Tabei Uplift (Figures 1(a) and 1(b)).

The warm and humid Ordovician climate provided favorable conditions for carbonate deposition on the Tarim Plate, which was situated at 20°S (Fang et al. 2001). From bottom to top, the Lower-Middle Ordovician strata are divided into the Penglaiba Formation (O<sub>1p</sub>), Yingshan Fm. (O<sub>1-2y</sub>), and Yijianfang Formation (O<sub>2yj</sub>), whereas the Upper Ordovician strata are divided into the Qiaerbak Formation (O<sub>3q</sub>), Lianglitag Formation (O<sub>3l</sub>), and Sangtamu Formation (O<sub>3s</sub>) (Figure 2). The Early Ordovician paleogeographic framework of the study area was characterized by the widespread development of carbonate platforms that were open to the sea in an extensional setting [14]. The buildup of carbonate platforms of the Lianglitag Formation was much lower than that of typical Early to Middle Ordovician platforms as a result of the sea-level rise [34], with a maximum thickness of 145.5 m.

Core and detailed well log, seismic, and other exploration well data analyses indicate that, during the early stage, the Tahe region was characterized by a gentle slope with

few high-energy depositions and characterized by grey to dark grey, thick-bedded micrites and microcrystalline marls interbedded with brown to grey-brown, thin- to medium-bedded bioclastic micrites and granular, microcrystalline limestones, whereas, at the late stage, it evolved into a weak-rimmed platform, characterized by the deposition of high-energy platform margin facies. The platform margin facies are distributed in TP5, S116, S110, and S107 wells, which are characterized by sparite oolitic limestone, calcarenite, and bioclastic limestone. Towards the south, the platform was mainly composed of dark grey, thinly laminated, nodular micrite, indicative of slope deposition (Figure 1(b)) [22, 23].

Previous studies [23, 35] have shown that there is an unconformity between the top of the Lianglitag Formation and the overlying Sangtamu Formation (EPU) (Figure 2), indicating a regional exposure surface and depositional break. The southward subduction of the Tianshan Ocean and formation of its associated suture at the end of Middle Devonian time resulted in thrusting and uplifting in the north of the Tahe Oilfield was significantly greater than in the south [31, 36] and led to the Upper Ordovician Lianglitag strata in the north being completely or partly removed by erosion, showing as the Lianglitag Fm. strata were overlain by the Carboniferous, the Devonian, or Silurian strata (LPU) (Figures 1(c) and 2), whereas the Lianglitag strata remained in the south (Figures 1(b) and 1(c)). In this paper, based on previous works on the basic geology of the Tarim Basin [31, 37–39], the burial history of well S109 was rebuilt by the Basinmod 1D software and the Easy% Ro model. During the deposition of the Ordovician, the uplift of the Tahe area led to the denudation of the strata. After the Ordovician deposited, the burial history was roughly divided into two stages by the two periods of uplift at the Silurian-Carboniferous and Permian. There are many periods of weak erosion events, and, during the Neogene and Quaternary, the strata experienced rapid subsidence, leading to thick deposition. The Upper Ordovician strata have been buried to >4500 m, with paleotemperatures up to approximately 130°C (Figure 3).

## 3. Methods

This study is based on a detailed examination of 32 wells from the Tahe Oilfield. The description of cores focused on diagenetic features and also noted the lithology, depositional composition, and textures, as well as sedimentary structures. The petrographic examination of 120 thin sections of the diagenetic features and associated fabrics was completed using transmitted light and cathodoluminescence microscopy (CL, using a RELIOTRON, model RELION III; 5–8 kV and 300–400 μA gun current) at the Diagenesis Laboratory of Institute of Geology and Geophysics, Chinese Academy of Sciences (IGGCAS).

To study the fluid nature of vug-filling calcite cement, in situ δ<sup>13</sup>C and δ<sup>18</sup>O measurements were conducted using an in situ SIMS (Secondary Ion Mass Spectrometry) Cameca IMS-1280 ion microprobe at IGGCAS. The analytical procedures were similar to those described by Rollion-Bard et al. (2003). A 10–15 μm diameter Cs ion beam was used to

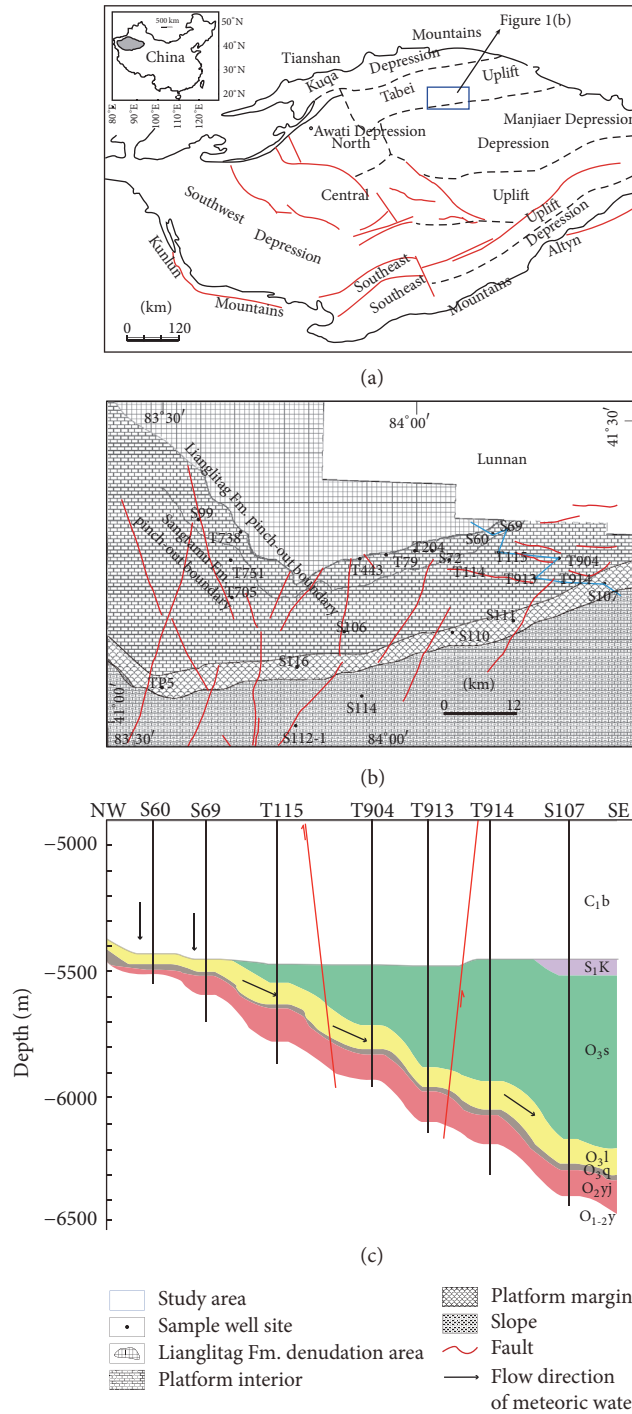


FIGURE 1: Tectonic subdivisions and location of the study areas. (a) Tectonic unit divisions of the Tarim Basin and location of the study areas. (b) Distribution of sample wells in the Tahe study region. (c) Strata profile from Well S60 to Well S107 (please see the blue line in (b)).

ablate 10–15  $\mu\text{m}$  diameter spots from the sample. The internal precision for each spot ranged between 0.009 and 0.015 (% Standard Error). The external precision was estimated to be 0.4‰ for oxygen and 0.6‰ for carbon as determined by consecutive analysis of a UWC (international calcite standard from University of Wisconsin) standard and OKA (Chinese primary calcite standard number GBW04481) standard.

44 core samples from 15 wells were collected for conventional oxygen and carbon isotope analyses. The samples analyzed in this study were whole rocks and fracture- and vug-filling calcite cement. Samples were taken using a dental drill. The analyses were carried out at the C-O Isotope Laboratory at IGGCAS. The carbon and oxygen isotope compositions were determined using a MAT-251 mass spectrometer

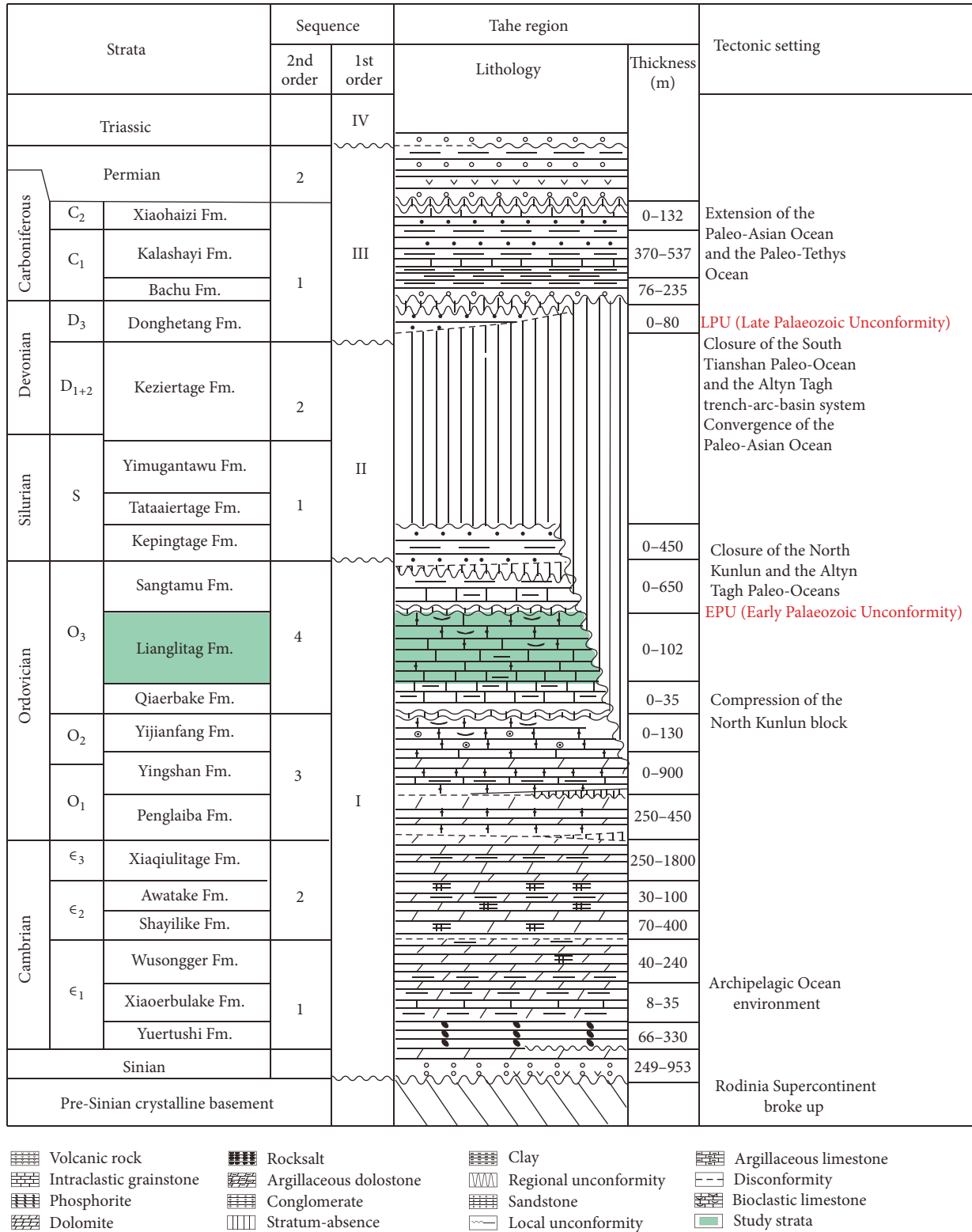


FIGURE 2: Stratigraphic chart showing the formations and hiatuses, modified after Lin et al. [31].

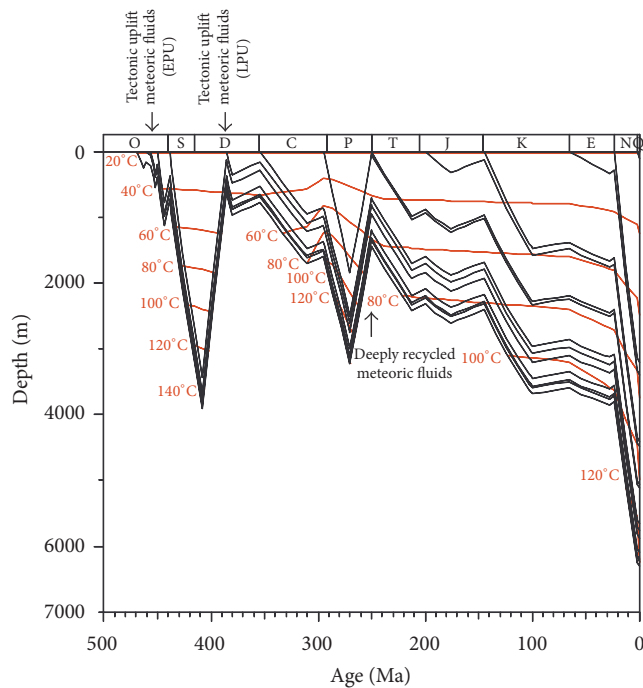


FIGURE 3: Burial history diagram of Well S109 in the Tahe Oilfield.

(Vienna PeeDee belemnite [VPDB] standard), and the results were expressed in parts per thousand (delta units). Reproducibility was checked by replicate analysis of laboratory standards and was  $\pm 0.05\%$  ( $1\sigma$ ) for oxygen isotopes and  $\pm 0.02\%$  ( $1\sigma$ ) for carbon isotopes.

26 core samples from 7 wells were collected for  $^{87}\text{Sr}/^{86}\text{Sr}$  analyses. Strontium isotope analyses were performed at the Rb-Sr Isotope Ultraclean Laboratory at IGGCAS. HAc was used to dissolve calcite to release Sr. The isotopic ratios were measured on a VG354 solid source mass spectrometer. The measured  $^{87}\text{Sr}/^{86}\text{Sr}$  values were corrected using a quality fractionation standard of  $^{86}\text{Sr}/^{88}\text{Sr} = 0.1194$ ; the mean value of the measured strontium isotope NBS987 (standard sample) was  $0.710272 \pm 0.000012$ .

Fluid inclusion petrography and microthermometry were conducted on 25 samples of intergranular calcite cement and vug-fill calcite cement to measure the homogenization temperature ( $T_h$ , uncorrected for pressure) and salinity of the aqueous fluid inclusions. The salinity, in weight percent of NaCl equivalents, was calculated from the ice melting temperature ( $T_m$  ice) using the Bodnar [40] equation with a temperature step increase of  $2^\circ\text{C}/\text{min}$ . Special emphasis was placed on fluid inclusion assemblages (FIAs) [41], which represent the most finely discriminated petrographically associated groups of fluid inclusions, which were presumably trapped at approximately the same time. The measurements were performed using a Linkam THMGS600 heating-freezing stage with a  $0.1^\circ\text{C}$  precision and calibrated with synthetic pure water and  $\text{CO}_2$  inclusions. The analyses were conducted at the Diagenesis Laboratory at IGGCAS.

## 4. Results

### 4.1. Petrographic Description

#### 4.1.1. Cement Sequences

**Calcite Cement 1 (C1).** C1 consists of isopachous fringe or fibrous (IFC) and early inclusion-poor calcite cement, constituting the first diagenetic phase to occlude the depositional pore space. IFC cement is noted for its blotchy to nonluminescent appearance under cathodoluminescence (CL) microscopy and is consistently present in grainstones and packstones (Figures 4(a) and 4(b)).

**Calcite Cement 2 (C2).** C2 is characterized by drusy calcite cement postdating calcite C1 and displays growth zones of dark red luminescence under CL (Figures 4(a) and 4(b)).

**Calcite Cement 3 (C3).** C3 is a blocky calcite and is characterized by nonluminescence (Figures 4(c)–4(f)). C3 occurs not only in intraparticle and interparticle pores but also in vug. The volume of C3 varies with its stratigraphic position. It has been widely observed in cores within the Lianglitag Formation pinch-out boundary and Sangtamu Formation pinch-out boundary, shown in Figures 5(a) and 5(b). At the south of the Sangtamu Formation pinch-out, C3 mainly occurs in the wells that are close to the fracture.

**Calcite Cement 4 (C4).** C4 grows on top of C3 crystals and exhibits a bright orange luminescent zoned CL pattern. It has euhedral surfaces that show no signs of dissolution. The percentage of C3 and C4 can reach 80% in some wells (Figures 4(c) and 4(d)).

**Calcite Cement 5 (C5).** C5 is a clear calcite with brown to dull luminescence (Figures 4(e) and 4(f)). It occurs as isolated rhombic crystals or completely fills the pore space with blocky textures. Some dissolution likely occurred in C5 filled with oil and/or bitumen (Figures 4(e) and 4(f)).

**Calcite Cement 6 (C6).** The mineralogical characteristics of C6 are similar to those of C5, which has bright and thick crystals. Under luminescence, C6 mainly shows red luminescence (Figures 5(c) and 5(d)). C6 is closely associated with fractures that only present in wells where fractures were developed (Figures 5(e) and 5(f)).

**4.1.2. Dissolution and Fracturing.** Millimeter- to meter-scale dissolution features and fractures were observed in cores and suggestive of multiple dissolution events.

Early meteoric dissolution occurred locally in high-energy carbonate shoals, but this dissolution pore space was subsequently filled by late calcite cement (Figure 6(a)), with few effective fabric-selected pores reserved. Dissolution vugs and channels, with sizes up to several centimeters, were observed locally, and these vugs were mainly filled by calcite C3. The dissolution vugs were non-fabric-selective (Figure 6(b)) and were distributed along fractures (Figure 6(c)). Meter scale dissolution cavities were detected in some cores, with two types of cavity fillings. One was characterized by

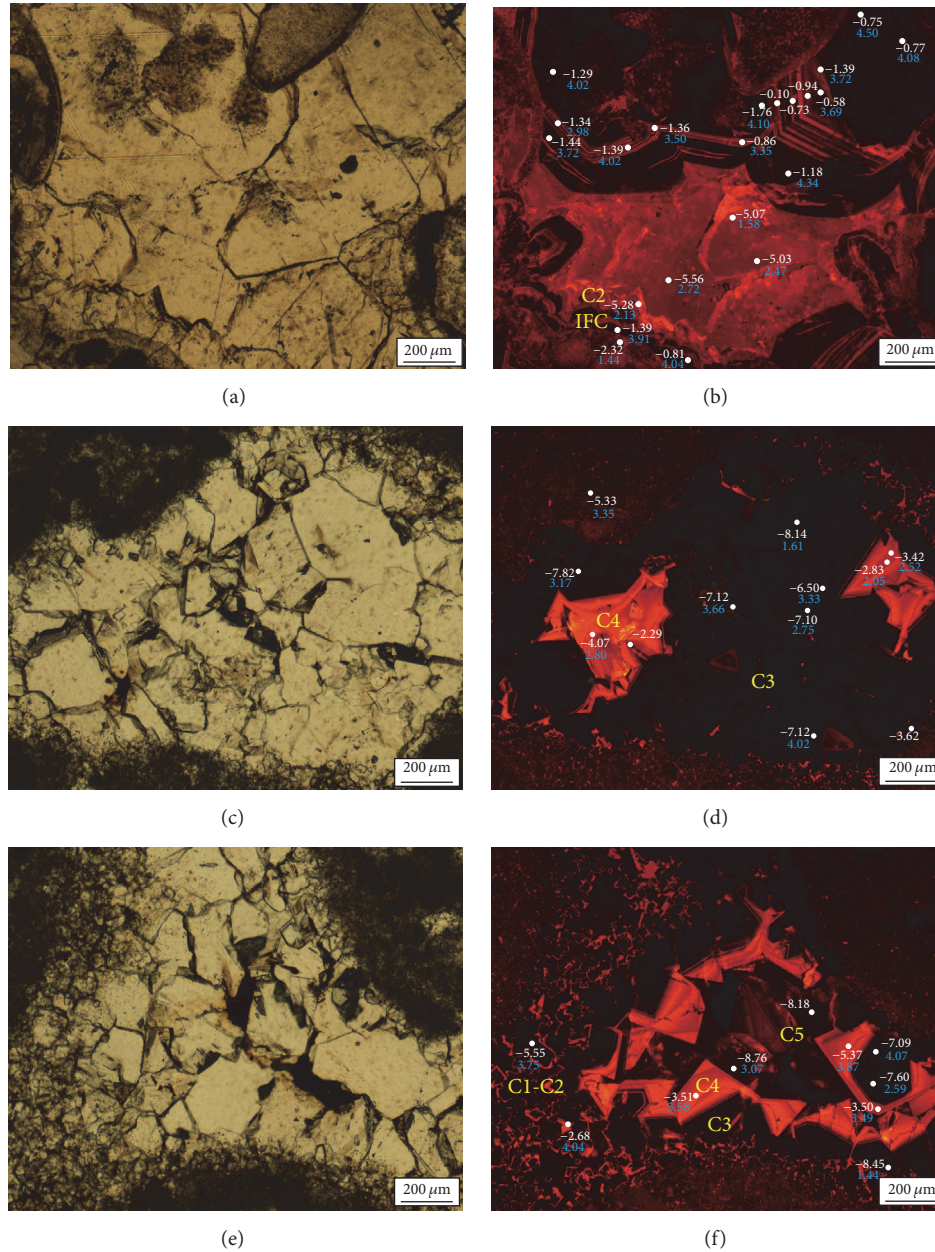


FIGURE 4: Photomicrograph pairs in transmitted light (a, c, and e) and cathodoluminescence (b, d, and f) of samples illustrating the main cement features in Lianglitag Fm. carbonate rocks. The white circle is the position of the SIM analysis point; the white digit is  $\delta^{18}\text{O}$  and the blue digit is  $\delta^{13}\text{C}$ . (a, b) The interparticle porosity is first cemented by nonluminescent isopachous fibrous cement (IFC), followed by C2. Under CL, C1 is nonluminescent and occasionally displays several thin yellow bands, whereas C2 shows red luminescence. Sample from 5885.92 m, well S106. (c, d) Pore space is mainly filled by nonluminescent C3, and C4, exhibiting a bright orange luminescent zoned CL pattern, continued growth on C3 crystals and the filling of the remaining space. Sample from 5838.00 m, well T751. (e, f) Dissolution pores are sequentially filled by C1–C5 cement. C5 exhibits brown dull luminescence. Some corrosion of calcite C5 and oil input are detectable. Sample from 5838.00 m, well T751.

sands, silts, marls, and breccias (Figure 6(d)); and the other was characterized by calcite cement and marl, with little detrital quartz sand (Figure 6(e)). During drilling, lost cores, bit drops, and lost circulation occurred in nine wells (e.g., wells S106 and S110). The above observations suggest the development of large cavities in these carbonates.

Based on core measurements, the total fracture frequency is 8 fractures per meter, whereas the open fracture frequency is only 1.6 fractures per meter. Therefore, approximately 80% of the observed fractures are infilled, which limits fracture connectivity. Most of the fractures are partially or completely occluded by green marl (Figure 6(f)).

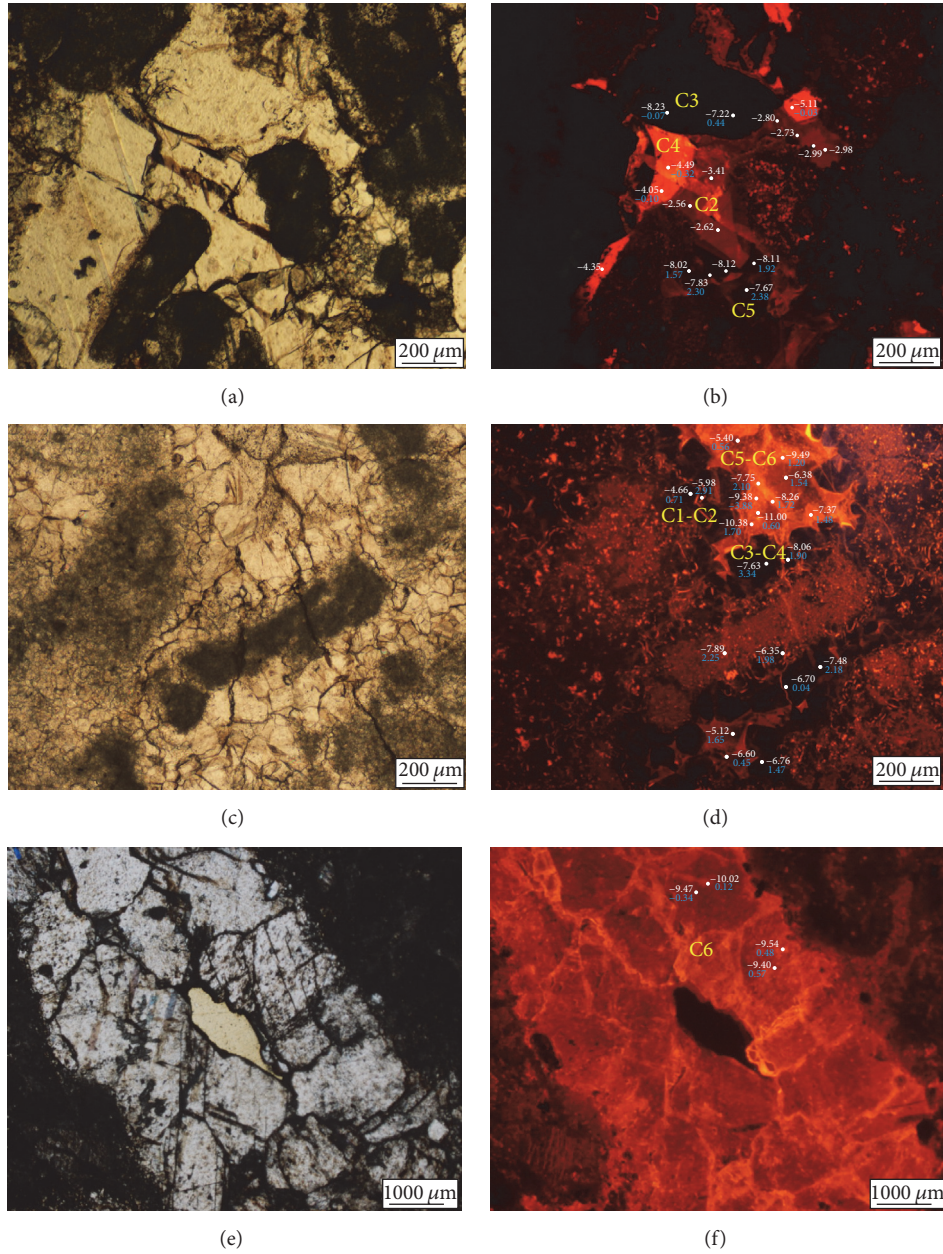


FIGURE 5: Photomicrograph pairs in transmitted light (a, c, and e) and cathodoluminescence (b, d, and f) of samples illustrating the main cement features in the Lianglitag Fm. carbonate rocks. The white circle is the position of the SIM analysis point; the white digit is  $\delta^{18}\text{O}$  and the blue digit is  $\delta^{13}\text{C}$ . (a, b) The dissolution pore is mainly cemented by C2–C5, and C2 is obviously cut by C3, indicating that it predated the formation. Sample from 5893.10 m, well T738. (c, d) The dissolution pore is cemented by C1–C6. Sample from 5779.36 m, well T904. (e, f) C6 with red luminescence fills the pore and the remaining effective pore is seen. Sample from 6089.9 m, well S110.

4.2. Isotope Geochemistry and Fluid Inclusion Microthermometry

4.2.1. In Situ Carbon and Oxygen Isotopes by SIMS. Carbon and oxygen isotopic data for pore-filling calcite cement from SIMS measurement were presented in Figure 7 and listed in Table 1.

C1. This calcite has  $\delta^{18}\text{O}$  values ranging from  $-3.62$  to  $-0.10\%$  VPDB, with a mean value of  $-1.32\%$  ( $n = 23$ ). The range of

$\delta^{13}\text{C}$  values on C1 fluctuates from  $1.44\%$  to  $4.50\%$  VPDB, with a mean value of  $3.72\%$  VPDB ( $n = 16$ ).

C2. Compared with C1, the  $\delta^{18}\text{O}$  values of C2 are more negative, ranging between  $-6.35$  and  $-2.56\%$  VPDB, with a mean value of  $-4.24\%$  VPDB ( $n = 15$ ). The range of  $\delta^{13}\text{C}$  values on C2 fluctuates from  $-0.91$  to  $3.75\%$ , with a mean value of  $1.55\%$  VPDB ( $n = 11$ ).

C3. The oxygen isotope values on C3 are more negative than C2, ranging from  $-8.45$  to  $-6.50\%$  VPDB, with a mean value

TABLE 1: Carbon and oxygen isotopic data of different stages of pore-filling calcite cement by in situ SIMS of Lianglitag Formation carbonates in the Tahe Oilfield.

Well	Number	Depth (m)	Stage	$\delta^{18}\text{O}$ (‰ VPDB)	2SE	$\delta^{13}\text{C}$ (‰ VPDB)	2SE
S106	1	5885.92	C1	-0.77	0.33	4.08	0.34
S106	2	5885.92	C1	-0.75	0.26	4.50	0.43
S106	3	5885.92	C1	-1.39	0.35	3.72	0.49
S106	4	5885.92	C1	-0.58	0.30	3.69	0.48
S106	5	5885.92	C1	-1.62	0.34	—	—
S106	6	5885.92	C1	-0.94	0.33	—	—
S106	7	5885.92	C1	-0.73	0.22	—	—
S106	8	5885.92	C1	-1.05	0.25	—	—
S106	9	5885.92	C1	-0.10	0.34	—	—
S106	10	5885.92	C1	-0.94	0.28	—	—
S106	11	5885.92	C1	-1.76	0.33	4.10	0.43
S106	12	5885.92	C1	-1.18	0.32	4.34	0.45
S106	13	5885.92	C1	-1.36	0.43	3.50	0.56
S106	14	5885.92	C1	-0.86	0.31	3.35	0.45
S106	15	5885.92	C1	-1.44	0.29	3.72	0.44
S106	16	5885.92	C1	-1.34	0.21	2.98	0.55
S106	17	5885.92	C1	-1.29	0.29	4.02	0.49
S106	18	5885.92	C1	-1.39	0.32	4.02	0.45
S106	19	5885.92	C2	-5.03	0.34	2.47	0.39
S106	20	5885.92	C2	-5.07	0.35	1.58	0.37
S106	21	5885.92	C2	-5.56	0.23	2.72	0.39
S106	22	5885.92	C2	-5.28	0.26	2.13	0.45
S106	23	5885.92	C1	-1.39	0.33	3.91	0.48
S106	24	5885.92	C1	-0.81	0.29	4.04	0.43
S106	25	5885.92	C1	-2.32	0.38	1.44	0.39
S110	1	6089.90	C6	-9.43	0.35	0.92	0.44
S110	2	6089.90	C6	-9.16	0.30	-0.88	0.70
S110	3	6089.90	C6	-9.69	0.29	0.13	0.42
S110	4	6089.90	C6	-9.14	0.28	—	—
S110	5	6089.90	C6	-9.19	0.29	0.91	0.39
S110	6	6089.90	C6	-9.47	0.43	-0.34	0.48
S110	7	6089.90	C6	-10.02	0.35	-0.12	0.42
S110	8	6089.90	C6	-9.54	0.26	0.48	0.36
S110	9	6089.90	C6	-9.40	0.26	0.57	0.48
T738	1	5893.10	C2	-2.56	0.19	—	—
T738	2	5893.10	C3	-8.23	0.25	-0.07	0.58
T738	3	5893.10	C3	-7.22	0.30	0.12	0.44
T738	4	5893.10	C2	-2.98	0.22	—	—
T738	5	5893.10	C2	-2.62	0.30	—	—
T738	6	5893.10	C5	-8.02	0.14	1.57	0.53
T738	7	5893.10	C5	-8.12	0.27	—	—
T738	8	5893.10	C5	-7.67	0.22	2.38	0.44
T738	9	5893.10	C2	-3.41	0.25	—	—
T738	10	5893.10	C4	-4.05	0.20	-0.10	0.58
T738	11	5893.10	C4	-4.49	0.22	-0.32	0.54
T738	12	5893.10	C5	-7.83	0.27	2.30	0.44
T738	13	5893.10	C5	-8.11	0.30	1.92	0.49

TABLE 1: Continued.

Well	Number	Depth (m)	Stage	$\delta^{18}\text{O}$ (‰ VPDB)	2SE	$\delta^{13}\text{C}$ (‰ VPDB)	2SE
T738	14	5893.10	C2	-2.99	0.28	—	—
T738	15	5893.10	C2	-2.73	0.21	—	—
T738	16	5893.10	C2	-2.80	0.25	—	—
T738	17	5893.10	C4	-5.11	0.22	-0.03	0.31
T738	18	5893.10	C4	-4.35	0.27	—	—
T751	1	5838.00	C3	-7.10	0.26	2.75	0.62
T751	2	5838.00	C3	-6.50	0.28	3.33	0.44
T751	3	5838.00	C3	-8.14	0.28	1.61	0.45
T751	4	5838.00	C4	-2.83	0.35	2.05	0.47
T751	5	5838.00	C4	-3.42	0.34	2.52	0.51
T751	6	5838.00	C1	-3.62	0.38	—	—
T751	7	5838.00	C4	-4.07	0.30	2.80	0.50
T751	8	5838.00	C4	-2.29	0.37	—	—
T751	9	5838.00	C3	-7.82	0.34	3.17	0.51
T751	10	5838.00	Matrix	-5.33	0.41	3.35	0.67
T751	11	5838.00	C3	-7.12	0.22	3.66	0.28
T751	12	5838.00	C3	-7.88	0.34	4.02	0.37
T751	13	5838.00	C4	-5.07	0.34	4.9	0.57
T751	14	5838.00	C3	-8.45	0.38	2.59	0.51
T751	15	5838.00	C3	-7.60	0.29	4.07	0.47
T751	16	5838.00	C3	-7.09	0.24	3.87	0.48
T751	17	5838.00	C4	-5.37	0.41	3.75	0.58
T751	18	5838.00	C4	-3.51	0.33	3.07	0.55
T751	19	5838.00	C3	-8.76	0.34	1.44	0.59
T751	20	5838.00	C4	-3.50	0.29	3.49	0.24
T751	21	5838.00	C3	-8.18	0.22	—	—
T751	22	5838.00	C2	-5.55	0.23	3.75	0.28
T751	23	5838.00	C1	-2.68	0.23	4.04	0.32
T904	1	5779.36	C6	-9.38	0.27	-3.88	0.32
T904	2	5779.36	C6	-10.38	0.26	1.70	0.44
T904	3	5779.36	C5	-8.26	0.24	1.72	0.43
T904	4	5779.36	C5	-7.75	0.28	2.10	0.43
T904	5	5779.36	C6	-9.49	0.27	1.20	0.48
T904	6	5779.36	C5	-7.37	0.22	1.48	0.42
T904	7	5779.36	C3	-8.06	0.27	1.90	0.53
T904	8	5779.36	C3	-7.63	0.19	3.34	0.62
T904	9	5779.36	C2	-4.66	0.28	0.71	0.51
T904	10	5779.36	C2	-5.98	0.39	2.91	0.59
T904	11	5779.36	C5	-6.38	0.28	1.54	0.47
T904	12	5779.36	C6	-11.00	0.38	0.60	0.46
T904	13	5779.36	C5	-5.40	0.20	0.56	0.47
T904	14	5779.36	Matrix	-7.89	0.36	2.25	0.45
T904	15	5779.36	C2	-6.35	0.32	1.98	0.48
T904	16	5779.36	C3	-7.48	0.34	2.18	0.46
T904	17	5779.36	C3	-6.70	0.25	0.04	0.56
T904	18	5779.36	C5	-5.12	0.29	1.65	0.51
T904	19	5779.36	C5	-6.60	0.33	0.45	0.41
T904	20	5779.36	C3	-6.76	0.24	1.47	0.58

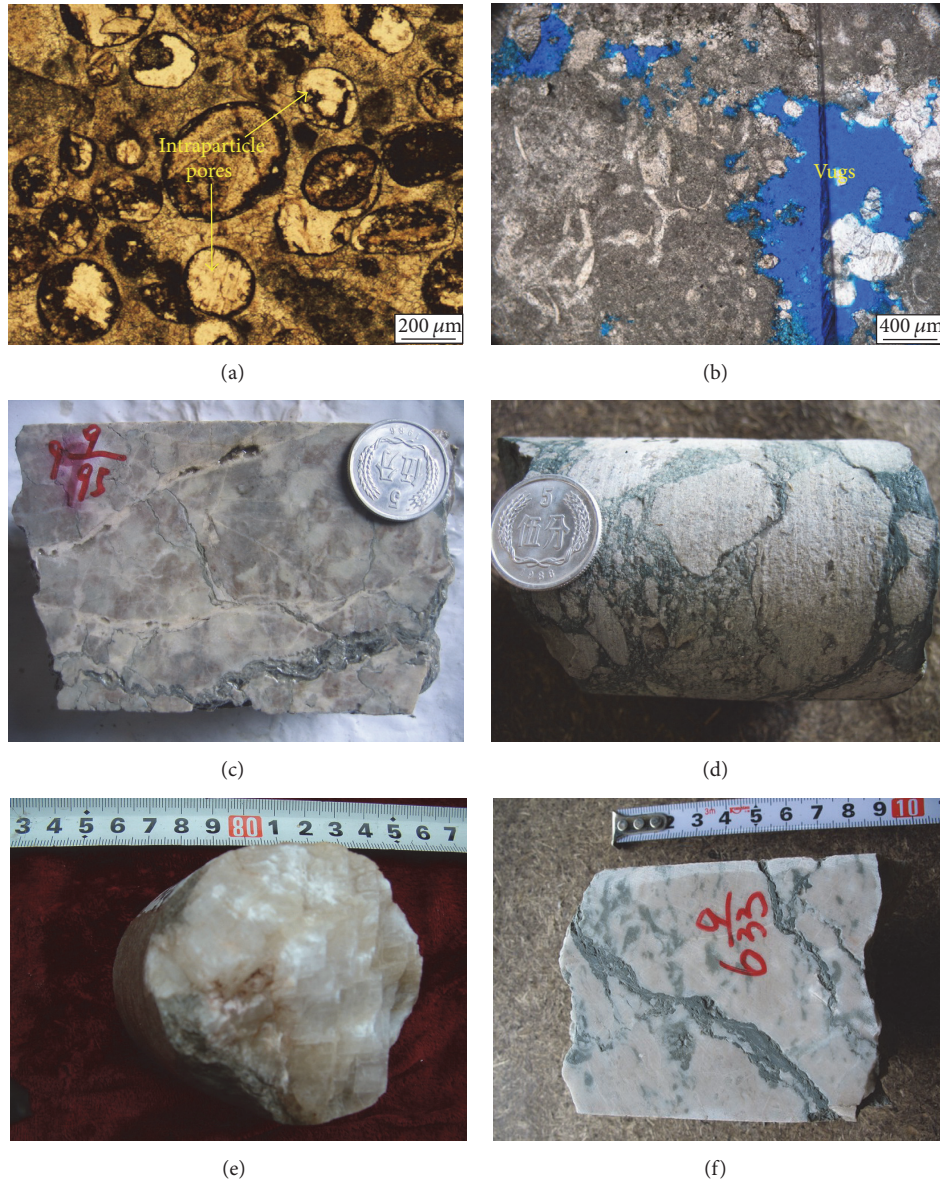


FIGURE 6: Photographs showing typical diagenetic features in the carbonate rocks of the Lianglitag Fm. (a) Early intragranular dissolution of carbonate minerals developed (most of them were filled during diagenesis), well S111, depth 6108.7 m. (b) Non-fabric-selective dissolution pores and vugs developed, well AD4, depth 6463.42 m. (c) Dissolution vug developed along fractures. Sample from 5794.1 m, well T904. (d) Cavern breccias developed in the Tahe Oilfield, well TH204, depth 5469.2 m. (e) Giant crystal calcite filling the cave. Sample from 6245.95 m, well S116. (f) Fracture filled by green marl in the Tahe Oilfield, well T904, depth 5773.21 m.

of  $-7.59\text{‰}$  VPDB ( $n = 18$ ), and the  $\delta^{13}\text{C}$  values are from  $-0.07$  to  $4.07\text{‰}$  VPDB, with a mean value of  $2.32\text{‰}$  VPDB ( $n = 17$ ).

C4. The  $\delta^{18}\text{O}$  values are typically  $3\text{‰}$  higher than those of C3, lying between  $-5.37$  and  $-2.29\text{‰}$  VPDB, with a mean value of  $-4.01\text{‰}$  VPDB ( $n = 12$ ), and the  $\delta^{13}\text{C}$  values on C4 are close to those of C3, ranging from  $-0.32$  to  $4.90\text{‰}$  VPDB, with a mean value of  $2.21\text{‰}$  VPDB ( $n = 10$ ).

C5. C5 shows more negative  $\delta^{18}\text{O}_{\text{VPDB}}$  values ( $-8.26\text{‰}$  to  $-5.12\text{‰}$  VPDB) than those of C4, with a mean value of

$-7.14\text{‰}$  VPDB ( $n = 11$ ), and similar  $\delta^{13}\text{C}_{\text{VPDB}}$  values ( $0.45\text{‰}$  to  $2.38\text{‰}$  VPDB).

C6. C6 displays low  $\delta^{18}\text{O}$  values ranging from  $-11.00$  to  $-9.14\text{‰}$  VPDB, with a mean value of  $-9.64\text{‰}$  VPDB ( $n = 13$ ), and  $\delta^{13}\text{C}$  values ranging from  $-0.88$  to  $1.70\text{‰}$  VPDB ( $n = 12$ ), except one low value ( $-3.88\text{‰}$ ) of VPDB.

4.2.2. *Traditional Carbon and Oxygen Isotopes.* The micrite ranges between  $-8.05$  and  $-3.78\text{‰}$  VPDB for  $\delta^{18}\text{O}$  (mean  $-6.53\text{‰}$  VPDB,  $n = 14$ ) and between  $0.56\text{‰}$  and  $2.48\text{‰}$  VPDB for  $\delta^{13}\text{C}$  (mean  $1.92\text{‰}$  VPDB,  $n = 14$ ). The oxygen

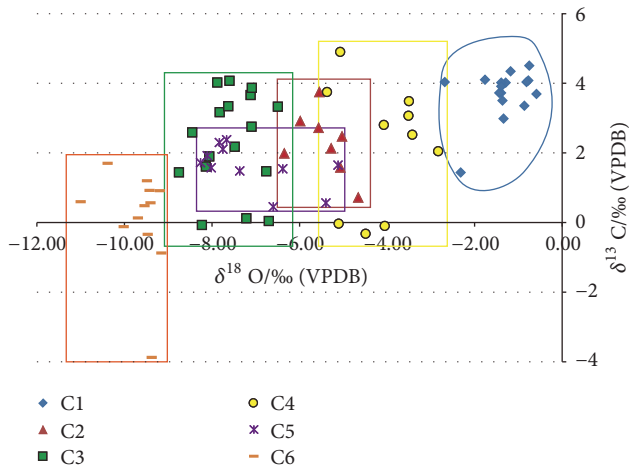


FIGURE 7:  $\delta^{13}\text{C}$  and  $\delta^{18}\text{O}$  values of different stages of pore-filling calcite cement by in situ SIMS.

isotopic compositions of grainstone are close to those of micrite, ranging from  $-8.45$  to  $-3.23\text{‰}$  VPDB (mean  $-5.98\text{‰}$  VPDB,  $n = 20$ ), and the carbon isotopic compositions of grainstone varies from  $-0.64\text{‰}$  to  $2.27\text{‰}$  VPDB (mean  $0.97\text{‰}$  VPDB,  $n = 20$ ). Fracture- and cave-filling calcite cement have  $\delta^{18}\text{O}_{\text{VPDB}}$  values ranging from  $-11.02\text{‰}$  to  $-8.16\text{‰}$  VPDB (mean  $-9.71\text{‰}$  VPDB,  $n = 10$ ) and  $\delta^{13}\text{C}_{\text{VPDB}}$  values ranging from  $-2.16\text{‰}$  to  $3.16\text{‰}$  VPDB (mean  $-0.02\text{‰}$  VPDB,  $n = 10$ ), respectively. The analytical results are listed in Table 2 and shown in Figure 8.

**4.2.3. Strontium Isotopes.** The analytical results are listed in Table 2 and shown in Figure 9(a). The micrite spans a broad range from 0.709005 to 0.711927 (mean value of 0.710418,  $n = 3$ ). The grainstone yields  $^{87}\text{Sr}/^{86}\text{Sr}$  ratios of 0.708136 to 0.709119 (mean value of 0.708659,  $n = 12$ ). The fracture and vug fillings present much higher  $^{87}\text{Sr}/^{86}\text{Sr}$  ratios, ranging from 0.709103 to 0.712863 (mean value of 0.710377,  $n = 10$ ).

**4.2.4. Fluid Inclusions (FI).** 25 doubly polished detachable wafers of calcite samples were prepared and analyzed for FI. Petrography, both transmitted light and UV fluorescence, was performed on doubly polished wafers to identify inclusion types for further analysis and to determine their relationship to the host minerals. The large and/or elongate inclusions were disregarded, which could mean stretching and resetting since their formation [41].

The fluid inclusion homogenization temperatures  $T_h$  and salinity (weight percent of NaCl equivalent) results of the cementing phases are shown in Figure 10. C1 is inclusion poor; therefore, no microthermometry was conducted in this cement.

C2 contains a few fluid inclusions, and the shape of the fluid inclusion is much more regular. The homogenization temperatures ( $T_h$ ) range from  $72^\circ\text{C}$  to  $91^\circ\text{C}$ . The salinity, derived from the final melting temperature of ice using the equation from Bodnar [40], ranges from 4.96 wt% to 10.73 wt% NaCl equiv.

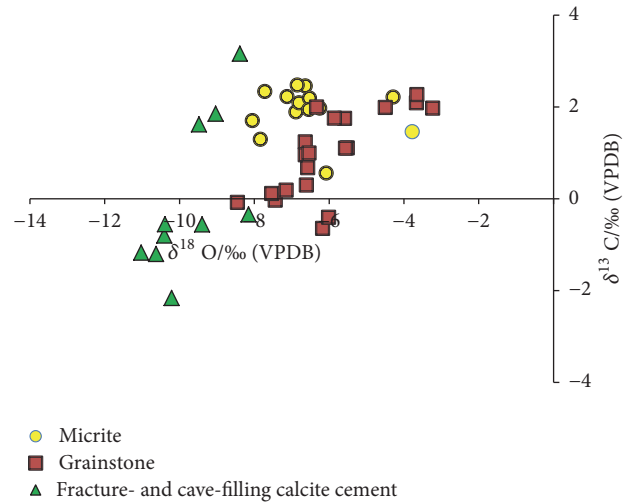


FIGURE 8:  $\delta^{13}\text{C}$  and  $\delta^{18}\text{O}$  values of host rocks and fracture- and cave-filling calcite cement by conventional methods.

Fluid inclusions in C3 are more abundant and mainly occur as single-phase aqueous inclusions with sizes  $< 4\ \mu\text{m}$  in general, which are too small to be measured.

The characteristics of inclusions in C4 are very similar to those of C2, with fewer numbers and the shape of fluid inclusion being more regular.  $T_h$  is less than  $90^\circ\text{C}$ , and salinity is moderate, ranging from 6.45 wt% to 9.98 wt% NaCl equiv.

C5 contains abundant aqueous fluid inclusions, sizes from 3 to  $15\ \mu\text{m}$ , and a vapor-to-liquid ratio of  $< 15\%$  in general. C5 shows a wide range of  $T_h$  varying from  $91^\circ\text{C}$  to  $129^\circ\text{C}$  ( $n = 58$ ). Water salinities at the time of C5 are variable, ranging from 0.71 wt% to 23.18 wt% NaCl equiv. ( $n = 58$ ). Oil-filled fluid inclusions were observed and showed yellow or blue UV fluorescence.

Aqueous fluid inclusions in calcite cement C6 have a vapor-to-liquid ratio of  $< 15\%$  and sizes of 4 to  $12\ \mu\text{m}$ . The average homogenization temperature is high, ranging from  $132.6^\circ\text{C}$  to  $200^\circ\text{C}$ . Note that C6 with relatively high temperatures has relatively low-salinity values, less than 10.61 wt% NaCl equiv. Oil inclusions were observed with blue-white UV fluorescence emission colors.

## 5. Discussion

### 5.1. Origin of Diagenetic Fluids

**5.1.1. Stable Isotopes and Fluid Inclusion Constraints on Fluids.** The combination of stable isotopic components and fluid inclusions can be used to estimate the formation temperature of diagenetic cement, which can further refine the diagenetic sequences and define the fluid properties.

Fibrous isopachous calcites are considered to be early marine cement that formed in the marine phreatic zone [42]. Therefore, C1 in this study formed in the early marine diagenesis environment. One type of blocky calcite cement surrounding bioclasts shows nonluminescence with several thin yellow bands (Figures 4(a) and 4(b)) based on similar

TABLE 2: Carbon, oxygen, and strontium isotopic data of host rocks and fracture- and vug-filling calcite cements by conventional methods of Lianglitag Formation carbonates in the Tahe Oilfield.

Well	Depth (m)	Sample type	Host lithology	$\delta^{18}\text{O}$ (‰ VPDB)	$\delta^{13}\text{C}$ (‰ VPDB)	$\text{Sr}^{87}/\text{Sr}^{86}$
S79	5499.96	Whole rock	Micritic limestones	-3.777	1.463	—
T443	5515.90	Whole rock	Micritic limestones	-7.837	1.296	—
T751	5838	Whole rock	Micritic limestones	-6.639	2.457	—
T904	5776	Whole rock	Micritic limestones	-6.885	1.892	—
T751	5840.20	Whole rock	Micritic limestones	-7.125	2.229	0.709005*
T751	5835.70	Whole rock	Micritic limestones	-7.718	2.337	—
T751	5776	Whole rock	Micritic limestones	-6.801	2.091	0.710323*
T751	5772.7	Whole rock	Micritic limestones	-6.523	2.194	—
S106	5884.14	Whole rock	Micritic limestones	-4.288	2.215	0.710756*
T751	5833.9	Whole rock	Micritic limestones	-6.85	2.48	—
T705	5657.95	Whole rock	Micritic limestones	-6.08	0.563	0.711927*
T904	5803	Whole rock	Micritic limestones	-6.542	1.944	—
T904	5792.54	Whole rock	Micritic limestones	-8.05	1.704	—
T904	5779.36	Whole rock	Micritic limestones	-6.247	1.975	—
S106	5934.86	Whole rock	Grainstone	-4.493	1.988	—
S110	6088.43	Whole rock	Grainstone	-8.448	-0.078	0.708904*
S99	5925.06	Whole rock	Grainstone	-6.335	1.999	—
S110	6089.9	Whole rock	Grainstone	-7.44	-0.028	0.709088*
S107	6186.86	Whole rock	Grainstone	-6.635	1.238	—
S107	6188.9	Whole rock	Sparry bioclastic limestone	-6.635	0.959	—
T705	5638.99	Whole rock	Sparry oolitic limestone	-6.171	-0.643	—
T705	5648.6	Whole rock	Grainstone	-6.607	0.3	0.708659*
T738	5883.9	Whole rock	Grainstone	-6.535	0.996	—
T114	6299.39	Whole rock	Grainstone	-3.23	1.977	0.70856*
S107	6230.33	Whole rock	Grainstone	-5.51	1.107	—
S110	6086.52	Whole rock	Grainstone	-7.149	0.19	0.709119*
S110	6083.91	Whole rock	Grainstone	-7.532	0.115	0.708919*
TP5	6158.68	Whole rock	Grainstone	-6.568	0.679	—
T114	6304.17	Whole rock	Grainstone	-3.664	2.091	0.708596*
S106	5885.92	Whole rock	Sparry bioclastic limestone	-3.653	2.268	0.708353*
T705	5638.3	Whole rock	Bioclastic limestone	-6.01	-0.403	0.708261*
S111	6108.7	Whole rock	Sparry bioclastic limestone	-5.582	1.75	—
S111	6105.89	Whole rock	Sparry bioclastic limestone	-5.86	1.757	0.708202*
S111	6104.96	Whole rock	Sparry bioclastic limestone	-5.558	1.105	0.708136*
S106	5885.92	Fracture-filling calcite cements	Sparry bioclastic limestone	-9.481	1.622	0.711119
S110	6098.3	Cavern-filling calcite cements	Marly limestone	-11.023	-1.175	0.712863
S110	6096.61	Vug-filling calcite cements	Micritic oolitic limestone	-10.624	-1.201	—
S110	6089.9	Cavern-filling calcite cements	Grainstone	-10.408	-0.799	—
S110	6083.91	Fracture-filling calcite cements	Grainstone	-9.393	-0.559	—
T79	5515.75	Cavern-filling calcite cements	Siltstone	-10.213	-2.159	—
T79	5509.3	Cavern-filling calcite cements	Siltstone	-8.155	-0.341	—
T204	5466.19	Cavern-filling calcite cements	Breccia	-10.389	-0.554	—
T751	5840.20	Vug-filling calcite cements	Micritic limestones	-8.383	3.16	0.709103
T904	5779.36	Vug-filling calcite cements	Micritic limestones	-9.033	1.854	—

\* After Liu et al. [23].

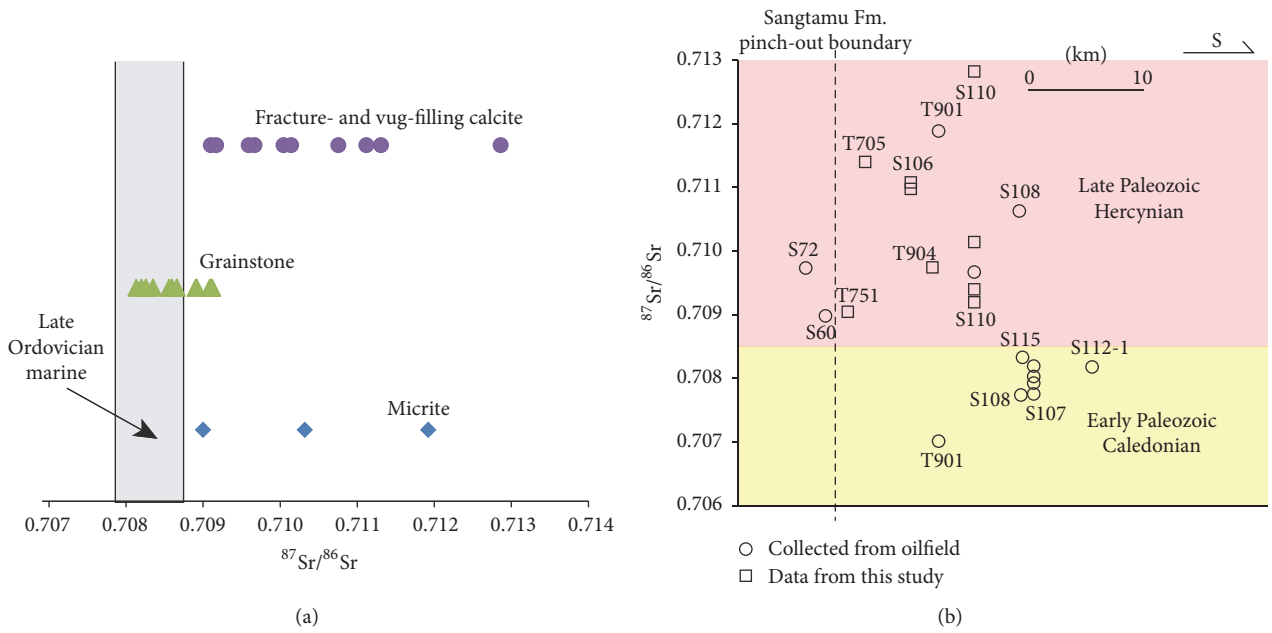


FIGURE 9: Characteristics of  $^{87}\text{Sr}/^{86}\text{Sr}$  values from the Lianglitag Formation. (a)  $^{87}\text{Sr}/^{86}\text{Sr}$  values of micrite, grainstone, and fractures and vug-filling calcite. (b) Distribution of  $^{87}\text{Sr}/^{86}\text{Sr}$  values from different wells in plane.

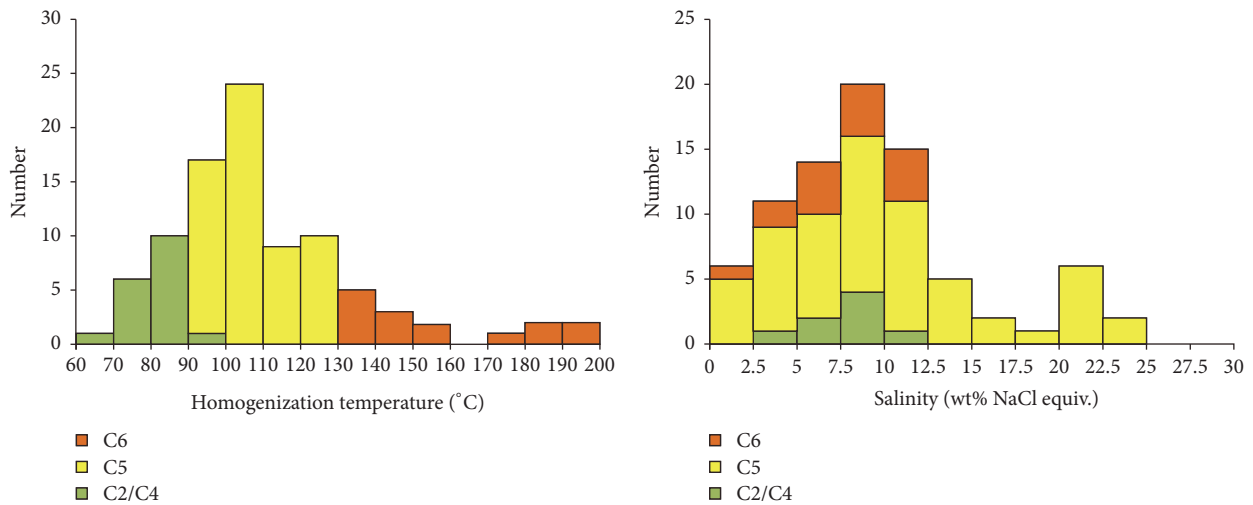


FIGURE 10: Histograms showing homogenization temperatures and salinities measured from fluid inclusions of different stages of pore-filling calcite cement.

$\delta^{18}\text{O}$  values and  $\delta^{13}\text{C}$  values with fibrous isopachous calcites (C1) (Figure 7). Hence, this blocky calcite cement should precipitate in marine diagenesis environment as well. Shields et al. [43] have reported that  $\delta^{18}\text{O}$  values of  $-6\text{‰}$  to  $-4\text{‰}$  VPDB and  $\delta^{13}\text{C}$  of  $-2\text{‰}$  to  $2\text{‰}$  VPDB characterize the global marine carbonates carbon and oxygen isotope values during the Late Ordovician. Assuming that the Late Ordovician limestones originally had a temperature of  $25^\circ\text{C}$  for subtropical seawater [44, 45] and using the O'Neil et al. [46] calcite-water oxygen isotope fractionation equation, the  $\delta^{18}\text{O}$  value of the water present during the growth of C1 was between  $-1.22\text{‰}$  and  $2.4\text{‰}$  V-SMOW, higher than

that of Late Ordovician seawater, that is  $-3$  to  $-6\text{‰}$  V-SMOW [43]. The slightly higher oxygen isotope values can be achieved by evaporation [47]. Therefore, the higher  $\delta^{18}\text{O}$  value suggests that evaporative concentration of seawater may have occurred during precipitation of C1. The higher  $\delta^{18}\text{O}$  value was mainly found in well S106, located at the southern part of the study area and characterized by deep slope facies (Figure 1(b)). Hence, environmental influence may be an alternative interpretation for oxygen isotopic changes in carbonate.

Compared with C1, the C2 shows slightly lower  $\delta^{18}\text{O}$  values ( $-6.35$  to  $-2.56\text{‰}$  VPDB; Figure 7), and homogenization

temperature  $T_h$  from fluid inclusion study indicates that C2 with coarser crystal was formed during burial diagenesis at approximately 60–90°C (Figure 10).

C3 shows lower oxygen values compared with C2. The more negative  $\delta^{18}\text{O}$  values could be due either to precipitation at a higher temperature or to precipitation from waters with lower  $\delta^{18}\text{O}$  values [48, 49]. The single-phase aqueous fluid inclusion petrographic evidence, which indicates a capture temperature of less than 50°C [41], suggests that C3 probably was in meteoric origin. Previous studies have indicated that the Lianglitag Formation carbonates are affected by both Caledonian and Hercynian orogenic events [50–53]. Hence, C3 probably precipitated as a result of meteoric water diagenesis during Caledonian and/or Hercynian orogenic events.

Compared with C3, C4 shows much more positive  $\delta^{18}\text{O}$  values. Most of the  $\delta^{18}\text{O}$  values for C4 lie within the marine calcite ranges [43], indicating that C4 was most likely influenced by marine fluid.  $T_h$  data from the fluid inclusions in C4 shows that it formed in temperatures up to 90°C; hence, C4 probably precipitated during the shallow buried stage after the tectonic uplift. Melim et al. [54] also showed that the carbon and oxygen isotopes changed from negative to positive from the meteoric phreatic zone to a seawater-shallow buried environment.

C5 has relatively negative  $\delta^{18}\text{O}_{\text{VPDB}}$  values, with  $\delta^{18}\text{O}_{\text{VPDB}}$  values ranging from –8.26 to –5.12‰ VPDB. The high fluid inclusion temperatures (91°C to 129°C) and wide range of salinity (0–23.18 wt%) imply that C5 blocky spars may have precipitated during burial environment from the mixing of multiple sources of fluids.

The  $\delta^{18}\text{O}_{\text{VPDB}}$  values of C6 are obviously negative and could be as low as –11‰ VPDB. Fluid inclusions in C6 are shown to have relatively low salinities (from 0 to 10.61 wt% equiv. NaCl) but highest homogenization temperatures (132.6 to 200°C). Based on the  $\delta^{18}\text{O}$  values and measured  $T_h$  temperatures, the isotopic signature of the parent fluid ranges from 5.57‰ to 11.96‰ (SMOW). Combined with the regional burial history curve (Figure 3), the homogeneous temperature of C6 exceeded the maximum burial experience of the strata. This type of calcite may have precipitated from a variety of processes: (1) the mixing of meteoric water with hydrothermal water, (2) thermochemical sulfate reduction, and (3) deeply recycled meteoric water. Hence, the high precipitation temperatures and relatively low salinity of the fluids indicate that C6 may have precipitated from meteoric water mixed with hydrothermal fluids. However, if this model applies, fluid inclusions with high temperatures are expected to have high salinities rather than low salinities, as was found in this area. The second possibility is that C6 with high homogenization temperatures and low salinities may have precipitated from thermochemical sulfate reduction (TSR) derived water [15, 55]. TSR is redox reactions between hydrocarbon and dissolved sulfates in temperatures >120°C [56–58]. TSR is well documented in Tazhong area [57, 59]. However, this proposal is discounted by the nonisotopically light carbon in both vug fillings and intergranular cement. Alternatively, deeply recycled meteoric water could have flowed down along faults to deep strata and thus became

significantly heated. Subsequently, the heated meteoric water underwent upward migration, leading to the precipitation of hydrothermal calcite. This model of water flow was previously proposed by Qing and Mountjoy [60] to explain the variation of homogenization temperatures as well as the  $^{87}\text{Sr}/^{86}\text{Sr}$  and  $\delta^{18}\text{O}$  values from saddle dolomite cement from the west towards the east in the Western Canada sedimentary basin as a result of tectonic thrusting and compression, sedimentary loading, and tectonic uplift on the western margin. The structural history of the Western Canada basin is broadly analogous to that of the Tahe area. Thus, it is possible for a similar model of water flow to have occurred in the study area as previously proposed by Li et al. [15], Jiang et al. [61], and Jiang et al. [62].

Different from  $\delta^{18}\text{O}$ ,  $\delta^{13}\text{C}$  is mainly controlled by carbon sources [63]. Most of the  $\delta^{13}\text{C}$  values from C1 to C6 lie between –2‰ and 4‰ (Figure 7), close to the  $\delta^{13}\text{C}$  range of contemporaneous seawater, indicating a local source of C.

Compared with the  $\delta^{18}\text{O}$  and  $\delta^{13}\text{C}$  analysis results of matrix pore-filling calcite cement by the SIMS method, the  $\delta^{18}\text{O}$  and  $\delta^{13}\text{C}$  data of fracture- and cave-filling calcite cement obtained by traditional methods are more negative (Figure 8), most likely due to the results of karst, which had been discussed by Li et al. [15] in detail. Most of the oxygen isotopes of micrite and grainstone are obviously more negative than those of the Late Ordovician marine carbonate (from –6 to –4‰ VPDB) [43], which indicates that the matrix limestone in the Lianglitag Formation is strongly affected by the late diagenetic fluid.

**5.1.2. Strontium Isotopes.** During the Late Ordovician, the carbonate strontium isotope composition of the global ocean ranged from 0.7078 to 0.7082 [64, 65]. The seawater  $^{87}\text{Sr}/^{86}\text{Sr}$  record is controlled by two main strontium fluxes and their isotopic compositions: the hydrothermal brines at midocean ridges (MOR flux), characterized by  $^{87}\text{Sr}/^{86}\text{Sr}$  ratios being close to 0.703, and the continental input (river flux), which has a modern global average  $^{87}\text{Sr}/^{86}\text{Sr}$  ratio of 0.712 [66–68].

Both micrite and fracture-vug-fill calcite present much higher  $^{87}\text{Sr}/^{86}\text{Sr}$  ratio values than Late Ordovician seawater, indicating largely introduced radiogenic Sr (Figure 9(a)). The higher  $^{87}\text{Sr}/^{86}\text{Sr}$  ratios of some micrite samples may be the result of recrystallization, which was commonly observed under the microscope (Figures 5(c) and 5(d)); it could also reflect the introduction of radiogenic strontium from terrigenous clastic internal to the Lianglitag Formation [23]. For radiogenic Sr in calcite cement, the stratigraphic hiatuses identified in Figure 2 and burial history diagrams shown in Figure 3 suggest that there are several uplift and erosion events which could have involved the weathering of radiogenic source terrains. Radiogenic strontium could also be derived from the Precambrian basement or Lower Cambrian clastic section via circulating fluids within conductive faults and fractures that penetrate the basement in the Tazhong area [69].  $^{87}\text{Sr}/^{86}\text{Sr}$  ratio shows increasing trends from lower to upper part of the formation. Therefore, the  $^{87}\text{Sr}$ -rich fluid is probably from meteoric water leaching of clastic material in the Tahe area during the periods of tectonic uplift, and

this is supported by a recent study from formation water geochemistry in the Tabei area [70].

Previous studies have indicated that the Lianglitag Formation carbonates are likely affected by both Early Paleozoic Caledonian and Late Paleozoic Hercynian karstification [50–53]. However, because of the relatively similar characteristics in the minerals and cathodoluminescence, it is difficult to distinguish these phases. According to the stratigraphic distribution characteristics (Figure 2), one of the distinguished features of the Late Paleozoic is that the clastics are more obvious. Hence, strontium isotope may be useful in distinction between the two karsts. The strontium isotopic composition could be broadly divided into two groups (Figure 9(b)): the first group represent the Early Paleozoic karst, characterized by  $^{87}\text{Sr}/^{86}\text{Sr}$  ratios that range from 0.70712 to 0.7085, which is close to the strontium isotopic composition of the Late Ordovician seawater; the second group shows  $^{87}\text{Sr}/^{86}\text{Sr}$  ratios ranging from 0.7085 to 0.71188, significantly higher than the Late Ordovician marine strontium isotopic composition. This group represents Late Paleozoic karst, which indicates that strontium may be added by continental weathering through the river. In addition, the strontium isotopic composition of the northern part of the Tahe Oilfield (the north of the Sangtamu Fm. pinch-out boundary) is much higher, which is mainly due to the Late Paleozoic karst, whereas the strontium isotopic composition of the middle and southern parts of the Tahe Oilfield (the south of the Sangtamu Fm. pinch-out boundary) are broad and are both influenced by the Early Paleozoic and the Late Paleozoic karst, such as well S108 and well T901, which are superimposed on the two karst interactions.

*5.2. Diagenetic Fluid Evolution and Its Influence on Reservoir Properties.* Based on petrographic, isotopic, and fluid inclusion data, the diagenetic sequence is identified and divided into three main episodes. The eogenetic, mesogenetic, and telogenetic stages were used in this study [71].

During the deposition of the Lianglitag Formation, the Tahe region was characterized by a ramp and/or weakly rimmed platform, with a low-gradient slope and small-scale reefs and shoals [23]. Marine calcite cement (C1) is commonly observed (Figures 4(a) and 4(b)), especially in the southern slope facies, indicating that the Lianglitag Formation carbonates experienced strong marine cementation in the eogenetic stage. Minor fabric-selective pores occur in high-energy shoals; however, they are more commonly partly or completely filled by calcite cement (Figure 6(a)). Therefore, the carbonates exhibit intensive marine cementation and weak syndepositional freshwater dissolution during the eogenetic diagenetic stage (Figure 11(a)). Thereafter, the strata enter a shallow burial diagenetic environment where C2 calcite cement was precipitated.

The large volume of C3 precipitated at the wells demonstrates that the telogenetic meteoric impact is ubiquitous. In the Caledonian, the arch developed as a monocline dipping gently to the SE; as the arch was uplifted several times, three episodes of karstification, designated episodes I, II, and III, occurred during this period [52, 53]. Episode I occurred

between the deposition of the Yijianfang and Qiaerbake Formations. Episode II occurred between the deposition of the Lianglitag and Sangtamu Formations. Episode III occurred between the deposition of the Ordovician Sangtamu Formation and Silurian strata. The Lianglitag Formation is mainly affected by Episode II [17]. The Lianglitag Formation carbonates were exposed to the surface and infiltrated by ground water, leading to significant dissolution of the carbonates and formation of dissolution vugs and caves with sizes from centimeters to meters (Figure 11(b)). Some vugs and caverns have been filled by minerals and/or sediments during the following mesogenetic stage (Figure 11(c)).

At the end of the Middle Devonian, because of the proximity to the South Tianshan Ocean, the northern part of the Tahe Oilfield was uplifted and subjected to subaerial erosion once again [31, 36]. The Lianglitag subcrop shown in Figure 1(b) and erosional removal of the Middle Ordovician through Carboniferous section shown in Figure 2 are both the result of Hercynian uplift and erosion. Therefore, Hercynian telogenetic fluids could have laterally access to the Lianglitag Formation via the subcrop limit and result in the development of dissolution cavities (Figures 1(c) and 11(d)). Access would not necessarily require transit through the overlying Sangtamu section. Additionally, fractures are important diagenetic fluid channels for karstification. There are four periods of fault structures recognizable in the Tahe seismic profiles at present [14], which from the bottom up are as follows: (1) thrust faults developed in Cambro-Ordovician strata that formed during the Middle-Late Ordovician; (2) a strike-slip fault that developed under the  $T_6^0$  reflecting layer (i.e., Carboniferous base boundary) and formed in the Middle-Late Devonian; (3) normal faults cutting Permian and older strata associated with early to middle Permian magmatism; and (4) thrust faults that developed in pre-Jurassic strata and formed during the latest Permian to earliest Triassic. The Late Ordovician strata in the Tahe region are mainly affected by mid to late Devonian strike-slip faulting. Other periods of faulting are of subsidiary importance. Therefore, strike-slip faults in the Middle-Late Devonian developed and freshwater along fractures could affect the Lianglitag Formation strata.

Subsequently, the sediments were again influenced by marine to shallow burial, from which bright orange CL calcite (Cement 4) precipitated. Burial dissolution pores are locally visible (Figures 4(e), 4(f), 5(e), and 5(f)). Although late burial dissolution does occur, it is volumetrically minor. Previous studies have shown that burial dissolution mainly includes organic acids,  $\text{CO}_2$ ,  $\text{H}_2\text{S}$  [72], and deep hydrothermal dissolution [12, 73, 74]. According to Section 5.1.1, TSR and thermal fluid activity are not obvious in the Upper Ordovician Lianglitag Formation, which is consistent with the results of Li et al. [14]. Deeply recycled meteoric water may have entered the carbonate rocks during the late Permian favored by fracturing [75] and generated both dissolution and subsequent cementation C6 in vugs. As noted above, C6 was precipitated at temperatures from 130 to 200°C and showed significantly higher  $^{87}\text{Sr}/^{86}\text{Sr}$  ratios and lighter  $\delta^{18}\text{O}$  and  $\delta^{13}\text{C}$  values. We have observed some C6 temperature and oxygen isotopic decreasing trend in distance, and the trend of

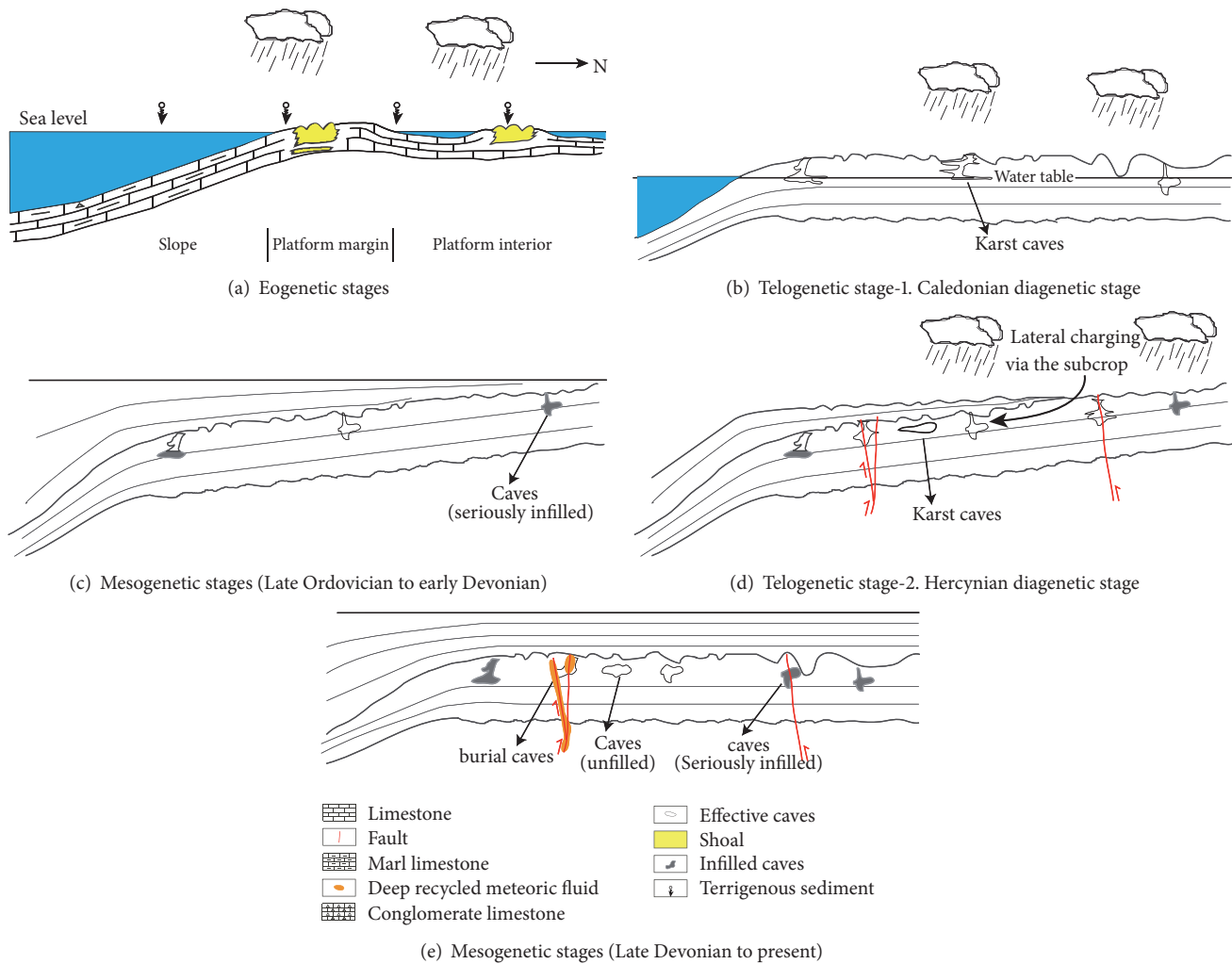


FIGURE 11: Diagenetic evolution and reservoir formation models of Lianglitag Formation carbonates.

oxygen isotope values and temperatures during its pathway suggest that C6 was likely precipitated from recycling of meteoric water. Unfortunately, the data are not enough. Combined with previous works in Tarim Basin [15, 61, 62], C6 was probably closely related to deeply recycled meteoric water. The reduced water coexisted with highly mature oils with blue-white UV fluorescence emission colors. However, because most fractures in the Tahe region are partially or completely occluded by green marl, the development of deeply recycled meteoric water is very local (Figure 11(e)).

Non-fabric-selective vug and cave were produced during near-surface karst processes and later burial diagenesis forms an important class of carbonate reservoir in the Lianglitag Formation in the Tahe Oilfield. Being near surface combined with burial diagenesis produced the complex reservoirs with several scales of heterogeneity. The main controlling factor of the reservoir distribution was multistage karstification and fracturing.

## 6. Conclusions

(1) Combined with isotopic geochemical and fluid inclusion data, the corresponding diagenetic fluid was identified. The

early nonluminescent C1 to growth zones of dark red luminescent C2 is a syngenetic seawater-shallow burial diagenetic environment; the subsequent nonluminescent C3 is related to the meteoric fluid system resulting from tectonic uplift and exposure. Then, the strata were buried again and the bright orange luminescent C4 zone was formed during shallow burial. The C5 precipitated in a middle-deep burial environment and was characterized by brown to dull luminescence. In addition, an abnormally high temperature and low salinity were found in C6 along fractures, which may be the product of deeply recycled meteoric water.

(2) The abundance of C1 indicates that the Lianglitag Formation carbonate suffered strong marine cementation and weak meteoric dissolution and cementation during the eogenetic diagenetic stage. The paleokarst during Caledonian II and Hercynian telogenetic karstification closely related to C3 constitutes the most constructive diagenesis. In addition, the carbonate was locally infected by deeply recycled meteoric water during burial. Compared with the Early Paleozoic fracture- and vug-filling calcite, the Late Paleozoic fracture- and vug-filling calcite have a significantly higher  $^{87}\text{Sr}/^{86}\text{Sr}$  ratio due to the presence of more terrigenous clastic material.

(3) The reservoir system in the Tahe carbonates is dominated by non-fabric-selective pores and remanent (unfilled) karst caves. The development of the reservoir is closely related to fractures. The vugs and caves may be the result of the infiltration and dissolution of meteoric fluid along the fractures when the strata are tectonically uplifted, of high-temperature and low-salinity meteoric water circulating along the deep basin, or of the two superimposed transformations. Multistage karstification and fracturing are the main controlling factors of reservoir development, which can provide important guidance for future deep-buried oil and gas exploration, and have important economic implications.

### Conflicts of Interest

The authors declare that there are no conflicts of interest regarding the publication of this paper.

### Acknowledgments

This work is financially supported by the National Natural Science Foundation of China (Grant no. 41302084), Strategic Priority Research Program Grant of the Chinese Academy of Sciences (XDA14010201-02), and National Science and Technology Major Project of China (2017ZX05008-003). The authors thank Drs. Xiaoxiao Ling, Guoqiang Tang, Yu Liu, Qiuli Li, and Xianhua Li for their help during SIMS analyses in IGGCAS. Dr. Lei Jiang gave constructive advice both in English language and in logic arrangement. Many thanks are also due to Professor Chunfang Cai for constructive comments that helped to improve the manuscript.

### References

- [1] C. Cai, B. Mei, T. Ma, C. Chen, W. Li, and C. Liu, *Approach to Fluid-Rock Interaction in the Tarim Basin*, Geological Publishing House, Beijing, China, 1997.
- [2] S. Morad, J. M. Ketzer, and L. R. De Ros, "Spatial and temporal distribution of diagenetic alterations in siliciclastic rocks: implications for mass transfer in sedimentary basins," *Sedimentology*, vol. 47, no. 1, pp. 95–120, 2000.
- [3] B. Rasmussen and B. Krapez, "Evidence of hydrocarbon and metalliferous fluid migration in the Palaeoproterozoic Earaheedy Basin of Western Australia," *Journal of the Geological Society*, vol. 157, no. 2, pp. 355–366, 2000.
- [4] J. J. Packard, I. Al-Aasm, I. Samson, Z. Berger, and J. Davies, "A Devonian hydrothermal chert reservoir: the 225 bcf parkland field, british columbia, Canada," *AAPG Bulletin*, vol. 85, no. 1, pp. 51–84, 2001.
- [5] J. R. Boles, P. Eichhubl, G. Garven, and J. Chen, "Evolution of a hydrocarbon migration pathway along basin-bounding faults: evidence from fault cement," *AAPG Bulletin*, vol. 88, no. 7, pp. 947–970, 2004.
- [6] S. N. Ehrenberg, G. P. Eberli, M. Keramati, and S. A. Moallemi, "Porosity-permeability relationships in interlayered limestone-dolostone reservoirs," *AAPG Bulletin*, vol. 90, no. 1, pp. 91–114, 2006.
- [7] Z. Li, D. Han, and J. Shou, "Diagenesis systems and their spatio-temporal attributes in sedimentary basins," *Acta Petrologica Sinica*, vol. 22, no. 8, pp. 2151–2164, 2006.
- [8] S. N. Ehrenberg, P. H. Nadeau, and A. A. M. Agrawi, "A comparison of Khuff and Arab reservoir potential throughout the Middle East," *AAPG Bulletin*, vol. 91, no. 3, pp. 275–286, 2007.
- [9] M. Moradpour, Z. Zamani, and S. A. Moallemi, "Controls on reservoir quality in the lower triassic kangany formation, Southern Persian gulf," *Journal of Petroleum Geology*, vol. 31, no. 4, pp. 367–385, 2008.
- [10] Z. Li and J. Liu, "Key problems and research trend of diagenetic geodynamic mechanism and spatio-temporal distribution in sedimentary Basins," *Acta Sedimentologica Sinica*, vol. 27, pp. 837–848, 2009.
- [11] Z. Li, "Research frontiers of fluid-rock interaction and oil-gas formation in deep-buried basins," *Bulletin of Mineralogy, Petrology and Geochemistry*, vol. 35, 2016.
- [12] C. Cai, K. Li, B. Li, L. Cai, and L. Jiang, "Geochemical characteristics and origins of fracture- and vug-filling of the Ordovician in Tahe Oilfield, Tarim Basin," *Acta Petrologica Sinica*, vol. 25, pp. 91–96, 2009.
- [13] Z. Jin, D. Zhu, W. Hu, X. Zhang, J. Zhang, and Y. Song, "Mesogenetic dissolution of the middle Ordovician limestone in the Tahe oilfield of Tarim basin, NW China," *Marine and Petroleum Geology*, vol. 26, no. 6, pp. 753–763, 2009.
- [14] Z. Li, S. Huang, J. Liu et al., "Buried diagenesis, structurally controlled thermal-fluid process and their effect on Ordovician carbonate reservoir in Tahe, Tarim Basin," *Acta Sedimentologica Sinica*, vol. 28, pp. 969–979, 2010.
- [15] K. Li, C. Cai, H. He et al., "Origin of palaeo-waters in the Ordovician carbonates in Tahe oilfield, Tarim Basin: constraints from fluid inclusions and Sr, C and O isotopes," *Geofluids*, vol. 11, no. 1, pp. 71–86, 2011.
- [16] H. Zeng, R. Loucks, X. Janson et al., "Three-dimensional seismic geomorphology and analysis of the Ordovician paleokarst drainage system in the central Tabei Uplift, northern Tarim Basin, western China," *AAPG Bulletin*, vol. 95, no. 12, pp. 2061–2083, 2011.
- [17] F. Tian, Q. Jin, X. Lu et al., "Multi-layered ordovician paleokarst reservoir detection and spatial delineation: a case study in the Tahe Oilfield, Tarim Basin, Western China," *Marine and Petroleum Geology*, vol. 69, pp. 53–73, 2016.
- [18] C. Jia, S. Zhang, and S. Wu, *Tarim Basin and the Surrounding Strata (Part II)*, Science Press, 2004.
- [19] Z. Zhao and Z. Huang, "Ordovician conodont zones and sedimentary sequences of the Tarim Basin, Xinjiang, NW China," *Journal of Stratigraphy*, vol. 30, pp. 193–203, 2006.
- [20] X. Cai, X. Jin, L. Zhao, Y. Yang, Z. Zhu, and M. Hu, "Classification and correlation of Lianglitag Formation of Upper Ordovician in Tarim Basin," *Xinjiang Petroleum Geology*, pp. 447–449, 2012.
- [21] M.-C. Hou, L. Wan, H. Fu, L.-M. Zhou, L.-X. Qi, and R.-L. Yu, "Study on the sedimentary environment of the Upper Ordovician Lianglitage Formation in the south of Tarim River, China," *Journal of Chengdu University of Technology*, vol. 33, pp. 509–516, 2006.
- [22] J. Liu, Z. Li, Y. Han, S. Peng, D. Han, and C. Xu, "Characteristics of sedimentary geochemistry and evolution of platform of the Lianglitag formation carbonate, Upper Ordovician in Tahe Oilfield," *Chinese Journal of Geology*, vol. 45, no. 1, pp. 278–291, 2010.
- [23] J. Liu, Z. Li, J. Huang, and L. Yang, "Distinct sedimentary environments and their influences on carbonate reservoir evolution

- of the Lianglitag Formation in the Tarim Basin, Northwest China," *Science China Earth Sciences*, vol. 55, no. 10, pp. 1641–1655, 2012.
- [24] Y. Lu, C. Liu, C. Du, H. Jiang, and F. Liang, "Reservoir characteristics and control factors of Lianglitag Formation of Upper Ordovician in The Tahe Oilfield," *Xinjiang Geology*, vol. 29, pp. 198–202, 2011.
- [25] S. Buschaert, S. Fourcade, M. Cathelineau et al., "Widespread cementation induced by inflow of continental water in the eastern part of the Paris basin: O and C isotopic study of carbonate cements," *Applied Geochemistry*, vol. 19, no. 8, pp. 1201–1215, 2004.
- [26] B. Vincent, L. Emmanuel, P. Houel, and J.-P. Loreau, "Geodynamic control on carbonate diagenesis: petrographic and isotopic investigation of the Upper Jurassic formations of the Paris Basin (France)," *Sedimentary Geology*, vol. 197, no. 3–4, pp. 267–289, 2007.
- [27] J. Bourdet, J. Pironon, G. Levresse, and J. Tritlla, "Petroleum accumulation and leakage in a deeply buried carbonate reservoir, Nispero field (Mexico)," *Marine and Petroleum Geology*, vol. 27, no. 1, pp. 126–142, 2010.
- [28] P. A. Cox, R. A. Wood, J. A. D. Dickson, H. B. Al Rougha, H. Shebl, and P. W. M. Corbett, "Dynamics of cementation in response to oil charge: evidence from a Cretaceous carbonate field, U.A.E." *Sedimentary Geology*, vol. 228, no. 3–4, pp. 246–254, 2010.
- [29] J. Sample, "Stable isotope constraints on vein formation and fluid evolution along a recent thrust fault in the Cascadia accretionary wedge," *Earth and Planetary Science Letters*, vol. 293, no. 3–4, pp. 300–312, 2010.
- [30] R. I. Gabitov, A. C. Gagnon, Y. Guan, J. M. Eiler, and J. F. Adkins, "Accurate Mg/Ca, Sr/Ca, and Ba/Ca ratio measurements in carbonates by SIMS and NanoSIMS and an assessment of heterogeneity in common calcium carbonate standards," *Chemical Geology*, vol. 356, pp. 94–108, 2013.
- [31] C. Lin, H. Yang, J. Liu, Z. Rui, Z. Cai, and Y. Zhu, "Distribution and erosion of the Paleozoic tectonic unconformities in the Tarim Basin, Northwest China: significance for the evolution of paleo-uplifts and tectonic geography during deformation," *Journal of Asian Earth Sciences*, vol. 46, pp. 1–19, 2012.
- [32] C. Jia, *Tectonic Characteristic and Petroleum in Tarim Basin, China*, Performance Industry Press, Beijing, China, 1997.
- [33] Q. Wang and Z. Li, *Basin-Mountain System and Oil and Gas in Kuche-Tianshan*, Science Press, 2007.
- [34] M. Jiang, J. Zhu, D. Chen, R. Zhang, and G. Qiao, "Carbon and strontium isotope variations and responses to sea-level fluctuations in the Ordovician of the Tarim Basin," *Science in China Series D: Earth Sciences*, vol. 44, no. 9, pp. 816–823, 2001.
- [35] X. Lou, "The seismic reflection boundary T7<sup>2</sup> and the Upper Ordovician carbonate karst reservoirs on the Tazhong uplift, Xinjiang," *Sedimentary Geology and Tethyan Geology*, vol. 25, pp. 24–32, 2005.
- [36] J. Charvet, L. Shu, S. Laurent-Charvet et al., "Palaeozoic tectonic evolution of the Tianshan belt, NW China," *Science China Earth Sciences*, vol. 54, no. 2, pp. 166–184, 2011.
- [37] N. Qiu, S. Hu, and L. He, *Theory and Application of Thermal System in Sedimentary Basin*, Petroleum Industry Press, 2004.
- [38] C. S. Lin, H. J. Yang, J. Y. Liu et al., "Paleostructural geomorphology of the Paleozoic central uplift belt and its constraint on the development of depositional facies in the Tarim Basin," *Science in China Series D: Earth Sciences*, vol. 52, no. 6, pp. 823–834, 2009.
- [39] N.-S. Qiu, R. Peter, Q.-H. Mei, G. Jiang, S. Nicolesco, and C. Tao, "Application of the (U-Th)/He thermochronometry to the tectono-thermal evolution of sedimentary basin—a case history of well KQ1 in the Tarim basin," *Chinese Journal of Geophysics*, vol. 52, no. 7, pp. 1825–1835, 2009.
- [40] R. J. Bodnar, "Revised equation and table for determining the freezing point depression of H<sub>2</sub>O-NaCl solutions," *Geochimica et Cosmochimica Acta*, vol. 57, no. 3, pp. 683–684, 1993.
- [41] R. H. Goldstein and T. J. Reynolds, *Fluid inclusion, microthermometry*, 1994.
- [42] C. H. Moore, *Carbonate Diagenesis And Porosity*, Elsevier, Amsterdam, Netherlands, 1989.
- [43] G. A. Shields, G. A. F. Carden, J. Veizer, T. Meidla, J.-Y. Rong, and R.-Y. Li, "Sr, C, and O isotope geochemistry of Ordovician brachiopods: a major isotopic event around the Middle-Late Ordovician transition," *Geochimica et Cosmochimica Acta*, vol. 67, no. 11, pp. 2005–2025, 2003.
- [44] D. Fang and Z. Shen, "Phanerozoic apparent polar-wander paths of Tarim and plate motion," *Journal of Zhejiang University (Science Edition)*, vol. 28, pp. 100–106, 2001.
- [45] L. Li, N. Qiu, Z. Jin, and Z. He, "Geothermal history of Tarim Basin," *Oil & Gas Geology*, vol. 26, pp. 613–617, 2005.
- [46] J. R. O'Neil, R. N. Clayton, and T. K. Mayeda, "Oxygen isotope fractionation in divalent metal carbonates," *The Journal of Chemical Physics*, vol. 51, no. 12, pp. 5547–5558, 1969.
- [47] B. W. Robinson and A. Gunatilaka, "Stable isotope studies and the hydrological regime of sabkhas in southern Kuwait, Arabian Gulf," *Sedimentary Geology*, vol. 73, no. 1–2, pp. 141–159, 1991.
- [48] J. Veizer, P. Bruckschen, F. Pawellek et al., "Oxygen isotope evolution of Phanerozoic seawater," *Palaeogeography, Palaeoclimatology, Palaeoecology*, vol. 132, no. 1–4, pp. 159–172, 1997.
- [49] A. Immenhauser, J. A. M. Kenter, G. Ganssen, J. R. Bahamonde, A. Van Vliet, and M. H. Saher, "Origin and significance of isotopes shifts in Pennsylvanian carbonates (Asturias, NW Spain)," *Journal of Sedimentary Research*, vol. 72, no. 1, pp. 82–94, 2002.
- [50] X. Yan, Z. Han, and Y. Li, "Reservoir characteristics and formation mechanism of the Ordovician carbonate pools in the Tahe Oilfield," *Geological Review*, vol. 48, pp. 619–626, 2002.
- [51] R. Yu, "Characteristics and significance of the Caledonian karst in the Tahe Oilfield, the Tarim basin," *Petroleum Geology & Experiment*, vol. 27, pp. 468–472, 2005.
- [52] R. Yu and H. Fu, "Influence of tectonic movement on Ordovician carbonates of Tahe Oilfield," *Nature Gas Exploration and Development*, vol. 29, pp. 1–5, 2006.
- [53] T. Zhang and X. Cai, "Caledonian paleo-karstification and its characteristics in Tahe area, Tarim basin," *Acta Geologica Sinica*, vol. 81, no. 8, pp. 1125–1134, 2007.
- [54] L. A. Melim, H. Westphal, P. K. Swart, G. P. Eberli, and A. Munnecke, "Questioning carbonate diagenetic paradigms: evidence from the Neogene of the Bahamas," *Marine Geology*, vol. 185, no. 1–2, pp. 27–53, 2002.
- [55] R. H. Worden, P. C. Smalley, and N. H. Oxtoby, "The effects of thermochemical sulfate reduction upon formation water salinity and oxygen isotopes in carbonate gas reservoirs," *Geochimica et Cosmochimica Acta*, vol. 60, no. 20, pp. 3925–3931, 1996.
- [56] R. H. Worden, P. C. Smalley, and N. H. Oxtoby, "Gas souring by thermochemical sulfate reduction at 140°C," *AAPG Bulletin*, vol. 79, no. 6, pp. 854–863, 1995.
- [57] C. Cai, W. Hu, and R. H. Worden, "Thermochemical sulphate reduction in Cambro-Ordovician carbonates in Central Tarim," *Marine and Petroleum Geology*, vol. 18, no. 6, pp. 729–741, 2001.

- [58] H. G. Machel, "Bacterial and thermochemical sulfate reduction in diagenetic settings—old and new insights," *Sedimentary Geology*, vol. 140, no. 1-2, pp. 143–175, 2001.
- [59] C. Cai, Q. Xiao, C. Fang, T. Wang, W. He, and H. Li, "The effect of thermochemical sulfate reduction on formation and isomerization of thiadiamondoids and diamondoids in the Lower Paleozoic petroleum pools of the Tarim Basin, NW China," *Organic Geochemistry*, vol. 101, pp. 49–62, 2016.
- [60] H. Qing and E. Mountjoy, "Large-scale fluid flow in the Middle Devonian Presqu'ile barrier, western Canada sedimentary basin," *Geology*, vol. 20, no. 10, article 903, 1992.
- [61] L. Jiang, W. Pan, C. Cai et al., "Fluid mixing induced by hydrothermal activity in the ordovician carbonates in Tarim Basin, China," *Geofluids*, vol. 15, no. 3, pp. 483–498, 2015.
- [62] L. Jiang, C. Cai, R. H. Worden et al., "Multiphase dolomitization of deeply buried Cambrian petroleum reservoirs, Tarim Basin, north-west China," *Sedimentology*, vol. 63, no. 7, pp. 2130–2157, 2016.
- [63] J. D. Hudson, "Stable isotopes and limestone lithification," *Journal of the Geological Society*, vol. 133, no. 6, pp. 637–660, 1977.
- [64] R. E. Denison, R. B. Koepnick, W. H. Burke, and E. A. Hetherington, "Construction of the Cambrian and Ordovician seawater  $^{87}\text{Sr}/^{86}\text{Sr}$  curve," *Chemical Geology*, vol. 152, no. 3-4, pp. 325–340, 1998.
- [65] J. M. McArthur, R. J. Howarth, and T. R. Bailey, "Strontium isotope stratigraphy: LOWESS version 3: best fit to the marine Sr-isotope curve for 0–509 Ma and accompanying look-up table for deriving numerical age," *Journal of Geology*, vol. 109, no. 2, pp. 155–170, 2001.
- [66] G. Faure, *Principles of Isotope Geology*, 2nd edition, 1986.
- [67] J. D. Marshall, "Climatic and oceanographic isotopic signals from the carbonate rock record and their preservation," *Geological Magazine*, vol. 129, no. 2, pp. 143–160, 1992.
- [68] J. L. Banner, "Application of the trace element and isotope geochemistry of strontium to studies of carbonate diagenesis," *Sedimentology*, vol. 42, no. 5, pp. 805–824, 1995.
- [69] C. Cai, K. Li, H. Li, and B. Zhang, "Evidence for cross formational hot brine flow from integrated  $^{87}\text{Sr}/^{86}\text{Sr}$ , REE and fluid inclusions of the Ordovician veins in Central Tarim, China," *Applied Geochemistry*, vol. 23, no. 8, pp. 2226–2235, 2008.
- [70] J. Chen, D. Liu, P. Peng, C. Yu, B. Zhang, and Z. Xiao, "The sources and formation processes of brines from the Lunan Ordovician paleokarst reservoir, Tarim Basin, northwest China," *Geofluids*, vol. 13, no. 3, pp. 381–394, 2013.
- [71] P. W. Choquette and L. C. Pray, "Geologic nomenclature and classification of porosity in sedimentary carbonates," *AAPG Bulletin*, vol. 54, no. 2, pp. 207–250, 1970.
- [72] S. J. Mazzullo and P. M. Harris, "Mesogenetic dissolution: its role in porosity development in carbonate reservoirs," *AAPG Bulletin*, vol. 76, no. 5, pp. 607–620, 1992.
- [73] G. R. Davies and L. B. Smith Jr., "Structurally controlled hydrothermal dolomite reservoir facies: an overview," *AAPG Bulletin*, vol. 90, no. 11, pp. 1641–1690, 2006.
- [74] Z. Jin, D. Zhu, W. Hu, X. Zhang, Y. Wang, and X. Yan, "Geological and geochemical signature of hydrothermal activity and their influence on carbonated reservoir bedside in the Tarim Basin," *Acta Geologica Sinica*, vol. 80, pp. 245–253, 2006.
- [75] J.-W. Li, Z. Li, N.-S. Qiu, Y.-H. Zuo, J.-B. Yu, and J.-Q. Liu, "Carboniferous-Permian abnormal thermal evolution of the Tarim basin and its implication for deep structure and magmatic activity," *Chinese Journal of Geophysics*, vol. 59, no. 9, pp. 3318–3329, 2016.

## Research Article

# Origin and Distribution of Carbonate Cement in Tight Sandstones: The Upper Triassic Yanchang Formation Chang 8 Oil Layer in West Ordos Basin, China

Jin Lai,<sup>1,2</sup> Guiwen Wang,<sup>1,2</sup> Jing Chen,<sup>1</sup> Shuchen Wang,<sup>1</sup> Zhenglong Zhou,<sup>1</sup> and Xuqiang Fan<sup>1</sup>

<sup>1</sup>College of Geosciences, China University of Petroleum, Beijing 102249, China

<sup>2</sup>State Key Laboratory of Petroleum Resources and Prospecting, China University of Petroleum, Beijing 102249, China

Correspondence should be addressed to Jin Lai; [sisylaijin@163.com](mailto:sisylaijin@163.com)

Received 13 February 2017; Revised 25 April 2017; Accepted 14 June 2017; Published 30 July 2017

Academic Editor: Xiaorong Luo

Copyright © 2017 Jin Lai et al. This is an open access article distributed under the Creative Commons Attribution License, which permits unrestricted use, distribution, and reproduction in any medium, provided the original work is properly cited.

Two generations of carbonate cement as Type I (microcrystalline calcite and dolomite) and Type II (mainly Fe-calcite and Fe-dolomite) are recognized in Chang 8 sandstones, Ordos basin. Carbonate cement in Chang 8 sandstones is closely related to the dissolved carbon from thermal maturation of organic matters. Carbonate cement in the loosely packed framework grains precipitated shortly after deposition, and late-stage ferroan calcite and ferroan dolomite formed with progressive burial. The early diagenetic carbonate cement is partially to completely replaced by late-stage ferroan calcite and ferroan dolomite. Carbonate cement is much more commonly observed in sand bodies adjacent to Chang 7 source rocks. With increasing distance from the Chang 7 oil layers, the carbonate cement content gradually decreases. However, some tight carbonate cemented zones also occur at the sandstone-mudstone interfaces. Dissolution of Ca-feldspars by organic acids-rich fluids, together with clay mineral transformations such as illitization of smectite, would provide  $\text{Ca}^{2+}$  and  $\text{Mg}^{2+}$  ions for carbonate cementation. Organic acids and  $\text{CO}_2$  rich fluids would charge into the reservoirs with the hydrocarbons, and when the  $\text{CO}_2$  and acids were buffered by the framework grain dissolution, carbonate cement would precipitate with a decrease in  $\text{CO}_2$  concentration.

## 1. Introduction

The Ordos basin is the second largest petroliferous sedimentary basin in China [1, 2]. The basin was part of the North China Craton prior to the Paleozoic, and it became an isolated lake basin during the Middle and Late Triassic [3]. A series of lacustrine and deltaic clastic sediments, which were known as the Yanchang Formation, were deposited during this time [3]. The Upper Triassic Yanchang Formation, which is underlain by the Middle Zhifang Formation and overlain by the Lower Jurassic Yanan Formation (Figure 1; [4]), is a significant oil-producing bed in the Ordos basin [3, 5]. The Chang 8 (eighth member of Yanchang Formation) sandstones, which consist of braided-delta subaqueous distributary channels, are important reservoir units [4]. However, the Chang 8 sandstones, which had experienced various types and degrees of diagenesis such as compaction

and cementation by carbonates and clays, are typical tight reservoirs with low porosity, low permeability, and strong microscopic heterogeneity (Zeng and Li 2009; [4, 6, 7]).

Understanding diagenetic heterogeneity is vital for hydrocarbon exploration in tight sandstone reservoirs [8]. Carbonate cementation is an important diagenetic alteration that has profound impact on sandstone reservoir quality and heterogeneity [9–12]. Precipitation of carbonate cement is an important agent of lithification [11], and it often contributes to the poor reservoir property. When the carbonate cement fills the pore space completely, the reservoir quality will become so poor that they may act as baffles or seepage barriers to fluid flow [13, 14]. The carbonate cementation in sedimentary rocks may be spatially discontinuous, producing conspicuous structures called concretions [11].

Carbonate cement is the predominant diagenetic minerals in Chang 8 sandstones [6]. Mineralogical, petrographic,

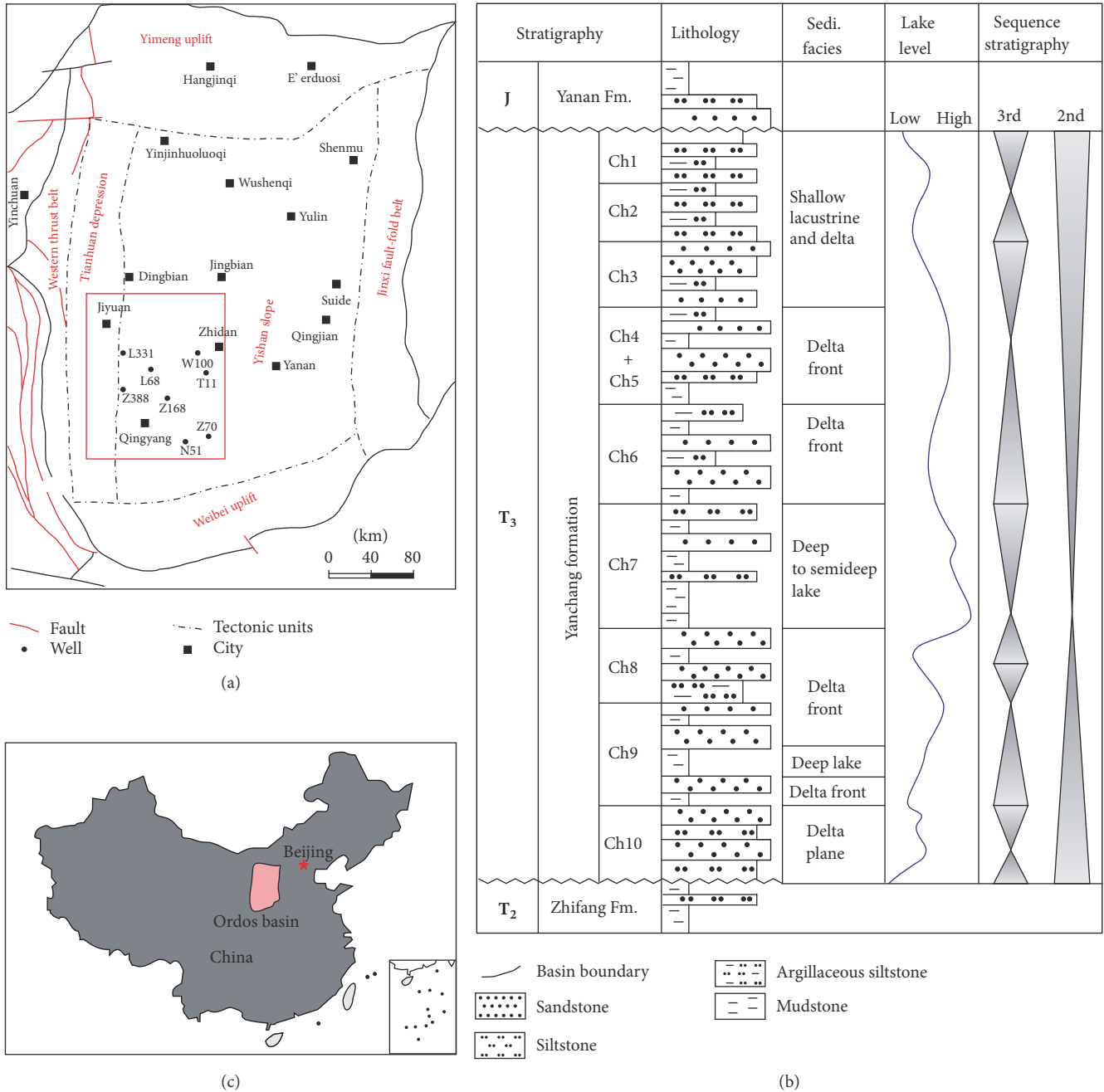


FIGURE 1: (a) The tectonic divisions of Ordos basin (after [6, 18, 24, 25]); (b) sequence stratigraphic column of Upper Triassic Yanchang Formation in Ordos basin, Ch = Chang (after [4]); and (c) map showing the location of the Ordos basin within China.

and geochemical analyses combined with ECS log data were used to describe the petrography and geochemistry of the carbonate cement and associated features in Chang 8 sandstones, with the special aim to unravel the origins, paragenesis, and distribution patterns of carbonate cement. This multidisciplinary work would provide insights into distribution patterns of carbonate cement within a siliciclastic succession and will have scientific significance in similar sandstone successions worldwide.

## 2. Geologic Setting

The Ordos basin is located in the western part of the North China block [1, 3, 15] and across five provinces: Shaanxi, Gansu, Ningxia, Inner Mongolia, and Shanxi (Figure 1(a); [16]). A series of Cenozoic rift basins separate the Ordos basin from adjoining mountains [17]. The Ordos basin can be divided into six structural units: the Yimeng uplift zone in the north, the Weibei uplift zone in the south, the Jinxi flexural

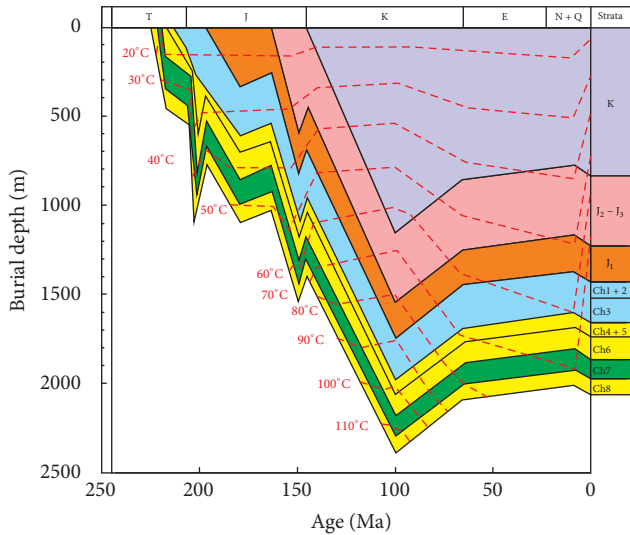


FIGURE 2: Burial and thermal histories of the Upper Triassic Yanchang Formation for Well L47 in Ordos basin (after [26]).

fold zone in the east, the Yishan slope in the midsection, the Xiyuan obduction zone, and the Tianhuan depression in the west (Figure 1(a); [16, 18–23]). The study area of this paper is located in the west Ordos basin (mainly the Yishan Slope and Tianhuan Depression), and abundant hydrocarbons are produced from the oil fields located in this area, including the Jiyuan, Heshui, Wu 464, Zhengning, and Huachi oil fields (Figure 1). Burial history reconstructions were based on the work of Shi et al., 2012 (Figure 2), and from Figure 2 it can be concluded that the Yanchang Formation had its maximum burial depth at about 100 Ma, then followed by an uplift and erosion of 400–500 m of sedimentary strata.

The Ordos basin is a gently dipping, very stable intracratonic basin [32]. The surrounding Yinshan and Qinling Mountains were thought to be the primary provenances for the Upper Triassic fluvial-deltaic sequences [17]. From the aspect of exploration and exploitation purposes, the Yanchang Formation could be subdivided into 10 informal oil reservoir units named Chang 10 to Chang 1 from the bottom to the top based on marker beds, lithological association, and sedimentary cycles, and these oil reservoir units are in conformity contact with each other [4, 17, 19, 33, 34]. Among them, the Chang 7 oil layers were deposited in a deep lacustrine environment [5, 35, 36], and the Chang 7 oil layers are good to very good source rocks [2, 37]. Sections from Chang 10 to Chang 8 represent a transgression sequence deposited at shallow water level, whereas those from Chang 6 to Chang 2 are regression sequences deposited at lake fading stage [5], and Chang 1 oil layer was deposited during the peneplain period [17]. The lithology of Chang 8 sandstones is mainly composed of grey fine to medium-grained sandstones and siltstones interbedded with dark mudstones [6]. Parallel bedding and wedge-shaped cross bedding can be observed in the fine- to medium-grained sandstones, and these clean sandstones are formed in a relatively high water energy environment, for example, the underwater distributary channel and mouth

bar of a delta front [27, 28, 38]. The siltstones with parallel bedding are mainly deposited in the distal bar microfacies. In contrast, the horizontal bedding can be observed in the dark mudstones, representing a low water energy environment [6].

### 3. Samples and Methods

Core samples and related thin sections were collected from more than 120 wells in the oilfield in the west Ordos basin. Standard modern wire-line logs comprise gamma-ray (GR), spontaneous potential (SP), bulk density (DEN), compensated neutron (CNL), borehole-compensated sonic (AC), and resistivity logs (RT and Rxo). The core-to-log depth matching is done by correlating the GR signature with the core description. ECS logging data is available in some wells such as An 157, Cheng 96, Yue 37, Hao 22, Zheng 53, Ban 28, and Xi 236.

The geochemical ECS logging tool uses a standard americium beryllium (AmBe) neutron source and bismuth germanate (BGO) detector to measure the released gamma rays [39]. By processing the measured  $\gamma$ -ray energy spectra using an oxide closure method, the ECS can provide information on the mineralogy including the mass fractions of certain components of carbonates, total clay, Q-F-M (quartz, feldspar, and mica), siderite, and pyrite, as well as anhydrite, salt, and coal [39, 40]. Compared with the standard set of logging data, the high vertical resolution (1.5 ft), open-hole ECS well logs can provide insight into predicting the distribution of carbonates in wells that lack core control.

Core samples and some cutting samples representative of noncored intervals were collected. Diagenesis and petrophysical properties were interpreted from petrographic data and core analyses. A total of 1735 samples analyses of He-porosity and air permeability were obtained. However, there are only 242 samples with their lithology known, and these 242 samples have also measured the carbonate content.

Cathode Luminescence (CL) analyses were performed on polished thin sections to characterize different cement generations using a Technosyn cold cathode luminescope.

Representative thin sections examined with a petrographic microscope were point counted (300 points per sample) to calculate the relative amounts of detrital framework grains, matrix, authigenic cement, interstitial minerals, and porosity. To examine the volume and distribution of porosity, the thin sections were impregnated with red-dye resin. To distinguish the mineralogy of carbonate cement, they were stained with Alizarin Red S and potassium ferricyanide for identification of ferroan dolomites, ferroan calcites, and nonferroan calcites in thin sections.

### 4. Results

**4.1. Reservoir Characteristics.** The Chang 8 sandstones are classified as lithic arkose, feldspathic litharenites, and litharenites according to Folk (1980) [6]. Detrital mineralogy is dominated by quartz (mostly monocrystalline), and the dominant feldspars are Ca-feldspars and Na-feldspars. The main types of rock fragments consist mainly of metamorphic rock fragments and volcanic rock fragments (Lai et al., 2014a; [6]).

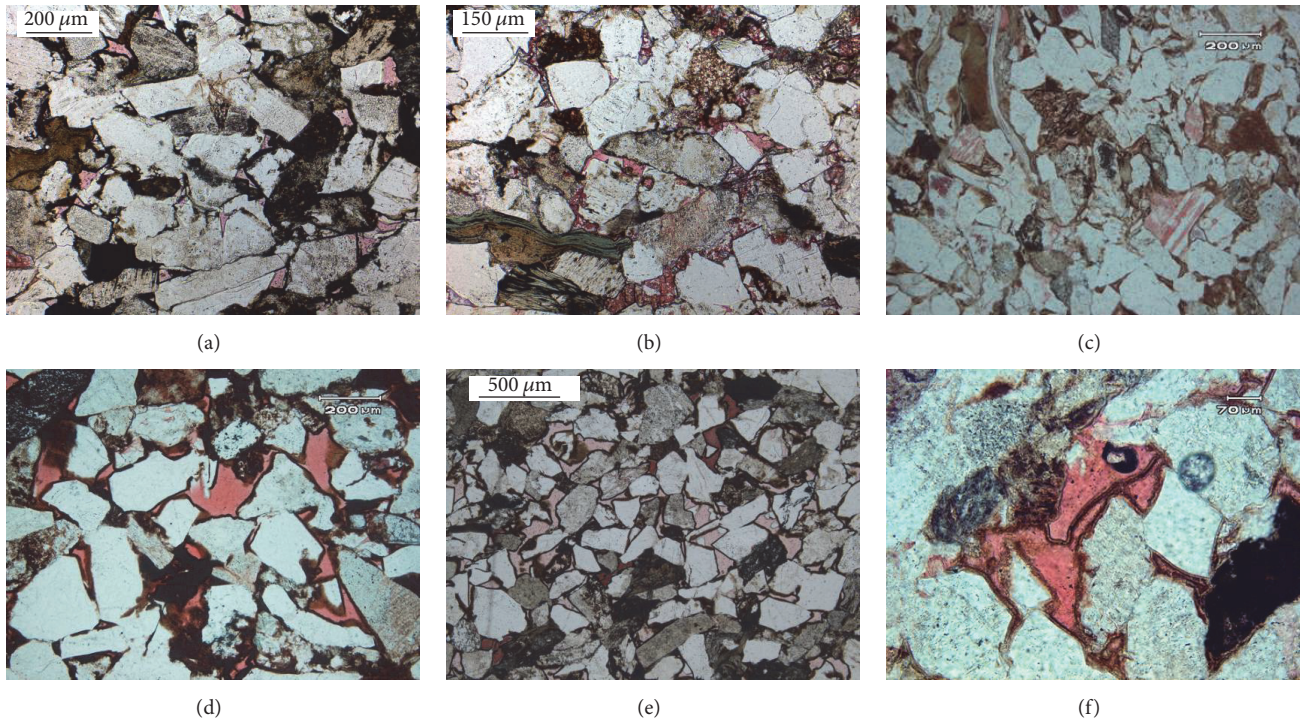


FIGURE 3: The lithology characteristics and reservoir pore systems of Chang 8 sandstones. (a) Medium-grained, subrounded to subangular, well sorted sandstone grains exhibit planar grain contacts, Zhuang 211, 1733.8 m, plane-polarized light (PPL); (b) medium-grained, well sorted, framework grains are heavily compacted due to its abundance in soft rock fragments, Zhuang 211, 1714.7 m, PPL; (c) grain contact is dominated by concave-convex due to its abundance in soft rock fragment, Yuan 177, 2466.7 m, PPL; (d) primary intergranular pore coexisting with the moldic pore, Luo 3, 2690.75 m, PPL; (e) porosity is shown in red, with intergranular pores, Zhuang 199, 1673.81 m, PPL; (f) primary intergranular pores showing the irregular polygon morphology, Feng 2, 2433.4 m, PPL.

On average the sandstones are fine- to medium-grained, typically nonequant, and moderately to well sorted. The grain shape is subrounded to subangular, and the types of grain contacts are dominated by planar type (Figures 3(a) and 3(b)). However, some samples show concavo-convex grain contacts due to its abundance in soft rock fragments (Figure 3(c); [6]). Thin section analyses (presence of red epoxy) indicate that pore systems in Chang 8 oil layers are of primary and secondary origins. In addition to the remaining primary intergranular porosity (Figures 3(d), 3(e), and 3(f)), variable amounts of secondary intragranular porosity due to partial to pervasive dissolution of detrital framework grains (feldspars and rock fragments) occur in many samples (Figures 3(e) and 3(f)) [6, 41].

The lithology has a primary control on the reservoir property of the Chang 8 sandstones. Figure 4 shows the cross-plot of permeability and porosity for various lithology within the Chang 8 reservoirs. It can be concluded that the medium-grained sandstone samples have the highest average porosity and permeability, whereas the reservoir quality of the siltstones and the mudstones are poor. In contrast, the fine-grained sandstones show a wide range of porosity and permeability due to various diagenetic modifications such as carbonate cementations. Some medium-grained sandstones also show very poor reservoir property, which are suggested to have experienced extensive carbonate cementation (Figure 4).

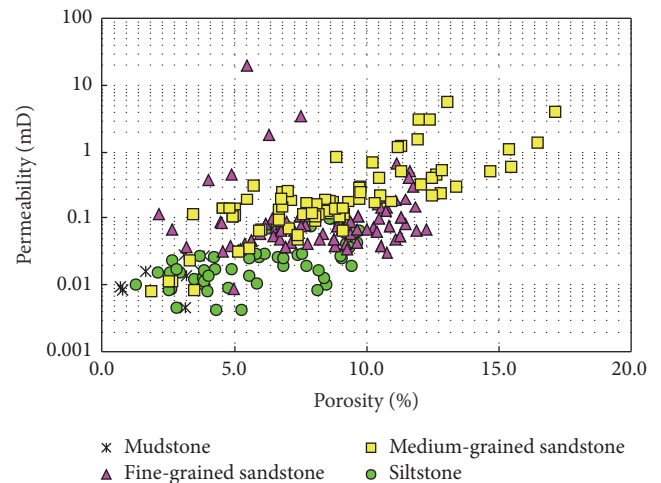


FIGURE 4: Core porosity versus core permeability cross-plots for various lithologies within Chang 8 oil layers in Ordos basin.

**4.2. Carbonate Cement.** Carbonate skeletal grains are rare in Chang 8 sandstones. Carbonate cementation has a profound impact on reservoir heterogeneity and quality, which often contributes to the poorest reservoir quality (Figure 5). Under microscopic observations, the total carbonate cement content in Chang 8 sandstones ranges from trace levels (<1%) to

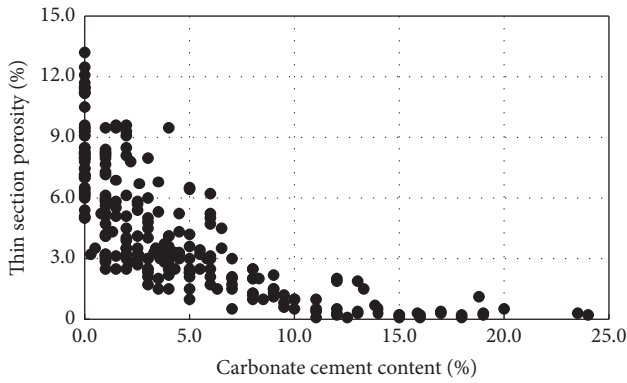


FIGURE 5: Scatter diagram showing the relationship of thin section porosity versus carbonate cement content.

24.0% with an average of 5.1%, and there is a trend that the thin section porosity would decrease rapidly with the increasing carbonate cement content (Figure 5). When the carbonate cement content is greater than 5.0%, the thin section porosity became very low (<3.0%) (Figure 5), and the thin section porosity is less than 1.0% when the carbonate cement content is greater than 15.0%; therefore it can be concluded that the carbonate cementation is one of the major causes contributing to the poor reservoir property in Chang 8 sandstones. Additionally, in Figure 5, there are also some samples with low content of carbonate cement but have low thin section porosity, and these samples are suggested to be those tightly compacted (Figure 5), which can be evidenced by the deformation of micas as well as the planar grain contacts (Figures 3(b) and 3(c)). According to conventional plug samples analysis, the carbonate content has also a negative impact of the core-measured porosity (Figure 6). Figure 6 exhibits core-measured porosity plotted against carbonate cement content for various lithologies within Chang 8 sandstones. Generally, the siltstones have the lowest porosity due to the extensive carbonate cement, while the carbonate cement content in fine-grained sandstones are relatively less than that in the medium-grained sandstones. Samples abundant in carbonate cement have very low porosity, which is consistent with the observations in Figure 4. The mudstones have the lowest carbonate cement content; however, the porosity in mudstones is very low due to the extensive diagenetic modifications such as compaction (Figure 6).

Carbonate cement is commonly observed to have replaced other detrital components, such as feldspar and rock fragment grains (Figures 7(a) and 7(b); [41]). It appears that the carbonate cement as well as compaction has collectively controlled the reservoir quality evolution of sandstones [10]. Among the carbonate cement, calcite and Fe-calcite are the major cement types in Chang 8 sandstones, ranging in volume abundance from trace amounts (<1%) to 24.0% of the rock, with an average of 3.73%, while dolomites and Fe-dolomites are relatively less commonly observed (ranges: trace to 14.0%, averaged as 1.37%). According to the thin section petrography, there exist three types of carbonate

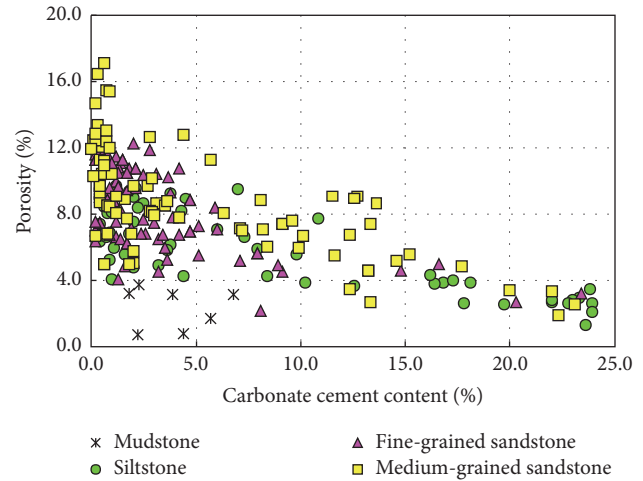


FIGURE 6: Core-measured porosity plotted against carbonate cement content of various lithology.

cement in sandstones of the Chang 8 sandstones: (1) carbonates as the dominant pore-filling constituents; (2) carbonates replacing framework grains; and (3) carbonates precipitating in intergranular pores before or after other cement types (Figures 7(a)–7(d)).

Thin section petrography and CL analysis confirm that two generations of carbonate cement are recognized and hereafter are referred to as Type I (mainly pore-filling and grain-replacing calcite and minor dolomite) and Type II (mainly grain-replacing Fe-calcite, Fe-dolomite and minor amount of calcite, and the carbonate cement precipitating in intergranular pores). Type I tends to fill the relatively large pores or replace the framework grains (Figures 7(c) and 7(d)) [6]. The eogenetic cement may have supported the framework grains and prevented extensive compaction [42], resulting in the floating grain texture and high volume of high minus-cement porosity [43]. The pore-filling cement is suggested to have precipitated before significant compaction and thus support eogenetic origin [44, 45]; however, the carbonate cement replacing framework grains may also precipitate after significant compaction. They display bright orange-red and yellow luminescence patterns under cathodoluminescence analysis (Figures 7(e) and 7(f)). Type II tends to occupy much smaller intergranular pores in tightly packed sandstones or, in some cases, partly and/or totally replaced the detrital grains (Figures 7(g) and 7(h)). They commonly precipitate along the edge of the preexisting Type I carbonate cement, indicating precipitation after considerable compaction and thus a mesogenetic origin [44]. Petrography and CL analysis show that calcite is often replaced by ferroan calcite, indicating that the formation timing of the Fe-calcite is after that of calcite (Figures 7(e)–7(h)). Isolated Fe-calcite also occurs in intragranular feldspar dissolution pores (Figure 7(g)), which indicates that the reservoirs experienced dissolution before the precipitation of Fe-calcite [12]. Type II carbonates can be distinguished from Type I carbonate cement since they display weak dull red/orange colors and blotchy luminescence patterns due to the presence of Fe and Mn ions (Figures 7(i)

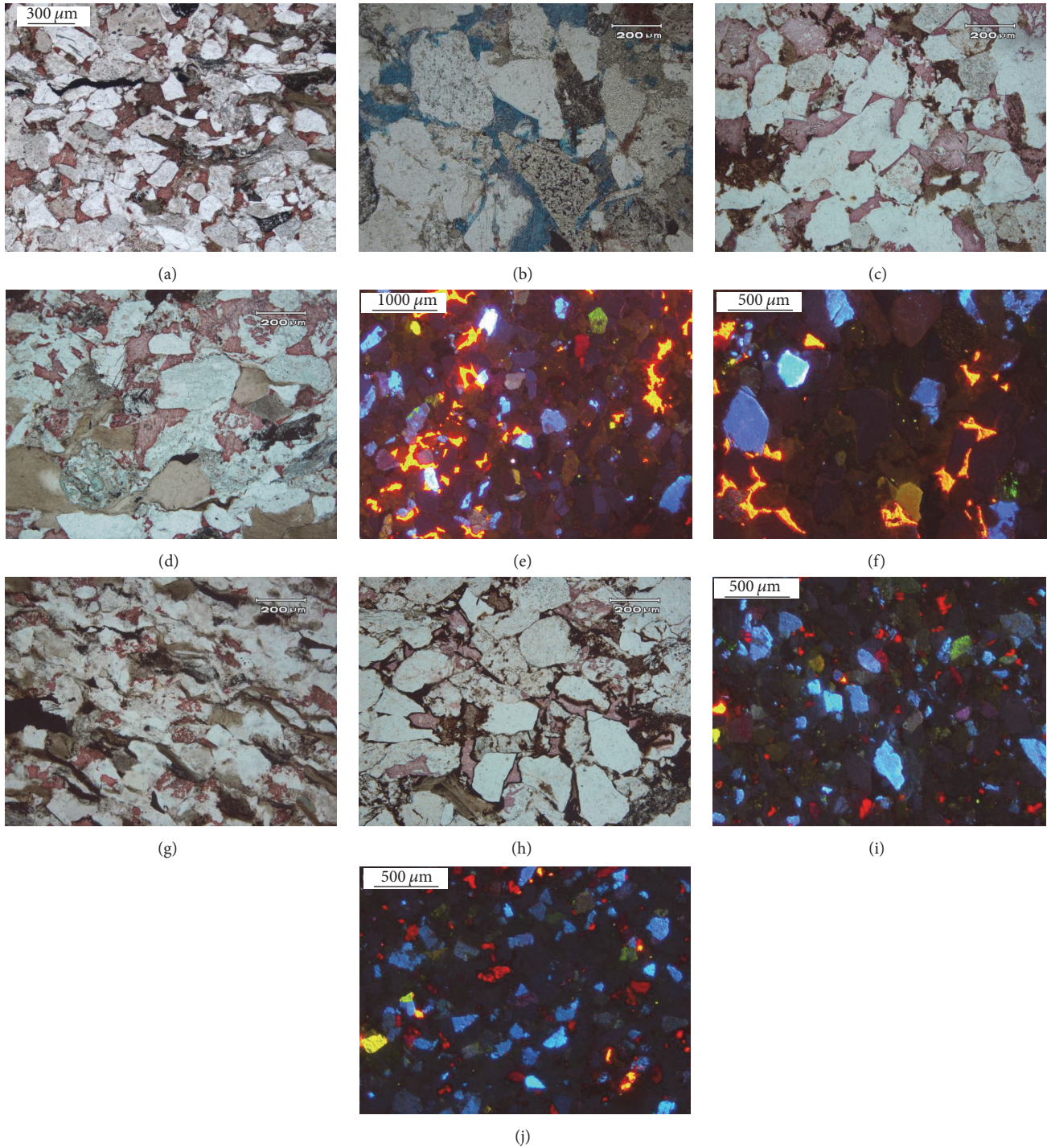


FIGURE 7: Photomicrographs showing the petrography, geochemistry, and distribution of carbonate cement for Chang 8 sandstones in Ordos basin; (a) calcites are the dominant pore-filling constituents, and they also replace framework grains; intergranular macropores are rarely observed in this sandstone, Zhuang 75, 2116 m, PPL; (b) dolomites are the most common pore-filling constituents. Dolomite also replaces framework grains, Yuan 43, 2270.56 m, PPL; (c) calcite fills large intergranular pores between loosely packed framework grains and replaces the framework grains, Luo 1, 2499.07 m; (d) calcite fills large intergranular pores between loosely packed framework grains and replaces the framework grains, Feng 9, 2512.92 m; (e) Type I calcites fill large pores between loosely packed framework grains, which display bright orange-red and yellow luminescence patterns, Zhuang 214, 1890.37 m, Cathode Luminescence (CL); (f) Type I calcites display bright orange-red and yellow luminescence patterns, Zhuang 214, 1890.37 m, CL; (g) Type II calcites occupy much smaller intergranular pores in tightly packed sandstones and replaced the detrital grains, An 62, 2396.47 m, PPL; (h) Type II calcites occupy much smaller intergranular pores in tightly packed sandstones and replaced the detrital grains, Luo 13, 2750.62, PPL; (i) Type II calcites occupy much smaller intergranular pores in tightly packed sandstones, and they precipitate along the edge of the preexisting Type I carbonate cement, and they display a weak dull red/orange and blotchy luminescence, Zhuang 240, 1785.6 m, CL; (j) Type II calcites display a weak dull red/orange and blotchy luminescence, Zhuang 214, 1782.85 m, CL.

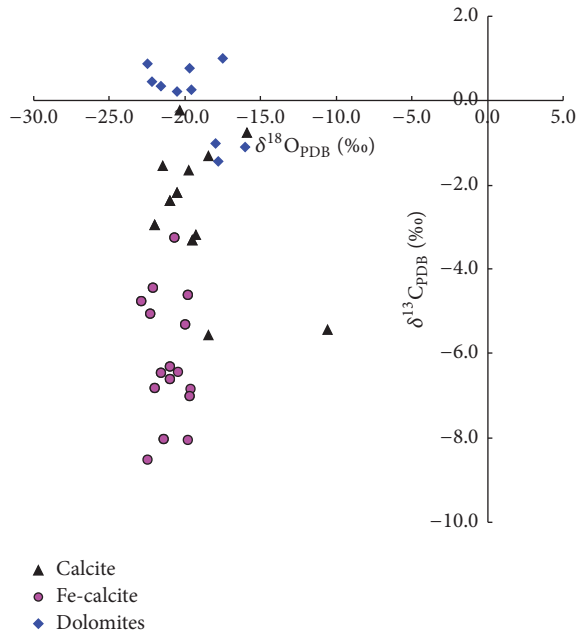


FIGURE 8: Scatter diagram showing the oxygen versus carbon stable isotopes for all types of carbonate cement of Yanchang Formation sandstones in Ordos basin (after [27–30]).

and 7(j)). Thin section analysis shows that no dissolution of carbonate cement is observed.

## 5. Discussions

**5.1. Isotope Analysis and Origins of Carbonate Cement.** Determining the origin of carbonate cement can improve our ability to predict its distribution (Liu et al., 2015). Bulk isotopic signature of carbonate cement would provide some additional clues to clarify their origin [43, 46]. According to the results published by Shi et al. [29], Wang et al. [30], Zhixue et al. [27], and Tian et al. [28], the  $\delta^{13}\text{C}$  values (PDB) are in the range from  $-8.51\text{‰}$  to  $1.00\text{‰}$  with an average of  $-3.55\text{‰}$ , whereas the  $\delta^{18}\text{O}$  values (PDB) range from  $-22.9\text{‰}$  to  $-10.58\text{‰}$  and have an average of  $-19.62\text{‰}$  (Figure 8).

The isotope analysis shows that the carbonate cement has relatively lighter oxygen and carbon isotopes. The negative  $\delta^{13}\text{C}$  values could be attributed to a variety of sources and/or processes, such as the derivation of carbon from thermal maturation of organic matter during burial [10, 47, 48].

All the carbonate cement types have very negative  $\delta^{18}\text{O}$  values (Figure 8). Depletion of  $\delta^{18}\text{O}$  in carbonates is attributed to (i) incursion of meteoric water; (ii) precipitation and recrystallization at higher temperatures; and (iii) microbial fractionation of oxygen isotopes [44]. Lighter oxygen isotopes and negative  $\delta^{13}\text{C}$  values in Chang 8 sandstones may suggest the role of freshwater influence on carbonates development. However, the Yanchang Formation had been continuously buried to larger than 2 km since its initial deposition (Figure 2), and there are no unconformities developed in the Chang 8 sandstones; therefore the Chang 8 sandstones had never been exposed to surface and meteoric

flushing. In contrast, reprecipitation and recrystallization during burial (increase in burial and temperature) would lead to a further negative shift in  $\delta^{18}\text{O}$  values [49]. The high  $^{18}\text{O}$ -depleted signature, negative  $\delta^{13}\text{C}$  values, and high Fe and Mg contents suggest that the late replacive carbonate cement (Fe-calcite and Fe-dolomite) including Fe-dolomite and Fe-calcite formed in burial conditions via the replacement of early diagenetic carbonate cement by the influence of deep formation water [45]. The positive  $\delta^{13}\text{C}$  values of some dolomite cement in Chang 8 sandstones are compatible with early marine carbonates but not the oxygen isotopes (Figure 8; [27]).

**5.2. Paragenetic Sequence of Carbonate Cement.** It is difficult to define precisely the timing of the cementation processes [45, 50]. Two diagenetic stages of carbonate cement are recognized according to petrographic and textural relationships and elemental and stable isotopic composition: the early diagenetic stage in shallow depth, represented by pore-filling and grain-replacing calcite and dolomite, and the late mesogenetic deep burial diagenetic stage, represented by ferroan calcite and ferroan dolomite replacing framework grains and precipitating in intergranular pores. Eogenetic diagenetic alterations also include mechanical compaction and formation of kaolinite and grain-coating chlorites, while mesogenetic diagenesis is characterized by continued mechanical compaction, dissolution of framework grain by organic acids, and subsequent precipitation of quartz and clay minerals such as illite and mixed-layer illite/smectite (Figure 9). Immediately after deposition, the mechanical compaction occurred, resulting in a significant reduction in the intergranular porosity [51]. Then grain-coating chlorites formed, and some kaolinites precipitated due to feldspar alteration. In mesodiagenesis, mechanical compaction continued to reduce the intergranular porosity. With progressive burial and increasing temperature, organic acids charged into the reservoirs, and feldspars were dissolved to form intra-granular dissolution pores [4]. As the byproducts of feldspar dissolution, the quartz cement and clay minerals such as illite and mixed-layer illite/smectite precipitated (Figure 9; [6]).

The presence of carbonate cement in the loosely packed framework grains indicates that cementation commenced shortly after deposition [45]. The slightly negative  $\delta^{13}\text{C}$  values of the dolomite and calcite cement would indicate its precipitation in slightly reducing conditions with minor contribution of organic carbon derived from soil-derived  $\text{CO}_2$  [45]. Indeed, soil  $\text{CO}_2$  could also give the depleted  $\delta^{13}\text{C}$  values, and it depends on how much soil  $\text{CO}_2$  was incorporated into the diagenetic fluids.

With progressive burial, the late-stage ferroan calcite and ferroan dolomite formed (Figures 7(e) and 7(f)). Under CL analysis, the early diagenetic carbonate cement is commonly observed to be partially to completely replaced by ferroan calcite and ferroan dolomite (Figures 7(g) and 7(h)). Alteration of eogenetic carbonate cement by fluids rich in Fe and/or Mg is regarded as a source of late precipitation of Type II carbonates during burial [45]. The Chang 8 sandstones had been buried deeper than 2000 m and were suggested to have

Diagenetic stage	Eodiagenesis				Mesodiagenesis		
Temperature (°C)	10–25		70		120		
Age (Ma)	208	135			65	0	
Epoch	T <sub>3</sub>	J <sub>1</sub>	J <sub>2</sub>	J <sub>3</sub>	K <sub>1</sub>	K <sub>2</sub>	E + Q
Compaction	.....						
Kaolinite	.....						
Quartz	.....						
I/S mixed layer	.....						
Illite	.....						
Chlorite	.....						
Calcite and Fe-calcite	.....						
Dolomite and Fe-dolomite	.....						
Dissolution	.....						

FIGURE 9: Paragenetic sequence of diagenesis in the Chang 8 sandstones in west Ordos basin. The boundary between eodiagenesis and mesodiagenesis is according to Morad et al. [31].

experienced various types and degrees of diagenesis such as compaction, cementation, and dissolution during the long geological history. The isotopic composition may also be modified during burial diagenesis, such as thermal evolution of organic matters during progressive burial and increasing temperature [52].

**5.3. Distribution Patterns of Carbonate Cement.** As discussed above, no carbonate rock fragments are observed in thin sections; therefore the carbonates detected by ECS logs are mainly cement. According to the interpretation results of ECS data, there is a downward decrease in the abundance of carbonate cement in Chang 8 sandstones (Figures 10 and 11). The tight carbonate cemented zones with carbonate cement greater than 10% are relatively shallowly buried and more adjacent to the overlying Chang 7 source rocks. With increasing distance from the Chang 7 oil layer, the carbonate cement content gradually decreases (Figures 10 and 11). However, there are also some carbonate cementation zones further down, and these layers with high percentage of carbonate cement are mainly associated with the sandstone-mudstone contacts (Figures 10 and 11), for example, the 2345–2350 m depth intervals in Figure 10 and 2528–2529 m depth intervals in Figure 11. Areas that have high percentages of carbonate cemented sandstones often occur along the margins of the sandstone bodies, where sandstone pinches out into mudstone [9, 53]. Since sandstone reservoirs interbedded with mudstones are readily influenced by a variety of sources of fluids, the sandstone-mudstone interface is the area with strong water-rock interactions [11, 12].

Diagenetic mineral assemblages from ECS logging data show that carbonate cement has a highly zonal distribution,

confined to thin beds or concretions in general, and the carbonate cement is much more commonly observed in sand bodies which are adjacent with the Chang 7 source rocks (Figures 10 and 11). Type I carbonates precipitated at eogenetic stage in the whole Chang 8 sandstones, resulting in the highly zonal distribution of carbonate cement, while the late-stage carbonate cement is mainly associated with the mudrocks of Chang 7 oil layer. Carbon isotope of CO<sub>2</sub> from volcanic rock is between –5 and +7‰; from carbonate decomposition is between –3.5 and +3.57‰; from carbonate cement of mudstones should be between –15 and –9‰; from the thermal evolution of organic matter should be –20‰ or so and even more negative [54, 55]. By isotope analysis (Figure 8), it can be concluded that the Fe-calcite should come from the carbonate cement source of mudrocks. Particularly the late-stage carbonate cement (Fe-calcite and Fe-dolomite) is mainly associated with release of acidic fluids from the mudrock intervals. Organic acid generations from mudrocks during late-stage burial would result in a reducing environment, which is favorable for the late-stage carbonate cementations [56]. Therefore these late carbonate (Fe-calcite and Fe-dolomite) cement types are related to thermal evolution of mudrocks and the availability of Ca<sup>2+</sup>, Mg<sup>2+</sup>, and Fe<sup>2+</sup> in the formation water (e.g., [57]).

The mudstones and oil shales of the Chang 7 oil layers are thought to be the best source rocks for Chang 8 sandstone reservoirs [35, 37]. The organic acids and CO<sub>2</sub> generated by thermal maturation of these source rocks would firstly charge into the sandstones adjacent to Chang 7 mudstones and shales, and these organic acids and CO<sub>2</sub> are mostly buffered by feldspar (especially Ca-feldspar grains) and rock fragments (the pH would be buffered by silicates) in sand

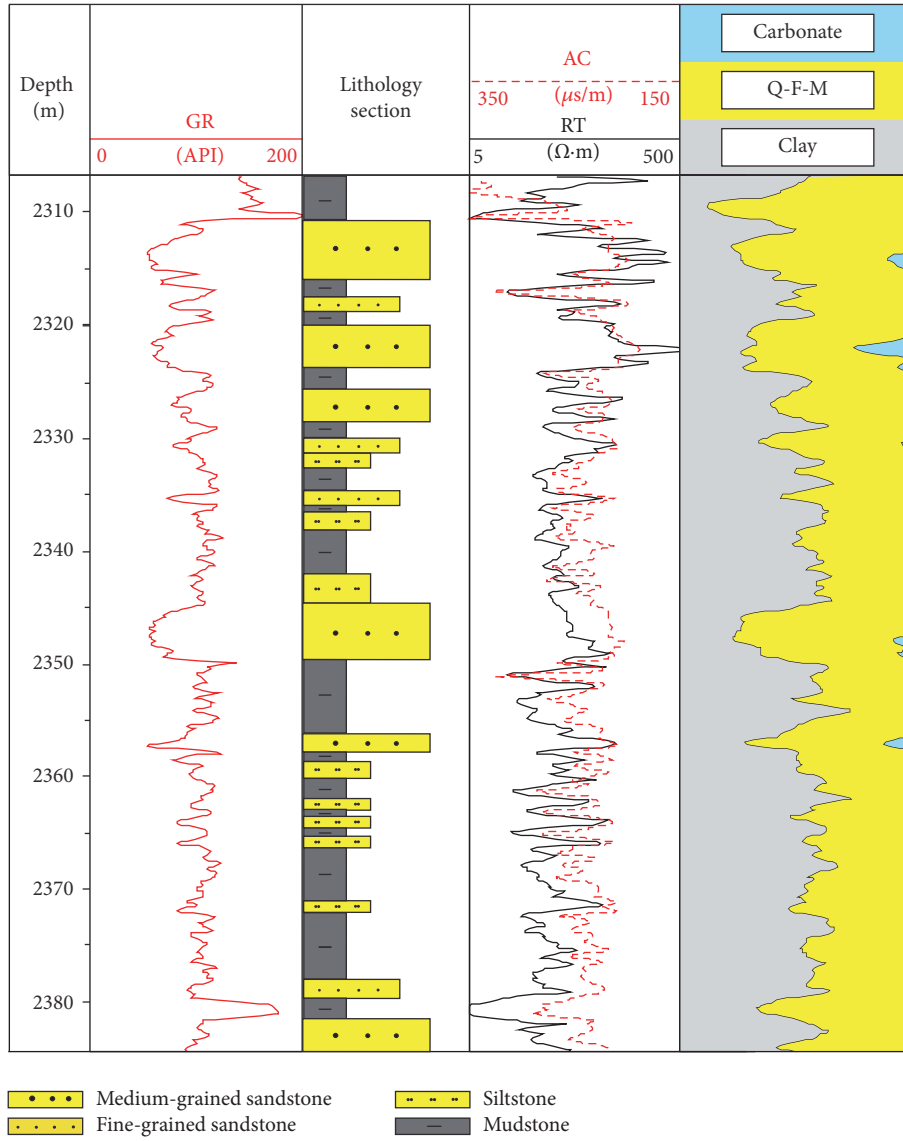


FIGURE 10: Diagenetic mineral assemblage characteristics interpreted by ECS logging in Well 22.

bodies adjacent to the Chang 7 oil layers. Feldspar dissolution pores are commonly observed while the carbonates show no evidence of dissolution (Figures 3(d), 3(e), and 3(f)). Besides the dissolution of Ca-feldspars, clay mineral transformations such as illitization of smectite are also accompanied by a release of  $\text{Ca}^{2+}$  and  $\text{Mg}^{2+}$  into solution [12, 53]. Carbonate cement (mainly Type II) would precipitate with enrichment of  $\text{Ca}^{2+}$  and  $\text{Mg}^{2+}$  ions and a decrease in  $\text{CO}_2$  concentration under Fe- and Mn-reducing, suboxic to sulfate-reduction geochemical conditions [57–60]. With increasing burial depth and temperature, the decomposition of organic acid decarboxylation would be enhanced, and more clay mineral transformation would occur [12]. The sand bodies which are more adjacent to the overlying Chang 7 mudrocks are more favorable for the late-stage carbonate cementation. These carbonate cement types will fill porosity where framework grains were previously dissolved.

## 6. Conclusions

- (1) Two generations of carbonate cement were recognized as Type I (calcite and dolomite) and Type II (mainly Fe-calcites and Fe-dolomites).
- (2) Carbonate cement is closely related to the dissolved carbon from thermal maturation of organic matters. High-temperature burial diagenesis would lead to a further negative shift in  $\delta^{18}\text{O}$  values.
- (3) Carbonate cement is much more commonly observed in sand bodies adjacent to Chang 7 source rocks. Dissolution of Ca-feldspars by organic acids-rich fluids, together with illitization of smectite, provides  $\text{Ca}^{2+}$  and  $\text{Mg}^{2+}$  ions for carbonate cementation, and carbonate cement would precipitate with a decrease in  $\text{CO}_2$  concentration.

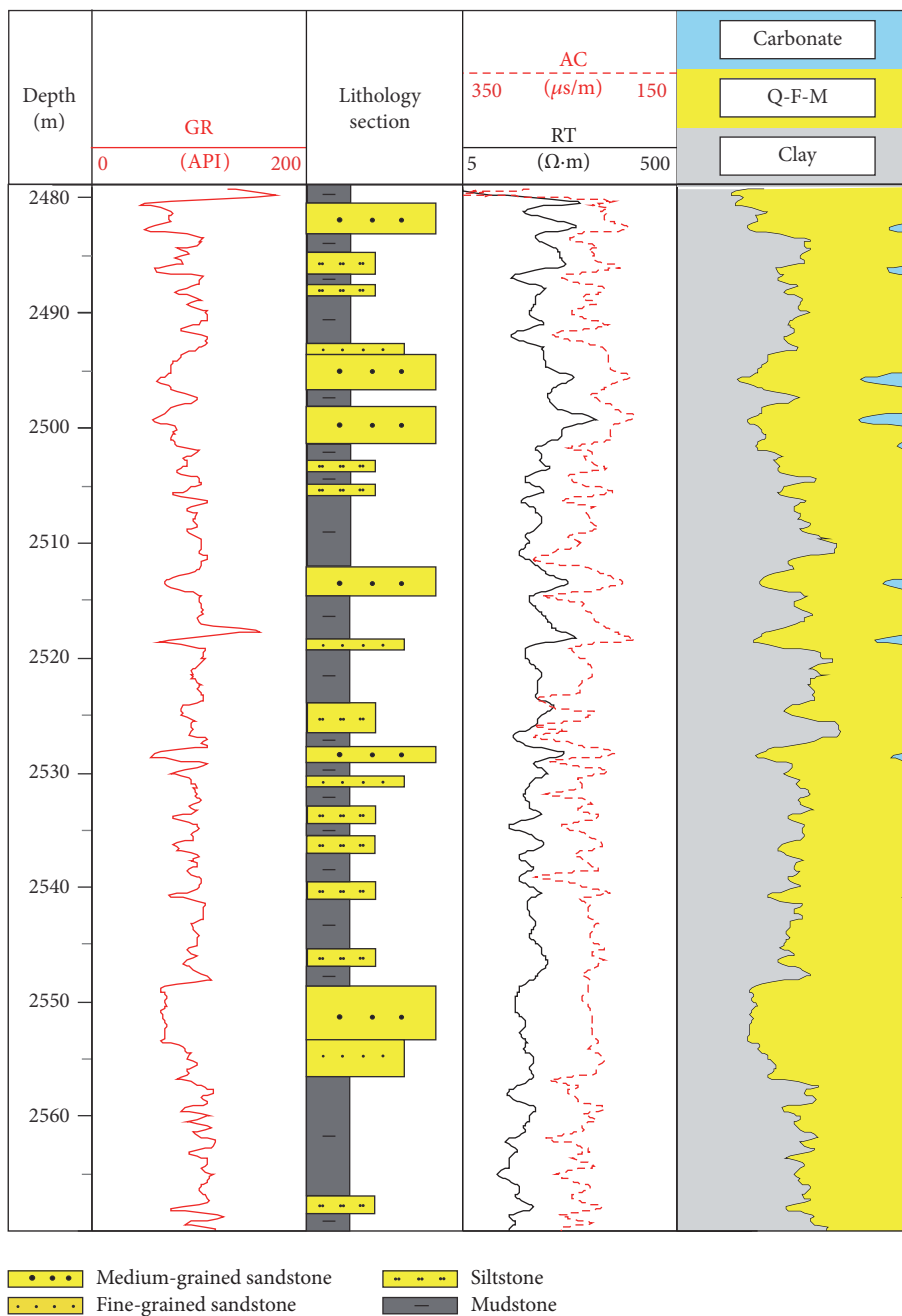


FIGURE II: Diagenetic mineral assemblage characteristics interpreted by ECS logging in Well 157.

### Conflicts of Interest

No conflicts of interest exist in the submission of this manuscript.

### Acknowledgments

The authors acknowledge PetroChina Changqing Oilfield Company and PetroChina Research Institute of Petroleum Exploration and Development for providing samples and data access and for permission to publish this work. This study

was supported by the National Natural Science Foundation of China (no. 41472115) and Science Foundation of China University of Petroleum, Beijing (no. 2462017YJRC023). The authors thank Professor Zhiqiang Mao and Professor Yujiang Shi for their data support.

### References

- [1] H. Zhu, K. Chen, K. Liu, and S. He, "A sequence stratigraphic model for reservoir sand-body distribution in the Lower Permian Shanxi Formation in the Ordos Basin, northern China,"

- Marine and Petroleum Geology*, vol. 25, no. 8, pp. 731–743, 2008.
- [2] C. Zou, L. Wang, Y. Li, S. Tao, and L. Hou, “Deep-lacustrine transformation of sandy debrites into turbidites, Upper Triassic, Central China,” *Sedimentary Geology*, vol. 265–266, pp. 143–155, 2012.
  - [3] L.-M. Ji, F.-W. Meng, J. D. Schiffbauer, J.-L. Xu, K. Yan, and J.-W. Shu, “Correlation between highly abundant oil-prone leiosphaerid acritarchs and hydrocarbon source rocks from the Triassic Yanchang Formation, eastern Gansu Province, North-western China,” *Gondwana Research*, vol. 14, no. 3, pp. 554–560, 2008.
  - [4] G. Wang, X. Chang, W. Yin, Y. Li, and T. Song, “Impact of diagenesis on reservoir quality and heterogeneity of the Upper Triassic Chang 8 tight oil sandstones in the Zhenjing area, Ordos Basin, China,” *Marine and Petroleum Geology*, vol. 83, pp. 84–96, 2017.
  - [5] L. Rongxi, T. Guzmics, L. Xiaojie, and X. Guangcheng, “Migration of immiscible hydrocarbons recorded in calcite-hosted fluid inclusions, Ordos Basin: a case study from Northern China,” *Russian Geology and Geophysics*, vol. 52, no. 11, pp. 1491–1503, 2011.
  - [6] J. Lai, G. Wang, Y. Chai, and Y. Ran, “Prediction of diagenetic facies using well logs: evidences from Upper Triassic Yanchang Formation Chang 8 sandstones in Jiyuan region, Ordos basin, China,” *Oil & Gas Science and Technology—Rev. IFP Energies nouvelles*, vol. 71, article 34, 2016.
  - [7] X. Luo, J. Yu, L. Zhang et al., “Numerical modeling of secondary migration and its applications to Chang-6 Member of Yanchang Formation (Upper Triassic), Longdong area, Ordos Basin, China,” *Science in China, Series D: Earth Sciences*, vol. 50, no. 2, pp. 91–102, 2007.
  - [8] Y. Cui, G. Wang, S. J. Jones et al., “Prediction of diagenetic facies using well logs—a case study from the upper Triassic Yanchang Formation, Ordos Basin, China,” *Marine and Petroleum Geology*, vol. 81, pp. 50–65, 2017.
  - [9] S. P. Dutton, “Calcite cement in permian deep-water sandstones, delaware basin, west Texas: origin, distribution, and effect on reservoir properties,” *AAPG Bulletin*, vol. 92, no. 6, pp. 765–787, 2008.
  - [10] H. Mansurbeg, S. Morad, A. Salem et al., “Diagenesis and reservoir quality evolution of palaeocene deep-water, marine sandstones, the Shetland-Faroes Basin, British continental shelf,” *Marine and Petroleum Geology*, vol. 25, no. 6, pp. 514–543, 2008.
  - [11] S. J. Loyd, F. A. Corsetti, J. M. Eiler, and A. K. Tripathi, “Determining the diagenetic conditions of concretion formation: assessing temperatures and pore waters using clumped isotopes,” *Journal of Sedimentary Research*, vol. 82, no. 12, pp. 1006–1016, 2012.
  - [12] J. Wang, Y. Cao, K. Liu, J. Liu, X. Xue, and Q. Xu, “Pore fluid evolution, distribution and water-rock interactions of carbonate cements in red-bed sandstone reservoirs in the Dongying Depression, China,” *Marine and Petroleum Geology*, vol. 72, pp. 279–294, 2016.
  - [13] K. G. Taylor, R. L. Gawthorpe, C. D. Curtis, J. D. Marshall, and D. N. Awwiller, “Carbonate cementation in a sequence-stratigraphic framework: upper cretaceous sandstones, book cliffs, utah-colorado,” *Journal of Sedimentary Research*, vol. 70, no. 2, pp. 360–372, 2000.
  - [14] A. A. Taghavi, A. Mørk, and M. A. Emadi, “Sequence stratigraphically controlled diagenesis governs reservoir quality in the carbonate Dehloran Field, southwest Iran,” *Petroleum Geoscience*, vol. 12, no. 2, pp. 115–126, 2006.
  - [15] Q. Liu, L. Chan, Q. Liu et al., “Relationship between magnetic anomalies and hydrocarbon microseepage above the Jingbian gas field, Ordos basin, China,” *AAPG Bulletin*, vol. 88, no. 2, pp. 241–251, 2004.
  - [16] J. Li, W. Zhang, X. Luo, and G. Hu, “Paleokarst reservoirs and gas accumulation in the Jingbian field, Ordos Basin,” *Marine and Petroleum Geology*, vol. 25, no. 4–5, pp. 401–415, 2008.
  - [17] X. Qiu, C. Liu, G. Mao, Y. Deng, F. Wang, and J. Wang, “Late Triassic tuff intervals in the Ordos basin, Central China: their depositional, petrographic, geochemical characteristics and regional implications,” *Journal of Asian Earth Sciences*, vol. 80, pp. 148–160, 2014.
  - [18] J. Lai, G. Wang, M. Chen et al., “Pore structures evaluation of low permeability clastic reservoirs based on petrophysical facies: a case study on Chang 8 reservoir in the Jiyuan region, Ordos Basin,” *Petroleum Exploration and Development*, vol. 40, no. 5, pp. 566–573, 2013.
  - [19] L.-M. Ji, K. Yan, F.-W. Meng, and M. Zhao, “The oleaginous *Botryococcus* from the Triassic Yanchang Formation in Ordos Basin, Northwestern China: morphology and its paleoenvironmental significance,” *Journal of Asian Earth Sciences*, vol. 38, no. 5, pp. 175–185, 2010.
  - [20] Z. Jiang, J. Xu, and G. Wang, “The discovery and significance of a sedimentary hiatus within the Carboniferous Taiyuan Formation, northeastern Ordos Basin, China,” *AAPG Bulletin*, vol. 96, no. 7, pp. 1173–1195, 2012.
  - [21] S. Guo, “Experimental study on isothermal adsorption of methane gas on three shale samples from Upper Paleozoic strata of the Ordos Basin,” *Journal of Petroleum Science and Engineering*, vol. 110, pp. 132–138, 2013.
  - [22] C.-Y. Wang, E. Sandvol, L. Zhu, H. Lou, Z. Yao, and X. Luo, “Lateral variation of crustal structure in the Ordos block and surrounding regions, North China, and its tectonic implications,” *Earth and Planetary Science Letters*, vol. 387, pp. 198–211, 2014.
  - [23] Z. Xu, L. Liu, T. Wang et al., “Characteristics and controlling factors of lacustrine tight oil reservoirs of the Triassic Yanchang Formation Chang 7 in the Ordos Basin, China,” *Marine and Petroleum Geology*, vol. 82, pp. 265–296, 2017.
  - [24] J. Lai, G. Wang, Y. Ran, Z. Zhou, and Y. Cui, “Impact of diagenesis on the reservoir quality of tight oil sandstones: The case of Upper Triassic Yanchang Formation Chang 7 oil layers in Ordos Basin, China,” *Journal of Petroleum Science and Engineering*, vol. 145, pp. 54–65, 2016.
  - [25] Z. Cao, G. Liu, H. Zhan et al., “Pore structure characterization of Chang-7 tight sandstone using MICP combined with N<sup>2</sup> GA techniques and its geological control factors,” *Scientific Reports*, vol. 6, Article ID 36919, 2016.
  - [26] B. Shi, Y. Zhang, L. Zhang, Y. Yang, and H. Li, “Hydrocarbon accumulation dating by fluid inclusion characteristics in Chang 7 tight sandstone reservoirs of Yanchang Formation in Ordos Basin,” *Petroleum Exploration and Development*, vol. 34, no. 6, pp. 599–603, 2012.
  - [27] S. Zhixue, S. Zhilei, L. Hongjiang, and Y. Xijie, “Characteristics of carbonate cements in sandstone reservoirs: a case from Yanchang Formation, middle and southern Ordos Basin, China,” *Petroleum Exploration and Development*, vol. 37, no. 5, pp. 543–551, 2010.
  - [28] Y. Tian, Z. Shi, and J. Song, “Characteristics of carbonate cements of Member 8 of Yanchang Formation in the Yichuan-Xunyi area, Ordos Basin, China,” *Journal of Chengdu University of Technology*, vol. 38, no. 4, pp. 378–384, 2011.

- [29] J. Shi, J. Wang, M. Mao et al., "Reservoir sandstone diagenesis of Member 6 to 8 in Yanchang Formation (Triassic), Xifeng oilfield, Ordos basin," *Acta Sedimentologica Sinica*, vol. 21, no. 3, pp. 373–380, 2003.
- [30] Q. Wang, X. Zhuo, G. Chen, and X. Li, "Characteristics of carbon and oxygen isotopic compositions of carbonate cements in Triassic Yanchang sandstone in Ordos basin," *Natural Gas Industry*, vol. 27, no. 10, pp. 28–34, 2007.
- [31] S. Morad, J. M. Ketzer, and L. R. De Ros, "Spatial and temporal distribution of diagenetic alterations in siliciclastic rocks: implications for mass transfer in sedimentary basins," *Sedimentology*, vol. 47, supplement 1, pp. 95–120, 2000.
- [32] M. Yang, L. Li, J. Zhou et al., "Structural Evolution and Hydrocarbon Potential of the Upper Paleozoic Northern Ordos Basin, North China," *Acta Geologica Sinica*, vol. 89, no. 5, pp. 1636–1648, 2015.
- [33] Y. Lei, X. Luo, X. Wang et al., "Characteristics of silty laminae in Zhangjiatan shale of southeastern Ordos Basin, China: implications for shale gas formation," *AAPG Bulletin*, vol. 99, no. 4, pp. 661–687, 2015.
- [34] W. Lyu, L. Zeng, Z. Liu, G. Liu, and K. Zu, "Fracture responses of conventional logs in tight-oil sandstones: a case study of the Upper Triassic Yanchang Formation in southwest Ordos Basin, China," *AAPG Bulletin*, vol. 100, no. 9, pp. 1399–1417, 2016.
- [35] Y. Duan, "Geochemical characteristics of crude oil in fluvial deposits from Maling oilfield of Ordos basin, China," *Organic Geochemistry*, vol. 52, pp. 35–43, 2012.
- [36] Y. Duan, Y. Yuan, and R. Qian, "Migration features of crude oil in fluvial deposits of Maling oilfield in Ordos Basin, China," *Organic Geochemistry*, vol. 58, pp. 78–85, 2013.
- [37] L. M. Ji, F. W. Meng, T. Wu, J. L. Xu, and L. T. Li, "Fluorescence intensity in Triassic acritarchs from the Yanchang Formation of the Ordos Basin, Northwestern China," *Acta Micropalaeontologica Sinica*, vol. 23, no. 3, pp. 309–312, 2006.
- [38] C. Zou, S. Tao, X. Yuan et al., "The formation conditions and distribution characteristics of continuous petroleum accumulations," *Acta Petrolei Sinica*, vol. 30, no. 3, pp. 324–331, 2009.
- [39] R. G. Maliva, E. A. Clayton, and T. M. Missimer, "Application of advanced borehole geophysical logging to managed aquifer recharge investigations," *Hydrogeology Journal*, vol. 17, no. 6, pp. 1547–1556, 2009.
- [40] H.-L. Wu, N. Li, C.-L. Lan, X.-Z. Kong, and H. Chai, "Standard spectrum measurement and simulation of elemental capture spectroscopy log," *Applied Geophysics*, vol. 10, no. 1, pp. 109–116, 2013.
- [41] J. Lai, G. Wang, Y. Chai et al., "Mechanism analysis and quantitative assessment of pore structure for tight sandstone reservoirs: an example from Chang 8 oil layer in the Jiyuan area of Ordos basin," *Acta Geologica Sinica*, vol. 88, no. 11, pp. 2119–2130, 2014.
- [42] F. H. Nader, E. De Boever, M. Gasparrini et al., "Quantification of diagenesis impact on the reservoir properties of the Jurassic Arab D and C members (Offshore, U.A.E.)," *Geofluids*, vol. 13, no. 2, pp. 204–220, 2013.
- [43] J. Lai, G. Wang, Y. Chai et al., "Deep burial diagenesis and reservoir quality evolution of high-temperature, high-pressure sandstones: Examples from Lower Cretaceous Bashijiqike Formation in Keshen area, Kuqa depression, Tarim basin of China," *AAPG Bulletin*, vol. 101, no. 06, pp. 829–862, 2017.
- [44] M. A. K. El-ghali, H. Mansurbeg, S. Morad, I. Al-Aasm, and G. Ajdanlisky, "Distribution of diagenetic alterations in fluvial and paralic deposits within sequence stratigraphic framework: evidence from the Petrohan Terrigenous Group and the Svidol Formation, Lower Triassic, NW Bulgaria," *Sedimentary Geology*, vol. 190, no. 1–4, pp. 299–321, 2006.
- [45] A. S. Mansour, R. I. Rifai, and M. N. Shaaban, "Geochemical constraint on the origin of the multi-mineralogic carbonate cements in the subsurface Middle Jurassic sandstones, Central Sinai, Egypt," *Journal of Geochemical Exploration*, vol. 143, pp. 163–173, 2014.
- [46] R. Calvo, A. Ayalon, A. Bein, and E. Sass, "Chemical and isotopic composition of diagenetic carbonate cements and its relation to hydrocarbon accumulation in the Heletz-Kokhav oil field (Israel)," *Journal of Geochemical Exploration*, vol. 108, no. 1, pp. 88–98, 2011.
- [47] J. M. Ketzer, M. Holz, S. Morad, and I. S. Al-Aasm, "Sequence stratigraphic distribution of diagenetic alterations in coal-bearing, paralic sandstones: evidence from the Rio Bonito Formation (early Permian), southern Brazil," *Sedimentology*, vol. 50, no. 5, pp. 855–877, 2003.
- [48] B. Cao, X. Luo, L. Zhang, F. Sui, H. Lin, and Y. Lei, "Diagenetic evolution of deep sandstones and multiple-stage oil entrapment: a case study from the Lower Jurassic Sangonghe Formation in the Fukang Sag, central Junggar Basin (NW China)," *Journal of Petroleum Science and Engineering*, vol. 152, pp. 136–155, 2017.
- [49] M. I. Odigi and L. C. Amajor, "Geochemistry of carbonate cements in Cretaceous sandstones, southeast Benue Trough, Nigeria: implications for geochemical evolution of formation waters," *Journal of African Earth Sciences*, vol. 57, no. 3, pp. 213–226, 2010.
- [50] J. Lai, G. Wang, C. Cai et al., "Diagenesis and reservoir quality in tight gas sandstones: the fourth member of the Upper Triassic Xujiahe Formation, Central Sichuan Basin, Southwest China," *Geological Journal*, pp. 1–18, 2017.
- [51] J. Lai, G. Wang, Y. Ran, and Z. Zhou, "Predictive distribution of high-quality reservoirs of tight gas sandstones by linking diagenesis to depositional facies: evidence from Xu-2 sandstones in the Penglai area of the central Sichuan basin, China," *Journal of Natural Gas Science and Engineering*, vol. 23, pp. 97–111, 2015.
- [52] S. M. Zamanzadeh, A. Amini, and M. Ghavidel-Syooki, "Sequence stratigraphic controls on early-diagenetic carbonate cementation of shallow marine clastic sediments (the Devonian Zakeen Formation, southern Zagros, Iran)," *Geosciences Journal*, vol. 13, no. 1, pp. 31–57, 2009.
- [53] H. G. Dill, S. Khishigsuren, F. Melcher et al., "Facies-related diagenetic alteration in lacustrine-deltaic red beds of the Paleogene Ergeliin Zoo Formation (Erdene Sum area, S. Gobi, Mongolia)," *Sedimentary Geology*, vol. 181, no. 1–2, pp. 1–24, 2005.
- [54] F. E. Wickman, "The cycle of carbon and the stable carbon isotopes," *Geochimica et Cosmochimica Acta*, vol. 9, no. 3, pp. 136–153, 1956.
- [55] R. G. Pankina, "Origin of CO<sub>2</sub> in petroleum gases (from the isotopic composition of carbon)," *International Geology Review*, vol. 21, no. 5, pp. 535–539, 1979.
- [56] S. M. Rogers, "Deposition and diagenesis of mississippian chat reservoirs, North-central Oklahoma," *AAPG Bulletin*, vol. 85, no. 1, pp. 115–129, 2001.
- [57] A. Karim, G. Pe-Piper, and D. J. W. Piper, "Controls on diagenesis of Lower Cretaceous reservoir sandstones in the western Sable Subbasin, offshore Nova Scotia," *Sedimentary Geology*, vol. 224, no. 1–4, pp. 65–83, 2010.
- [58] K. Al-Ramadan, S. Morad, J. N. Proust, and I. Al-Aasm, "Distribution of diagenetic alterations in siliciclastic shoreface

deposits within a sequence stratigraphic framework: evidence from the Upper Jurassic, Boulonnais, NW France,” *Journal of Sedimentary Research*, vol. 75, no. 5, pp. 943–959, 2005.

- [59] K. E. Higgs, H. Zwingmann, A. G. Reyes, and R. H. Funnell, “Diagenesis, porosity evolution, and petroleum emplacement in tight gas reservoirs, Taranaki Basin, New Zealand,” *Journal of Sedimentary Research*, vol. 77, no. 12, pp. 1003–1025, 2007.
- [60] A. Khidir and O. Catuneanu, “Predictive diagenetic clay-mineral distribution in siliciclastic rocks as a tool for identifying sequence boundaries in non-marine successions: the Coalspur Formation, west-central Alberta,” *Geologos*, vol. 15, no. 3-4, pp. 169–180, 2009.

## Research Article

# A Geochemical Model of Fluids and Mineral Interactions for Deep Hydrocarbon Reservoirs

Jun Li,<sup>1</sup> Raheel Ahmed,<sup>2</sup> Qian Zhang,<sup>1</sup> Yongfan Guo,<sup>1</sup> and Xiaochun Li<sup>1</sup>

<sup>1</sup>State Key Laboratory of Geomechanics and Geotechnical Engineering, Institute of Rock and Soil Mechanics, Chinese Academy of Sciences, Wuhan 430071, China

<sup>2</sup>Dimue Technology Ltd. Co., Wuhan, China

Correspondence should be addressed to Jun Li; lijun2009s@gmail.com

Received 19 February 2017; Accepted 12 June 2017; Published 16 July 2017

Academic Editor: Keyu Liu

Copyright © 2017 Jun Li et al. This is an open access article distributed under the Creative Commons Attribution License, which permits unrestricted use, distribution, and reproduction in any medium, provided the original work is properly cited.

A mutual solubility model for CO<sub>2</sub>-CH<sub>4</sub>-brine systems is constructed in this work as a fundamental research for applications of deep hydrocarbon exploration and production. The model is validated to be accurate for wide ranges of temperature (0–250°C), pressure (1–1500 bar), and salinity (NaCl molality from 0 to more than 6 mole/KgW). Combining this model with PHREEQC functionalities, CO<sub>2</sub>-CH<sub>4</sub>-brine-carbonate-sulfate equilibrium is calculated. From the calculations, we conclude that, for CO<sub>2</sub>-CH<sub>4</sub>-brine-carbonate systems, at deeper positions, magnesium is more likely to be dissolved in aqueous phase and calcite can be more stable than dolomite and, for CO<sub>2</sub>-CH<sub>4</sub>-brine-sulfate systems, with a presence of CH<sub>4</sub>, sulfate ions are likely to be reduced to S<sup>2-</sup> and H<sub>2</sub>S in gas phase could be released after S<sup>2-</sup> saturated in the solution. The hydrocarbon “souring” process could be reproduced from geochemical calculations in this work.

## 1. Introduction

With the exploration and production of middle-shallow oil and gas reservoirs, the main oil/gas fields have come to the late stages of production. More and more intensive exploration work has been done on middle-shallow fields and it is not easy to achieve more breakthroughs. So, researchers are devoting more efforts in deep reservoirs (with depth more than 5000 m). In China, the depositional environment is quite complex and special, so abundant hydrocarbon resources are possible. From the drilling evidence, an effective hydrocarbon reserve was found at more than 7000 m depth in China [1]. More and more research on deep layer hydrocarbon exploration has been carried out in recent years.

For deep hydrocarbon research, fluid-rock interaction is an important topic, as it will influence the fluid composition, physical and chemical properties, and transportation in porous media. The geochemical reactions are more active at locations with both gas and water, such as so-called gas-water transition zones [2, 3]. When gas and water contact, both gas components and mineral will be dissolved in water, and many

geochemical reactions could be triggered. In Sichuan basin, H<sub>2</sub>S can usually be found from gas reservoirs. The existence of H<sub>2</sub>S can be a result of geochemical reactions of dissolved hydrocarbon and sulfates. It is called “souring” process in some literature [2].

Numerical modeling of geochemistry is a useful tool to understand the mechanism of fluid-mineral interactions in deep reservoirs. PHREEQC is one of the most popular geochemistry software packages in hydrological applications [4]. The speciation in water associated with hundreds of chemical reactions can be dealt with. TOUGHREACT is a 3D reactive transportation simulator which is able to calculate geochemical reactions with similar database as PHREEQC [5]. This simulator has been widely used in CO<sub>2</sub> geological storage and geothermal recovery projects. Both of the software programs are powerful for geochemical reaction analysis in porous media. However, for fluid-mineral interactions in deep reservoir, gas-brine phase partitioning and speciation should be carefully considered due to high temperature and pressure. In gas reservoirs, CO<sub>2</sub> usually exists with quite a bit amount of hydrocarbons. So, in this work, we establish a

mutual solubility model for CO<sub>2</sub>-CH<sub>4</sub>-brine systems, which is accurate for a pressure range of 1 bar to 1500 bar, temperature range of 0°C to 250°C, and salinity range of 0 to 6 m. With the solubility calculated by the model, PHREEQC is used to calculate equilibrium of CO<sub>2</sub>-CH<sub>4</sub>-brine-minerals (carbonates and sulfates).

## 2. CO<sub>2</sub>-CH<sub>4</sub>-Brine Mutual Solubility Modeling

We assume that there are two fluid phases (i.e., aqueous phase and nonaqueous phase) existing at given temperature, pressure, and feed composition. CO<sub>2</sub> or CH<sub>4</sub> always dominates nonaqueous phase. Their solubilities in water and H<sub>2</sub>O content in nonaqueous phase are desired to be accurately reproduced by a thermodynamic model. In equilibrium state, for each component in the system (e.g., component  $i$ ), the chemical potential in each phase should be equal. Then we have,

$$\mu_i^{\text{NA}} = \mu_i^{\text{AQ}}. \quad (1)$$

For nonaqueous phase,

$$\begin{aligned} \mu_i^{\text{NA}}(T, P, y_i) &= \mu_i^{\text{NA}(0)}(T) + RT \ln f_i(T, P, y_i) \\ &= \mu_i^{\text{NA}(0)}(T) + RT \ln y_i P \\ &\quad + RT \ln \varphi_i(T, P, y_i), \end{aligned} \quad (2)$$

where  $\mu_i^{\text{NA}(0)}(T)$  stands for standard chemical potential of component  $i$ , which is the ideal gas chemical potential at the pressure of 1 bar [6, 7];  $y_i$  is mole fraction of component  $i$  in nonaqueous phase;  $f_i$  is fugacity and  $\varphi_i$  is fugacity coefficient;  $R$  is the gas constant (8.31446 J/K/mol);  $T$  is temperature in K; and  $P$  is pressure in bar hereafter.

For aqueous phase,

$$\begin{aligned} \mu_i^{\text{AQ}}(T, P, m_{\text{sol}}) &= \mu_i^{\text{AQ}(0)}(T, P) + RT \ln a_i(T, P, m_{\text{sol}}) \\ &= \mu_i^{\text{AQ}(0)}(T, P) + RT \ln (Nw \times x_i) \\ &\quad + RT \ln \gamma_i(T, P, m_{\text{sol}}), \end{aligned} \quad (3)$$

where  $\mu_i^{\text{AQ}(0)}$  is the standard chemical potential of species  $i$  in an ideal aqueous solution with a hypothetical unit molality [8];  $m_{\text{sol}}$  is the molality (in mole/Kg water, molal for short hereafter) of salt in the aqueous phase;  $Nw$  is the mole number of 1kg water (55.508);  $x_i$  is the mole fraction of species  $i$  dissolved in the aqueous phase;  $a_i$  is activity of component  $i$  in aqueous phase; and  $\gamma_i$  is activity coefficient of component  $i$ .

With (1) to (3), we have

$$\frac{\mu_i^{\text{AQ}(0)} - \mu_i^{\text{NA}(0)}}{RT} = \ln \left( \frac{f_i}{a_i} \right). \quad (4)$$

Here, equilibrium constant is defined as  $\ln(K_i) = (\mu_i^{\text{AQ}(0)} - \mu_i^{\text{NA}(0)})/RT$ , so we have

$$y_i \varphi_i P = Nw K_i x_i \gamma_i. \quad (5)$$

TABLE 1: Parameters of H<sub>2</sub>O equilibrium constant in (6).

Parameters	$T > 373.15 \text{ K}$	$T \leq 373.15 \text{ K}$
$a_1$	$-9.0283127E - 1$	$9.31063597E0$
$a_2$	$3.6492938E - 2$	$-1.892867005E - 1$
$a_3$	$4.3610019E - 4$	$1.307135652E - 3$
$a_4$	$-3.10936036E - 6$	$-3.800223763E - 6$
$a_5$	$4.5920530E - 9$	$4.0091369717E - 9$
$a_6$	$1.62996873E1$	$2.2769246863E1$
$a_7$	$2.81119409E - 2$	$-1.1291330188E - 2$

The mutual solubility model of CO<sub>2</sub>-CH<sub>4</sub>-brine system is established based on the above principle. Equilibrium constants ( $K_i$ ), fugacity coefficients ( $\varphi_i$ ), and activity coefficients ( $\gamma_i$ ) should be properly carefully obtained.

*2.1. Equilibrium Constants.* For equilibrium constant of H<sub>2</sub>O, we follow the work of Li et al. [7] with an empirical equation revised from Spycher et al. (2003):

$$\begin{aligned} K_{\text{H}_2\text{O}}(T, P) &= (a_1 + a_2 T + a_3 T^2 + a_4 T^3 + a_5 T^4) \\ &\quad \cdot \exp \left( 0.1 \frac{(P - 1)(a_6 + a_7 T)}{RT} \right). \end{aligned} \quad (6)$$

The parameters ( $a_1$  to  $a_7$ ) in (6) are all from Li et al. [7], listed in Table 1.

For equilibrium constants of CO<sub>2</sub> and CH<sub>4</sub>, we follow the form of Mao et al. (2013):

$$\begin{aligned} \ln K_i &= b_1 + b_2 T + \frac{b_3}{T} + b_4 T^2 + \frac{b_5 P}{T^2} + b_6 P + b_7 P T \\ &\quad + \frac{b_8 P}{T} + b_9 P T^2 + b_{10} P^2 T + b_{11} P^3, \end{aligned} \quad (7)$$

where  $i = \text{CO}_2, \text{CH}_4$ .  $b_i$  ( $i = 1, 2, \dots, 11$ ) are parameters. The parameters are determined from experimental data of gas solubility in aqueous phase. See Table 2 for more details.

*2.2. Fugacity Coefficients.* Peng-Robinson equation of state (PR-EOS for short [9]) is used from CO<sub>2</sub>, CH<sub>4</sub>, and H<sub>2</sub>O fugacity coefficients in the nonaqueous phase. PR-EOS is a classic two-parameter equation of state of cubic form. The related parameters of pure component systems can be found from the original work of Peng and Robinson [9]. For gas mixtures, mixing rule is used for the two parameters.

$$\begin{aligned} a &= \sum_i \sum_j y_i y_j a_{ij} \\ b &= \sum_i b_i y_i, \end{aligned} \quad (8)$$

where  $a_{ij} = \sqrt{a_i a_j} (1 - \delta_{ij})$  and  $\delta_{ij}$  are binary interaction parameters of species  $i$  and  $j$ . Binary interaction parameters for CO<sub>2</sub>, CH<sub>4</sub>, and H<sub>2</sub>O can be found in Table 3 according to Søreide and Whitson [10].

TABLE 2: Parameters of CO<sub>2</sub> and CH<sub>4</sub> equilibrium constants in (7).

	$b_1$	$b_2$	$b_3$	$b_4$	$b_5$	$b_6$	$b_7$	$b_8$	$b_9$	$b_{10}$	$b_{11}$
CO <sub>2</sub>	2.302E-1	-3.654E-2	-1.8367E3	2.0331E-5	-3.9072E5	-5.8269E-2	1.5062E-4	7.8087E0	-1.3013E-7	1.1145E-9	-1.3074E-10
CH <sub>4</sub>	-1.6388E1	3.2371E-2	9.4682E3	-2.6573E-5	-1.4353E6	-1.3225E-2	3.1305E-5	2.2605E0	-2.9063E-8	3.4408E-9	-6.11809E-10

TABLE 3: Binary interaction parameter in PR-EOS.

$\delta_{ij}$	H <sub>2</sub> O	CO <sub>2</sub>	CH <sub>4</sub>
H <sub>2</sub> O	—	0.19014	0.485
CO <sub>2</sub>	0.19014	—	0.1196
CH <sub>4</sub>	0.485	0.1196	—

2.3. *Activity Coefficients.* For activity coefficients, Pitzer model [11] was successfully used in gas-water-mineral modeling for high salinities in previous works [12–15]. Cations, anions, and interaction between particle pairs are considered to influence the component activity behaviors in aqueous phase. The activity coefficient equations are as follows:

$$\ln \gamma_i = \sum_c 2m_c \lambda_{i-c} + \sum_a 2m_a \lambda_{i-a} + \sum_c \sum_a m_a m_c \zeta_{i-a-c}, \quad (9)$$

where  $m_c$  is cation molality,  $m_a$  is anion molality, and  $\lambda_{i-c}$ ,  $\lambda_{i-a}$ , and  $\zeta_{i-a-c}$  are parameters that are functions of temperature and pressure.  $\lambda_{i-c}$ ,  $\lambda_{i-a}$ , and  $\zeta_{i-a-c}$  are known as Pitzer parameters and they are usually estimated from gas solubility data from aqueous solutions with dissolved salts. In this work, Pitzer parameters are usually calibrated from gas solubility from NaCl solutions.  $\lambda_{i-\text{Cl}^-}$  is assumed to be 0. As the approximation in Duan and Sun [14] and Duan et al. [16],  $\lambda_{i-\text{monovalent}}$  and  $\lambda_{i-\text{bivalent}}$  are estimated as  $\lambda_{i-\text{Na}^+}$  and  $2\lambda_{i-\text{Na}^+}$ . All ternary parameters are estimated as  $\zeta_{i-\text{Na}-\text{Cl}}$ . Pitzer parameters are listed in Table 4.

2.4. *Model Validation.* The model performance is evaluated from comparison of model results and related experimental data of CO<sub>2</sub>-CH<sub>4</sub>-brine systems (including the subsystems).

For CO<sub>2</sub>-H<sub>2</sub>O-NaCl systems, the experimental studies [17–19] are sufficient, which cover temperature from 0°C to more than 250°C and pressure from 1 bar to more than 1500 bar. From our comparison, the average absolute derivations for most of the data points are less than 10%. Figures 1(a) and 1(b) show a comparison of CO<sub>2</sub> solubilities in pure water and NaCl solutions calculated from this model and related experimental data. We can find that the model solutions agree with the experimental data in the wide ranges of temperature, pressure, and salinity. Figure 1(c) shows the H<sub>2</sub>O solubility in nonaqueous (CO<sub>2</sub>-rich) phase of the model solutions and experimental data. From the figure, the model can well reproduce H<sub>2</sub>O solubility in nonaqueous phase.

Experimental data of CH<sub>4</sub>-H<sub>2</sub>O-NaCl system are also sufficient with temperature from 0 to more than 250°C and pressure from 1 bar to more than 1500 bar [20]. Figures 2(a) and 2(b) show the comparison of CH<sub>4</sub> solubilities in water and NaCl solutions of experimental data and this model. Figure 2(c) shows the experimental data of H<sub>2</sub>O in nonaqueous (CH<sub>4</sub>-rich) phase and the related model solutions. From the comparisons, the experimental data can be well reproduced by the model.

Compared with single gas (CO<sub>2</sub> or CH<sub>4</sub>)-brine systems, gas mixture (CO<sub>2</sub> and CH<sub>4</sub> existing at the same time)-brine systems have less experimental data. The existing data are also not systematic. Qin et al. [21] have studied phase equilibria for CO<sub>2</sub>-CH<sub>4</sub>-H<sub>2</sub>O system at 325 K and 376 K and with pressure

from 100 bar to 500 bar. 21 data points were generated in the work. We compared their results with our model. From the comparison (see Figure 3), we can conclude that the model can predict mutual solubilities for CO<sub>2</sub>-CH<sub>4</sub>-H<sub>2</sub>O system.

In summary, the comparison of the model solutions with existing experimental data shows that the model can well reproduce and predict mutual solubility data of CO<sub>2</sub>-CH<sub>4</sub>-brine systems in wide ranges of temperature, pressure, and salinity. The model is reliable to be used in gas-water-mineral equilibrium analysis.

### 3. CO<sub>2</sub>/CH<sub>4</sub>-Water-Mineral Interactions in Deep Environments

In Sichuan basin, carbonates (such as dolomite or calcite) are the dominant minerals in some natural gas reservoirs; meanwhile sulfates (such as gypsum or anhydrite) and clay minerals are also commonly found [22, 23]. In Sichuan natural gas reservoirs, CH<sub>4</sub> is always accompanied with other components such as CO<sub>2</sub>, N<sub>2</sub>, or H<sub>2</sub>S [24]. PHREEQC is a famous software package for water-mineral interaction calculations. Pressure effects can be considered using its third version [4]. With an accurate mutual solubility model of CO<sub>2</sub>-CH<sub>4</sub>-brine systems, geochemical reactions in CO<sub>2</sub>-CH<sub>4</sub>-water-mineral systems can be calculated by combining this model and the PHREEQC functionality. Through this research, we aim to find out

- (i) the influences on geochemical reactions in depth (i.e., temperature and pressure increase or decrease);
- (ii) sensitivity of gas components (i.e., CO<sub>2</sub> or CH<sub>4</sub>) to water composition, mineral dissolution, or precipitation.

In this work, the calculations are based on Sichuan basin background. The hydrostatic pressure is assumed to be 100 bar/Km, and geothermal gradient is assumed as 25°C/Km according to a previous work [25] with surface temperature set as 25°C. The depth range of the research is from 3000 m to 6000 m. Relationships of depth, temperature, and pressure are shown in Figure 4. To clarify the influences from gas components, sodium chlorite is considered as the only salt that is dissolved in water as an initial solution. Geochemistry equilibrium of CO<sub>2</sub>-CH<sub>4</sub>-brine-dolomite, CO<sub>2</sub>-CH<sub>4</sub>-brine-calcite, and CO<sub>2</sub>-CH<sub>4</sub>-brine-gypsum/anhydrite systems is studied. Two gas compositions are considered, pure CH<sub>4</sub> or 10% CO<sub>2</sub> + 90% CH<sub>4</sub>, to evaluate CO<sub>2</sub> influences.

Table 5 lists the species of ions, minerals, and gases which get involved in geochemical reactions in CO<sub>2</sub>-CH<sub>4</sub>-brine-carbonate systems and CO<sub>2</sub>-CH<sub>4</sub>-brine-sulfate systems.

3.1. *CO<sub>2</sub>-CH<sub>4</sub>-Brine-Carbonate Systems.* For CO<sub>2</sub>-CH<sub>4</sub>-brine-carbonate systems, cases of fluid equilibrium with calcite and dolomite are studied, respectively. Figure 5 shows the molality of carbon (including HCO<sub>3</sub><sup>-</sup>, CO<sub>2</sub>, CaHCO<sub>3</sub><sup>+</sup>, CaCO<sub>3</sub>, CO<sub>3</sub><sup>2-</sup>, MgHCO<sub>3</sub><sup>-</sup>, and MgCO<sub>3</sub>) dissolved in aqueous phase with different depths, gas compositions, and salinities. Figure 6 shows the molality of calcium (including Ca<sup>2+</sup>, CaCO<sub>3</sub>, CaHCO<sub>3</sub><sup>+</sup>, and CaOH<sup>+</sup>) and magnesium

TABLE 4: Pitzer parameters for activity coefficients.

Parameters	Equations
$\lambda_{\text{CO}_2\text{-Na}^+}$	$-3.1312239 \times 10^{-1} + 5.532647 \times 10^{-4}T + 7.5844401 \times 10^1/T - 1.8950519 \times 10^{-4}P + 7.1628762 \times 10^{-5}P/T - 1.458572 \times 10^{-8}P^2T$
$\lambda_{\text{CH}_4\text{-Na}^+}$	$-5.7066455 \times 10^{-1} + 7.2997588 \times 10^{-4}T + 1.5176903 \times 10^2/T + 3.1927112 \times 10^{-5}P - 1.642651 \times 10^{-5}P/T$
$\lambda_{\text{H}_2\text{S-Na}^+}$	$1.03658689 - 1.1784797 \times 10^{-3}T - 1.7754826 \times 10^2/T - 4.5313285 \times 10^{-4}P + 4.775165 \times 10^1P/T^2$
$\zeta_{\text{CO}_2\text{-Na}^+\text{-Cl}^-}$	$-1.14462 \times 10^{-2} + 2.8274958 \times 10^{-5}T + 1.3980876 \times 10^{-2}P/T - 1.4349005 \times 10^{-2}P/(630 - T)$
$\zeta_{\text{CH}_4\text{-Na}^+\text{-Cl}^-}$	$-2.9990084 \times 10^{-3}$
$\zeta_{\text{H}_2\text{S-Na}^+\text{-Cl}^-}$	$-1.0274152 \times 10^{-2}$

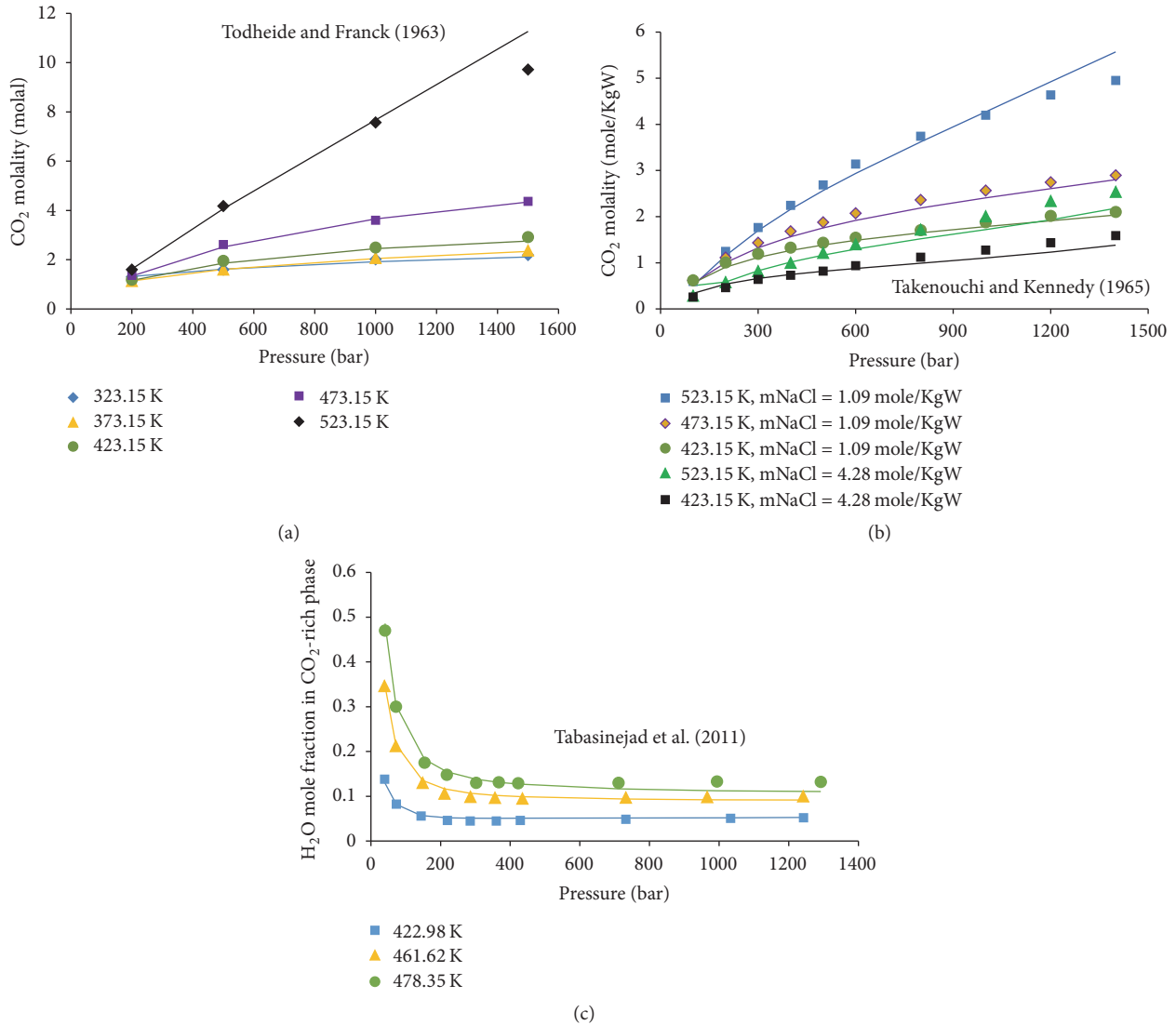


FIGURE 1: Mutual solubilities of CO<sub>2</sub>-brine systems. Lines are calculated results from this model, and dots are from experimental data. (a) CO<sub>2</sub> solubility in pure water; (b) CO<sub>2</sub> solubility in NaCl solutions; (c) H<sub>2</sub>O solubility in CO<sub>2</sub>-rich phase.

(including Mg<sup>2+</sup>, MgOH<sup>+</sup>, MgCO<sub>3</sub>, and MgHCO<sub>3</sub><sup>+</sup>) that is dissolved in aqueous phase. From Figure 6, it is shown that CO<sub>2</sub> in the gas phase will promote calcite or dolomite dissolution. From the calculations, we find that, with CO<sub>2</sub> existing in the system, carbon concentration in aqueous

phase increases with depth. From 3000 m to 6000 m, the carbon molality is almost doubled in Figure 5 at different salinities. However, compared with calcium, magnesium is more soluble and increases with depth. From our calculation, in fluid-dolomite systems, with an increase in

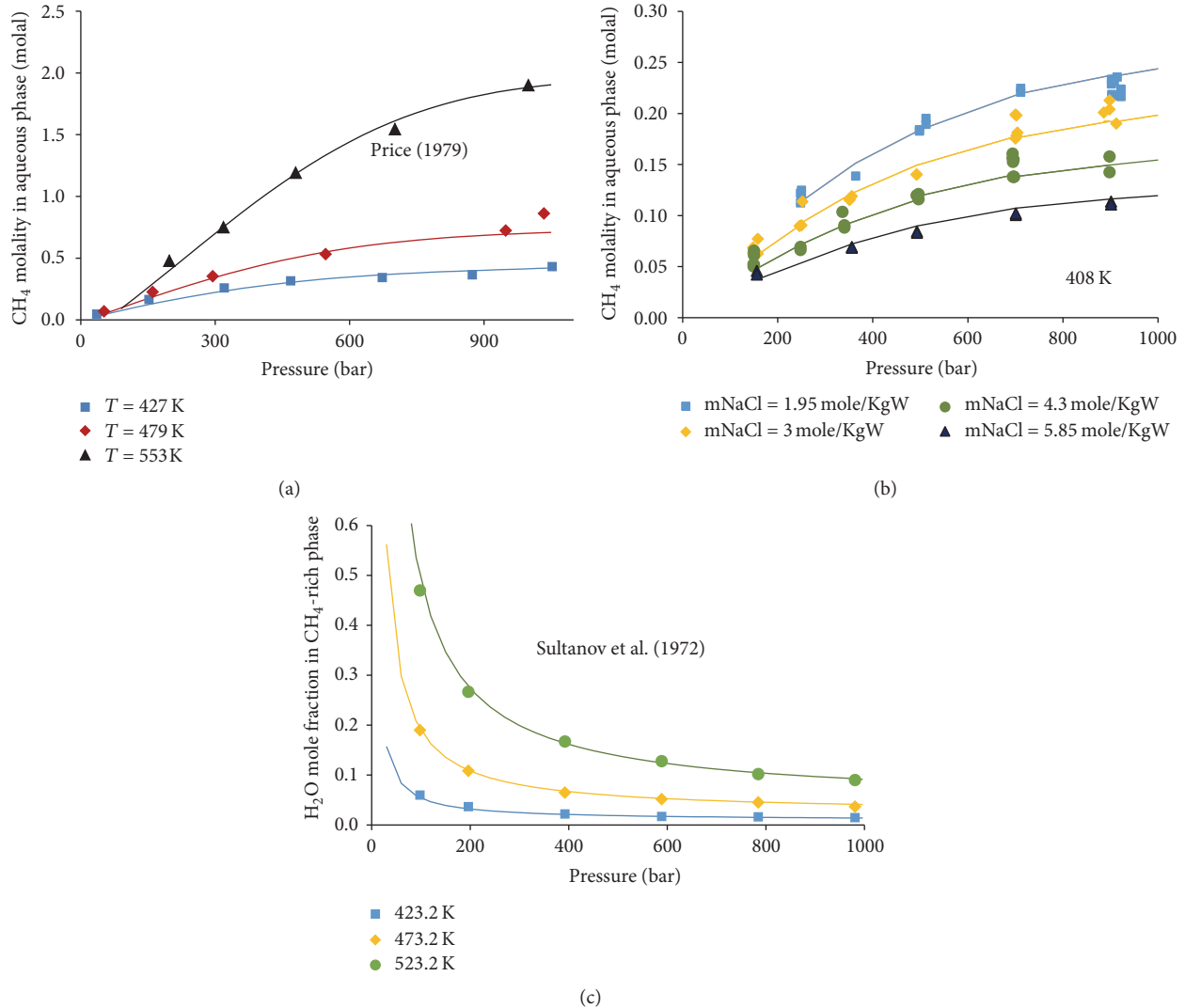


FIGURE 2: Mutual solubilities of CH<sub>4</sub>-brine systems. Lines are calculated results from this model, and dots are from experimental data. (a) CH<sub>4</sub> solubility in pure water; (b) CH<sub>4</sub> solubility in NaCl solutions; (c) H<sub>2</sub>O solubility in CH<sub>4</sub>-rich phase.

temperature and pressure, more calcite precipitates. We can conclude that, in deep carbonate environments, calcium is more likely to precipitate and magnesium ion is more likely to be rich in aqueous phase and transport to shallower areas due to diffusion gradient. So, in general, calcite approaches being existing in deeper environments and dolomite is more likely to be existing in shallower environments.

**3.2. CO<sub>2</sub>-CH<sub>4</sub>-Brine-Sulfate Systems.** The element sulfur can have different chemical valences such as -2, 0, +4, and +6 in nature. When sulfates are dissolved in water, sulfur is usually in +6 valence state. It could be reduced to other valence states when reducer exists in the solution. In deep gas reservoirs in Sichuan basin, sulfates commonly exist. Different fluid compositions may trigger different redox geochemical reactions and lead to different forms of sulfur or even reservoir properties.

In this work, we perform several numerical experiments to evaluate the influence of gas composition and depth on fluid-mineral equilibrium. For gas composition, we considered three cases: pure CH<sub>4</sub>, 10% CO<sub>2</sub> + 90% CH<sub>4</sub>, and pure CO<sub>2</sub>. The calculations covered depth from 3000 m to 6000 m. Figure 7 presents S(-2) (i.e., sulfur dissolved in water with chemical valence -2, which can be S<sup>2-</sup>, HS<sup>-</sup>, and H<sub>2</sub>S as ions) and S(+6) (i.e., sulfur dissolved in water in chemical valence +6, which can be SO<sub>4</sub><sup>2-</sup>, HSO<sub>4</sub><sup>-</sup>, CaSO<sub>4</sub>, and CaHSO<sub>4</sub><sup>+</sup>) concentration in equilibrium of gas-water-gypsum. From Figure 7, we can find the following:

- (1) With pure CO<sub>2</sub> in gas, S(-2) in water is extremely low, and more CH<sub>4</sub> is dissolved in water leading to higher S(-2) concentration.
- (2) Higher CO<sub>2</sub> mole fraction in gas phase will lead to higher S(+6) concentration in water phase.

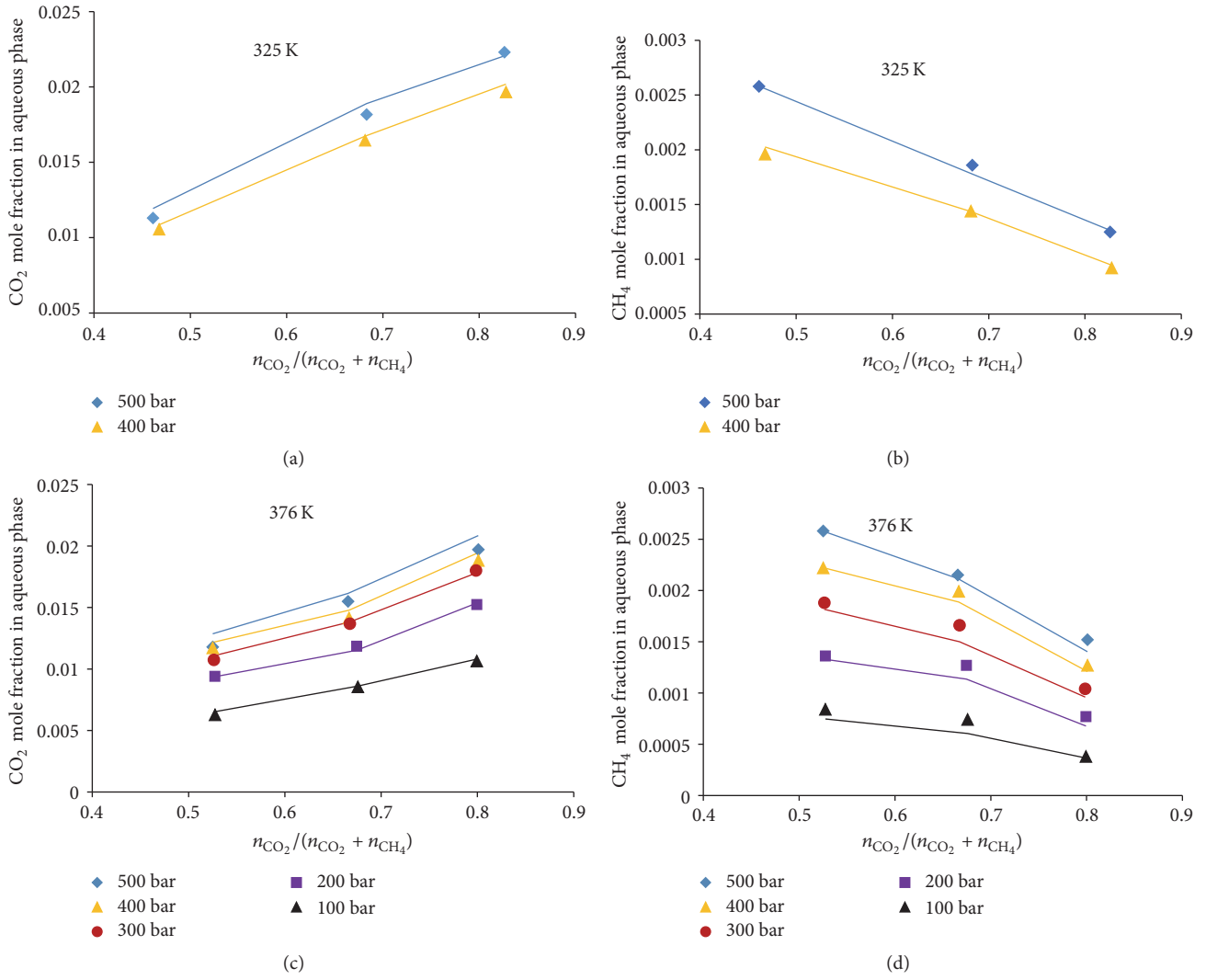


FIGURE 3: CO<sub>2</sub>/CH<sub>4</sub> solubilities in water in CO<sub>2</sub>-CH<sub>4</sub>-H<sub>2</sub>O systems at different temperature and pressure. Dots are from Qin et al.'s [21] experimental data, and lines are from this model.

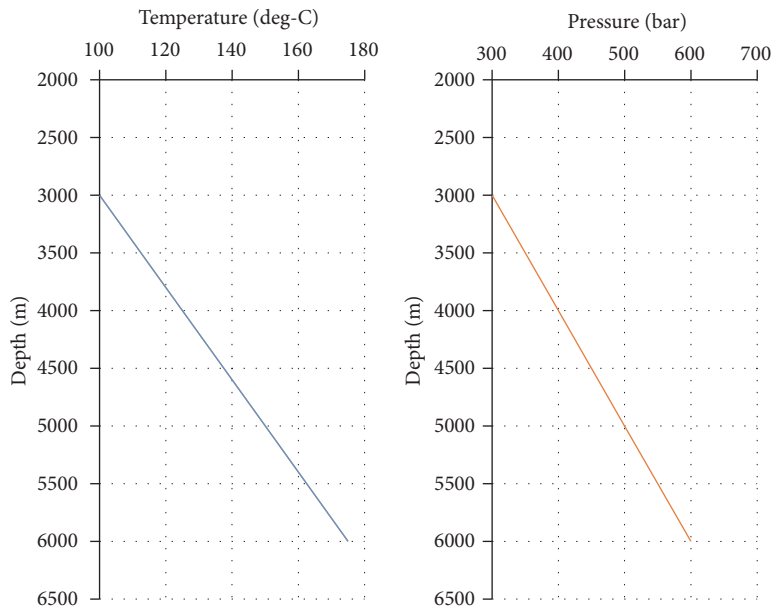


FIGURE 4: Temperature, pressure, and depth relationships.

TABLE 5

(a) Ions, minerals, and gases involved in CO<sub>2</sub>-CH<sub>4</sub>-brine-carbonate systems

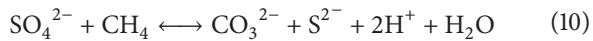
Cations	Anions	Neutral ions	Minerals and gases
H <sup>+</sup>	OH <sup>-</sup>	H <sub>2</sub> O	Aragonite
Ca <sup>2+</sup>	HCO <sub>3</sub> <sup>-</sup>	CH <sub>4</sub>	Calcite
CaHCO <sub>3</sub> <sup>+</sup>	CO <sub>3</sub> <sup>2-</sup>	CO <sub>2</sub>	Dolomite
CaOH <sup>+</sup>	Cl <sup>-</sup>	(CO <sub>2</sub> ) <sub>2</sub>	Halite
Mg <sup>2+</sup>	NaCO <sub>3</sub> <sup>-</sup>	CaCO <sub>3</sub>	CH <sub>4</sub> (g)
MgHCO <sub>3</sub> <sup>+</sup>		H <sub>2</sub>	CO <sub>2</sub> (g)
MgOH <sup>+</sup>		MgCO <sub>3</sub>	H <sub>2</sub> (g)
Na <sup>+</sup>		NaHCO <sub>3</sub>	H <sub>2</sub> O (g)
		NaOH	O <sub>2</sub> (g)
		O <sub>2</sub>	

(b) Ions, minerals, and gases involved in CO<sub>2</sub>-CH<sub>4</sub>-brine-sulfate systems

Cations	Anions	Neutral ions	Minerals and gases
H <sup>+</sup>	OH <sup>-</sup>	H <sub>2</sub> O	Anhydrite
Ba <sup>2+</sup>	HCO <sub>3</sub> <sup>-</sup>	BaSO <sub>4</sub>	Aragonite
BaHCO <sub>3</sub> <sup>+</sup>	NaCO <sub>3</sub> <sup>-</sup>	BaCO <sub>3</sub>	Barite
BaOH <sup>+</sup>	CO <sub>3</sub> <sup>2-</sup>	NaHCO <sub>3</sub>	Calcite
CaHCO <sub>3</sub> <sup>+</sup>	Cl <sup>-</sup>	CaCO <sub>3</sub>	Dolomite
MgHCO <sub>3</sub> <sup>+</sup>	NaSO <sub>4</sub> <sup>-</sup>	(CO <sub>2</sub> ) <sub>2</sub>	Gypsum
Ca <sup>2+</sup>	HS <sup>-</sup>	MgCO <sub>3</sub>	Halite
CaHSO <sub>4</sub> <sup>+</sup>	S <sup>2-</sup>	CaSO <sub>4</sub>	Sulfur
CaOH <sup>+</sup>	SO <sub>4</sub> <sup>2-</sup>	MgSO <sub>4</sub>	Witherite
Mg <sup>2+</sup>	HSO <sub>4</sub> <sup>-</sup>	NaOH	H <sub>2</sub> (g)
MgOH <sup>+</sup>		O <sub>2</sub>	H <sub>2</sub> O (g)
Na <sup>+</sup>		H <sub>2</sub> S	H <sub>2</sub> S (g)
		H <sub>2</sub>	O <sub>2</sub> (g)
		CH <sub>4</sub>	CH <sub>4</sub> (g)
		CO <sub>2</sub>	CO <sub>2</sub> (g)

(3) With higher depth, higher S(+6) concentration can be found, but depth influence on S(-2) concentration is not clear.

It is clear that CH<sub>4</sub> is the key component for S(+6) to be reduced to S(-2) species in water. The related redox geochemical reaction is



When CH<sub>4</sub> and SO<sub>4</sub><sup>2-</sup> are dissolved in water, the above reaction is triggered, and CH<sub>4</sub> is oxidized from C(-4) to C(+4). In the meantime, SO<sub>4</sub><sup>2-</sup> is reduced to S<sup>2-</sup>.

Figure 8(a) shows the amount of calcite precipitation for different cases of geochemical equilibrium. Referring to Figure 8(a), in case of pure CO<sub>2</sub> in gas phase, there is no calcite precipitation; with higher CH<sub>4</sub> mole fraction in gas phase, more calcite can be precipitated; in deeper environments, more calcite can be precipitated. This phenomenon is also connected with sulfur reduction. With CH<sub>4</sub> dissolved in water, more sulfate is consumed and more calcium ions are dissolved in water. In this process, carbanions are generated because of the redox reaction. With more and more calcium

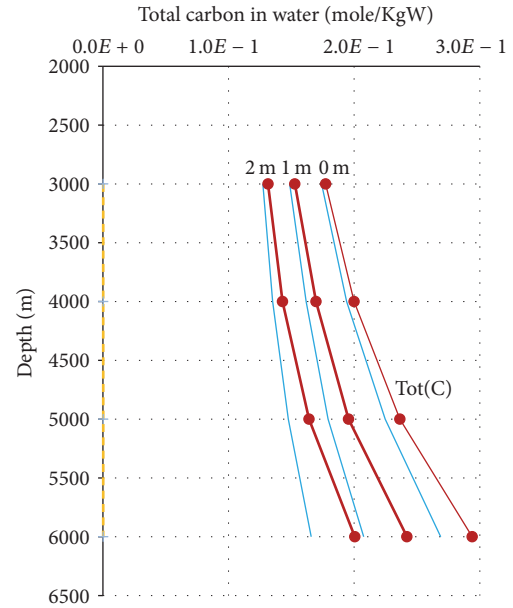


FIGURE 5: Molality of total carbon dissolved in water varying with depth at different salinities and gas compositions. Dashed yellow line represents the case of pure CH<sub>4</sub> of gas in the system. Blue lines represent results from fluid-calcite systems (with gas composition CO<sub>2</sub>:CH<sub>4</sub> = 1:9 in mole). Red lines with dots represent the result from fluid-dolomite systems (with gas composition CO<sub>2</sub>:CH<sub>4</sub> = 1:9 in mole).

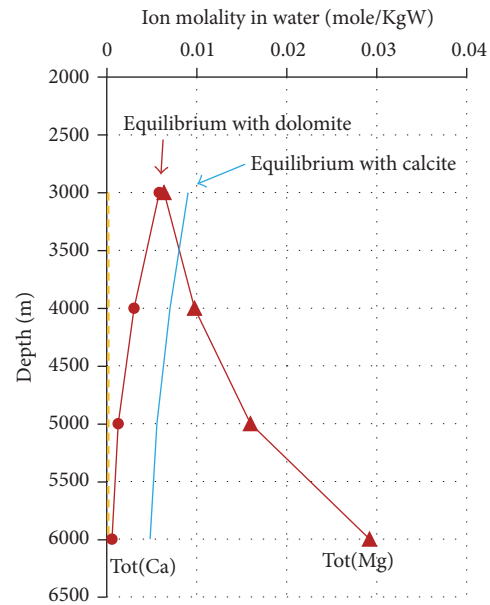


FIGURE 6: Molality of elements Ca and Mg dissolved in water varying with depth (with sodium chlorite molality 0). Yellow line represents the case of pure CH<sub>4</sub> of gas in the system. Red lines with dots represent results from fluid-dolomite systems (with gas composition CO<sub>2</sub>:CH<sub>4</sub> = 1:9 in mole). Blue line represents results from fluid-calcite systems (with gas composition CO<sub>2</sub>:CH<sub>4</sub> = 1:9 in mole).

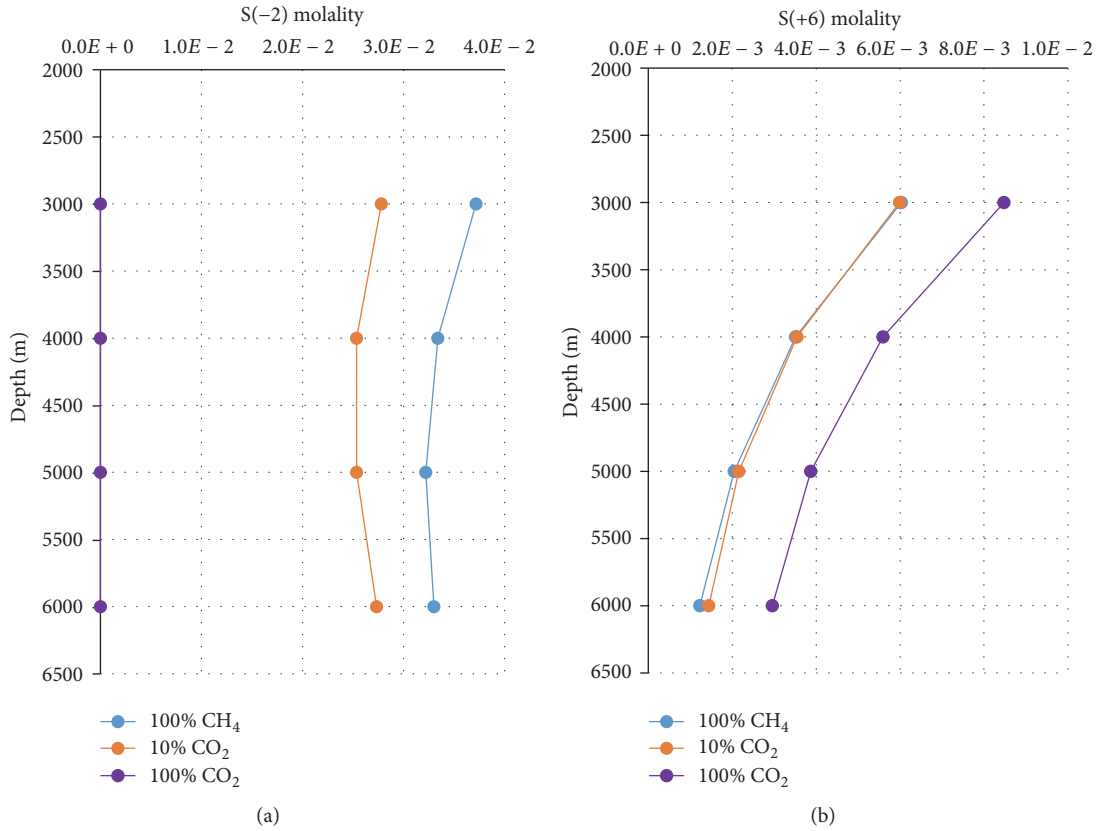


FIGURE 7: Concentration of S(+6) and S(-2) in aqueous phase varying with depth in equilibrium of gas (pure CH<sub>4</sub>, 10% CO<sub>2</sub> + 90% CH<sub>4</sub>, or pure CO<sub>2</sub>), water, and gypsum.

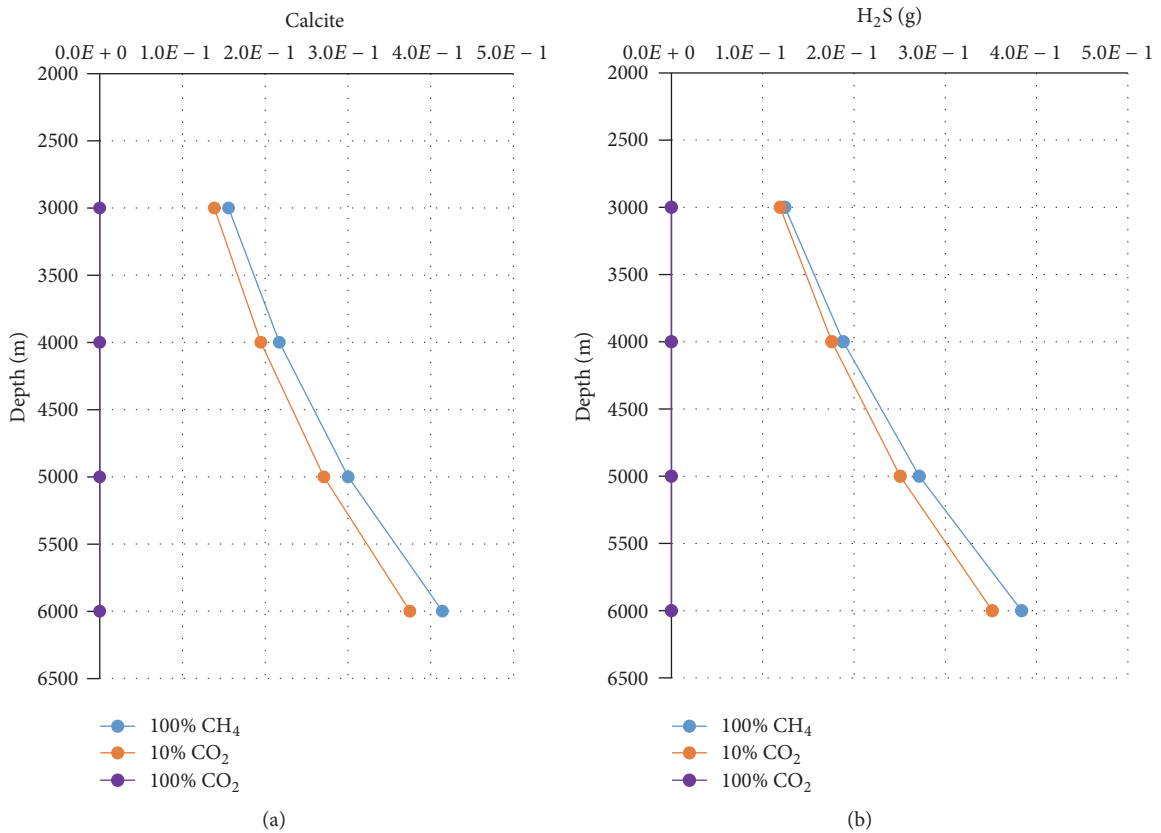


FIGURE 8: (a) Mole number of calcite precipitated and (b) mole number of H<sub>2</sub>S released to gas with 1 KG water in equilibrium with gas (pure CH<sub>4</sub>, 10% CO<sub>2</sub> + 90% CH<sub>4</sub>, or pure CO<sub>2</sub>) and gypsum at different depths.

and carbanion in the solution, calcite becomes saturated and precipitates. Another product is  $\text{H}_2\text{S}$  in gas phase. With more and more  $\text{S}(-2)$  generated in water,  $\text{S}^{2-}$  and  $\text{H}^+$  approach combining with one another, and  $\text{H}_2\text{S}$  becomes saturated and is released in gas phase. As shown in Figure 8(b), with more  $\text{CH}_4$  in gas phase, more  $\text{H}_2\text{S}$  will be generated in gas phase at equilibrium states. From this study, we can find that  $\text{CH}_4$ -water-sulfate redox reaction could be a mechanism of  $\text{H}_2\text{S}$  origin in gas reservoirs [2]. From the figure, we can also find that, at higher depth, more  $\text{H}_2\text{S}$  can be generated. This result agrees with the statement from Li et al. [2].

#### 4. Conclusions

In this work, an accurate mutual solubility model is constructed with “fugacity-activity” method for  $\text{CO}_2$ - $\text{CH}_4$ -brine systems. This model has a wide application range of pressure, temperature, and salinity, which can be used for fluid phase equilibrium in deep hydrocarbon reservoirs.

Combined with the mutual solubility model and PHREEQC, the equilibrium  $\text{CO}_2$ - $\text{CH}_4$ -brine-mineral systems under deep reservoir conditions can be calculated. The mutual solubility model can be used to calculate the mole numbers of  $\text{CO}_2/\text{CH}_4$  dissolved in brine at given temperature, pressure, and salinity. With the dissolved mole numbers of  $\text{CO}_2/\text{CH}_4$ , PHREEQC is used to calculate the speciation between aqueous phase and mineral.

$\text{CO}_2/\text{CH}_4$ -brine-carbonate (i.e., dolomite or calcite) and  $\text{CO}_2/\text{CH}_4$ -brine-sulfate (i.e., gypsum or anhydrite) equilibria were studied with the above methodology. From the study, we find the following:

- (1) For  $\text{CO}_2/\text{CH}_4$ -brine-carbonate (calcite or dolomite) systems, with an increase in depth, calcium is more likely to precipitate as calcite and magnesium is more likely dissolved in aqueous phase. In other words, dolomite could be rich in shallower position and calcite may approach being existing at deeper locations.
- (2) With  $\text{CH}_4$  present in the  $\text{CO}_2/\text{CH}_4$ -brine-sulfate (gypsum or anhydrite) systems, redox reaction is triggered and  $\text{S}(+6)$  is reduced to  $\text{S}(-2)$ .  $\text{H}_2\text{S}$  will be released when  $\text{S}(-2)$  becomes saturated in aqueous phase. This process could be one of the origins for  $\text{H}_2\text{S}$  in gas reservoirs in Sichuan basin, China.

This work is an attempt to do preliminary fluid-mineral interaction calculations with a new established accurate mutual solubility model of  $\text{CO}_2$ - $\text{CH}_4$ -brine systems combined with PHREEQC, version 3. The geochemical reaction parameters are still needed to be validated for high temperature and pressure. Also, more systematic research work of gas-water-minerals is still required in the future according to real depositional environments.

#### Conflicts of Interest

The authors declare that there are no conflicts of interest regarding the publication of this paper.

#### Acknowledgments

This work is supported by National Natural Science Foundation of China (Grant no. 41502246). Dimue Tech. Ltd. Co. provided technical support during the research. The authors also acknowledge the sponsorship from National Key R&D Program of China (2016YFE0102500).

#### References

- [1] G. Zhu and S. Zhang, “Hydrocarbon accumulation conditions and exploration potential of deep reservoirs in China,” *Acta Petrolei Sinica*, vol. 30, no. 10, 2009 (Chinese).
- [2] K. Li, C. Cai, D. Hou et al., “Origin of high  $\text{H}_2\text{S}$  concentrations in the Upper Permian Changxing reservoirs of the Northeast Sichuan Basin, China,” *Marine and Petroleum Geology*, vol. 57, pp. 233–243, 2014.
- [3] H. G. Machel, H. R. Krouse, and R. Sassen, “Products and distinguishing criteria of bacterial and thermochemical sulfate reduction,” *Applied Geochemistry*, vol. 10, no. 4, pp. 373–389, 1995.
- [4] D. L. Parkhurst and C. A. J. Appelo, *Description of Input and Examples for PHREEQC Version 3 - A Computer Program for Speciation, Batch-Reaction, One-Dimensional Transport, and Inverse Geochemical Calculations*, U.S. Geological Survey Techniques and Methods, 2013.
- [5] T. Xu, N. Spycher, E. Sonnenthal, G. Zhang, L. Zheng, and K. Pruess, “TOUGHREACT version 2.0: a simulator for subsurface reactive transport under non-isothermal multiphase flow conditions,” *Computers and Geosciences*, vol. 37, no. 6, pp. 763–774, 2011.
- [6] J. Li, L. Wei, and X. Li, “An improved cubic model for the mutual solubilities of  $\text{CO}_2$ - $\text{CH}_4$ - $\text{H}_2\text{S}$ -brine systems to high temperature, pressure and salinity,” *Applied Geochemistry*, vol. 54, pp. 1–12, 2015.
- [7] J. Li, Z. Zhang, X. Luo, and X. Li, “Modelling of phase equilibria in  $\text{CH}_4$ - $\text{C}_2\text{H}_6$ - $\text{C}_3\text{H}_8$ - $n\text{C}_4\text{H}_{10}$ - $\text{NaCl}$ - $\text{H}_2\text{O}$  systems,” *Applied Geochemistry*, vol. 56, pp. 23–36, 2015.
- [8] J. Li and Z. Duan, “A thermodynamic model for the prediction of phase equilibria and speciation in the  $\text{H}_2\text{O}$ - $\text{CO}_2$ - $\text{NaCl}$ - $\text{CaCO}_3$ - $\text{CaSO}_4$  system from 0 to 250°C, 1 to 1000 bar with  $\text{NaCl}$  concentrations up to halite saturation,” *Geochimica et Cosmochimica Acta*, vol. 75, no. 15, pp. 4351–4376, 2011.
- [9] D.-Y. Peng and D. B. Robinson, “A new two-constant equation of state,” *Industrial Engineering Chemistry Fundamentals*, vol. 15, pp. 59–64, 1976.
- [10] I. Søreide and C. H. Whitson, “Peng-Robinson predictions for hydrocarbons,  $\text{CO}_2$ ,  $\text{N}_2$ , and  $\text{H}_2\text{S}$  with pure water and  $\text{NaCl}$  brine,” *Fluid Phase Equilibria*, vol. 77, no. C, pp. 217–240, 1992.
- [11] K. S. Pitzer, “Thermodynamics of electrolytes. I. theoretical basis and general equations,” *Journal of Physical Chemistry*, vol. 77, no. 2, pp. 268–277, 1973.
- [12] C. E. Harvie, N. Møller, and J. H. Weare, “The prediction of mineral solubilities in natural waters: The  $\text{Na}$ - $\text{K}$ - $\text{Mg}$ - $\text{Ca}$ - $\text{H}$ - $\text{Cl}$ - $\text{SO}_4$ - $\text{OH}$ - $\text{HCO}_3$ - $\text{CO}_3$ - $\text{CO}_2$ - $\text{H}_2\text{O}$  system to high ionic strengths at 25°C,” *Geochimica et Cosmochimica Acta*, vol. 48, no. 4, pp. 723–751, 1984.
- [13] J. P. Greenberg and N. Møller, “The prediction of mineral solubilities in natural waters: A chemical equilibrium model for the  $\text{Na}$ - $\text{K}$ - $\text{Ca}$ - $\text{Cl}$ - $\text{SO}_4$ - $\text{H}_2\text{O}$  system to high concentration from 0 to 250°C,” *Geochimica et Cosmochimica Acta*, vol. 53, no. 10, pp. 2503–2518, 1989.

- [14] Z. Duan and R. Sun, "An improved model calculating CO<sub>2</sub> solubility in pure water and aqueous NaCl solutions from 273 to 533 K and from 0 to 2000 bar," *Chemical Geology*, vol. 193, no. 3-4, pp. 257-271, 2003.
- [15] Z. Duan and D. Li, "Coupled phase and aqueous species equilibrium of the H<sub>2</sub>O-CO<sub>2</sub>-NaCl-CaCO<sub>3</sub> system from 0 to 250°C, 1 to 1000 bar with NaCl concentrations up to saturation of halite," *Geochimica et Cosmochimica Acta*, vol. 72, no. 20, pp. 5128-5145, 2008.
- [16] Z. Duan, N. Møller, and J. H. Weare, "An equation of state for the CH<sub>4</sub>-CO<sub>2</sub>-H<sub>2</sub>O system: I. Pure systems from 0 to 1000°C and 0 to 8000 bar," *Geochimica et Cosmochimica Acta*, vol. 56, no. 7, pp. 2605-2617, 1992.
- [17] K. Tödheide and E. U. Franck, "Das zweiphasengebiet und die kritische kurve im system kohlendioxid-wasser bis zu drucken von 3500 bar," *Zeitschrift für Physikalische Chemie*, vol. 37, no. 5-6, pp. 387-401, 1963.
- [18] S. Takenouchi and G. C. Kennedy, "The solubility of carbon dioxide in NaCl solutions at high temperatures and pressures," *American Journal of Science*, vol. 263, no. 5, pp. 445-454, 1965.
- [19] F. Tabasinejad, R. G. Moore, S. A. Mehta et al., "Water solubility in supercritical methane, nitrogen, and carbon dioxide: Measurement and modeling from 422 to 483 K and pressures from 3.6 to 134 MPa," *Industrial and Engineering Chemistry Research*, vol. 50, no. 7, pp. 4029-4041, 2011.
- [20] R. G. Sultanov, V. G. Skripka, and A. Y. Namoit, "Phase equilibrium and critical effect of water-methane system under increased temperature and pressure," *Zhurnal Fizicheskoi Khimi*, vol. 46, p. 2160, 1972.
- [21] J. Qin, R. J. Rosenbauer, and Z. Duan, "Experimental measurements of vapor-liquid equilibria of the H<sub>2</sub>O + CO<sub>2</sub> + CH<sub>4</sub> ternary system," *Journal of Chemical and Engineering Data*, vol. 53, no. 6, pp. 1246-1249, 2008.
- [22] H. Wen, L. Wen, H. Chen, R. Zheng, L. Dang, and Y. Li, "Geochemical characteristics and diagenetic fluids of dolomite reservoirs in the Huanglong Formation, Eastern Sichuan Basin, China," *Petroleum Science*, vol. 11, no. 1, pp. 52-66, 2014.
- [23] C. Liu, Q. Xie, G. Wang et al., "Rare earth element characteristics of the carboniferous Huanglong Formation dolomites in eastern Sichuan Basin, southwest China: implications for origins of dolomitizing and diagenetic fluids," *Marine and Petroleum Geology*, vol. 81, pp. 33-49, 2017.
- [24] S. Qin, G. Zhou, W. Li, Y. Hou, and F. Lü, "Geochemical evidence of water-soluble gas accumulation in the Weiyuan gas field, Sichuan Basin," *Natural Gas Industry B*, vol. 3, no. 1, pp. 37-44, 2016.
- [25] Y. Han and C. Wu, "Geothermal gradient and heat flow values of some deep wells in sichuan basin," *Oil Gas Geology*, vol. 14, pp. 80-84, 1993.

## Research Article

# Pore Fluid Evolution Influenced by Volcanic Activities and Related Diagenetic Processes in a Rift Basin: Evidence from the Paleogene Medium-Deep Reservoirs of Huanghekou Sag, Bohai Bay Basin, China

Zhongheng Sun,<sup>1,2</sup> Hongtao Zhu,<sup>1,2</sup> Changgui Xu,<sup>3</sup> Xianghua Yang,<sup>1,2</sup>  
Xiaofeng Du,<sup>3</sup> Qingbin Wang,<sup>3</sup> and Jinyang Qiao<sup>1,2</sup>

<sup>1</sup>Key Laboratory of Tectonics and Petroleum Resources, China University of Geosciences, Ministry of Education, Wuhan 430074, China

<sup>2</sup>Faculty of Earth Resources, China University of Geosciences, Wuhan 430074, China

<sup>3</sup>Tianjin Branch of China National Offshore Oil Company Ltd., Tianjin 300452, China

Correspondence should be addressed to Hongtao Zhu; htzhu@cug.edu.cn

Received 3 March 2017; Revised 20 May 2017; Accepted 6 June 2017; Published 13 July 2017

Academic Editor: Shuichang Zhang

Copyright © 2017 Zhongheng Sun et al. This is an open access article distributed under the Creative Commons Attribution License, which permits unrestricted use, distribution, and reproduction in any medium, provided the original work is properly cited.

Volcanic activities exert a significant influence on pore fluid property and related diagenetic processes that substantially controlled reservoirs quality. Analysis of Paleogene medium-deep sandstones on the Huanghekou Sag provides insight into relating the diagenetic processes to pore fluid property evolution influenced by volcanic activities. Three distinct types of pore fluids were identified on the basis of an integrated and systematic analysis including core and thin section observation, XRD, SEM, CL, and trace element. Alkaline aqueous medium environment occurred in  $E_2s_{1+2}$  where volcanic activities have insignificant influence on pore fluids, evidenced by typical alkaline diagenetic events such as K-feldspar albitization, quartz dissolution, feldspar dissolution, and carbonate cementation. During the deposition of  $E_3d_3$ , influx of terrestrial freshwater and alteration of ferromagnesian-rich pore water result in the formation of mixing aqueous medium environment through volcanic eruption dormancy causing zeolite dissolution, clay mineral transformation, and K-feldspar albitization. Ferromagnesian-rich aqueous medium environment developed resulting from the intensive hydrolysis of the unstable ferromagnesian minerals formed due to intense volcanic activities during  $E_3d_{1+2}$  and corresponding predominant diagenetic processes were characterized by the precipitation and dissolution of low-silica zeolites. Therefore, the differential properties of pore fluids caused various diagenetic processes controlling reservoir quality.

## 1. Introduction

It has been documented that thousands of drilled wells show the tremendously exploratory potential of deep sedimentary formations, which has recently drawn great attention of petroleum geologists worldwide (e.g., [1–3]). The definition of the medium-deep or deep reservoirs differs from basin to basin conventionally depending on basin type and exploration degree. Bohai Bay Basin, one of the most petroliferous basins in China [4], and the medium-deep reservoirs are significant exploration interests commonly defined as those Paleogene intervals at burial depth more than 2500 m (e.g., [5–7]) but in the study area of Huanghekou Sag it is generally

referred to those not deeper than 3500 m due to special geological settings. A clear understanding of Paleogene reservoirs development is therefore of great significance for optimizing petroleum exploration and increasing reserves.

Pore fluid evolution exerts a critical role in fluid-rock interactions (e.g., [9–12]). Sources of pore fluids are variable which mainly derived from connate water [13], meteoric water [14–16], dehydration of minerals (e.g., gypsum or clay mineral [17–19]), deep compaction brines [20], and hydrothermal water introduced by igneous activities [18]. In most cases, however, the pore fluids are initially only one of them or mixture of them geochemically with different signatures. Thus, the pore fluids are easily altered by dissolution

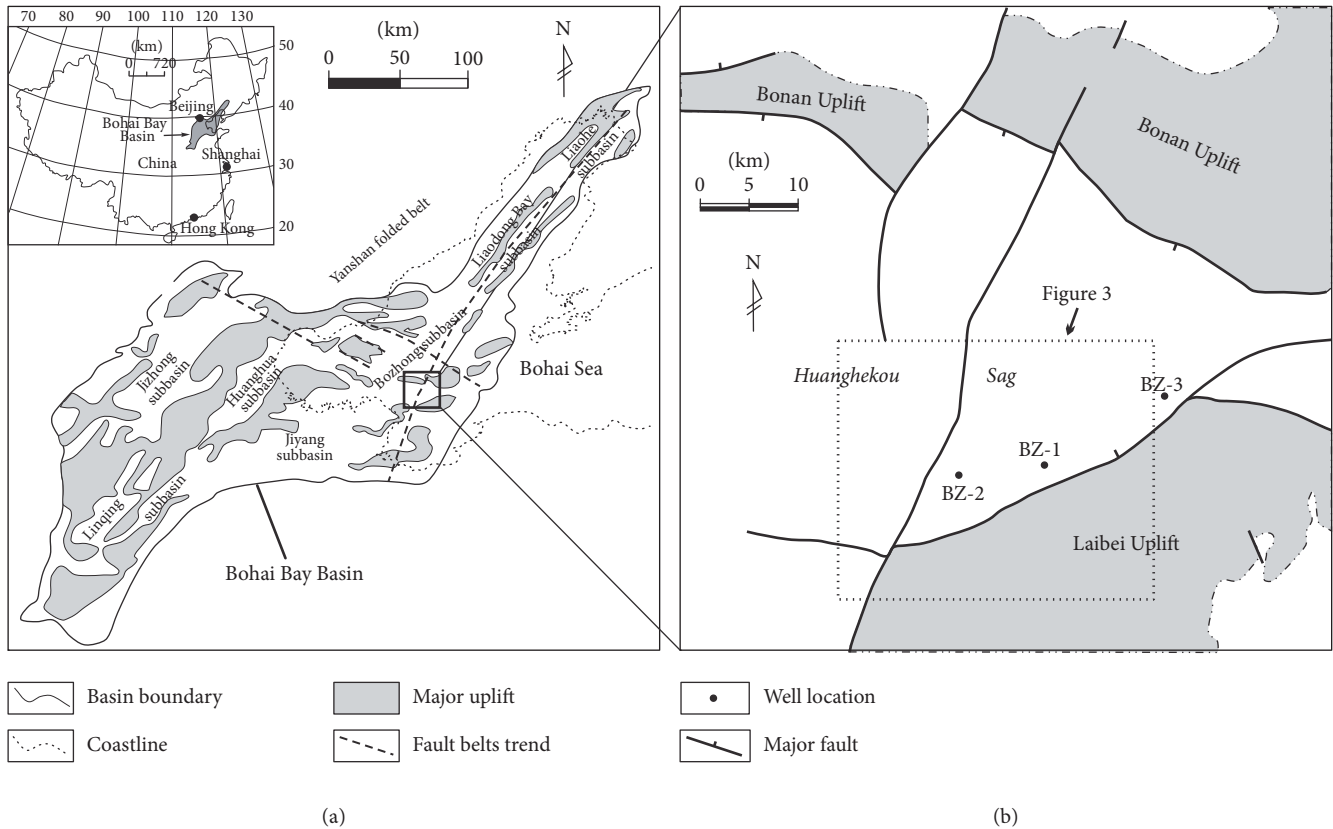


FIGURE 1: (a) Location map of subbasins of the Bohai Bay Basin, eastern China (modified from [8]). (b) Map of the Huanghekou Sag showing the distribution of major faults and wells.

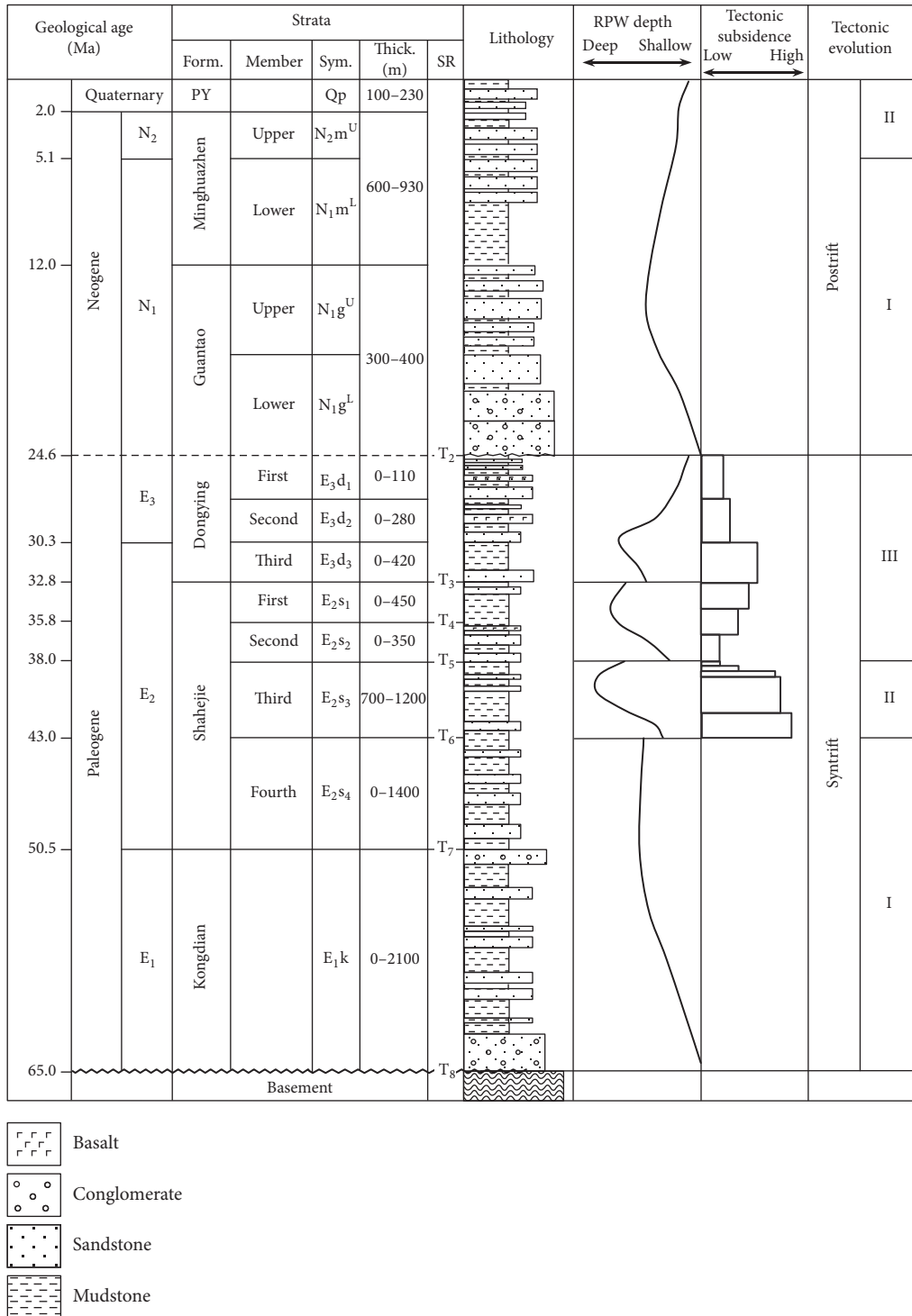
and precipitation of minerals, expulsion of organic  $\text{CO}_2$  and acids, volcanic eruption (e.g., [15, 16, 21, 22]), or mixing with other fluids (e.g., abundance of ferromagnesian caused by basalt eruption) during progressive burial. Different fluid sources and interactions in the reservoir pore have a vital impact on pore fluid property evolution, and thus, to a large extent, will influence the diagenesis and reservoir quality (denotes reservoir porosity and permeability in this paper). Therefore, pore fluid evolution and related diagenetic processes are complicated and variable [2, 23], which can induce strong reservoir heterogeneity [24, 25]. In an attempt to shed light on pore fluid evolution during progressive burial it is thus essential for predicting diagenetic processes and development of hydrocarbon reservoirs (e.g., [10, 26]).

A large number of case studies associated with pore fluid evolution and diagenesis have been made over the past decades, with most works focused on the small scale sandstone reservoirs with nonvolcanic development [9–12, 21, 22]. So far, however, there are few reports that have focused on the reservoir quality in the study area sandstone influenced by volcanic activities but had not investigated the pore fluid evolution associated with volcanic activities and their impacts on diagenetic process [27]. The study area of Huanghekou Sag had undergone multiphase of volcanic eruption during the Paleogene where the aqueous medium is strongly altered by hydrolyzation of chemically unstable ferromagnesian minerals. Various types of pore fluids developed in Paleogene

medium-deep reservoirs ( $\text{E}_2\text{s}_{1+2}$ ,  $\text{E}_3\text{d}_3$ ,  $\text{E}_3\text{d}_{1+2}$ ), which controlled the reservoir quality that is better than that of adjacent areas with no volcanic eruption, providing an excellent example to investigate the properties of pore fluid aqueous medium evolution influenced by volcanic activities. The objectives of this study are to (1) understand pore fluid evolution influenced by volcanic activities, (2) relate the diagenetic processes to pore fluid property evolution, and (3) evaluate controls of different diagenesis on reservoir quality. These objectives will be achieved by an integrated analysis of petrology, mineralogy and trace element compositions combined with a range of analytical techniques. The study provides a useful analogue for understanding the pore fluid evolution of the medium-deep reservoirs that share similar geological settings.

## 2. Geological Setting

The Bohai Bay Basin, one of the most petroliferous basins in China [4], is located on the eastern coast of China (Figure 1), covering an area of approximately  $200,000 \text{ km}^2$  ( $77,220 \text{ mi}^2$ ). The Bohai Bay Basin is a complex Cenozoic lacustrine rift basin that formed in the Late Jurassic through the early Tertiary on the north China craton. Generally, the tectonic evolution of the basin is subdivided into two major stages ([28–30]; Figure 2), namely, a synrift stage between 65 and 24.6 Ma and a postrift stage from 24.6 Ma to the present, respectively. The Bohai Bay Basin contains several



Form. = formation; PY = pingyuan; SR = seismic reference; RPW depth = relative paleowater depth; Sym. = symbol.

FIGURE 2: Generalized stratigraphic column of the Bohai Bay Basin (modified from [8]). Labels I, II, and III in the far right column mark the tectonic substages of the synrift and postrift.

subbasins (Figure 1(a)). The Huanghekou Sag is located in the southern part of the Bozhong Subbasin of the Bohai Bay Basin and has an area of approximately 3,600 km<sup>2</sup> (1,390 mi<sup>2</sup>), bordered in the north by the Bonan Uplift

and in the south by the Laibei Uplift (Figures 1(a) and 1(b)).

Sediments filled in the Huanghekou Sag, in ascending order, are composed of the the Paleogene Kongdian

TABLE 1: Percentages of detrital grains and structural characteristic from the Paleogene sandstones of well BZ-1, Huanghekou Sag.

Strata	Depth (m [ft])	Structure			Detrital grains (%)					
		Gs	Psephicity	Sorting	Q	Pl	Kf	Vd	Md	M
E <sub>3</sub> d <sub>1</sub>	2255 (7398)	Mcg	Sa-Sr	Moderate	25	15	22	28	10	0
E <sub>3</sub> d <sub>1</sub>	2258 (7408)	Fmg	Sa-Sr	Moderate	33	5	43	6	12	1
E <sub>3</sub> d <sub>1</sub>	2265 (7431)	Mg	Sa-Sr	Good	32	4	44	5	14	1
E <sub>3</sub> d <sub>1</sub>	2280 (7480)	Mg	Sa-Sr	Good	18	0	33	30	16	3
E <sub>3</sub> d <sub>1</sub>	2354 (7723)	Fg	Sa-Sr	Good	34	5	40	6	14	1
E <sub>3</sub> d <sub>1</sub>	2356 (7730)	Hg	Sa-Sr	Poor	35	5	31	9	20	0
E <sub>3</sub> d <sub>3</sub>	2826 (9271)	Mfg	Sa-Sr	Poor	33	10	30	18	9	0
E <sub>3</sub> d <sub>3</sub>	2903 (9524)	Fg	Sr	Good	30	12	27	22	8	1
E <sub>3</sub> d <sub>3</sub>	2925 (9596)	Mg	Sa-Sr	Good	28	8	24	28	11	1
E <sub>3</sub> d <sub>3</sub>	2944 (9659)	Fg	Sa-Sr	Good	35	7	28	17	9	4
E <sub>3</sub> d <sub>3</sub>	2953 (9688)	Mg	Sa-Sr	Moderate	30	5	40	17	8	0
E <sub>3</sub> d <sub>3</sub>	2957 (9701)	Mg	Sa-Sr	Moderate	30	6	36	19	9	0
E <sub>2</sub> s <sub>1</sub>	3045 (9990)	Fg	Sa-Sr	Good	33	5	36	16	8	2
E <sub>2</sub> s <sub>1</sub>	3060 (10,039)	Fmg	Sa-Sr	Moderate	32	10	27	19	12	0
E <sub>2</sub> s <sub>2</sub>	3081 (10,108)	Fmg	Sa-Sr	Moderate	31	5	34	22	8	0
E <sub>2</sub> s <sub>2</sub>	3084 (10,118)	Cmg	Sa-Sr	Moderate	32	6	32	18	12	0
E <sub>2</sub> s <sub>2</sub>	3090 (10,138)	Fmg	Sa-Sr	Moderate	30	5	36	20	8	1

BZ-1 = Bozhong-1; Cmg = coarse-medium grained; E<sub>3</sub>d<sub>1</sub> = first member of the Paleogene Dongying Formation; E<sub>3</sub>d<sub>3</sub> = third member of the Paleogene Dongying Formation; E<sub>2</sub>s<sub>1</sub> = first member of the Paleogene Shahejie Formation; E<sub>2</sub>s<sub>2</sub> = second member of the Paleogene Shahejie Formation; Fg = fine grained; Fmg = fine-medium grained; Gs = grain size; Hg = heterogranular; Kf = K-feldspar; M = mica; Mcg = medium-coarse grained; Md = metamorphic detritus; Mfg = medium-fine grained; Mg = medium grained; Pl = plagioclase; P = psephicity; Q = quartz; Sa-Sr = subangular-subrounded; Sr = subrounded; Vd = volcanic detritus.

(Ek), Shahejie (Es) and Dongying (Ed) formations, Neogene Guantao (Ng) and Minghuazhen (Nm) formations, and the Quaternary Pingyuan (Qp) Formation (Figure 2). The Paleogene Shahejie (Es) interval in the Huanghekou Sag is subdivided into four units (E<sub>2</sub>s<sub>4</sub>, E<sub>2</sub>s<sub>3</sub>, E<sub>2</sub>s<sub>2</sub>, and E<sub>2</sub>s<sub>1</sub> [the first member of the Paleogene Shahejie Formation]), whereas the Dongying (Ed) Formations are composed of three units (E<sub>3</sub>d<sub>3</sub>, E<sub>3</sub>d<sub>2</sub>, and E<sub>3</sub>d<sub>1</sub> [the first member of the Paleogene Dongying Formation]). Note that E<sub>2</sub>s<sub>2</sub> and E<sub>2</sub>s<sub>1</sub> intervals are referred to as E<sub>2</sub>s<sub>1+2</sub> for short in this paper and E<sub>3</sub>d<sub>2</sub> and E<sub>3</sub>d<sub>1</sub> intervals are referred to as E<sub>3</sub>d<sub>1+2</sub> because of similar deposition settings. The Paleogene Shahejie (Es) and Dongying (Ed) Formations, apart from the E<sub>2</sub>s<sub>4</sub> and E<sub>2</sub>s<sub>3</sub> interval, are the subject of this study. During the deposition of E<sub>2</sub>s<sub>1+2</sub> intervals, braided river deltas developed overall the study area with volcanics distributed sporadically at the bottom and top of the E<sub>2</sub>s<sub>2</sub> interval and drilled thickness approximately 26 m accounting for 13.16 percent of the total formation thickness of the E<sub>2</sub>s<sub>2</sub> interval. However, there is no significant volcanics drilled for E<sub>3</sub>d<sub>3</sub> that experienced rapid subsidence and lacustrine mudstones are developed in the central of the Huanghekou Sag interfingered with more proximal sandstones of braided river delta. With the continuous volcanic eruption of the lower unit of the second member of the Paleogene Dongying Formation (E<sub>3</sub>d<sub>2</sub><sup>1</sup>), high paleogeomorphology developed around the well BZ-1 of the research area, which impeded the supply of clastic materials and development of braided river delta. Volcanic eruption in the E<sub>3</sub>d<sub>1+2</sub> intervals is characterized by more active, multiperiod eruption and widespread distribution [8].

According to the drilling results of well BZ-1, volcanics are drilled up to 91.7 m with percentage of 21.3 of the total formation thickness of the E<sub>3</sub>d<sub>1+2</sub> interval. Examination of thin section in volcanics drilled in the study area indicates that lithology of igneous is mainly basalt.

Most samples in the Paleogene E<sub>2</sub>s<sub>1+2</sub>, E<sub>3</sub>d<sub>3</sub>, and E<sub>3</sub>d<sub>1+2</sub> intervals are mainly lithic arkoses. Sandstones of E<sub>2</sub>s<sub>1+2</sub> intervals are fine to medium-grained and moderately sorted sandstones of subangular to subrounded psephicity. Based on point-count data (Table 1), detrital quartz (30%–33%) and feldspar (37%–41%) are the predominant framework grain and detrital feldspar includes K-feldspar and plagioclase. Detrital K-feldspar is more abundant than plagioclase. Rock fragments (24%–31%) are less significant and include metamorphic and igneous grains, with acidic igneous rock most. Comparing to E<sub>2</sub>s<sub>1+2</sub> intervals, samples in E<sub>3</sub>d<sub>3</sub> and E<sub>3</sub>d<sub>1+2</sub> have similar framework compositions and rock fragments constituents, but the percentages of each component are substantially different. The content of detrital feldspar in E<sub>3</sub>d<sub>3</sub> ranges between 32% and 45%, detrital quartz varies from 25% to 35%, and rock fragments range from 25% to 39%. However, for E<sub>3</sub>d<sub>1+2</sub>, the contents of detrital feldspar, detrital quartz, and rock fragments are 33%–48%, 18%–35%, and 18%–46%, respectively.

### 3. Samples and Methods

The study was focused on the Paleogene medium-deep reservoirs (E<sub>2</sub>s<sub>1+2</sub>, E<sub>3</sub>d<sub>3</sub>, and E<sub>3</sub>d<sub>1+2</sub>) of Huanghekou sag where most of the producing oil fields occur and volcanic

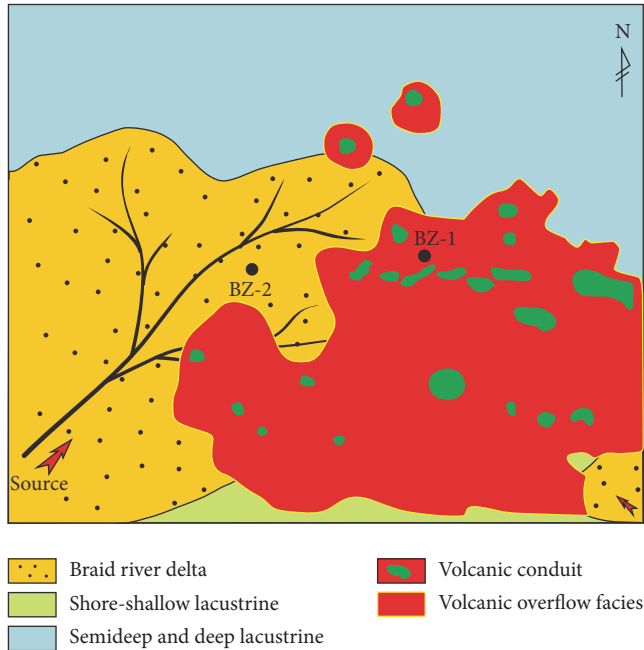


FIGURE 3: Sedimentary facies and volcanics distribution of the first and second members of Dongying Formation ( $E_3d_{1+2}$ ) based on the interpretation of well and seismic data. The mapping area is shown in Figure 1(b).

activities developed pervasively. Three main oil-producing wells drilled in the study area marked in black dotted line (Figure 1(b)). Previous studies demonstrated the fact that volcanic activities in the first and second members of Dongying Formation ( $E_3d_{1+2}$ ) are characterized by more active, multiphase eruption and widespread distribution [8]. Well- and seismic-based sedimentary facies and volcanics distribution of  $E_3d_{1+2}$  indicate that the well BZ-1 located in volcanic overflow facies, surrounded by volcanic conduits displaying beads-shaped distribution (Figure 3). However, both well BZ-2 and well BZ-3 have no significant volcanic overflow facies developed. In other words, well BZ-1 may have experienced stronger influence of volcanic activities than that of the other two wells. Data from well BZ-1 are therefore of optimum choice for investigating the pore fluid evolution influenced by volcanic activities. Core and cuttings samples were collected from well BZ-1 borehole in the Paleogene at depths ranging from 2000 to 3500 m (6562–11,483 ft).

To quantify different diagenetic products, more than 60 polished thin sections and about 40 blue epoxy resin impregnated thin sections were prepared for rock mineralogy, diagenesis, and visual pore characteristics. Point counting was carried out on thin sections with at least 300 points to examine the correctness of the selected rock composition data. To determine the compositions of authigenic minerals and understand their spatial relationships, an amount of 15 representative samples was prepared using a Quanta 200 environmental scanning electron microscope (ESEM). Ten representative samples were viewed under a FEI Quanta 450 FEG field emission scanning electron microscope (BSE) equipped with backscatter detector (BSE) under an

acceleration voltage of 20 kV and sample dip of  $70^\circ$ . In addition, different mineral phases were determined based on highly magnified backscatter electron image methods.

Reconstruction of paleosalinity based on boron in clays is an effective approach documented by using sediments at various time scale [31–34]. Boron-derived paleosalinity reconstructions are based on the direct positively linear relationship between boron in ancient clays and the paleosalinity of the depositional environment [34, 35]. Hence, to restore the paleosalinity, trace element analysis was carried out using ELE-MENTXR plasma mass spectrum analyzer with ELANDRC-e, measured following the rules of Methods for Chemical Analysis of Silicate Rocks-Part 30: Determination of 44 Elements (National Standard GB/T 14506.30-2010). Measured temperature and relative moisture for trace element are  $20^\circ\text{C}$  and 30%, respectively.

Samples were collected for mineralogical analyses using X-ray diffraction (XRD). The XRD patterns of sandstone were obtained using X'pert Pro MPD X-ray diffractometer made in Netherlands with measured temperature of  $20^\circ\text{C}$  and moisture of 65% whereas the XRD patterns of mudstone were finished using D/max-2500 X-ray diffractometer with measured temperature of  $20^\circ\text{C}$  and moisture of 50%. Preparation, analysis, and interpretation procedures are modified from Moore and Reynolds [36] and Hillier [37]. Cathode luminescence (CL) analyses for 10 typical samples were performed using an Olympus microscope equipped with a CL8200-MK5 CL instrument.

Among all the analyses above, point counting, XRD of sandstones, SEM, and CL were done in Key Laboratory of China University of Geosciences, whereas XRD of mudstones and trace element analysis were carried out in Institute of Bohai Oilfield.

## 4. Results

A series of diagenetic processes are identified in the Paleogene medium-deep reservoirs, Huanghekou Sag, including precipitation of carbonate, zeolite minerals and dissolution of feldspar, quartz, and zeolite minerals. Precipitation and dissolution of these minerals played a significant role in reservoir quality of the Paleogene medium-deep reservoirs. In addition, these diagenetic products developed in specified aqueous medium environment that can be effectively used to trace pore fluid properties, combined with analysis of trace elements and X-ray diffraction. Minor diagenetic phases (e.g., ferroan dolomite) are not depicted in this study because of leanly abundant through the Paleogene medium-deep intervals.

**4.1. Precipitation and Dissolution of Zeolite.** Discrete plot of mineral compositions based on XRD analysis of sandstone reservoirs indicates that zeolites occur mainly in the  $E_3d_{1+2}$  interval with high content, which may be controlled by aqueous medium environment enriched ferromagnesian minerals (Figure 4). Similarly, precipitation and dissolution of zeolites are observed commonly in the  $E_3d_{1+2}$  interval. In thin sections, zeolites occur as intergranular cements with prismatic perpendicular to basalt rock fragments filling

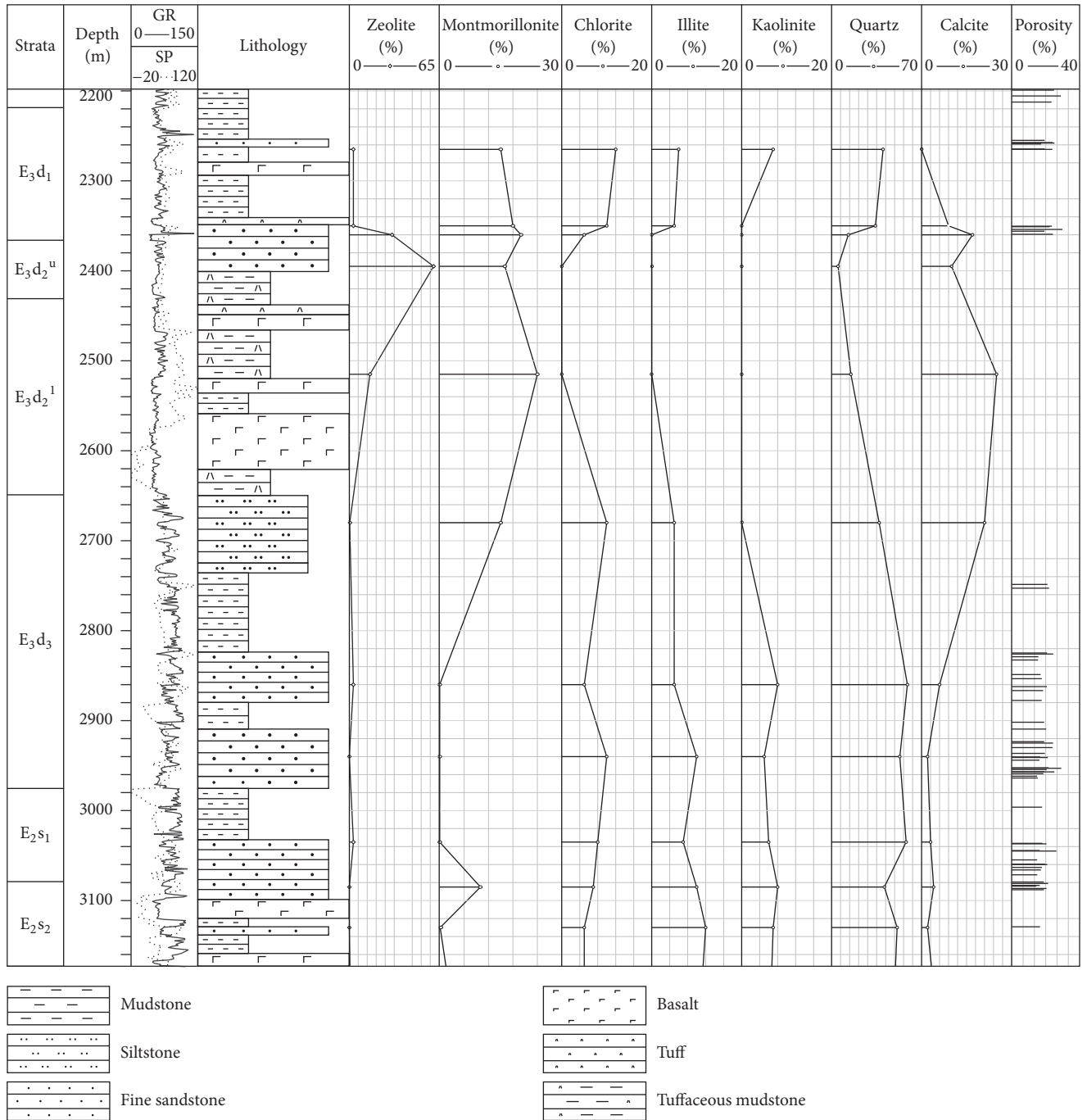


FIGURE 4: Mineralogical composition vertical distribution of reservoir sandstones in BZ-1 well based on X-ray diffraction (XRD) analysis.

intergranular pores (Figure 5(a)). In addition, some interesting phenomena are observed that zeolites replace volcanic fragments, feldspars, and quartz that line intergranular pores. Pore types of the E<sub>3</sub>d<sub>1+2</sub> interval occur mainly as zeolite dissolution pore, amygdala dissolution pore based on thin section observation.

**4.2. Dissolution of Quartz and Feldspar.** Partial to extensive dissolution of detrital quartz grains was observed in the E<sub>2</sub>s<sub>1+2</sub> interval (Figures 6(a), 6(b), and 6(c)). Based on

microscope observations, two types of quartz dissolution can be identified: (1) quartz grains dissolution occurred along the boundaries and interior of grains, with embayed boundary and vugular shape, respectively; (2) quartz grains dissolution occurred along the internal fracture of grains. Dissolution of detrital feldspar grains is pervasively developed in the Paleogene reservoirs of study area. The predominant dissolved feldspars are K-feldspar grains (Figure 7(a)). Locally, dissolved plagioclase can be observed but is not common.

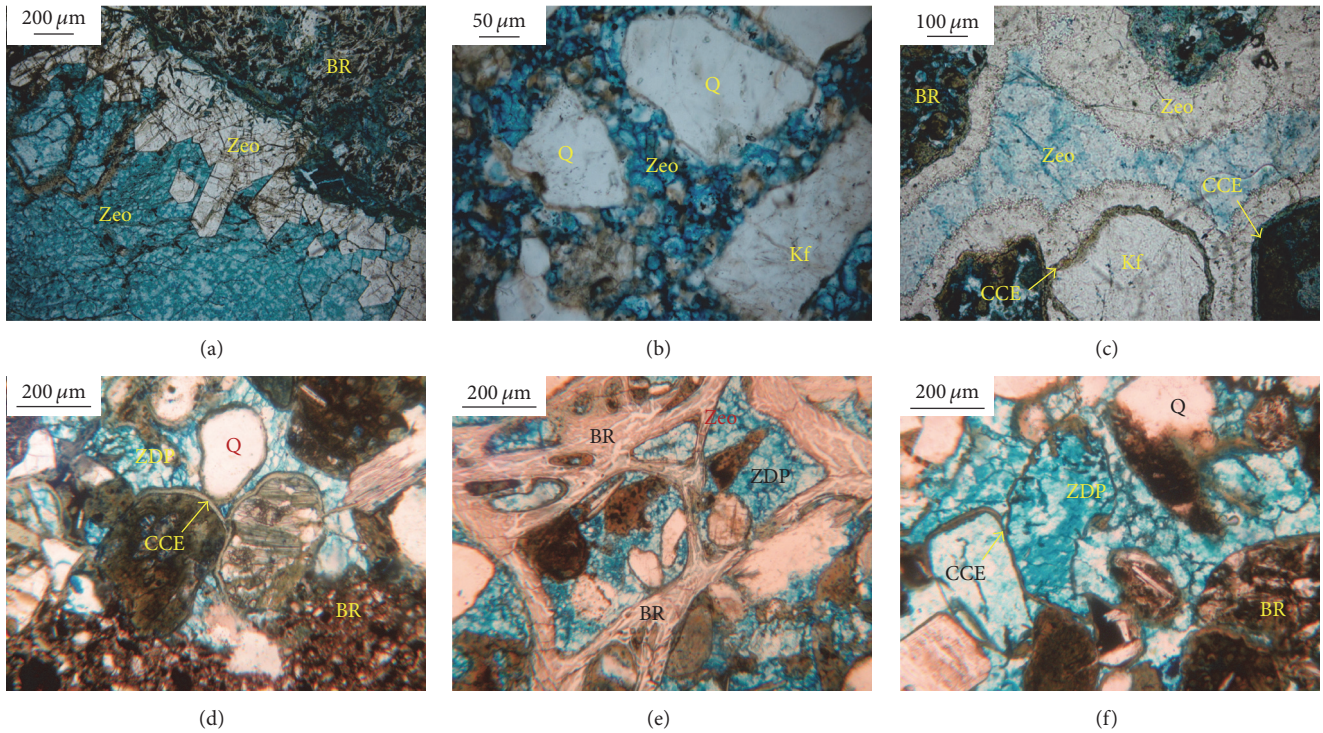


FIGURE 5: Photomicrographs of zeolite diagenesis and dissolved zeolite related to basalt eruption of the Paleogene sandstone reservoirs in well BZ-1. (a) Zeolite precipitated perpendicular to basalt rock fragments, E<sub>3</sub>d<sub>1</sub>, 2259 m (7411 ft). (b) Zeolite filled in intergranular pores, E<sub>3</sub>d<sub>1</sub>, 2265 m (7431 ft). (c) Zeolite developed pervasively and chlorite clay envelope occurred, E<sub>3</sub>d, 2351 m (7713 ft). (d) Micrograph of thin section showing the zeolite partly and completely dissolved and chlorite clay envelope occurred, E<sub>3</sub>d<sub>1</sub>, 2280 m (7480 ft). (e) Micrograph of thin section showing dissolved amygdaloid pores of zeolite, E<sub>3</sub>d<sub>1</sub>, 2280 m (7480 ft). (f) Micrograph of thin section showing the zeolite partly and completely dissolved, E<sub>3</sub>d<sub>1</sub>, 2280 m (7480 ft). BR = basalt rock fragments, CCE = chlorite clay envelope, Kf = K-feldspar, Q = quartz, Zeo = zeolite, and ZDP = zeolite dissolved pore.

**4.3. K-Feldspar Albitization.** On the basis of environmental scanning electron microscope (ESEM) and backscattered electron (BSE) image analysis, albitization occurred mainly in the E<sub>2</sub>s<sub>1+2</sub> interval. Albitization of K-feldspar is predominant the interest area, whereas albitization of plagioclase only can be observed locally (Figures 6(d), 6(e), and 6(f)). In addition, euhedral albite crystals are developed as pore-filling cements and as replacement of dissolved K-feldspar and plagioclase (Figure 6(e)). Albitization of K-feldspar is displayed commonly along cleavage planes of detrital feldspar grains (Figure 6(f)).

**4.4. Carbonate Cements.** Carbonate cements are the volumetrically predominant authigenic minerals in the E<sub>2</sub>s<sub>1+2</sub> interval and mainly include calcite, dolomite, and ferroan dolomite. The CL micrograph of calcite cements displays a homogeneous orange luminescence color (Figure 7(c)). In thin sections, dolomite cements cause mainly ctenoid dolomite encrustation around the surface of detrital grains or partly epidermis oolite formed by engulfing quartz grains (Figures 7(d) and 7(f)). Ferroan dolomite is the most pore-filling cements remaining in intergranular pores which resulted in the pore connectivity becoming worse. Ctenoid dolomite encrustation adheres to the surface of detrital grains but inhabited the overgrowth of

quartz grains which effectively preserved intergranular pore.

**4.5. X-Ray Diffraction of Clay Mineral.** Various types of clay minerals with different abundances occur in the Paleogene interbedded mudstones of sandstone reservoirs, as revealed by XRD, composed of illite, mixed-layer illite/smectite (I/S), kaolinite, chlorite, and mixed-layer chlorite/smectite (C/S). XRD analysis data of interbedded mudstones indicates that illite and mixed-layer illite/smectite are the dominating clay minerals in the whole Paleogene intervals except the E<sub>3</sub>d<sub>1+2</sub> interval which may be associated with the eruption of basalt and the content of illite shows positive correlation with increasing burial depth, particularly, deeper than about 2700 m where it increases sharply (Figure 8). Mixed-layer chlorite/smectite mainly exists at depths shallower than 2800 m corresponding to the E<sub>3</sub>d<sub>1+2</sub> interval and the upper part of E<sub>3</sub>d<sub>3</sub> interval and shows decreasing trends with increased burial depth (Figure 8). The content of kaolinite is characterized by significant increase in the lower part of E<sub>3</sub>d<sub>3</sub> interval between 2900 m and 3000 m with percentage ranging from 10 to 30 m. On the contrary, the percentage of mixed-layer illite/smectite decreases quickly deeper than 2800 m to 3000 m. Therefore, the contents of the two-clay minerals variation with depth show that obviously

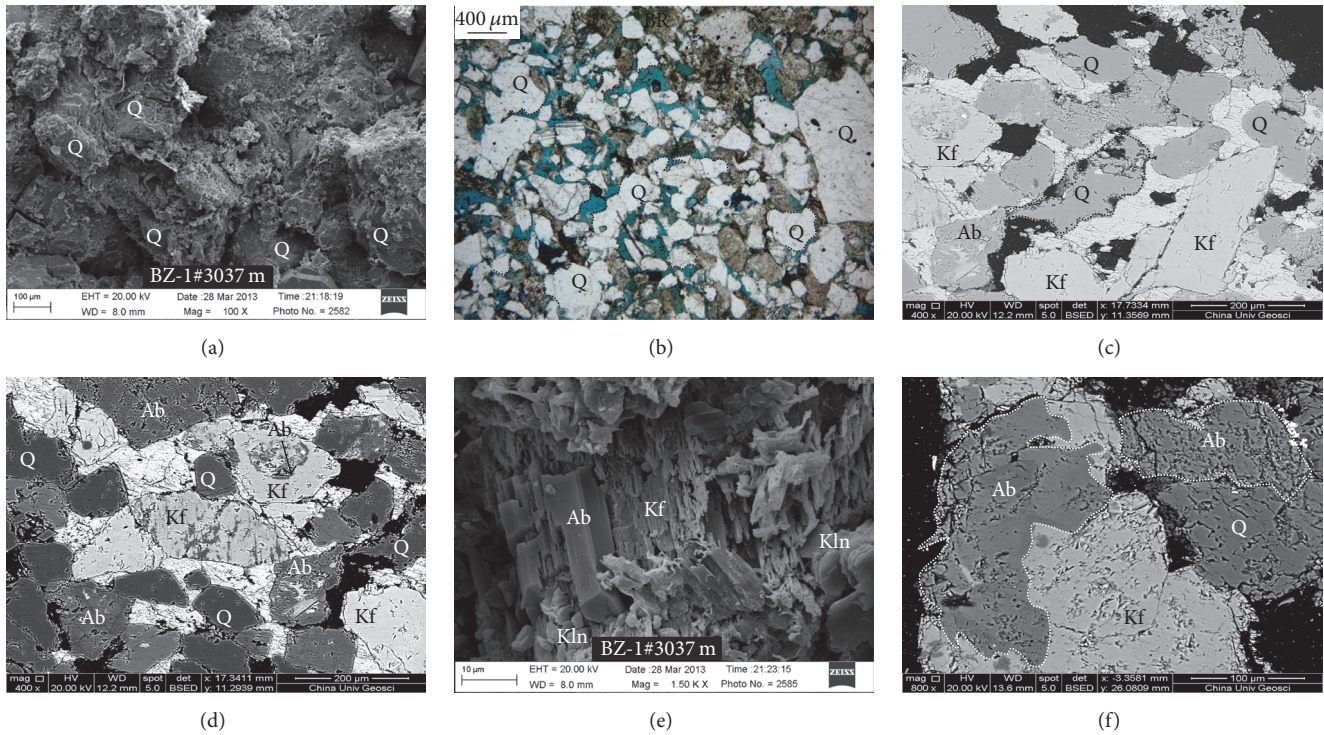


FIGURE 6: Photomicrographs of quartz grains dissolution and K-feldspar albitization in the Paleogene sandstone reservoirs in the well BZ-1 of Huanghekou Sag. (a) Environmental scanning electron microscope (ESEM) image of dissolved quartz (Q),  $E_2s_1$ , 3037 m (9964 ft). (b) Dissolution of quartz showing embayed shape (marked with black dot line),  $E_2s_1$ , 3037 m (9964 ft). (c) Backscattered electron (BSE) image of quartz dissolution along grain boundary and fracture,  $E_3d_3$ , 2944 m (9659 ft). (d) Albitization (Ab) of K-feldspar along cleavage plane,  $E_3d_3$ , 2944 m, BSE image (9659 ft). (e) SEM photograph of albite crystals in partly dissolved K-feldspar grain,  $E_2s_1$ , 3037 m (9964 ft). (f) K-feldspar was replaced by albite,  $E_2s_1$ , 3037 m (9964 ft). Ab = albitization, Kf = K-feldspar, Kln = kaolinite, and Q = quartz.

mirror trends occurred in the lower part of  $E_3d_3$  interval (Figure 8).

**4.6. Trace Element Distribution of Paleogene Mudstone.** Trace element distribution of well BZ-1 between  $E_2s_{1+2}$ ,  $E_3d_3$ , and  $E_3d_{1+2}$  is characterized by three types of stepped reduction where boron concentrations decrease significantly. Based on analysis of trace elements, boron concentrations of  $E_2s_{1+2}$  interval and  $E_3d_{1+2}$  interval are the most and the least, respectively, and  $E_3d_3$  interval is intermediate. Within the  $E_2s_{1+2}$  interval, concentration of boron increases slightly with increased burial depth ranging from 32.6 to 46.6  $\mu\text{g/g}$  with an average value of 38.16  $\mu\text{g/g}$  (Figure 9). During the  $E_3d_3$  interval, however, the content of boron reduces to level ranging from 15.4 to 33.9  $\mu\text{g/g}$  with an average of 26.8  $\mu\text{g/g}$  (Figure 9). For  $E_3d_{1+2}$  interval, boron concentrations decrease to a lower interval ranging from 5.51 to 26.5  $\mu\text{g/g}$  with an average value of 10.7  $\mu\text{g/g}$  (Figure 9). Similar trend is shown in the ratios of B/Ga element, as revealed in Figure 9, but different in numeric value.

## 5. Discussion

**5.1. Evolution of Pore Fluids.** The various diagenetic processes in the Paleogene medium-deep reservoirs in the Huanghekou Sag record the pore varying fluid properties. The typically

diagenetic events, clay mineral compositions, and trace elements distribution characteristics discussed above demonstrate large difference in the pore fluid properties with different intervals during the burial process of the sandstone reservoirs accompanied by basalt eruption. Therefore, in an attempt to investigate these differences using XRD data and trace elements are necessary.

Different diagenetic events developed in various deposition environment with diverse pore fluid properties that effectively help us understand the pore fluid evolution [12]. Based on thin section observation, as discussed above, typically diagenetic events developed in Paleogene sandstone reservoirs include precipitation and dissolution of zeolite, dissolution of quartz and feldspar, and K-feldspar albitization.

**5.1.1. Ferromagnesian Aqueous Medium Environment.** Zeolite is alkaline metal aluminum silicate mineral of framework structure essentially formed through the water-rock interactions of volcanic glass whether exogenous or endogenous origin [38]. Previous studies demonstrated that zeolite may develop with various sedimentary environments but commonly formed during the medium-alkaline water environment with pH value ranging from 7 to 10 and generally related to alteration of volcanic tuff and volcanic glass [39–41]. Furthermore, zeolite concentrated on saline alkaline environment which provides the source of  $\text{SiO}_2$  and  $\text{Al}_2\text{O}_3$  for

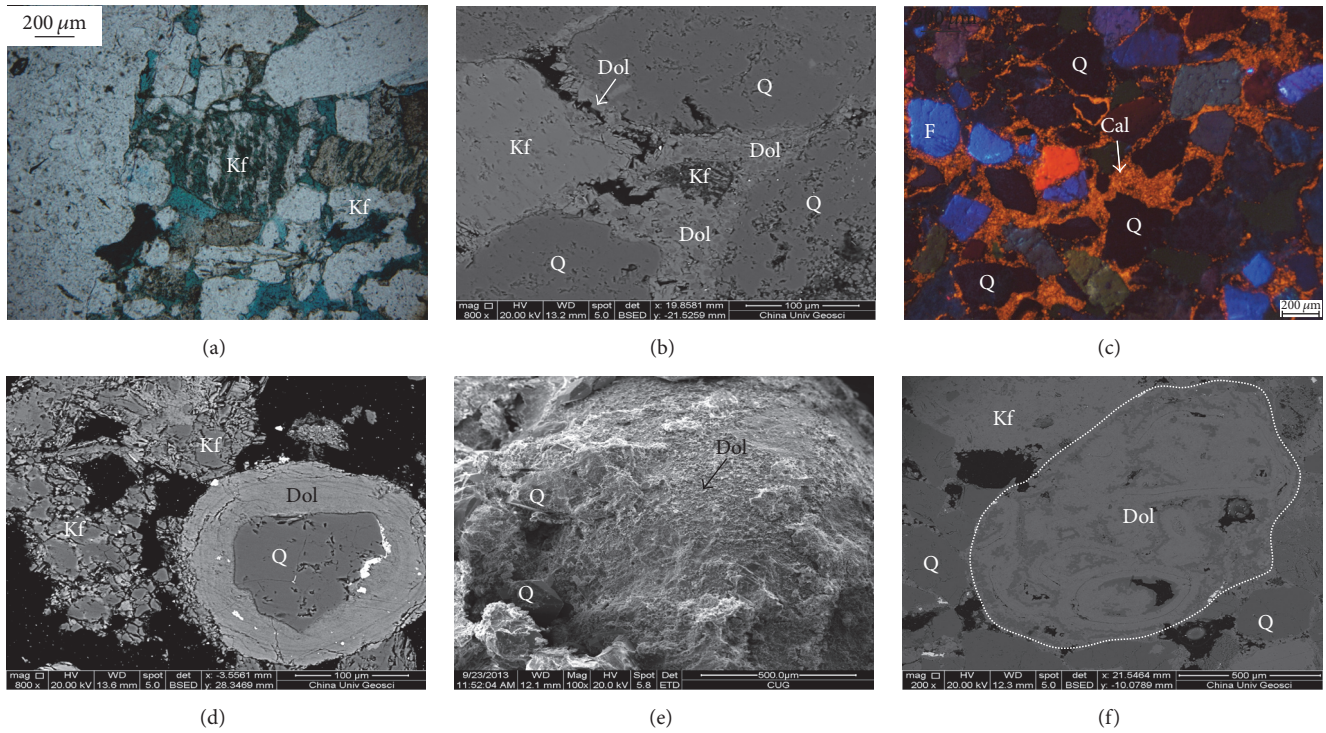
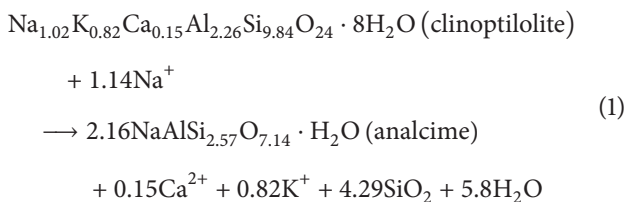


FIGURE 7: Photomicrographs of feldspar dissolution and dolomite encrustation in the Paleogene sandstone reservoirs in the well BZ-1 of Huanghekou Sag. (a) K-feldspar (Kf) dissolution,  $E_{2s_1}$ , 3037 m (9964 ft). (b) Backscattered electron (BSE) image of dolomite encrustation,  $E_{2s_2}$ , 3084 m (10,118 ft). (c) Micrograph of CL showing the calcite cements (orange luminescent),  $E_{2s_2}$ , 3084 m (10,118 ft). (d) Micrograph of BSE showing dolomite encrustation around the detrital quartz,  $E_{2s_1}$ , 3037 m (9964 ft). (e) Idem with D but ESEM micrograph,  $E_{2s_1}$ , 3037 m (9964 ft). (f) Micrograph of BSE showing dolomite debris (within the white dotted line) and pectinate dolomite encrustation (outside the white dotted line),  $E_{2s_2}$ , 3084 m (10,118 ft). Cal = calcite, Dol = dolomite, F = feldspar, Kf = K-feldspar, Kln = kaolinite, and Q = quartz.

the precipitation of zeolite. When formation water medium flows through the basalt strata, the released  $K^+$ ,  $Na^+$ ,  $Ca^{2+}$ ,  $Al^{3+}$ ,  $Fe^{3+}$ , and  $Mg^{2+}$  of basalt resulted in the formation of alkaline water environment with increased pH and enrichment of ferromagnesian minerals which favors generation of zeolite. Thus, interaction of alkaline aqueous medium and volcanic glass leads to generation of zeolite minerals [40, 42–44]. Previous study based on electron microprobe analysis demonstrated that zeolites in well BZ-1 of the study area are mainly analcimes [27]. Analcimes might not be directly formed by the alteration of volcanic glass but transformed by other zeolites (commonly clinoptilolites). Early formed zeolites (clinoptilolite) may react at shallow depths to form analcime, albite, and K-feldspar as a function of either age or salinity. The transformation of clinoptilolite to analcime can be idealized as the following reaction [45], but the actual chemical change is commonly more complex than this.



Given that, it is well explained that high contents of zeolite based on thin section observations and XRD data occurred

mainly in the layer ( $E_3d_{1+2}$ ) containing basalt (Figures 4 and 5). With the influence of basalt eruption, ferromagnesian minerals of basalt in sandstone reservoirs of  $E_3d_{1+2}$  dissolved led to development of ferromagnesian aqueous medium environments that benefits the formation of zeolite. However,  $E_3d_3$  with no significant influence of basalt eruption is corresponding to less abundance of zeolite. This phenomenon is consistent with clay minerals dominated by mixed layers C/S in  $E_3d_{1+2}$  (Figure 8), which can be interpreted as strong hydration and hydrolysis of tuff and eruptive rock detritus precipitated voluminous authigenic smectite at an early diagenesis stage [46–48]. Smectite can easily transform to mixed-layer I/S or discrete illite with increasing temperature where a potassium source exist ([49–52]; Cama et al. 2000). Meanwhile, the conversion of smectite to mixed-layer C/S occurred where aqueous medium environments were enriched in magnesium. Large amounts of  $Fe^{2+}$  and  $Mg^{2+}$  released due to intense hydrolyzation of unstable volcanic rock fragments that resulted in pore fluids rich in ferromagnesian provided the condition for the formation of chlorite. Therefore, that is why the content of mixed-layer C/S of  $E_3d_{1+2}$  increases abruptly as shown by XRD analysis (Figure 8).

**5.1.2. Alkaline Aqueous Medium Environment.** For a long time, quartz is considered to be chemically stable mineral

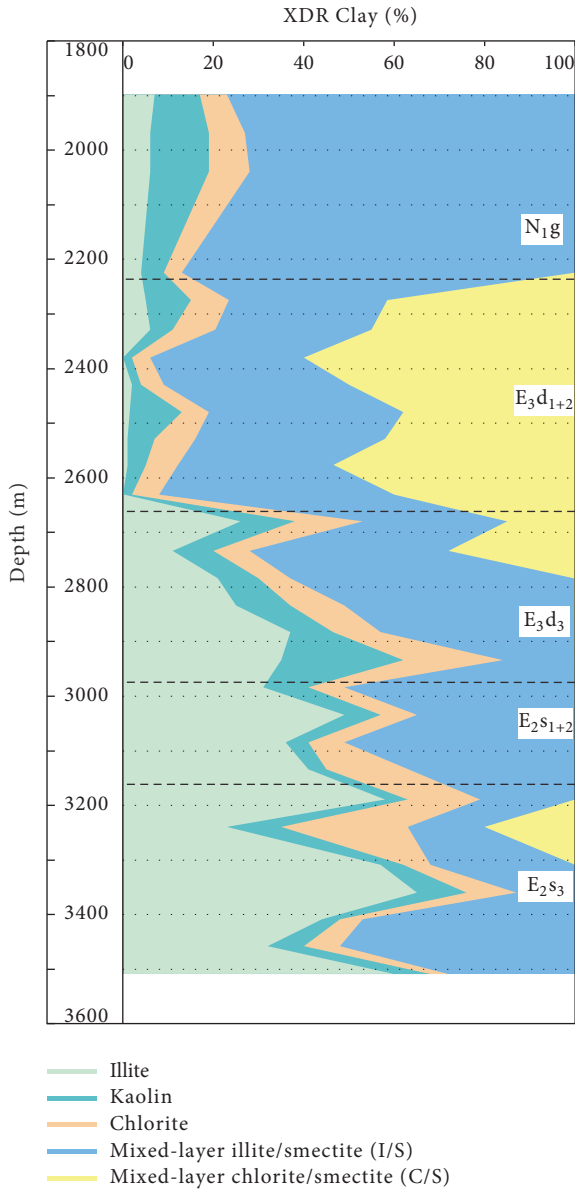


FIGURE 8: Mineralogical composition vertical distribution of interbedded mudstones based on XRD analysis.

that barely participates chemical diagenetic reactions except quartz overgrowth. As the research goes, however, more and more scholars realized that the dissolution of quartz grains and quartz overgrowth occurred during diagenesis stage [53–59]. Experimental simulation also confirmed the dissolution of quartz occurred and, based on determinations of simulation experiment, experimental formula was obtained that quartz dissolution rates are a function of pH, temperature, and alkaline ions concentration [55]. Although multiple factors can affect quartz dissolution, the predominant factor controlled quartz dissolution is pore fluid geochemical property [55, 59, 60]. Because of the stability of quartz, it is difficult to dissolve and commonly will become unstable in alkaline environments where dissolution and alternation is developed. Therefore, the dissolution of quartz, generally, indicates the

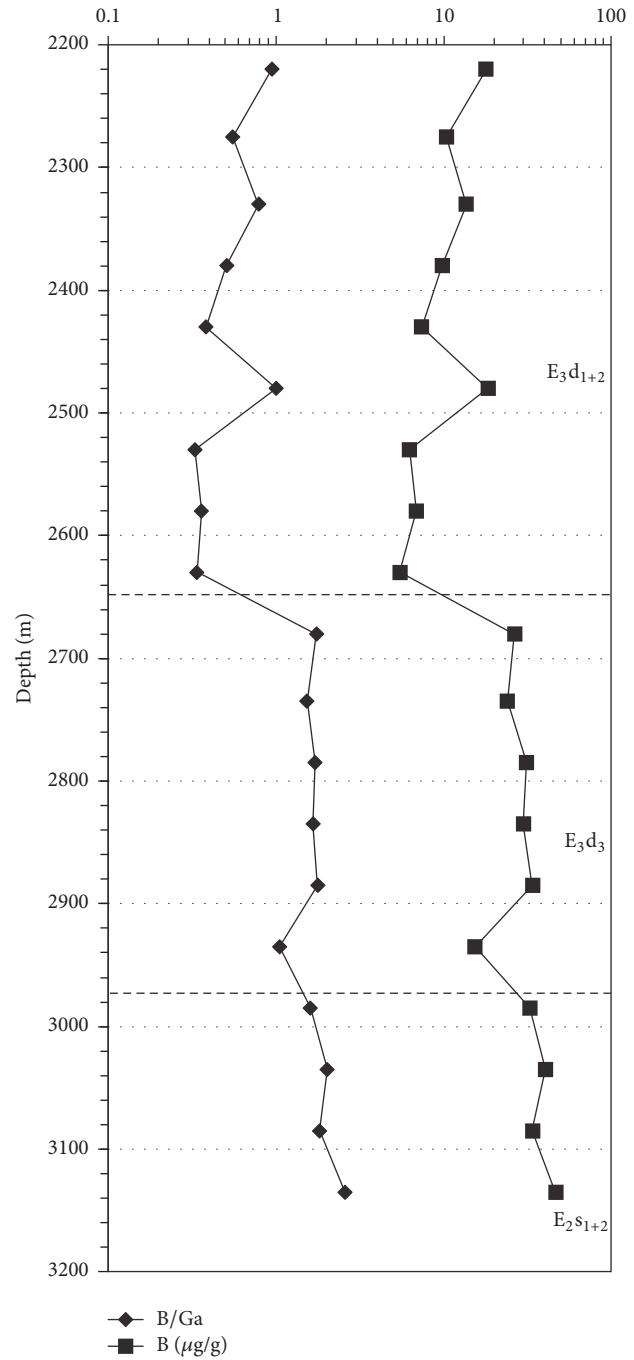


FIGURE 9: Plots showing the variations in the concentrations of B element and the ratio of B/Ga with depth in mudstone of well BZ-1. B = boron; Ga = gallium.

alkaline aqueous medium environments as exemplified by many case studies [58–60]. The quartz dissolution in the study area is mainly observed in  $E_2s_{1+2}$  (Figure 6). During  $E_2s_{1+2}$ , lacustrine basin experienced the arid climate of alkaline aqueous medium coupled with part hydrolysis of ferromagnesian-rich minerals, resulting in enrichment of sodium and potassium. With the enrichment of the alkaline ions, pH value of pore fluids became high. It thus can be

concluded that the deposition aqueous medium environment may be alkaline during the period of diagenesis. In addition, local dissolution of detrital quartz grains can be observed in the  $E_3d_3$  interval but is less common (Figure 6), which indicates that the aqueous medium environment was inferred to be affected by that of the  $E_2s_{1+2}$  interval.

Similarly conclusion can be drawn by the study on the analysis of trace element. Trace element is substantially sensible parameter indicating the salinity change which can be used to trace the pore fluid aqueous medium condition and therefore to deduce the deposition environment [61–64]. The content of boron is positively correlated with the salinity, that is, the higher content of boron the higher salinity [32, 65]. As is shown by the distribution of trace element of well BZ-1, the content of boron displays three stages increased with progressively increasing burial depth between  $E_3d_{1+2}$ ,  $E_3d_3$ , and  $E_2s_{1+2}$  (Figure 9). This trend indicates that the paleosalinity of  $E_2s_{1+2}$  is the highest,  $E_3d_3$  is second, and  $E_3d_{1+2}$  is the least. It is worth noting that the layer containing the lowest paleosalinity in  $E_3d_{1+2}$  is well correlated with the layer containing widespread distribution of basalt in  $E_3d_{1+2}$ . Therefore, it is not difficult to deduce that, during the deposition of  $E_2s_{1+2}$ , lake basin is narrow and shallow with high salinity of alkaline aqueous medium environment. During the sedimentation of  $E_3d_3$ , the basin experienced rapid subsidence and resulted in increasing in water depth and development of braided river delta. As a consequence, strong inputs of terrestrial deltaic fresh water significantly accelerated the pore fluids dilution causing decrease in salinity. However, braided river delta is not developed in  $E_3d_{1+2}$  which experienced weak inputs of terrestrial fresh water. Hence, the lowest paleosalinity in  $E_3d_{1+2}$  might not be the cause of input of terrestrial fresh water but interaction of pore fluids and basalt. Volcanic activities might have influenced the pore fluid salinity and further research is needed to understand the mechanism how volcanic activities influence the pore fluid salinity. Another parameter can be used to reveal that the paleosalinity is the ratios of B/Ga that display the corresponding trend with the content of boron. All of this reveals that the pore fluid aqueous medium environment of  $E_2s_{1+2}$  is alkalinity with high salinity. Besides that, the valuable information for the pore fluid aqueous medium environment of sandstone reservoirs can be provided by clay minerals composition. During the period of sedimentary process of  $E_2s_{1+2}$ , lake water was saline associated with arid climatic environments that favored enrichment of potassium and, with the increasing burial of depth as well as the increase of temperature and press, kaolinite transforms to illite based on XRD data.

The albitization of detrital K-feldspar and plagioclase is one of the most important diagenetic changes occurring in sandstone reservoir [66–68]. Many previous studies documented that the albitization of detrital K-feldspar commonly occurred in the alkaline aqueous medium environment [60, 69]. The presence of detrital K-feldspar albitization is observed mainly in  $E_2s_{1+2}$  and also can be found in  $E_3d_3$ , but less common, indicating the alkaline aqueous medium environment during the sedimentary process of  $E_2s_{1+2}$  as well as the weak alkaline condition of  $E_3d_3$ .

In summary, based on the analysis of petrologic characteristics and pore fluid properties, evolution of pore fluids was investigated and three of distinguished stages are identified. (1) During  $E_2s_{1+2}$ , lacustrine basin experienced the arid climate of alkaline aqueous medium coupled with part hydrolysis of ferromagnesian-rich minerals, resulting in enrichment of sodium and potassium with the highest content of boron and predominant clay minerals are potassium-rich illite and mixed-layer I/S (Figures 8, 9, and 10). (2) During  $E_3d_3$ , influx of fluvial fresh water together with hydrolysis of ferromagnesian mineral developed mixing aqueous medium environment diagenetic model (Figure 10). Mixing aqueous medium pore fluids in  $E_3d_3$  are characterized by interaction of pore fluids in both  $E_2s_{1+2}$  and  $E_3d_{1+2}$  and diagenetic processes exhibit integrated characteristic of both  $E_2s_{1+2}$  and  $E_3d_{1+2}$ . The composition of the primary clay minerals is illite and mixed-layer I/S which may be caused by interaction of potassium-rich brine. (3) During  $E_3d_{1+2}$ , strong hydrolysis of unstable ferromagnesian mineral and weak influx of fluvial fresh water resulted in the pore fluids enriched in ferromagnesian minerals and ferromagnesian aqueous medium environment diagenetic model developed due to volcanic activities (Figure 10).

## 5.2. Factors Controlling the Reservoir Quality

**5.2.1. Early Precipitation of Zeolite Associated with Basaltic Eruption.** The pore fluids flow through the basalt strata dissolving the  $Fe^{2+}$  and  $Mg^{2+}$  of the igneous rocks to form a ferromagnesian aqueous medium environment where zeolite is precipitated in the intergranular pores. The presence of zeolite precipitation increases the resistance to compaction favoring the preservation of primary pores. However, during the thermal evolution stage of the source rocks, dissolution of zeolite developed due to expulsion of organic acid forming secondary pores (Figure 5). Therefore, it is easily inferred that proximal sandstone formations combined with the influence of strong hydrolysis of ferromagnesian minerals commonly are favorable for the development of sandstone porosity, such as transition zone of braided river delta development zone and basaltic eruption zone.

**5.2.2. Impacting of Compaction on Reservoir Quality.** A large number of exploration practices show that compaction is the main factor leading to the reduction of primary porosity of sandstone reservoirs. Therefore, the effective inhibition of compaction can significantly affect the preservation of pores and improve the reservoir quality. The volcanic rocks are widely distributed in the study area and vertical distribution is mainly focused in  $E_2s_{1+2}$  and  $E_3d_{1+2}$ . During the volcanic eruption stage, volcanic conduit facies and overflow facies constructed I-shaped volcanic structure which formed roof support effect weakening the compaction of overlying formation [70]. Therefore, the primary pores can be substantially preserved improving the reservoir physical property.

**5.2.3. Inhibition of Quartz Overgrowth and Dissolution of Detrital Quartz Grain.** Quartz overgrowth is considered

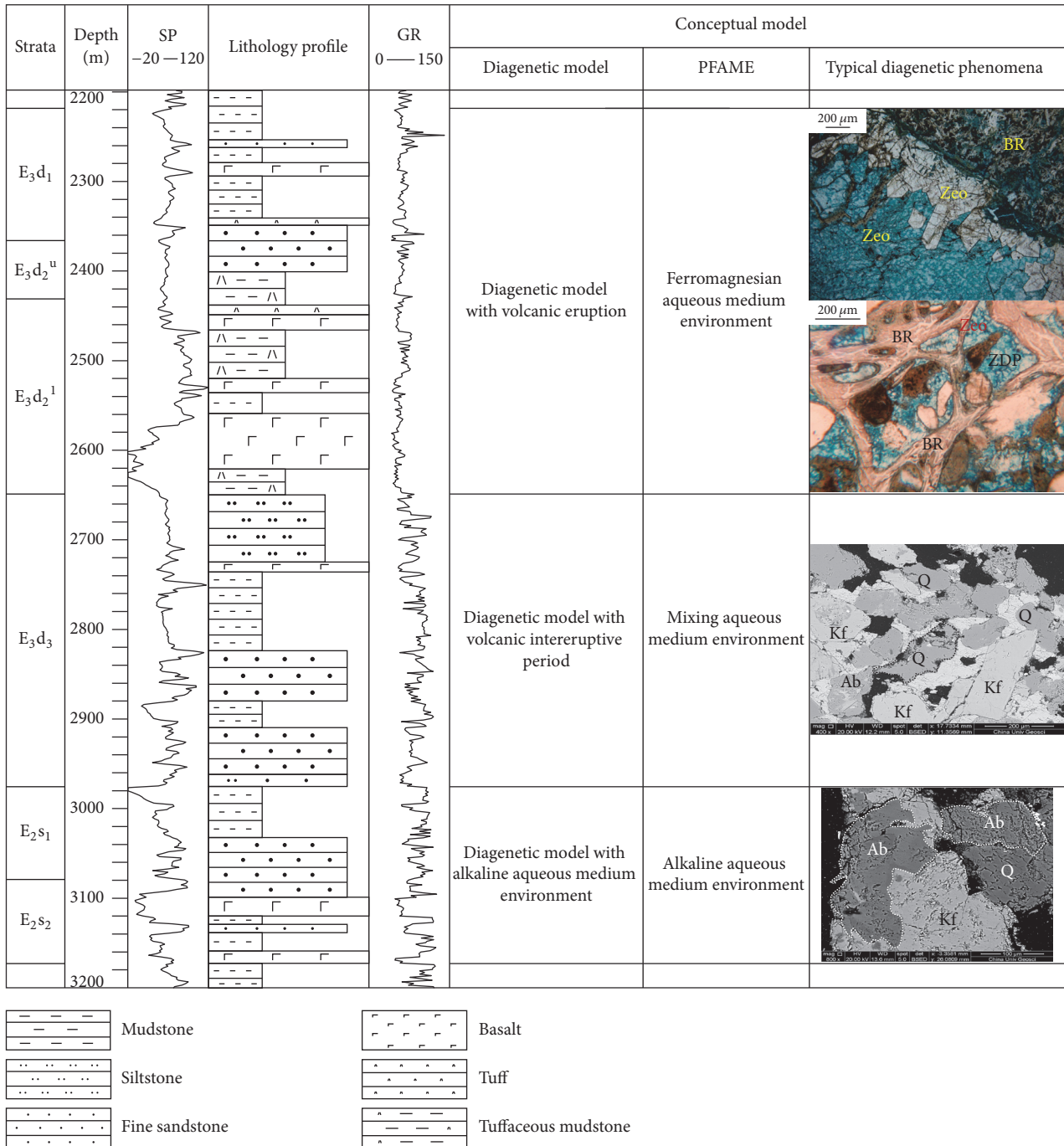


FIGURE 10: Vertical evolution of pore fluids properties and typical diagenetic phenomena of well BZ-1, Huanghekou Sag. Ab = albitization, BR = basalt rock fragment, Kf = K-feldspar, PFAME = pore fluid aqueous medium environment, Q = quartz, ZDP = zeolite dissolution pore, and Zeo = zeolite.

the main factor that reduced the porosity of medium-deep reservoirs and commonly 1% of quartz overgrowth resulted in 10% of the pore loss [71]. Therefore, the pore preservation of medium-deep reservoirs can be achieved by inhibiting the chemical compaction of quartz. In the study area, the quartz grain surface observed the presence of ctenoid dolomite encrustation developed under the alkaline aqueous medium environment, effectively inhibiting the overgrowth of quartz

(Figure 7(d)). As a result, the pores can be better preserved. As is shown by the porosity data in well BZ-1, there is no significant decrease in porosity with progressively increasing burial depth between E<sub>3</sub>d<sub>1+2</sub>, E<sub>3</sub>d<sub>3</sub>, and E<sub>2</sub>s<sub>1+2</sub> (Figure 3). Furthermore, secondary pores produced resulted from the dissolution of detrital quartz also found based on thin section observation which improved the quality of reservoir (Figures 6(a), 6(b), and 6(c)).

**5.3. Implications for Petroleum Exploration.** The study has broad implications for exploration and development in other deeply buried sandstone reservoirs, especially but not exclusively related to volcanic activities. Sandstone reservoirs with development of volcanic rocks have not been considered prime potential hydrocarbon reservoirs due to poor reservoir quality. The present study, however, demonstrated that ferromagnesian-rich pore fluid aqueous medium environment resulted from volcanic activities developing typical diagenetic events such as precipitation and dissolution of zeolite associated with basaltic eruption effectively improving the reservoir quality. In turn, related diagenetic processes record the pore fluid property which provides us with new insight into investigating the pore fluid evolution and predicting the reservoir quality. Meanwhile, volcanic conduit facies and overflow facies constructed I-shaped volcanic structure which increased resistance but reduced compaction of strata, preserving the primary pores and improving the reservoir quality.

## 6. Conclusions

Pore fluid evolution influenced by volcanic activities in sandstone reservoirs has a critical impact on diagenetic processes which controlled the reservoir quality, as exemplified by deeply buried sandstone reservoirs in the Huanghekou Sag, Bohai Bay Basin, China. On the basis of our studies, the following conclusions can be drawn.

- (1) Volcanic activities exert a significant influence on pore fluid properties depending on volcanic activity intensity. Evolution of pore fluids can be divided into three stages corresponding to volcanic activities:
    - ①  $E_2s_{1+2}$ : alkaline aqueous medium environment is developed with insignificant influence by volcanic activities, which can be interpreted as alkaline lake basin aqueous medium diagenetic model;
    - ②  $E_3d_3$ : affected by influx of fluvial fresh water together with hydrolysis of ferromagnesian mineral, mixing aqueous medium environment occurred and volcanic intereruptive period diagenetic model was established;
    - ③  $E_3d_{1+2}$ : multiphase volcanic activities resulted in the formation of ferromagnesian aqueous medium environment and development of basal eruption diagenetic model.
  - (2) The vertical distribution of pore fluids with varied properties in different intervals controls the diagenetic processes and reservoir quality.
    - ① Alkaline aqueous medium pore fluids formed in  $E_2s_{1+2}$ , causing quartz dissolution, K-feldspar albitization, and dolomite encrustation.
    - ② Ferromagnesian pore fluids in  $E_3d_{1+2}$  resulted in zeolite precipitation in early diagenesis and zeolite dissolution during thermal evolution stage due to expulsion of organic acid. In addition, the predominant clay mineral is mixed-layer C/S influenced by hydrolysis of unstable ferromagnesian-rich mineral resulting from volcanic activities.
    - ③ Mixing aqueous medium pore fluids in  $E_3d_3$  are characterized by interaction of pore fluids
- in both  $E_2s_{1+2}$  and  $E_3d_{1+2}$ . Therefore, the diagenetic processes exhibits integrated characteristic of both  $E_2s_{1+2}$  and  $E_3d_{1+2}$ .
- (3) A series of controlling factors that played positive effect in the reservoirs quality are concluded including dolomite encrustation inhibited quartz overgrowth developments, quartz and zeolite dissolution formed secondary pores, and I-shaped igneous structure increased the resistance of compaction.

## Conflicts of Interest

The authors declare that there are no conflicts of interest regarding the publication of this paper.

## Acknowledgments

This research was funded by the National Natural Science Foundation of China (no. 41572084) and the National Science and Technology Major Project (no. 2016ZX05024-003-007). Thanks are due to the Tianjin Branch of the China National Offshore Oil Corporation for providing data used in this study and the permission to publish the results.

## References

- [1] S. Bloch, R. H. Lander, and L. Bonnell, "Anomalously high porosity and permeability in deeply buried sandstone reservoirs: Origin and predictability," *AAPG Bulletin*, vol. 86, no. 2, pp. 301–328, 2002.
- [2] J. M. Ajdukiewicz, P. H. Nicholson, and W. L. Esch, "Prediction of deep reservoir quality using early diagenetic process models in the jurassic norphlet formation, gulf of Mexico," *AAPG Bulletin*, vol. 94, no. 8, pp. 1189–1227, 2010.
- [3] X. Pu, L. Zhou, W. Wang et al., "Medium-deep clastic reservoirs in the slope area of Qikou sag, Huanghua depression, Bohai Bay Basin," *Petroleum Exploration and Development*, vol. 40, no. 1, pp. 38–51, 2013.
- [4] F. Hao, X. Zhou, Y. Zhu, X. Bao, and Y. Yang, "Charging of the Neogene Penglai 19-3 field, Bohai Bay Basin, China: Oil accumulation in a young trap in an active fault zone," *AAPG Bulletin*, vol. 93, no. 2, pp. 155–179, 2009.
- [5] C. G. Xu and W. C. Lai, "Predication technologies of Paleogene mid-deep reservoir and their application in Bohai Sea," *China offshore oil and gas*, vol. 4, pp. 231–236, 2005.
- [6] S. Jiang, D. S. Cai, X. M. Zhu, G. H. Zhu, and X. L. Hu, "Diagenesis of Liaozhong sag in Liaohe depression and pore evolution in its middle-deep strata," *Oil and Gas Geology*, vol. 28, no. 3, pp. 362–369, 2007, [In Chinese with English abstract].
- [7] Y.-J. Wang, M.-S. Feng, J. Wang, Q.-L. Xia, X.-H. Zhou, and W.-C. Lai, "Characteristics of high-quality reservoir of medium-deep paleogene in shinan slope area, bozhong depression," *Journal of Mineralogy and Petrology*, vol. 32, no. 3, pp. 77–84, 2012.
- [8] H. Zhu, Y. Liu, Y. Wang, X. Zhou, and X. Yang, "Volcanic eruption phases and 3-D characterization of volcanic rocks in BZ34-9 block of Huanghekou Sag, Bohai Bay Basin," *Earth Science - Journal of China University of Geosciences*, vol. 39, no. 9, pp. 1309–1316, 2014.

- [9] B. L. Winter, C. M. Johnson, J. A. Simo, and J. W. Valley, "Paleozoic fluid history of the Michigan basin: Evidence from dolomite geochemistry in the middle Ordovician St. Peter Sandstone," *Journal of Sedimentary Research*, no. 65, pp. 306–320, 1995.
- [10] S. Morad, K. Al-Ramadan, J. M. Ketzer, and L. F. De Ros, "The impact of diagenesis on the heterogeneity of sandstone reservoirs: A review of the role of depositional facies and sequence stratigraphy," *AAPG Bulletin*, vol. 94, no. 8, pp. 1267–1309, 2010.
- [11] K. Bjørlykke and J. Jahren, "Open or closed geochemical systems during diagenesis in sedimentary basins: Constraints on mass transfer during diagenesis and the prediction of porosity in sandstone and carbonate reservoirs," *AAPG Bulletin*, vol. 96, no. 12, pp. 2193–2214, 2012.
- [12] B. Ma, K. A. Eriksson, Y. Cao, Y. Jia, Y. Wang, and B. C. Gill, "Fluid flow and related diagenetic processes in a rift basin: Evidence from the fourth member of the Eocene Shahejie Formation interval, Dongying depression, Bohai Bay Basin, China," *AAPG Bulletin*, vol. 100, no. 11, pp. 1633–1662, 2016.
- [13] L. C. Amajor and A. M. Gbadebo, "Oilfield brines of meteoric and connate origin in the eastern Niger Delta," *Journal of Petroleum Geology*, vol. 15, no. 4, pp. 481–488, 1992.
- [14] K. Bjørlykke, "Fluid flow in sedimentary basins," *Sedimentary Geology*, vol. 86, no. 1-2, pp. 137–158, 1993.
- [15] M. A. Bustillo and A. M. Alonso-Zarza, "Overlapping of pedogenesis and meteoric diagenesis in distal alluvial and shallow lacustrine deposits in the Madrid Miocene Basin, Spain," *Sedimentary Geology*, vol. 198, no. 3-4, pp. 255–271, 2007.
- [16] J. W. Bishop, D. A. Osleger, I. P. Montáez, and D. Y. Sumner, "Meteoric diagenesis and fluid-rock interaction in the middle Permian capitan backreef: Yates formation, slaughter canyon, New Mexico," *AAPG Bulletin*, vol. 98, no. 8, pp. 1495–1519, 2014.
- [17] K. Bjørlykke, "Clay mineral diagenesis in sedimentary basins - A key to the prediction of rock properties. Examples from the North Sea Basin," *Clay Minerals*, vol. 33, no. 1, pp. 14–34, 1998.
- [18] K. Bjørlykke, "Petroleum geoscience: From sedimentary environments to rock physics," *Petroleum Geoscience: From Sedimentary Environments to Rock Physics*, pp. 1–508, 2010.
- [19] F. O. Amadi, R. P. Major, and L. R. Baria, "Origins of gypsum in deep carbonate reservoirs: Implications for hydrocarbon exploration and production," *AAPG Bulletin*, vol. 96, no. 2, pp. 375–390, 2012.
- [20] C. M. Bethke and S. Marshak, "Brine migrations across North America - the plate tectonics of groundwater," *Annual Review of Earth & Planetary Sciences*, vol. 18, pp. 287–315, 1990.
- [21] B. H. Hartmann, K. Ramseier, and A. Matter, "Diagenesis and pore-water evolution in permian sandstones, gharif formation, Sultanate of Oman," *Journal of Sedimentary Research*, vol. 70, no. 3, pp. 533–544, 2000.
- [22] J. Wang, Y. Cao, K. Liu, J. Liu, X. Xue, and Q. Xu, "Pore fluid evolution, distribution and water-rock interactions of carbonate cements in red-bed sandstone reservoirs in the Dongying Depression, China," *Marine and Petroleum Geology*, vol. 72, pp. 279–294, 2016.
- [23] S. P. Dutton and R. G. Loucks, "Reprint of: Diagenetic controls on evolution of porosity and permeability in lower Tertiary Wilcox sandstones from shallow to ultradeep (200-6700m) burial, Gulf of Mexico Basin, U.S.A.," *Marine and Petroleum Geology*, vol. 27, no. 8, pp. 1775–1787, 2010.
- [24] S. Morad, J. M. Ketzer, and L. R. De Ros, "Spatial and temporal distribution of diagenetic alterations in siliciclastic rocks: Implications for mass transfer in sedimentary basins," *Sedimentology*, vol. 47, no. 1, pp. 95–120, 2000.
- [25] K. Bjørlykke, "Relationships between depositional environments, burial history and rock properties. Some principal aspects of diagenetic process in sedimentary basins," *Sedimentary Geology*, vol. 301, pp. 1–14, 2014.
- [26] H. L. Wycherley, J. Parnell, G. R. Watt, H. Chen, and A. J. Boyce, "Indicators of hot fluid migration in sedimentary basins: Evidence from the UK Atlantic margin," *Petroleum Geoscience*, vol. 9, no. 4, pp. 357–374, 2003.
- [27] W. Wang, X. H. Yang, Q. B. Wang, J. R. Ye, H. T. Zhu, and H. Li, "Characterization and controlling factors of sandstone reservoirs in basalt development areas: an example from comparison between BZ3-9 and KL6 area in South of Bohai Sea," *Earth Science*, vol. 42, no. 4, pp. 570–586, 2017, [In Chinese with English abstract].
- [28] M. B. Allen, D. I. M. Macdonald, Z. Xun, S. J. Vincent, and C. Brouet-Menzies, "Early Cenozoic two-phase extension and late Cenozoic thermal subsidence and inversion of the Bohai Basin, northern China," *Marine and Petroleum Geology*, vol. 14, no. 7-8, pp. 951–972, 1997.
- [29] L.-Y. Hsiao, S. A. Graham, and N. Tilander, "Seismic reflection imaging of a major strike-slip fault zone in a rift system: Paleogene structure and evolution of the Tan-Lu fault system, Liaodong Bay, Bohai, offshore China," *AAPG Bulletin*, vol. 88, no. 1, pp. 71–97, 2004.
- [30] J. Qi and Q. Yang, "Cenozoic structural deformation and dynamic processes of the Bohai Bay basin province, China," *Marine and Petroleum Geology*, vol. 27, no. 4, pp. 757–771, 2010.
- [31] C. T. Walker, "Evaluation of boron as a paleosalinity indicator and its application to offshore prospects," *AAPG Bulletin*, vol. 52, no. 5, pp. 751–766, 1968.
- [32] E. L. Couch, "Calculation of paleosalinities from boron and clay mineral data," *American Association of Petroleum Geologists Bulletin*, vol. 55, no. 10, pp. 1829–1837, 1971.
- [33] B. Legler, J. W. Schneider, U. Gebhardt, D. Merten, and R. Gaupp, "Lake deposits of moderate salinity as sensitive indicators of lake level fluctuations: Example from the Upper Rotliegend saline lake (Middle-Late Permian, Northeast Germany)," *Sedimentary Geology*, vol. 234, no. 1-4, pp. 56–69, 2011.
- [34] C. Ye, Y. Yang, X. Fang, and W. Zhang, "Late Eocene clay boron-derived paleosalinity in the Qaidam Basin and its implications for regional tectonics and climate," *Sedimentary Geology*, vol. 346, pp. 49–59, 2016.
- [35] S. Landergren, "On the Distribution of Boron on Different Size Classes in Marine Clay Sediments," *GFF*, vol. 80, no. 1, pp. 104–107, 1958.
- [36] D. M. Moore and R. C. Reynolds, *X-ray Diffraction and the Identification and Analysis of Clay Minerals*, Oxford University Press, 1997.
- [37] S. Hillier, "Quantitative Analysis of Clay and other Minerals in Sandstones by X-Ray Powder Diffraction (XRPD)," *Clay Mineral Cements in Sandstones*, pp. 663–676, 2003.
- [38] G. Chen, "Zeolite minerals and their relation to oil and gas accumulation in the reservoir formations in karamay oil field," *Acta Petrolei Sinica*, vol. 13, no. 3, pp. 45–51, 1992, [In Chinese with English abstract].

- [39] R. H. Mariner and R. C. Surdam, "Alkalinity and formation of zeolites in saline alkaline lakes," *Science*, vol. 170, no. 3961, pp. 979–980, 1970.
- [40] S. Han, H. Yu, C. Si, S. Chen, N. Chen, and L. Yu, "Corrosion of analcite in reservoir of Junggar Basin," *Shiyou Xuebao/Acta Petrolei Sinica*, vol. 28, no. 3, pp. 51–62, 2007.
- [41] S. F. Zhu, X. M. Zhu, X. L. Wang, and Z. Y. Liu, "Zeolite diagenesis and its control on petroleum reservoir quality of Permian in northwestern margin of Junggar Basin, China," *Science China Earth Sciences*, vol. 55, no. 3, pp. 386–396, 2012.
- [42] R. L. Hay, "Zeolites and zeolitic reactions in sedimentary rocks," *Special Paper of the Geological Society of America*, vol. 85, pp. 1–122, 1966.
- [43] M. D. Su and C. L. Dai, "Geological feature and genesis of zeolite in the Mesozoic Volcanic Rocks in east China," *Scientia Geologica Sinica*, vol. 2, pp. 116–125, 1983, [In Chinese with English abstract].
- [44] H. Li, Y. Q. Liu, H. Liang et al., "Lithology and original analysis of sublacustrine hydrothermal deposits characterized by analcime, sanidine, dolomite, quaterz, etc. in Lucaogou Formation, Middle Permian, Santanghu Basin, Northeast Xinjiang, China," *Acta Petrolei Sinica*, vol. 30, no. 2, pp. 205–218, 2012, [In Chinese with English abstract].
- [45] G. K. Moncure, R. C. Surdam, and H. L. McKague, "Zeolite diagenesis below pahute mesa, nevada test site," *Clays and Clay Minerals*, vol. 29, no. 5, pp. 385–396, 1981.
- [46] L. Bettison-Varga and I. D. R. Mackinnon, "The role of randomly mixed-layered chlorite/smectite in the transformation of smectite to chlorite," *Clays and Clay Minerals*, vol. 45, no. 4, pp. 506–516, 1997.
- [47] H. Lindgreen, V. A. Drits, B. A. Sakharov et al., "The structure and diagenetic transformation of illite-smectite and chlorite-smectite from North Sea Cretaceous-Tertiary chalk," *Clay Minerals*, vol. 37, no. 3, pp. 429–450, 2002.
- [48] S. M. Xu, C. M. Lin, X. F. Wang et al., "Diagenesis and Its Effect on Reservoir of Member 2-3 of the Lower Shihezi Formation in Daniudi Gas Field, Ordos Basin," *Geoscience*, vol. 25, no. 5, pp. 909–916, 2011, [In Chinese with English abstract].
- [49] K. Bjørlykke, "Open-system chemical behaviour of Wilcox Group mudstones. How is large scale mass transfer at great burial depth in sedimentary basins possible? A discussion," *Marine and Petroleum Geology*, vol. 28, no. 7, pp. 1381–1382, 2011.
- [50] F. L. Lynch, L. E. Mack, and L. S. Land, "Burial diagenesis of illite/smectite in shales and the origins of authigenic quartz and secondary porosity in sandstones," *Geochimica et Cosmochimica Acta*, vol. 61, no. 10, pp. 1995–2006, 1997.
- [51] Y. M. Metwally and E. M. Chesnokov, "Clay mineral transformation as a major source for authigenic quartz in thermomature gas shale," *Applied Clay Science*, vol. 55, pp. 138–150, 2012.
- [52] B. Thyberg, J. Jahren, T. Winje, K. Bjørlykke, J. I. Faleide, and Ø. Marcussen, "Quartz cementation in Late Cretaceous mudstones, northern North Sea: Changes in rock properties due to dissolution of smectite and precipitation of micro-quartz crystals," *Marine and Petroleum Geology*, vol. 27, no. 8, pp. 1752–1764, 2010.
- [53] P. C. Bennett, "Quartz dissolution in organic-rich aqueous systems," *Geochimica et Cosmochimica Acta*, vol. 55, no. 7, pp. 1781–1797, 1991.
- [54] A. J. Gratz and P. Bird, "Quartz dissolution: Theory of rough and smooth surfaces," *Geochimica et Cosmochimica Acta*, vol. 57, no. 5, pp. 977–989, 1993.
- [55] P. M. Dove, "The dissolution kinetics of quartz in sodium chloride solutions at 25° to 300°C," *American Journal of Science*, vol. 294, no. 6, pp. 665–712, 1994.
- [56] J. W. Tester, W. G. Worley, B. A. Robinson, C. O. Grigsby, and J. L. Feerer, "Correlating quartz dissolution kinetics in pure water from 25 to 625°C," *Geochimica et Cosmochimica Acta*, vol. 58, no. 11, pp. 2407–2420, 1994.
- [57] W. G. Worley, J. W. Tester, and C. O. Grigsby, "Quartz Dissolution Kinetics from 100–200°C as a Function of pH and Ionic Strength," *AIChE Journal*, vol. 42, no. 12, pp. 3442–3455, 1996.
- [58] L. W. Qiu, Z. X. Jiang, W. X. Chen, X. H. Li, and Z. D. Xiong, "A new type of secondary porosity Quartz Dissolution Porosity," *Acta Petrolei Sinica*, vol. 20, no. 4, pp. 621–627, 2002, [In Chinese with English abstract].
- [59] D. L. Han, Z. Li, and W. F. Li, "Heterogeneous Features of Quartz Grain Dissolution of Cretaceous Sandstone Reservoir in the Kuqa Depression and Its Major Controlling factors," *Acta Geologica Sinica*, vol. 85, no. 2, pp. 257–261, 2011, [In Chinese with English abstract].
- [60] H. Zhu, D. Zhong, J. Yao et al., "Alkaline diagenesis and its effects on reservoir porosity: a case study of Upper Triassic Chang 7 tight sandstones in Ordos Basin, NW China," *Petroleum Exploration and Development*, vol. 42, no. 1, pp. 51–59, 2015.
- [61] R. L. Cullers, "The controls on the major and trace element variation of shales, siltstones, and sandstones of Pennsylvanian-Permian age from uplifted continental blocks in Colorado to platform sediment in Kansas, USA," *Geochimica et Cosmochimica Acta*, vol. 58, no. 22, pp. 4955–4972, 1994.
- [62] Y. Miao, S. X. Sang, S. Y. Chen, C. J. Liu, and J. B. Ouyang, "Trace element characteristics and their geological significances in Permo-Carboniferous dark mudstone in Jiyang Depression," *Geochimica*, vol. 38, no. 1, pp. 57–67, 2009, [In Chinese with English abstract].
- [63] R. C. Zheng and M. Q. Liu, "Study on Palaeosalinity of Chang-6 oil Reservoir set in Ordos Basin," *Oil and Gas Geology*, vol. 20, no. 1, pp. 20–25, 1999, [In Chinese with English abstract].
- [64] Z. J. Zhu, H. D. Chen, L. B. Lin, and Y. Fan, "Signification and characteristic of the trace element ratios of the sandstone in silurian xiaoheba formation in southeastern sichuan province and western hunan province," *Geological Sciences and Technology Information*, vol. 29, no. 2, pp. 24–30, 2010, [In Chinese with English abstract].
- [65] G. Liu and D. S. Zhou, "Application of microelements analysis in identifying sedimentary environment," *Petroleum Geology and Experiment*, vol. 29, no. 3, pp. 307–310, 2007, [In Chinese with English abstract].
- [66] E. F. McBride, "Diagenetic processes that affect provenance determination in sandstones," in *Provenance of arenites*, pp. 95–113, Spring Netherlands, 1985.
- [67] S. Morad, "Albitized microcline grains of post-depositional and probable detrital origins in Brøttum Formation sandstones (Upper Proterozoic), Sparagmite Region of southern Norway," *Geological Magazine*, vol. 125, no. 3, pp. 229–239, 1988.
- [68] K. L. Milliken, "Late Diagenesis and Mass Transfer in Sandstone-Shale Sequences," *Treatise on Geochemistry*, vol. 7-9, pp. 159–190, 2003.

- [69] G. F. Yang, S. G. Zhuo, B. Niu, and J. J. Er, "Albitization of detrital feldspar in cretaceous sandstones from the songliao basin," *Geological Review*, vol. 49, no. 2, pp. 155–161, 2003.
- [70] YB. Chai, B. Yang, QB. Wang, CM. Niu, and H. Li, "A contrastive analysis on the impact of volcanic rock on compaction of BZ34 area in Huanghekou Depression," *Geological Science and Technology Information*, no. 1, pp. 80–86, 2016, [In Chinese with English abstract].
- [71] S. T. Paxton, J. O. Szabo, J. M. Ajdukiewicz, and R. E. Klimentidis, "Construction of an intergranular volume compaction curve for evaluating and predicting compaction and porosity loss in rigid-grain sandstone reservoirs," *AAPG Bulletin*, vol. 86, no. 12, pp. 2047–2067, 2002.

## Research Article

# Deep-Buried Triassic Oil-Source Correlation in the Central Junggar Basin, NW China

Ming Wu,<sup>1,2</sup> Jun Jin,<sup>3</sup> Wanyun Ma,<sup>3</sup> Baoli Xiang,<sup>3</sup> Ni Zhou,<sup>3</sup> Jiangling Ren,<sup>3</sup> and Jian Cao<sup>1</sup>

<sup>1</sup>State Key Laboratory for Mineral Deposits Research, Department of Earth Sciences, Nanjing University, Nanjing, Jiangsu 210023, China

<sup>2</sup>Department of Earth and Planetary Sciences, Washington University, St. Louis, MO 63130, USA

<sup>3</sup>Research Institute of Experiment and Testing, PetroChina Xinjiang Oilfield Company, Karamay, Xinjiang 843000, China

Correspondence should be addressed to Jian Cao; [jcao@nju.edu.cn](mailto:jcao@nju.edu.cn)

Received 26 February 2017; Accepted 4 May 2017; Published 11 June 2017

Academic Editor: Shuichang Zhang

Copyright © 2017 Ming Wu et al. This is an open access article distributed under the Creative Commons Attribution License, which permits unrestricted use, distribution, and reproduction in any medium, provided the original work is properly cited.

Whether there is an effective deep-buried lacustrine Triassic petroleum system in the Junggar Basin, NW China, has been enigmatic and debated for a long time. Here we conduct an oil-source correlation to address this issue. Results show that the extracted bitumens from the Triassic mudstones in the central basin have distinctive stable carbon isotope and biomarker compositions compared to the Permian-sourced and Jurassic-sourced hydrocarbons, the other two recognized sources in the study area. These characteristics include  $\delta^{13}\text{C}$  value of  $-30.46 \sim -26.30\%$ ,  $\beta$ -carotane/maximum *n*-alkane of 0.22–0.41, Pr/Ph of 1.00–1.51,  $\text{C}_{24}$  tetracyclic terpane/ $\text{C}_{26}$  tricyclic terpane of 0.43–0.96, Ts/Tm of 0.34–0.64, gammacerane/ $\text{C}_{30}$  hopane of 0.10–0.14, and regular steranes  $\text{C}_{27} > \text{C}_{28} < \text{C}_{29}$  with  $\text{C}_{29}$  sterane in dominance (40–50%). These suggest that the Triassic mudstones in the study area host fresh lacustrine organic matters with high input of higher plants. The Triassic-reservoired crude oils and extracts can be divided into two types. Through oil-source correlation, we infer that both type A and type B oils are derived from mixed Permian and Triassic source rocks. Linear regression analysis shows that the contribution from Triassic mudstones to type A and B oils is 67% and 31%, respectively. This implies that the deep-buried Triassic lacustrine mudstones in the Junggar Basin may have some oil-generation potential and thus might represent a new case of Triassic petroleum systems in China and deserves a more detailed and thorough study in future exploration and exploitation.

## 1. Introduction

The Triassic sediments have contributed to global petroleum reserves and production at approximately 2.0% [1, 2]. The major Triassic source rocks are deposited in marginal marine, marine shelf settings, or other shallow marine environments, such as the Lower–Middle Triassic Locker Shale in Northwest Australia, the Middle–Upper Triassic Carbonates in Arabian Platform, and the Middle–Upper Triassic Shublik–Otuk interval in Alaska [3]. In China, the major Triassic source rocks include both lacustrine mudstones deposited during flooding periods, such as the Upper Triassic Yanchang Formation in the Erdos Basin [4] and Huangshanjie Formation in the Tarim Basin [5], and marine limestone and argillaceous rocks such as the Upper Triassic Xiaochaka Formation in the Qiangtang Basin [6].

The Junggar Basin, located in northwestern China and being one of the most petroliferous basins in NW China, is typified by development of multiple source rocks, from old to young including Carboniferous, Permian, Jurassic, Cretaceous, and Paleogene [7–13]. In addition, Triassic has been proposed to be a candidate for source rock [14–16]. This understanding was obtained mainly based on two reasons. First, a flooding event in a lacustrine basin is commonly accompanied by development of high-quality hydrocarbon source rocks, which lay the foundation for formation of large oil and gas fields; notable examples include the Late Triassic to Early Jurassic lake system in the Jameson Land Basin, East Greenland [17, 18] and the Late Cretaceous lake system in the Songliao Basin, China [19, 20]. In the Junggar Basin, the Triassic, particularly the Upper Triassic Baijiantan Formation ( $\text{T}_3b$ ), has been proved to be deposited during a lacustrine

flooding period [21–23] and shown to be an important set of regional caprock [24–26]. Thus, theoretically, Triassic formation in the Junggar Basin may be an important set of hydrocarbon source rocks. Second, for the Triassic the underlying Permian and overlying Jurassic have both been validated to be effective source rocks [7, 11, 27–29]. This implies that the Triassic has the maturity condition for hydrocarbon generation given that the Triassic is organic-rich.

Wu et al. [16] conducted a pilot study on the geochemical evaluation of the Triassic mudstones in the central Junggar Basin and concluded that the Triassic has hydrocarbon generation potential, with gas in dominance and some oil. This, in turn, implies that the established petroleum systems in the basin might need to be reevaluated. It seems that there are no large amounts of generated gas [30] because the maturity of the Triassic has not reached the gas-generation window [16]. Thus, the critical issue in the study of whether the Triassic can be effective hydrocarbon source rocks in the Junggar Basin is oil-generation ability and associated resource prospects.

However, this issue has not received large research attention because petroleum resources have been believed to be sufficient in the basin. Only a few preliminary studies have noted that there are possible Triassic oil-source rocks in the basin. Chen et al. [14] analyzed the geochemical features of Carboniferous, Permian, Triassic, and Jurassic source rocks as well as the crude oils in the eastern Junggar Basin. The geochemical assessment of the genetic potential of the multiple source rocks showed that the Triassic source rocks should have generated certain amounts of oils. Late on, Chen et al. [15] quantified the Triassic contribution to the mixed oils at 15% based on artificial mixing experiments and mixing calculations by using whole-oil carbon isotope ratios and absolute concentrations of biomarkers.

Along with the increasing exploration level in the basin, it becomes more and more important to know if there are additional source rock sequences in the basin. Thus, this paper aims to clarify the oil-generation potential of the Triassic mudstones in the basin by using an oil-source correlation study. We focused on the central Junggar Basin because it is the typical area reported to develop Triassic source rocks [16].

## 2. Geologic Setting

The Junggar Basin of NW China, which covers an area of ca.  $1.3 \times 10^5$  km<sup>2</sup>, is located in the northern Xinjiang Uygur Autonomous Region and is a superimposed petroliferous basin (Figure 1(a)). This triangular basin is bounded by mountains from four sides, including the Qinggelidi-Kelameili Mountains to the east, the Zhayier Mountains to the west, the Tianshan Mountains (i.e., Yilinheibiergen and Bogeda Mountains) to the south, and the Altai Mountains (i.e., Delun Mountains) to the north (Figure 1(a)). The Junggar Basin comprises Paleozoic, Mesozoic, and Cenozoic strata [32, 33] (Figure 1(a)) deposited on a pre-Carboniferous folding and crystallized two-story basement [34, 35]. The location of the studied central Junggar Basin is indicated in Figure 1(b).

The Junggar Basin was subject to a continuous subsidence during the Triassic and the crust mainly experienced vertical rising and sinking [21–23]. Because of basin subsidence and

expansion, especially the deposition of the Upper Triassic, the fault depression and fault-uplift belts throughout the basin formed during the Permian rifting [36] were gradually uniformized, providing favorable conditions for development of hydrocarbon source rocks [37].

The Triassic formation in the central Junggar Basin from bottom to up consists of the Lower Baikouquan Formation ( $T_1b$ ), the Middle Karamay Formation ( $T_2k$ ), and the Upper Baijiantan Formation ( $T_3b$ ). The sedimentary facies evolved from alluvial fan plains, to shore-shallow lakes, to braided-river deltaic fronts, to shore-shallow lakes, to swamps, to shallow lakes, and to deep lakes (Figure 2) [22].  $T_1b$  consists of brown/gray siltstone, fine-grained sandstone, and gray/brown mudstones.  $T_2k$  presents as gray and dark gray mudstone, silty mudstone, and carbonaceous mudstone, interbedded with some laminated coal seams.  $T_3b$  is lithologically dominated by gray and dark gray mudstones, interbedded with thin layers of siltstones and fine-grained to medium-grained sandstones.

## 3. Samples and Methods

Samples used in this oil-source correlation study include mudstone source rocks, reservoir oils, and sandstone extracts. The Triassic mudstones over the central Junggar Basin have different organic matter types and maturities [16]. Based on the dataset reported by Wu et al. [16], eight mudstone samples with hydrogen index (HI) > 100 mg/g TOC from well SM 1 are collected to represent Triassic possible hydrocarbon source rocks. For oil-source correlation, we also collect three Triassic-reservoired crude oils and five oil-bearing sandstones (Tables 1 and 2).

Fresh mudstones were crushed into powders which were used for geochemical analysis. For TOC analysis, sample splits (200 mg) were treated with 10% by volume HCl at 60°C to remove any carbonate, before the samples were washed with distilled water to remove the HCl. The samples were then dried overnight at 50°C before analysis with a LECO SC-144DR Carbon-Sulfur Analyzer.

Rock-Eval pyrolysis was performed using 100-mg crushed mudstone samples and a Rock-Eval VI instrument. These samples were heated to 600°C in a helium atmosphere, thus generating values for four main parameters, including  $S_1$ ,  $S_2$ ,  $S_3$ , and  $T_{max}$ , where  $S_1$  is the amount of free hydrocarbon that can be volatilized from the rock sample (in mg HC/g rock),  $S_2$  is the amount of hydrocarbon produced by cracking of organic matter in the rock (mg HC/g rock),  $S_3$  is the amount of CO<sub>2</sub> produced during the analysis (mg HC/g rock), and  $T_{max}$  (°C) is the temperature at which the maximum  $S_2$  yield is reached, which gives a rough estimate of thermal maturity.

Vitrinite reflectance ( $R_o$ ) measurements were performed using a Zeiss Axioskop 40 Pol incident light microscope at a wavelength ( $\lambda$ ) of 546 nm with a 50x/0.85 oil objective. Yttrium aluminum garnet standard (GWB13401) with a reflectance of 0.588% was used for calibration during analysis, and at least 50 measurements were performed on each sample analyzed during the study.

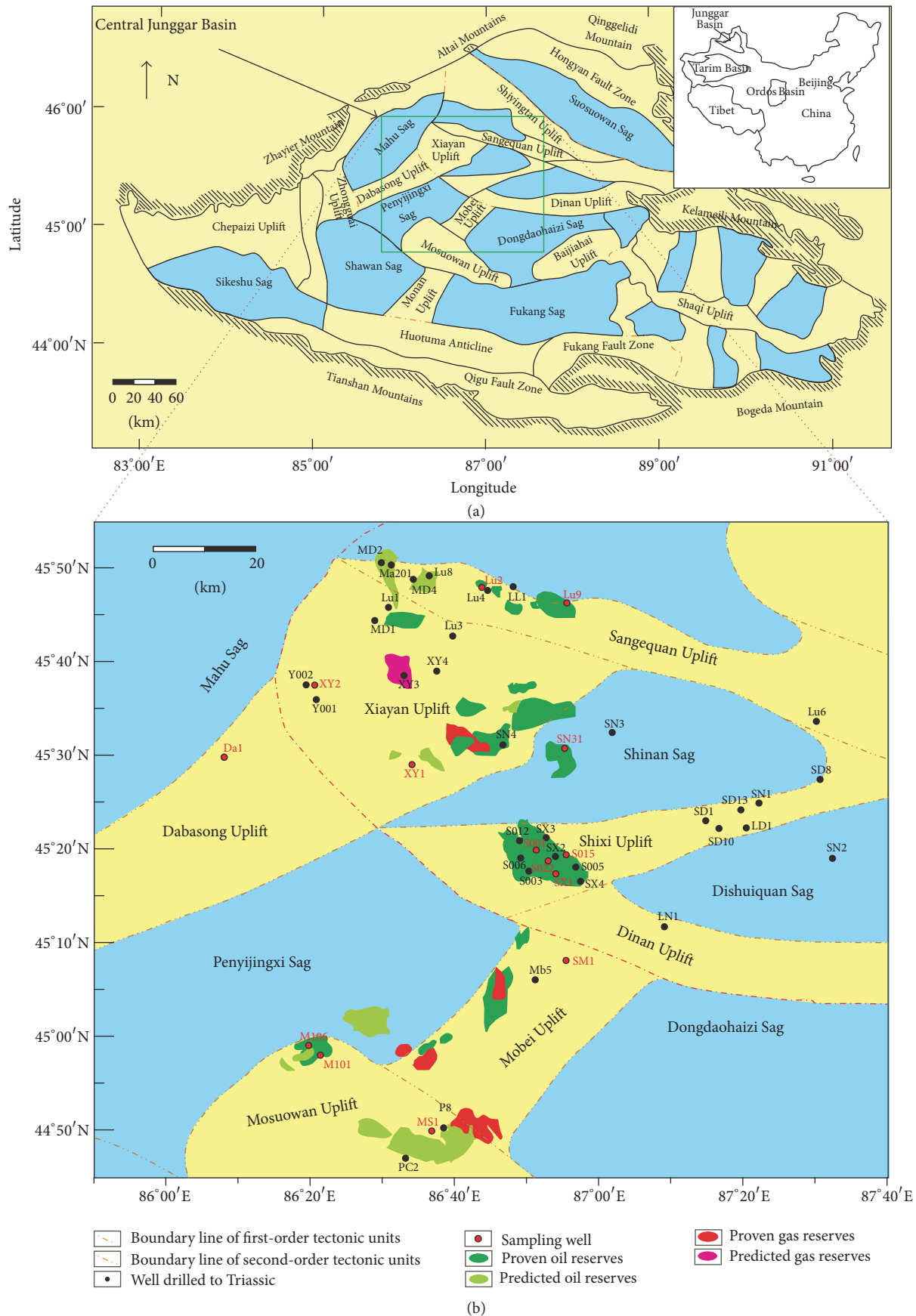


FIGURE 1: (a) Structural units of the Junggar Basin and (b) structural units and key wells of the studied central basin.

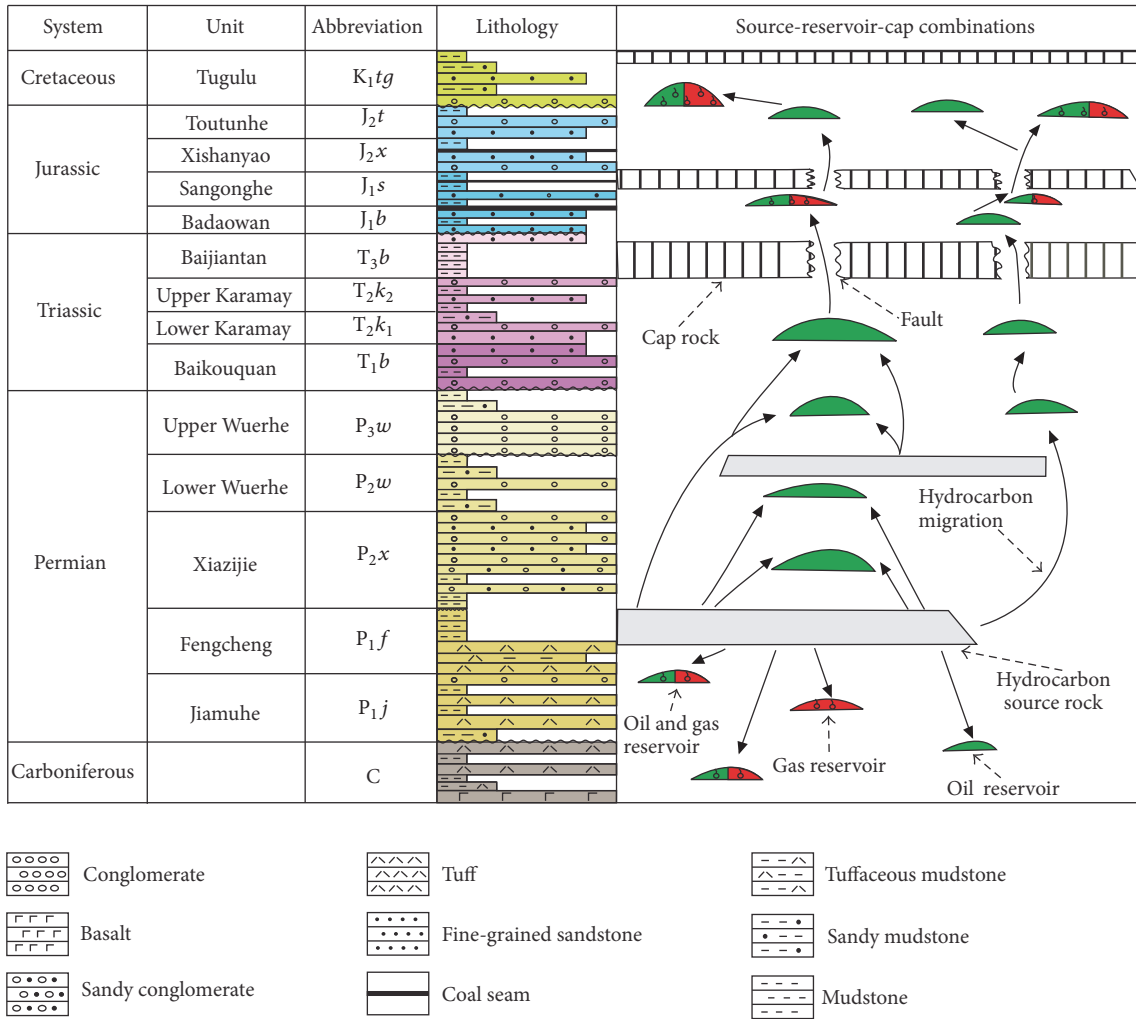


FIGURE 2: Generalized stratigraphy and source-reservoir-cap rock combinations in the central Junggar Basin.

TABLE 1: Bulk geochemical parameters of Triassic potential mudstone source rocks in the central Junggar Basin.

Well	Depth (m)	Fm.	Lithology	TOC (%)	$\delta^{13}C^1$ (‰)	$\delta^{13}C^2$ (‰)	$S_1$ (mg/g)	$S_2$ (mg/g)	PG (mg/g)	HI (mg/g)	$R_o$ (%)	$T_{max}$ (°C)
SM 1	4180	$T_3b$	Dark gray mudstone	1.17	-26.81	-28.47	0.40	1.84	2.24	157.26	0.79	440
SM 1	4190	$T_3b$	Dark gray mudstone	1.49	-26.58	-28.14	0.61	2.90	3.51	194.63	0.80	444
SM 1	4200	$T_3b$	Dark gray mudstone	1.26	-25.70	-26.30	0.36	1.68	2.04	133.33	0.82	442
SM 1	4210	$T_3b$	Dark gray mudstone	1.34	-26.12	-28.45	0.69	3.67	4.36	273.88	0.83	444
SM 1	4218	$T_3b$	Dark gray mudstone	1.36	-27.08	-29.65	0.56	2.88	3.44	211.76	0.83	445
SM 1	4230	$T_3b$	Dark gray mudstone	1.40	-26.73	-29.09	0.98	4.82	5.80	211.76	0.85	443
SM 1	4294	$T_3b$	Dark gray mudstone	1.57	-28.86	-30.46	0.40	1.96	2.36	124.84	0.88	445
SM 1	4324	$T_2k$	Dark gray mudstone	1.02	-26.33	-28.01	0.43	2.22	2.65	217.65	0.90	446

Note. 1, kerogen carbon isotope; 2, carbon isotope of rock extracts.

TABLE 2: Molecular parameters of Triassic mudstone source rocks in the central Junggar Basin.

Well	Depth (m)	Fm.	Lithology	Type*	<i>n</i> -Alkanes <sup>1</sup>	Maximum <i>n</i> -alkanes <sup>2</sup>	Pr/Ph <sup>3</sup>	Pr/ <i>n</i> C <sub>17</sub>	Ph/ <i>n</i> C <sub>18</sub>	OEP <sup>4</sup>	$\beta$ -Carotane/maximum <i>n</i> -alkane	$(nC_{21} + nC_{22})/(nC_{28} + nC_{29})$	$nC_{21}^-/nC_{22}^+$
SM1	4180	T <sub>3b</sub>	Dark gray mudstone	N/A	C <sub>11</sub> -C <sub>35</sub>	C <sub>20</sub>	1.36	0.54	0.40	0.98	0.22	7.00	2.30
SM1	4190	T <sub>3b</sub>	Dark gray mudstone	N/A	C <sub>11</sub> -C <sub>35</sub>	C <sub>20</sub>	1.33	0.61	0.43	1.00	0.27	4.11	1.68
SM1	4200	T <sub>3b</sub>	Dark gray mudstone	N/A	C <sub>13</sub> -C <sub>35</sub>	C <sub>21</sub>	1.51	0.66	0.43	1.02	0.19	3.86	1.43
SM1	4210	T <sub>3b</sub>	Dark gray mudstone	N/A	C <sub>11</sub> -C <sub>35</sub>	C <sub>21</sub>	1.00	0.55	0.53	1.01	0.41	3.44	1.37
SM1	4218	T <sub>3b</sub>	Dark gray mudstone	N/A	C <sub>11</sub> -C <sub>35</sub>	C <sub>21</sub>	1.11	0.51	0.44	1.00	0.33	7.15	1.82
SM1	4230	T <sub>3b</sub>	Dark gray mudstone	N/A	C <sub>11</sub> -C <sub>35</sub>	C <sub>21</sub>	1.04	0.53	0.42	1.00	0.38	5.63	1.36
SM1	4324	T <sub>2k</sub>	Dark gray mudstone	N/A	C <sub>11</sub> -C <sub>35</sub>	C <sub>21</sub>	1.01	0.50	0.45	1.01	0.40	8.21	1.85
MS1	5649.19	T <sub>2k</sub>	Sandstone extract	A	C <sub>9</sub> -C <sub>35</sub>	C <sub>17</sub>	1.30	0.44	0.38	1.06	0.19	2.75	1.72
MS1	5796	T <sub>2k</sub>	Sandstone extract	A	C <sub>12</sub> -C <sub>35</sub>	C <sub>20</sub>	0.75	0.43	0.53	0.99	0.12	3.87	1.38
MS1	5955	T <sub>1b</sub>	Sandstone extract	A	C <sub>14</sub> -C <sub>35</sub>	C <sub>19</sub>	0.88	0.41	0.40	1.00	0.08	4.66	1.68
MS1	5981.48	T <sub>1b</sub>	Sandstone extract	A	C <sub>12</sub> -C <sub>35</sub>	C <sub>17</sub>	1.23	0.38	0.33	1.06	0.06	2.92	1.65
XY1	4493	T <sub>1b</sub>	Crude oil	B	C <sub>10</sub> -C <sub>35</sub>	C <sub>17</sub>	0.98	0.70	0.80	1.09	0.62	2.45	2.18
XY2	4325	T <sub>2k</sub>	Crude oil	B	C <sub>9</sub> -C <sub>35</sub>	C <sub>20</sub>	0.91	0.96	1.19	1.03	0.97	2.63	2.56
Da1	4244	T <sub>2k</sub>	Crude oil	B	C <sub>9</sub> -C <sub>35</sub>	C <sub>15</sub>	1.11	0.78	0.76	0.98	0.47	2.62	3.42
SM1	4508.2	T <sub>1b</sub>	Sandstone extract	B	C <sub>12</sub> -C <sub>35</sub>	C <sub>21</sub>	0.98	0.62	0.68	1.00	0.48	2.71	1.29

Note. \*Type of end-member oil; N/A, not applicable; 1, *N*-alkane distribution; 2, main peak (maximum concentration) of *n*-alkanes; 3, pristane/phytane; 4, calculated after Scalan and Smith [31], defined as OEP =  $[(C_{i-2} + 6C_i + C_{i+2})/(4C_{i-1} + 4C_{i+1})]^{(-1)^{i+1}}$ , C<sub>*i*</sub> is the relative weight percent of an *n*-alkane containing *i* carbon atoms per molecule which has the maximum concentration in *n*-alkanes.

Source rocks and reservoir samples were crushed by the use of a handheld jaw crusher and a shatter box. The powders were then extracted using Soxhlet apparatus by a mixture of dichloromethane:methanol (93:7) for 72 h. The rock extracts were evaporated through rotary evaporation and dried using nitrogen gas. Then the dried extracts were weighed. Then, asphaltenes were removed from the rock extracts and the three crude oils by precipitation with hexane, followed by filtration. The deasphalted extracts and oils were subsequently separated into saturated hydrocarbons, aromatic hydrocarbons, and polar compound (NSO) through column chromatography, using hexane, a mixture of dichloromethane and hexane (1:1), and a mixture of dichloromethane and methanol (1:1). The alkanes were analyzed by gas chromatography-mass spectrometry (GC-MS). GC-MS analysis was carried out using an Agilent 5975 interfaced to an Agilent 6890 chromatograph fitted with a 30 m × 0.32 mm i.d. HP-5 column with a film thickness of 0.25 μm, and He was used as carrier gas. The GC oven temperature was held initially at 75°C (2 min), ramped from 75 to 200°C at 5°C/min, and finally ramped to 310°C at 3°C/min (held for 8 min). The GC-MS system was operated in the electron impact (EI) mode at electron energy of 70 eV, with an emission current of 200 μA. The data acquisition mode is selected ion model (SIM).

For the stable carbon isotopic analysis of the crude oils, mudstone kerogen, and rock extracts, the samples were added to a quartz tube with CuO wire (1.0 g) and were then combusted at 500°C for 1 h and 850°C for another 3 h. Isotopic ratios were analyzed using cryogenically purified CO<sub>2</sub> in a Finnigan MAT-253 mass spectrometer and are reported in standard δ-notation relative to the Vienna Pee Dee Belemnite (VPDB) standard. The working standard used was NBS-19.

For comparison, analytical results of some typical Permian-derived oils and Jurassic mudstone source rocks are retrieved from the geochemical database of PetroChina Xinjiang Oilfield Company. Note that there are no effective Permian source rocks available in the study area because rocks in the sag area are too deep to drill. Thus, to compensate, we use the Permian-derived oils to indicate the characteristics of source rock.

## 4. Results and Discussion

**4.1. Basic Geochemical Characteristics of Triassic Potential Mudstone Source Rocks.** Table 1 presents the basic geochemical characteristics of the Triassic possible source rocks in this study. Results show that the mudstones are organic-rich [38], shown by TOC values higher than 1.0% and petroleum generation (PG = S<sub>1</sub> + S<sub>2</sub>) contents higher than 2.0 mg/g rock. HI values of these samples are > 100 mg/g TOC, the kerogen δ<sup>13</sup>C value ranges from -28.86‰ to -25.70‰, and the δ<sup>13</sup>C value of the mudstone extracts varies between -26.30‰ and -30.46‰. These are indicative of type III kerogen in general and some having high HI values can be relatively oil-prone [38]. R<sub>o</sub> and T<sub>max</sub> values of these samples are generally in the range of 0.79–0.90% and 440–446°C, respectively, implying that the organic matters in the mudstones have entered the

oil-generation window [38]. Thus, the mudstones can generate both oil and gas and be regarded as potential source rocks.

**4.2. Biomarkers of Triassic Potential Mudstone Source Rocks and Their Difference to the Permian and Jurassic Source Rocks.** The biomarker composition of the eight Triassic mudstones in this study is similar and can be distinguished from the other three identified source rocks present in the central Junggar Basin (i.e., the Permian two sequences and Jurassic), setting up a good foundation for oil-source correlation and mixing calculation (Figure 3, Tables 2 and 3).

In terms of paraffin compositions, the Triassic mudstones have a carbon number of *n*-alkanes ranging from C<sub>11</sub> to C<sub>35</sub>, peaking at *n*-C<sub>20</sub> or *n*-C<sub>21</sub>. The ratios of Pr/Ph, Pr/*n*-C<sub>17</sub>, and Ph/*n*-C<sub>18</sub> range in 1.00–1.51 (averages at 1.19), 0.50–0.66 (averages at 0.56), and 0.40–0.53 (averages at 0.44), respectively, implying type II–III kerogen mixtures (Figure 4) [39]. This is consistent with the understanding obtained from the basic geochemistry above (Section 4.1). The ratio of β-carotane/*n*-alkane main peak ranges in 0.19–0.47 with an average of 0.34, suggesting that the water body of the depositional environment has certain salinity, potentially stratifying water column which provides favorable preservation of organic matter [40]. These characteristics are generally similar to typical Permian-derived oils, which are indicative of Permian mudstone source rocks (Figures 3 and 4), but are fundamentally different from typical Jurassic mudstone source rocks in the study area, which are commonly characterized by Pr/Ph values > 3.0 and low to no concentration of carotanes (Figures 3 and 4).

As for terpanes, the abundance of tricyclic terpanes (TTs) is relatively less than pentacyclic terpanes (PTs), with the ratio of main TT peak to main PT peak ranging between 0.21 and 0.34 with an average of 0.24. This implies that the organic matter in the Triassic mudstones is moderately mature in general and has a relatively big contribution from higher plants and/or prokaryotes regarding bioprecursors [3, 41]. Such characteristics are sharply different from the Jurassic mudstone source rocks in the study area, which have extremely low abundance of TTs relative to PTs (the ratio of TTs/PTs commonly less than 0.1; Figure 3(a)). Among the TT compounds, C<sub>19</sub>TT has a relatively high abundance, such that the ratios of C<sub>19</sub>TT/C<sub>21</sub>TT and C<sub>19</sub>TT/C<sub>23</sub>TT were around 0.2; this is also different from the characteristics of the Jurassic mudstone source rocks in the study area (Figures 3(c) and 3(d)). No defined distribution pattern of C<sub>20</sub>, C<sub>21</sub>, or C<sub>23</sub>TT can be observed, which is commonly regarded as a fingerprint of Permian-sourced oils indicative of source rocks in the study area [42]. The ratios of C<sub>24</sub>TeT/C<sub>26</sub>TT, Ts/Tm, and gammacerane/C<sub>30</sub> hopane average at 0.65, 0.51, and 0.12, respectively, indicative of a dual input of terrigenous higher plants and aquatic organisms from lacustrine environments [3, 21, 22]. These values provide clues to distinguish the Triassic-derived oils from the Permian- and Jurassic-derived oils in the study area (Table 4).

In terms of the sterane composition, the Triassic mudstone source rocks have relatively high abundance of pregnane and homopregnanes, as indicated by a pregnane/αααC<sub>29</sub>R

TABLE 3: Biomarker composition of saturated hydrocarbons of Triassic mudstone source rocks in the central Junggar Basin.

Well	Depth (m)	Fm.	Lithology	Type*	1	2	3	4	5	6	7	8	9	10	11	12	13	14	15	16	17	18
SM1	4180	T <sub>3b</sub>	Dark gray mudstone	N/A	8.41	33.4	30.6	27.6	0.61	0.21	0.46	0.16	0.17	0.47	0.40	0.11	0.46	0.50	34.0	25.1	41.0	0.17
SM1	4190	T <sub>3b</sub>	Dark gray mudstone	N/A	7.81	32.7	30.5	29.0	0.77	0.22	0.46	0.19	0.17	0.54	0.48	0.12	0.41	0.47	30.6	22.9	46.6	0.21
SM1	4200	T <sub>3b</sub>	Dark gray mudstone	N/A	8.29	33.1	32.5	26.2	0.96	0.23	0.34	0.23	0.20	0.58	0.66	0.10	0.39	0.44	24.9	21.6	53.5	0.18
SM1	4210	T <sub>3b</sub>	Dark gray mudstone	N/A	6.76	27.3	30.7	35.2	0.43	0.28	0.62	0.17	0.15	0.47	0.45	0.13	0.42	0.48	28.2	24.5	47.4	0.16
SM1	4218	T <sub>3b</sub>	Dark gray mudstone	N/A	7.43	32.3	29.4	30.9	0.64	0.34	0.56	0.20	0.19	0.52	0.48	0.14	0.39	0.45	26.9	24.1	49.0	0.19
SM1	4230	T <sub>3b</sub>	Dark gray mudstone	N/A	6.70	30.0	29.9	33.4	0.62	0.22	0.51	0.20	0.17	0.52	0.47	0.12	0.41	0.45	29.2	24.6	46.3	0.12
SM1	4324	T <sub>2k</sub>	Dark gray mudstone	N/A	7.10	30.5	29.5	32.9	0.51	0.22	0.64	0.16	0.18	0.48	0.44	0.14	0.40	0.46	28.1	25.1	46.8	0.14
MS1	5649.19	T <sub>2k</sub>	Sandstone extract	A	8.28	26.5	36.5	28.7	0.31	4.85	2.32	0.21	0.34	0.70	0.40	0.15	0.49	0.64	30.6	25.2	44.2	0.17
MS1	5796	T <sub>2k</sub>	Sandstone extract	A	8.06	21.8	38.6	31.5	0.63	1.23	1.00	0.20	0.13	0.48	0.39	0.09	0.53	0.49	30.2	28.4	41.3	0.15
MS1	5955	T <sub>1b</sub>	Sandstone extract	A	7.99	29.6	35.8	26.6	0.47	1.62	1.49	0.36	0.12	0.77	0.53	0.12	0.44	0.54	27.9	25.4	46.7	0.16
MS1	5981.48	T <sub>1b</sub>	Sandstone extract	A	4.98	20.0	42.3	32.7	0.40	1.32	1.02	0.17	0.14	0.42	0.45	0.14	0.42	0.46	29.3	27.1	43.5	0.22
XY1	4493	T <sub>1b</sub>	Crude oil	B	3.25	20.9	31.6	44.3	0.12	4.89	4.21	0.15	0.16	0.66	0.43	0.36	0.49	0.69	29.7	28.3	41.9	0.13
XY2	4325	T <sub>2k</sub>	Crude oil	B	3.99	24.4	32.0	39.6	0.20	1.78	3.54	0.13	0.20	0.58	0.35	0.32	0.45	0.62	22.0	29.4	48.6	0.10
Da1	4244	T <sub>2k</sub>	Crude oil	B	5.47	27.9	29.1	37.6	0.15	3.15	3.76	0.21	0.13	0.66	0.54	0.28	0.44	0.67	21.9	25.0	53.1	0.09
SM1	4508.2	T <sub>1b</sub>	Sandstone extract	B	2.79	18.6	43.0	35.6	0.15	5.74	7.54	0.11	0.25	0.70	0.46	0.34	0.61	0.73	16.3	19.9	63.8	0.17

Note. \* Type of end-member oil; N/A, not applicable; 1, C<sub>19</sub> tricyclic terpane/(C<sub>19</sub> + C<sub>20</sub> + C<sub>21</sub> + C<sub>23</sub>) tricyclic terpane (%); 2, C<sub>20</sub> tricyclic terpane/(C<sub>19</sub> + C<sub>20</sub> + C<sub>21</sub> + C<sub>23</sub>) tricyclic terpane (%); 3, C<sub>21</sub> tricyclic terpane/(C<sub>19</sub> + C<sub>20</sub> + C<sub>21</sub> + C<sub>23</sub>) tricyclic terpane (%); 4, C<sub>23</sub> tricyclic terpane/(C<sub>19</sub> + C<sub>20</sub> + C<sub>21</sub> + C<sub>23</sub>) tricyclic terpane (%); 5, C<sub>24</sub> tetracyclic terpane/C<sub>26</sub> tricyclic terpane; 6, main peak (maximum concentration) of tricyclic terpanes/main peak of hopanes; 7, Ts/Tm; 8, Tm/C<sub>30</sub>H; 9, C<sub>30</sub> moretane/C<sub>30</sub> hopane; 10, C<sub>29</sub>H/C<sub>30</sub>H; 11, C<sub>31</sub>H/C<sub>30</sub>H; 12, Gammacerane/C<sub>30</sub> hopane; 13, Sterane C<sub>29</sub>20S/(20S + 20R); 14, Sterane C<sub>29</sub>ββ/(αα + ββ); 15, Sterane αααC<sub>27</sub>20R/ααα(C<sub>27</sub>20R + C<sub>28</sub>20R) × 100%; 16, Sterane αααC<sub>28</sub>20R/ααα(C<sub>27</sub>20R + C<sub>28</sub>20R) × 100%; 17, Sterane αααC<sub>29</sub>20R/ααα(C<sub>27</sub>20R + C<sub>28</sub>20R + C<sub>29</sub>20R) × 100%; 18-Diasteranes/regular steranes.

SM 1 well, 4218 m, T<sub>3</sub>b, dark gray mudstone,

TOC = 1.36%, PG = 3.44 mg/g, HI = 211.76 mg/g,

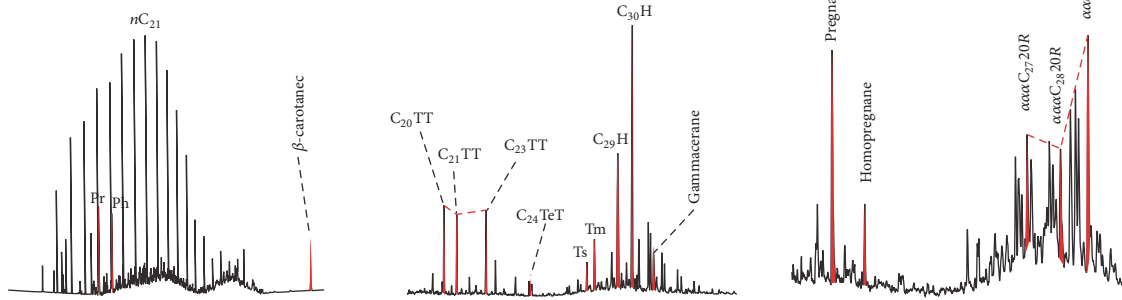
$\delta^{13}\text{C} = -29.65\text{‰}$ , Pr/Ph = 1.11,

$R_o = 0.83$ ,  $T_{\text{max}} = 445^\circ\text{C}$ ,  $C_{29} \text{ 20S}/(20\text{S} + 20\text{R}) = 0.39$ .

GC

$m/z = 191$

$m/z = 217$



(a) Triassic mudstone source rock

MO 008 well, 2926 m, J<sub>1</sub>s, carbonaceous mudstone,

TOC = 5.87%, PG = 4.93 mg/g, HI = 81.09 mg/g,

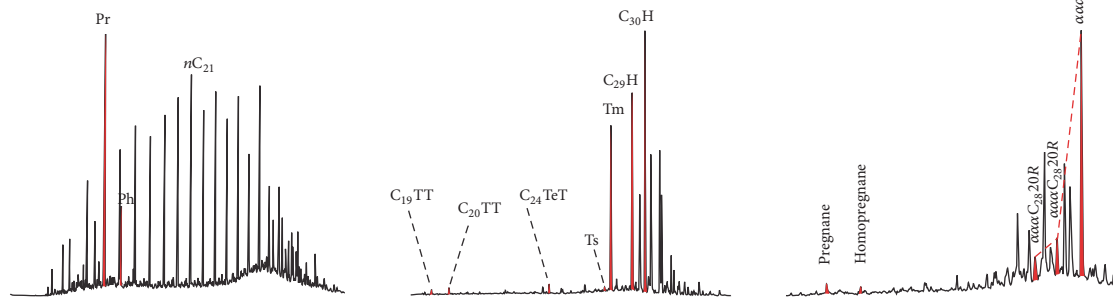
$\delta^{13}\text{C} = -26.40\text{‰}$ , Pr/Ph = 5.6,

$R_o = 1.0\%$ ,  $T_{\text{max}} = 443^\circ\text{C}$ ,  $C_{29} \text{ 20S}/(20\text{S} + 20\text{R}) = 0.40$ .

GC

$m/z = 191$

$m/z = 217$



(b) Jurassic mudstone source rock

M13 well, 4546 m, J<sub>1</sub>s<sub>2</sub><sup>2</sup>, crude oil,

Density = 0.84 g/cm<sup>3</sup>,

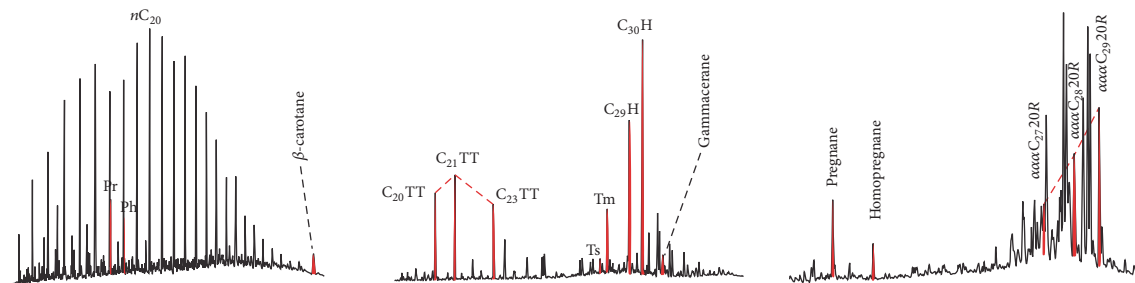
Saturate hydrocarbons = 81.02%, aromatic hydrocarbons = 8.25%, NSO = 3.01%, asphaltene = 1.27%,

$\delta^{13}\text{C} = -29.30\text{‰}$ , Pr/Ph = 1.33,  $C_{29} \text{ 20S}/(20\text{S} + 20\text{R}) = 0.48$ .

GC

$m/z = 191$

$m/z = 217$



(c) P<sub>2</sub>w mudstone source rock

FIGURE 3: Continued.

PC 2 well, 4605 m, J<sub>1</sub>s<sub>1</sub>, crude oil,  
 Density = 0.82 g/cm<sup>3</sup>,  
 Saturate hydrocarbons = 78.93%, aromatic hydrocarbons = 4.58%, NSO = 2.76%, asphaltene = 0.97%,  
 $\delta^{13}\text{C} = -30.40\text{‰}$ , Pr/Ph = 1.04, C<sub>29</sub> 20S/(20S + 20R) = 0.44.

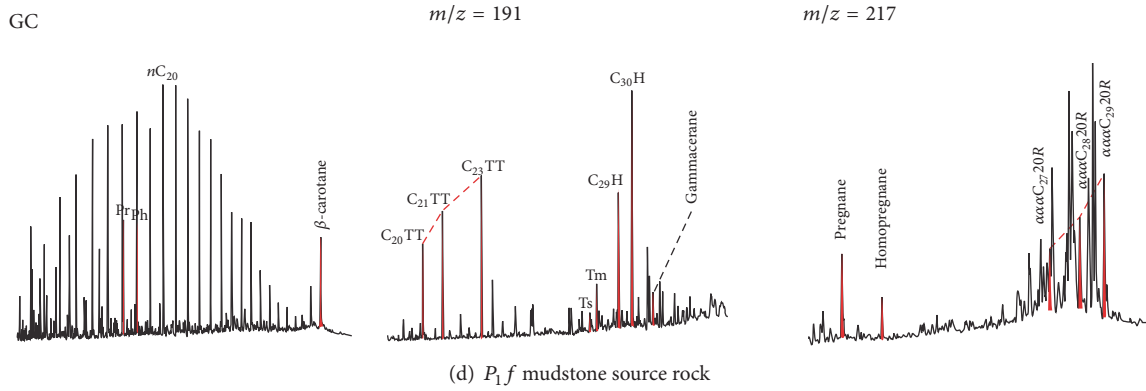


FIGURE 3: Gas chromatograms (GC) and GC-mass spectra (MS) of Triassic, Jurassic, and Permian mudstone source rocks in the central Junggar Basin. (a) Triassic mudstone source rock; (b) Jurassic mudstone source rock; (c) P<sub>2</sub>w-derived oil indicating P<sub>2</sub>w mudstone source rock; (d) P<sub>1</sub>f-derived oil indicating P<sub>1</sub>f mudstone source rock.

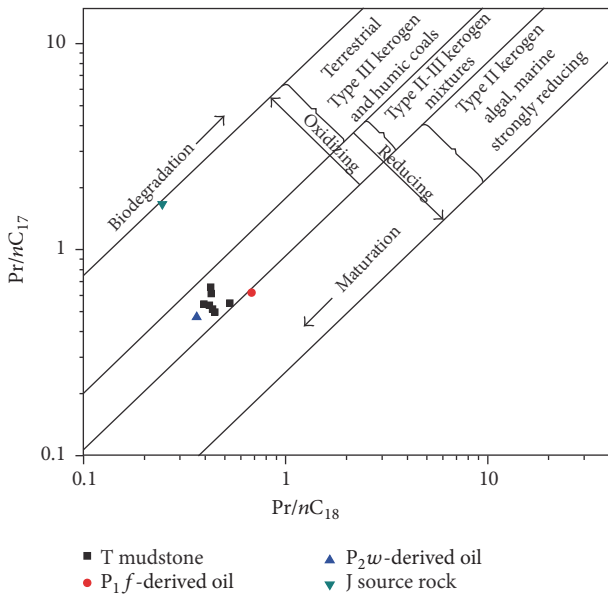


FIGURE 4: Ph/n-C<sub>18</sub> versus Pr/n-C<sub>17</sub> of the Triassic mudstone source rocks collected in this study. Average values of Permian-derived oils and Jurassic mudstone source rocks are plotted for comparison.

regular sterane ratio of nearly 1.0. Among C<sub>27</sub>, C<sub>28</sub>, and C<sub>29</sub> regular steranes, C<sub>29</sub> was the most abundant, as its percentage among the three regular steranes is between 41.0% and 53.5%; in addition, the abundance of the C<sub>27</sub> sterane is higher than that of the C<sub>28</sub> sterane, as indicated by their relative contents among the three regular steranes being 24.9–34.0% and 21.6–25.1%, respectively. These features are also suggestive of nonmarine shales [43]. These mudstones have relatively low level of diasteranes to regular steranes, with a ratio being 0.12–0.21. High diasteranes/regular steranes are typical of

petroleum derived from clay-rich mineral [44, 45]. Also, alternatively, acidic and oxic conditions facilitate diasterane formation [46, 47]. Thus, the low values of diasteranes/regular steranes of the Triassic mudstone probably are indicative of reduced to suboxic depositional environment.

In summary, the Triassic mudstone source rocks can be distinguished from Permian and Jurassic mudstone source rocks in five aspects (Table 4, Figure 5). Note that these parameters should be used in integration but not individually.

(1) *Carbon Isotope*. Compared to Permian-derived hydrocarbons indicative of source rocks (P<sub>1</sub>f < -30‰, P<sub>2</sub>w < -28‰, PDB) and Jurassic mudstone source rocks (> -28‰, PDB), the  $\delta^{13}\text{C}$  value of the Triassic mudstone source rocks is distributed in -30.46‰~-26.30‰, which is generally heavier than Jurassic mudstone source rocks and lighter than Permian-derived hydrocarbons and associated mudstone source rocks, indicative of different depositional environments and organic matter precursors.

(2) *Paraffin Composition*. The Pr/Ph value of the Triassic mudstone source rocks ranges between 1.0 and 2.0, which is similar to the P<sub>2</sub>w-derived hydrocarbons and associated mudstone source rocks, higher than the P<sub>1</sub>f-derived hydrocarbons and associated mudstone source rocks (<1.0) and lower than Jurassic mudstone source rocks (>3.0).

(3) *β-Carotane Abundance*. The value β-carotane/maximum n-alkanes of the Triassic mudstone source rocks is between 0.2 and 0.4, which is lower than the P<sub>1</sub>f-derived hydrocarbons and associated mudstone source rocks (>0.4) and higher than Jurassic-derived hydrocarbons and associated mudstone source rocks (<0.2).

(4) *Terpanes Composition*. Compared to Jurassic mudstone source rocks, the ratios of TTs/PTs of Triassic mudstone

TABLE 4: Key geochemical differences between Triassic mudstone source rocks and other three identified end-member source rocks (i.e., Jurassic and Permian) in the central Junggar Basin.

End-member source rocks		T	J	P <sub>2w</sub>	P <sub>1f</sub>
$\delta^{13}\text{C}$		-26‰~ -30‰	>-28‰	<-28‰	<-30‰
Paraffins	Main peak (maximum concentration) of <i>n</i> -alkanes	C <sub>20</sub> , C <sub>21</sub>	Mostly C <sub>23</sub> or C <sub>25</sub>	C <sub>19</sub> , C <sub>20</sub>	C <sub>17</sub>
	Pr/Ph	1.0–2.0	>3.0	1.0–2.0	<1.0
	Pr/ <i>n</i> -C <sub>17</sub> Ph/ <i>n</i> -C <sub>18</sub>	0.3–0.6	Pr/ <i>n</i> -C <sub>17</sub> > 1.0, Ph/ <i>n</i> -C <sub>18</sub> < 0.5	0.3–0.6	>0.5
$\beta$ -Carotane	$\beta$ -Carotane/maximum <i>n</i> -alkane	0.2–0.4	Very less/no	<0.2	>0.4
Terpanes	C <sub>19</sub> /C <sub>21</sub> TT	<0.2	>1.0	<0.2	<0.2
	C <sub>19</sub> /C <sub>23</sub> TT	<0.2	>1.0	<0.3	<0.2
	Distribution pattern of C <sub>20</sub> , C <sub>21</sub> or C <sub>23</sub> TT	No defined distribution pattern	C <sub>20</sub> > C <sub>21</sub> > C <sub>23</sub> , C <sub>20</sub> > C <sub>21</sub> < C <sub>23</sub>	C <sub>20</sub> < C <sub>21</sub> > C <sub>23</sub>	C <sub>20</sub> < C <sub>21</sub> < C <sub>23</sub>
	Main peak of TT/main peak of hopanes	<0.5	<0.1	0.2–1.0	0.2–1.0
	C <sub>24</sub> TeT/C <sub>26</sub> TT	>0.5	>3.0	0.2–0.5	<0.3
	Gammacerane/C <sub>30</sub> hopane	~0.1	Very less/no	<0.2	>0.3
	Ts/Tm	<1.0	<0.1	<0.5	<0.5
Steranes	C <sub>27</sub> , C <sub>28</sub> , C <sub>29</sub> regular steranes	Predominance of C <sub>29</sub> = 40–60%, C <sub>27</sub> > C <sub>28</sub>	Predominance of C <sub>29</sub> > 70%, C <sub>27</sub> < C <sub>28</sub>	Predominance of C <sub>29</sub> = 40–50%, generally C <sub>27</sub> < C <sub>28</sub>	Predominance of C <sub>29</sub> = 40–60%, generally C <sub>27</sub> < C <sub>28</sub>
	Diasteranes/regular steranes	0.1–0.2	>0.4	<0.4	<0.4

source rocks are higher (0.2–1.0). The values of C<sub>19</sub>TT/C<sub>21</sub>TT and C<sub>19</sub>TT/C<sub>23</sub>TT are both less than 0.2, which is also different from the characteristics of the Jurassic mudstone source rocks in the study area (>1.0). Ts/Tm values of Triassic mudstone source rocks (<0.4) are obviously higher than Jurassic mudstone source rocks (<0.1). Compared to Permian-derived hydrocarbons indicative of source rocks, no defined distribution pattern of C<sub>20</sub>, C<sub>21</sub>, or C<sub>23</sub>TT can be observed in Triassic mudstone source rocks, which is commonly regarded as a fingerprint of Permian-sourced oils indicative of source rocks in the study area (C<sub>20</sub> < C<sub>21</sub> > C<sub>23</sub> for P<sub>2w</sub> and C<sub>20</sub> < C<sub>21</sub> < C<sub>23</sub> for P<sub>1f</sub>) [48]. The value of gammacerane/C<sub>30</sub> hopane is also generally less than P<sub>1f</sub>-sourced hydrocarbons indicative of source rocks (>0.3). The ratio of C<sub>24</sub>TeT/C<sub>26</sub>TT of Triassic mudstone source rocks (>0.5) is higher than Permian-sourced hydrocarbons indicative of source rocks (0.2–0.5) but not as high as Jurassic mudstone source rocks (>3.0).

(5) *Steranes Composition*. Similar to Permian and Jurassic mudstone source rocks, Triassic mudstone source rocks also have a predominance of C<sub>29</sub> steranes but the percent of C<sub>29</sub> steranes is much less than Jurassic mudstone source rocks. Value of diasteranes/steranes of Triassic mudstone source rocks (0.1–0.2) is also much less than Jurassic mudstone source rocks (>0.4). Triassic mudstone source rocks show a distinct feature of C<sub>27</sub> > C<sub>28</sub> steranes which are not observed in Permian and Jurassic mudstone source rocks.

#### 4.3. Geochemistry of Triassic-Reservoired Oils and Reservoir Extracts

4.3.1. *General Geochemistry*. As shown in Table 5, the Triassic-reservoired oils collected in this study have a density of 0.81–0.86 g/cm<sup>3</sup>, a viscosity of 2.98–10.69 mPa·s, and high abundance of wax compounds (3.82–14.08%). Thus, these oils are light oils with low viscosity, which is consistent with high concentrations of saturated hydrocarbons (>75%), aromatic hydrocarbons (4.43–16.23%), and low concentrations of NSO and asphaltene (<5%) in terms of group compositions.

The abundance of reservoir extracts is all above 1000 ppm with a maximum of 11035 ppm. In terms of group compositions, a relatively large variation is observed; for example, the content of saturated hydrocarbons ranges between 52 and 92%, while asphaltenes vary between 0.75 and 10.08%. This variation implies that the reservoired hydrocarbons may have experienced complex secondary alterations, such as water washing, biodegradation, and oxidation [49, 50].

The bulk  $\delta^{13}\text{C}$  of the crude oils and extracts range within -30.27‰ ~ -27.75‰.

4.3.2. *Biomarkers*. As shown in Figure 6 and Tables 2 and 3, the biomarker compositions of the Triassic-reservoired crude oils and reservoir extracts in the study area can be generally divided into two types. Note that molecular compositions of oil are influenced by maturity and secondary alterations [3].

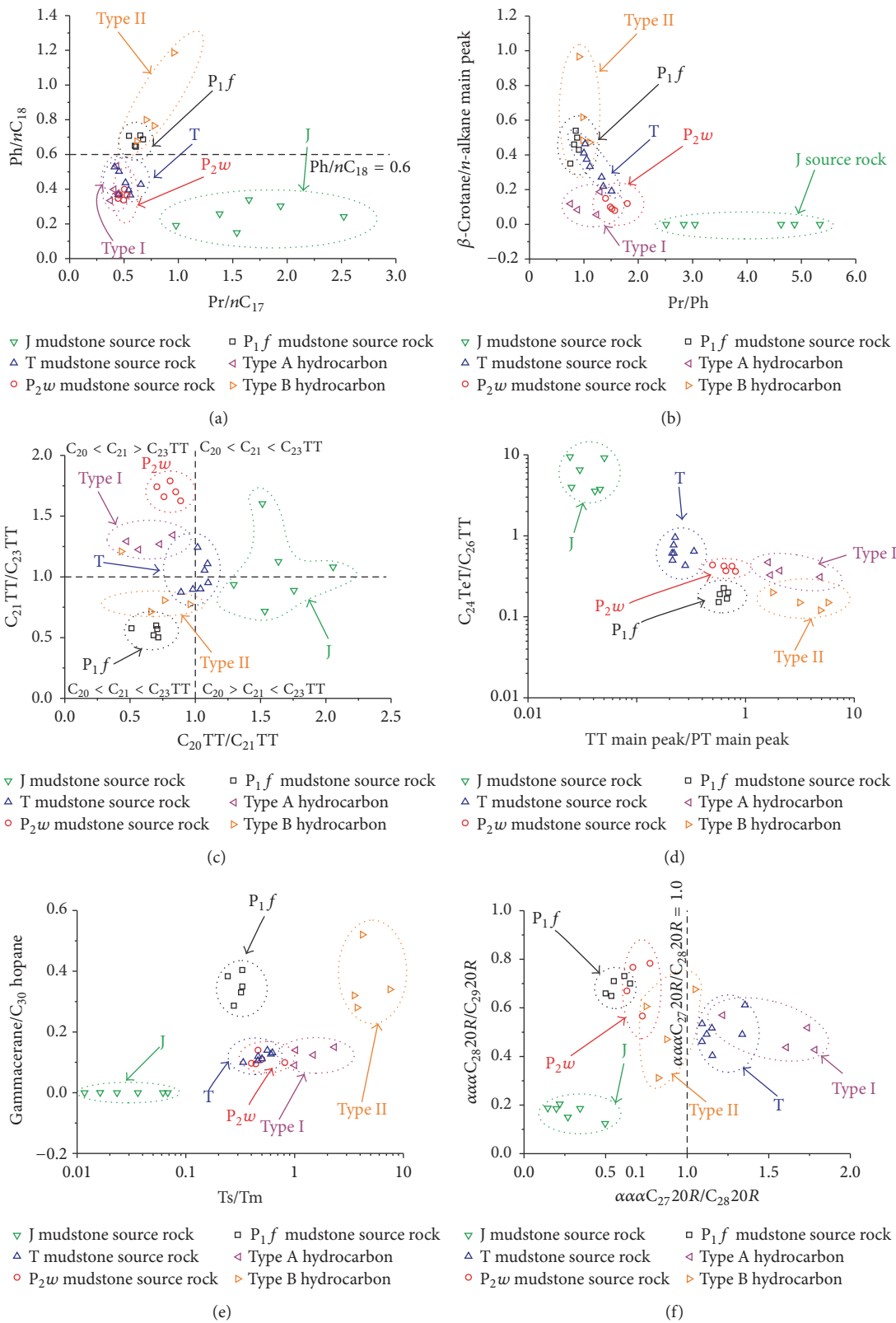


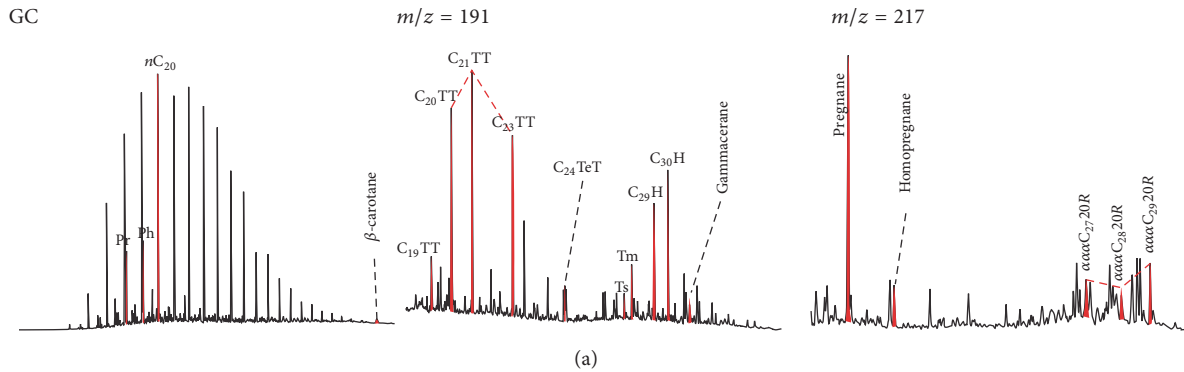
FIGURE 5: Correlation of key biomarkers that distinguish the Permian, Jurassic, and Triassic mudstone source rocks and Triassic oil-source correlation in the central Junggar Basin. (a)  $Pr/n-C_{17}$  versus  $Ph/n-C_{18}$ ; (b)  $Pr/Ph$  versus  $\beta$ -carotane/*n*-alkane main peak; (c)  $C_{20}/C_{21}TT$  versus  $C_{21}/C_{23}TT$ ; (d) regular sterane  $\alpha\alpha C_{27}20R/C_{28}20R$  versus  $\alpha\alpha C_{28}20R/C_{29}20R$ ; (e)  $Ts/Tm$  versus gammacerane/ $C_{30}$  hopane; (f)  $TT$  main peak/ $PT$  main peak versus  $C_{24}TeT/C_{26}TT$ .  $TT$ : tricyclic terpane.  $TeT$ : tetracyclic terpane.  $PT$ : pentacyclic terpane.

TABLE 5: Basic geochemical characteristics of Triassic reservoir crude oils and extracts in the central Junggar Basin.

Well	Depth (m)	Fm.	Sample type	1	2	3	4	5	6	7	8	9	10
MS1	5649.19	T <sub>2</sub> k	Sandstone extract	1132	N/A	N/A	N/A	N/A	89.64	5.12	2.75	0.75	-30.11
MS1	5796.00	T <sub>2</sub> k	Sandstone extract	3602	N/A	N/A	N/A	N/A	67.03	15.52	12.37	3.36	-29.19
MS1	5955.00	T <sub>1</sub> b	Sandstone extract	1570	N/A	N/A	N/A	N/A	69.69	15.64	8.93	2.77	-30.27
MS1	5981.48	T <sub>1</sub> b	Sandstone extract	2002	N/A	N/A	N/A	N/A	91.66	5.30	1.26	1.38	-29.70
XY1	4493.00	T <sub>1</sub> b	Crude oil	N/A	0.84	10.69	14.08	23	85.05	6.69	0.51	0.45	-28.98
XY2	4325.00	T <sub>2</sub> k	Crude oil	N/A	0.86	10.58	3.82	13	75.97	16.23	3.03	0.22	-29.03
Da 1	4244.00	T <sub>2</sub> k	Crude oil	N/A	0.81	2.98	5.67	11	88.87	4.43	3.46	1.48	-27.75
SMI	4508.20	T <sub>1</sub> b	Sandstone extract	11035	N/A	N/A	N/A	N/A	51.87	4.41	4.65	10.08	-29.61

Note. 1, chloroform A (ppm); 2, oil density ( $\text{g}/\text{cm}^3$ ); 3, viscosity @ 50°C (mPa·s); 4, wax content (%); 5, freezing point (°C); 6, saturated hydrocarbons (%); 7, aromatic hydrocarbons (%); 8, NSO (%); 9, asphaltene (%), and 10,  $\delta^{13}\text{C}$  (‰). N/A, not applicable.

MS 1 well, 5955 m, T<sub>1</sub>b, sandstone extract,  
 Chloroform bitumen content = 1570 ppm,  
 Saturate hydrocarbons = 69.69%, aromatic hydrocarbons = 15.64%, NSO = 8.93%, asphaltene = 2.77%,  
 $\delta^{13}\text{C} = -30.11\text{‰}$ , Pr/Ph = 0.88,  
 $C_{29}\text{-}20\text{S}/(20\text{S} + 20\text{R}) = 0.44$ ,  $C_{29}\text{-}\beta\beta/(\alpha\alpha + \beta\beta) = 0.54$ .



Da 1 well, 4244 m, T<sub>2</sub>k, crude oil,  
 Density =  $0.81\text{ g/cm}^3$ ,  
 Saturate hydrocarbons = 88.87%, aromatic hydrocarbons = 4.43%, NSO = 3.46%, asphaltene = 1.48%,  
 $\delta^{13}\text{C} = -27.75\text{‰}$ , Pr/Ph = 1.11,  
 $C_{29}\text{-}20\text{S}/(20\text{S} + 20\text{R}) = 0.44$ ,  $C_{29}\text{-}\beta\beta/(\alpha\alpha + \beta\beta) = 0.67$ .

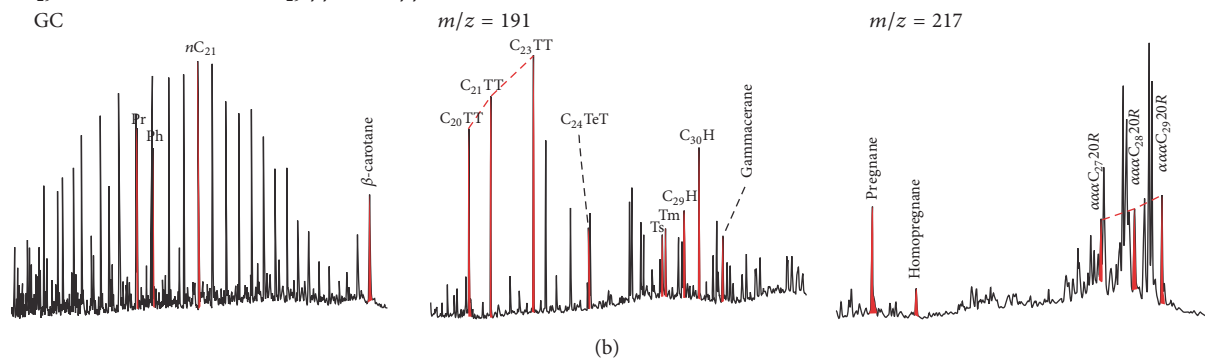


FIGURE 6: Gas and mass chromatograms of Triassic-reservoired oils and reservoir extracts in the central Junggar Basin. (a) The end-member type A. (b) The end-member type B. See text for the classification of these two types.

In this study, the maturity of oils and reservoir extracts only has a slight variation according to the two sterane parameters, that is,  $C_{29}\text{ }20\text{S}/(20\text{S} + 20\text{R})$  and Sterane  $C_{29}\beta\beta/(\alpha\alpha + \beta\beta)$  (Table 3). Secondary alterations of oil (e.g., water washing, biodegradation, and oxidation) are weak (Figure 6). Thus, these two effects cannot influence the determination of oil classification and oil-source correlation.

The type A oils in this study can be exemplified by the sandstone extracts from well MS 1. These samples have relatively low Pr/*n*-C<sub>17</sub> and Ph/*n*-C<sub>18</sub> ratios, which are in the ranges of 0.38–0.44 and 0.33–0.53, respectively. They have low  $\beta$ -carotane contents, as the ratio of  $\beta$ -carotane/*n*-alkane main peak ranges between 0.06 and 0.19. The distribution patterns of C<sub>20</sub>, C<sub>21</sub>, and C<sub>23</sub> TT all follow the order of C<sub>20</sub> < C<sub>21</sub> > C<sub>23</sub> with the C<sub>23</sub> abundance mostly being higher than that of the C<sub>20</sub>TT. Relatively high concentrations of C<sub>24</sub>TeT were observed, such that all the samples have C<sub>24</sub>TeT/C<sub>26</sub>TT ratios greater than 0.3. The Ts/Tm ratios of these samples are 1.0–3.0. The concentrations of gammacerane are low in these samples,

as evidenced by the ratio of gammacerane to C<sub>30</sub> hopane being less than 0.2. The regular steranes are dominated by C<sub>29</sub> and the C<sub>27</sub> > C<sub>28</sub> regular steranes.

The type B oils in this study consist of the crude oils from the Da 1, XY 1, and XY 2 wells and one sandstone extract from well SM 1. These oils and extracts have biomarker characteristics remarkably different from those of type A. They have relatively high Pr/*n*-C<sub>17</sub> and Ph/*n*-C<sub>18</sub> ratios, which are in the ranges of 0.91–1.11 and 0.62–0.96, respectively. These samples have very high concentrations of  $\beta$ -carotane, as demonstrated by ratios of  $\beta$ -carotane/*n*-alkane main peak between 0.47 and 0.97. The distribution patterns of C<sub>20</sub>, C<sub>21</sub>, and C<sub>23</sub> TT all follow the order of C<sub>20</sub> < C<sub>21</sub> < C<sub>23</sub>. The C<sub>24</sub>TeT content is significantly low as the C<sub>24</sub>TeT/C<sub>26</sub>TT ratios are all less than 0.2. The samples have abundant gammacerane, as evidenced by the ratios of gammacerane to C<sub>30</sub> hopane in the range of 0.28–0.52. The regular steranes are dominated by C<sub>29</sub> (40–60%) and the concentration of the C<sub>27</sub> regular sterane is generally close to that of C<sub>28</sub>.

#### 4.4. Oil-Source Correlation

**4.4.1. Insights from Stable Carbon Isotopes.** The bulk  $\delta^{13}\text{C}$  of the type A and type B Triassic-reservoired crude oils and reservoir extracts is similar which varies within  $-30.27\sim-29.70\%$  and  $-29.61\sim-27.75\%$ , respectively. These values are generally consistent with the Triassic mudstone source rocks, whose bulk  $\delta^{13}\text{C}$  ranges between  $-30.46\%$  and  $-26.30\%$  and different to Jurassic and Permian source rocks, whose bulk  $\delta^{13}\text{C}$  values are generally  $>-28\%$  and  $<-30\%$ , respectively. This might suggest that Triassic mudstone source rocks have contributions to the Triassic-reservoired hydrocarbons.

**4.4.2. Insights from Biomarkers.** To perform the oil-source correlation, we use some indicative biomarker ratios (Figure 5). Results show that the type A oils and extracts have similar Pr/ $n\text{-C}_{17}$  and Ph/ $n\text{-C}_{18}$  ratios to  $P_2w$  sourced hydrocarbons and Triassic source rocks (Figure 5(a)). In contrast, the type B oils and extracts are very close to those of the  $P_1f$  sourced hydrocarbons (Figure 5(a)).

An examination of  $\beta$ -carotane (Figure 5(b)) indicates that the type A oils and extracts are similar to  $P_2w$  sourced hydrocarbons, as the ratios of  $\beta$ -carotane/ $n$ -alkane main peak are all less than 0.2. In contrast, the type B oils and extracts exhibit the ratios similar to  $P_1f$  sourced hydrocarbons, with the values of  $\beta$ -carotane/ $n$ -alkane main peak all greater than 0.4. The Triassic source rocks have values of  $\beta$ -carotane/ $n$ -alkane main peak generally between type A and type B oils and extracts.

In terms of the distribution pattern of  $C_{20}$ ,  $C_{21}$ , and  $C_{23}$  TT (Figure 5(c)), the type A oils and extracts are similar to  $P_2w$  sourced hydrocarbons in the order of  $C_{20} < C_{21} > C_{23}$ . The type B oils and extracts are similar to  $P_1f$  sourced hydrocarbons, as the pattern of  $C_{20} < C_{21} < C_{23}$  is dominant. In contrast, the Triassic source rocks exhibit diverse distribution patterns of  $C_{20}$ ,  $C_{21}$ , and  $C_{23}$  TT, with  $C_{20} > C_{21} > C_{23}$  in dominance.

Figure 5(d) shows that both the type A and type B oils and extracts have the ratio of the TT main peak/PT main peak (0.74–5.74) significantly higher than those of the Triassic and Jurassic source rocks. As this ratio is not only controlled by the hydrocarbon source but also influenced by hydrocarbon maturity [3, 51], the high value  $> 1.0$  might also be influenced by higher levels of maturity of the oils and extracts [46]. As indicated in Figure 5(d), the high Ts/Tm ratios correlate well with the highly mature Permian oil [48, 52].

Figure 5(e) shows that the Ts/Tm ratios of the two types of oils and extracts are significantly higher than those of the Triassic and Jurassic-sourced rocks. Similar to the relative abundance of TT/PT, the Ts/Tm ratio is also influenced by both organic facies and maturity of the organic matter [46]. As such, such high Ts/Tm ratios could also be caused by high maturity of the Triassic-reservoired hydrocarbons, similar to the TT/PT ratio as discussed above. Shown by Figure 5(e), the high Ts/Tm ratios correlate well with the highly mature Permian oil [48, 52].

Regarding the gammacerane concentration (Figure 5(e)), the type A oils and extracts are similar to the  $P_2w$  sourced

hydrocarbons and Triassic mudstone source rocks in their low content, as the ratios of gammacerane/ $C_{30}$  hopane are all less than 0.2. In contrast, type B oils and extracts exhibit the ratios of gammacerane/ $C_{30}$  hopane greater than 0.2, similar to those of the  $P_1f$  source hydrocarbons.

Figure 5(f) reveals that each type of oils and extracts has samples with regular sterane compositions of either  $C_{27} < C_{28}$  or  $C_{27} > C_{28}$ . As discussed above, the Permian and Jurassic-sourced hydrocarbons are generally characterized by  $C_{27} < C_{28}$ , whereas the  $C_{27} > C_{28}$  pattern is found only in Triassic source rocks in the study area. This suggests that the Triassic oils and extracts are likely influenced by the contribution of Triassic-generated oils, especially for the type A samples.

Based on the above results and discussion, it appears that both the two types of oils and extracts are derived little from the Jurassic source rocks in terms of either carbon isotopes or biomarker compositions. In contrast, there are many overlaps in carbon isotopes and biomarker compositions between the Triassic-reservoired hydrocarbons and the Permian and Triassic source rocks. Thus, we interpret the Triassic-reservoired crude oils and reservoir extracts as a mix of Permian and Triassic source rocks. The contribution from the Triassic source rocks is particularly exemplified by the distribution pattern of regular steranes  $C_{27}$ ,  $C_{28}$ , and  $C_{29}$ . This pattern is characterized by  $C_{27} < C_{28} < C_{29}$  for both  $P_1f$ - and  $P_2w$ -sourced hydrocarbons [48, 53, 54]. However, Triassic-sourced hydrocarbons have distinctive pattern of  $C_{27} > C_{28} < C_{29}$  which is also observed in the eastern Junggar Basin [14, 15]. This strongly implies that the Triassic-reservoired oils and extracts in the central Junggar Basin have some contributions from Triassic source rocks, especially those having regular steranes  $C_{27} > C_{28}$ .

**4.4.3. Rough Evaluation of Oil-Source Contributions.** To quantitatively constrain the contribution from Triassic source rocks to Triassic-reservoired hydrocarbons, a mathematical calculation method was employed, although it is rather difficult to determine the relative contribution to mixed oils of three or more source rocks [3, 14, 15]. We estimate the proportional contributions by using the end-member oils from the different source rocks. In theory, representative end-member Permian- and Triassic-sourced oils that have similar maturity with the Triassic-reservoired hydrocarbons should be used. However, the Permian-sourced end-member oils used in this study may have different maturities to the Triassic-reservoired crude oils and extracts shown by the higher values of Ts/Tm and TTs/PTs of the Triassic-reservoired crude oils and extracts. Thus, only the biomarker ratios independent of maturity were selected for the calculation. As such, the parameters used in this study include  $\delta^{13}\text{C}$ ,  $C_{24}\text{TeT}/C_{26}\text{TT}$ , Pr/Ph,  $C_{27}/C_{28}$  regular sterane, and gammacerane/ $C_{30}$  hopane.

However, due to complex mixing mechanism and possible alteration during and after mixing, the relationship between sources and mixed oils might be nonlinear and the calculation of mixing proportion based on biomarker ratios may lead to incorrect results. Under these circumstances, average values of biomarker ratios were used. Therefore, average values of the  $P_2w$ - and  $P_1f$ -sourced oils are used

TABLE 6: Representative parameters and their values used in calculation of oil-source contribution.

Well/Fm.	Source	$\delta^{13}\text{C}$	Pr/Ph	$\text{C}_{24}\text{TeT}/\text{C}_{26}\text{TT}$	$\text{C}_{27}/\text{C}_{28}$ sterane	Gammacerane/ $\text{C}_{30}$ hopane
M101/ $J_1s$	$P_2w$	-28.82	1.48	0.44	0.72	0.10
M106/ $J_1s$	$P_2w$	-28.81	1.57	0.42	0.63	0.15
SN31/ $K_1tg$	$P_2w$	-28.34	1.80	0.39	0.67	0.10
S015/ $J_1s$	$P_2w$	-29.15	1.52	0.37	0.77	0.11
S022/ $J_1b$	$P_2w$	-29.36	1.40	0.36	0.75	0.14
S001/ $J_1b$	$P_1f$	-30.83	0.85	0.15	0.61	0.32
S022/ $J_1b$	$P_1f$	-30.64	0.91	0.17	0.54	0.36
SX1/ $J_1b$	$P_1f$	-30.60	0.88	0.20	0.50	0.42
Lu9/ $K_1tg$	$P_1f$	-30.44	0.75	0.23	0.65	0.40
Lu12/ $K_1tg$	$P_1f$	-30.39	0.82	0.19	0.55	0.35
N/A	$P_2w^*$	-28.90	1.55	0.40	0.71	0.12
N/A	$P_1f^*$	-30.58	0.84	0.19	0.57	0.37
N/A	Triassic*	-28.57	1.19	0.65	1.20	0.12

Note. \* Average value of the source, that is, value used to represent each group. N/A, not applicable.

as representative values of Permian-sourced hydrocarbons. Average values of the Triassic mudstone extracts are used to represent values of Triassic-sourced hydrocarbons. Average values of the type A and type B crude oils and extracts are used as representative features of mixed oils to calculate proportions of different sources to the type A and type B hydrocarbons, respectively. The values are listed in Table 6. Secondly, for the three-sourced mixed oil, the following equations can be used to estimate the contribution of each input:

$$\begin{aligned}
 f_1 + f_2 + f_3 &= 1, \\
 X_{11}f_1 + X_{12}f_2 + X_{13}f_3 &= Y_1, \\
 X_{21}f_1 + X_{22}f_2 + X_{23}f_3 &= Y_2, \\
 0 < f_1, f_2, f_3 < 1,
 \end{aligned} \tag{1}$$

where  $X_{ij}$  refers to biomarker ratio of each source,  $Y_i$  refers to the biomarker ratio of mixed oils and  $f_i$  refers to the proportion of each source. Based on those constrained mathematical conditions above, linear regression shows that contributions of Triassic source rocks to the type A and type B hydrocarbons are 67% and 31%, respectively. The contributions of  $P_2w$  source rocks to the type A and type B hydrocarbons are 22% and 5%, respectively. The contributions of  $P_1f$  source rocks to the type A and type B hydrocarbons are 11% and 64%, respectively. Thus, the mixing calculation results show that both the type A and type B hydrocarbons have contributions from Triassic source rocks to varying degrees.

**4.5. Implications for Oil-Generation Potential of the Triassic Lacustrine Mudstone.** As outlined above, the critical issue for the hydrocarbon potential of Triassic mudstones in the Junggar Basin is its oil generation. The discovered oil accumulations in the study area to date are mainly Permian-sourced. However, our study suggests that the two types of Triassic-reservoired oils and extracts cannot be fully excluded from the infiltration of Triassic-generated oils. Thus, the Triassic

mudstones in the Junggar Basin might have oil-generation potential, although the contribution from these Triassic-generated oils may be relatively small. This suggests that the Triassic mudstones are likely a set of important oil-source rocks that have been overlooked in previous exploration and studies. Triassic-sourced hydrocarbons might be accumulated in depressions which are poorly explored, as mudstones in these areas have organic matter of higher organic abundance and better organic matter type relative to those in uplifts [55, 56].

However, note that both the two types of Triassic-reservoired hydrocarbons in this study are similar to the Permian-sourced oils in terms of overall geochemical characteristics. Thus, the subsequent studies should focus on elucidating the Triassic evolution of hydrocarbon generation and accumulation and on more reliably quantifying the contribution from the Triassic-generated oils, thereby providing more accurate information for exploration.

In summary, the Triassic lacustrine mudstones in the Junggar Basin could be another set of effective source rocks and thus a new Triassic petroleum system might exist.

## 5. Conclusions

(1) The deep-buried Triassic lacustrine mudstone source rocks in the central Junggar Basin have distinctive bulk carbon isotopes and biomarker compositions that are distinguishable from the generally accepted Permian and Jurassic source rocks. The average  $\delta^{13}\text{C}$  values of the kerogen and extracts from the Triassic mudstones are  $-26.77\text{‰}$  and  $-28.57\text{‰}$ , respectively. In terms of biomarkers, these mudstones have Pr/Ph of approximately 1.2,  $\text{C}_{24}\text{TeT}/\text{C}_{26}\text{TT}$  around 0.65, and gammacerane/ $\text{C}_{30}$  hopane averaging at 0.12. In addition, the rocks contain more  $\text{C}_{27}$  than  $\text{C}_{28}$  regular steranes.

(2) The deep-buried Triassic-reservoired oils and extracts in the central Junggar Basin can be geochemically divided into two types. Both of these two types, especially type A, have oil contribution from the Triassic mudstones. The

proportions for type A and type B hydrocarbons are 67% and 31%, respectively. This implies the oil-generation potential of the Triassic lacustrine mudstones in the central Junggar Basin.

(3) Given the wide distribution of the Triassic mudstones throughout the Junggar Basin and favorable geochemical features, the deep-buried Triassic lacustrine mudstones are likely another set of important hydrocarbon source rocks in the basin. As such, the Triassic mudstones deserve more attention and require further study to elucidate their hydrocarbon potential and an evaluation of the Triassic petroleum system is required.

## Conflicts of Interest

The authors declare that they have no conflicts of interest.

## Acknowledgments

The authors thank Professors Xiaorong Luo and Shuichang Zhang for their encouragement to complete the manuscript. This work was jointly funded by National Science and Technology Major Project of China (Grant no. 2016ZX05001-005) and National Natural Science Foundation of China (Grant nos. 41322017 and 41472100).

## References

- [1] H. R. Grunau, "Abundance of source rocks for oil and gas worldwide," *Journal of Petroleum Geology*, vol. 6, pp. 39–54, 1983.
- [2] H. D. Klemme and G. F. Ulmishek, "Effective petroleum source rocks of the world: stratigraphic distribution and controlling depositional factors," *AAPG Bulletin*, vol. 75, no. 12, pp. 1809–1851, 1991.
- [3] K. E. Peters, C. C. Walters, and J. M. Moldowan, *The Biomarker Guide: Interpreting Molecular Fossils in Petroleum and Ancient Sediments*, Cambridge University Press, UK, second edition, 2005.
- [4] A. D. Hanson, B. D. Ritts, and J. M. Moldowan, "Organic geochemistry of oil and source rock strata of the Ordos Basin north-central China," *AAPG Bulletin*, vol. 91, no. 9, pp. 1273–1293, 2007.
- [5] D. Liang, S. Zhang, J. Chen, F. Wang, and P. Wang, "Organic geochemistry of oil and gas in the Kuqa depression, Tarim Basin, NW China," *Organic Geochemistry*, vol. 34, no. 7, pp. 873–888, 2003.
- [6] W. Ding, H. Wan, A. Su, and Z. He, "Characteristics of Triassic marine source rocks and prediction of favorable source kitchens in Qiangtang Basin, Tibet," *Energy Exploration and Exploitation*, vol. 29, no. 2, pp. 143–160, 2011.
- [7] G. Ulmishek, "Geology and petroleum resources of basins," *Argonne National Laboratory ANL/ES-146*, p. 131, 1984.
- [8] A. R. Carroll, L. Yunhai, S. A. Graham et al., "Junggar basin, northwest China: trapped Late Paleozoic ocean," *Tectonophysics*, vol. 181, no. 1–4, pp. 1–14, 1990.
- [9] S. A. Graham, S. Brassell, A. R. Carroll et al., "Characteristics of selected petroleum source rocks, Xinjiang Uygur Autonomous Region, Northwest China," *AAPG Bulletin*, vol. 74, pp. 493–512, 1990.
- [10] A. R. Carroll, S. C. Brassell, and S. A. Graham, "Upper Permian lacustrine oil shales, southern Junggar Basin, northwest China," *AAPG Bulletin*, vol. 76, pp. 1874–1902, 1992.
- [11] M. S. Hendrix, S. C. Brassell, A. R. Carroll, and S. A. Graham, "Sedimentology, organic geochemistry, and petroleum potential of Jurassic Coal Measures: Tarim, Junggar, and Turpan Basins, Northwest China," *AAPG Bulletin*, vol. 79, pp. 929–958, 1995.
- [12] J. L. Clayton, J. Yang, J. D. King, P. G. Lillis, and A. Warden, "Geochemistry of oils from the Junggar basin, northwest China," *AAPG Bulletin*, vol. 81, pp. 1926–1944, 1997.
- [13] Z. Jin, J. Cao, W. Hu et al., "Episodic petroleum fluid migration in fault zones of the northwestern Junggar Basin (northwest China): Evidence from hydrocarbon-bearing zoned calcite cement," *AAPG Bulletin*, vol. 92, no. 9, pp. 1225–1243, 2008.
- [14] J. Chen, D. Liang, X. Wang et al., "Mixed oils derived from multiple source rocks in the Cainan oilfield, Junggar Basin, Northwest China. Part I: Genetic potential of source rocks, features of biomarkers and oil sources of typical crude oils," *Organic Geochemistry*, vol. 34, no. 7, pp. 889–909, 2003.
- [15] J. Chen, C. Deng, D. Liang et al., "Mixed oils derived from multiple source rocks in the Cainan oilfield, Junggar Basin, Northwest China. Part II: Artificial mixing experiments on typical crude oils and quantitative oil-source correlation," *Organic Geochemistry*, vol. 34, no. 7, pp. 911–930, 2003.
- [16] M. Wu, J. Cao, X. Wang et al., "Hydrocarbon generation potential of Triassic mudstones in the Junggar Basin, northwest China," *AAPG Bulletin*, vol. 98, no. 9, pp. 1885–1906, 2014.
- [17] G. Dam and F. G. Christiansen, "Organic geochemistry and source potential of the lacustrine shales of the Upper Triassic - Lower Jurassic Kap Stewart Formation, East Greenland," *Marine and Petroleum Geology*, vol. 7, no. 4, pp. 428–443, 1990.
- [18] L. B. Clemmensen, D. V. Kent, and F. A. Jenkins Jr., "A Late Triassic lake system in East Greenland: Facies, depositional cycles and palaeoclimate," *Palaeogeography, Palaeoclimatology, Palaeoecology*, vol. 140, no. 1–4, pp. 135–159, 1998.
- [19] Z. H. Zhang, Y. Y. Wu, K. Yu et al., "Geochemical characteristics of source rocks in Changling area, Songliao Basin," *Xinjiang Petroleum Geology*, vol. 23, pp. 501–506, 2002 (Chinese).
- [20] Z. H. Feng, W. Fang, Z. G. Li et al., "Depositional environment of terrestrial petroleum source rocks and geochemical indicators in the Songliao Basin," *Science China Earth Sciences*, vol. 54, no. 9, pp. 1304–1317, 2011.
- [21] S. S. Luo, Z. Z. Gao, and X. W. Yang, "Sedimentary system in Baixiantan formation of Baikouquan oilfield in Xinjiang," *Journal of Oil and Gas Technology*, vol. 28, pp. 15–17, 2006 (Chinese).
- [22] B. L. Liu, Q. F. Wang, and S. M. Yan, "Triassic stratigraphic and sedimentary characteristics of Well Z2 from central Junggar Basin, Xinjiang," *Journal of Stratigraphy*, vol. 32, pp. 188–193, 2008 (Chinese).
- [23] B. Z. Xian, H. B. Xu, Z. K. Jin et al., "Sequence stratigraphy and subtle reservoir exploration of Triassic system in northwestern margin of Junggar Basin," *Geological Journal of China Universities*, vol. 14, pp. 139–146, 2008 (Chinese).
- [24] D. F. He, X. F. Chen, Y. J. Zhang et al., "Enrichment characteristics of oil and gas in Junggar Basin," *Acta Petrolei Sinica*, vol. 25, pp. 1–10, 2004 (Chinese).
- [25] J. Cao, Y. Zhang, W. Hu et al., "The Permian hybrid petroleum system in the northwest margin of the Junggar Basin, northwest China," *Marine and Petroleum Geology*, vol. 22, no. 3, pp. 331–349, 2005.

- [26] Y. Q. Zhang and N. F. Zhang, "Oil/gas enrichment of large superimposed basin in Junggar Basin," *China Petroleum Exploration*, vol. 11, pp. 59–65, 2006 (Chinese).
- [27] A. R. Carroll, "Upper Permian lacustrine organic facies evolution, Southern Junggar Basin, NW China," *Organic Geochemistry*, vol. 28, no. 11, pp. 649–667, 1998.
- [28] M. J. Zhang and P. Yang, "The characteristics and analysis of reservoir-forming conditions of the Carboniferous oil and gas pools in Junggar Basin," *Journal of Xinjiang Petroleum Institute*, vol. 2, pp. 8–13, 2000 (Chinese).
- [29] G. L. Tao, W. X. Hu, J. Cao et al., "Exploration prospect of Jurassic source derived oils in the Central Junggar Basin, NW China," *Geological Review*, vol. 54, pp. 478–484, 2008 (Chinese).
- [30] J. Cao, X. Wang, P. Sun et al., "Geochemistry and origins of natural gases in the central Junggar Basin, northwest China," *Organic Geochemistry*, vol. 53, pp. 166–176, 2012.
- [31] E. S. Scalani and J. E. Smith, "An improved measure of the odd-even predominance in the normal alkanes of sediment extracts and petroleum," *Geochimica et Cosmochimica Acta*, vol. 34, no. 5, pp. 611–620, 1970.
- [32] G. R. Wang, "Classification of tectonic units and geologic evolution in the northern Xinjiang and neighboring areas," *Xinjiang Geology*, vol. 14, pp. 12–27, 1996 (Chinese).
- [33] J. Y. Li, G. Q. He, X. Xu et al., "Crustal tectonic framework of Northern Xinjiang and adjacent regions and its formation," *Acta Sedimentologica Sinica*, vol. 80, 2006 (Chinese).
- [34] Z. R. Yang and H. M. Gu, "Preliminary results of aeromagnetic data: implication for property and evolution of basement of the Junggar Basin," *Xinjiang Petroleum Geology*, vol. 8, pp. 37–45, 1987 (Chinese).
- [35] B. Zhao, "Nature of basement of Junggar Basin," *Xinjiang Petroleum Geology*, vol. 13, pp. 95–99, 1992 (Chinese).
- [36] B. Lu, J. Zhang, T. Li, and M. A. Lu, "Analysis of tectonic framework in Junggar Basin," *Xinjiang Petroleum Geology*, vol. 29, pp. 284–289, 2008 (Chinese).
- [37] F. Hao, X. Zhou, Y. Zhu, and Y. Yang, "Lacustrine source rock deposition in response to co-evolution of environments and organisms controlled by tectonic subsidence and climate, Bohai Bay Basin, China," *Organic Geochemistry*, vol. 42, no. 4, pp. 323–339, 2011.
- [38] D. F. Huang, J. C. Li, and D. J. Zhang, "Kerogen types and study on effectiveness, limitation and interrelation of their identification parameters," *Acta Sedimentologica Sinica*, vol. 2, pp. 18–33, 1984 (Chinese).
- [39] J. Hunt, *Petroleum geochemistry and geology*, W. H. Freeman and Co., New York, NY, USA, 1995.
- [40] K. E. Peters and J. M. Moldowan, "Effects of source, thermal maturity, and biodegradation on the distribution and isomerization of homohopanes in petroleum," *Organic Geochemistry*, vol. 17, no. 1, pp. 47–61, 1991.
- [41] J. K. Volkman, M. R. Banks, K. Denwer, and F. R. Aquino Neto, "Biomarker composition and depositional settings of Tasmanite oil shale from northern Tasmania, Australia," in *Proceedings of the 14th International Meeting on Organic Geochemistry*, Paris, September 18–22, 1989.
- [42] J. Cao, S. Yao, Z. Jin et al., "Petroleum migration and mixing in the northwestern Junggar Basin (NW China): constraints from oil-bearing fluid inclusion analyses," *Organic Geochemistry*, vol. 37, no. 7, pp. 827–846, 2006.
- [43] J. M. Moldowan, W. K. Seifert, and E. J. Gallegos, "Relationship between petroleum composition and depositional environment of petroleum source rocks," *AAPG Bulletin*, vol. 69, pp. 1255–1268, 1985.
- [44] I. Rubinstein, O. Sieskind, and P. Albrecht, "Rearranged sterenes in a shale: occurrence and simulated formation," *Journal of the Chemical Society: Perkin Transactions*, vol. 1, no. 19, pp. 1833–1836, 1975.
- [45] O. Sieskind, G. Joly, and P. Albrecht, "Simulation of the geochemical transformations of sterols: superacid effect of clay minerals," *Geochimica et Cosmochimica Acta*, vol. 43, no. 10, pp. 1675–1679, 1979.
- [46] J. M. Moldowan, P. Sundararaman, and M. Schoell, "Sensitivity of biomarker properties to depositional environment and/or source input in the Lower Toarcian of SW-Germany," *Organic Geochemistry*, vol. 10, no. 4–6, pp. 915–926, 1986.
- [47] D. Brincaat and G. Abbott, "Some aspects of the molecular biogeochemistry of laminated of massive rocks from the Naples Beach Section (Santa Barbara-Ventura Basin)," in *The Monterey Formation: From Rocks to Molecules*, C. M. Isaacs and J. J. Rulkötter, eds., pp. 140–149, Columbia University Press, New York, NY, USA, 2001.
- [48] X. L. Wang, *Research on hydrocarbon source and accumulation of Penljingxi depression, Junggar Basin*. Nanchong, Sichuan [Ph.D. thesis], Southwest Petroleum University, Chengdu, China, 2001.
- [49] S. Larter, A. Wilhelms, I. Head et al., "The controls on the composition of biodegraded oils in the deep subsurface - Part I: Biodegradation rates in petroleum reservoirs," *Organic Geochemistry*, vol. 34, no. 4, pp. 601–613, 2003.
- [50] C. M. Aitken, D. M. Jones, and S. R. Larter, "Anaerobic hydrocarbon biodegradation in deep subsurface oil reservoirs," *Nature*, vol. 431, no. 7006, pp. 291–294, 2004.
- [51] W. K. Seifert and J. Michael Moldowan, "Applications of steranes, terpanes and monoaromatics to the maturation, migration and source of crude oils," *Geochimica et Cosmochimica Acta*, vol. 42, no. 1, pp. 77–95, 1978.
- [52] X. L. Wang and S. F. Kang, "Analysis of crude origin in hinterland and slope of northwestern margin, Junggar Basin," *Xinjiang Petroleum Geology*, vol. 20, pp. 109–112, 1999 (Chinese).
- [53] X. B. Shi, X. L. Wang, J. Cao et al., "Genetic type of oils and their migration/accumulation in the Mobei-Mosuowan area, central Junggar Basin," *Acta Sedimentologica Sinica*, vol. 28, pp. 380–387, 2010, 2010 (Chinese).
- [54] F. Hao, Z. Zhang, H. Zou, Y. Zhang, and Y. Yang, "Origin and mechanism of the formation of the low-oil-saturation Moxizhuang field, Junggar Basin, China: Implication for petroleum exploration in basins having complex histories," *AAPG Bulletin*, vol. 95, no. 6, pp. 983–1008, 2011.
- [55] K. Kelts, "Environments of deposition of lacustrine petroleum source rocks: An introduction," *Geological Society Special Publication*, vol. 40, pp. 3–26, 1988.
- [56] B. J. Katz, "Controlling factors on source rock development—a review of productivity, preservation and sedimentation rate," *SEPM Special Publication*, vol. 82, N.B. Harris edition, pp. 7–16, 2005.

## Research Article

# Genetic Types and Source of the Upper Paleozoic Tight Gas in the Hangjinqi Area, Northern Ordos Basin, China

Xiaoqi Wu,<sup>1</sup> Chunhua Ni,<sup>1</sup> Quanyou Liu,<sup>2,3</sup> Guangxiang Liu,<sup>1</sup>  
Jianhui Zhu,<sup>1</sup> and Yingbin Chen<sup>1</sup>

<sup>1</sup>Wuxi Research Institute of Petroleum Geology, Petroleum Exploration and Production Research Institute, SINOPEC, Wuxi, Jiangsu 214126, China

<sup>2</sup>State Key Laboratory of Shale Oil and Gas Enrichment Mechanisms and Effective Development, Beijing 100083, China

<sup>3</sup>Petroleum Exploration and Production Research Institute, SINOPEC, Beijing 100083, China

Correspondence should be addressed to Quanyou Liu; qyouliu@sohu.com

Received 21 December 2016; Accepted 24 April 2017; Published 29 May 2017

Academic Editor: Xiaorong Luo

Copyright © 2017 Xiaoqi Wu et al. This is an open access article distributed under the Creative Commons Attribution License, which permits unrestricted use, distribution, and reproduction in any medium, provided the original work is properly cited.

The molecular and stable isotopic compositions of the Upper Paleozoic tight gas in the Hangjinqi area in northern Ordos Basin were investigated to study the geochemical characteristics. The tight gas is mainly wet with the dryness coefficient ( $C_1/C_{1-5}$ ) of 0.853–0.951, and  $\delta^{13}C_1$  and  $\delta^2H-C_1$  values are ranging from  $-36.2\text{‰}$  to  $-32.0\text{‰}$  and from  $-199\text{‰}$  to  $-174\text{‰}$ , respectively, with generally positive carbon and hydrogen isotopic series. Identification of gas origin indicates that tight gas is mainly coal-type gas, and it has been affected by mixing of oil-type gas in the wells from the Shilijiahan and Gongkahan zones adjacent to the Wulanjilinmiao and Borjianghaizi faults. Gas-source correlation indicates that coal-type gas in the Shiguhao zone displays distal-source accumulation. It was mainly derived from the coal-measure source rocks in the Upper Carboniferous Taiyuan Formation ( $C_3t$ ) and Lower Permian Shanxi Formation ( $P_1s$ ), probably with a minor contribution from  $P_1s$  coal measures from in situ Shiguhao zone. Natural gas in the Shilijiahan and Gongkahan zones mainly displays near-source accumulation. The coal-type gas component was derived from in situ  $C_3t$ - $P_1s$  source rocks, whereas the oil-type gas component might be derived from the carbonate rocks in the Lower Ordovician Majiagou Formation ( $O_1m$ ).

## 1. Introduction

Geochemical characteristics of natural gas are fundamental to the study on the origin, migration, accumulation, and alteration of natural gas and have played an important role in revealing the organic type, thermal evolution degree, and sedimentary environment of source rocks of natural gas [1–8]. The studies on the origin and source of natural gas especially unconventional gas in China have achieved significant progress in recent years [9–15]. Tight gas has made the most contribution to the rapid increase of unconventional gas output and reserves in China, and the reserves and annual production of tight gas in China at the end of 2010 accounted for 39.2% and 24.6% of the total natural gas, respectively [16]. Therefore, tight gas has been considered in priority in the exploration and exploitation of unconventional gas in

China [16]. There were 16 tight gas fields in the 48 large gas fields discovered in China by the end of 2011, suggesting the crucial importance of this type of reservoirs in China. The gas production of these 16 large tight gas fields in 2011 was  $26.799 \times 10^9 \text{ m}^3$ , accounting for 26.1% of the total gas production in China [17].

The Ordos Basin, a petroliferous basin located in central China, is the most productive basin with the highest annual gas output in China [18]. The exploration targets for natural gas in the Ordos Basin mainly consist of the Upper Paleozoic Carboniferous-Permian tight sandstone and the Lower Paleozoic Ordovician carbonate reservoirs. Several giant Upper Paleozoic tight gas fields with proven reserves over  $100 \times 10^9 \text{ m}^3$  have been discovered in the Carboniferous-Permian tight sandstone, for example, Sulige,

Yulin, Daniudi, Wushenqi, and Zizhou. The Upper Paleozoic natural gas is commonly considered as coal-type gas from the Carboniferous-Permian coal-measure source rocks [19–26]. However, the Lower Paleozoic natural gas was generally believed to be mixed by both coal-type gas from the Upper Paleozoic coal measures and oil-type gas from the marine source rocks [27–29].

The Hangjinqi area is located in northern Ordos Basin, and the gas exploration has achieved continuous breakthroughs in recent years. Natural gas is mainly enriched in the Upper Paleozoic tight sandstone reservoirs, with few discoveries in the Mesoproterozoic strata such as wells J3 and J13 [30]. The geological reserves of tight gas in the Hangjinqi area are higher than  $700 \times 10^9 \text{ m}^3$ , and the Upper Paleozoic tight gas reservoirs are characterized by the lithological traps, large gas-bearing area, and low abundance of reserves [31]. Previous studies have been conducted on the Mesozoic tectonic evolution [32], segmentation of the faults [33], geochemical characteristics of the source rocks [34, 35], and the origin of natural gas [36]. Moreover, Hao et al. [31] demonstrated the forming conditions of the gas reservoirs, and Wang et al. [37] proposed the accumulating mechanism of natural gas based on the analysis of trap conditions. However, there is no consensus on the source and accumulating pattern of natural gas. Although the Upper Paleozoic tight gas in the Hangjinqi area was commonly believed to be sourced from the Carboniferous-Permian coal measures, it is still controversial whether the gas was derived from the source rocks in situ Hangjinqi area [34, 35] or the Wushenqi area in central Ordos Basin [37]. Wang et al. [37] proposed that advantageous sandbody, unconformity, faults, and fissures constituted favorable migration pathways for the northward migration natural gas. Nevertheless, Xue et al. [34] considered that the strata in the Ordos Basin were gentle with a low dip angle, and the conditions for large-scale lateral migration were undeveloped in consideration of the Upper Paleozoic tight sandstone reservoirs. Hao et al. [31] and Chen et al. [36] demonstrated that the Upper Paleozoic natural gas to the south and north of the Sanyanjing-Wulanjilinmiao-Borjiangaizi fault zones displayed near-source and distal-source accumulation, respectively. However, Xue et al. [34] proposed that the Upper Paleozoic natural gas in the Hangjinqi area displayed near-source accumulation and was derived from in situ Upper Paleozoic coal-measure source rocks.

The above controversy is mainly derived from the different understandings on the geological conditions of tight gas in the Hangjinqi area, and geochemical characteristics of tight gas in the area have been weakly studied with a few confusions. Chen et al. [36] demonstrated that natural gas in the Shiguhao zone in northern Hangjinqi area was partially derived from source rocks in the Shilijiahan area to the south of the Borjiangaizi fault, and the gas had been affected by compositional geochromatographic effect and carbon isotopic fractionation. However, natural gas in the Shiguhao zone displayed obviously higher  $\delta^{13}\text{C}_1$  values and  $\text{C}_1/\text{C}_{1-5}$  ratios than those in the Shilijiahan zone [36], suggesting higher maturity rather than the migration effect.

The generation and alteration processes of natural gas can be revealed by the study of genetic and postgenetic molecular and isotopic fractionations based on the gas geochemical characteristics [2, 38]. Therefore, the authors intend to document the geochemical characteristics of the Upper Paleozoic tight gas based on the analyses of molecular and stable isotopic compositions in this study. We further demonstrate the origin, source, and possible postgenetic processes of tight gas in comparison with the Lower Paleozoic gas in the Jingbian gas field. This would provide valuable information for the accumulation and resource evaluation of natural gas in the Ordos Basin.

## 2. Geological Setting

The Ordos Basin is a multicycle cratonic basin with stable subsidence and located at the western margin of the North China Block covering an area of  $37 \times 10^4 \text{ km}^2$  [44]. Based on the basement property and the present tectonic morphology and characteristics, the Ordos Basin can be divided into 6 tectonic units (Figure 1), that is, Yimeng Uplift, Weibei Uplift, Jinxi Fault-fold Belt, Yishan Slope, Tianhuan Depression, and West Margin Thrust Belt [24, 45].

The Hangjinqi area is located tectonically in the Yimeng Uplift and northern Yishan Slope covering an area of  $9825 \text{ km}^2$ . It can be subdivided into 5 secondary structural units according to the fluctuation characteristics and structural configuration of the top surface of the basement, that is, Wulangeer uplift, Gongkahan uplift, Hangjinqi fault terrace, northern Yishan Slope, and the northeastern corner of the Tianhuan Depression (Figure 1). Three main faults are distributed in the Hangjinqi area from west to east, in which the Sanyanjing and Wulanjilinmiao faults are south-dipping normal faults, whereas the Borjiangaizi fault is north-dipping thrust fault (Figure 1). Seven gas zones, that is, Haoraozhao, Shiguhao, Shilijiahan, Azhen, Gongkahan, Wulanjilinmiao, and Xinzhaio, are classified according to the fault distribution (Figure 1). The Hangjinqi area was topographically a long-term inherited paleohigh in northern Ordos Basin and was considered as the favorable oriented region for oil and gas migration [46]. Gas reservoirs are found mainly in the Shiguhao and Shilijiahan zones.

The Upper Paleozoic strata in the Hangjinqi area unconformably overlie the Lower Ordovician Majiagou Formation ( $\text{O}_1\text{m}$ ) or Meso-Neoproterozoic strata ( $\text{Pt}_2\text{-Pt}_3$ ), and they consist upward of the Upper Carboniferous Taiyuan Fm. ( $\text{C}_3\text{t}$ ), Lower Permian Shanxi Fm. ( $\text{P}_1\text{s}$ ), and Lower Shihezi Fm. ( $\text{P}_1\text{x}$ ), as well as Upper Permian Upper Shihezi Fm. ( $\text{P}_2\text{sh}$ ) and Shiqianfeng Fm. ( $\text{P}_2\text{s}$ ) (Figure 2). Natural gas is mainly reservoired in the  $\text{P}_1\text{x}$  tight sandstone with only a few discoveries in the  $\text{P}_1\text{s}$  and  $\text{C}_3\text{t}$  sandstones, and these sandstone reservoirs are generally characterized by low porosity and permeability [37]. The  $\text{P}_2\text{sh}$  and  $\text{P}_2\text{s}$  strata are mainly composed of thick-layer lacustrine mudstone interbedded with sandstone, and the mudstone is widely and stably distributed with the thickness of 130 m–160 m, constituting the regional caprock for the underlying  $\text{P}_1\text{x}$  and  $\text{P}_1\text{s}$  tight gas reservoirs [31]. Moreover, natural gas has also



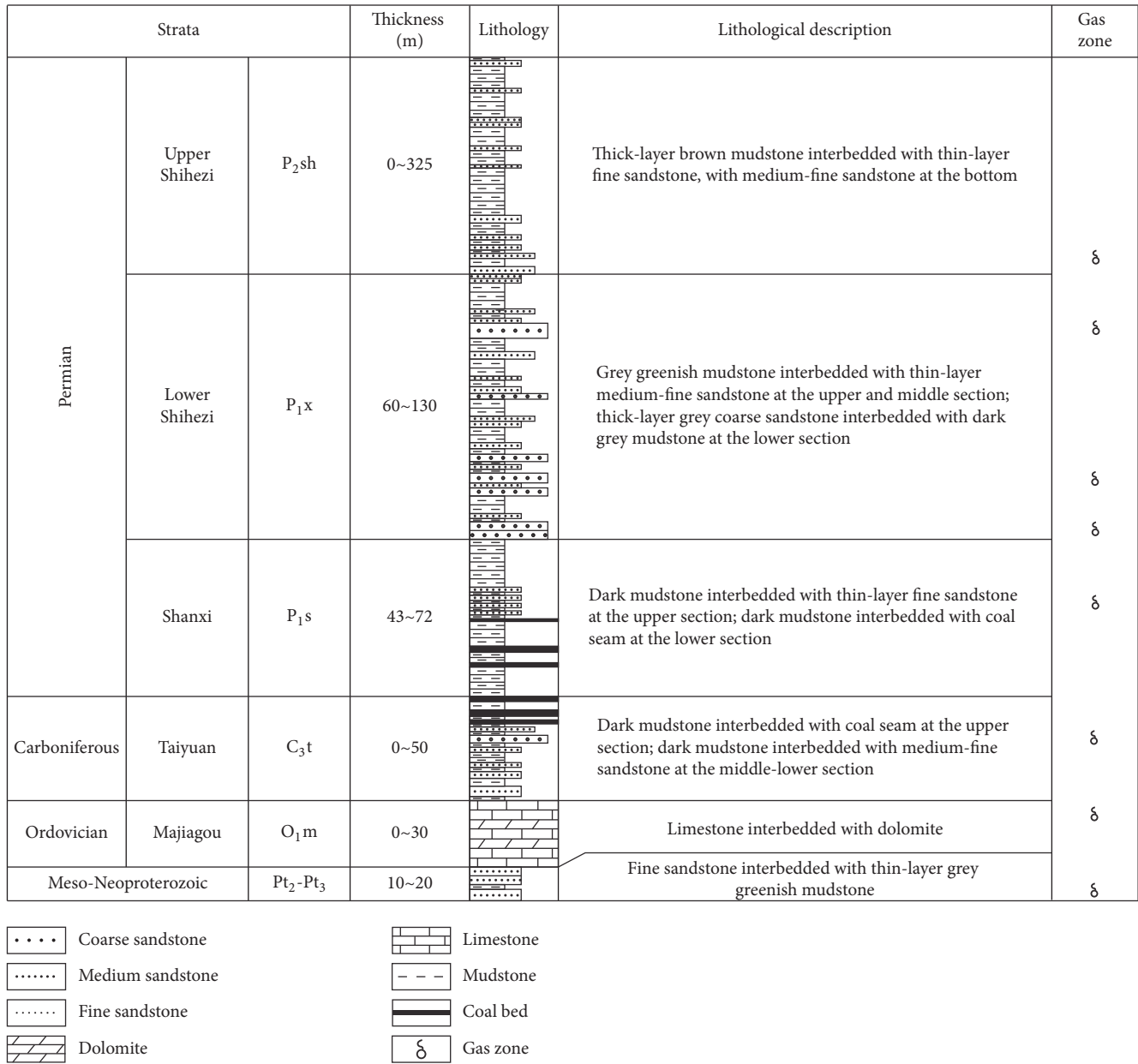


FIGURE 2: Stratigraphic column of the Hangjinqi area in the Ordos Basin.

reported in the  $\delta$  notation in permil (‰) relative to VPDB, and the measurement precision is estimated to be  $\pm 0.5\text{‰}$  for  $\delta^{13}\text{C}$ .

Stable hydrogen isotopic composition of alkane gases was measured on a Thermo Scientific Delta V Advantage mass spectrometer (GC/TC/IRMS). The alkane gas components were separated on a HP-PLOT Q column (30 m  $\times$  0.32 mm  $\times$  20  $\mu\text{m}$ ) with helium carrier gas at 1.5 ml/min. The GC oven was initially held at 30°C for 5 min and then programmed to 80°C at 8°C/min and then heated to 260°C at 4°C/min where it was held for 10 min. Each gas sample was measured in triplicate and the results were averaged. The measurement precision is estimated to be  $\pm 3\text{‰}$  for  $\delta^2\text{H}$  with respect to VSMOW.

## 4. Results

The molecular and stable isotopic compositions of the Upper Paleozoic tight gas from the Hangjinqi area are listed in Table 1.

**4.1. Chemical Composition of Natural Gas.** The P<sub>1</sub>s-P<sub>1</sub>x tight gas in the Hangjinqi area in northern Ordos Basin is dominated by methane with CH<sub>4</sub> and C<sub>2-5</sub> contents in the ranges of 83.48%–93.72% and 4.81%–14.49%, respectively. The gas is generally wet with dryness coefficient (C<sub>1</sub>/C<sub>1-5</sub>) in the range of 0.853–0.951, which is mainly lower than 0.95 (Table 1), and CH<sub>4</sub> content is positively correlated with the C<sub>1</sub>/C<sub>1-5</sub> ratio (Figure 3(a)). The Pt<sub>2</sub> gas sample from Well J101 displays CH<sub>4</sub>

TABLE 1: Molecular and stable isotopic compositions of natural gas from the Hangjinqi area in the Ordos Basin.

Gas zone	Gas well	Strata	CH <sub>4</sub>	C <sub>2</sub> H <sub>6</sub>	C <sub>3</sub> H <sub>8</sub>	iC <sub>4</sub> H <sub>10</sub>	nC <sub>4</sub> H <sub>10</sub>	iC <sub>5</sub> H <sub>12</sub>	nC <sub>5</sub> H <sub>12</sub>	N <sub>2</sub>	CO <sub>2</sub>	Chemical composition (%)					δ <sup>13</sup> C (‰, VPDB)				δ <sup>2</sup> H (‰, VSMOW)				R <sub>o</sub> (%)ⓐ	R <sub>o</sub> (%)ⓑ
												C <sub>2</sub> H <sub>4</sub>	C <sub>2</sub> H <sub>6</sub>	C <sub>3</sub> H <sub>8</sub>	iC <sub>4</sub> H <sub>10</sub>	nC <sub>4</sub> H <sub>10</sub>	iC <sub>5</sub> H <sub>12</sub>	nC <sub>5</sub> H <sub>12</sub>	C <sub>1</sub> /C <sub>1-5</sub>	δ <sup>13</sup> C <sub>1</sub>	δ <sup>13</sup> C <sub>2</sub>	δ <sup>13</sup> C <sub>3</sub>	δ <sup>13</sup> C <sub>3</sub>	δ <sup>2</sup> H-C <sub>1</sub>		
Shiguohao	J11	P <sub>1</sub> x	93.47	3.62	0.84	0.12	0.18	0.05	0.05	1.36	0.30	0.950	-32.2	-24.9	-24.5	-174	-153	-139	1.43	0.50						
	J26	P <sub>1</sub> x	93.66	3.59	0.81	0.11	0.19	0.06	0.05	1.16	0.35	0.951	-32	-25.4	-24.8	-175	-153	-146	1.48	0.52						
	J66P5H	P <sub>1</sub> x	93.22	4.33	0.94	0.11	0.21	0.05	0.07	0.84	0.21	0.942	-32.9	-24.5	-22.9	-191	-170	-156	1.28	0.45						
	J66P8H	P <sub>1</sub> x	84.35	8.32	3.28	0.68	1.12	0.56	0.53	0.25	0.00	0.853	-32.7	-26.0	-22.7	-187	-161	-124	1.32	0.46						
	J66P9H	P <sub>1</sub> x	87.04	7.79	2.50	0.45	0.72	0.34	0.30	0.39	0.00	0.878	-32.3	-25.7	-23.4	-190	-164	-126	1.41	0.49						
	JPH-13	P <sub>1</sub> x	87.28	7.36	2.52	0.43	0.70	0.34	0.31	0.27	0.00	0.882	-32.7	-26.6	-23.0	-191	-148	/	1.32	0.46						
	YS1	P <sub>1</sub> x	90.04	6.49	1.92	0.31	0.50	0.26	0.22	0.24	0.00	0.903	-32.7	-27.1	-23.2	-186	-169	-143	1.32	0.46						
	J66	P <sub>1</sub> x	88.27	7.28	2.36	0.41	0.61	0.27	0.22	0.18	0.00	0.888	-32.4	-26.3	-20.7	-184	-159	-109	1.38	0.48						
	J77	P <sub>1</sub> x	89.47	6.18	2.03	0.33	0.48	0.16	0.16	0.1	0.77	0.45	0.906	-34.7	-24.7	-25.0	-199	-171	-176	0.95	0.33					
	J55	P <sub>1</sub> s	83.48	7.14	1.86	0.18	0.38	0.08	0.07	0.07	6.76	0.03	0.896	-36.2	-24.8	-26.4	/	/	/	0.74	0.26					
Shilijiahan	J111	P <sub>1</sub> x	90.88	5.47	1.57	0.29	0.46	0.27	0.23	0.42	0.00	0.916	-32.4	-26.5	-23.3	-185	-159	-109	1.38	0.48						
	J58P13H	P <sub>1</sub> x	93.72	3.77	1.05	0.22	0.33	0.17	0.14	0.46	0.00	0.943	-32.8	-27.6	-21.3	-182	-132	/	1.30	0.45						
	J98	P <sub>1</sub> x	92.67	4.63	1.18	0.24	0.35	0.21	0.17	0.16	0.00	0.932	-32.8	-27.8	-19.5	-185	-150	-126	1.30	0.45						
	J58	P <sub>1</sub> x	90.02	5.31	1.52	0.35	0.53	0.25	0.22	1.10	0.00	0.917	-32.6	-26.3	-21.7	-180	-129	/	1.34	0.47						
	J99	P <sub>1</sub> x	90.97	5.69	1.52	0.32	0.48	0.30	0.26	0.35	0.00	0.914	-32.8	-28.7	-22.3	-184	-152	-100	1.30	0.45						
Gongkahan	J110	P <sub>1</sub> x	87.34	6.79	2.71	0.66	0.86	0.41	0.32	0.19	0.00	0.881	-32.4	-28.9	-26.6	-180	-137	-105	1.38	0.48						
	J101	Pt <sub>2</sub>	82.75	5.02	2.70	0.46	0.84	0.28	0.28	7.10	0.00	0.896	-34.5	-30.1	-31.1	-173	/	/	0.98	0.34						

Note. R<sub>o</sub> (%) (ⓐ, ⓑ) values were calculated according to the δ<sup>13</sup>C<sub>1</sub>-R<sub>o</sub> empirical equations for coal-type gas proposed by Dai and Qi [48] and Stahl [49], respectively. “/” indicates no data.

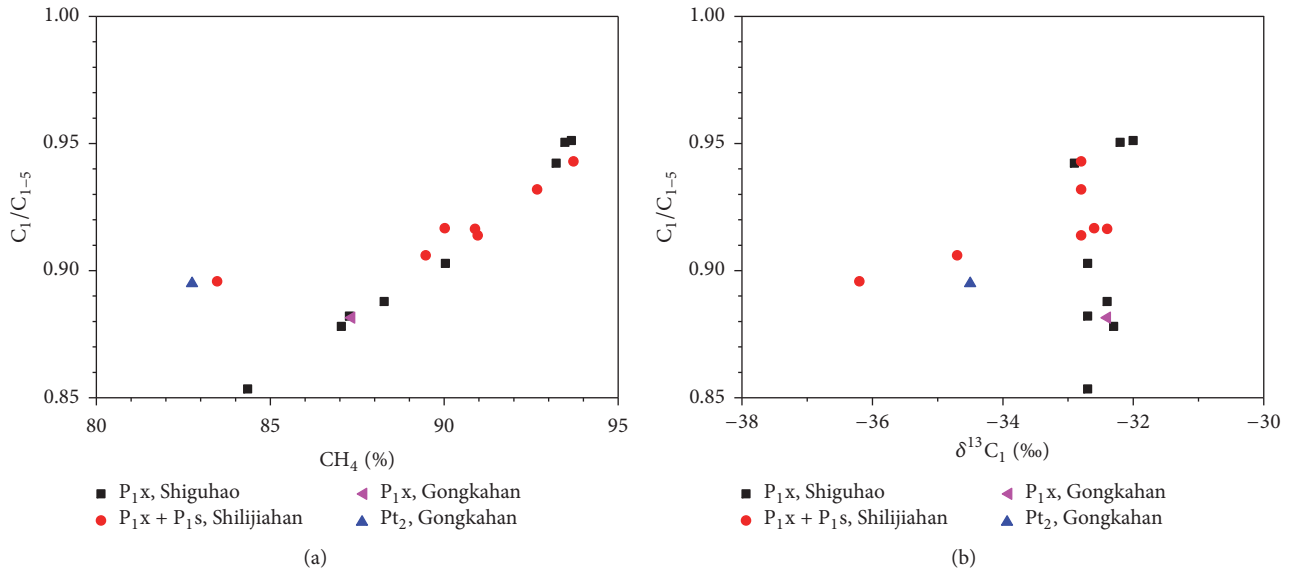


FIGURE 3: Correlation diagrams of dryness coefficient ( $C_1/C_{1-5}$ ) versus  $CH_4\%$  (a) and  $C_1/C_{1-5}$  ratio versus  $\delta^{13}C_1$  value (b) of tight gas from the Hangjinqi area in the Ordos Basin.

content of 82.75%, which is lower than the  $P_1s$ - $P_1x$  tight gas, and it is also wet gas with  $C_1/C_{1-5}$  ratio of 0.896 (Table 1, Figure 3(a)).

The  $P_1s$ - $P_1x$  tight gas in the Hangjinqi area contains few amount of  $CO_2$  with the content of 0%–0.45%, and the nonhydrocarbon component is mainly  $N_2$  with the content mainly in the range of 0.16%–1.36% (Table 1). Only one sample (J55) has  $N_2$  content of 6.76%, which is similar to the  $Pt_2$  gas sample from Well J101 (Table 1). This might be caused by the application of the technology of nitrogen gas-lift recovery, which would not affect the carbon and hydrogen isotopic compositions of alkane gas. Therefore, the carbon and hydrogen isotopic compositions of the gas samples could be used to identify the gas origin.

**4.2. Carbon Isotopic Composition.**  $\delta^{13}C_1$  value of the alkanes in the  $P_1s$ - $P_1x$  tight gas in the Hangjinqi area is from  $-36.2\%$  to  $-32.0\%$ , and it is uncorrelated with the dryness coefficient ( $C_1/C_{1-5}$ ) (Table 1, Figure 3(b)). The  $P_1s$ - $P_1x$  alkane gas displays variable  $C_1/C_{1-5}$  ratio and nearly constant  $\delta^{13}C_1$  value (from  $-32.9\%$  to  $-32.0\%$ ) except two gas samples (J55, J77) (Table 1, Figure 3(b)).  $\delta^{13}C_1$  value of the  $Pt_2$  gas sample from Well J101 is  $-34.5\%$ , which is slightly lower than the main value of the  $P_1s$ - $P_1x$  gas (Table 1, Figure 3(b)).

$\delta^{13}C_2$  and  $\delta^{13}C_3$  values of the  $P_1s$ - $P_1x$  alkane gas are from  $-28.9\%$  to  $-24.5\%$  and from  $-26.6\%$  to  $-19.5\%$ , respectively, whereas those of the  $Pt_2$  gas sample are  $-30.0\%$  and  $-31.1\%$ , respectively (Table 1, Figure 4). The  $P_1s$ - $P_1x$  alkane gas generally displays positive carbon isotopic series ( $\delta^{13}C_1 < \delta^{13}C_2 < \delta^{13}C_3$ ), with only two gas samples (J55, J77) displaying partial reversal between  $C_2H_6$  and  $C_3H_8$  carbon isotopes ( $\delta^{13}C_2 > \delta^{13}C_3$ ), which are consistent with the  $Pt_2$  gas sample from Well J101 (Figure 4).

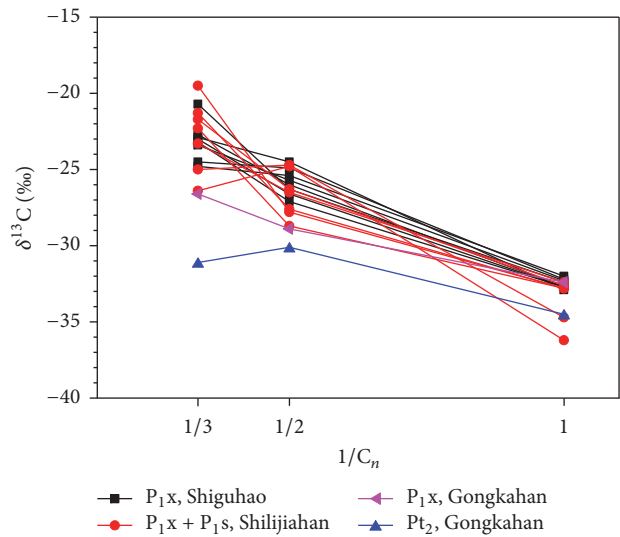


FIGURE 4: Carbon isotopic series of alkane gas in the Hangjinqi area in the Ordos Basin.

**4.3. Hydrogen Isotopic Composition.**  $\delta^2H$ - $C_1$  value of the  $P_1s$ - $P_1x$  alkane gas in the Hangjinqi area is from  $-199\%$  to  $-174\%$ , whereas that of the  $Pt_2$  gas sample from Well J101 is  $-173\%$ , and it is slightly higher than that of the  $P_1s$ - $P_1x$  gas (Table 1, Figure 5).  $\delta^2H$ - $C_2$  and  $\delta^2H$ - $C_3$  values of the  $P_1s$ - $P_1x$  alkane gas are from  $-171\%$  to  $-129\%$  and from  $-176\%$  to  $-100\%$ , respectively. The alkane gas generally displays positive hydrogen isotopic series ( $\delta^2H-C_1 < \delta^2H-C_2 < \delta^2H-C_3$ ) with only one gas sample (J77) being partially reversed between  $C_2H_6$  and  $C_3H_8$  hydrogen isotopes ( $\delta^2H-C_2 > \delta^2H-C_3$ ) (Table 1, Figure 5).

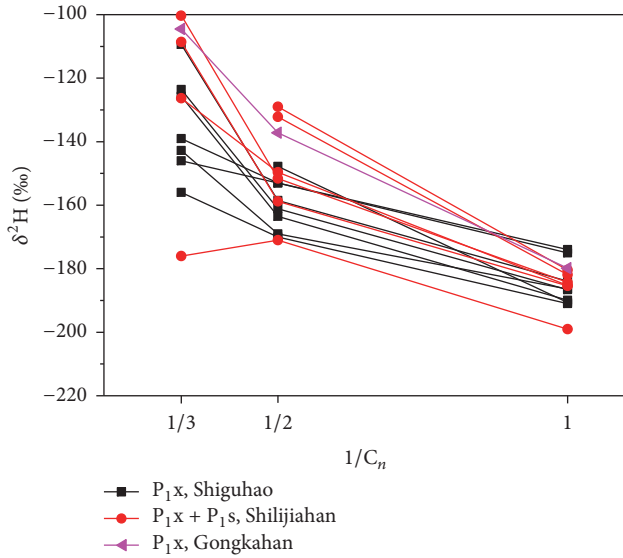


FIGURE 5: Hydrogen isotopic series of alkane gas from the Hangjinqi area in the Ordos Basin.

**5. Discussion**

*5.1. Origin of Tight Gas.* The Upper Paleozoic (P<sub>1s</sub>-P<sub>1x</sub>) alkane gas in the Hangjinqi area in northern Ordos Basin mainly displays positive carbon and hydrogen isotopic series (Figures 4 and 5) with δ<sup>13</sup>C<sub>1</sub> value higher than -30‰ (Figure 3(b)), suggesting the typically biogenic gas rather than the abiogenic one [50]. The biogenic gas can be divided into bacterial gas and thermogenic gas, in which the bacterial gas is dominated by CH<sub>4</sub> and extremely dry with C<sub>1</sub>/C<sub>1-5</sub> ratio higher than 0.99 and δ<sup>13</sup>C<sub>1</sub> value lower than -55‰, whereas thermogenic gas generally displays δ<sup>13</sup>C<sub>1</sub> value higher than -50‰ [4, 50]. The P<sub>1s</sub>-P<sub>1x</sub> and Pt<sub>2</sub> gases in the Hangjinqi area display δ<sup>13</sup>C<sub>1</sub> value and dryness coefficient ranging from -36.2‰ to -32.0‰ and from 0.853 to 0.951, respectively (Figure 3(b)). They are significantly different from the bacterial gas, and they follow the maturity trend rather than the biodegradation trend in correlation diagram between C<sub>2</sub>/C<sub>3</sub> and C<sub>2</sub>/iC<sub>4</sub> (Figure 6).

The P<sub>1s</sub>-P<sub>1x</sub> and Pt<sub>2</sub> gases in the Hangjinqi area display typical characteristics of thermogenic gas in the modified Bernard diagram (Figure 7). Thermogenic gas can be generally divided into coal-type gas from humic organic matter and oil-type gas from sapropelic organic matter [3, 50]. The Upper Paleozoic tight gas in the Hangjinqi area follows the trend of natural gas from type III kerogen, suggesting the origin of coal-type gas (Figure 7). However, the O<sub>1m</sub> gas in the Jingbian gas field lies in the mixing or transitional zone between gases from types II and III kerogens, which may indicate the trend of mixing between oil-type and coal-type gases (Figure 7). The P<sub>1s</sub>-P<sub>1x</sub> tight gas in the Hangjinqi area mainly displays a wide range of C<sub>1</sub>/C<sub>2+3</sub> ratio (7.27-21.30) with nearly constant δ<sup>13</sup>C<sub>1</sub> value (from -32.9‰ to -32.0‰), indicating certain migration trend (Figure 7).

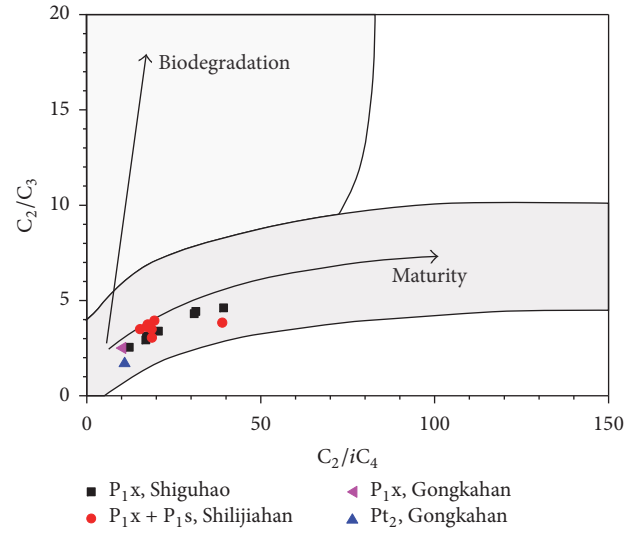


FIGURE 6: Correlation diagram between C<sub>2</sub>/C<sub>3</sub> and C<sub>2</sub>/iC<sub>4</sub> values of tight gas from the Hangjinqi area (modified after Prinzhofer and Battani [39]).

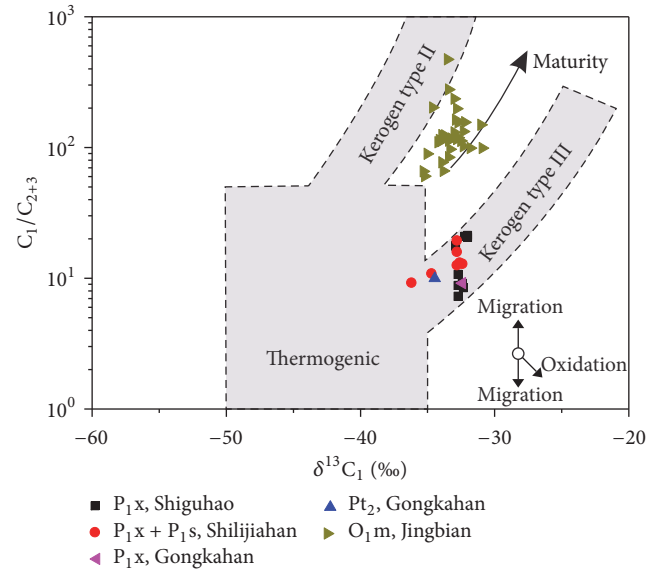


FIGURE 7: Modified Bernard diagram of tight gas from the Hangjinqi area (modified after Bernard et al. [40]). Data of the O<sub>1m</sub> gas in the Jingbian gas fields are from Dai [18].

Since coal-type gas sourced from humic organic matter has relatively higher δ<sup>13</sup>C<sub>2</sub> value than oil-type gas from sapropelic organic matter with similar δ<sup>13</sup>C<sub>1</sub> value, they follow different evolution trends in correlation diagram between δ<sup>13</sup>C<sub>1</sub> and δ<sup>13</sup>C<sub>2</sub> values [3]. The P<sub>1s</sub>-P<sub>1x</sub> gas in the Hangjinqi area generally follows the trends of gases derived from type III kerogen in the Niger Delta [3] and Sacramento Bain [41], indicating the genetic type of coal-type gas (Figure 8(a)). Several P<sub>1x</sub> gas samples are distributed in the transitional zone between gases from types II and III kerogens, and they display the characteristics of gas mixed by oil-type and

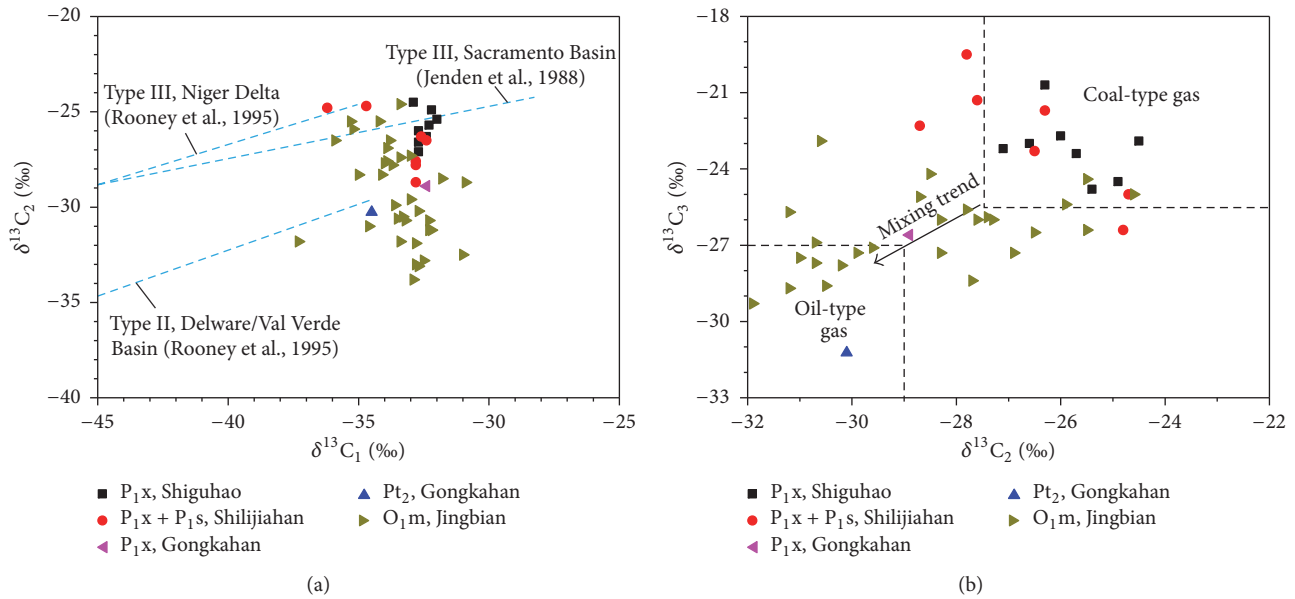


FIGURE 8: Cross-plots of  $\delta^{13}C_2$  versus  $\delta^{13}C_1$  (a) and  $\delta^{13}C_3$  versus  $\delta^{13}C_2$  (b) of tight gas from the Hangjinqi area. The trend lines for gases from kerogen type III of Niger Delta and kerogen type II of Delaware/Val Verde Basin are from Rooney et al. [3], and the trend lines for gas from kerogen type III of Sacramento Basin are from Jenden et al. [41].  $\delta^{13}C_2$  and  $\delta^{13}C_3$  ranges for coal-type and oil-type gases in (b) are from Dai [42]. Data of the  $O_{1m}$  gas in the Jingbian gas fields are from Dai [18].

coal-type gases, which are similar to the  $O_{1m}$  gas in the Jingbian gas field (Figure 8(a)). The  $Pt_2$  gas sample from the Gongkahan zone follows the trend of gas derived from type II kerogen in the Delaware/Val Verde Basin [3], indicating the characteristics of oil-type gas (Figure 8(a)).

The carbon isotopes of ethane and propane generally inherited those of original organic matter and were effective indexes to identify the coal-type and oil-type gases [50]. Empirical observations indicated that  $\delta^{13}C_2$  and  $\delta^{13}C_3$  values of coal-type gas were generally higher than  $-27.5\text{‰}$  and  $-25.5\text{‰}$ , respectively, whereas those of oil-type gas were lower than  $-29.0\text{‰}$  and  $-27.0\text{‰}$ , respectively [42]. The  $Pt_2$  gas in the Gongkahan zone displays the characteristics of oil-type gas with low  $\delta^{13}C_2$  and  $\delta^{13}C_3$  values (Figure 8(b)). The  $P_{1s}$ - $P_{1x}$  tight gas in the Hangjinqi area mainly displays the characteristics of coal-type gas, with several  $P_{1x}$  gas samples from the Shilijiahan and Gongkahan zones displaying the trend of mixing with oil-type gas, and the proportion of oil-type gas seems generally lower than that in the  $O_{1m}$  gas in the Jingbian gas field (Figure 8(b)).

The hydrogen isotopic composition of natural gas is controlled by the type of organic matter, thermal maturity, and the environmental condition of the aqueous medium and has been effectively used to identify the gas origin [1, 50–52]. The coal-type and oil-type gases display different distribution trends in correlation diagrams of both  $\delta^2H-C_1$  versus  $\delta^{13}C_1$  and  $\delta^2H-C_1$  versus  $\delta^{13}C_2$  [13]. The  $P_{1s}$ - $P_{1x}$  gas in the Hangjinqi area displays the characteristics of gases from humic organic matter and generally follows the maturity trend in correlation diagram of  $\delta^2H-C_1$  versus  $\delta^{13}C_1$  (Figure 9(a)), suggesting the genetic type of coal-type

gas. The  $O_{1m}$  gas in the Jingbian gas field also displays the characteristics of gases from humic organic matter, which indicates that the gas is dominated by coal-type gas, and this is consistent with the conclusions of previous studies [19, 53]. The  $Pt_2$  gas from the Gongkahan zone is plotted in the mixing or transitional zone, and it is adjacent to the zone of humic gases in correlation diagram of  $\delta^2H-C_1$  versus  $\delta^{13}C_1$  (Figure 9(a)), which indicates that the  $Pt_2$  gas is dominated by coal-type gas and has been mixed by a small amount of oil-type gas.

In correlation diagram of  $\delta^2H-C_1$  versus  $\delta^{13}C_2$  (Figure 9(b)), the  $P_{1x}$  tight gas from the Shiguahao zone mainly displays the characteristics of coal-type gas, whereas the  $P_{1s}$ - $P_{1x}$  gas in the Shilijiahan and Gongkahan zones generally follows the trend of mixing with oil-type gas, although it is adjacent to the range of coal-type gas. The  $O_{1m}$  gas in the Jingbian gas field also displays the mixing trend (Figure 9(b)), which is consistent with previous studies [28, 54]. However, it is generally closer to the range of oil-type gas than the  $P_{1s}$ - $P_{1x}$  tight gas in the Shilijiahan and Gongkahan zones, and this indicates that the proportion of oil-type gas in the  $O_{1m}$  gas in the Jingbian gas field is probably higher (Figure 9(b)).

Therefore, the Upper Paleozoic tight gas in the Hangjinqi area in northern Ordos Basin is mainly composed of coal-type gas.  $\delta^{13}C_2$  and  $\delta^{13}C_3$  values indicate that tight gas in the Shilijiahan and Gongkahan zones has been generally mixed by oil-type gas, and it displays similar characteristics with the  $Pt_2$  gas from the Gongkahan zone and the  $O_{1m}$  gas in the Jingbian gas field. The proportion of oil-type gas in the Upper Paleozoic gas in the Shilijiahan and Gongkahan zones is slightly lower than that in the  $O_{1m}$  gas in the Jingbian gas field.

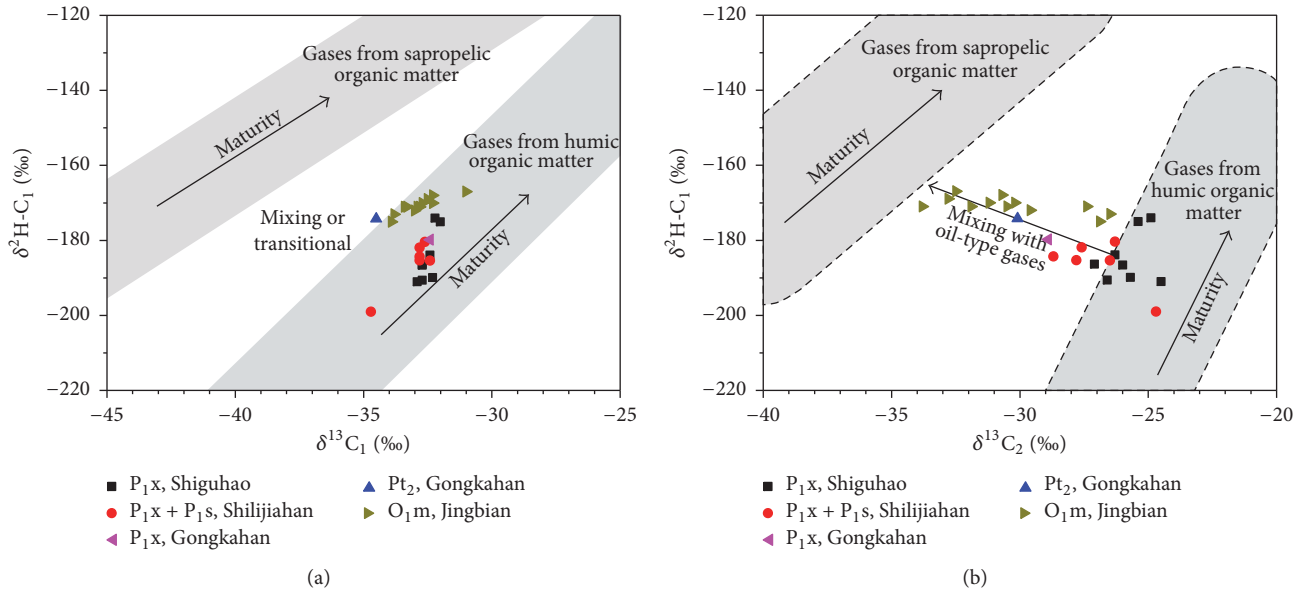


FIGURE 9: Correlation diagrams of  $\delta^2\text{H-C}_1$  versus  $\delta^{13}\text{C}_1$  (a) and  $\delta^2\text{H-C}_1$  versus  $\delta^{13}\text{C}_2$  (b) of tight gas from the Hangjinqi area (modified after Wang et al. [13]). Data of the  $\text{O}_{1m}$  gas in the Jingbian gas fields are from Dai [18].

**5.2. Source of Tight Gas.** The Upper Paleozoic coal-type gas in the Ordos Basin has been commonly accepted to be derived from the  $\text{C}_3\text{t-P}_1\text{s}$  coal-measure source rocks [19–26]. Only a set of humic source rocks, that is, the  $\text{C}_3\text{t-P}_1\text{s}$  coal measures, is developed in the Hangjinqi area in northern Ordos Basin. It is believed to be the source of the Upper Paleozoic coal-type gas in this area. However, it is controversial whether the gas was generated from in situ source rocks in the Hangjinqi area [34, 35] or had been contributed by source rocks in the Wushenqi area in central Ordos Basin [37]. Since the  $\text{C}_3\text{t}$  coal-measure source rocks are undeveloped to the north of the Borjianghaizi fault [47], there is no consensus on whether the  $\text{C}_3\text{t-P}_1\text{s}$  coal measures to the south of the fault have contributed to the  $\text{P}_1\text{s-P}_1\text{x}$  tight gas in the Shiguhao zone to the north of the Borjianghaizi fault [31, 34–36].

The  $\text{C}_3\text{t-P}_1\text{s}$  coal-measure source rocks in the Hangjinqi area are gas-prone with kerogen type III; however, the development of the  $\text{C}_3\text{t-P}_1\text{s}$  source rocks to the south and north of the Borjianghaizi fault is significantly different. Only the  $\text{P}_1\text{s}$  coal-measure source rocks are generally developed in the Shiguhao zone to the north of the Borjianghaizi fault with the thickness and  $R_0$  value generally lower than 30 m and 1.1% (Figure 1), respectively, and the cumulative gas generation intensity is in the range of  $0\text{--}10 \times 10^8 \text{ m}^3/\text{km}^2$  [31, 35]. However, both the  $\text{C}_3\text{t}$  and  $\text{P}_1\text{s}$  source rocks are developed in the Shilijiahan zone to the south of the Borjianghaizi fault with the thickness and  $R_0$  value generally higher than 30 m and 1.1% (Figure 1), respectively. The cumulative gas generation intensity is mainly in the range of  $(15\text{--}30) \times 10^8 \text{ m}^3/\text{km}^2$  [31, 35]. The exploration in recent years indicates that the gas production and reserves in the Shiguhao zone to the north of the Borjianghaizi fault with relatively poor source condition are commonly higher than those in the Shilijiahan

zone to the south of the fault with favorable source condition, respectively [31].

Thermal maturity of the source rocks could be indicated by  $\delta^{13}\text{C}_1$  value of the natural gas, and the comparison between the measured  $R_0$  values of source rocks and the calculated  $R_0$  values based on  $\delta^{13}\text{C}_1$  values provides an important approach for gas-source correlation. The  $\delta^{13}\text{C}_1\text{-}R_0$  empirical equation for coal-type gas proposed by Stahl [49] was based on the coal gas from the NW Germany, and it was suitable for the instantaneous gas generation in high-mature stage [55, 56]. The  $\delta^{13}\text{C}_1\text{-}R_0$  empirical equation for coal-type gas proposed by Dai and Qi [48] was based on the statistics of coal-type gases from main Chinese petroliferous basins and has been widely and effectively applied in China, and it was appropriate for the continuous and cumulative gas generation [55, 56].

The burial history in the Hangjinqi area indicated that the  $\text{P}_1\text{s}$  coal-measure source rocks in the Shiguhao zone had just entered the threshold of the hydrocarbon generation and had been uplifted in the Late Jurassic, and they had been continuously buried and gradually entered the mature stage in the Early Cretaceous (Figure 10(a)). The  $\text{C}_3\text{t-P}_1\text{s}$  coal-measure source rocks in the Shilijiahan zone had been continuously buried from the deposition to the end of the Early Cretaceous and continuously generated hydrocarbons from the Early Jurassic to the Early Cretaceous (Figure 10(b)). Both the Shiguhao and Shilijiahan zones have been uplifted since the Late Cretaceous with the stagnation of the hydrocarbon generation of the source rocks (Figure 10). Therefore, the hydrocarbon generation history of the  $\text{C}_3\text{t-P}_1\text{s}$  coal-measure source rocks in the Hangjinqi area is similar to the cumulative model proposed by Dai and Qi [48] rather than the instantaneous model in high-mature stage proposed by

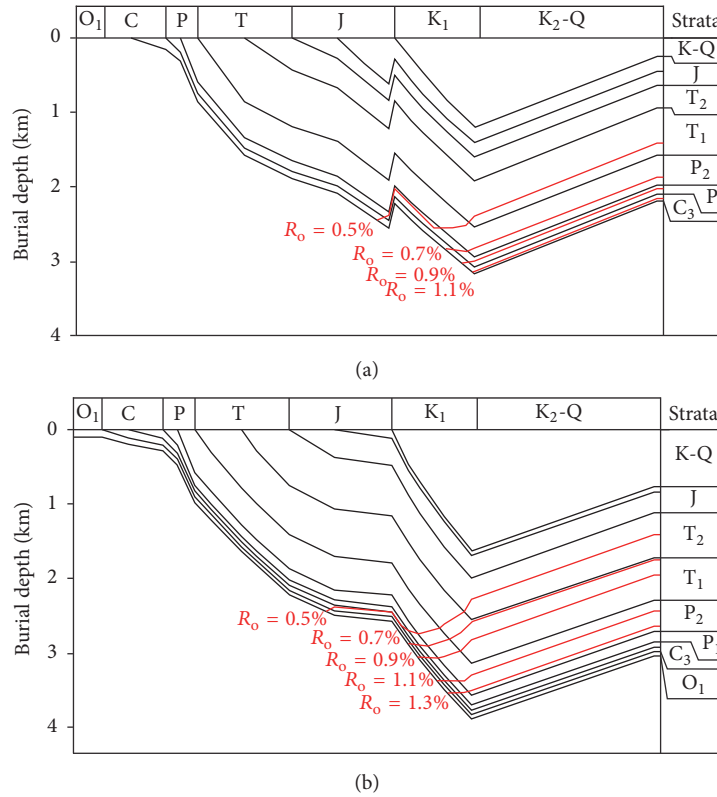


FIGURE 10: Burial and thermal evolution histories of the major stratigraphic intervals at the locations of Well JP1 in the Shiguohao gas zone (a) and Well J10 in the Shilijiahan gas zone (b) in the Hangjinqi area (modified after Hao et al. [31]).

Stahl [49]. The calculation results indicate that the calculated  $R_o$  value according to Stahl's equation is generally lower than 0.5% (Table 1), which is significantly different from the main measured  $R_o$  value of 0.8%–1.7% of the source rocks; therefore, Stahl's equation is unsuitable for tight gas in the Hangjinqi area.

The calculated  $R_o$  values of natural gas from the Shilijiahan and Gongkahan zones based on the  $\delta^{13}C_1$ - $R_o$  empirical equation for coal-type gas proposed by Dai and Qi [48] are in the ranges of 0.74%–1.38% and 0.98%–1.38% with the average values of 1.19% and 1.18%, respectively (Table 1). These calculated  $R_o$  values are mainly higher than 1.1% and consistent with the measured  $R_o$  values of the  $C_3$ t- $P_1$ s source rocks to the south of the Borjianghai fault (Figure 1), which indicates that the coal-type gas from the Shilijiahan and Gongkahan zones is mainly derived from in situ  $C_3$ t- $P_1$ s source rocks. The calculated  $R_o$  value of natural gas from the Shiguohao zone based on the  $\delta^{13}C_1$ - $R_o$  empirical equation for coal-type gas proposed by Dai and Qi [48] is in the range of 1.28%–1.48% with an average of 1.37%, which is significantly higher than the measured  $R_o$  value (<1.1%) of in situ  $P_1$ s source rocks (Figure 1). This indicates that the Upper Paleozoic tight gas in the Shiguohao zone was mainly derived from the coal-measure source rocks with high maturity to the south of the Borjianghai fault rather than in situ  $P_1$ s source rocks.

Although the source rocks in the Wushenqi area had been considered to contribute to the natural gas in the Hangjinqi

area [37], the measured  $R_o$  value of the  $C_3$ t- $P_1$ s source rocks in the Wushenqi area is generally in the range of 1.6%–1.8% [19]. It is obviously higher than both the measured  $R_o$  value of the source rocks (Figure 1) and the calculated  $R_o$  value of natural gas in the Hangjinqi area. Since the strata in the Ordos Basin are generally flat with a low dip angle, and the Upper Paleozoic reservoirs are mainly tight sandstone with low porosity and permeability, the conditions for large-scale lateral migration were undeveloped [25, 34]. Therefore, natural gas generated by the coal-measure source rocks in the Wushenqi area seems unlikely to migrate laterally to the Hangjinqi area by a long distance of nearly one hundred kilometers. Moreover, the Upper Paleozoic tight gas in the Hangjinqi area is generally wet with the average  $C_1/C_{1-5}$  ratio and  $\delta^{13}C_1$  value of 0.910 and  $-32.9\%$ , respectively (Table 1, Figure 3(b)). However, the Upper Paleozoic tight gas in the Wushenqi area is mainly dry with the average  $C_1/C_{1-5}$  ratio and  $\delta^{13}C_1$  value of 0.952 and  $-32.7\%$ , respectively [18], which are both slightly higher, indicating the maturity difference rather than the migration fractionation [38]. Therefore, there is little contribution from the source rocks in the Wushenqi area in central Ordos Basin to the Upper Paleozoic tight gas in the Hangjinqi area in northern Ordos Basin.

The calculated  $R_o$  value of coal-type gas from the Shiguohao zone based on the  $\delta^{13}C_1$ - $R_o$  empirical equation for coal-type gas proposed by Dai and Qi [48] is in the range of 1.28%–1.48%. It is consistent with the thermal maturity of the  $C_3$ t- $P_1$ s coal measures (Figure 1) in the northern margin of

the Yishan Slope to the south of the Borjiangaizi such as the Shilijiahan zone. Therefore, the coal-type gas in the Shiguhaio zone was mainly derived from the  $C_3t$ - $P_1s$  coal measures to the south of the Borjiangaizi zone such as the Shilijiahan zone, with probably a small amount of contribution by in situ  $P_1s$  coal measures in the Shiguhaio zone.

Although several tight gas samples (J58, J58P13H, J98, J99, and J111) from the Shilijiahan zone are mainly coal-type gas, they display significant mixing by oil-type gas as indicated by low  $\delta^{13}C_2$  value ( $-28.7\text{‰}$ ~ $-26.3\text{‰}$ ) (Figures 8(a) and 9(b)). The  $P_1x$  (J110) and  $Pt_2$  (J101) tight gas samples from the Gongkahan zone also display similar characteristics with  $\delta^{13}C_2$  values of  $-28.9\text{‰}$  and  $-30.1\text{‰}$ , respectively. These gas samples were all collected from the wells located adjacent to the Wulanjilinmiao and Borjiangaizi faults. Those tight gas samples collected from the wells (J55, J77) in the Shilijiahan zone away from the faults are typically coal-type gas with relatively higher  $\delta^{13}C_2$  values ( $-24.8\text{‰}$ ,  $-24.7\text{‰}$ ), and they have not been mixed by the oil-type gas (Figures 8(a) and 9(b)).

The Paleozoic oil-type gas is mainly distributed in the  $O_1m$  carbonate reservoirs, and it is believed to be derived from the  $O_1m$  carbonate rocks [27, 29, 57] or  $C_3t$  limestone [19, 20, 58]. The  $C_3t$  limestone is mainly distributed in central Ordos Basin such as the Jingbian area and has been considered to contribute to the Lower Paleozoic gas in the Jingbian gas field; however, the  $C_3t$  limestone is undeveloped in northern Ordos Basin such as the Hangjinqi area [19]. Although the  $O_1m$  carbonate rocks in the Ordos Basin mainly have not reached the standard of hydrocarbon generation due to the low TOC content [20], they display certain hydrocarbon generation potential; for example, the self-generated and self-reservoired oil-type gas has been discovered in the presalt  $O_1m$  reservoirs in central-eastern Ordos Basin. The presalt  $O_1m$  source rocks display an average TOC content of 0.3% with kerogen type I, and the  $O_1m$  source rocks could generate a certain amount of oil-type gas since the samples with TOC content higher than 0.4% account for 28.2% of the total [59]. Therefore, the oil-type gas component in tight gas from the Gongkahan and Shilijiahan zones in the Hangjinqi area is inferred to be derived from the  $O_1m$  carbonate rocks, and it migrated upwards along the Wulanjilinmiao and Borjiangaizi faults.

Moreover, the  $Pt_2$  gas sample (J101) from the Hangjinqi area also displays the mixing characteristics of coal-type gas and oil-type gas, and relatively low  $\delta^{13}C_2$  and  $\delta^{13}C_3$  values indicate that the proportion of oil-type gas is slightly higher than that in the Upper Paleozoic tight gas. This may explain the reason why the calculated  $R_o$  value (0.98%) of the  $Pt_2$  gas sample according to the  $\delta^{13}C_1$ - $R_o$  empirical equation for coal-type gas proposed by Dai and Qi [48] is significantly lower than that of the  $P_1s$ - $P_1x$  tight gas. The Proterozoic mudstone in the Hangjinqi area has certain hydrocarbon generation potential with mainly kerogen type III, and the distribution range and thickness are both limited [30]. Since only a small amount of the  $Pt_2$  gas has been discovered in Wells J3, J13 and J101, it is inferred that the  $Pt_2$  gas was mainly derived from the mixing of coal-type

gas from the  $Pt_2$  mudstone and oil-type gas from the  $O_1m$  carbonate rocks. The  $Pt_2$  mudstone or  $O_1m$  carbonate core samples have not been obtained in the Hangjinqi area till now. Therefore, further study needs to be conducted on the geochemical characteristics and hydrocarbon potential of the  $Pt_2$  mudstone and  $O_1m$  carbonate source rocks.

**5.3. Filling Patterns of Tight Gas.** The accumulation and distribution of the Upper Paleozoic tight gas in the Hangjinqi area were controlled by the Borjiangaizi fault. It experienced three obvious peaks of activity in the evolution history, that is, the Caledonian to the Early Hercynian fracture period, the Indosinian to the Early Yanshanian squeezing thrust activity period, and the Middle-Late Yanshanian strike-slip tearing activity period [43]. The studies on the homogenization temperature of the fluid inclusions and the accumulation history indicated that two periods of gas filling occurred to the Upper Paleozoic strata in the Hangjinqi area in the Middle-Late Jurassic and the Early Cretaceous, respectively [43, 46]. The  $C_3t$ - $P_1s$  coal-measure source rocks in the Shilijiahan and Shiguhaio zones entered the peak stage ( $R_o > 0.8\%$ ) of hydrocarbon generation in the early and middle periods of the Early Cretaceous, respectively; that is, both the  $C_3t$ - $P_1s$  source rocks in these two zones started to generate a large amount of natural gas in the Early Cretaceous (Figure 10). Therefore, the strike-slip activity of the Borjiangaizi fault in the Middle-Late Yanshanian effectively matched with the main gas filling period in the Early Cretaceous, and the intensive fault activity in the gas filling period was favorable for the effective expulsion of hydrocarbons from the source rocks and migration and accumulation of natural gas [43].

The study on the fault sealing ability indicated that the fault plane of the Borjiangaizi fault was vertically sealed in the  $P_2sh$  and  $P_2s$  strata with the fault sealing coefficients almost less than 1.0, whereas the fault plane was vertically open in the  $P_1s$  and  $P_1x$  strata with the fault sealing coefficients mostly ranging from 4.0 to 10.0 [43]. Moreover, the  $P_2sh$  and  $P_2s$  mudstones constituted the favorable regional caprock since they display a large thickness and stable lateral distribution. Therefore, the large amount of natural gas generated by the  $C_3t$ - $P_1s$  coal-measure source rocks to the south of the Borjiangaizi fault firstly migrated vertically along the fault and then migrated laterally across the fault to the north along the  $P_1x$  stripped sand bodies (Figure 11). It finally accumulated in the favorable traps during the migration (Figure 11); that is, natural gas in the Shiguhaio zone to the north of the Borjiangaizi fault mainly displayed distal-source accumulation.

Molecular fractionation of natural gas occurs during the migration process. Since the diffusion coefficient of the hydrocarbon decreases with the increase of the molecular weight [60], the diffusive gas is enriched in  $CH_4$  and displays higher  $C_1/C_{1-5}$  ratio. As indicated from the section A-A' (Figure 11), the  $P_1s$  gas sample from Well J55 to the south of the Borjiangaizi fault displays  $C_1/C_{1-5}$  ratio of 0.896, whereas the  $P_1x$  gas samples from Wells J66P5H, YS1, J11, and J26 to the north of the fault display  $C_1/C_{1-5}$  ratios higher than 0.900 (Figure 11). This suggests that the  $P_1x$  gas in the

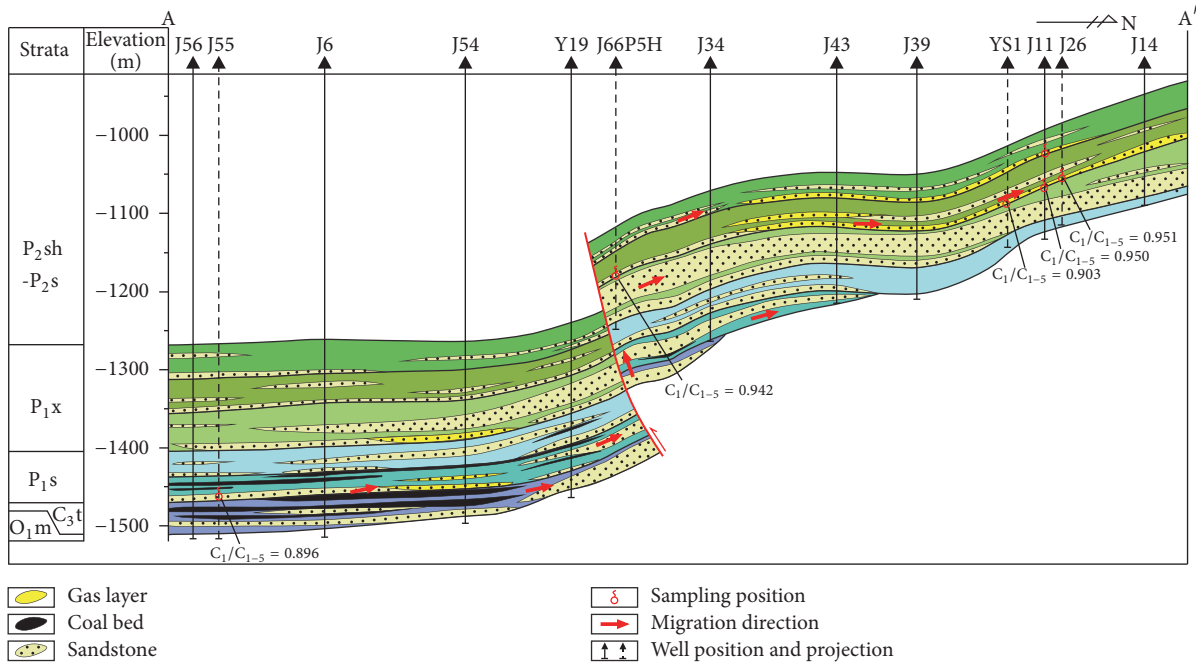


FIGURE 11: Gas filling model of the Upper Paleozoic tight gas in the Hangjinqi area, and the position of the section A-A' is indicated in Figure 1 (modified after Li et al. [43]).

reservoirs to the north of the fault has been migrated from the  $C_3t$ - $P_1s$  coal-measure source rocks to the south of the fault.

As to the Shilijiahan zone to the south of the Borjianghaizi fault, since the strata dipped to the south due to the effect of the thrusting in the Late Jurassic, natural gas which had migrated upwards along the fault seemed unfavorable to fill into in situ  $P_1s$  and  $P_1x$  sand bodies (Figure 11). Therefore, natural gas in the Shilijiahan zone was mainly derived from in situ  $C_3t$  and  $P_1s$  source rocks. The migration pathways were mainly the sand bodies and fissures with the driving force of the pressure difference between source rocks and the reservoirs, which affected the degree of gas accumulation. Consequently, tight gas in the Shilijiahan and Gongkahan zones mainly displayed near-source accumulation. Moreover, the gas samples which had been mixed by the oil-type gas were all collected from the wells adjacent to the Borjianghaizi and Wulanjilinmiao faults, and the oil-type gas component was inferred to be derived from the  $O_1m$  carbonate rocks and migrate upwards along the two faults.

## 6. Conclusions

(1) The Upper Paleozoic tight gas in the Hangjinqi area in northern Ordos Basin is mainly wet gas with the dryness coefficient ( $C_1/C_{1-5}$ ) of 0.853–0.951, which is positively correlated with the  $CH_4$  content. The  $\delta^{13}C_1$ ,  $\delta^{13}C_2$ , and  $\delta^{13}C_3$  values are ranging from  $-36.2\text{‰}$  to  $-32.0\text{‰}$ , from  $-28.9\text{‰}$  to  $-24.5\text{‰}$ , and from  $-26.6\text{‰}$  to  $-19.5\text{‰}$ , respectively, with the  $\delta^2H$ - $C_1$  values from  $-199\text{‰}$  to  $-174\text{‰}$ . The alkane gas generally displays positive carbon and hydrogen isotopic series, with only a few gas samples being partially reversed between  $C_2H_6$  and  $C_3H_8$ .

(2) Integrated analysis on geochemical characteristics from the alkane carbon and hydrogen isotopes demonstrates that the Upper Paleozoic tight gas in the Hangjinqi area is mainly coal-type gas. The carbon isotopic compositions of ethane and propane indicate that tight gas from the wells in the Shilijiahan and Gongkahan zones adjacent to the Wulanjilinmiao and Borjianghaizi faults has been affected by the mixing of oil-type gas, and it displays similar geochemical characteristics with the  $O_1m$  gas in the Jingbian gas field. However, the proportion of oil-type gas in the Upper Paleozoic gas in the Shilijiahan and Gongkahan zones is slightly lower than that in the  $O_1m$  gas in the Jingbian gas field.

(3) Gas-source correlation indicated that the coal-type gas in the Shiguhaio zone displayed distal-source accumulation, and it was mainly derived from the  $C_3t$ - $P_1s$  coal-measure source rocks, probably with a minor contribution from the  $P_1s$  coal measures in in situ Shiguhaio zone. Tight gas in the Shilijiahan and Gongkahan zones mainly displayed near-source accumulation. The coal-type gas component was derived from in situ  $C_3t$ - $P_1s$  source rocks, whereas the oil-type gas component might be derived from the  $O_1m$  carbonate rocks, and it migrated upwards along the Wulanjilinmiao and Borjianghaizi faults.

## Conflicts of Interest

The authors declare that there are no conflicts of interest regarding the publication of this paper.

## Acknowledgments

The authors would like to thank Professor Jinxing Dai and Deliang Liu for generous guidance and assistance, the North

China Branch Company of SINOPEC for sample collection and technical support, and Key Laboratory for Hydrocarbon Accumulation Mechanism of SINOPEC for chemical analyses of natural gas. This work was supported by the National Natural Science Foundation of China (Grants nos. 41625009, U1663201, and 41302118) and the National Science & Technology Special Project (Grant no. 2016ZX05002-006).

## References

- [1] M. Schoell, "The hydrogen and carbon isotopic composition of methane from natural gases of various origins," *Geochimica et Cosmochimica Acta*, vol. 44, no. 5, pp. 649–661, 1980.
- [2] A. A. Prinzhofer and A. Y. Huc, "Genetic and post-genetic molecular and isotopic fractionations in natural gases," *Chemical Geology*, vol. 126, no. 3–4, pp. 281–290, 1995.
- [3] M. A. Rooney, G. E. Claypool, and H. Moses Chung, "Modeling thermogenic gas generation using carbon isotope ratios of natural gas hydrocarbons," *Chemical Geology*, vol. 126, no. 3–4, pp. 219–232, 1995.
- [4] M. J. Whiticar, "Carbon and hydrogen isotope systematics of bacterial formation and oxidation of methane," *Chemical Geology*, vol. 161, no. 1, pp. 291–314, 1999.
- [5] Y. Tang, J. K. Perry, P. D. Jenden, and M. Schoell, "Mathematical modeling of stable carbon isotope ratios in natural gases," *Geochimica et Cosmochimica Acta*, vol. 64, no. 15, pp. 2673–2687, 2000.
- [6] Y. Ni, Q. Ma, G. S. Ellis et al., "Fundamental studies on kinetic isotope effect (KIE) of hydrogen isotope fractionation in natural gas systems," *Geochimica et Cosmochimica Acta*, vol. 75, no. 10, pp. 2696–2707, 2011.
- [7] Q. Y. Liu, R. H. Worden, Z. J. Jin et al., "TSR versus non-TSR processes and their impact on gas geochemistry and carbon stable isotopes in carboniferous, permian and lower triassic marine carbonate gas reservoirs in the Eastern Sichuan Basin, China," *Geochimica et Cosmochimica Acta*, vol. 100, no. 1, pp. 96–115, 2013.
- [8] Q. Y. Liu, R. H. Worden, Z. J. Jin et al., "Thermochemical sulphate reduction (TSR) versus maturation and their effects on hydrogen stable isotopes of very dry alkane gases," *Geochimica et Cosmochimica Acta*, vol. 137, no. 0, pp. 208–220, 2014.
- [9] Q. Liu, J. Dai, Z. Jin et al., "Abnormal carbon and hydrogen isotopes of alkane gases from the Qingshen gas field, Songliao Basin, China, suggesting abiogenic alkanes?" *Journal of Asian Earth Sciences*, vol. 115, no. 1, pp. 285–297, 2016.
- [10] Q. Liu, Z. Jin, J. Li, A. Hu, and C. Bi, "Origin of marine sour natural gas and gas-filling model for the wolonghe gas field, Sichuan Basin, China," *Journal of Asian Earth Sciences*, vol. 58, pp. 24–37, 2012.
- [11] F. Hao, X. Zhang, C. Wang et al., "The fate of CO<sub>2</sub> derived from thermochemical sulfate reduction (TSR) and effect of TSR on carbonate porosity and permeability, Sichuan Basin, China," *Earth-Science Reviews*, vol. 141, pp. 154–177, 2015.
- [12] Y. Ni, J. Dai, C. Zou, F. Liao, Y. Shuai, and Y. Zhang, "Geochemical characteristics of biogenic gases in China," *International Journal of Coal Geology*, vol. 113, pp. 76–87, 2013.
- [13] X. Wang, W. Liu, B. Shi, Z. Zhang, Y. Xu, and J. Zheng, "Hydrogen isotope characteristics of thermogenic methane in chinese sedimentary basins," *Organic Geochemistry*, vol. 83–84, no. 1, pp. 178–189, 2015.
- [14] F. Hao and H. Zou, "Cause of shale gas geochemical anomalies and mechanisms for gas enrichment and depletion in high-maturity shales," *Marine and Petroleum Geology*, vol. 44, pp. 1–12, 2013.
- [15] J. Dai, C. Zou, D. Dong et al., "Geochemical characteristics of marine and terrestrial shale gas in China," *Marine and Petroleum Geology*, vol. 76, pp. 444–463, 2016.
- [16] J. Dai, Y. Ni, and X. Wu, "Tight gas in China and its significance in exploration and exploitation," *Petroleum Exploration and Development*, vol. 39, no. 3, pp. 277–284, 2012.
- [17] J. Dai, C. Yu, S. Huang et al., "Geological and geochemical characteristics of large gas fields in China," *Petroleum Exploration and Development*, vol. 41, no. 1, pp. 1–13, 2014.
- [18] J. Dai, *Giant Coal-Derived Gas Fields and the Source in China*, Science Press, Beijing, China, 2014.
- [19] J. Dai, J. Li, X. Luo et al., "Stable carbon isotope compositions and source rock geochemistry of the giant gas accumulations in the Ordos Basin, China," *Organic Geochemistry*, vol. 36, no. 12, pp. 1617–1635, 2005.
- [20] A. Hu, J. Li, W. Zhang, Z. Li, L. Hou, and Q. Liu, "Geochemical characteristics and origin of gases from the Upper, Lower Paleozoic and the Mesozoic reservoirs in the Ordos Basin, China," *Science in China, Series D: Earth Sciences*, vol. 51, supplement I, pp. 183–194, 2008.
- [21] H. Yang, J. Fu, X. Liu, and P. Meng, "Accumulation conditions and exploration and development of tight gas in the Upper Paleozoic of the Ordos Basin," *Petroleum Exploration and Development*, vol. 39, no. 3, pp. 295–303, 2012.
- [22] G. Hu, J. Li, X. Shan, and Z. Han, "The origin of natural gas and the hydrocarbon charging history of the Yulin gas field in the Ordos Basin, China," *International Journal of Coal Geology*, vol. 81, no. 4, pp. 381–391, 2010.
- [23] S. Huang, X. Fang, D. Liu, C. Fang, and T. Huang, "Natural gas genesis and sources in the Zizhou gas field, Ordos Basin, China," *International Journal of Coal Geology*, vol. 152, part A, pp. 132–143, 2015.
- [24] H. Yang, J. Fu, X. Wei, and X. Liu, "Sulige field in the Ordos Basin: geological setting, field discovery and tight gas reservoirs," *Marine and Petroleum Geology*, vol. 25, no. 4–5, pp. 387–400, 2008.
- [25] C. N. Zou, Z. Yang, S. Z. Tao et al., "Continuous hydrocarbon accumulation over a large area as a distinguishing characteristic of unconventional petroleum: the Ordos Basin, North-Central China," *Earth-Science Reviews*, vol. 126, pp. 358–369, 2013.
- [26] Q. Liu, Z. Jin, Q. Meng, X. Wu, and H. Jia, "Genetic types of natural gas and filling patterns in Daniudi gas field, Ordos Basin, China," *Journal of Asian Earth Sciences*, vol. 107, pp. 1–11, 2015.
- [27] Q. Y. Liu, Z. J. Jin, Y. Wang et al., "Gas filling pattern in Paleozoic marine carbonate reservoir of Ordos Basin," *Acta Petrologica Sinica*, vol. 28, no. 3, pp. 847–858, 2012.
- [28] C. Cai, G. Hu, H. He, J. Li, J. Li, and Y. Wu, "Geochemical characteristics and origin of natural gas and thermochemical sulphate reduction in Ordovician carbonates in the Ordos Basin, China," *Journal of Petroleum Science and Engineering*, vol. 48, no. 3–4, pp. 209–226, 2005.
- [29] Q. Liu, M. Chen, W. Liu, J. Li, P. Han, and Y. Guo, "Origin of natural gas from the Ordovician paleo-weathering crust and gas-filling model in Jingbian gas field, Ordos Basin, China," *Journal of Asian Earth Sciences*, vol. 35, no. 1, pp. 74–88, 2009.

- [30] S. Peng, *The Analyzation of Middle-Late Proterozoic Hydrocarbon Geologic Feature and Exploration Potential in Hangjinqi Area*, Northwest University, Xi'an, China, 2009.
- [31] S. Hao, L. Li, W. Zhang, R. Qi, C. Ma, and J. Chen, "Forming conditions of large-scale gas fields in Permo-Carboniferous in the northern Ordos Basin," *Oil and Gas Geology*, vol. 37, no. 2, pp. 149–154, 2016.
- [32] M. Yang, L. Li, J. Zhou et al., "Mesozoic structural evolution of the Hangjinqi area in the northern Ordos Basin, North China," *Marine and Petroleum Geology*, vol. 66, pp. 695–710, 2015.
- [33] M. Yang, L. Li, J. Zhou, X. Qu, and D. Zhou, "Segmentation and inversion of the Hangjinqi fault zone, the Northern Ordos Basin (North China)," *Journal of Asian Earth Sciences*, vol. 70–71, no. 1, pp. 64–78, 2013.
- [34] H. Xue, J.-C. Zhang, B. Xu, Y. Wang, and X.-P. Mao, "Evaluation of Upper Paleozoic source rocks of the Hangjinqi block in the northern Ordos Basin, China," *Journal of Chengdu University of Technology (Science and Technology Edition)*, vol. 37, no. 1, pp. 21–28, 2010.
- [35] W.-M. Ji, W.-L. Li, Z. Liu, and T. Lei, "Research on the Upper Paleozoic gas source of the Hangjinqi block in the northern Ordos Basin," *Natural Gas Geoscience*, vol. 24, no. 5, pp. 905–914, 2013.
- [36] J. Chen, H. Jia, Y. Li, C. An, W. Li, and S. Liu, "Origin and source of natural gas in the Upper Paleozoic of the Yimeng Uplift, Ordos Basin," *Oil and Gas Geology*, vol. 37, no. 2, pp. 205–209, 2016.
- [37] M. Wang, D. He, H. Bao, R. Lu, and B. Gui, "Upper Palaeozoic gas accumulations of the Yimeng Uplift, Ordos Basin," *Petroleum Exploration and Development*, vol. 38, no. 1, pp. 30–39, 2011.
- [38] A. Prinzhofer and E. Pernaton, "Isotopically light methane in natural gas: bacterial imprint or diffusive fractionation?" *Chemical Geology*, vol. 142, no. 3–4, pp. 193–200, 1997.
- [39] A. Prinzhofer and A. Battani, "Gas isotopes tracing: An important tool for hydrocarbons exploration," *Oil and Gas Science and Technology*, vol. 58, no. 2, pp. 299–311, 2003.
- [40] B. B. Bernard, J. M. Brooks, and W. M. Sackett, "Natural gas seepage in the Gulf of Mexico," *Earth and Planetary Science Letters*, vol. 31, no. 1, pp. 48–54, 1976.
- [41] P. D. Jenden, I. R. Kaplan, R. Poreda, and H. Craig, "Origin of nitrogen-rich natural gases in the California Great Valley: evidence from helium, carbon and nitrogen isotope ratios," *Geochimica et Cosmochimica Acta*, vol. 52, no. 4, pp. 851–861, 1988.
- [42] J. Dai, "Significant advancement in research on coal-derived gas in China," *Petroleum Exploration and Development*, vol. 26, no. 3, pp. 1–10, 1999.
- [43] W. Li, W. Ji, and Z. Liu, "Control of Boerjianghaizi fault on gas accumulation of Upper Paleozoic in northern Ordos Basin," *Geoscience*, vol. 29, no. 3, pp. 584–590, 2015.
- [44] J. Yang and X. Pei, *Natural Gas Geology in China*, vol. 4, Petroleum Industry Press, Beijing, China, 1996.
- [45] Y. Yang, W. Li, and L. Ma, "Tectonic and stratigraphic controls of hydrocarbon systems in the Ordos Basin: a multicycle cratonic basin in central China," *AAPG Bulletin*, vol. 89, no. 2, pp. 255–269, 2005.
- [46] H. Xue, Y. Wang, and X. Mao, "The timing of gas pooling in the Upper Paleozoic in the northern Ordos Basin: A case study of the Hangjinqi Block," *Natural Gas Industry*, vol. 29, no. 12, pp. 9–12, 2009.
- [47] B. Xu, H. Nie, and M. Wang, "A study of hydrocarbon-generating potential of Hangjinqi prospect area in ordos basin," *Petroleum Geology and Recovery Efficiency*, vol. 16, no. 4, pp. 38–39, 2009.
- [48] J. Dai and H. Qi, "The  $\delta^{13}\text{C}$ -Ro relationship of coal-derived alkane gases in China," *Chinese Science Bulletin*, vol. 34, no. 9, pp. 690–692, 1989.
- [49] W. J. Stahl, "Carbon and nitrogen isotopes in hydrocarbon research and exploration," *Chemical Geology*, vol. 20, no. C, pp. 121–149, 1977.
- [50] J. Dai, X. Pei, and H. Qi, *Natural Gas Geology in China*, vol. 1, Petroleum Industry Press, Beijing, China, 1992.
- [51] Q. Liu, J. Dai, J. Li, and Q. Zhou, "Hydrogen isotope composition of natural gases from the Tarim Basin and its indication of depositional environments of the source rocks," *Science in China, Series D: Earth Sciences*, vol. 51, no. 2, pp. 300–311, 2008.
- [52] J. Dai, Y. Ni, and C. Zou, "Stable carbon and hydrogen isotopes of natural gases sourced from the Xujiahe Formation in the Sichuan Basin, China," *Organic Geochemistry*, vol. 43, no. 1, pp. 103–111, 2012.
- [53] G. Hu and S. Zhang, "Characterization of low molecular weight hydrocarbons in Jingbian gas field and its application to gas sources identification," *Energy Exploration and Exploitation*, vol. 29, no. 6, pp. 777–796, 2011.
- [54] Y.-R. Zou, Y. Cai, C. Zhang, X. Zhang, and P. Peng, "Variations of natural gas carbon isotope-type curves and their interpretation—a case study," *Organic Geochemistry*, vol. 38, no. 8, pp. 1398–1415, 2007.
- [55] W. Liu and Y. Xu, "A two-stage model of carbon isotopic fractionation in coal-gas," *Geochimica*, vol. 28, no. 4, pp. 359–365, 1999.
- [56] E. M. Galimov, "Isotope organic geochemistry," *Organic Geochemistry*, vol. 37, no. 10, pp. 1200–1262, 2006.
- [57] S. Hao, Y. Gao, and Z. Huang, "Characteristics of dynamic equilibrium for natural gas migration and accumulation of the gas field in the center of the Ordos Basin," *Science in China, Series D: Earth Sciences*, vol. 40, no. 1, pp. 11–15, 1997.
- [58] X. Xia, L. Zhao, W. Zhang, and J. Li, "Geochemical characteristics and source rock of Ordovician gas reservoir, Changqing Gasfield," *Chinese Science Bulletin*, vol. 44, no. 20, pp. 1917–1920, 1999.
- [59] D. Liu, W. Zhang, Q. Kong, Z. Feng, C. Fang, and W. Peng, "Lower Paleozoic source rocks and natural gas origins in Ordos Basin, NW China," *Petroleum Exploration and Development*, vol. 43, no. 4, pp. 591–601, 2016.
- [60] B. M. Krooss and D. Leythaeuser, "Experimental measurements of the diffusion parameters of light hydrocarbons in water-saturated sedimentary rocks-II. Results and geochemical significance," *Organic Geochemistry*, vol. 12, no. 2, pp. 91–108, 1988.

## Research Article

# Hydrothermal Dissolution of Deeply Buried Cambrian Dolomite Rocks and Porosity Generation: Integrated with Geological Studies and Reactive Transport Modeling in the Tarim Basin, China

Wenwen Wei,<sup>1,2</sup> Daizhao Chen,<sup>1,2</sup> Hairuo Qing,<sup>3</sup> and Yixiong Qian<sup>4</sup>

<sup>1</sup>Key Laboratory of Petroleum Resources Research, Institute of Geology and Geophysics, Chinese Academy of Sciences, Beijing 100029, China

<sup>2</sup>University of Chinese Academy of Sciences, No. 19A Yuquan Road, Beijing 100049, China

<sup>3</sup>Department of Geology, University of Regina, Regina, SK, Canada S4S 0A2

<sup>4</sup>Wuxi Research Institute of Petroleum Geology, SINOPEC, Wuxi 214151, China

Correspondence should be addressed to Daizhao Chen; [dzh-chen@mail.iggcas.ac.cn](mailto:dzh-chen@mail.iggcas.ac.cn)

Received 12 January 2017; Accepted 20 March 2017; Published 4 May 2017

Academic Editor: Keyu Liu

Copyright © 2017 Wenwen Wei et al. This is an open access article distributed under the Creative Commons Attribution License, which permits unrestricted use, distribution, and reproduction in any medium, provided the original work is properly cited.

The burial dissolution of carbonate rocks has long been an interesting topic of reservoir geologists. Integrated with geological studies and reactive transport modeling, this study investigated the Cambrian dolomites that were buried at depths up to 8408 m and still preserved a large amount of unfilled dissolution vugs from the borehole TS1 in the northern Tarim Basin. Studies indicate that these vugs were formed in association with fault-channeled hydrothermal fluids from greater depth through “retrograde dissolution” as the fluid temperature dropped during upward migration. The reactive transport modeling results suggest an important control of the vertical permeability of wall-rock on fluid and temperature patterns which, in turn, would control the spatial distribution of dissolving-originated porosity. The hydrothermal dissolution mainly occurred in dolomite wall-rocks with higher vertical permeability (extensive development of tensional fractures and connected pore spaces), producing additional dissolved porosity there during deep burial. This study implicates the importance of multidisciplinary approaches for understanding the burial/hydrothermal dissolution of dolomite rocks and predicting favourable deep/ultradeep carbonate reservoirs.

## 1. Introduction

It is commonly believed that about 50–60% of oil and gas reservoirs in the world occur in carbonate rocks [1]. Carbonate reservoirs are commonly heterogeneous as a result of complicated diagenetic processes which could have substantially modified the pore systems [2]. For this reason, understanding of spatial diagenetic differences and subsequent predicting of “sweet” reservoirs are quite a challenge for recovery of carbonate hydrocarbon resources.

The porosity in carbonate reservoirs usually decreases with increasing burial depth due to mechanical-chemical compaction and subsequent cementation [3, 4]. According to

Schmoker and Halley [3], most petroleum producing reservoirs are buried at depths less than 6000 m subsurface. However, the borehole TS1, one of the deepest petroleum wells (to the depth of 8408 m) in the world, was drilled in the northern uplift of the Tarim Basin, northwestern China, and revealed a large number of dissolution pores and vugs, notably a downward increase in porosity, in the deeply buried Cambrian dolomites from 6884 to 8408 m deep [5]. Therefore, modeling the fluid property, pathway, and dissolution/precipitation is of great significance in understanding the formation of vuggy pore systems and controls in such a great depth, facilitating exploration for the ultradeep hydrocarbon reservoirs which were poorly constrained and understood in general.

In recent years, reactive transport modeling (RTM) has become an important tool for understanding the diagenetic process and predicting their spatial patterns [6–8]. RTM couples mineral reactions with groundwater flow, heat, and solute transport [9]. Previous applications of reactive transport models have gained a better insight into dolomitization process [7, 10]. Based on reactive transport modeling, Lu and Cantrell [11] predicted the dolomite pattern that agrees with observed distribution of dolomites. RMT has also been successfully applied for prediction of reservoir quality in different geologic settings [8, 12, 13].

Fault-related hydrothermal alteration of carbonate rocks, especially dolomitization, was a very important mechanism controlling the reservoir development [14–16]. However, rare numerical simulations have been carried out to investigate the hydrothermal alteration (or dolomitization) on carbonate reservoirs developed in the fault systems [8]. To improve our understanding of diagenetic process and reservoir development through numerical simulations, a solid study on the geological setting and processes was the basis on which the reservoir model is better refined and established. However, many numerical simulations did not pay enough attention to the geological setting and processes, limiting their application for the complex geological realities.

In this study, we investigated the diagenetic processes and porosity development tied to fault-controlled hydrothermal fluids in the deep Cambrian dolomite reservoir revealed in the ultradeep borehole TS1 (~8408 m deep) in Tarim Basin, based on the petrographic investigation, petrophysical data integrated with fluid reactive transport modeling using TOUGHREACT V2 [9]. Our reactive transport modeling focused on the critical diagenetic processes and their roles in pore generation and plugging. This would improve our understanding for diagenetic processes and porosity generation/reduction, facilitating prediction for the deep carbonate (dolomite) reservoirs.

## 2. Geologic Setting

**2.1. Depositional Setting and Stratigraphy.** The Tarim Basin, one of the biggest hydrocarbon-producing basins (with an area of 530,000 km<sup>2</sup>) in China, is located in the northwest China (Figure 1). From the Cambrian to Middle Ordovician, a thick carbonate succession, up to 2000 m thick, was deposited in northern Tarim Basin (Figures 2 and 3). A summary of stratigraphic units and their main lithologies in platform interior of Cambrian and Ordovician is illustrated in Figure 2, and relevant information can also be found in [17, 18]. In ascending order, the Lower Cambrian includes the Yurtus, Xiaoerbulake, and Wusonger formations. Of these, the Yurtus Formation is characterized by the bedded chert, black shale in the lower part, and argillaceous dolomite in the upper part. The Xiaoerbulake Formation is characterized by banded lenticular-like dolomite in the lower part and banded to thin-bedded dolomite intercalated with microbialite in the upper part. The Wusonger Formation is characterized by argillaceous dolomite intercalated with thin- to medium-bedded dolomite. The Middle Cambrian includes the Shayilike and Arwatage formations; they are

characterized by variable stromatolites and reddish dolomitic mudrock (or argillaceous dolomite) intercalated with subordinate evaporites. The Upper Cambrian includes the Lower Qilitage Group, is characterized by cyclic peritidal facies (thrombolite, stromatolite, and laminite) in the lower part and oolites/grainstones with minor microbialites in the upper part. Toward the platform margin where the borehole TS1 is located, the equivalent strata are dominated by massive microbial reefs (or buildups) which initially occur from the middle Xiaoerbulake Formation (Figure 3).

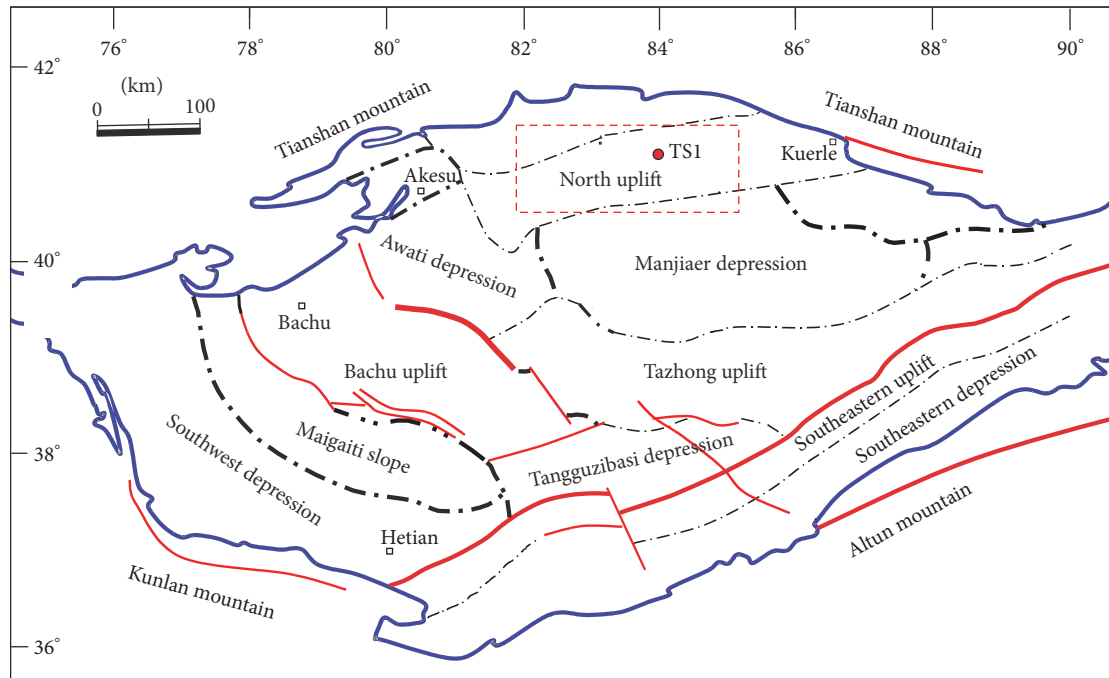
In the northern Tarim Basin, a ramp carbonate platform was built on the antecedent (Neoproterozoic) palaeohigh during the Early Cambrian [19]; it then evolved into a carbonate platform rimmed with microbial buildups and sandy shoals from the late Early Cambrian and further evolved into sandy shoal-protected platform system from the late Late Cambrian to the Early Ordovician (Figures 1(b) and 3). From the Late Ordovician, the carbonate depositional system gradually evolved into a mixed carbonate-siliciclastic system and finally was replaced by a complete siliciclastic system near the end of Ordovician, due to the progressive long-term marine regression in response to the tectonic inversion to a convergent continental margin [20, 21].

**2.2. Burial History and Tectonic Evolution.** Seven tectonic units were identified in the Tarim Basin by previous extensive seismic investigations, including three topographic uplifts (the North, Central, and South uplifts) and four depressions (the Kuche, North, Southwest, and Southeast depressions) (Figure 1(a); [22]). All these had experienced multiple deformations after the burial in response to multiple tectonic movements during the Caledonian, Hercynian, Yanshanian, and Himalayan orogenic episodes (Figure 4(a)).

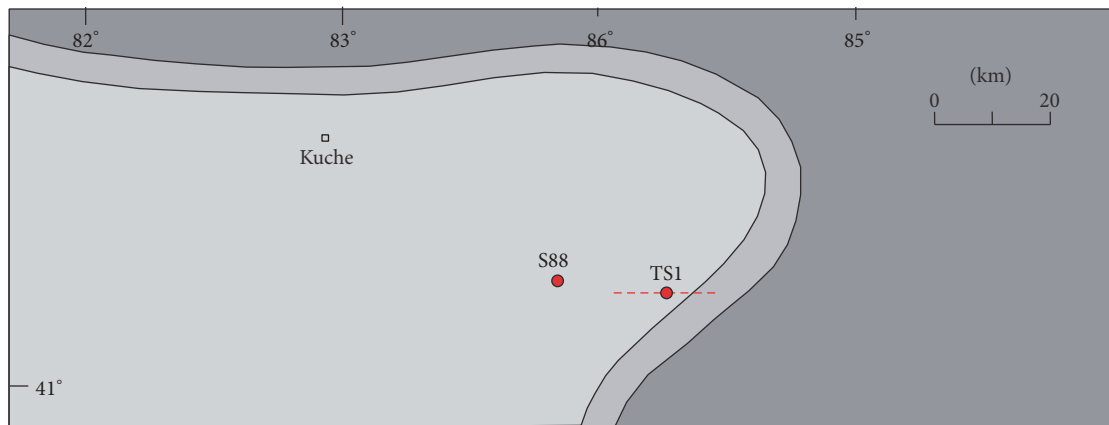
The study area is located in the North Uplift which was mainly activated during the Caledonian to Hercynian phases. The burial history for the Cambrian to Ordovician successions is illustrated in Figure 4(a) which shows that these carbonates experienced three episodes of significant uplift after burial. The first episode occurred in relation to the Middle Caledonian Orogeny during the Late Ordovician, the second one in association with the Early Hercynian Orogeny during the Late Devonian, and the third one in response to the Late Hercynian Orogeny during the Late Permian [23, 24].

Three major episodes of abnormal thermal events took place in the basin scale after the burial of Cambrian carbonate successions. The first episode occurred during the Early Ordovician but only localized in the central-western part of the basin [28]. The second one, also the most intense one, took place extensively in the entire basin during the Early Permian [26–30] and was characterized by basic basalt lavas and/or intrusive diabases, and intermediate acidic magmas in the central and northern parts of the basin, respectively [28]. The last one was active during the Cretaceous but was only restricted around the margin of the basin [28].

**2.3. Fault/Fracture System.** In the dip-trending seismic profile across the well TS1 in the North Uplift of Tarim Basin, several high-angle (nearly vertical) tensional (or transtensional) faults with small displacement (downthrowing) are



(a)



(b)

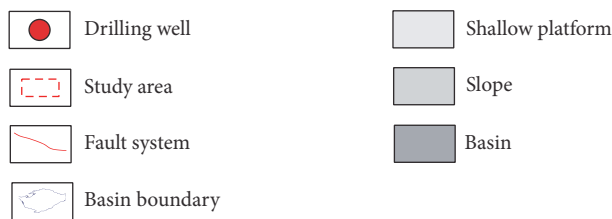


FIGURE 1: (a) Map of the Tarim Basin showing the main tectonic units (modified from He et al., [23]). Dashed rectangle denotes the location of study area and TS1. (b) Palaeogeographic setting of the northern Tarim Basin (study area) during the Cambrian period (modified from [17–21]). Dashed line indicates the location of seismic profile shown in Figure 3.

identified, which cut the Precambrian-Cambrian boundary and partially extend upwards into the Ordovician (Figure 3). Extensive interpretations from the 3D seismic datasets demonstrate a dominance of conjugate (wrench) fault pattern

composed mainly of NE- and NW-trending fault (or fracture) (X-shaped) series, respectively, with subordinate N-S-trending tensional fault series in the Cambrian dolomites. In the northeastern part of this area, some E-W-trending

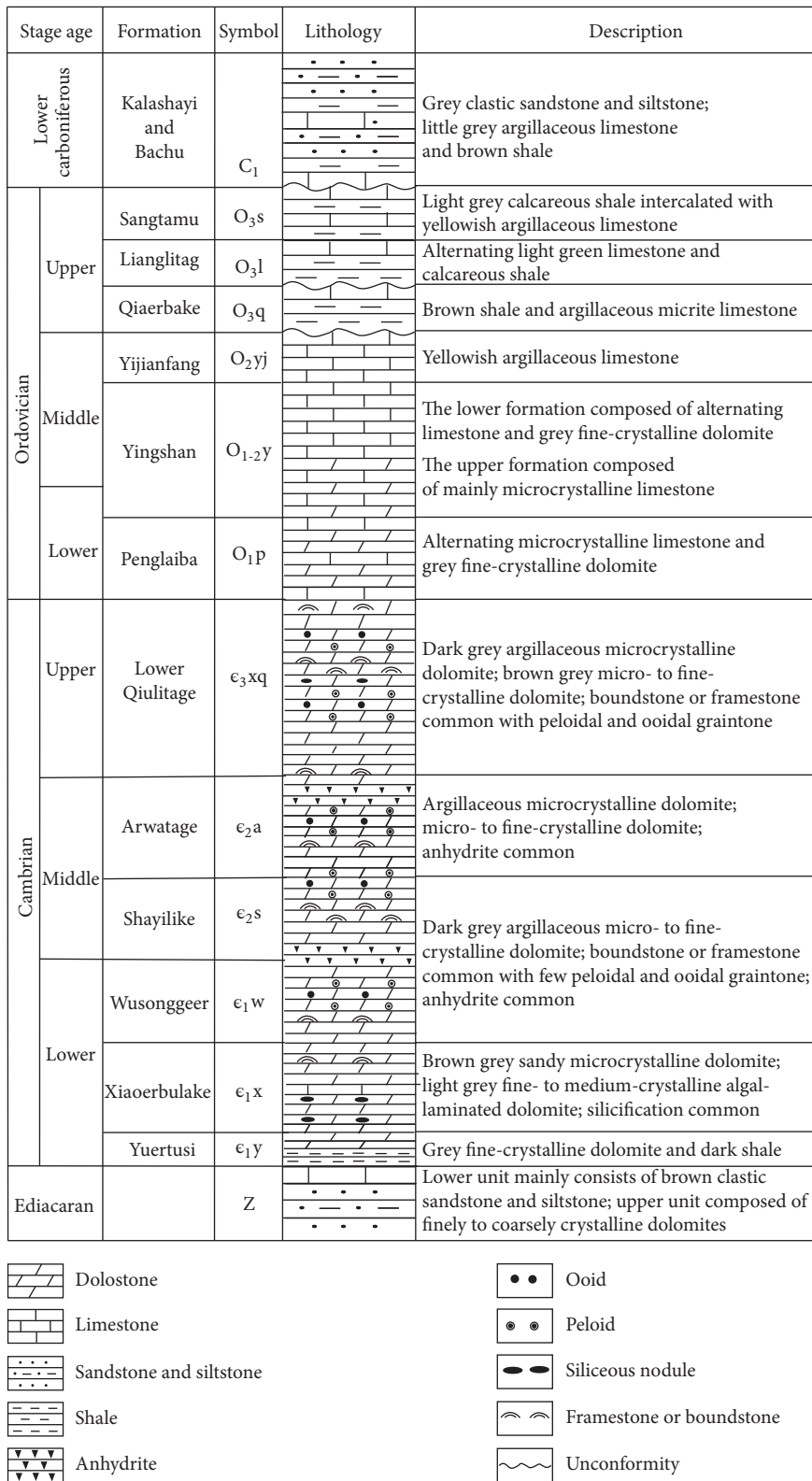
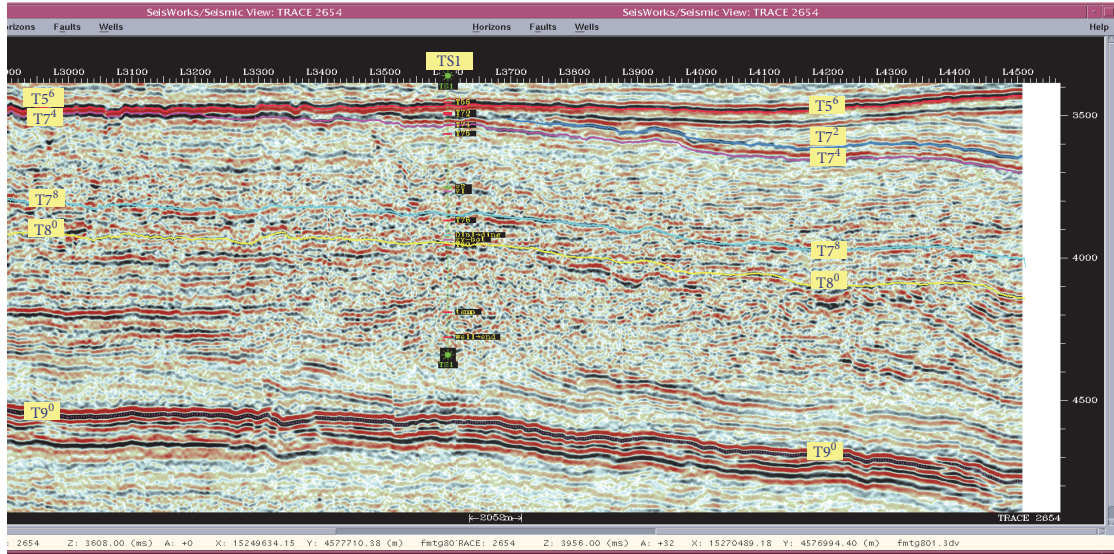
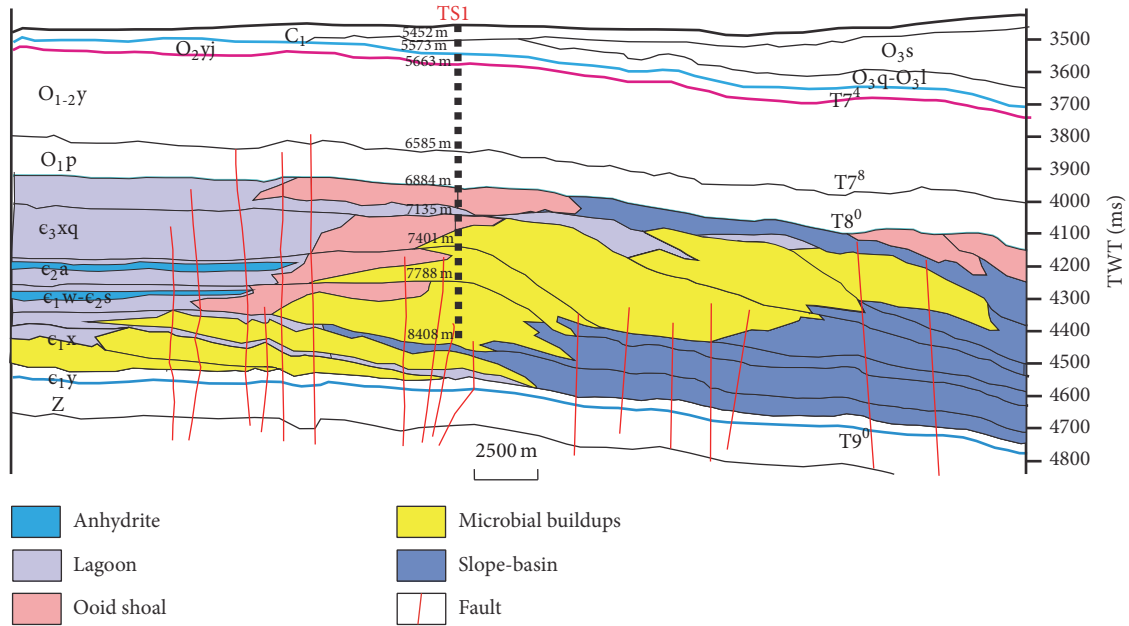


FIGURE 2: Generalized stratigraphic column from the Cambrian to Lower Carboniferous successions in the northern Tarim Basin, based on data from [5, 25].



(a)



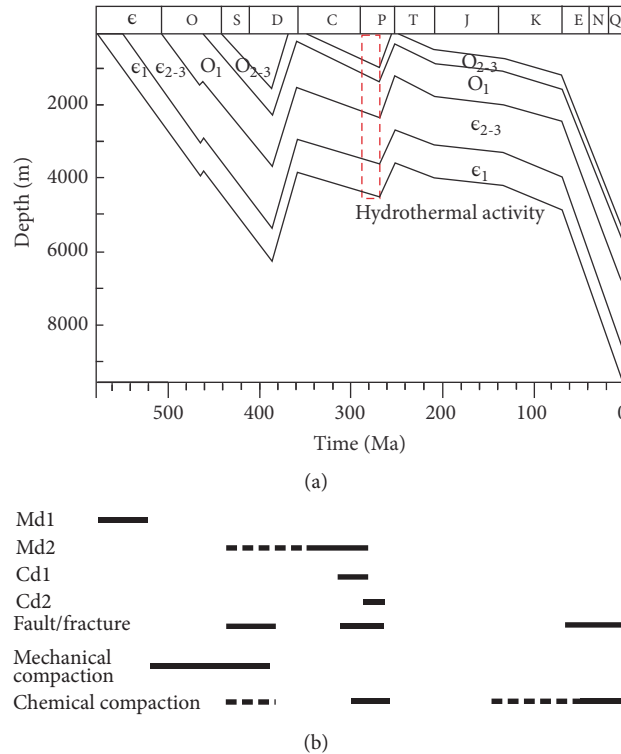


FIGURE 4: (a) Burial history curves of the Cambrian and Ordovician strata from well TS1 in the North Uplift (modified from Zhu et al., 2015). Dashed rectangle denotes the periods of Early Permian hydrothermal activity, based on data from [5, 26, 27]. (b) Paragenetic sequence of the main diagenetic events of Cambrian strata in the studied well. Dashed lines indicate uncertain timing or a long-term event.

shear fractures and tensional fractures (joints). The shear fractures are typically inclined (mostly less than  $45^\circ$ ) to the horizontal strata and can be easily observed in cores and wellbore image (Figures 6(a) and 6(b)). The shear fracture was formed by compressive stress, which is generally required to overcoming the large compressive strength of carbonate rocks. Although it is difficult to determine the critical condition for shear failure, this scenario mostly occurs in or near fault zones [34]. Our observation also indicates that the shear fractures were more frequently encountered in the deep part of well TS1 near the fault zone (Figures 2, 6(a), and 6(b)).

The tensional fractures (joints) in sedimentary successions are commonly normal to the bed interfaces; however, they are rarely found in cores and wellbore image logging although some researchers [35] claimed the predominance of such fractures in the Cambrian strata. In relatively less deformed sedimentary rocks, the density of tensional fractures is typically controlled by stratification rather than faulting or folding [36]. The tensional fractures are generally more abundant than shear fractures in the country rocks. This is attributed to the fact that the tensile strength is much lower than the compressive strength, so it can be easily formed in shallow crustal conditions [34]. The distance of adjacent tensional fractures is generally larger than or equal to the thickness of complete stratigraphic (mechanic) unit (i.e., integrated stratified beds) known as fracture-saturation (Figure 6(c); [36]). In this case, the density of tensional

fractures was much lower than that of shear fractures in fault zones which were more or less connected with stratigraphic (stratified) interface, serving as an effective network for fluid flow (Figure 6(c)).

**2.4. Diagenesis and Dolomitization.** Several hydrocarbon wells have been drilled to the depth over 8000 m in the northern uplift of Tarim Basin [5]. Of these, the borehole TS1 is the deepest one penetrated up to 8408 m deep with abundant dissolution pore spaces (vugs and fractures) preserved in the cores samples of Cambrian, providing an unique dataset for understanding how these pore spaces were generated by basinal or hydrothermal fluids during burial and/or structural diagenetic processes. The diagenetic processes of dolomite rocks in the North Uplift have been studied by several researchers [5, 25, 37, 38]. The main diagenetic events including dolomitization, mechanical and chemical compaction, fracturing, and structural-related hydrothermal dissolution and pore plugging (cementation) (Figure 4(b)).

Based on petrographic observations, four types of dolomite are recognized in the matrix and cement. Of these, two types are matrix dolomites (Figures 7(a)–7(e)): (1) fabric-retentive (mimetic) dolomite (Md1) and (2) medium to coarse crystalline fabric-obiterated nonplanar-a (anhedral) dolomite (Md2), and two types are cement dolomites: (3) medium to coarsely crystalline planar-s (subhedral) dolomite (Cd1) and (4) coarsely crystalline nonplanar-a saddle dolomite (Cd2) (Figure 7(f)).

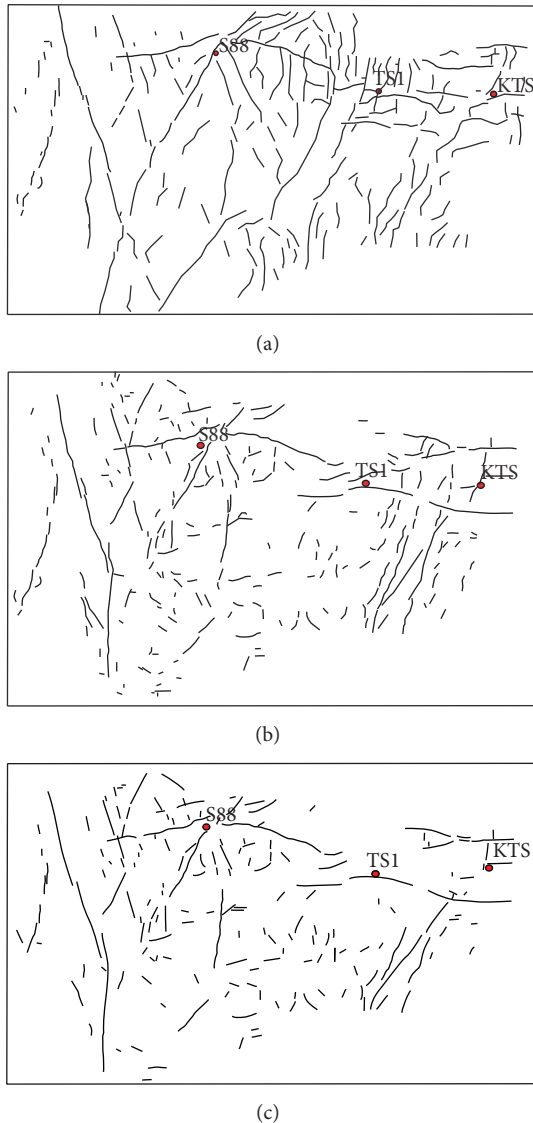


FIGURE 5: Spatial patterns of fault/fracture systems on some important stratal levels traced by seismic reflection surfaces in northern Tarim. (a)  $T9^0$  (lower surface of Cambrian formation), (b)  $T8^0$  (upper surface of Cambrian formation), and (c)  $T7^8$  (upper surface of Lower Ordovician Penglaiba Formation) as indicated in Figure 3. Note the location of borehole TS1.

The Md1 dolomites are the most abundant matrix dolomites with a wide spectrum of retentive fabrics (or texture) including mudstone to grainstone and diversified microbialites (microbial laminite, stromatolite, and thrombolite) and other subordinate fabrics (or textures) such as dissolution fabrics so that crystals vary widely in size from dolomiticrites within primary grains and/or microbial framework, to medium equant crystals in intercrystalline pores of packstone to grainstone or fenestral and framework pores of microbialites (Figures 7(a)–7(d)). Locally, extracellular polymeric substances (EPS) are found in microbially originated fabrics [39]. This type of dolomite generally demonstrates similar isotope (O-C-Sr) values to those of coeval seawater [5, 25, 38].

The primary depositional environments of these diverse Md1 dolomites varied from microbial reefs (or buildups) to ooidal shoal which could have aggraded to the tidal flat (Figure 1(b)). The preservation of mimetic fabrics (or textures) of primary sediments suggests they could have been formed either by microbial mediation, particularly for those microbial dolomites (Figures 7(a) and 7(b)) during deposition [39], or by penecontemporaneous dolomitization driven by reflux of more saline seawater in the protected lagoon through the ooidal shoal-microbial reefs on the platform margin [25, 38] (Figure 7(c)).

The Md2 dolomites, the second important matrix dolomites, are fabric-obliterated with rare ghosts of primary fabrics/textures. These dolomites, generally 100 to 200  $\mu\text{m}$  in size, are exclusively composed of nonplanar-a dolomite mosaics with few intercrystalline pore spaces (Figures 7(d) and 7(e)). This type of dolomite generally demonstrates similar  $\delta^{13}\text{O}$  and  $^{87}\text{Sr}/^{86}\text{Sr}$  values to those of Md1 dolomite although more negative  $\delta^{13}\text{O}$  values and radiogenic  $^{87}\text{Sr}/^{86}\text{Sr}$  ratios are present as well [5, 25]. All these data suggest a similar fluid in which Md2 dolomites had precipitated, at elevated temperature [5, 25, 38].

The Cd1 dolomites, 50 to 500  $\mu\text{m}$  in size, are characterized by planar-s to planar-e crystals which commonly occur as the initial cements lining the vuggy and fracture pore spaces (Figure 7(f)). Their close association with fracture implies that fracturing could have provided necessary conduits for fluid migration from depth, promoting initial dissolution and subsequent precipitation of Cd1 dolomite along the walls of vugs and fractures.

The Cd2 dolomites, 200  $\mu\text{m}$  to 2 mm in size, are composed of coarse nonplanar-a saddle dolomites with half-moon termination (Figure 7(f)). These saddle dolomites are mostly grown directly over the walls and rarely sit over the Cd1 crystals in vugs and fractures so that their precipitation was also closely associated with fracturing as well. The Cd2 dolomites generally have similar C but more negative O isotope values to those of matrix dolomites [38], suggesting that the Cd2 dolomites likely precipitated from higher-temperature dolomitizing fluids mostly sourced from the ambient aquifer in the host dolomite rocks [16].

### 2.5. Hydrothermal Activity and Dolomite Dissolution.

Numerous studies have demonstrated a strong Early Permian large igneous province (LIP) (mantle plume?) activity in the Tarim Basin [40, 41]; this could have exerted a substantial influence on the carbonate rocks including the Cambrian dolomites as they were penetrated by the intrusive diabases and volcanic eruptive edifice through thermal baking, enhanced thermal anomaly (or gradient), and/or hydrothermal fluid inputs [5, 25, 27, 38]. On the other hand, the high-angle conjugate (wrench) fault system that penetrated the Cambrian dolomites may have been developed and/or reactivated from the latest Carboniferous to the Early Permian as a result of collision of Tianshan arc accretionary to the north with Tarim block [31, 33]. Under this overall compressional (or transpressional) tectonic regime in the Tarim block, particularly in the northern part where the deep well TS is located, these faults and associated fractures could have

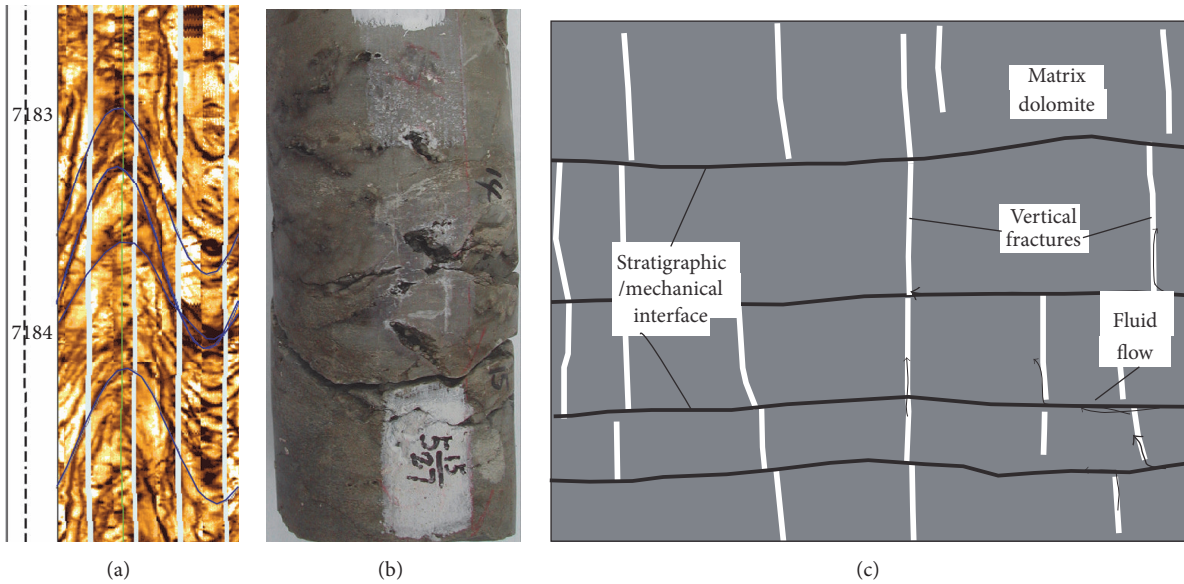


FIGURE 6: (a) Wellbore image logging shows the development of shear fractures on the wall, well TS1. (b) Borehole cores show the development of low-angle shear fractures at depths of 8407 m, well TS1. Note the vugs developed by dissolving enlargement along the fractures. (c) Stratigraphic controls tensional fracture patterns. Fractures develop within mechanical units and normal to the stratigraphic interfaces. The tensional fractures can serve as an effective network for fluid flow.

formed a complicated conduit network through which the hydrothermal fluids from depth could have readily migrated upwards and caused dissolution upon the host dolomites. The preferential occurrence of large less-filled vugs (up to several centimeters in size and 10% in porosity) along fractures in the Cambrian dolomites, particularly in the lower part of this drilled well (~8408 m deep) close to the fault (Figure 8), generally supports intensive dissolution upon the host dolomites and fracture enlargement likely by the fracture/fault-channeled, upflowing hydrothermal fluids from a greater depth; otherwise, few porosities could have remained at such a great depth [3]. The subsequent precipitation of more or less saddle dolomite cements further attests to a hydrothermal fluid in which they were precipitated as the Mg ions increased and reached the saturation relative to dolomite [5]. This scenario also agrees with upward-increasing distribution of pore-filling saddle dolomite cements (Figure 8). Moreover, the higher homogenization temperatures (122–153°C) of Cd2 dolomite in the Cambrian succession than the normal burial temperatures (68–105°C) during the Early Permian [5, 25] confirm the attribute of hydrothermal fluids.

### 3. Reactive Transport Modeling

**3.1. Methods.** In this study, the numerical program TOUGHREACT V2 [9] was used to investigate the hydrothermal dissolution and porosity generation in the deepest borehole TS1 in the Tarim Basin (Figure 1). This program is a nonisothermal RTM coupled code capable of simulating multiphase fluid flow, heat, and chemically reactive solution transport and has been used previously to simulate carbonate diagenesis, notably dolomitization [7, 11].

The numerical model is based on the geological architecture along the E-W trending transection across the well

TS1 in the northern Tarim Basin along which stratal and structural patterns were unveiled by 3D seismic reflectors and more specifically constrained by the borehole data of TS1 on aspects of horizon calibration, subsurface strata, and petrophysics. During the Early Permian, subsurface strata, in ascending order, include the Neoproterozoic, Cambrian, Ordovician, and Carboniferous successions (Figures 2 and 3). The model domain covers an area with a width of 35 km from west to east and a height of 3700 to 4000 m eastward; it is further divided into cells 350 m wide and decreased to 100 m close to the well TS1 area to give a higher-resolution characterization for the permeability heterogeneity around the fault zone. The whole grid system comprises 7320 active cells (Figure 9). The unstructured grid system is created by PetraSim which is an interactive graphical interface preprocessor for TOUGHREACT. In the model domain, it is assumed that all boundaries (including right, left, bottom, and top boundaries) are fluid-pressure boundaries, allowing recharge or discharge of fluids driven by hydrostatic pressure. The top boundary represents an earth surface condition with a temperature of 25°C and one atmospheric pressure. Initial burial temperature for all boundaries and model domain is determined specifically with a thermal gradient of 3.5°C/100 m based on the regional geothermal history [26]. The fluid pressure for the model domain and boundaries is presumably dominated by hydrostatic pressure with a gradient of 1 MP/100 m.

**3.2. Petrophysical Model.** The permeability of Cambrian dolomite rocks could have been influenced by the primary deposition, multiple diagenesis, and fracturing- or faulting-related fluid activity. Many permeability data show that most of the Cambrian dolomite samples yield the permeability values lower than the detection limits, but a few samples still follow the porosity-permeability (P-P) relationship

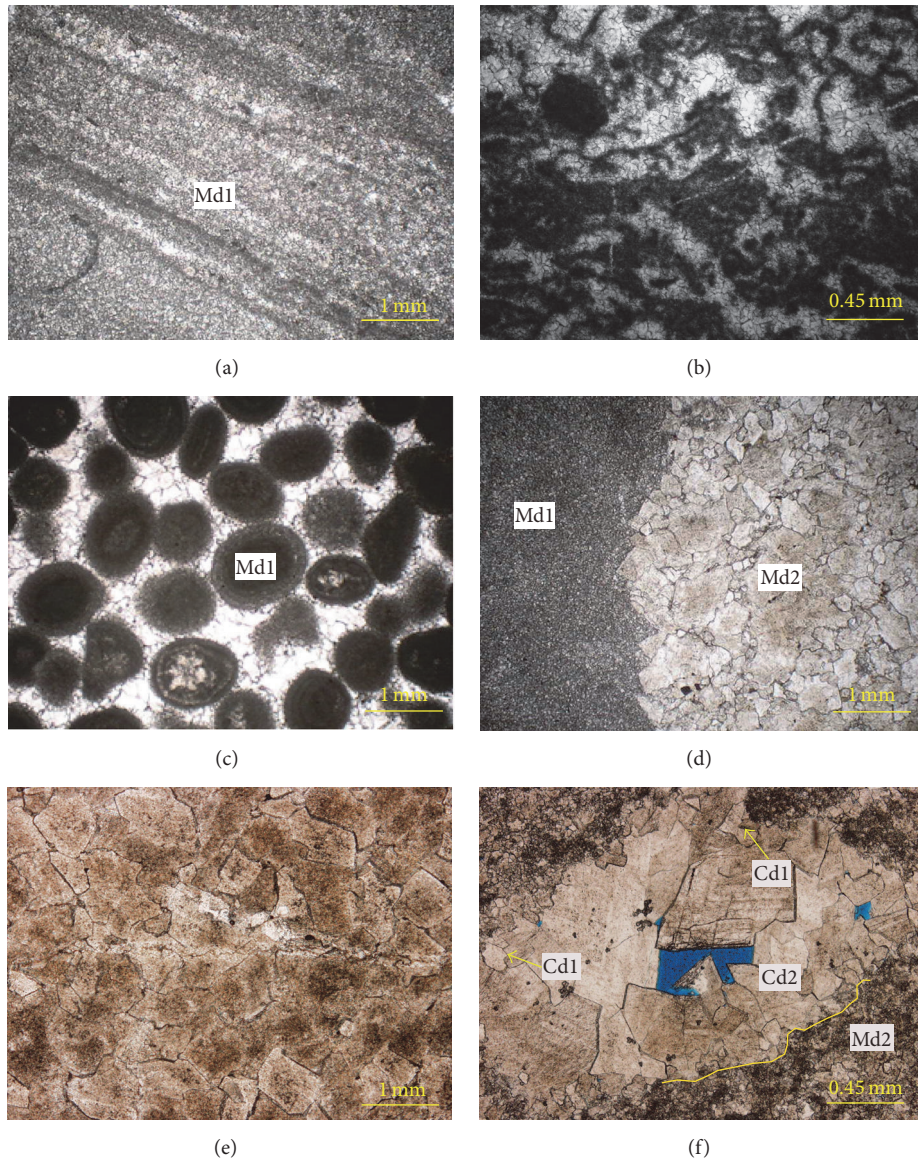


FIGURE 7: Photomicrographs showing different types of dolomites in Cambrian strata in well TS1. (a) Dark-brown to black, organic-rich laminated microbial dolomite (Md1), 7690 m. (b) Photomicrographs of microbial boundstones in platform margin reefs. Note the well-preserved original microbial fabric (Md2), 7875.7 m. (c) Photomicrographs of fabric-retentive dolomite (ooidal grainstone) (Md2) cemented with thin fibrous (or bladed) and equant dolomite crystals, 7710 m. (d) Very finely crystalline, fabric-retentive micrite (dolomicrite) (Md1) with medium-crystalline fabric-obliterative dolomite (Md2), 8030 m. (e) Medium to coarse crystalline fabric-obliterative dolomite (Md2), 7155 m. (f) Photomicrograph showing cement dolomites in the vug developed in the matrix dolomite: the initial medium-crystalline planar-s (subhedral) dolomites (Cd1) and subsequent coarse crystalline saddle dolomites (Cd2) which are characterized by curved crystal faces and undulose extinction. 7875 m. Note the relict pore space in vug center (blue resin).

(Figure 10). This implies that the P-P relationship proposed by Lucia [42] can still be used to estimate the permeability of the Cambrian dolomites during the Permian Period, but the impact of diagenesis should also be considered. In the studied borehole section of TS1 and adjacent area, there are five major primary lithological types in the Cambrian succession: peloidal-ooidal grainstone (Gs), packstone (Ps), wackestone (Ws), mudstone (Ms), and microbial boundstone (Bs) (Figure 9).

Based mainly on the permeability data, the dolomite rocks are tentatively classified into three classes: classes 1 to 3 with decreasing permeability (Figure 10). In view of the high uncertainty for the P-P relationship due to strong diagenetic alterations on the dolomite rocks, three scenarios (I to III) (Table 1) are further presumed to test which case is more close to the reality during the course of intense dissolution on the dolomite host. As documented above, the primary dolograins were strongly cemented (Figure 7(c)) and/or

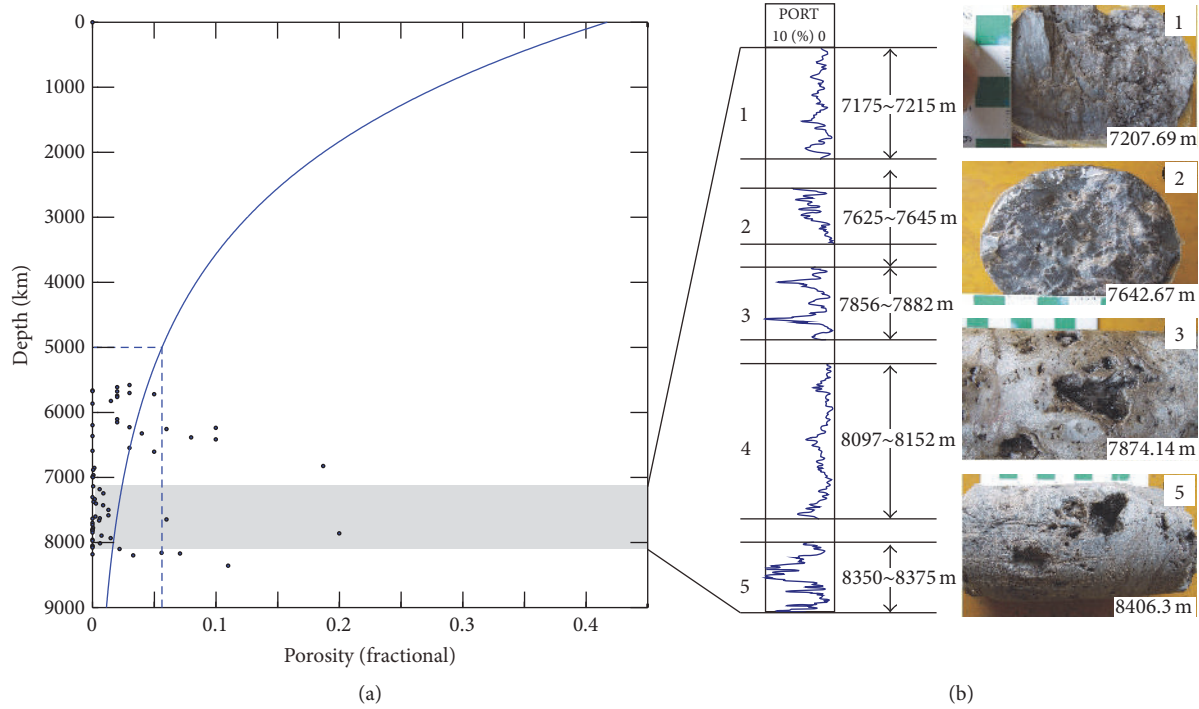


FIGURE 8: (a) Plot of porosity derived from well logging interpretation against depth in well TS1. The solid line shows the porosity-depth relationship of carbonates according to Schmoker and Halley (1982). The dashed rectangle shows the porosity ranges of carbonates buried below depth of 5000 m. (b) Porosity variations interpreted from well logging in intervals 1–5 with core photos. Note prevalence of dissolved, less-cemented open vugs present in the deeper part of the well.

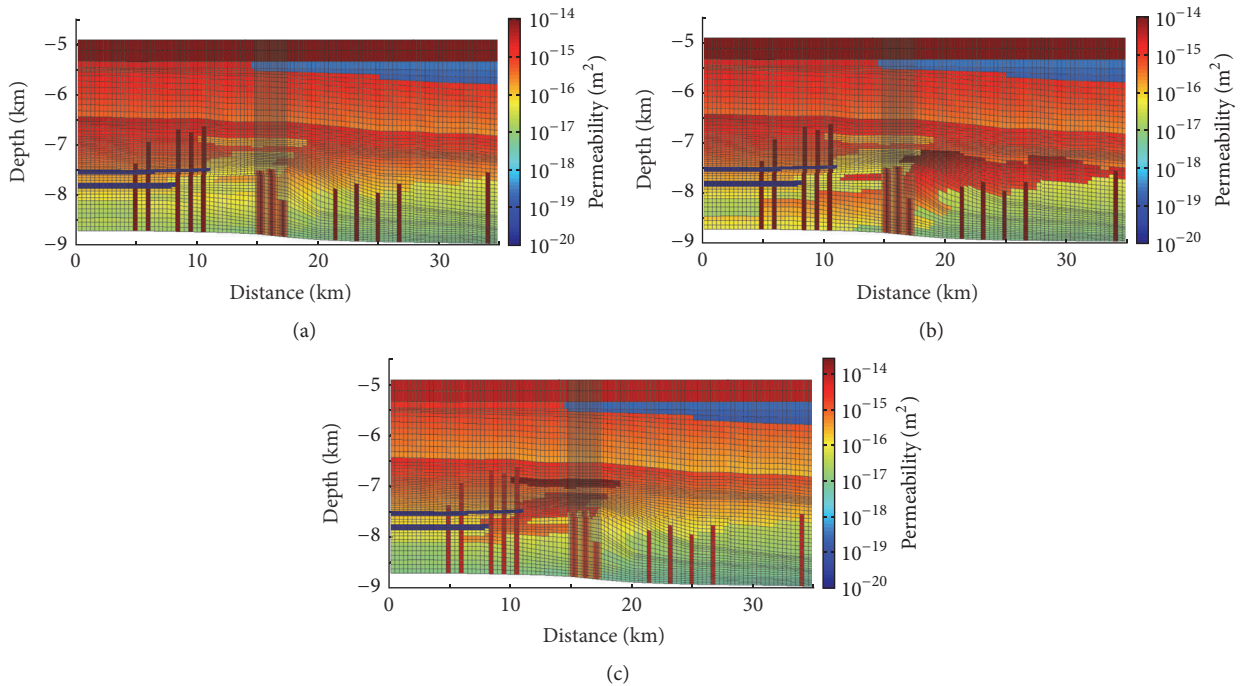


FIGURE 9: Initial values of horizontal permeability used in simulations for Scenario I (a), Scenario II (b), and Scenario III (c). Note that the permeability was assigned to different stratigraphic and lithologic units based on Figure 3. The lithologic units which are not displayed in Figure 3 are assigned based on the stratigraphic description in Figure 2.

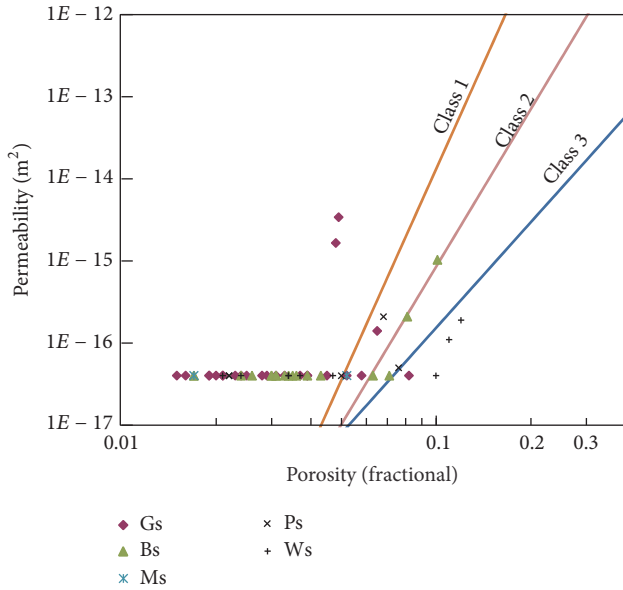


FIGURE 10: Crossplots of porosity and permeability for different types of dolomite rocks. Note the three lines which show the three classes of porosity-permeability relationship according to Lucia (1995). The permeability of the detection limit is  $4 \times 10^{-17} \text{ m}^2$ .

TABLE 1: Assignment of permeability class and scenario for dolomite rocks used in simulation.

	Scenario I	Scenario II	Scenario III
Grainstone	Class 3	Class 3	Class 1
Microbial reefs	Class 2	Class 1	Class 2
Packstone	Class 2	Class 2	Class 2
Wackestone/mudstone	Class 3	Class 3	Class 3

recrystallized (Figure 7(e)) mostly with extremely low porosity and permeability (Figure 10) so that this type of dolomite is initially assigned to class 3. For comparison, it is also assigned to class 1 in another scenario (III) in view of the relatively high permeability in some of this type of dolomite which may have been not substantially plugged before or during the significant dissolution. Although the microbial reefs or buildups (boundstones) on the platform margin may have relatively high volumes of primary fenestral or framework porosity, their permeability, which is highly dependent on whether the pores are connected or not, is not necessarily high accordingly. Therefore, this type of dolomite is assigned to class 2 (intermediate) in two scenarios (I and III) and to class 1 in one scenario (II) for a comparison (or sensitivity test). Dolopackstone, dolowackestone, and dolomudstone are generally fabric-retentive, with rare cements and weak diagenetic modification. Of these, dolopackstones roughly yield an intermediate permeability (Figure 10), so that it is tentatively assigned to class 2 in all scenarios. In contrast, dolowackestone and dolomudstone generally yield the lowest permeability, so that they are collectively set to class 3 in all scenarios.

Other rocks except dolomites are set with a consistent permeability without sensitivity test for the P-P relationship.

As documented above, in the Cambrian platform interior succession, there are widespread evaporites (mostly anhydrites) occurring in the Awatage Formation (Figure 3) which are generally thought as the impermeable aquitard; its permeability is thus set to  $1 \times 10^{-20} \text{ m}^2$  [43], almost impermeable to fluids. Above the Cambrian, the Lower Ordovician Penglaiba Formation is dominated by the shoal dolomites (grainstone) in the lower part which pass upward into shelfal interbedded dolomites and limestones, so it is tentatively set to class 3 in the lower part and class 2 in the upper part. The overlying Yinghshan and Yijianfang formations of the Lower-Middle Ordovician mainly comprise the wackestone and lime mudstone with relatively low porosity and permeability; they are thus assigned to class 3. Further upwards, the Upper Ordovician comes which mainly comprises the argillaceous limestones (wackestones and mudstones) intercalated with black shales deposited on the offshore shelf; this argillaceous-rich succession is thus regarded approximately as corresponding to the shale. The permeability of shales is estimated based on the P-P relationship proposed by Harrison and Summa [44]. The Upper Ordovician is overlapped by the major unconformity surface on which it is overlain by the Carboniferous strata which are mainly composed of sandstones (Figure 2). These sediments were laid near the Earth surface during the Early Permian. The permeability near Earth surface may have significantly increased so that it cannot be reasonably described by the P-P relationship [45]. In our model, the permeability of Carboniferous sandstones is set to  $1 \times 10^{-14} \text{ m}^2$ , consistent with the previously reported permeability values near the Earth surface [45]. Petrophysical variations along the profile across the well TS1 are illustrated in Figure 9.

The development of tensional or transtensional fracture networks in wall-rock (Figure 6(c)) commonly increases the vertical permeability substantially. To study the influence of tensional/transtensional fractures, the permeability anisotropy ( $k_{\text{horizontal}} : k_{\text{vertical}}$ ) ranging from 1 to 100 was tested in the simulations.

The permeability in fault zones varies significantly in space and time [46]. Ingebritsen and Manning [47] observed that the drastic increase in crust permeability (100 to 1000 times) could occur through the tectonic activity (e.g., seismic rupturing). In our baseline modeling, the fault permeability is set to  $1 \times 10^{-14} \text{ m}^2$  which is approximately 100 times higher than that of the host rock. In addition, sensitivity tests for permeability in fault zone were conducted by one order of increase or decrease in magnitude.

The initial fluid composition was constrained by fluid inclusion data derived from hydrothermal-originated minerals such as saddle dolomite, fluorite, barite, and quartz present in the Paleozoic carbonates [48], which is assumed to be equilibrium with dolomite at the temperature of the bottom influx boundary (Table 2). In contrast to the precipitation of dolomite, the dissolution of dolomite is generally considered as an equilibrium reaction process [9, 49]. Although kinetic reaction process can also be modeled by the TOUGHREACT [9], thermodynamic reaction modeling can reach convergence through iteration more rapidly (or efficiently), leading to more precise results [9] due to the small variance of saturation index in the simulation.

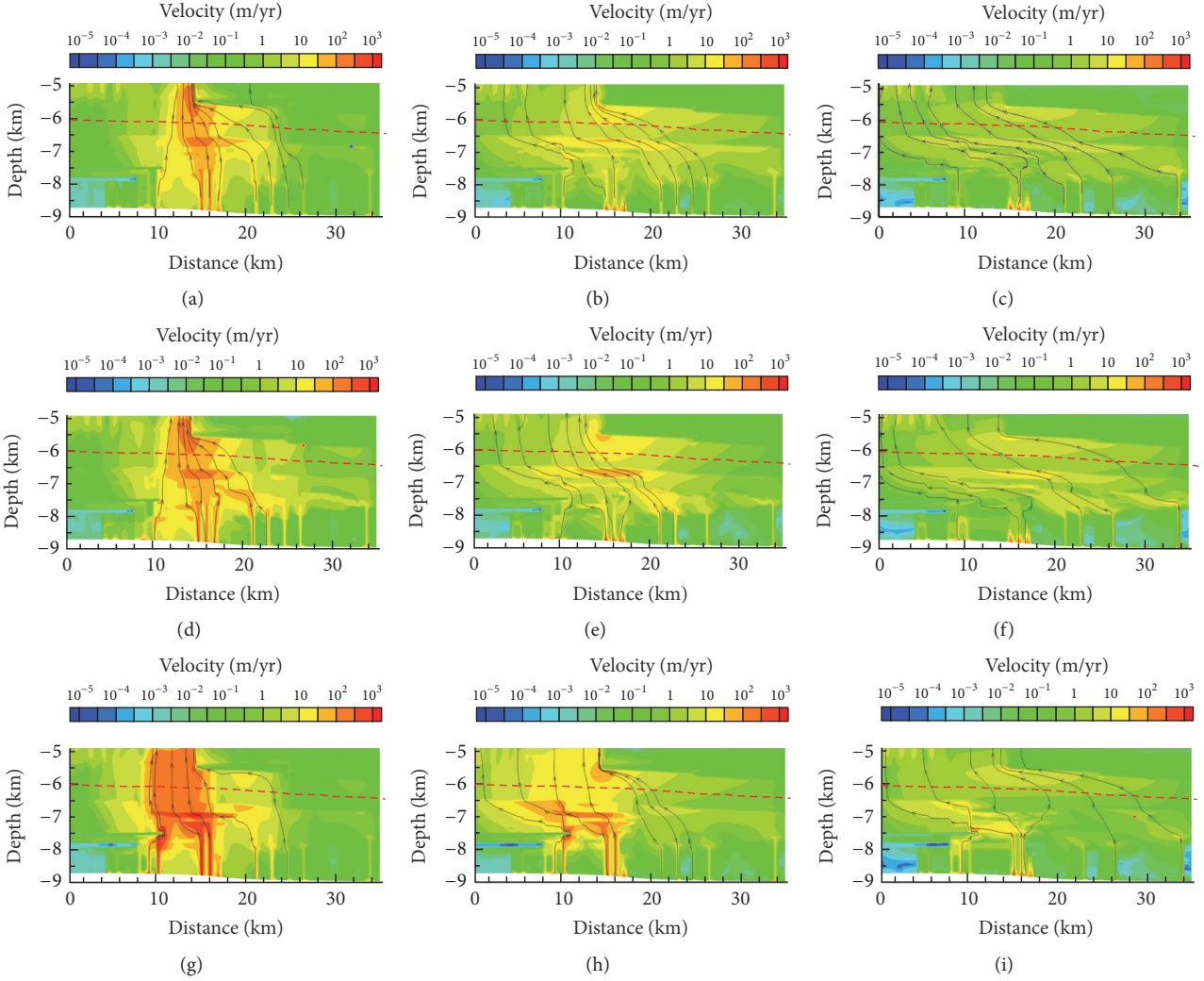


FIGURE 11: The fluid velocity for Scenario I: (a)  $k_h : k_v = 1$ , (b)  $k_h : k_v = 10$ , and (c)  $k_h : k_v = 100$ , Scenario II: (d)  $k_h : k_v = 1$ , (e)  $k_h : k_v = 10$ , and (f)  $k_h : k_v = 100$ , and Scenario III: (g)  $k_h : k_v = 1$ , (h)  $k_h : k_v = 10$ , and (i)  $k_h : k_v = 100$ . The arrow lines indicate the general pathways of fluids. Note the model domains below the dashed lines which were arranged for plotting dissolved porosity in Figure 15.

TABLE 2: Initial fluid composition.

Component	Total aqueous concentration (mol/kg)
Na <sup>+</sup>	1.13
K <sup>+</sup>	0.05773
Ca <sup>+2</sup>	0.206
Mg <sup>+2</sup>	0.0438
Cl <sup>-</sup>	1.686
HCO <sub>3</sub> <sup>-</sup>	0.57179
SO <sub>4</sub> <sup>-2</sup>	0.0193
pH	7

## 4. Results

The reactive transport model is mainly used to analyze the fluid flow, accompanying formation temperature, and spatial distribution of dissolved porosity as well as sensitivity of

fault zone permeability. The spatial pattern of fluid flow and temperature will determine the final distribution of dissolved porosity.

**4.1. Spatial Pattern of Fluid Flow.** Modeling results show that the fluid was dominantly driven to flow in the dolomites of platform margin and was significantly suppressed in dolomites of platform interior and slope due to the presence of Middle Cambrian low permeable evaporative deposits and Upper Ordovician shaly limestones and shales, respectively (Figure 11).

In platform margin dolomites, upward-flowing fluids driven by the difference of formation pressure predominated. In the low part of model domain, upflowing fluids were focused in the fault zones which would flow laterally into the permeable country dolomites near the top of faults.

Permeability anisotropy has an important control on fluid and temperature patterns. For the low permeability anisotropy ( $k_h : k_v = 1$ ), the fluids mainly flow vertically

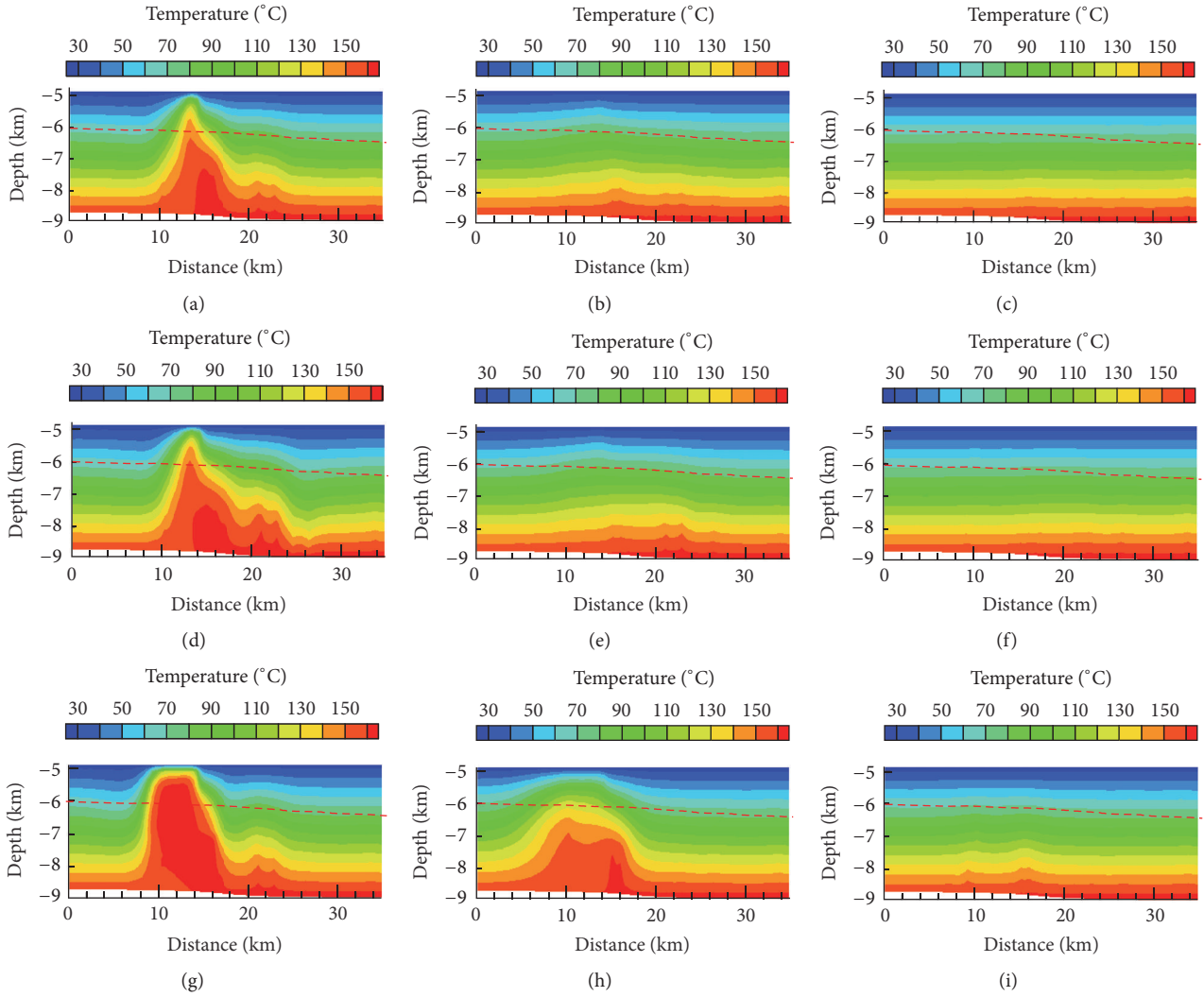


FIGURE 12: The temperature patterns of Scenario I: (a)  $k_h:k_v = 1$ , (b)  $k_h:k_v = 10$ , and (c)  $k_h:k_v = 100$ ; Scenario II: (d)  $k_h:k_v = 1$ , (e)  $k_h:k_v = 10$ , and (f)  $k_h:k_v = 100$ ; and Scenario III: (g)  $k_h:k_v = 1$ , (h)  $k_h:k_v = 10$ , and (i)  $k_h:k_v = 100$ . Note the model domains below the dashed lines which were arranged for plotting dissolved porosity in Figure 15.

(Figures 11(a), 11(d), and 11(g)). As permeability anisotropy increases ( $k_h:k_v = 10$ ), some of fluids tend to flow laterally, and they would almost completely flow laterally as the anisotropy increases further ( $k_h:k_v = 100$ ). Furthermore, permeability anisotropy, particularly the vertical permeability, also controls the fluid velocity which would decrease as the vertical permeability decreases. The fluid velocity varies from 1000 to 10 m/yr with a low permeability anisotropy ( $k_h:k_v = 1$ ). It varies from 100 to 1 m/yr with a moderate permeability anisotropy ( $k_h:k_v = 10$ ). It will decrease further, varying from 10 to 0.1 m/yr, while the permeability anisotropy increases further ( $k_h:k_v = 100$ ).

By comparing the permeability in different scenarios, the permeability heterogeneity of host rock mainly influences the fluid velocity but exerts few impacts on general pattern of fluid flow. In addition, the well-cemented or strongly recrystallized grainstones (scenarios I and II) could have reduced the fluid velocity 10–100 times in comparison to

the grainstones with a little early cements (scenario III) (Figure 11).

**4.2. Temperature Patterns.** Similar to the fluid flow pattern, formation temperature is also controlled by permeability anisotropy (Figure 12). In the context of low permeability anisotropy ( $k_h:k_v = 1$ ) and high fluid velocity, the formation temperature is dominated by fluid convective heat transfer, which would decrease significantly in the front zone of hydrothermal invasion and generate thermal anomalies of 50°C higher than normal temperature (Figures 12(a), 12(d), and 12(g)). In contrast, in the context of moderate permeability anisotropy, the thermal anomalies would wane apparently, only giving rise to an increase on formation temperature of 1–10°C (Figures 12(b), 12(e), and 12(h)). Furthermore, as permeability anisotropy is enhanced further ( $k_h:k_v = 100$ ), vanishingly weak thermal anomaly is observed probably as

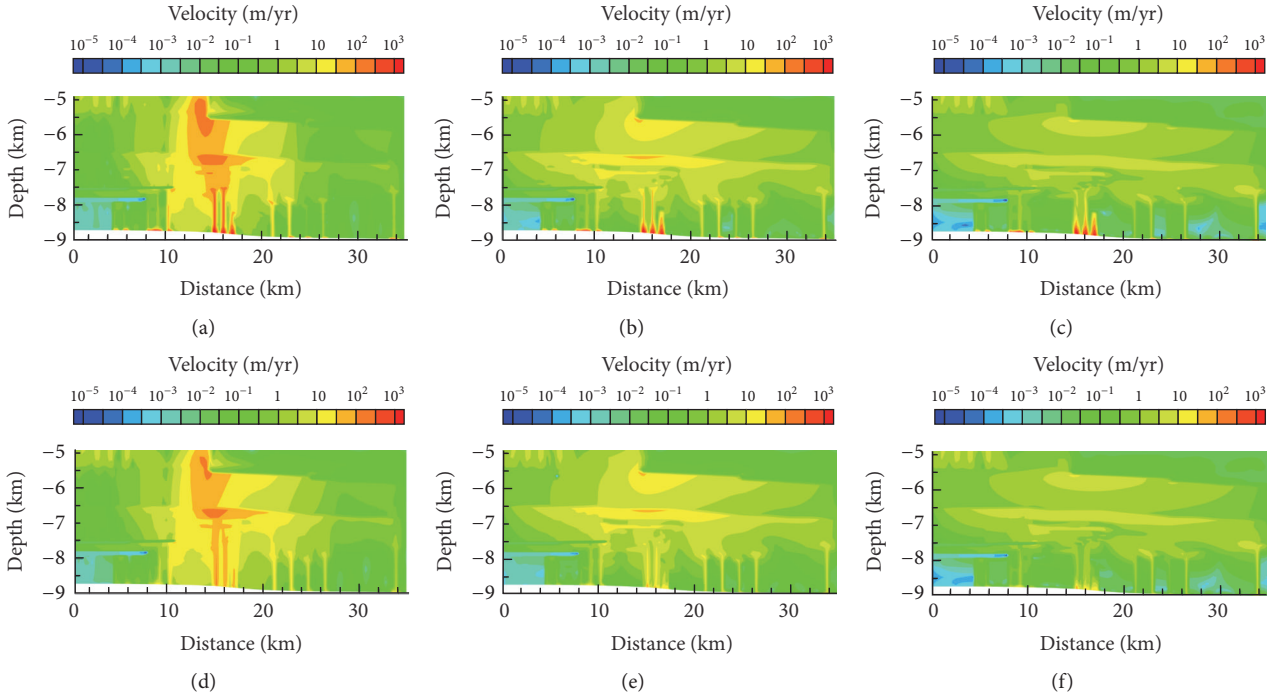


FIGURE 13: The fluid velocity for Scenario I with fault permeability of  $1 \times 10^{-13} \text{ m}^2$ : (a)  $k_h : k_v = 1$ , (b)  $k_h : k_v = 10$ , and (c)  $k_h : k_v = 100$  and fault permeability of  $1 \times 10^{-15} \text{ m}^2$ : (d)  $k_h : k_v = 1$ , (e)  $k_h : k_v = 10$ , and (f)  $k_h : k_v = 100$ .

a result of enhanced heat conduction in rocks (Figures 12(c), 12(f), and 12(i)).

Besides the permeability anisotropy, temperature patterns can also be influenced by the permeability heterogeneity because this heterogeneity can increase the fluid velocity and enhance the convective heat. In scenario III, if the shoal-deposited grainstones were rarely cemented with high porosity and permeability during the Early Permian, a thermal anomaly of about  $10\text{--}30^\circ\text{C}$  could have been induced in these sediments relative to well-cemented grainstones (scenarios I and II) around the well TS1.

**4.3. Influence of Fault Permeability.** Taking scenario I as an example, the sensitivity of fault permeability to the modeling results was tested. The fault permeability varies from the baseline value ( $1 \times 10^{-14} \text{ m}^2$ ) to the values by plus or minus one order of magnitude relative to the consistent permeability of country rocks. The modeling results show vanishingly small influences of fault permeability on the fluid velocity and temperature patterns in comparison to the baseline modeling (Figures 13 and 14).

The fluid velocity and temperature patterns changed slightly in the condition with a low permeability anisotropy ( $k_h : k_v = 1$ ) (Figures 13(a), 13(d), 14(a), and 14(d)) which have the highest vertical permeability and strong fluid transport ability. For a comparison, in the conditions with moderate and large permeability anisotropies, the fault permeability almost exerts no influence on the simulation results.

**4.4. Spatial Patterns of Dolomite Dissolution.** Our simulation on dolomite dissolution runs for three scenarios for a time

interval of 10 Ma (Figure 15) in view of long-lasting compression from the north by the collision of Tarim block and Tianshan accretionary complex during the Late Carboniferous–Early Permian ( $\sim 306\text{--}270 \text{ Ma}$ ) [31–33]. The simulation results indicate that the porosity can be produced continuously by dissolution in dolomite rocks within fault zones due to a higher fluid velocity there. The dolomite dissolution generally occurred in the hydrothermal invasion zones of the wall-rock. In addition, the development of porosity is also controlled by the permeability anisotropy. For a low permeability anisotropy ( $k_h : k_v = 1$ ), a large amount of dissolved porosity, with a maximum up to 5%, occur in the upper part of wall-rock and gradually decrease downward (Figures 15(a), 15(d), and 15(g)). Combined with fluid velocity and temperature patterns together, dissolved porosity was produced mainly in the place where formation temperature decreases significantly.

In contrast, with a moderate permeability anisotropy ( $k_h : k_v = 10$ ), the dissolved porosity, although decreasing to ca. 2%, takes place more widely (Figures 15(b), 15(e), and 15(h)). In view of fluid velocity and temperature patterns together, the porosity occurs mainly in the place where fluids flow rapidly as in scenarios I and II. But in scenario III, the dissolved porosity is controlled mainly by the temperature pattern due to enhanced thermal anomaly.

As permeability anisotropy increases further ( $k_h : k_v = 100$ ), dissolution on dolomites is dramatically reduced for the simulation time interval. In the most part of the model domain, less than 0.2% of dissolved porosity can be generated, even in local places where more pore or vuggy spaces (ca. 0.3–0.5%) can be dissolved (Figures 15(c), 15(f), and 15(i)).

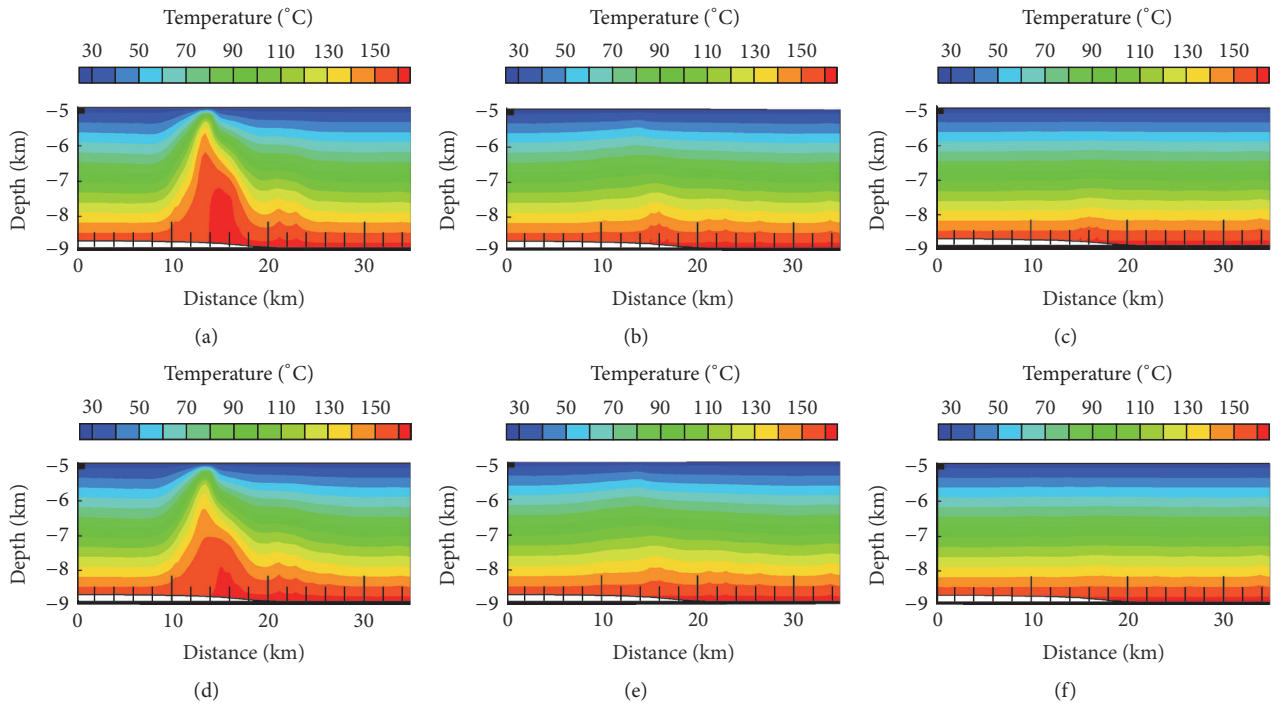


FIGURE 14: The temperature patterns for Scenario I with fault permeability of  $1 \times 10^{-13} \text{ m}^2$ : (a)  $k_h : k_v = 1$ , (b)  $k_h : k_v = 10$ , and (c)  $k_h : k_v = 100$  and fault permeability of  $1 \times 10^{-15} \text{ m}^2$ : (d)  $k_h : k_v = 1$ , (e)  $k_h : k_v = 10$ , and (f)  $k_h : k_v = 100$ .

This is mainly because the fluids dominantly flow laterally along the isotherms of temperature. As a result, the dissolving capacity of fluid is drawn down rapidly in response to temperature decrease. In addition, the fluid velocity has also played a role in dolomite dissolution. The fluid velocity has slightly increased from scenarios I to III (Figures 11(c), 11(f), and 11(i)), increasing the dissolved porosity to some extent (Figures 15(c), 15(f), and 15(i)). However, the fluid velocity only plays a subordinate role in the formation of dissolved porosity in comparison to the isothermal flow which causes one-order magnitude reduction of porosity in contrast to the high vertical permeability ( $k_h : k_v = 10$ ) (Figures 15(b), 15(e), and 15(h)).

### 5. Discussion

This study aimed to investigate the dissolution upon the dolomites at great depth within the fault zones induced by the upflowing hydrothermal fluids around the deeply penetrated well TS1 and adjacent area in the North Uplift of Tarim Basin. This could provide an alternative insight on processes and controls of burial and/or hydrothermal dissolution on dolomites, porosity generation and preservation in deeply buried fault-related carbonate reservoirs, facilitating a better understanding for the formation of deeply buried carbonate reservoirs, and more efficient prediction and exploration of hydrocarbon to greater depths.

#### 5.1. Deep Burial/Hydrothermal Dissolution of Carbonates.

The burial dissolution of carbonates is still a controversial

topic for reservoir geologists [50]. Many authors have proposed that deep-burial dissolution of carbonate could have been induced by a series of acidic fluids, such as  $\text{CO}_2$ -  $\text{H}_2\text{S}$ - and organic acidic-rich fluids, which could be produced by different geological process. The strong large igneous province (LIP) activity in the Tarim Basin during the Early Permian could have caused intense thermal anomaly [26, 41], which in turn could have promoted organic matter maturation, organic acid production, and thermochemical sulfate reduction in the Cambrian strata [48, 51]. As a result, the acidic anions may have increased in the hydrothermal fluids by mixing with the formation and magmatic-originated fluids at depth. However, Ehrenberg et al. [50] pointed out that the dissolving fluids could quickly reach equilibrium with carbonate minerals due to the rapid kinetic dissolution of carbonate minerals. In this case, acid-induced dissolution on carbonates could have only occurred locally in the place where the acidic fluid was generated or injected.

Many researchers proposed that widespread dissolution of carbonates may have been caused by retrograde dissolution during the course of temperature falling [8, 43]. As fluids from depths flow upward, fluid temperature decreases gradually. In this condition, the original carbonate-saturated fluids then tend to be undersaturated relative to carbonate minerals, thereby causing carbonate dissolution. In burial condition, the basinal fluid undoubtedly has a higher temperature, which will lead to a faster rate of chemical reaction, but characterizes a fairly slow velocity relative to the near surface conditions. These factors make the formation fluids quickly reach the equilibrium with carbonate minerals. In this light,

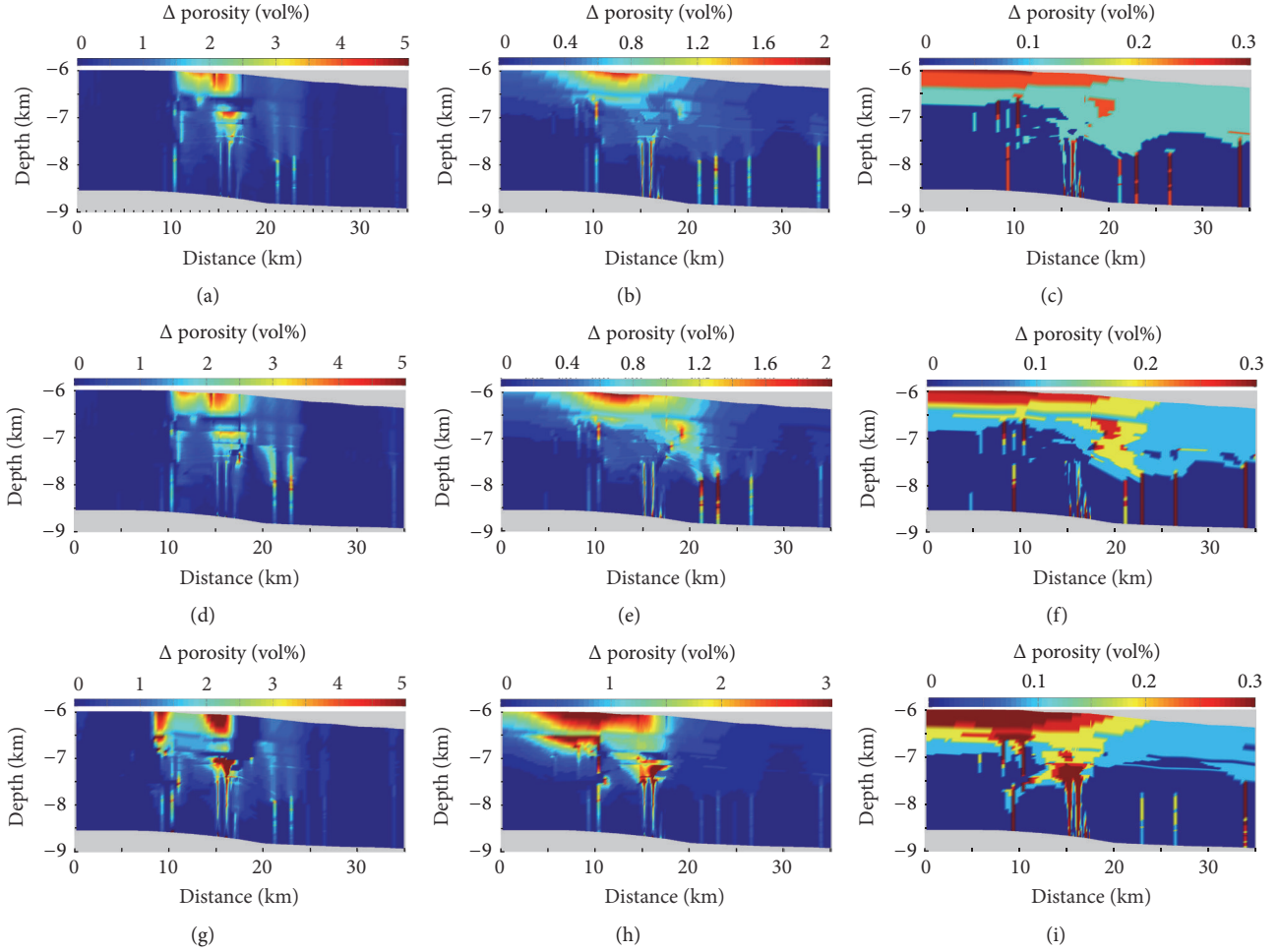


FIGURE 15: The dolomite dissolution patterns simulated for an interval of 10 Ma for Scenario I: (a)  $k_h:k_v = 1$ , (b)  $k_h:k_v = 10$ , and (c)  $k_h:k_v = 100$ ; Scenario II: (d)  $k_h:k_v = 1$ , (e)  $k_h:k_v = 10$ , and (f)  $k_h:k_v = 100$ ; and Scenario III: (g)  $k_h:k_v = 1$ , (h)  $k_h:k_v = 10$ , and (i)  $k_h:k_v = 100$ . The plotting area is referred to the model domain below dashed lines in Figure 11 which is mainly composed of dolomite formation.

we believe that retrograde dissolution may have played the most important role in carbonate dissolution during deep burial. Under this circumstance, in view of the fast reaction rate and retrograde dissolution behaviour, substantial dissolution and subsequent pore development require a much high volume of fluid relative to the host carbonate rock which is favoured in the connected pore spaces such as open fracture networks.

This is generally consistent with our observation on the deeply buried Cambrian dolomite rocks in which the intensive dissolution and abundant vuggy spaces occurred mainly in connected fracture networks and pores system close to the fault zone around the bottom of penetrated borehole TS1 (Figure 8(b)). In contrast, dolomite (mostly saddle dolomite) precipitation in the vuggy and fracture spaces and matrix recrystallization in the Mid-upper Cambrian dolomites were likely associated with the closed (or semiclosed) pore systems which were generally more distal to the fault zone.

*5.2. Importance of the Wall-Rock Vertical Permeability.* The modeling results have demonstrated that wall-rock

permeability exerts a fundamental control on the fluid flow, formation temperature, and dolomite dissolution as well. The permeability anisotropy is the most important parameter that controls the general patterns of fluid flow, fluid velocity and temperature. In comparison, the permeability heterogeneity could have mainly influenced the fluid velocity and temperature patterns.

Despite the fast rate of carbonate dissolution, our simulation results suggest that the burial or hydrothermal dissolution of carbonates at depths was not simply a transport-limited process; rather it could be an integrative effect of both fluid velocity and temperature gradients. With a high vertical permeability of wall-rock ( $k_h:k_v = 1$ ) in the fracture/fault zone, although the higher-speed fluids could have delivered more ample dissolved matter, the stronger thermal anomaly around the area of well TS1 only with a slight temperature decrease (Figures 12(a), 12(d), and 12(g)) seemingly limited the dolomite dissolution. In contrast, the hydrothermal front with a maximum decrease in temperature led to substantial dissolution on dolomites (Figures 15(a), 15(d), and 15(g)). As the vertical permeability decreased, the fluid velocity could

have reduced accordingly through which the dissolution tended to be a transport-limited process (Figures 15(b), 15(e), and 15(h)). In this case, the distribution of dissolved porosity may have mirrored the variation of fluid velocity (Figures 11(b), 11(e), and 11(h)).

As vertical permeability further decrease ( $k_h : k_v = 100$ ), the dissolved porosity is reduced significantly (Figures 15(c), 15(f), and 15(i)) due to isothermal flowing (Figures 11(c), 11(f), and 11(i)). Therefore, the deeply buried carbonate reservoir was unlikely favoured by the hydrothermal dissolution if the vertical permeability of wall-rocks was too low.

**5.3. Influence of Fault Zone Permeability.** The sensitivity test indicates that the fault permeability has a little influence on burial/hydrothermal dissolution. Since the internal architecture of fault zone is too complicated, it is difficult to estimate permeability variations across the fault zone [47, 52, 53]. Alternatively, this research implies that fault-related hydrothermal dissolution on dolomite rocks could be potentially predicted by studying the permeability pattern of the wall-rock.

With progressive burial of sediments, the geological fluid would have stagnated in the deep part of basins due to the dramatic decrease of rock permeability [54, 55]. However, tectonic activity accompanying with increasing fault permeability could have enhanced crossing-stratal fluid flow and basin-scale deep circulation of geological fluids [54, 55]. In general, after seismic rupturing and subsequent abrupt permeability increase, the permeability in fault zones will gradually decrease with times [14, 47] which would influence the hydrothermal fluid flow as well. Our simulations have tested the influence of this process on the fluid flow, temperature pattern, and induced carbonate dissolution. The modeling results indicate that, as the fault permeability decreases, burial dissolution can still persist onwards in view of the small influences of fault permeability on the fluid velocity and temperature patterns (Figures 13 and 14) which will control the distribution of dissolved porosity.

**5.4. Function of Cap Aquitards and Internal Aquifers.** The hydrothermal dissolution mainly occurred in dolomites deposited on platform margin but did not occur in dolomites of platform interior and slope environments (Figure 15), probably resulting from the presence of low permeable cap aquitards which may have prevented vertical crossing-formational flowing (Figure 11). This implies that occurrence of low permeable cap aquitards is an important indicator for predicting of deeply buried carbonate reservoirs.

The internal aquifers in which fluids mainly flow horizontally are not favourable for burial/hydrothermal dissolution due to a constant temperature if they are laid horizontally during burial. The unconformities which have high horizontal permeability were generally considered as important exploration targets for carbonate reservoirs [1, 2]. However, the modeling result suggests that the porosity along the horizontally buried unconformity surfaces within carbonate successions, although acting as internal aquifers, may have not been enhanced necessarily by hydrothermal dissolution due to insignificant temperature drawdown.

**5.5. Predictions of Deep/Ultradeep Carbonate Reservoirs.** As the burial depth increases, the primary porosity of carbonates will be significantly lost due to the mechanical and chemical compaction [3, 5] (Figures 4(b) and 8(a)), thus burial/hydrothermal dissolution could have played a critical role in pore generation, preservation, and subsequent reservoir development.

Our modeling demonstrates the importance of vertical permeability of wall-rocks on burial or hydrothermal dissolution. Those dolomites (or carbonates), as if tensional or transtensional fractures (joints) were extensively developed, would have a higher potential to develop dissolution vugs or cavities, facilitating formation of deeply buried carbonate reservoirs (Figure 15). Moreover, studies on the style and mechanism of fracturing and/or faulting would be much helpful for better understanding for the flow patterns and pathway of basinal thermal fluids. In turn, if integrated with reactive transport modeling, the deeply buried carbonate reservoirs could be more precisely predicted.

## 6. Conclusions

The Cambrian dolomite strata penetrated by the deep well TS1 in the northern Tarim Basin are characterized by microbial reefs (or buildups) deposited on the platform margin. Four types of dolomite texture are identified, including two types of matrix dolomites, (1) fabric-retentive dolomite (Md1) and (2) fabric-obliterated nonplanar dolomite (Md2), and two types of cement dolomite, (3) medium to coarsely crystalline planar-s (e) dolomite (Cd1) and (4) coarsely crystalline nonplanar saddle dolomite (Cd2). The dolomites were subject to complicated diagenetic events and alteration, such as early dolomitization, compaction, fracturing, and hydrothermal dissolution and alteration (precipitation and recrystallization).

In the northern Tarim Basin where the well TS1 is located, a series of high-angle X-shaped (wrench) fault complex dominate the dolomite strata with subordinate N-S and E-W trending fault series; they cut off the Cambrian base and partially extend into the Ordovician. These fault/fracture complexes may have been formed during the Late Ordovician while the Tarim plate was subducted northward beneath the Central Tianshan arc and was further reactivated while it was finally collided with the Tianshan arc accretionary complex (collage) during the Permian. A series of X-shaped wrench fracture system also extensively occur in the cored dolomite samples particularly near the main fault zones.

The dissolved vuggy pores preferentially take place along the fractures particularly in the lower part of well TS1 where they are also less plugged by dolomite cements. All these features demonstrate the interaction of fracture- or fault-channeled upward-flowing hydrothermal fluids with the host dolomites through which intense dissolution occurred preferentially in the lower part of dolomites having been penetrated. The enhanced hydrothermal activity was likely linked to the LIP activity in the Tarim block during the Early Permian.

The reactive transport modeling demonstrates the importance of wall-rock permeability on fluid and temperature

patterns, particularly the vertical permeability dependent on the connectedness of fractures; it could have further controlled the spatial distribution of dissolved vuggy porosity. In contrast, the fault permeability has little influence on the distribution of dissolved porosity.

The hydrothermal dissolution mainly occurred in platform margin dolomites penetrated by the high-angle fault series and was fairly weak in platform interior and slope-basinal dolomites due to the presence of cap aquitards (evaporites and shales) which could have prohibited upward flowing of fluid. The presence of internal aquifers, such as horizontally buried unconformity surface, did not necessarily enhance the hydrothermal dissolution.

This study provides an integrated approach with geological analysis and reactive transport modeling to unveil the process of hydrothermal dissolution on dolomite rocks associated with faults or fractures from a deep-penetrated well TS1 in northern Tarim Basin; this would further improve our understanding for the development and distribution of deeply buried carbonate reservoirs.

## Conflicts of Interest

The authors declare that they have no conflicts of interest.

## Acknowledgments

This study was supported by the National Natural Science Foundation of China (Grant no. U1663209) and National Science and Technology Priority Special Project of China (Grant no. 2011ZX0500803). The authors are much grateful to the reviewer (Y. Xiao) for his positive comments on this study.

## References

- [1] P. O. Roehl and P. W. Choquette, *Carbonate Petroleum Reservoirs*, Springer, Berlin, Germany, 1985.
- [2] J. Garland, J. Neilson, S. E. Laubach, and K. J. Whidden, "Advances in carbonate exploration and reservoir analysis," *Geological Society Special Publication*, vol. 370, no. 1, pp. 1–15, 2012.
- [3] J. W. Schmoker and R. B. Halley, "Carbonate porosity versus depth: a predictable relation for south Florida," *American Association of Petroleum Geologists Bulletin*, vol. 66, no. 12, pp. 2561–2570, 1982.
- [4] S. N. Ehrenberg, G. P. Eberli, M. Keramati, and S. A. Moallemi, "Porosity-permeability relationships in interlayered limestone-dolomite reservoirs," *AAPG Bulletin*, vol. 90, no. 1, pp. 91–114, 2006.
- [5] D. Zhu, Q. Meng, Z. Jin, Q. Liu, and W. Hu, "Formation mechanism of deep Cambrian dolomite reservoirs in the Tarim basin, northwestern China," *Marine and Petroleum Geology*, vol. 59, pp. 232–244, 2015.
- [6] F. F. Whitaker, P. L. Smart, and G. D. Jones, "Dolomitization: from conceptual to numerical models," *Geological Society Special Publication*, vol. 235, pp. 99–139, 2004.
- [7] F. F. Whitaker and Y. Xiao, "Reactive transport modeling of early burial dolomitization of carbonate platforms by geothermal convection," *AAPG Bulletin*, vol. 94, no. 6, pp. 889–917, 2010.
- [8] G. D. Jones and Y. Xiao, "Geothermal convection in South Atlantic subsalt lacustrine carbonates: developing diagenesis and reservoir quality predictive concepts with reactive transport models," *AAPG Bulletin*, vol. 97, no. 8, pp. 1249–1271, 2013.
- [9] T. Xu, E. Sonnenthal, N. Spycher, and K. Pruess, *TOUGHREACT User's Guide: A Simulation Program for Non-Isothermal Multiphase Reactive Geochemical Transport in Variable Saturated Geologic Media*, Lawrence Berkeley National Laboratory, Berkeley, Calif, USA, 2008.
- [10] G. D. Jones and Y. Xiao, "Dolomitization, anhydrite cementation, and porosity evolution in a reflux system: insights from reactive transport models," *AAPG Bulletin*, vol. 89, no. 5, pp. 577–601, 2005.
- [11] P. Lu and D. Cantrell, "Reactive transport modelling of reflux dolomitization in the Arab-D reservoir, Ghawar field, Saudi Arabia," *Sedimentology*, vol. 63, no. 4, pp. 865–892, 2016.
- [12] B. Garcia-Fresca, F. Jerry Lucia, J. M. Sharp Jr., and C. Kerans, "Outcrop-constrained hydrogeological simulations of brine reflux and early dolomitization of the Permian San Andres Formation," *AAPG Bulletin*, vol. 96, no. 9, pp. 1757–1781, 2012.
- [13] Y. Xiao, G. D. Jones, F. F. Whitaker et al., "Fundamental approaches to dolomitization and carbonate diagenesis in different hydrogeological systems and the impact on reservoir quality distribution," in *Proceedings of the sixth International Petroleum Technology Conference (IPTC '13)*, pp. 1164–1179, Beijing, China, March 2013.
- [14] G. R. Davies and L. B. Smith Jr., "Structurally controlled hydrothermal dolomite reservoir facies: an overview," *AAPG Bulletin*, vol. 90, no. 11, pp. 1641–1690, 2006.
- [15] H. R. Qing and E. W. Mountjoy, "Formation of coarsely crystalline, hydrothermal dolomite reservoirs in the Presquile Barrier, Western Canada Sedimentary Basin," *AAPG Bulletin*, vol. 78, no. 1, pp. 55–77, 1994.
- [16] H. G. Machel, "Concepts and models of dolomitization: a critical reappraisal," in *The Geometry and Petrogenesis of Dolomite Hydrocarbon Reservoirs*, vol. 235, pp. 7–63, Geological Society London Special Publications, London, UK, 2004.
- [17] Z. Gao, T. Fan, Z. Jiao, and Y. Li, "The structural types and depositional characteristics of carbonate platform in the cambrian-ordovician of tarim basin," *Acta Sedimentologica Sinica*, vol. 24, no. 1, pp. 19–27, 2006.
- [18] Z. Zhao, Y. Zhang, M. Pan, W. U. Xingning, and W. Pan, "Cambrian sequence stratigraphic framework in Tarim Basin," *Geological Review*, vol. 56, pp. 609–620, 2010.
- [19] Z. Feng, Z. Bao, M. Wu, Z. Jin, and X. Shi, "Lithofacies palaeogeography of the Cambrian in Tarim area," *Journal of Palaeogeography*, vol. 8, pp. 427–439, 2006.
- [20] Z. Feng, Z. Bao, M. Wu, Z. Jin, X. Shi, and A. R. Luo, "Lithofacies palaeogeography of the Ordovician in Tarim area," *Journal of Palaeogeography*, vol. 9, no. 5, pp. 447–460, 2007.
- [21] Z. Zhao, W. Pan, L. Zhang, S. Deng, and Z. Huang, "Sequence stratigraphy in the ordovician in the Tarim Basin," *Geotectonica et Metallogenia*, vol. 33, no. 1, pp. 175–188, 2009.
- [22] Z. Jin, Y. Zhang, and S. Chen, "Wave tectono-sedimentary processes in Tarim basin," *Science in China, Series D: Earth Sciences*, vol. 48, no. 11, pp. 1949–1959, 2005.
- [23] Z. L. He, H. B. Mao, X. F. Zhou, M. Cong, and X. Y. She, "Complex petroleum system and multicycle basin in Tarim," *Oil & Gas Geology*, vol. 21, no. 3, pp. 207–213, 2000.
- [24] Y. Kang and Z. Kang, "Tectonic evolution and oil and gas of Tarim basin," *Journal of Southeast Asian Earth Sciences*, vol. 13, no. 3–5, pp. 317–325, 1996.

- [25] C. Guo, D. Chen, H. Qing et al., "Multiple dolomitization and later hydrothermal alteration on the Upper Cambrian-Lower Ordovician carbonates in the northern Tarim Basin, China," *Marine and Petroleum Geology*, vol. 72, pp. 295–316, 2016.
- [26] Z. Jin, D. Zhu, W. Hu, X. Zhang, Y. Wang, and X. Yan, "Geological and geochemical signatures of hydrothermal activity and their influence on carbonate reservoir beds in the Tarim Basin," *Acta Geologica Sinica*, vol. 80, no. 2, pp. 245–253, 2006.
- [27] S. Dong, D. Chen, H. Qing et al., "Hydrothermal alteration of dolostones in the Lower Ordovician, Tarim Basin, NW China: multiple constraints from petrology, isotope geochemistry and fluid inclusion microthermometry," *Marine and Petroleum Geology*, vol. 46, pp. 270–286, 2013.
- [28] H. Chen, S. Yang, C. Dong et al., "Geological thermal events in Tarim Basin," *Chinese Science Bulletin*, vol. 42, no. 7, pp. 580–584, 1997.
- [29] S. Dong, D. Chen, H. Qing, M. Jiang, and X. Zhou, "In situ stable isotopic constraints on dolomitizing fluids for the hydrothermally-originated saddle dolomites at Keping, Tarim Basin," *Chinese Science Bulletin*, vol. 58, no. 23, pp. 2877–2882, 2013.
- [30] S. Zou, Z. Li, Z. Ren et al., "U-Pb dating and Hf isotopic compositions of detrital zircons from permian sedimentary rocks in keping area of Tarim Basin, Xinjiang, China: constraints on geological evolution of tarim block," *Acta Petrologica Sinica*, vol. 29, no. 10, pp. 3369–3388, 2013.
- [31] D. Zhou, S. A. Graham, E. Z. Chang, B. Wang, and B. Hacker, "Paleozoic amalgamation of the Chinese Tian Shan: evidence from a transect along the Dushanzi-Kuqa Highway," in *Paleozoic and Mesozoic Tectonic Evolution of Central and Eastern Asia: From Continental Assembly to Intracontinental Deformation*, M. S. Hendix and G. A. Davis, Eds., vol. 194 of *Geological Society of America Memoirs*, pp. 23–46, Geological Society of America, 2001.
- [32] W. Xiao, C. Han, C. Yuan et al., "Middle Cambrian to Permian subduction-related accretionary orogenesis of Northern Xinjiang, NW China: implications for the tectonic evolution of central Asia," *Journal of Asian Earth Sciences*, vol. 32, no. 2–4, pp. 102–117, 2008.
- [33] W.-J. Xiao, L.-C. Zhang, K.-Z. Qin, S. Sun, and J.-L. Li, "Paleozoic accretionary and collisional tectonics of the Eastern Tianshan (China): implications for the continental growth of central Asia," *American Journal of Science*, vol. 304, no. 4, pp. 370–395, 2004.
- [34] R. Caputo, "Why joints are more abundant than faults. A conceptual model to estimate their ratio in layered carbonate rocks," *Journal of Structural Geology*, vol. 32, no. 9, pp. 1257–1270, 2010.
- [35] P. Zhang, G. Hou, W. Pan et al., "Research on the effectiveness of fractures in Sinian-Cambrian dolomite reservoir in Tarim Basin," *Acta Scientiarum Naturalium Universitatis Pekinensis*, vol. 49, no. 6, pp. 993–1001, 2013.
- [36] C. A. Underwood, M. L. Cooke, J. A. Simo, and M. A. Muldoon, "Stratigraphic controls on vertical fracture patterns in Silurian dolomite, northeastern Wisconsin," *AAPG Bulletin*, vol. 87, no. 1, pp. 121–142, 2003.
- [37] D. Ye, "Deep dissolution of Cambrian-Ordovician carbonates in the Northern Tarim Basin," *Acta Sedimentologica Sinica*, vol. 12, pp. 66–71, 1994.
- [38] L. Jiang, W. Pan, C. Cai et al., "Fluid mixing induced by hydrothermal activity in the ordovician carbonates in Tarim Basin, China," *Geofluids*, vol. 15, no. 3, pp. 483–498, 2015.
- [39] X. You, S. Sun, J. Zhu, Q. Li, W. Hu, and H. Dong, "Microbially mediated dolomite in Cambrian stromatolites from the Tarim Basin, north-west China: implications for the role of organic substrate on dolomite precipitation," *Terra Nova*, vol. 25, no. 5, pp. 387–395, 2013.
- [40] G.-Y. Wu, Y.-J. Li, Y.-L. Liu, Y. Zhao, and H. Li, "Petrochemistry and regional tectonic implications of Permian-Early Triassic volcanic rocks in the Tabei rise, Tarim basin," *Journal of Mineralogy and Petrology*, vol. 32, no. 4, pp. 21–30, 2012.
- [41] Y.-G. Xu, X. Wei, Z.-Y. Luo, H.-Q. Liu, and J. Cao, "The Early Permian Tarim Large Igneous Province: main characteristics and a plume incubation model," *Lithos*, vol. 204, pp. 20–35, 2014.
- [42] F. J. Lucia, "Rock-fabric/petrophysical classification of carbonate pore space for reservoir characterization," *American Association of Petroleum Geologists Bulletin*, vol. 79, no. 9, pp. 1275–1300, 1995.
- [43] G. D. Jones and Y. Xiao, "Geothermal convection in the Tengiz carbonate platform, Kazakhstan: reactive transport models of diagenesis and reservoir quality," *AAPG Bulletin*, vol. 90, no. 8, pp. 1251–1272, 2006.
- [44] W. J. Harrison and L. L. Summa, "Paleohydrology of the Gulf of Mexico basin," *American Journal of Science*, vol. 291, no. 2, pp. 109–176, 1991.
- [45] C. E. Manning and S. E. Ingebritsen, "Permeability of the continental crust: implications of geothermal data and metamorphic systems," *Reviews of Geophysics*, vol. 37, no. 1, pp. 127–150, 1999.
- [46] V. F. Bense, T. Gleeson, S. E. Loveless, O. Bour, and J. Scibek, "Fault zone hydrogeology," *Earth-Science Reviews*, vol. 127, no. 2, pp. 171–192, 2013.
- [47] S. E. Ingebritsen and C. E. Manning, "Permeability of the continental crust: dynamic variations inferred from seismicity and metamorphism," *Geofluids*, vol. 10, no. 1–2, pp. 193–205, 2010.
- [48] C. Cai, S. G. Franks, and P. Aagaard, "Origin and migration of brines from Paleozoic strata in Central Tarim, China: constraints from  $^{87}\text{Sr}/^{86}\text{Sr}$ ,  $\delta\text{d}$ ,  $\delta^{18}\text{O}$  and water chemistry," *Applied Geochemistry*, vol. 16, no. 9–10, pp. 1269–1284, 2001.
- [49] J. L. Palandri and Y. K. Kharaka, "A compilation of rate parameters of water-mineral interaction kinetics for application to geochemical modeling," U.S. Geological Survey Open File Report 2004-1068, 2004.
- [50] S. N. Ehrenberg, O. Walderhaug, and K. Bjerlykke, "Carbonate porosity creation by mesogenetic dissolution: reality or illusion?" *AAPG Bulletin*, vol. 96, no. 2, pp. 217–225, 2012.
- [51] C. Cai, K. Li, H. Li, and B. Zhang, "Evidence for cross formational hot brine flow from integrated  $^{87}\text{Sr}/^{86}\text{Sr}$ , REE and fluid inclusions of the Ordovician veins in Central Tarim, China," *Applied Geochemistry*, vol. 23, no. 8, pp. 2226–2235, 2008.
- [52] M. Manga, I. Beresnev, E. E. Brodsky et al., "Changes in permeability caused by transient stresses: field observations, experiments, and mechanisms," *Reviews of Geophysics*, vol. 50, no. 2, Article ID RG2004, 2012.
- [53] T. M. Mitchell and D. R. Faulkner, "Towards quantifying the matrix permeability of fault damage zones in low porosity rocks," *Earth and Planetary Science Letters*, vol. 339–340, pp. 24–31, 2012.
- [54] G. Garven, "Continental-scale groundwater flow and geologic processes," *Annual Review of Earth Planetary Sciences*, vol. 23, no. 1, pp. 89–118, 2003.
- [55] G. Garven and R. A. Freeze, "Theoretical analysis of the role of groundwater flow in the genesis of stratabound ore deposits. 1. Mathematical and numerical model," *American Journal of Science*, vol. 284, no. 10, pp. 1085–1124, 1984.

## Research Article

# A New Method to Identify Reservoirs in Tight Sandstones Based on the New Model of Transverse Relaxation Time and Relative Permeability

Yuhang Guo, Baozhi Pan, and Lihua Zhang

College of Geo-Exploration Science and Technology, Jilin University, Changchun, China

Correspondence should be addressed to Yuhang Guo; 124563749@qq.com

Received 14 January 2017; Accepted 9 March 2017; Published 19 April 2017

Academic Editor: Xiaorong Luo

Copyright © 2017 Yuhang Guo et al. This is an open access article distributed under the Creative Commons Attribution License, which permits unrestricted use, distribution, and reproduction in any medium, provided the original work is properly cited.

Relative permeability and transverse relaxation time are both important physical parameters of rock physics. In this paper, a new transformation model between the transverse relaxation time and the wetting phase's relative permeability is established. The data shows that the cores in the northwest of China have continuous fractal dimension characteristics, and great differences existed in the different pore size scales. Therefore, a piece-wise method is used to calculate the fractal dimension in our transformation model. The transformation results are found to be quite consistent with the relative permeability curve of the laboratory measurements. Based on this new model, we put forward a new method to identify reservoir in tight sandstone reservoir. We focus on the Well M in the northwestern China. Nuclear magnetic resonance (NMR) logging is used to obtain the point-by-point relative permeability curve. In addition, we identify the gas and water layers based on new  $T_2$ - $K_r$  model and the results showed our new method is feasible. In the case of the price of crude oil being low, this method can save time and reduce the cost.

## 1. Introduction

The phenomenon of Nuclear Magnetic Resonance (NMR) was discovered in 1946, and since then NMR has been widely used in various fields. NMR logging technology has been rapidly developed in recent years, with confirmed favorable results in the evaluation of reservoir permeability. NMR logging technology has a unique fluid sensitivity and is able to provide information regarding the fluid number of rock pores, fluid properties, and fluid-bearing pore sizes. Since this data cannot be obtained by other conventional logging methods, it thereby provides very important information for reservoir descriptions and evaluations [1]. With regard to NMR logging, a spin echo string is collected to obtain stratum information, of which the distribution of the retrieved  $T_2$  (transverse relaxation time) is closely related to the pore size and can be expressed as the porosity distribution through calibration. The movable fluid (MFFI), unmovable fluid (BVI), and other information can also be obtained from the  $T_2$  distribution. Through the core experimental analysis of

the target area, accurate  $T_2$  cutoff values can be acquired to determine the irreducible water saturation measurements.

The relative permeability refers to the ratio between the effective permeability of each fluid type and the absolute permeability of the rock itself, in the cases of saturated multiphase fluid in the rock pores. The relative permeability is related to the rock's wettability and fluid saturation, and the relative permeability curve can be obtained by laboratory measurements. Purcell [2] proposed a model based on the capillary pressure curves. Burdine (1953) proposed similar equations in which the tortuosity ratio is introduced in the model. Brooks and Corey [3] made further research on calculating relative permeability based on capillary pressure. The model modified by Brooks and Corey has been widely used in many studies. Feng et al. (2016) proposed a new relative permeability model in which the pore size distribution, the tortuosity, and the gas-water spatial distribution were all considered. Combined with a capillary pressure curve, the shift of the transverse relaxation time ( $T_2$ ) distribution of Nuclear Magnetic Resonance is used to determine the parameters in

the model. But the model has too many variables, which is hard to apply in practical logging evaluation.

In recent years, more and more researches focused on using fractal theory to establish the relationship between the relative permeability and other parameters. The fractal theory, which was developed in the 1970s, is a rational tool used to describe complex and irregular phenomena and processes and provides a good method for research regarding the microscopic pore structure of porous media [4]. The fractal theory has been applied in the oil industry with fruitful results. A molecular adsorption method was applied by Pfeifer and Avnir [5] to obtain the pores of the reservoir rocks with fractal structure. On the basis of the fractal theory, the transformation relationship between the capillary pressure, relative permeability, and resistivity index was established by Li (2011). Then, Li's transformation model was improved by Pairoys (2013), and favorable sample effects have been achieved in particular regions. The transformation between  $T_2$  and the resistivity index was discussed by Ge et al. [6], based on the fractal theory and the linear relationship between  $P_C$  (the capillary pressure) and  $T_2$ . In accordance with the study results put forward by Li, the relationship between the permeability,  $T_2$ , and capillary pressure was used to achieve the transformation relationship between the relative permeability and  $T_2$  by Bai et al. [7]. However, it can be seen from the eventual transformation results that the residual water and oil saturation were not considered and have a certain deviation from experimental measurement results. In addition, in practical applications, such as oil shale, samples are difficult to obtain. Also, the experiment takes longer time, and it is impossible to measure all of the samples in well. A solution is necessary for finding a way to obtain the relative permeability curve with depth.

The novelty of this paper is using a combination of the previous research results regarding the links between capillary pressure, resistivity index, relative permeability, and transverse relaxation time; the transformation relationship between the transverse relaxation time and the relative permeability is derived. All experimental cores are taken from tight sandstone reservoir in northwest China. Based on the rock resistivity experiment experimental data and the mercury injection test data, the parameter expression in the transformation relationship is given in order to discuss the control factors and their influences. It is obvious that the transformation results are better than those of the known methods, which thereby provided a theoretical basis for the relative permeability curve with changes over depth through the NMR logging data. The model is applied in the northwest of China to obtain the relative permeability curve with depth, as well as identify the gas and water yield layers. It is a new and reliable reservoir identification method.

## 2. Theoretical Background

*2.1. Relationship between the Capillary Pressure ( $P_C$ ) and the Resistivity Index ( $I$ ).* In the Archie equation, the relationship

between the resistivity index and water saturation is shown as follows:

$$I = \frac{b}{S_w^n} = \frac{R_t}{R_0}. \quad (1)$$

$I$  is the resistivity index;  $b$  is the constant of the Archie equation;  $n$  is the saturation index;  $R_t$  is the sample resistivity;  $R_0$  is the rock resistivity in the case of 100% water bearing; and  $S_w$  is the water saturation. In this study, the  $I$ - $S_w$  curves are a single fractal dimension, and  $b$  and  $n$  are the fixed values throughout the saturation distribution.

The capillary pressure can be expressed as follows:

$$P_C = P_{nw} - P_w = \frac{2\sigma \cos \theta}{r}, \quad (2)$$

where  $P_{nw}$  and  $P_w$  are the pressures of the nonwetting phase and wetting phase fluids, respectively;  $P_C$  is the capillary pressure;  $r$  is the capillary radius;  $\sigma$  is the tension of the two-phase fluid boundary surface; and  $\theta$  is the wetting angle. It is clear that the capillary pressure is inversely proportional to the capillary radius. The relationship between the capillary pressure and the saturation can be established through a mercury injection experiment.

Toledo et al. [8] considered  $P_C$  is a function of wetting phase saturation and fractal dimension.

$$S_w \propto (P_C)^{-(3-D_f)}, \quad (3)$$

where  $D_f$  is the fractal dimension. Based on the fractal model of the porous media, the relationship between the capillary pressure and the resistivity index was given by Li [9].

$$P_{CD} = I^\beta = \frac{P_C}{P_e}. \quad (4)$$

Among these,  $\beta$  is the index related to the water-film thickness, which is the function of the fractal function  $D_f$ ;  $P_{CD}$  is the dimensionless capillary pressure; and  $P_e$  is the entry capillary pressure.

*2.2. Relationship between the Capillary Pressure ( $P_C$ ) and the Nuclear Magnetic Transverse Relaxation Time ( $T_2$ ).* The relationship between  $P_C$  and  $T_2$  is relatively well constrained due the relationship to the pore structure. The methods of using the  $T_2$  distribution for transforming the pseudo capillary pressure curve mainly include a linear method and a power function method.

In the linear method [10], it is assumed that a linear relationship exists between  $P_C$  and the reciprocal of  $T_2$  as detailed below:

$$P_C = \frac{2\sigma \cos \theta}{r} = \frac{C_1}{T_2}. \quad (5)$$

In the equation,  $C_1$  is the linear transformation coefficient and can be obtained by the core data analysis. The power function method is more frequently applied, and the relationship between  $T_2$  and the corresponding capillary radius has been given by He et al. [11, 12] as follows:

$$T_2 = m_t r^{n_t}, \quad (6)$$

where  $m_t$  and  $n_t$  are the empirical coefficients, obtained according to the core data analysis. The power function method is suitable for low-permeability reservoirs containing complex pore structure. Therefore, the power function relationship has been used in this study.

**2.3. Relationship between the Relative Permeability ( $K_r$ ) and the Resistivity Index ( $I$ ).** Based on Darcy's law and Ohm's law, Li [14] proposed a model to describe the relationship between the wetting phase relative permeability and the resistivity index:

$$k_{rw} = S_W^* \frac{1}{I}, \quad (7)$$

where  $k_{rw}$  is the relative permeability of the wetting phase.  $I$  is the resistivity index.  $S_W^*$  is effective saturation which can be written:

$$S_W^* = \frac{S_w - S_{wir}}{1 - S_{wir}}, \quad (8)$$

where  $S_w$  is the wetting phase saturation and  $S_{wir}$  is the irreducible wetting phase saturation of the wetting phase. Following Li's research, Pairoys introduced the residual non-wetting phase saturation into his model. At the same time,  $I^*$ , the normalized or effective resistivity index, and  $I_{\min}$ , the minimum resistivity index obtained at residual nonwetting phase saturation  $S_{mwr}$ , were proposed.

$$k_{rw} = S_W^* \frac{1}{I^*}, \quad (9)$$

$$S_W^* = \frac{S_w - S_{wir}}{1 - S_{wir} - S_{mwr}}.$$

### 3. New $T_2$ - $K_r$ Model and Validation

**3.1. Wetting Phase Relative Permeability Calculated by the New Model.** Although the relationships between  $T_2$  and  $P_C$ , as well as between  $P_C$  and  $I$ , have been extensively studied [10–14], research on the relationship between  $T_2$  and  $I$  must be established and requires further development. By combining the previous research on the relationship between the capillary pressure and the resistivity index, the relationship between  $T_2$  and  $I$  was studied incorporating the fractal theory [6, 7] (Zhang et al., 2015). The pore volume distribution expression of the known space is shown as follows:

$$V \propto r^{3-D_f}. \quad (10)$$

In the equation,  $V$  is the volume of the pores with the radius of  $r$  among rock samples; and this equation is used to derive  $r$ .

$$\frac{dV}{dr} \propto r^{2-D_f}. \quad (11)$$

In accordance with the principle of fractal geometry, the integral was carried out on the above equation in order to

obtain the expression of the cumulative pore volume  $V_r$  with a pore size less than  $r$ .

$$V_r = \int_{r_{\min}}^r a_v r^{2-D_f} dr = b_v (r^{3-D_f} - r_{\min}^{3-D_f}). \quad (12)$$

In the equation,  $r_{\min}$  is the minimum pore radius of the reservoir rocks; and  $a_v$  is the proportionality constant  $b_v = a_v/(3 - D_f)$ . The total pore volume  $V$  of the reservoir is as follows:

$$V = b (r_{\max}^{3-D_f} - r_{\min}^{3-D_f}). \quad (13)$$

Through (12) and (13), the expression of the cumulative volume fraction  $S_r$  of the pore with a size less than  $r$  can be obtained.

$$S_r = \frac{V_r}{V} = \frac{r^{3-D_f} - r_{\min}^{3-D_f}}{r_{\max}^{3-D_f} - r_{\min}^{3-D_f}}. \quad (14)$$

Due to  $r_{\min} \ll r_{\max}$  and  $r_{\min} \ll r$ , (14) can be simplified as follows:

$$S_r = \left( \frac{r}{r_{\max}} \right)^{3-D_f}. \quad (15)$$

In reservoir physics,  $S_r$  is the wetting phase saturation  $S_w$ . Equation (2) is substituted into (15) to obtain the following:

$$S_w = S_r = \left( \frac{P_c}{P_{cmin}} \right)^{D_f-3} = P_{CD}^{D_f-3}. \quad (16)$$

$P_{CD}$  is dimensionless, for the purpose of eliminating the influence of the fluid, rather than the fluid correction. In regard to the complex pore structure, the power function method was used to substitute (6) into (15), and the following could be obtained:

$$S_w = S_r = \left( \frac{T_2}{T_{2max}} \right)^{(3-D_f)/n_t} = (T_{2D})^{(3-D_f)/n_t}, \quad (17)$$

where  $T_{2max}$  is the maximum transverse relaxation time, corresponding to  $r_{\max}$ , and  $T_{2D}$  is the dimensionless transverse relaxation time  $T_{2D} = T_2/T_{2max}$ . Therefore, the relationship between the  $T_2$  distribution and the wetting phase saturation could be obtained. Equation (1) is substituted into (17), and the following equation was easily obtained:

$$T_{2D} = b_t (I)^{-\alpha}, \quad (18)$$

where  $\alpha$  is the index related to the pore radius distribution and relaxation time index and  $b_t$  is the transformation factor, which can be obtained from the rock experiment data.

$$\alpha = \frac{n_t}{n(3 - D_f)} = n_t \beta, \quad (19)$$

$$b_t = b^{n_t/n(3-D_f)} = b^\alpha.$$

Based on the fractal theory and the relationship between the transverse relaxation time  $T_2$ , capillary pressure  $P_C$ ,

resistivity index  $I$ , and relative permeability  $K_r$ , the transformation relationship between the water-phase relative permeability and the  $T_{2D}$  dimensionless transverse relaxation time was obtained, including the parameters  $\alpha$ ,  $n$ , and  $b$ . These parameters could be obtained from the experimental data. Combining (7) and (17)–(19), the  $k_{rw}$ - $T_2$  model can be derived as the following equation:

$$K_{rw} = \frac{T_{2D}^{1/\alpha}}{b} \left( \frac{T_{2D}^{1/\alpha n} - S_{ir}}{1 - S_{ir}} \right). \quad (20)$$

The parameters in (20) are all derived from the above equation. It is worth noting that  $b$  is equal to 1.0084 which is showed in Figure 2 (data from experiment). In general,  $b$  is a constant ( $b = 1$ ). The nonwetting phase's relative permeability was obtained by (21). This equation was derived from a Brooks-Corey model, which was applied by Li [14] to more effectively solve the nonwetting phase's relative permeability.

$$K_{rnw} = (1 - S_w^*)^2 \left( 1 - (S_w^*)^{\lambda/(2+\lambda)} \right). \quad (21)$$

In (20),  $S_{ir}$  is the residual water saturation. In many of the previous research results, the solution of  $S_w^*$  takes into account the residual gas saturation  $S_{or}$ .  $\lambda$  is the pore size distribution index and can be calculated from capillary pressure data [3]. Therefore, this model was also correspondingly changed into (22). However, it was found that, in the actual application, better effects could be achieved without consideration of the residual gas saturation.

$$K_{rw} = \frac{T_{2D}^{1/\alpha}}{b} \left( \frac{T_{2D}^{1/\alpha n} - S_{ir}}{1 - S_{ir} - S_{or}} \right). \quad (22)$$

It should be noted that the model proposed by Li [9] and Ma et al. [15] was based on Darcy's law, Ohm's law, and Poiseuille's law and expounded the relationship between the relative permeability and the resistivity index. In the derivation process of the model of Ma et al. [15], (23) was obtained, of which  $L_a$  and  $L_w$  were equivalent path lengths under the saturated and unsaturated water conditions, respectively. In this model, the pore radius is assumed as the cylinder, and  $r_a$  and  $r_w$  represent the equivalent pore radius under corresponding status, respectively. In (23),  $r_a^4$  is equivalent to the increase of the weight of the pore radius under saturated water conditions, which indicates that the relative permeability is strongly influenced by the pore radius, while the transverse relaxation time is the physical variable closely related to the pore radius. In combination with previous research views, it was also proven that the application of the nuclear magnetic  $T_2$  distribution for the purpose of establishing a new model of the relative permeability was reliable. Meanwhile, the related parameters in (20) characterized the internal relationship among the resistivity index, relative permeability, and transverse relaxation time.

$$K_{rw} = \frac{L_a}{L_w} \frac{\pi r_w^4}{\pi r_a^4}. \quad (23)$$

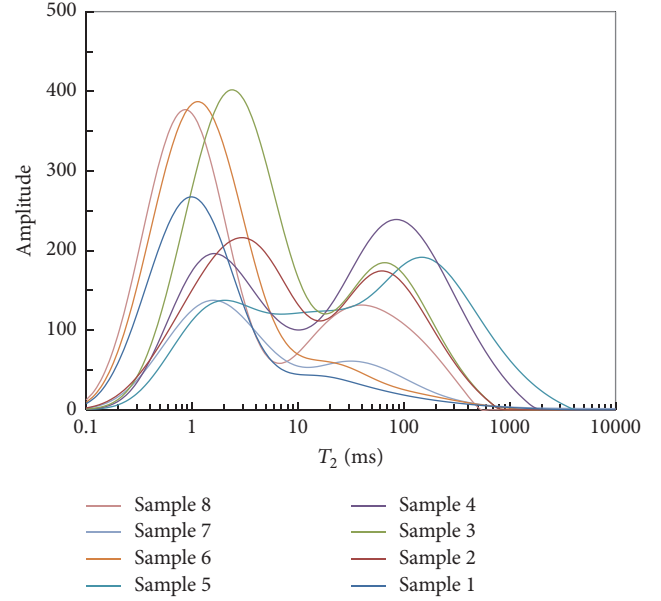


FIGURE 1:  $T_2$  distribution map of the 8 samples.

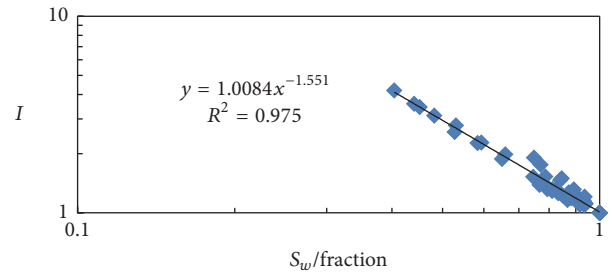


FIGURE 2: Relationship between the resistivity index and the water saturation of the 8 samples.

**3.2. Results and Discussion.** Tight sandstone reservoir samples were selected for the comprehensive laboratory measurements, in order to obtain the capillary pressure curve, relative permeability curve, core nuclear magnetic  $T_2$  distribution, and resistivity index curve. The capillary pressure and the resistivity index were measured in RCS760 equipment produced by the Coretest company at the same condition (temperature: 55°C, pore pressure: 14 Mpa, pressure of surrounding rock: 30 Mpa, and frequency: 1 KHz). The NMR experiments were performed in the modified MARAN II equipment operating at a Larmor frequency of 4 MHz at ambient pressure and 55°C. By using a CPMG pulse sequence, transverse relaxation time could be obtained [1]. The brine used for experiment had a salinity of 30000 ppm with a resistivity of 1.097  $\Omega$ -m at 55°C. Permeability and porosity were measured by AP608 (produced by the Coretest company). The relative permeability was measured by unsteady-state method (temperature: 55°C, pore pressure: 14 Mpa, and pressure of surrounding rock: 30 Mpa). Figure 1 shows the nuclear magnetic  $T_2$  distribution of each sample measured under the saturated water conditions. Figure 2 presents the relationship between the resistivity index and the water saturation.

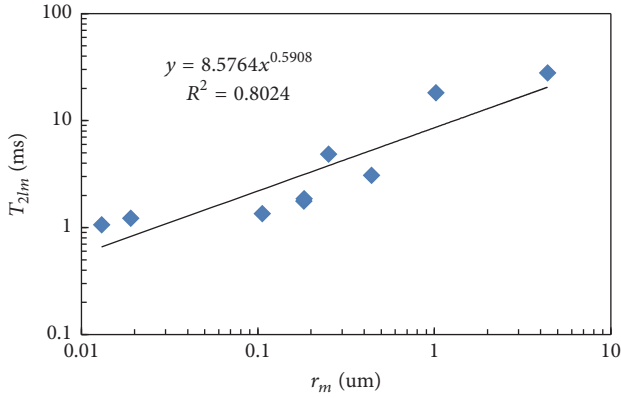


FIGURE 3: Relationship between  $T_{2lm}$  and  $r_m$  in the study area.

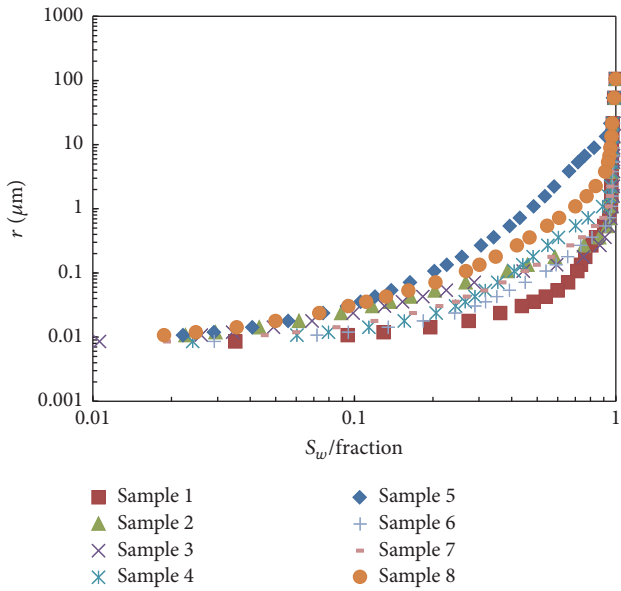


FIGURE 4: Relationship between the pore radius and wetting phase saturation transformed on the basis of a capillary pressure curve.

Figure 3 is the relationship between the  $T_2$  logarithmic average ( $T_{2lm}$ ) and average pore throat radius ( $r_m$ ) in the study area within the sample selection. The average pore throat radius ( $r_m$ ) can be obtained from mercury injection data. According to (6),  $m_t = 8.5764$  and  $n_t = 0.5908$  can be obtained.

As viewed from Figure 4, in combination with (15), a multifractal dimension phenomenon existed in this region. Through analysis of the data, the mutation position of the fractal dimension change was identified as the piece-wise point. According to the pore radius of  $0.03 \mu\text{m}$  and  $1 \mu\text{m}$  as the dividing point, the pores were divided into small, medium, and large categories. Equation (4) of the piece-wise method was applied for the transformation between the resistivity index and the capillary pressure, and the transformation results are as shown in Figure 5. The adoption of the piece-wise method was significantly more effective than the results of the model of Li [9], which indicated that it was more

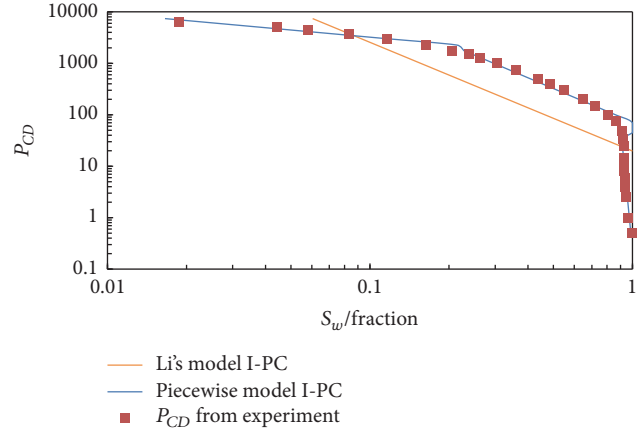


FIGURE 5:  $I-P_C$  transformed by the piece-wise method.

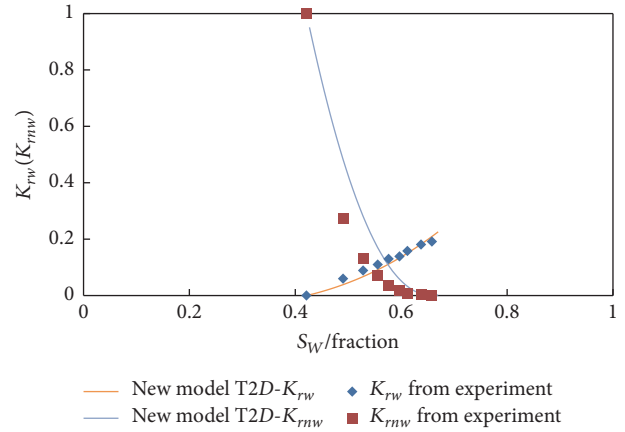


FIGURE 6: Transformation result contrast of Sample 4.

reasonable to use the described piece-wise transformation method in this region.

Table 1 lists the basic information of the cores which were taken from a tight sandstone reservoir in northwest China, including porosity, permeability, rock-electro parameters  $b$  and  $n$ , and the piece-wise fractal dimension of the  $T_2$  distribution. In the table, the last three columns were obtained on the basis of the piece-wise point in combination with (17). The lower  $D_f$  is found to be, the higher the pore frequency is. Therefore, the cores were clearly mainly composed of small pores, with fewer large pores present.

Figure 6 is the contrast diagram of the relative permeability curve of Sample 4, which was obtained through laboratory measurements and which was transformed by  $T_{2D}$ . It is worth nothing that the transformation parameter was solved by the previously determined piece-wise method. And the judgment coefficient of the wetting phase's relative permeability was 0.934. The nonwetting phase's relative permeability was calculated by (21). Results indicate that there is a certain error between the calculated value and actual value. Figure 7 shows the transformation results of Sample 5; the judgment coefficient of the wetting phase's relative permeability was 0.875. After analyzing the sample data in this region, (21)

TABLE I: Basic information of the rock samples.

Core number	$\Phi$ (%)	$K$ (md)	$n$	$b$	$D_{fT_2}$ (large)	$D_{fT_2}$ (medium)	$D_{fT_2}$ (small)
1	6.487	0.019	2.19	0.9924	2.9875	2.8631	1.7245
2	9.646	0.11	1.191	1.0003	2.9123	2.6573	1.6317
3	11.791	0.097	1.25	0.9943	2.9375	2.6445	1.2662
4	12.286	9.402	1.552	1.0210	2.8862	2.7258	1.2623
5	10.542	15.313	1.541	0.9963	2.8944	2.6689	1.2610
6	8.588	0.036	1.223	1.0169	2.9850	2.8330	1.6979
7	4.507	0.041	2.143	1.0245	2.9721	2.7554	1.6070
8	10.223	0.101	1.353	1.0097	2.9425	2.8911	1.7435

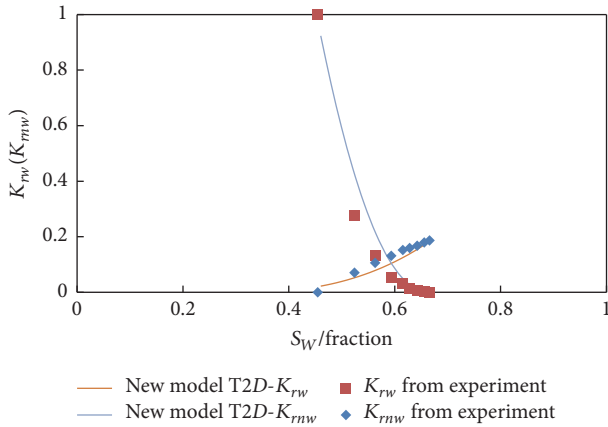


FIGURE 7: Transformation result contrast of Sample 5.

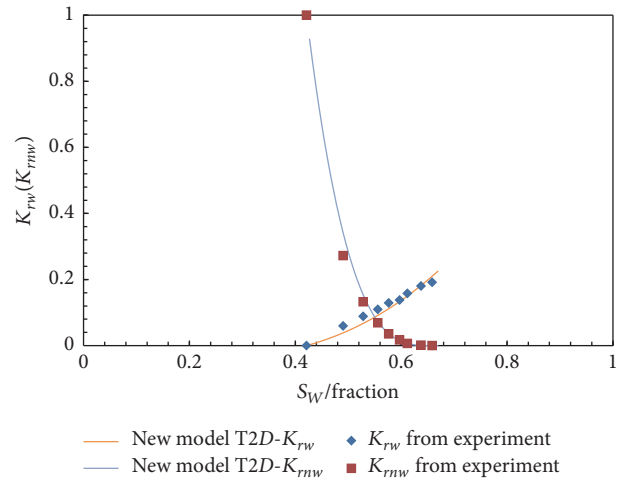


FIGURE 8: Nonwetting phase's relative permeability of Sample 4 calculated by (24).

was improved upon when calculating the nonwetting phase's relative permeability.

$$\begin{aligned}
 K_{rmw} &= (1 - S_w^*)^2 \left(1 - (S_w^*)^{\lambda/(2+\lambda)}\right) \left(\frac{1 - S_w - S_{or}}{1 - S_{or} - S_{ir}}\right) \\
 &= (1 - S_w^*)^3 \left(1 - (S_w^*)^{\lambda/(2+\lambda)}\right).
 \end{aligned} \quad (24)$$

Figures 8 and 9 show the nonwetting phase's relative permeability for Samples 4 and 5, which were calculated by (24), respectively. Table 2 lists the fitting coefficient  $R^2$ , as well as the error contrast of the two types of calculation methods. The calculation results of (24) were determined to be more accurate than that of (22). A similar factor was added by Ma et al. [15] to the model of Li [9] in the calculation of  $k_{rw}$ , in order to introduce the pore tortuosity. Equation (24) illustrated the improvement in  $K_{rmw}$  in accordance with  $k_{rw}$  model presented by Ma et al. [15]. However, the introduction of the factor and the relationship between the effective nonwetting phase flow path and the pore tortuosity require further research.

It is worth noting that we get the pseudo relative permeability curve by  $T_2$ - $K_r$  model, the same as Yokoyama and Lake [16] and Slijkerman et al. [17] get pseudo capillary pressure curve by  $T_2$ - $P_C$ . This is just a kind of approximate method

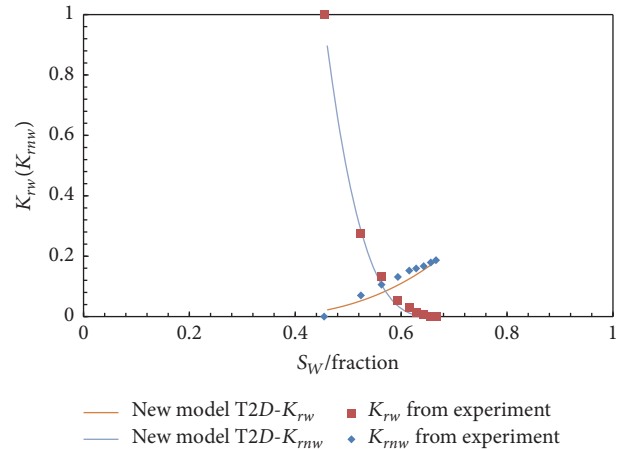


FIGURE 9: Nonwetting phase's relative permeability of Sample 5 calculated by (24).

to obtain relative permeability. In the case of the price of crude oil being low, this method can save time and reduce the cost. At the same time we also can anticipate  $T_2$ - $K_r$  model application prospect in the actual logging.

TABLE 2: Calculation result contrast of the different equations.

Core number	Equation (24)		Equation (21)	
	Mean absolute error	$R^2$	Mean absolute error	$R^2$
4	1.4488	0.9939	6.6979	0.8983
5	1.0624	0.9975	3.7613	0.9602

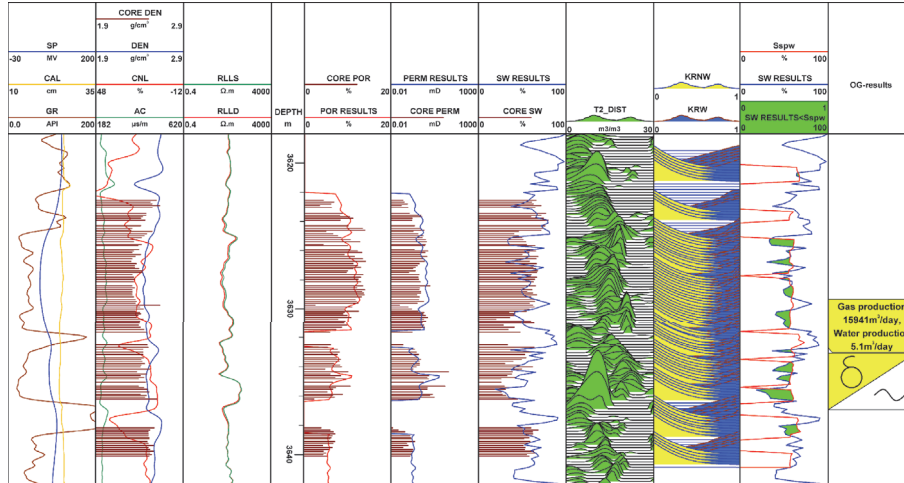


FIGURE 10: Comprehensive logging interpretation chart of Well M.

#### 4. Application Case Analysis

The transformation model of the relative permeability and transverse relaxation time is obtained and verified, based on the processing and research of the experimental data, and according to the regional characteristics, the piece-wise method is adopted. This model is applied for the processing of the nuclear magnetic logging data, in order to obtain the relative permeability curve with changes over depth. It must be pointed out that the results we get by this method are pseudo relative permeability curves, as well as using  $T_2$  spectrum to calculate pseudo capillary pressure curve which is widely used now. By simulating the underground conditions (temperature, pressure, the instrument measuring frequency, and fluid properties), we can obtain the results which were close to the real underground logging response value. Temperature impacts magnet magnetic field intensity; it has great influence on the result of the nuclear magnetic measurement. However, pressure mainly affects the structure of the rock itself. It should be pointed out that, due to the limitation of equipment, we cannot do nuclear magnetic experiment under the condition of high pressure. But the cores are measured after being saturated with water under high pressure, and the measured time is short. We hold the view that such a short time for the influence of the pore structure is negligible. At the same temperature and measuring frequency, NMR lab measurements results can be close to the actual logging data. We proposed a new method to identify the reservoir accurately based on  $T_2$ - $K_r$  model.

The processing was carried out on the target segment of Well M in the tight sandstone of the study area. Nuclear magnetic logging data were used to obtain the relative permeability curve with changes over depth. Figure 10 shows the comprehensive logging interpretation chart of Well M, in which Tracks 4–6 list the porosity, permeability, water saturation, and core data obtained by logging. Track 7 is  $T_2$  distribution from NMR logging. Track 8 is the relative permeability curve calculated by the  $T_2$ - $K_r$  model. It should be noted that the relative permeability curve could not be obtained at all of the depth points, and the mudstone layer influenced the transformation. In track 9, the  $S_{spw}$  is the saturation corresponding to the wetting and nonwetting phase permeability equal points, and SW RESULTS is the standardized wetting phase water saturation. The cases of the SW RESULTS greater than the  $S_{spw}$  indicate that this layer produced much water (per unit volume). In contrast, the cases of the  $Sw^*$  less than the  $S_{spw}$  indicate that this layer produced much gas (per unit volume), which is consistent with the gas testing results (in track 10). It is worth nothing that green overlapping in track 9 has shown the case of producing much gas ( $SW RESULTS < S_{spw}$ ). At the depth ranges from 3632.7 to 3636.6 m, there is a gas-water layer of which gas production is 15941 m<sup>3</sup>/day and water production is 5.1 m<sup>3</sup>/day. It has been proven that this method will be of a guiding significance for the exploration of oil and gas layers in hydrocarbon developments. We provide a very intuitive method to monitor reservoir production.

## 5. Conclusions

In this study, a transformation model between the transverse relaxation time  $T_2$  and the relative permeability  $K_r$  was established through the analysis of the physical rock experimental data. In the model, the transformation parameters were solved using the transformation relationship between the physical variables, such as the capillary pressure, transverse relaxation time, and resistivity index. In the processing of the experimental data, continuous fractal dimension phenomena were found to exist in the samples from the study area. Therefore, a piece-wise method was used to calculate the parameters. The piece-wise points were determined according to the mutation position of the fractal dimension, and the pore radiuses of  $0.03\ \mu\text{m}$  and  $1\ \mu\text{m}$  were selected as the dividing points. During the application of the Li model, the capillary pressure curve obtained by the piece-wise transformation of the resistivity index was shown to be relatively consistent with that obtained by the experiments, thereby proving the rationality of the piece-wise method. During the use of the piece-wise method and the new model, the wetting phase's relative permeability transformed by the transverse relaxation time was shown to be relatively consistent with that obtained by the experimental measurements. However, the nonwetting phase's relative permeability obtained by the improved model had better effects, which confirmed that this model was reasonable and effective. The model was applied to the evaluation of the reservoir logging. Meanwhile, the nuclear magnetic logging data were used in this study to obtain the relative permeability curve with depth and for identifying major water and gas production horizons, which were consistent with the gas testing results. It was indicated that this model had practical application significance. Our new method to identify the reservoir is effective and feasible.

It was also determined that a specific problem existed in this model. The  $T_2$  distribution measured under the wetting phase saturation state was applied for the calculation of the transformation parameters in this study. However, the oil and gas had in fact an impact on the  $T_2$  distribution, which was ignored in this study. The focus of future research should be to correct this impact through measuring the transverse relaxation time and relative permeability under different saturation states, in order to improve the model.

## Conflicts of Interest

The authors declare that they have no conflicts of interest.

## Acknowledgments

This work is supported in part by the National Natural Science Foundation of China under Grant 41174096 and the Graduate Innovation Fund of Jilin University under Project 2016103.

## References

- [1] L. Z. Xiao, Z. B. Qiang, W. S. Wu et al., *Frontiers Investigation in Well Logging*, vol. II, Petroleum Industry Press, 2007.
- [2] W. R. Purcell, "Capillary pressures—their measurement using mercury and the calculation of permeability therefrom," *Journal of Petroleum Technology*, vol. 1, no. 2, p. 39, 1949.
- [3] R. H. Brooks and A. T. Corey, "Properties of porous media affecting fluid flow," *Journal of the Irrigation and Drainage Division*, vol. 6, p. 61, 1966.
- [4] C. M. Zhang, Z. B. Chen, Z. S. Zhang et al., "Fractal characteristics of reservoir rock pore structure based on NMR  $T_2$  distribution," *Journal of Oil and Gas Technology*, vol. 29, no. 4, pp. 80–86, 2007.
- [5] P. Pfeifer and D. Avnir, "Chemistry in no integral dimensions between two and three: I. Fractal theory of heterogeneous surfaces," *Journal of Chemical Physics*, vol. 79, pp. 3369–3558, 1983.
- [6] X. M. Ge, Y. R. Fan, F. Wu et al., "Correspondence of core nuclear magnetic resonance  $T_2$  spectrum and resistivity index," *Journal of China University of Petroleum*, vol. 36, no. 6, pp. 53–56, 2012.
- [7] S.-T. Bai, J.-B. Wan, D.-J. Cheng et al., "Study of relationship between petrophysical experimental parameters: capillary pressure, NMR  $\tau_2$  distribution, resistivity index, relative permeability," *Journal of Chengdu University of Technology (Science & Technology Edition)*, vol. 41, no. 4, pp. 483–491, 2014.
- [8] P. G. Toledo, R. A. Novy, H. T. Davis, and L. E. Scriven, "Capillary pressure, water relative permeability, electrical conductivity and capillary dispersion coefficient of fractal porous media at low wetting phase saturations," *SPE Advanced Technology Series*, vol. 2, no. 1, pp. 136–141, 1994.
- [9] K. Li, "Calculation of gas-water relative permeability from resistivity and the comparison with experimental data," *GRC Transactions*, vol. 30, pp. 825–830, 2006.
- [10] Y. Volokitin and W. Looyestijn, "Constructing capillary pressure curves from NMR log data in the presence of hydrocarbons," in *Proceedings of the SPWLA 40th Annual Logging Symposium*, Oslo, Norway, 1999.
- [11] Y. D. He, Z. Q. Mao, L. Z. Xiao et al., "A new method to obtain capillary pressure curve using NMR  $T_2$  distribution," *Journal of Jilin University (Earth Science Edition)*, vol. 35, no. 2, pp. 177–181, 2005.
- [12] Y.-D. He, Z.-Q. Mao, L.-Z. Xiao, and X.-J. Ren, "An improved method of using NMR  $T_2$  distribution to evaluate pore size distribution," *Chinese Journal of Geophysics*, vol. 48, no. 2, pp. 373–378, 2005.
- [13] K. Li and R. N. Horne, "Comparison of methods to calculate relative permeability from capillary pressure in con-solidated water-wet porous media," *Water Resources Research*, vol. 42, no. 6, Article ID W06405, 2006.
- [14] K. Li, "A new method for calculating two-phase relative permeability from resistivity data in porous media," *Transport in Porous Media*, vol. 74, no. 1, pp. 21–33, 2008.
- [15] D. Ma, C. Liu, and C. Cheng, "New relationship between resistivity index and relative permeability," *Journal of Energy Resources Technology*, vol. 137, no. 3, Article ID 032904, 2015.
- [16] Y. Yokoyama and L. W. Lake, "The effects of capillary pressure on immiscible displacements in stratified porous media," in *Proceedings of the SPE Annual Technical Conference and Exhibition*, Society of Petroleum Engineers, 1981.
- [17] W. F. J. Slijkerman, J. P. Hofman, W. J. Looyestijn, and Y. Volokitin, "A practical approach to obtain primary drainage capillary pressure curves from NMR core and log data," *Petrophysics*, vol. 42, no. 4, 2001.